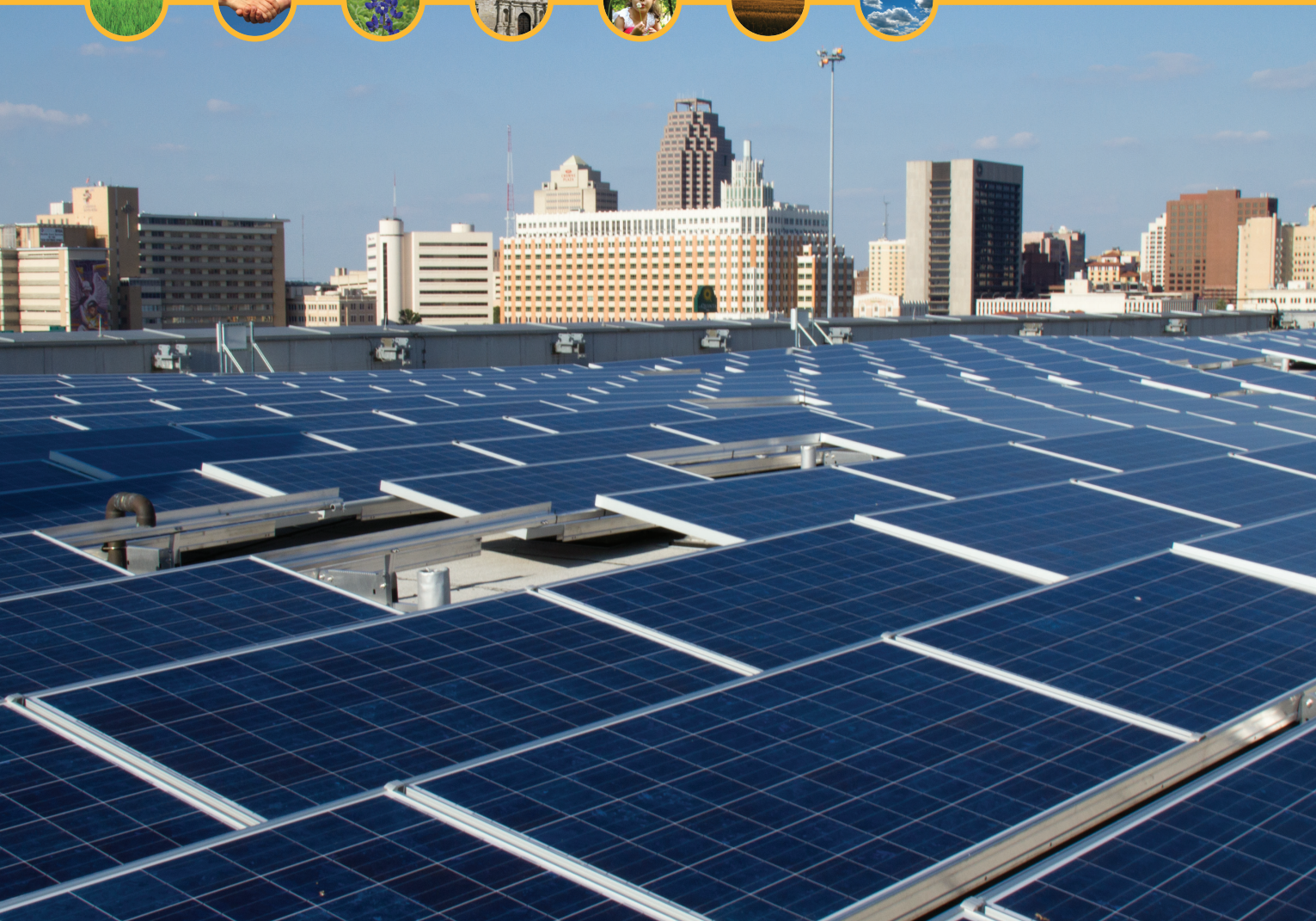


TEXAS SUSTAINABLE ENERGY RESEARCH INSTITUTE



Section 1:

Electric Vehicles

Investigation of the Topology and Control for A 4800-V Grid-Connected Electrical Vehicle Charging Station with STACOM-APF Functions Using A Bi-directional, Multi-level, Cascaded Converter

Russell Crosier, Shuo Wang and Mo Jamshidi

Power Electronics and Electrical Power Research Laboratory
Electrical and Computer Engineering Department
University of Texas at San Antonio
San Antonio, TX 78249

Abstract— This paper presents a new design for an ultra-fast, public electric vehicle (EV) charging station. Because of the multi-megawatt nature of such a station, the design is aimed at being appropriate for a medium voltage (MV) connection. Through the proper choice of a multi-level topology and staircase modulation, it is able to operate efficiently and provide galvanic isolation without the use of a large transformer. As a further benefit for this application, it is able to provide reactive, harmonic, and unbalanced load compensation. Simulation results are provided in Simulink to verify the effectiveness of the staircase modulation and capabilities of the topology.

I. INTRODUCTION

In comparison to conventional road vehicles, electric vehicles (EVs) suffer from a limited range and long (>15 min.) charging times. It has been suggested [1] that the existence of public, ultrafast (≤ 3 min.) charging stations will address this issue to some extent. However, such stations have numerous challenges to overcome. For reasons of cost and multi-megawatt power levels, one challenge is to interface directly with distribution-level voltages (MV) while drawing an acceptable harmonic profile. For reasons of footprint and safety, a second challenge is to do this without a conventional (50/60 Hz) transformer while providing galvanic isolation for safety reasons. A final challenge is to address the negative impact that such stations are predicted to have on the electrical grid [1].

In addition to these challenges, there is a strong preference from utilities and investors to invest in new infrastructure and technology when it can provide multiple services or benefits in addition to its primary purpose. Because a charging station does not always operate at full power, this translates into several MVA of capacity that could be utilized (e.g., to provide reactive power support). Therefore, we have identified the following goals in addition to challenges discussed above: (1) the ability to compensate existing reactive, harmonic, and negative-sequence currents on the distribution system; (2) the ability to provide

additional reactive support; and (3) the ability to provide load leveling (with the incorporation of a large battery or some other form of energy storage).

Existing topologies (for example, [1-7]) do not address all of these issues. In this paper, we present a modular design based on the isolated, DC-DC cell in [8]. These cells are connected and controlled in such a way to act as a MV, cascaded, multi-level inverter. Through an appropriate control and modulation scheme (described herein), our unique topology can draw arbitrary waveforms from the grid. This allows it to have STATCOM/APF and load-leveling capabilities to meet the goals above and to address its cost (both in capital expense and in negative impact on the grid). In addition, it draws current with an acceptable harmonic profile, is modular, provides galvanic isolation from the MV (4.8 kVrms, phase-phase or 3.92 kV) grid, and has a small footprint due to the absence of a 50/60 Hz transformer.

II. TOPOLOGY

A. Ultrafast Topology

We determined that the charging station (Fig. 1) should have a power rating of 2.4 MW (6 EVs, up to 400 kW each). In addition, we determined that the station should have an apparent power rating of 6 MVA to provide active and reactive power for grid support purposes. To achieve this MVA capacity and to achieve the current slew rate necessary for APF functionality, we determined that each phase should be able to produce ± 4800 V and that the inductor L of each phase should be equal to 1 mH.

To minimize the charging station's impact on the grid during peak loading, we propose using a large battery or other form of energy storage for the common DC-link. This will enable EV charging without drawing power from the grid during those times. Because the topology is bi-directional, the battery can also be used to supply the grid during when the marginal cost of generation is very high.

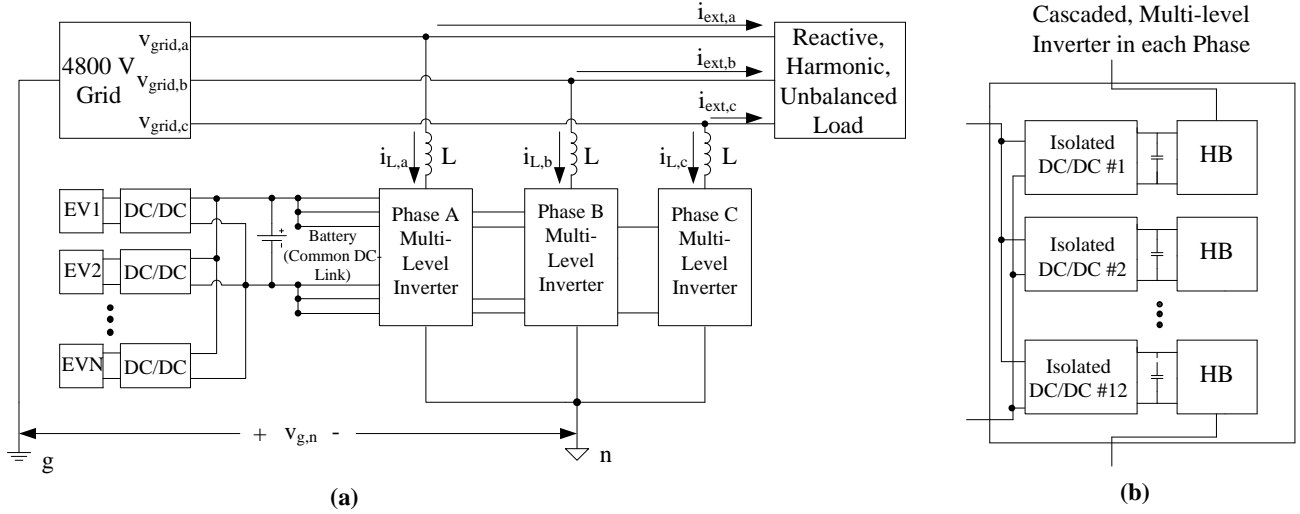


Figure 1: Layout of charging station with grid and load to be compensated (a) and the makeup of the multi-level inverter in each phase (b).

Our topology is unique in that power flows through a common DC-link (see Fig. 1a) without the use of a bulky transformer. We have selected the cascaded H-bridge (HB), multilevel inverter of Fig. 1b as one of the best practical alternative to using a large transformer (SiC devices promise to fulfill this task with two-level inverters and enhanced efficiency in the future [9]). In particular we use 12, cascaded HBs per phase, each with a floating, 400V DC-link. Whether or not Si-C is used in future implementations to enhance the efficiency of our topology, multilevel modulation of the output voltage is optimal for this particular application because, as detailed in section V, it has vastly superior harmonic performance.

Finally, because of the modularity inherent in Fig. 1B, our topology is easily adapted to other voltages (say 7.2 or 13.8 kV). Alternatively, the HBs in Fig. 1B can be designed with higher DC-link voltages. The choice between these two alternatives depends on whether improving efficiency or harmonic performance is a priority.

B. Isolated, Bi-directional, DC-DC Converters and the Common DC-Link

As mentioned above, in our topology all power flows through the common DC-link. Key to this are the isolated, bi-directional, DC-DC converters shown in Fig. 1b. By virtue of the isolation, the DC-links in Fig. 1b can be stacked by the HBs while still being able to transfer energy to and from the common DC-link. [8] discusses a zero-voltage-switching (ZVS) converter that is a possible candidate for this application. As this paper focuses on the control of the output current and the necessary modulation of the HBs to achieve that, readers interested in the design and control of the isolated converters are directed to [8].

However, it is worth analyzing the benefit of a common DC-link. The total, instantaneous power drawn by a 3-phase load is constant in time for balanced, sinusoidal conditions.

Therefore, when drawing/ supplying positive sequence current from/to the grid, our topology results in no low frequency power circulation in the battery (as shown in the simulation results). In theory, there are some other topologies that can draw a balanced, 3-phase power from MV levels and transfer it to a single DC load. However, they are unsuitable for this application because they either cannot function as a charging station [9], use a large transformer [1-3], draw unacceptable harmonics [4], have excessive capacitance requirements [1,3,5], do not provide galvanic isolation ([6] and [10]). Additionally, because the isolated, DC-DC converters are bidirectional and energy can be freely transferred between phases, our topology can correct any load imbalance upstream of it (as shown in Fig. 1a).

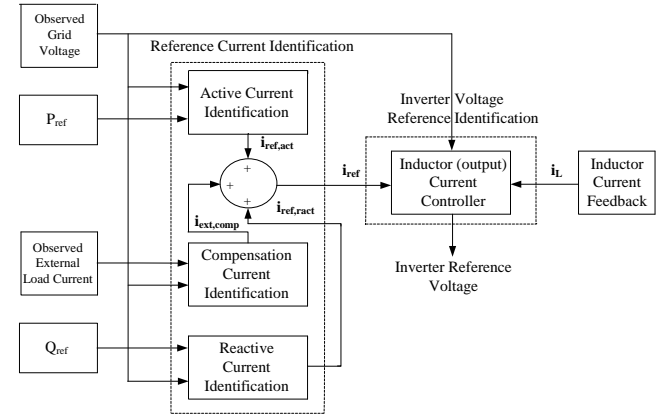


Figure 2: Overall control diagram showing how the reference current and then inverter reference voltage are determined.

III. REFERENCE CURRENT IDENTIFICATION

As shown in Fig. 2, the overall control process consists of two main steps which are the reference current identification (determining what current to draw from the grid) and the inverter voltage reference identification (the voltage necessary to control $i_{L,a}$, $i_{L,b}$, and $i_{L,c}$ in Fig. 1 so they follow

the reference current). In this section, we develop a reference current identification scheme to achieve the following tasks: draw the appropriate amount of power to charge the EVs, charge/discharge the battery as commanded to provide grid support, provide APF/STATCOM compensation of the external load in Fig. 1a, and supply reactive power (in addition to that supplied by the STATCOM functionality) when commanded.

The first two tasks both require active power. Therefore, the first component of the inductor reference current is the active reference current and is a function of the reference power, P_{ref} . We use the following equation which, according to [14], calculates the active, positive sequence current necessary to draw P_{ref} :

$$\mathbf{i}_{ref,active} = \frac{\mathbf{v}_{grid} \cdot \mathbf{P}_{ref}}{\mathbf{v}_{grid}^T \mathbf{v}_{grid}}, \quad (1)$$

where \mathbf{v}_{grid} is the observed, three-phase, grid voltage column, $\mathbf{v}_{grid}^T \mathbf{v}_{grid}$ is the dot product of the grid voltage with itself, and bold is used to indicate a three phase column vector. P_{ref} is a function of the power demanded by the EVs and the power commanded to charge/discharge the battery. However, it is determined by a feedback controller and, so, is discussed in section IV.B.

Next we write the reference current to provide STATCOM/APF functionality. First, need to determine the component of the load current that we don't want to compensate. To do this, we adapt (1) to yield the active, positive-sequence current of the external load:

$$\mathbf{i}_{ext,active} = \frac{\mathbf{v}_{grid} \cdot \mathbf{P}_{est,ext}}{\mathbf{v}_{grid}^T \mathbf{v}_{grid}}, \quad (2)$$

where $P_{est,ext}$ is the estimated, active power of the external load and is given by (6) and, again, bold indicates a three phase column vector.

Because the remaining components of the load current are what we wish to compensate, we write the compensation current reference as

$$\mathbf{i}_{ref,comp} = -(\mathbf{i}_{ext} - \mathbf{i}_{ext,active}) = \frac{\mathbf{v}_{grid} \cdot \mathbf{P}_{est,ext}}{\mathbf{v}_{grid}^T \mathbf{v}_{grid}} - \mathbf{i}_{ext}, \quad (3)$$

where \mathbf{i}_{ext} is the observed, external load current and the negative sign outside of the parentheses is due to the direction of the inductor current in Fig. 1a.

The final component of the reference current, is the component necessary to provide reactive support to the grid (in addition to reactive power supplied by compensating the external load). This is often desirable because supplying a net amount reactive power to the grid can help boost the voltage

at a load bus. In order for the incoming inductor current to supply reactive power to the grid, the current needs to lead the grid voltage by 90° . Therefore, (1) can be modified to give the equation for reactive current reference:

$$\mathbf{i}_{ref,react} = \frac{\mathbf{v}_{grid}(t - 3/(4 \cdot f_{line})) \cdot Q_{ref}}{\mathbf{v}_{grid}^T \mathbf{v}_{grid}}, \quad (4)$$

where Q_{ref} is the reference command to supply reactive power to the grid and f_{line} is line frequency. Because Q_{ref} results in a balanced reactive power being supplied, this function does impose any extra requirements on or incur any losses in the battery.

Now that we have (1-3), we can combine them to form the equation for the total reference current of the inductors:

$$\mathbf{i}_{ref} = \mathbf{i}_{ref,act} + \mathbf{i}_{ref,react} + \mathbf{i}_{ref,comp} = \frac{\mathbf{v}_{grid} \cdot (P_{ref} + P_{est,ext}) + \mathbf{v}_{grid}(t - 3/(4 \cdot f_{line})) \cdot Q_{ref}}{\mathbf{v}_{grid}^T \mathbf{v}_{grid}} - \mathbf{i}_{ext}, \quad (5)$$

where $P_{est,ext}$ is given by (6) and line frequency is 60Hz.

We discuss the determination of $P_{est,ext}$ last because it has a strong effect on APF/STATCOM performance. Various algorithms exist for this purpose with various trade-offs. We use the method developed in [11] which has an excellent trade-off between rapid transient response and robustness. It is also very simple:

$$P_{est,ext} = \frac{1 \text{ sec.}}{120} \int_{t-\text{sec.}/120}^t (\mathbf{v}_{grid}^T \mathbf{i}_{ext}) dt, \quad (6)$$

where $\mathbf{v}_{grid}^T \mathbf{i}_{ext}$ is dot product of the grid voltage and the external load current, and the integral is implemented with a moving average filter over the most recent half-cycle.

IV. CONTROL AND MODELING

A. Inductor Current Control

In order for the inductor current, \mathbf{i}_L , in Fig. 1a to follow the reference current, \mathbf{i}_{ref} , in equation (1), the correct voltage needs to applied to those inductors, and thus the correct inverter voltage \mathbf{v} must be synthesized for each phase. Again, bold variables indicate a three-phase vector. To begin, we write the basic equation for the inductor current:

$$\frac{d\mathbf{i}_{L,abc}}{dt} = L^{-1}(\mathbf{v}_{grid} + \mathbf{v}_{gn} - \mathbf{v}), \quad (7)$$

where \mathbf{v}_{grid} is the three phase grid voltage, \mathbf{v} is the three phase inverter voltage, and \mathbf{v}_{gn} is the common mode voltage between the grid ground and the floating inverter neutral.

Since there is no neutral current, we do not desire there to be any neutral component in the reference current. Therefore, there will no neutral component in $d\mathbf{i}/dt$. With this assumption, we can drop the ground to neutral voltage:

$$\frac{di_L}{dt} = L^{-1}(\mathbf{v}_{grid} - \mathbf{v}), \quad (8)$$

We are now going to approximate di/dt as being constant in the next T_s seconds (T_s is sampling time period or the dead-beat delay time in dead beat control and is set to 1/2880 or .000347 sec. as described at the end of section V). Therefore, we write:

$$\frac{\Delta \mathbf{I}_L}{T_s} = L^{-1}(\mathbf{v}_{grid} - \mathbf{v}), \quad (9)$$

Now we assume that we want \mathbf{i}_L to be \mathbf{i}_{ref} at the end of this period. Therefore, $\Delta \mathbf{i}_L = \mathbf{i}_{ref} - \mathbf{i}_L$. Substituting this expression into (4) yields:

$$\frac{\mathbf{i}_{ref} - \mathbf{i}_L}{T_s} = L^{-1}(\mathbf{v}_{grid} - \mathbf{v}), \quad (10)$$

and isolating \mathbf{v} yields

$$\mathbf{v}^{(*)} = \mathbf{v}_{grid} - L \frac{\mathbf{i}_{ref}^{(*)} - \mathbf{i}_L}{T_s}. \quad (11)$$

Equation (6) is the inverter voltage necessary to make $\Delta \mathbf{i}_L = \mathbf{i}_{ref} - \mathbf{i}_L$. That is, \mathbf{i}_L will equal \mathbf{i}_{ref} at the end of each T_s interval. Whenever a discrete-time controller is used to make a first-order system (as ours is) have zero error after one switching cycle, it known as deadbeat control (although this definition can be modified for n^{th} order systems). However, as we are using a natural form of modulation (Section V), the controller runs in continuous time and, strictly speaking, is not deadbeat.

Notice that there are “(*)” operators in (6). This is because we need to modify the expression for \mathbf{v} . As discussed in section V, to prevent multiple switching, we need to add a smoothing filter to the expression for \mathbf{v} . This expression is given by:

$$\begin{aligned} V(s) &= C_{smooth}(s) \cdot V(s)^{(*)} \\ &= \frac{.053s}{7 \cdot e^{-09 \cdot s^2} + .053 \cdot s + 1} \cdot V(s)^{(*)}, \end{aligned} \quad (12)$$

where $C_{smooth}(s)$ has unity gain at its resonance frequency of 60 Hz and a Q of 1/20.

In addition to $C_{smooth}(s)$, we need to compensate \mathbf{i}_{ref} so that the resulting \mathbf{i}_L will not have a steady-state, phase error at 60 Hz due to the delay of T_s . Therefore, we compensate \mathbf{i}_{ref} with a lead compensator:

$$\mathbf{I}_{ref}(s)^{(*)} = C_{lead}(s) \cdot \mathbf{I}_{ref}(s) = 1.413 \frac{s+266}{s+534} \cdot \mathbf{I}_{ref}(s), \quad (13)$$

where $C_{lead}(s)$ has unity gain and a phase lead of 19.6° at 60 Hz and minimal effect on other frequencies.

Combining (6), (7), and (8) yields the final equation for the inverter voltage:

$$\begin{aligned} V(s) &= \frac{.053s}{7 \cdot e^{-09 \cdot s^2} + .053 \cdot s + 1} \\ &\cdot \left[V_{grid}(s) - L \frac{1.413 \frac{s+266}{s+534} \mathbf{I}_{ref}(s) - \mathbf{I}_L(s)}{T_s} \right] \end{aligned} \quad (14)$$

When this equation and $L = 1$ mH are used, the inductor current has the per-phase transfer function of

$$\begin{aligned} \frac{\mathbf{I}_{L,phase}(s)}{\mathbf{I}_{L,ref}(s)} &= \frac{s+266}{s+534} \cdot \frac{.075}{2.44e-9 \cdot s^2 + 1.84e-5 \cdot s + .053} \end{aligned} \quad (15)$$

B. Battery Power Flow Control Loop and System Model

Under normal circumstances, the power demanded by the charging EVs (hereafter referred to as $P_{dem,EV}$) should be matched by power flowing from the grid, through the multi-level inverters to the DC-link (hereafter called P_{ret}). However, because ultra-fast vehicle charging presents a very transient load (especially if pulse-and-burp methods [12] are employed), we use an integral controller to soften the transients presented to the grid. In addition, integral control ensures that P_{ret} is exactly equal to $P_{dev,EV}$. To achieve this we have

$$P_{ref}^{(*)}(s) = \frac{10}{s} (P_{dem,EV}(s) - P_{ret}(s)), \quad (16)$$

where the integral gain of 10 is chosen to yield dominant pole in (20).

Equation (16) contains “(*)” because it needs modification. It does not allow the common DC-link’s battery to be discharged (for grid support) or charged back up. Instead, it ensures that, at steady state, the returned power will exactly match the power consumed by the EVs. Therefore, we modify the integrand of (16) to allow the returned power to be different from the power consumed by the EVs if desired:

$$P_{ref}(s) = \frac{10}{s} (P_{dem,EV}(s) - P_{ref,supp}(s) - P_{ret}(s)), \quad (17)$$

where $P_{ref,supp}$ is the reference power for grid support. When $P_{ref,supp}$ is negative, then the steady state value of P_{ret} will be greater than $P_{dem,EV}$. This discrepancy will flow into the battery causing the battery to be charged. Vice versa, when $P_{ref,supp}$ is positive, the battery will discharge providing grid support.

Because the relationship between P_{ref} and i_L is time-varying (1) and complicated (15), it is reasonable to first investigate the open-loop response of the system before further investigating the closed-loop performance. Therefore, equation below is based on open-loop simulation results. We used the same model described in the Simulation section except that we manually drove P_{ref} instead of using (17) to close the loop. Based on the open-loop step response of the observed P , we found the following pseudo-delay to be very accurate:

$$\frac{P(s)}{P_{ref}(s)} = \frac{1102}{s + 1102}, \quad (18)$$

where $P(s)$ is the actual resulting power drawn from the grid and the pole of $P(s)/P_{ref}(s)$ at $s = -1102$ corresponds to a time constant of 0.91 ms (i.e., it approximates a delay of 0.91ms).

To model the losses of the cascaded HBs and isolated converters (it is assumed that the dynamics of the isolated converters are fast enough so power flowing into them from the grid instantaneously appears at the battery), we assume a 97% efficiency [8]:

$$\frac{P_{ret}(s)}{P_{ref}(s)} = \frac{1102}{s + 1102} \alpha(s), \quad (19)$$

where $\alpha(t)$ is 97% or 1/97% depending on the direction of power flow. This reciprocation happens because the bi-directional capability of the topology. When power flows from the DC-link to the grid, then P (the grid power) is 97% of P_{ret} . However, when power flows the other direction P_{ret} is 97% of P .

We can now substitute this equation into (17) and rearrange to yield

$$\frac{P_{ref}(s)}{P_{dem,EV}(s) - P_{ref,supp}(s)} = \frac{10(s + 1102)}{s^2 + 1102 \cdot s + 11020 \cdot \alpha(s)}, \quad (20)$$

which, because $1 \approx \alpha(t) \approx \alpha(s)$, has a dominant pole at -10 rad./sec.

Because of the very dominant pole at -10 rad./sec., we can accurately model the power flow with the following approximations:

$$\begin{cases} \frac{P(s)}{P_{dem,EV}(s) - P_{ref,supp}(s)} = \frac{10}{s + 10} \cdot \frac{1}{\alpha(s)}, \\ \frac{P_{ret}(s)}{P_{dem,EV}(s) - P_{ref,supp}(s)} = \frac{10}{s + 10} \end{cases} \quad (21)$$

Fig. 3a shows the response of the power absorbed from the grid to a 2.4 MW step in $P_{dem,EV}$ and a -5 MW step in $P_{ref,supp}$. Likewise, Fig. 3b shows the step-response of the power supplied by the battery based on (21). Comparing Fig. 3 to Fig. 10 in the simulation section shows that (21) is indeed an accurate approximation.

C. Controller Limitations

In subsection A, we had to place some restrictions on (11) to arrive at (14). As discussed in more detail in the next section, this is because we are using a natural method to modulate the inverters and the reference voltage given by (11) contains frequency components near the switching frequency. Therefore, there is no guarantee that the average output voltage will equal the average reference voltage over a fixed interval T_s (the dead-beat delay time in (11)). This is especially apparent in Fig. 4 between $t=45$ ms and 47 ms.

These limitations, however, are not a fundamental limitation of our topology. Equation (11) could be used if a modulation method existed that could guarantee the average inverter output voltage is equal to a reference value over fixed, discrete-time intervals. Such a method, known as multi-level, space vector PWM (SVPWM) is the subject of Ch. 12 of [7]. While its implementation is far more complex than the staircase modulation we use in section V, the end result is very similar. Essentially, the only difference is that the edges of the output voltage in Fig. 4 timed to achieve a given average value. The rising and falling still happens in the same sequence.

To fully optimize the operation of the topology, we recommend the use of multi-level, SVPWM and synchronous, DQ-based, dead-beat controller. This will allow the bandwidth of dead-beat control to be achieved, without having a phase delay for the 60 Hz component [13] and without having to sacrifice the advantages of multi-level modulation discussed in the next section.

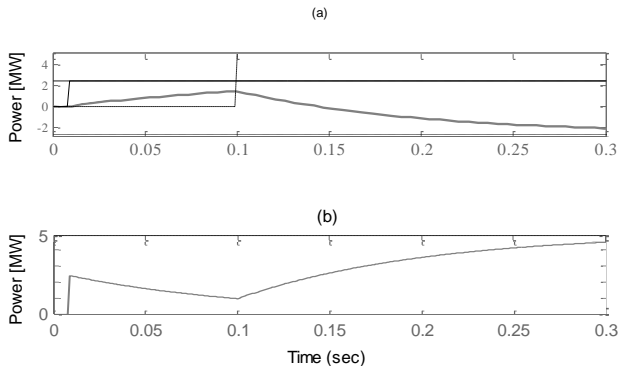


Figure 3: (a) Response of power consumed by station (gray) in response to step changes in EV charging power (solid) and grid support (dashed) according to equation (21) and (b) response of power supplied by battery.

V. MULTILEVEL, STAIRCASE MODULATION OF THE CASCADED HBs

To synthesize the inverter output voltage determined in section IV.A, we use a type of naturally-sampled modulation called staircase modulation (investigated in [15]). This is shown in Fig. 4, where the inverter voltage follows the reference voltage in discrete, 400V steps. To achieve this, the cascaded HBs in Fig. 1b are switched on in sequence to stack the DC-links voltages. The exact time at which a new HB switches on is when the reference voltage crosses the halfway point between two, discrete, 400 V level. Thus, the first HB switches on when reference voltage reaches 200 V. In this way there are 48 steps per 60-Hz cycle (generating a full scale 4800 V magnitude output voltage) for an effective switching of $F_s=2880$ Hz.

Besides allowing interface with voltages much higher than the device ratings, there are several other advantages of using a multilevel inverter over a two-level inverter. First and foremost, the di/dt of the ripple is inversely proportional to N , the number of levels in the inverter (Figs. 11.6 and 11.7 of [7]). However, the achievable current slew rate is not reduced because the output voltage in Fig. 4 is free to make more than one level transition at a time. Therefore, for a given switching speed, the ripple current magnitude is reduced by the same factor. With a two-level inverter, this is accomplished by increasing switching speed, but this does not decrease the di/dt in the ripple current. Alternatively, an LCL output filter can be used but this requires complex control and a higher switching speed, for the same bandwidth. Therefore, our use of a 13-level inverter vastly improves the harmonics of the output current without sacrificing transient response or bandwidth while allowing negligible switching losses and a small inductor size!

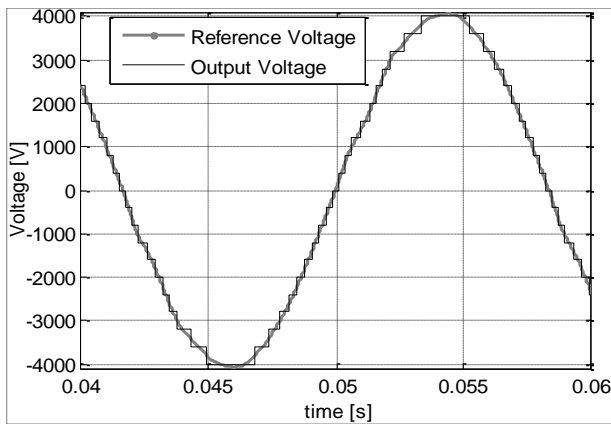


Figure 4: Phase A multi-level inverter output and reference voltages.

Another advantage of synthesizing the reference voltage in multiple steps is that it allows the use of the class of IGBTs with the lowest conduction losses. Typical devices (such as the IRG4PC50S) achieve forward voltage drops as low 1.1V but sacrifice the ability to switch faster than 1 kHz, preventing most PWM applications from exploiting their exceptional efficiency. However, they are very well suited for our topology because, as Fig. 4 shows, the topology enables an

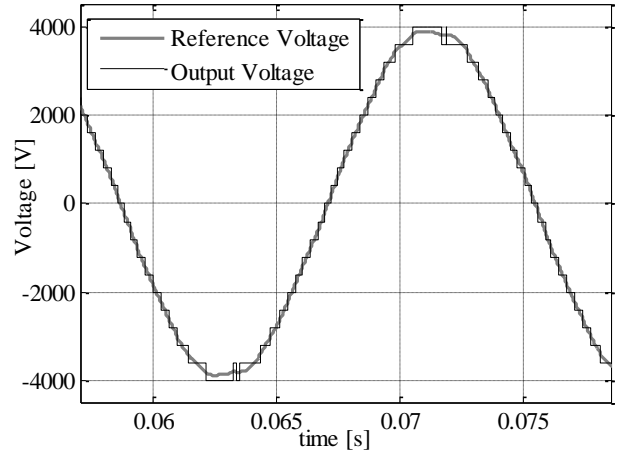


Figure 5: Phase A reference and output voltage while exhibiting multiple switching

accurate synthesis of a reference waveform while on require each HB to change state 4 times per cycle.

Fig. 5, however, shows an issue that must be addressed. Thus far in our implementation of staircase modulation, there is nothing to prevent the multiple switching shown at $t=0.063$ s. In a worst-case scenario, the reference voltage can dither at high frequency about the midpoint between two voltage levels, resulting in improper synthesis of the reference voltage. This can be addressed by using comparators with hysteresis. However, this degrades the accuracy of the synthesis of the reference voltage, and (7-15) were developed on the assumption that v of (14) is accurately synthesized. Instead, we use a smoothing filter, $C_s(s)$, as discussed in section IV. A to help prevent dithering in reference waveform and an algorithm intercept multiple switching and freeze the HB's state for predetermined amount of time. Either way, the price of using staircase modulation is reduced bandwidth compared to what is theoretically achievable with our topology.

There is another shortcoming of the staircase modulation method. Essentially, it does not optimally time its rising and falling edges when the slope of the reference voltage is non-constant. By Examining Fig. 4 between $t=45$ ms and 47 ms, one can see that there is no guarantee that the resulting output voltage has the same average value as that of the reference voltage during this time period. As discussed in detail in section IV, Multilevel, SVPWM can be used to address this issue as well as the multiple switching issue without requiring a smoothing filter. Additionally, by pairing SVPWM with a DQ-based controller the topology can achieve the maximum theoretical bandwidth of 1440 Hz ($F_s/2$).

VI. SIMULATION

A. Simulink Model

We simulated our topology and control system in Simulink using the SimPowerSystems add-on as shown in Fig. 6. For the multilevel inverters, ideal voltage sources are used (as we are not modeling the dynamics of the isolated DC-DC converters). However, we do model the structure of Fig. 1B as being 97% efficient, as in (19).

The other blocks in the figure are the power reference block, reference current identification, the current controller, the grid, the EV load, and the external load. The power

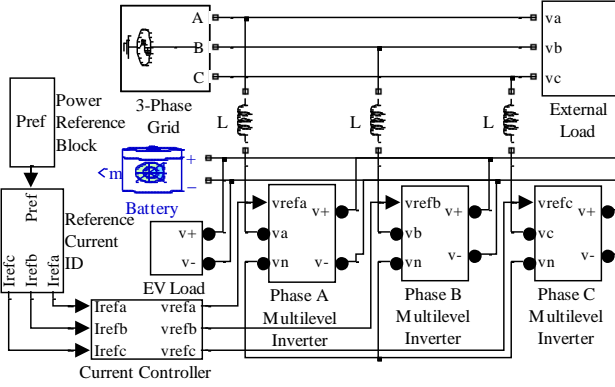


Figure 6: Simulink model.

reference block uses equation (17) to generate P_{ref} . The P_{ref} signal and several other inputs are fed into the reference current identification block which uses (5) to generate i_{ref} . The current control block uses (14) to generate the appropriate reference voltage, v , to control the inductor current to follow i_{ref} . The EV load models the power consumed by the EVs by drawing an appropriate amount of current from the battery.

B. Simulation Results for the Output Current and Compensation Effectiveness

To verify the transient and harmonic performance of the current control (14), we ran the following simulation: initially, the external load is drawing reactive, unbalanced, and harmonic currents (Fig. 7a, dashed curve), and then a 1 MW charging load is added at 0.05 sec. The phase A currents during this time are shown in Fig. 7. The dashed curve indicates that the load current has some harmonics and is out of phase with the grid voltage. The addition of the 1 MW charging load is indicated by the change in grid (solid curve) and charging station current (thick gray curve) after 0.05 sec. but no change in load current. The power flow during this time is shown for various parts of the system in Fig. 8.

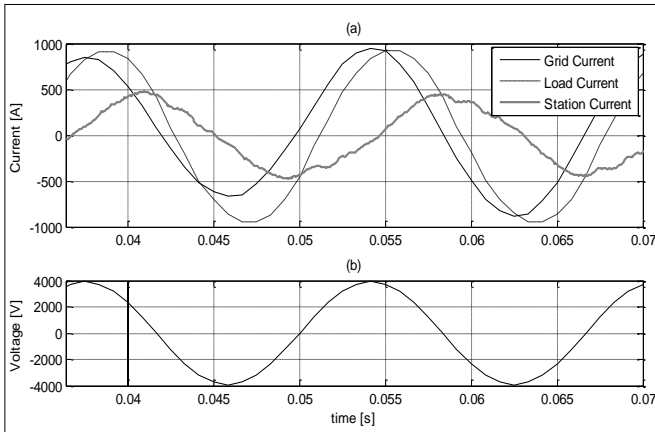


Figure 7: Phase A grid, charging station, and external load currents (a) and phase A grid voltage draw as a phase reference.

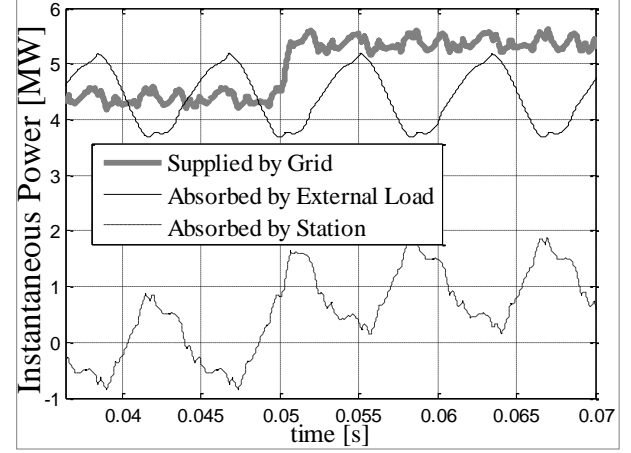


Figure 8: Instantaneous power supplied by the grid, absorbed by the external load, and absorbed by the charging station during simulation.

As the grid current (Fig. 7a) shows, the load current has been compensated so that the grid current is in phase with the voltage (plotted in Fig. 7b for reference). Thus the RMS current has been significantly reduced (Table I). As Table I shows, the overall harmonics have been reduced as well.

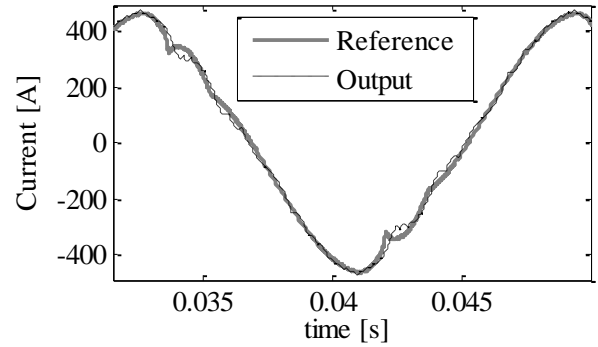


Figure 9: Output current (black) following phase A reference current (thick, gray).

The effectiveness of (14) can be verified visually as well. To do this, the phase A output current is compared to its reference in Fig. 9 when there is high harmonic content in the reference. Due to the limitations of our current control and modulation methods in section IV.C and the end of section V, there are some imperfections in the reference following. Overall, however, the figure indicates a decent ability to follow harmonics and transients.

C. Simulation Results of the Power Flow

Simulation was also used to verify (21), the system model of the power flow. In section IV, it was claimed that a dominant pole was introduced such that (21) becomes a very accurate approximation. To verify this we simulated the system with the same step changes in $P_{ref, EV}$ and $P_{ref, supp}$ that were used to generate Fig. 3. Comparing the power flow response of the full simulation model, Fig. 10, to Fig. 3 shows that (21) is indeed accurate.

Simulation was also used to verify (21), the system model of the power flow. In section IV, it was claimed that a dominant pole was introduced such that (21) becomes a very accurate approximation. To verify this we simulated the

Table I: Simulation Results Summary

	Active Phase Current (RMS)	Current THD	Phase Current RMS	Total PF	Total Apparent Power	Total Active Power
External Load	523	2.76%	680	77%	5.6 MVA	4.3 MW
Grid Current w/o EV Charging	523	2.19 %	523	>99%	4.3 MVA	4.3 MW
Grid Current with EV Charging	648	1.2%	648	>99%	5.3 MVA	5.3 MW

system with the same step changes in $P_{ref, EV}$ and $P_{ref, supp}$ that were used to generate Fig. 3. Comparing the power flow response of the full simulation model, Fig. 10, to Fig. 3 shows that (21) is indeed accurate.

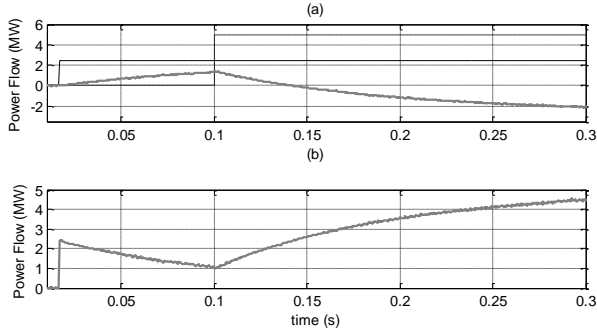


Figure 10: (a) Simulated response of power consumed by station (gray) in response to step changes in EV charging power (solid) and grid support (dashed) and (b) response of power supplied by battery.

VII. CONCLUSIONS

Because of the unique features of our topology (high power density, MV-level interface, excellent harmonic performance, and STATCOM/APF capabilities) it is ideally suited (from a utility point of view) for a public, ultra-fast, EV charging station. As the simulation results show it is capable of removing correcting a typical distribution load to 99% power factor (including harmonic, reactive, and negative-sequence currents). With the inclusion of the battery as the common DC-link, the charging station can operate without drawing power from the grid during heavy loads. In fact, with the bi-directional capability of the topology, the battery can be used to support the grid at strategic times.

As shown in section V, each H-bridge only changes state 240 times per second even though the effective switching frequency is 2880 Hz. This drastically reduces switching losses. With the use of staircase, multi-level modulation, we are able to achieve the bandwidth necessary to compensate harmonics while having small di/dt in the ripple current. However, as the bandwidth is still somewhat limited (15), any improvement in it is very valuable in this application. Theoretically, a 1440 Hz bandwidth should be achievable. Through the use of multi-level, SVPWM in conjunction with a DQ-based, dead-beat controller this can be realized.

ACKNOWLEDGMENT

The authors thank Dr. Les Shepherd in Civil and Environmental Engineering department for his generous support as well Yongbin Chu in UTSA Power Electronics and

Electrical Power Research Laboratory (PEEPRL) for his assistance in preparing this manuscript.

REFERENCES

- [1] D. Aggeler, F. Canales, H. Zelaya-De La Parra, A. Coccia, N. Butcher, O. Apeldoorn, "Ultra-fast DC-charge infrastructures for EV-mobility and future smart grids", in *IEEE 2010 Innovative Smart Grid Technologies Conference Europe*, 2010, pp.1-8.
- [2] S. Bai, D. Yu, S. Lukic, "Optimum design of an EV/PHEV charging station with DC bus and storage system", in *IEEE 2010 Energy Conversion Congress and Exposition*, 2010, pp. 1178-1184.
- [3] M. Malinowski, K. Gopakumar, J. Rodriguez, M. Perez, "A Survey on Cascaded Multilevel Inverters", *IEEE Transactions of Industrial Electronics*, vol. 57, no. 7, pp. 2197-2206, July 2010.
- [4] C. Liu, S. Ho, W. Fu, S. Hai, "Magnetic Design of Transformers for 20kW Charging Stations of Electrical Vehicles", in *2010 14th Biennial Conference on Electromagnetic Field Computation*, May 2010, p. 1.
- [5] L. Tolbert, F. Peng, T. Habetler, "Multilevel Inverters for Electric Vehicle Applications", in *1998 Power Electronics in Transportation*, 1998, pp. 79-84.
- [6] M. Hagiwara, H. Akagi, "Control and Experiment of Pulsewidth-Modulated Modular Multilevel Converters", *IEEE Transactions on Power Electronics*, vol. 24, no. 7, pp. 1737-1746, July 2009.
- [7] D. Holmes, T. Lipo, *Pulse Width Modulation for Power Converters: Principles and Practice*, Wiley-IEEE Press, 2003.
- [8] S. Inoue, H. Akagi, "A Bi-Directional Isolated DC/DC Converter as a Core Circuit of the Next-Generation Medium-Voltage Power Conversion System", in *IEEE 2006 Power Electronics Specialists Conference*, 2006, pp. 1-7.
- [9] G. Ortiz, J. Biela, D. Bortis, J. Kolar, "1 Megawatt, 20 kHz, Isolated, Bidirectional 12kV to 1.2kV DC-DC Converter for Renewable Energy Applications", in *IEEE 2010 International Power Electronics Conference*, 2010, pp. 3212-3219.
- [10] L. Maharjan, T. Yamagishi, H. Akagi, J. Asakura, "Fault-Tolerant Operation of a Battery-Energy-Storage System Based on a Multilevel Cascade With Star Configuration", *IEEE Transactions on Power Electronics*, vol. 25, no. 9, pp. 2386-2396, Sept. 2010.
- [11] L. da Silva, L. de Lacerda de Oliveira, V. da Silva, "Speeding-up dynamic response of active power conditioners", in *IEEE 2003 Canadian Conference Electrical and Computer Engineering*, 2003, pp. 347-350.
- [12] Y. Chu, R. Chen, T. Liang, S. Changchien, J. Chen, "Positive/negative pulse battery charger with energy feedback and power factor correction", in *IEEE 2005 Applied Power Electronics and Conference and Exposition*, 2005, pp. 986-990.
- [13] T. Saigusa, K. Imamura, T. Yokoyama, "100kHz Single Phase Utility Interactive Inverter with FPGA based Hardware Controller", in *IEEE 2010 International Power Electronics Conference*, 2010, pp. 1457-1462.
- [14] F. Peng, J. Lai, "Generalized Instantaneous Reactive Power Theory for Three-phase Power Systems", in *IEEE Transactions on Instrumentation and Measurement*, VOL. 45, NO. 1, pp. 293-297, February 1996.
- [15] F. Peng, J. Lai, J. McKeever, J. VanCoeveering, "A Multilevel Voltage-Source Inverter with Separate DC Sources for Static VAr Generation", in *IEEE Transactions on Industry Applications*, Vol 32, No 5, pp.1130-1138, September/October 1996.

Single-stage Isolated Bi-directional Converter Topology using High Frequency AC link for Charging and V2G Applications of PHEV

Shesh Narayan Vaishnav and H. Krishnaswami, *Member, IEEE*,

Department of Electrical and Computer Engineering

The University of Texas at San Antonio

San Antonio, Texas, USA

E-mail: sheshvaishnav@yahoo.co.in and Hariharan.Krishnaswami@utsa.edu

Abstract—In this paper, an isolated bi-directional ac/dc converter with a single power conversion stage is proposed for both charging and Vehicle-to-Grid (V2G) applications of PHEV. The converter consists of two active bridges connected through a series resonant tank and a high-frequency transformer. Steady-state analysis is presented for the proposed phase-shift modulation technique between active bridges, to control the bi-directional power flow in the converter. Simulation results are presented to augment the analysis. The proposed converter has the advantages of minimal power conversion stages, high switching frequency operation and low switching losses.

I. INTRODUCTION

Plug-in Hybrid Electric Vehicles (PHEV) are expected to capture significant market share of automobiles in next 10 years [1]. PHEV batteries will be charged from the power grid and hence, utilities nationwide have started exploring the effects of PHEVs on distribution infrastructure. Furthermore, a fleet of PHEV can act as a distributed energy storage for utilities to use under peak load condition, termed as Vehicle-to-Grid (V2G) functionality. A review of the V2G functionalities and the power electronics configurations associated with such vehicles is given in [2]. Hence, the bi-directional charger either on-board or off-board forms an important unit in PHEV. In this paper, a high-frequency ac link based power electronic topology is proposed for bi-directional charging applications.

Existing bi-directional chargers proposed in literature [3], [4], [5] use two stages of power conversion, an ac-dc converter and a dc-dc converter, both bi-directional in power flow. Several topologies for the ac-dc and dc-dc conversion stages are discussed in [3]. Two dc-dc converters are discussed, a dual active bridge high power converter [6] and the integrated buck-boost dc-dc converter [7]. A bi-directional battery charger for residential applications is discussed in [5] with an improved control method for V2G operating mode. Reactive power compensation, which is one of the V2G functionalities, is demonstrated in [4] with a bi-directional ac-dc front end converter. With two stages of power conversion, the intermediate link is mostly dc. Such two stage power conversion will lead to

increased part count, size and weight, which are major design challenges for on-board or external level 1 or level 2 chargers. To address these challenges, a single-stage power converter is proposed in this paper.

The proposed converter is shown in Fig. 1. It consists of two active bridges with an intermediate high frequency ac link. A series resonant tank is used as the impedance at the high frequency link. The high frequency transformer is used both for isolation and voltage conversion. Traditionally, resonant converters are controlled using frequency or Pulse Width Modulation (PWM) in only one bridge and is uni-directional due to the presence of a diode bridge at the load side. In this paper, a phase-shift modulation technique is proposed which controls the phase-shift between input and output-side active bridges at constant switching frequency. This proposed technique naturally allows bi-directional power flow and uses the principle of power flow in a dual active bridge converter [6]. A three-port dc-dc-dc converter using similar principle is explained in [8]. The proposed modulation technique in this paper allows for direct dc-ac or ac-dc conversion determined by power flow direction.

The advantages of the proposed converter are: (1) Single-stage conversion with high frequency ac link reduces component count and increases power density and (2) Soft-switching operation achieved due to the presence of resonant tank, reduces switching losses and increases efficiency. Analysis of the proposed converter is presented in the following section.

II. ANALYSIS

The converter shown in Fig. 1 has a series resonant circuit with inductance L and capacitance C . It switches at a frequency F_s which is above resonant frequency F_r formed by the series resonant tank. The input voltage $v_{in}(t) = \hat{V}_{in} \sin(2\pi F_o t)$ from grid, is connected to the active bridge through an input filter which filters the current ripple at switching frequency. The PHEV battery is connected at the output of the load-side active bridge. The input-side active bridge switches operate in four-quadrant mode, i.e., each switch uses two Mosfets connected back-back as shown in Fig. 1. V_b is the battery voltage at the output side, F_s is

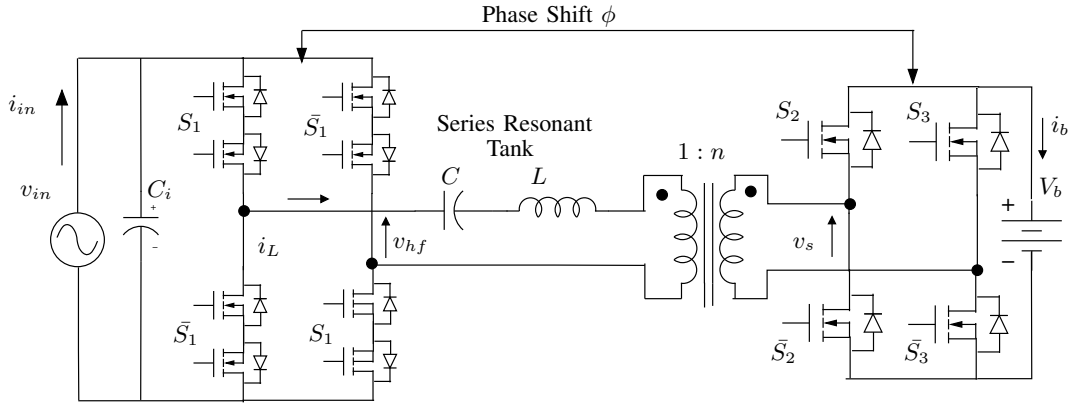


Fig. 1. Proposed Single-stage bi-directional converter with high frequency ac link for PHEV application

the switching frequency and F_o is the line frequency 60Hz. The high frequency transformer has a turns ratio of n . The transformer can be either step-down or step-up based on the design of battery voltage of PHEV.

Two modulation functions $m_1(t)$ and $m_2(t)$ are proposed. The input-side active bridge is controlled by $m_1(t)$ in (1) and the output-side active bridge by $m_2(t)$ in (2). The function $\text{sgn}(\cdot)$ is the signum function which denotes the sign of the signal and ϕ is the phase-shift angle between active bridges.

$$m_1(t) = \text{sgn}(\sin(\omega_s t)) \quad (1)$$

$$m_2(t) = \frac{1}{2} \left[\text{sgn}(\cos((\omega_s - \omega_o)t + \phi)) - \text{sgn}(\cos((\omega_s + \omega_o)t + \phi)) \right] \quad (2)$$

$$\text{Where } \omega_s = 2\pi F_s; \quad \omega_o = 2\pi F_o \quad (3)$$

Square wave modulation is represented as $m_1(t)$. It is known that when a low frequency voltage waveform is amplitude modulated with a high frequency square wave $m_1(t)$ as in an electronic transformer [9], the resultant Fourier spectrum has two fundamental frequencies $F_s - F_o$ and $F_s + F_o$ whose magnitudes are $\frac{2}{\pi} \hat{V}_{in}$. Since this voltage appears across the input of the series resonant tank, it is necessary to produce a voltage waveform across the secondary of the transformer with two fundamental frequencies. For this reason, the modulation function $m_2(t)$ takes the form given in (2). This modulation function produces two frequencies by introducing a slow varying phase-shift at a frequency of F_o between the left and right legs of the output-side active bridge such that the average value in each switching cycle $T_s = \frac{1}{F_s}$ varies sinusoidally at low frequency F_o . In other words, the function introduces zero voltage states in the output of the active bridge whose width varies at low frequency. In this way, the voltage across the resonant inductor and the transformer will have two fundamental frequencies $F_s - F_o$ and $F_s + F_o$. Finally, these two modulation functions have to allow for power flow control which is provided by the phase-shift angle ϕ between the fundamentals of the outputs of the input-side and output-side active bridges. This phase-shift angle, when varied from -90° to 90° , will allow for bi-directional power flow control

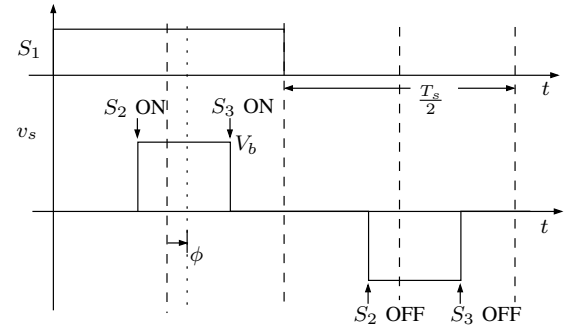


Fig. 2. Switching pulses derived from the proposed phase-shift modulation technique

between the utility and the battery.

The switching signals S_1 , S_2 and S_3 (Fig. 1) can be generated using (1) and (2) as detailed in [10]. The switching signals are shown in Fig. 2 where the pulse-width of the voltage waveform v_s varies sinusoidally at low frequency and the phase-shift ϕ is the angle between the fundamental of v_{hf} and v_s . It is to be noted that the output-side active bridge is controlled by center modulation and hence the phase-shift ϕ remains constant as the pulse-width of v_s varies.

The steady-state analysis assumes sinusoidal tank currents and voltages due to operation above resonant frequency. Hence, only two frequencies are used $F_s - F_o$ and $F_s + F_o$ for analysis. The tank currents in these two frequencies are calculated using phasor analysis and superposition theorem. The resultant sum, by superposition, flows through the secondary side active bridge and is rectified by the modulating signal (2). After integrating the resultant waveform, the average value of the current through the battery I_b is determined to be (4). It is to be noted that this current is independent of battery voltage V_b and the actual current waveform is at twice the line frequency. The expression in (4) is similar to the load current equation in a dual active bridge converter [6] with the difference being the resonant tank in Fig. 1.

While deriving (4), two simplifying assumptions were made: (a) Switching frequency $F_s \gg F_o$ and (b) The

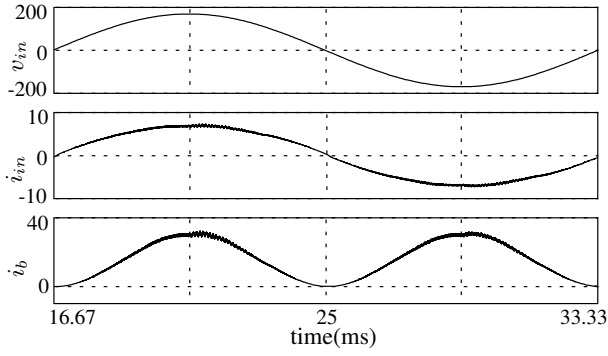


Fig. 3. Input voltage in volts $v_{in}(t)$, filtered input current $i_{in}(t)$ and battery current $i_b(t)$ in Amperes for power flow from AC input to battery

impedance of the resonant tank at $F_s + F_o$ and $F_s - F_o$ are equal.

$$I_b = \frac{4}{\pi^2} \frac{\hat{V}_{in}}{nZ(F - \frac{1}{F})} \sin \phi \quad (4)$$

$$\text{where } Z = \sqrt{\frac{L}{C}}; F = \frac{F_s}{F_r}; F_r = \frac{1}{2\pi\sqrt{LC}} \quad (5)$$

III. SIMULATION RESULTS

A charger with power level of $P_o = 650W$ is used for simulation purposes in order to verify the analysis results. The input ac voltage is chosen to be $V_{in(rms)} = 120V$ and the battery voltage V_b is chosen to be $36V$. The battery voltage is assumed fairly constant during the simulation time, since the battery charging current is independent of battery voltage. The switching frequency is chosen as $F_s = 100kHz$ close to and 1.1 times above resonant frequency. The value of turns ratio is chosen such that the overall voltage conversion ratio is unity [8] i.e., $\frac{n\hat{V}_{in}}{V_b} = 1$. With the required value of I_b and the maximum value of phase-shift angle, the value of the characteristic impedance Z can be calculated using (4). The values of the resonant inductor and capacitor can then be calculated from (5).

The results of the battery current along with input voltage and input current are shown in Fig. 3 for the specified power level and a phase-shift of $\phi = 90^\circ$. It can be observed that battery current waveform is at twice the line frequency and its average value matches (4). The high frequency ripple in input current is filtered by C_i . The input current is normally in phase with the input voltage for this type of modulation scheme.

The tank current and the applied tank voltage $v_{hf}(t)$ for few switching cycles are shown in Fig. 4. The phase-shift ϕ between the waveforms of $v_{hf}(t)$ and $v_s(t)$ can be observed to be 90° from Fig. 4 shown for three switching cycles around $\omega_o t = 60^\circ$. The pulse-width of the waveform $v_s(t)$ varies sinusoidally such that its fundamental has two frequencies $F_s + F_o$ and $F_s - F_o$. Due to the resonant nature of the circuit, soft-switching operation is possible in both the active bridges. Tank current $i_L(t)$ lags the applied voltage $v_{hf}(t)$

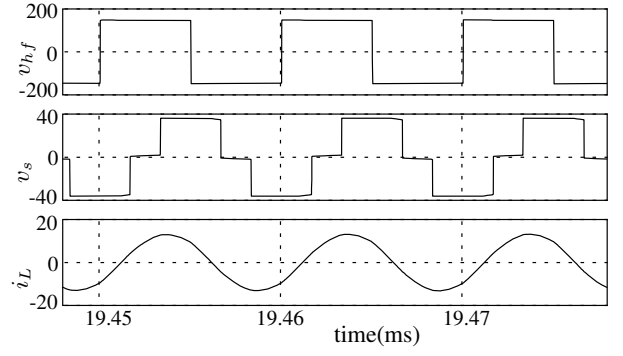


Fig. 4. Applied tank voltage $v_{hf}(t)$, transformer secondary voltage $v_s(t)$ and tank current $i_L(t)$ in Amperes for power flow from AC input to battery at time instant $\omega_o t = 60^\circ$ to illustrate the PWM from proposed phase-shift modulation and soft-switching operation

from input-side bridge as seen in Fig. 4. Since the current drawn from utility is in phase with the voltage, only one Mosfet can be switched in the four-quadrant switch enabling Zero Voltage Switching (ZVS) in all eight switches in the input side active bridge. This eliminates the commutation problem in four-quadrant switches. Although it adds drive circuitry to control each individual Mosfet in a four-quadrant switch, the efficiency gain is significant.

ZVS operation is possible in the battery side active bridge only when the the voltage conversion ratio is unity. The condition for ZVS is that this tank current lead the transformer secondary voltage $v_s(t)$ from the output-side active bridge based on current direction defined in Fig. 1. This lagging angle can be observed from Fig. 4 proving that ZVS is possible in secondary-side switches also. But, the voltage waveform v_s has zero voltage states and hence, when the pulse-width of $v_s(t)$ is lower than the phase-shift, ZVS is lost in one of the legs.

IV. BI-DIRECTIONAL POWER FLOW

Power flow from PHEV to utility is needed for V2G applications. This paper considers only real power flow into the grid with its application of peak load reduction. In the proposed converter, if the phase-shift is made negative, the power flows from the battery to the grid. Considering this mode, the average value of the current into utility can be derived using the same phasor analysis as in Section 2 and is given in (6). This result is equivalent to the one presented in [10] for photovoltaic inverter application.

$$\bar{i}_{in}(t) = \frac{8}{\pi^2} \frac{V_b \sin \phi}{nZ(F - \frac{1}{F})} \sin(2\pi F_o t) \quad (6)$$

Simulation results of the input current and battery current are shown in Fig. 5 to illustrate the bi-directional capability of the proposed converter. The average of the battery current is negative as seen in Fig. 5. The difference in phase-shifts between Fig. 3 and Fig. 4 can be seen. It is observed from Fig. 6 that the tank current still lags the applied voltage $v_{hf}(t)$ and hence ZVS is possible in the input-side active bridge with each

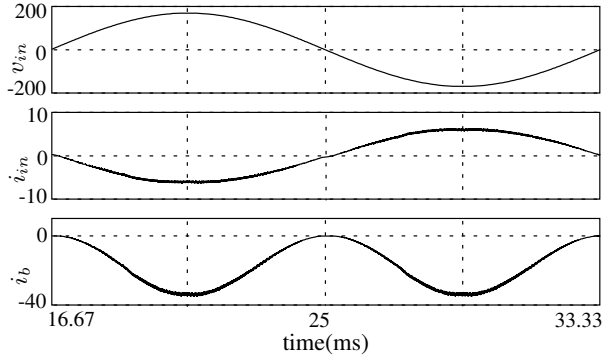


Fig. 5. Input voltage in volts $v_{in}(t)$, filtered input current $i_{in}(t)$ and battery current $i_b(t)$ in Amperes for power flow from Battery to ac input

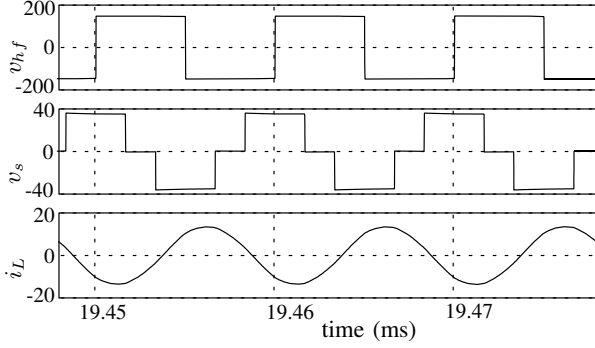


Fig. 6. Applied tank voltage $v_{hf}(t)$, transformer secondary voltage $v_s(t)$ and tank current $i_L(t)$ in Amperes for power flow from Battery to ac input, at time instant $\omega_o t = 60^\circ$ to illustrate the PWM from proposed phase-shift modulation and soft-switching operation

Mosfet in the four-quadrant switch controlled individually. In the output-side active bridge also, ZVS occurs in one of the legs based on the pulse-width of $v_s(t)$. Hence both active bridges can achieve soft-switching in V2G mode.

V. CONCLUSION

This paper proposes a single-stage isolated bi-directional high frequency link converter for both charging and V2G applications of PHEV that has advantages such as reduced size, part count, weight and switching losses when compared to two-stage power converters for the same application. A novel phase-shift modulation is proposed to control the bi-directional power flow in the converter. Steady-state analysis along with simulation results is presented.

REFERENCES

- [1] M. Duvall, "Grid integration of plug-in hybrid and electric vehicles," in *PHEV Executive Summit*, July 2009.
- [2] B. Kramer, S. Chakraborty, and B. Kroposki, "A review of plug-in vehicles and vehicle-to-grid capability," in *Industrial Electronics, 2008. IECON 2008. 34th Annual Conference of IEEE*, 2008, pp. 2278–2283.
- [3] D. Erb, O. Onar, and A. Khaligh, "Bi-directional charging topologies for plug-in hybrid electric vehicles," in *Applied Power Electronics Conference and Exposition (APEC), 2010 Twenty-Fifth Annual IEEE*, 2010, pp. 2066–2072.
- [4] M. Kisacikoglu, B. Ozpineci, and L. Tolbert, "Examination of a phev bidirectional charger system for v2g reactive power compensation," in *Applied Power Electronics Conference and Exposition (APEC), 2010 Twenty-Fifth Annual IEEE*, 2010, pp. 458–465.

- [5] X. Zhou, S. Lukic, S. Bhattacharya, and A. Huang, "Design and control of grid-connected converter in bi-directional battery charger for plug-in hybrid electric vehicle application," in *Vehicle Power and Propulsion Conference, 2009. VPPC '09. IEEE*, 2009, pp. 1716–1721.
- [6] M. H. Kheraluwala, R. W. Gascoigne, D. M. Divan, and E. D. Baumann, "Performance characterization of a high-power dual active bridge dc-to-dc converter," *IEEE Trans. Ind. Appl.*, vol. 28, no. 6, pp. 1294–1300, Nov. 1992.
- [7] Y.-J. Lee, A. Khaligh, and A. Emadi, "Advanced integrated bidirectional ac/dc and dc/dc converter for plug-in hybrid electric vehicles," *Vehicular Technology, IEEE Transactions on*, vol. 58, no. 8, pp. 3970–3980, oct. 2009.
- [8] H. Krishnaswami and N. Mohan, "Three-port series-resonant dc/dc converter to interface renewable energy sources with bidirectional load and energy storage ports," *Power Electronics, IEEE Transactions on*, vol. 24, no. 10, pp. 2289–2297, Oct. 2009.
- [9] H. Krishnaswami and V. Ramanarayanan, "Control of high-frequency ac link electronic transformer," *Electric Power Applications, IEE Proceedings -*, vol. 152, no. 3, pp. 509–516, May 2005.
- [10] H. Krishnaswami, "Photovoltaic microinverter using single-stage isolated high-frequency link series resonant topology," *Energy Conversion Congress and Exposition, ECCE'11*, 2011, to be published.

Section 2:

Microgrids

Fuzzy-Logic Based Control for Battery Management in Micro-Grid

Yashar Sahraei Manjili, *Student Member IEEE*, Amir Rajaei, *Student Member IEEE*
 Brian Kelley, *Senior Member IEEE*, Mo Jamshidi *Fellow IEEE*

Abstract— In this paper, a Fuzzy-Logic based control framework is proposed for Battery Management in Micro-Grid System. The Micro-Grid system operates synchronously with the main grid and also has the ability to operate independently from the power grid. Distributed renewable energy generators including solar, wind, and batteries supply power to the consumer in the Micro-Grid network. The goal is to control the amount of power given to the storage system in order to minimize a cost function based on payment/profit and distribution loss through reasonable decision making using predefined profiles of system variables such as Load Demand, Electricity Price, and Renewable Generation. Simulation results are presented and discussed. The proposed intelligent control system turns out to be capable of achieving effective energy management.

Index Terms—Micro-Grid, Control, Power Flow, Fuzzy-Logic, Load Demand.

I. INTRODUCTION

Micro-Grid is can be referred to as a small scale grid that is designed to provide power for small communities. A Micro-Grid is an aggregation of multiple distributed generators (DGs) such as renewable energy sources, conventional generators, and energy storage systems which work together as a power supply network in order to provide both electric power and thermal energy for small communities which may vary from one common building to a smart house or even a set of loads consisting of a mixture of different structures such as buildings, factories, etc. Typically, a Micro-Grid operates in parallel with the main grid. However, there are cases in which a Micro-Grid operates in islanded mode, or in a disconnected state [1]. In this article, in addition to both of the states already mentioned, a third state is assumed for operation of Micro-Grid in which excess power in the Micro-Grid is delivered to the main grid, i.e. the excess power is sold to the grid.

II. SYSTEM MODEL

A three bus system is used to model the Micro-Grid network for simulations in this article. One of the busses in the

distributed generation system model is assumed to serve the renewable generators which include either solar farm, wind farm, or any other renewable generation units. Another bus is assumed to be working as the grid (utility) bus which will provide the complement part of the power demand that renewable generation system cannot afford to the load. The third bus will be the specific load to which the demanded power is to be provided. This load can be anything from a common building or a smart house, to even a group of plants and factories or a mixture of all of them. Figure 1 shows an overall Micro-Grid schematic including Renewable Electricity Generators and Storage Unit, Utility, and Typical Load.



Figure 1 Micro-Grid Schematic

There are two scenarios assumed for simulation in this article, scenario 1 deals with a Micro-Grid which includes the renewable generation unit without any battery storage unit. Therefore there will not be any approaches required for controlling the battery storage system in this scenario. The second scenario deals with the same Micro-Grid system as mentioned in scenario 1 but with the battery storage unit considered to be connected to the same bus as the renewable generators. These two scenarios will be described in more detail in the next section “Problem Statement”. The characteristics of busses in each of the two scenarios are as follows:

Scenario 1:

- Bus1 is of type PQ and is used as the renewable generation unit's bus
- Bus2 is of type Slack (reference) and is used as the Utility (grid) bus
- Bus3 is of type PV and is used as the Load bus

Scenario 2:

- Bus1 is of type PQ and is used as the bus for renewable generation unit and the Battery storage unit
- Bus2 is of type Slack (reference) and is used as the Utility (grid) bus
- Bus3 is of type PV and is used as the Load bus

III. PROBLEM STATEMENT

Important point on this first idea is that we have assumed the time-varying pricing for electricity. The update duration of pricing is assumed to be 15 mins, which means that the price per kilowatt-hour of electricity consumed by the customers of the load region is updated every 15 minutes, and there will be a cost function determined by us as:

$$C = \sum_{t=1}^T (Pr(t) \cdot (S_U + S_L)) \quad (1)$$

where the electricity price is determined by the CPS energy every 15 minutes for the next 15 minute period. $S_U(t)$ is the amount of power transferred to/from the Grid during each 15 minute period. If power is received from the Grid $S_U(t)$ will be positive, and if power is delivered to the grid in case of excess power generation by the renewable generation system $S_U(t)$ will appear in the equations with a negative sign. $S_L(t)$ is the amount of distribution loss which will occur on the branches we have between these three Busses in the Micro-Grid system during each 15 minute period. Depending on whether the load is getting how much of its demanded power from renewable generation system and how much from the Grid, and also depending on whether the renewable generation system is producing excess power and is selling the excess power to the Grid, this power Loss will vary.

The simulation is done on the Micro-Grid system considering two scenarios. In the following the summary of the two scenarios is given:

Scenario 1: Analysis of the Micro-Grid system profits and costs under time-varying electricity pricing policy; in this scenario, the simulation, analysis and study will be done Micro-Grid which includes the renewable generation unit without any battery storage unit. Therefore there will not be any approaches required for controlling the battery storage system in this scenario.

Scenario 2: Fuzzy Control of the Micro-Grid system under time-varying electricity pricing policy; the cost function assumed in this scenario is the same as the cost function described in the scenario 1. The main difference here is that the storage system exists in the network and will appear to be on the same bus with the renewable generation unit.

The power flow calculation in the Micro-Grid is the key to simulate the whole system. There are a number of well-known methods for calculation of power flow in the distributed generation network [2]. There are four different types of busses considered in a distributed generation network, the characteristics of which will be calculated in power flow

algorithms. These four types include PQ, PV, Slack, and isolated [3,4].

IV. FUZZY CONTROL APPROACH

The control strategy implemented in this paper is to use the Fuzzy Logic [5] approach for controlling the power flow to/from the battery storage unit in order to minimize the cost function introduced in previous section “Problem Statement”. The three input variables to the fuzzy inference engine are Price, Renewable Generation, and Load Demand.

The numerical values for these three input variables are normalized to the [0 1] interval, and then are Fuzzified using three fuzzy sets defined as Low, Medium, and High. The input variables after fuzzification will be fed to a fuzzy inference engine where the rule-base is applied to the input-output variables and the output will be determined by human reasoning. There is only one output variable which determines the amount of power to be stored in the battery, or to be drawn from battery. Output variable fuzzy set is assumed to have five membership functions called Negative Large (NL), Negative Small (NS), Zero (Z), Positive Small (PS), and Positive Large (PL). The power drawn from the batteries can be used to provide the load in order to complement the renewable generation power for providing the load's demand, can be sold to the Grid, or can be partially used for both reasons [6]. The role of fuzzy inference engine is critically important for obtaining satisfactory results. For example, if the *Price* is *Low*, the *Renewable Generation* is *High*, and the *Load Demand* is *Medium*, then, the amount of *Power to Battery* storage system should be *Positive-Large*, even if this requires the system to get power from grid and store it in the battery storage unit, because the main point here is that Price is low, which means that by storing the energy in the batteries during low price times, the system will have enough stored energy in order to sell to the Grid during high-price periods. Even under cases of High Load demand this will be a good strategy. Therefore, having feasible rules predefined for the fuzzy system will help to minimize the cost function drastically. The proposed approach may sometimes result in making the cost function value negative, which means that the system is even making some profit out of this control approach instead of paying to the utility.

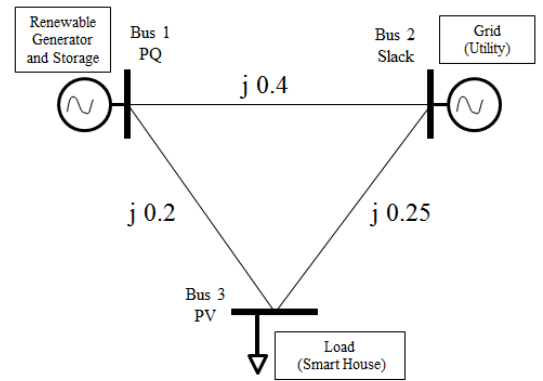


Figure 2 Three Bus Model for Micro-Grid

V. SIMULATION RESULTS & DISCUSSIONS

The simulation is done on the three bus system for power flow calculation. The Gauss-Seidel algorithm is implemented using Matlab for power flow calculation. Some typical data are generated for dynamic Load Demand and Renewable Generation rate.

The power demand of the Load on bus 3 (Smart House) is supplied by two generators on buses 1 and 2. Bus 1 includes solar panel and storage and bus 2 is slack which is connected to utility as shown in figure 2.

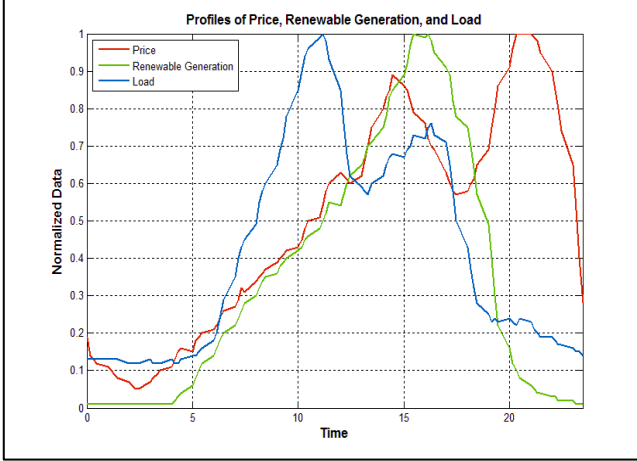


Figure 3 Profiles of Price, Renewable Generation, and the Load during a typical day for each 15min period

The numerical values of the data profile for the three input variables to the *fuzzy inference engine* are shown in figure 3. These variables include electricity price, renewable generation rate, and load demand. The data is generated typically for simulation purposes only with regard to the fact that the peak electricity consumption duration of the whole region of interest is around 8:30 pm where the price gets to its peak value. The simulation results for scenario 1 are represented in figures 4 to 6.

As it can be inferred from figure 4, the value of reactive power for bus 1 is constantly zero which corresponds to the assumption that the renewable generators do not provide reactive energy. Figure 5 shows that the active power is taken from the Utility during first half of the day time, and during the most of the second half of the day the active power is being delivered to the grid. Load is evidently consuming active power regarding the blue curve represented in figure 6.

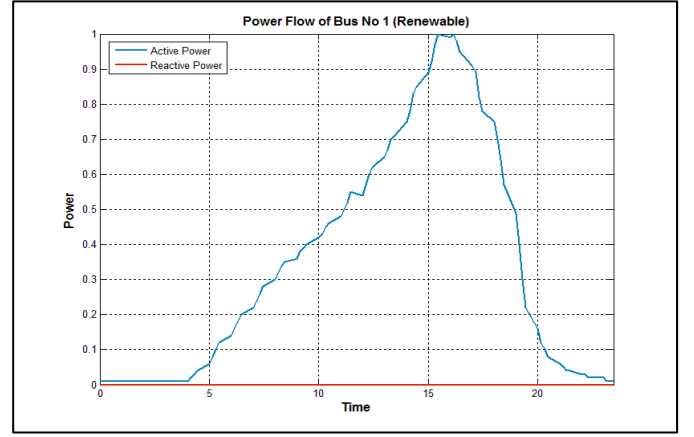


Figure 4 The Power Flow of Bus 1 including Solar Panel in a typical day for each 15min period

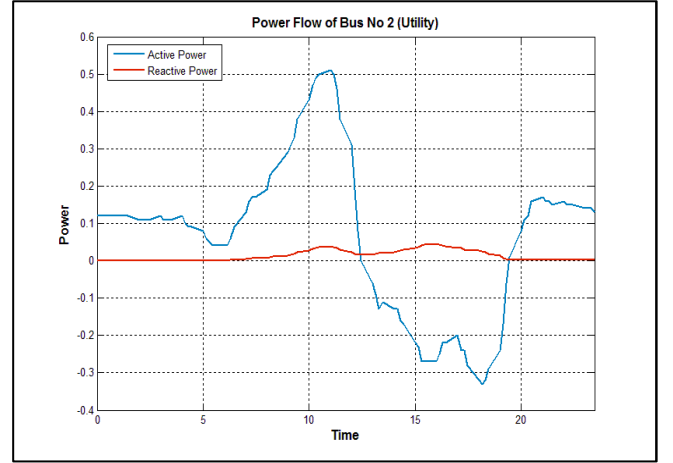


Figure 5 The Power Flow of Bus 2 connected to utility in a typical day for each 15min period

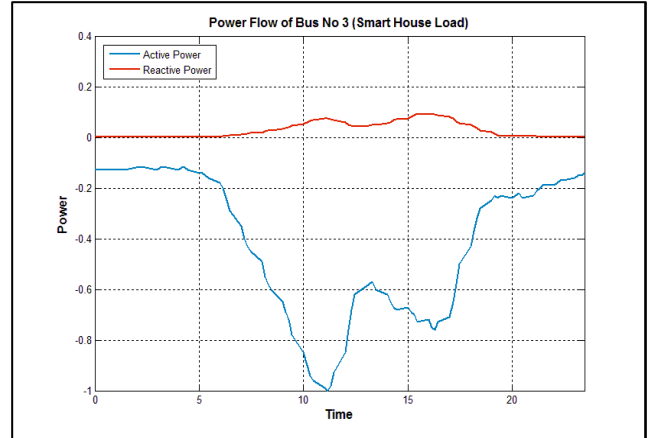


Figure 6 The Power Flow of Bus 3 including Load in a typical day for each 15min period

Output of the fuzzy inference engine which represents the power rate given to battery is shown in figure 7. Whenever the value of this variable is positive it means that power is delivered to the storage unit and if the power is drawn from the storage unit, the value will be negative.

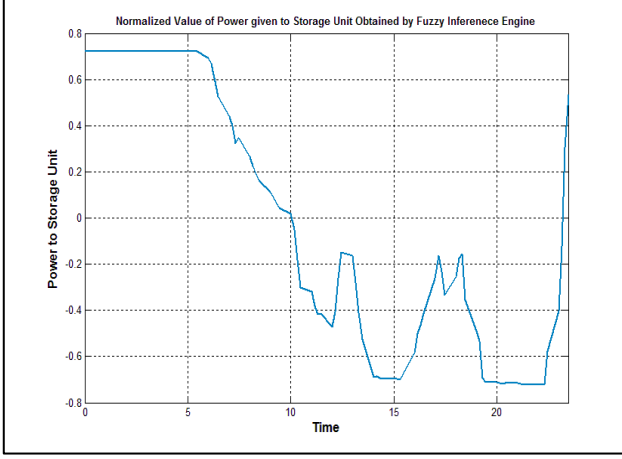


Figure 7 The normalized Value of Power given to Storage obtained by Fuzzy Inference Engine

Simulation results for scenario 2 which includes storage on bus 2 are represented in figures 8 to 10.

As one can infer from figure 8, the value of reactive power for bus 1 is again constantly zero – the same as it was in scenario 1 - which corresponds to the assumption that the renewable generators do not provide reactive energy. Figure 9 shows that the active power is taken from the utility during first half of the day time, and during the most of the second half of day the active power is being sold to the grid. The point is that the first part of the active power diagram is raised dramatically due to fuzzy decision making which means that the system is absorbing more active power from the grid during low-price hours and stores the power in the storage unit. Also, the second part of the active power diagram has fallen more in comparison to the same section of figure 5 which denotes on increase in the amount of power drawn from storage unit and using this power for partially charging the load and also selling the excess power to the grid during high-price hours. This strategy results in minimization of cost function or in other words maximizes the profit function. As shown in figure 10, load (smart house) is consuming active power.

Remembering that the pricing periods are assumed to be 15 minute periods and one day is 24 hours overallly there will be 96 periods of pricing during one day period. The summation of payment/profit and the loss during each of the periods will give us the overall value of cost function for one day. The process can be extended to one week, one month, one year etc.

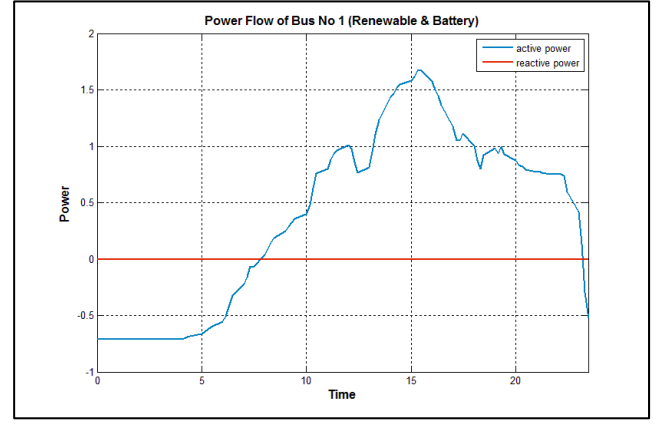


Figure 8 The Power Flow of Bus 1 including Solar Panel in a typical day for each 15min period with storage on bus 2

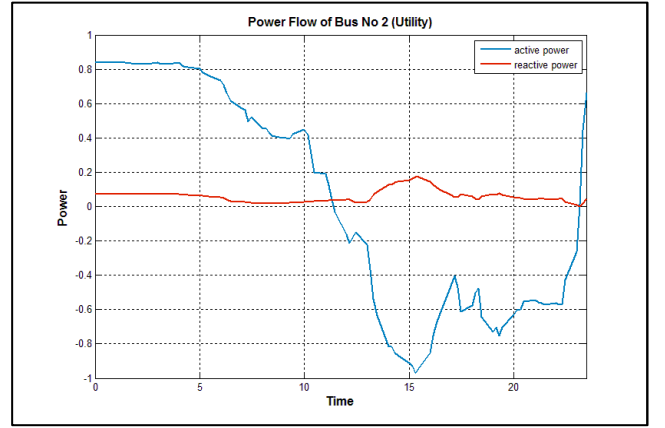


Figure 9 The Power Flow of Bus 2 connected to utility in a typical day for each 15min period with the Storage on bus 2

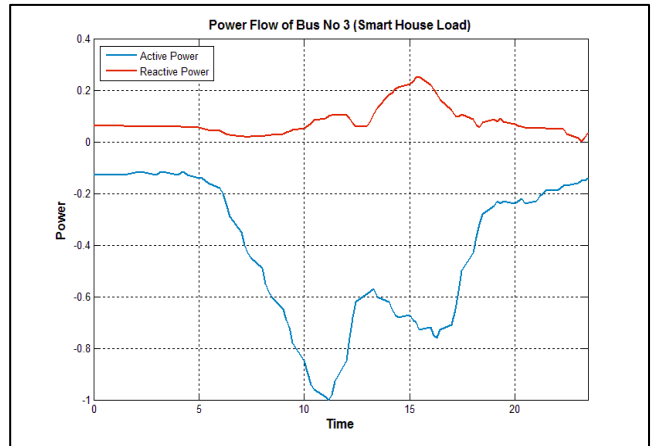


Figure 10 The Power Flow of Bus 3 including Load (Smart House) in a typical day for each 15min period with storage on bus 2

In table 1, total values of distribution loss, payment/profit, and the cost function on one typical day for the two scenarios mentioned in section III are summarized. It must be mentioned that the values in the table are dimension-less, and they can be regarded as the costs or the prices that the end-user should pay to the utility because of regular operation of Micro-Grid, or earns due to improved operation and control of the Micro-Grid.

Table 1. The simulation results for Loss, Payment, and Cost

	Loss	Payment	Cost
Scenario 1	0.1286	2.3433	2.4719
Scenario 2	6.3430	-11.8192	-5.4761

The Cost is equal to summation of Payment and Loss. Payment is simply the overall summation of power from/to grid multiplied by the relevant price for all 15 min periods, and the overall summation of multiplication of the price and consumed power on distribution branches for all 15 min periods is defined as Loss for one typical day. With no loss of generality, it is assumed that the active and reactive power have the same price.

VI. CONCLUSION

The proposed Fuzzy-Logic based control method is applied for Battery Management in Micro-Grid System. In the micro-grid system three buses are considered as renewable generator and Storage, utility, and load (smart house). The goal was to minimize the cost function which is based on distribution loss and payment/profit. The Micro-Grid was simulated under first scenario 1 without any storage units involved. Simulation results obtained for the same Micro-Grid under scenario 2 where the storage system is included with the Fuzzy controller show that scenario 2 outperforms the first scenario where no storage system with fuzzy controller is incorporated. Therefore, using fuzzy controller it is possible to reduce the cost of the Micro-Grid system, and even let the customers make profit from selling the excess power to the utility.

REFERENCES

- [1] Cho, C.; Jeon, J.; Kim, J.; Kwon, S.; Park, K.; Kim, S., 'Active Synchronizing Control of a Microgrid' IEEE Transactions on Power Electronics, issue 99, PP, 2011
- [2] N. L. Srinivasa Rao, G. Govinda Rao, B. Ragnath, "Power Flow Studies Of The Regional Grid With Inter State Tie-Line Constraints" IEEE Conference on Power Quality, pp. 165-171, 2002.
- [3] R. D. Zimmerman, C. E. Murillo-Sánchez, and R. J. Thomas, "MATPOWER's Extensible Optimal Power Flow Architecture," Power and Energy Society General Meeting, 2009 IEEE, pp. 1-7, July 26-30 2009.
- [4] R. D. Zimmerman, C. E. Murillo-Sánchez, and R. J. Thomas, "MATPOWER Steady-State Operations, Planning and Analysis Tools for Power Systems Research and Education," Power Systems, IEEE Transactions on, vol. 26, no. 1, pp. 12-19, Feb. 2011.
- [5] Chang, Sheldon S. L. ; Zadeh, Lofti A. ; "On Fuzzy Mapping and Control", IEEE Transactions on Systems, Man and Cybernetics, pp. 30-34, 1972.
- [6] Zhu Wang, Rui Yang and Lingfeng Wang, " Intelligent Multi-agent Control for Integrated Building and Micro-grid Systems" IEEE PES Innovative Smart Grid Technologies (ISGT), pp.1-7, 2011.

Fuzzy Control of Electricity Storage Unit for Energy Management of Micro-Grids¹

Yashar Sahraei Manjili^{*†}, Amir Rajaei^{*}, Mohammad Jamshidi^{*}, Brian T. Kelley^{*}

^{*}Department of Electrical and Computer Engineering
University of Texas at San Antonio
San Antonio, TX

[†]sca102@my.utsa.edu

Abstract— A Fuzzy Logic-based framework is proposed for control of Battery Storage Unit in Micro-Grid Systems to achieve Efficient Energy Management. Typically, a Micro-Grid system operates synchronously with the main grid and also has the ability to operate independently from the main power grid in an islanded mode. Distributed renewable energy generators including solar, wind in association with batteries and main grid supply power to the consumer in the Micro-Grid network. The goal here is to control the amount of power delivered to/taken from the storage unit in order to improve a cost function, defined based on summation of payment required for purchasing power from main grid or profit obtained by selling power to the main grid and distribution power loss, through reasonable decision making using predetermined human reasoning-based fuzzy rules. Profiles of system variables such as Consumer's Load Demand, Electricity Price Rate, and Renewable Electricity Generation Rate are assumed arbitrarily for obtaining general results. Measures of payment/profit will be extracted to compute amounts of cost and balance for the network which represent benefits of using Fuzzy logic for Storage Unit control with and without considering storage unit capacity limits. Simulation results are presented and discussed.

Keywords- *Micro-Grid Network, Intelligent Control, Power Flow Analysis, Fuzzy-Logic, Load Demand, Variable Electricity Price Rate.*

I. INTRODUCTION

Micro-Grid is a small-scale grid that is designed to provide power for local communities. A Micro-Grid is an aggregation of multiple distributed generators (DGs) such as renewable energy sources, conventional generators, in association with energy storage units which work together as a power supply network in order to provide both electric power and thermal energy for small communities which may vary from one common building to a smart house or even a set of complicated loads consisting of a mixture of different structures such as buildings, factories, etc [1]. Typically, a Micro-Grid operates synchronously in parallel with the main grid. However, there are cases in which a Micro-Grid operates in islanded mode, or in a disconnected state [2]. In this article we assume that when the Micro-grid is connected to the main grid and is working synchronously with it, the flow of electric power can be either from the main grid to the Micro-grid or vice-versa. If the flow

of electric power is from the main grid towards Micro-grid it means that the Micro-grid is consuming the main grid's energy for each KiloWatt-Hour of which the consumer, here Micro-grid, must pay to the Grid. This borrowed power can be either sent to local load to be consumed or can be stored in battery for future use. But, in case the flow of power is from the Micro-Grid towards the main grid, this means that Micro-Grid is delivering power to the main grid. In other words, the excess power generated currently by the renewable electricity generators or stored previously in the batteries is being sold to the main grid, and the Micro-Grid, or in general the consumer, is making profit by selling energy to the main grid. Without loss of generality, we have assumed that the price rate for buying energy from the main grid is equal to the electricity price rate which is sold to the grid. The excess power can be sold to the grid whenever the storage unit or load don't need that power or whenever it is more beneficial to sell power to grid than to use it for supplying the load. However, in this article the main goal is to have the load completely supplied by the required power demand at all conditions. Authors have previously simulated the Micro-Grid assuming no maximum and minimum limit for the amount of energy stored in the battery unit [1]. In this article, storage unit's limits on maximum and minimum amount of stored energy are considered and the results are compared to the results of the previous work.

II. SYSTEM MODEL

The model used for simulation of the Micro-grid network is a three-bus system. One of the busses in the distributed generation model is assumed to serve the renewable generators which include either solar farm, wind farm, or any other renewable generation units either in association with battery storage unit or without storage. Another bus is assumed to be there as the grid (utility) bus which will provide the complement part of the power demanded by the local load that renewable electricity generation system cannot afford. The third bus will be the specific load to which the demanded power is to be provided. This load can be anything from a common building or a smart house, to even a group of plants and factories or a mixture of all of them. Figure 1 shows an

¹This work is partially funded by CPS Energy through Texas Sustainable Energy Research Institute at the University of Texas at San Antonio.

overall Micro-Grid schematic including Renewable Electricity Generators and Storage Unit, Utility, and Local Load.



Figure 1 Micro-Grid Network Schematic

There are three scenarios defined for simulation in this article; scenario 1 deals with a Micro-Grid which includes the renewable electricity generators without any battery storage unit. Therefore there will not be any approaches required for controlling the battery storage system in this scenario. The second scenario deals with the same Micro-Grid system as mentioned in scenario one but after the battery storage unit is connected to the same bus with the renewable generators. Also, the fuzzy approach is applied in this scenario for energy management through battery unit control. The point in this scenario is that the battery storage is assumed to be an ideal battery without any maximum or minimum limits on stored energy, i.e. infinite battery capacity. In the third scenario which is the last one, the Micro-Grid is assumed to have everything mentioned in scenario two plus the fact that maximum and minimum limits of stored energy are taken into account for storage unit and are assumed to be 85% and 15% of the nominal maximum storable energy respectively. These three scenarios will be described in more detail in section III.

A. Characteristics of Buses in Scenario 1

The three buses in the model of Micro-Grid Network simulated in this article have the following characteristics in the first scenario:

- Bus 1 is of type PQ and is used as the renewable electricity generation unit's bus.
- Bus 2 is of type Slack (reference) and is used as the Utility (grid) bus.
- Bus 3 is of type PV and is used as the Local Load bus.

B. Characteristics of Buses in Scenario 2

The characteristics of the three buses in the Micro-Grid Network model simulated in this article are as follows in the second scenario:

- Bus 1 is a PQ bus and is used as the bus for renewable generation unit and infinite-capacity battery storage.
- Bus 2 will be the Slack (reference) bus and is used as the Utility (grid) bus.
- Bus 3 is of type PV and is used as the Local Load bus.

C. Characteristics of Buses in Scenario 3

Bus characteristics of the three buses in the Micro-Grid Network model simulated in this article are as follows in the third, i.e. last, scenario:

- Bus 1 is a PQ bus and is used as the bus for renewable generation unit and finite-capacity battery storage unit.
- Bus 2 will be the Slack (reference) bus and is used as the Utility (grid) bus.
- Bus 3 is of type PV and is used as the Local Load bus.

This must be noted that battery units are assumed to be ideal batteries, i.e. no dynamic transient of change in the amount of stored energy in batteries are assumed, i.e. the amount of stored energy in the batteries is assumed to be changing as a pure ramp by time in both ascending and descending direction.

III. PROBLEM STATEMENT

The important point which lies behind the idea of this article is that we have assumed the real-time pricing for electricity. The update duration of pricing is assumed to be 15 minutes, which means that the price per KiloWatt-Hour of electricity consumed by the customers of the load region is updated every 15 minutes. This means that the money consumers need to pay to the utility for the same amount of energy used during different time-intervals might be different. Therefore, a function is required to be defined which takes into account the difference between amount of power given to the utility by the Micro-Grid, and the amount of power taken from the utility by the Micro-Grid. The Equation 1 represents this cost function:

$$Cost = \sum_{t=1}^T (Pr(t) \cdot (S_U(t) + S_L(t))) \quad (1)$$

where the electricity price $Pr(t)$ is determined by the CPS energy every 15 minutes for the next 15 minute period. $S_U(t)$ is the amount of power transferred to/from the Grid during each 15 minute period. If power is received from the Grid $S_U(t)$ will be positive, and if power is delivered to the grid in case of excess power generation by the renewable generation system $S_U(t)$ will appear in the equations with a negative sign. $S_L(t)$ is the amount of distribution loss which will occur on the branches we have between these three buses in the Micro-Grid system during each 15 minute period. Depending on whether the load is getting how much of its demanded power from renewable generation system and how much from the Grid, and also depending on whether the renewable generation system is producing excess power and is selling the excess power to the Grid, this power Loss will vary.

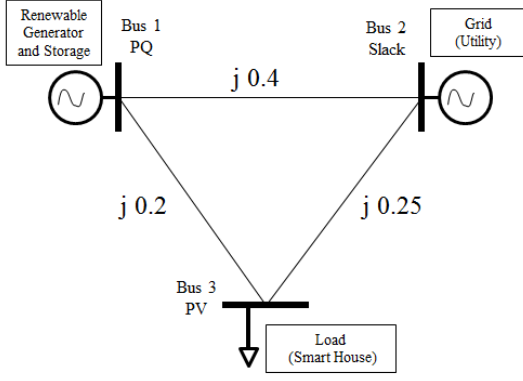


Figure 2 Three Bus Model for Micro-Grid

Figure 2 represents the three-bus model used for simulation of the Micro-Grid in different scenarios along with the branch impedances and the types of buses. Simulation is done on the Micro-Grid system considering three scenarios. In the following the summary of these scenarios is given:

A. Scenario 1

Analysis of the Micro-Grid system profits and costs under real-time electricity pricing policy; in this scenario the simulation, analysis and study will be done on a Micro-Grid model which includes the renewable generation unit without any battery storage unit. Therefore there will not be any approaches required for controlling the battery storage system.

B. Scenario 2

Fuzzy Control of the Micro-Grid system under real-time electricity pricing policy; the cost function assumed in this scenario is the same as the cost function used in the scenario 1. The main difference here is that the storage unit exists in the network and will appear to be on the same bus with the renewable electricity generation unit. The storage unit in this scenario is assumed to be ideal with infinite capacity.

C. Scenario 3

Fuzzy Control of the Micro-Grid system under real-time electricity pricing policy; the cost function assumed in this scenario is the same as the cost function described in the two scenarios 1 and 2. In this scenario also the storage unit exists in the network on the same bus with the renewable generation unit. The critical difference between this scenario and scenario 2 is that the storage unit in this scenario is assumed to be an ideal battery with finite capacity. Therefore, the maximum and minimum amounts of energy stored in the batteries are finite values and serve as boundaries which cannot be exceeded.

The power flow calculation and analysis in the Micro-Grid is the key to simulate the whole system. There are a number of well-known methods for calculation of power flow in the distributed generation network [3]. There are four different types of busses considered in a distributed generation network, the characteristics of which will be calculated in power flow

algorithms. These four types include PQ, PV, Slack, and isolated [4, 5].

IV. FUZZY CONTROL APPROACH

The control strategy implemented in this paper is to use Fuzzy Logic [6] for controlling the power flow to/from the battery storage unit in order to improve the value of the cost function introduced in section III. The three input variables to the fuzzy inference engine are Electricity Price, Renewable Generation Rate, and Load Demand. The Fuzzy inference engine serves as the controller which determines a measure of the amount of power that must be sent to/taken from the battery unit during the next time interval, i.e. 15 minute period, based on the current values of its three inputs.

The fuzzy membership functions for the three inputs price, load demand, and renewable generation rate, and also for the output variable which determines the amount of power transaction with the storage unit are shown in figure 3.

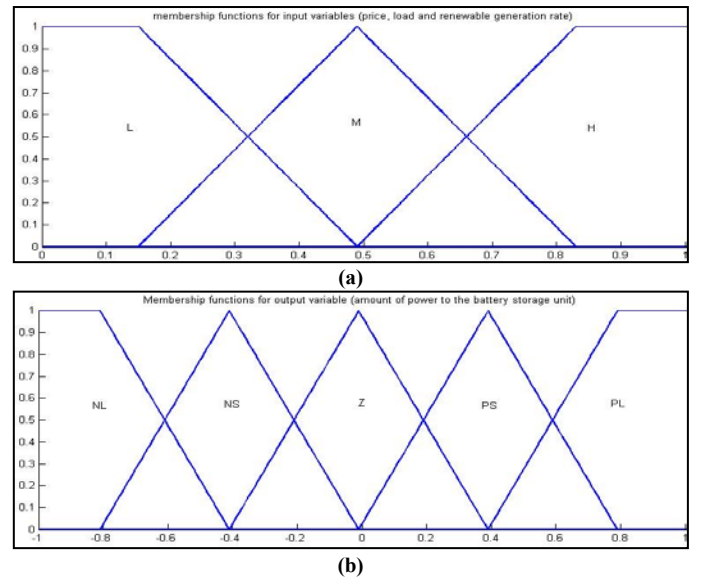


Figure 3 Fuzzy Membership functions for input and output variables of the Fuzzy Controller; (a) inputs (b) output

The numerical values for these three input variables are normalized to the [0 1] interval, and then are Fuzzified using three fuzzy sets defined as Low (L), Medium (M), and High (H) as can be seen in figure 3a. The input variables after fuzzification will be fed to a fuzzy inference engine where the rule-base is applied to the input-output variables and the output will be determined by human reasoning. There is only one output variable from the fuzzy controller. This variable determines the amount of power to be stored in the battery, or to be drawn out from battery in each 15 minute interval. As represented in figure 3b, output variable fuzzy set is assumed to have five membership functions called Negative Large (NL), Negative Small (NS), Zero (Z), Positive Small (PS), and Positive Large (PL). The power drawn from the batteries can be used to complement the renewable electricity generation unit's power for providing the load's demand, can be sold to the Grid, or can be partially used for both reasons [7]. The role of fuzzy inference engine is critically important for obtaining

satisfactory results. For example two of the rules can be as follows:

IF the *Price* is *Low*, AND the *Renewable Generation* rate is *High*, AND the *Load Demand* is *Medium*, THEN the amount of *Power to Battery* storage system should be *Positive-Large*.

IF the *Price* is *High*, AND the *Renewable Generation* rate is *Low*, AND the *Load Demand* is *Medium*, THEN the amount of *Power to Battery* storage system should be *Negative-Large*.

The primary goal in these simulations is to provide the local load with all the power it demands at any circumstances. Meanwhile, this must be noted that whenever the price is high or low, the secondary goal will be to sell the most power to the main grid, and to purchase the most power possible from the main grid respectively. Under low-price electricity conditions, the action required by the rules might even require the Micro-Grid network to purchase power from grid and store it in the battery storage unit because the main point here is that the Price is low. This means by storing the energy in the batteries during low price times, the system will have enough stored energy in order to sell to the Grid during high-price periods. Even under cases of High local Load demand this will be a rational strategy. Therefore, having feasible rules predefined for the fuzzy system will help improve the cost function drastically. The proposed approach may even sometimes result in making the cost function value negative, which means that the system is making some profit instead of paying to the utility by the use of this control approach.

V. SIMULATION RESULTS & DISCUSSIONS

The simulation is done on the three bus system shown in figure 2. The Gauss-Seidel algorithm is implemented using Matlab for power flow calculation [8]. Some typical data are generated for electricity price rate, time-varying Load Demand and Renewable Generation Rate.

The power demand of the Load on bus 3 (Smart House) is supplied by two generators on buses 1 and 2. Bus 1 includes solar panel and/or storage unit and bus 2 is slack which is connected to utility as shown in figure 2.

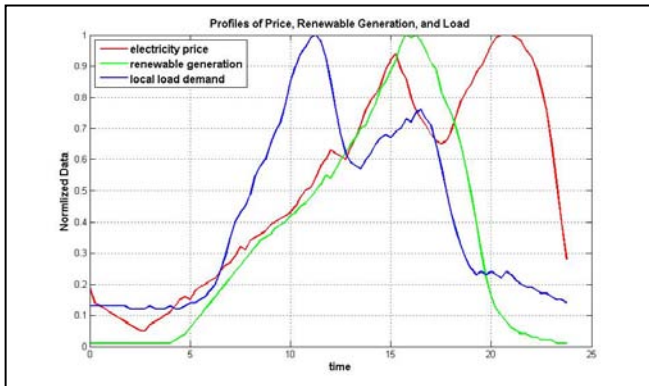


Figure 4 Profiles of Price, Renewable Generation, and the Load

The numerical values of the data profile for the three input variables which are fed to the fuzzy controller are shown in figure 4 during a typical day. These variables include electricity price which is assumed to be variable as time passes,

renewable electricity generation rate, and local load demand. The data is generated arbitrarily for simulation purposes only with regard to the fact that the peak electricity consumption duration of the whole region of interest for the main grid is around 8:30 pm where the electricity price gets to its maximum value. The simulation results for scenario 1 are represented in figures 5 to 7.

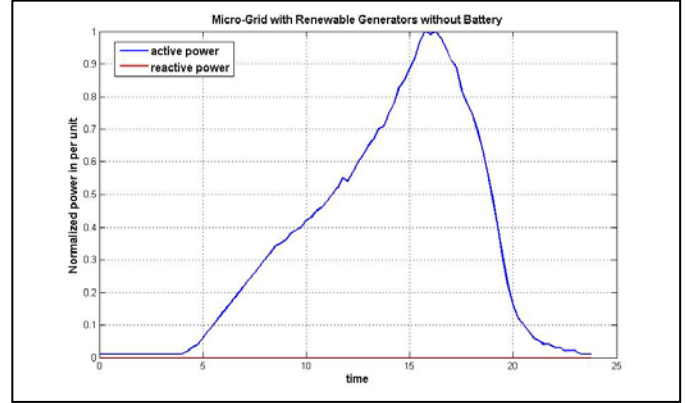


Figure 5 Power Flow of Bus 1 connected to Solar Panels; scenario 1

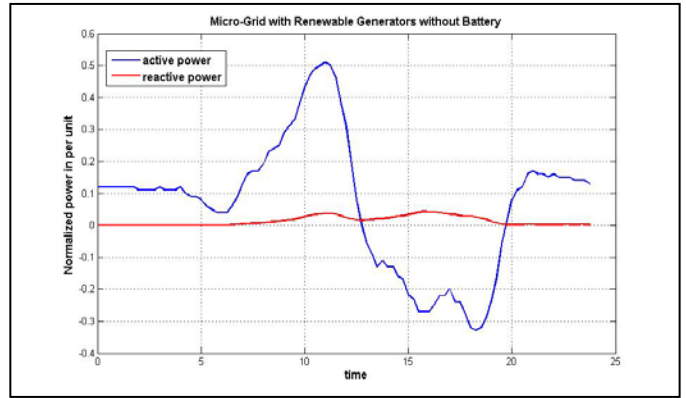


Figure 6 Power Flow of Bus 2 connected to Utility; scenario 1

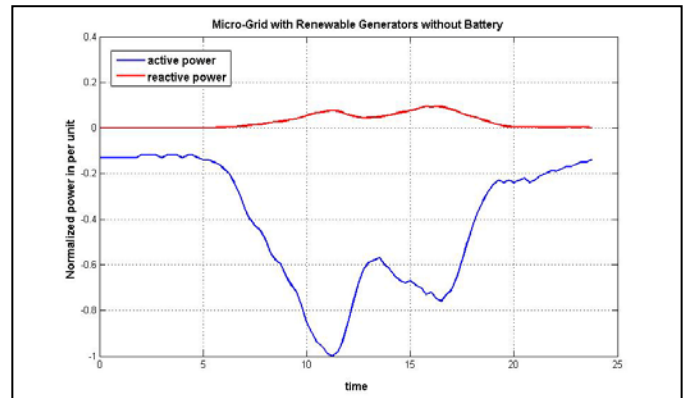


Figure 7 Power Flow of Bus 3 connected to Load; scenario 1

As it can be inferred from figure 5, the value of reactive power for bus 1 is constantly zero which corresponds to the assumption that the renewable generators do not provide reactive energy. Figure 6 shows that the active power is taken from the Utility during first half of the day time, and during

most of the second half of the day the active power is being delivered to the grid. Load is evidently consuming active power regarding the blue curve represented in figure 7.

Simulation results for scenario 2 which associates ideal storage with infinite capacity to the renewable electricity generators on bus 2 are represented in figures 8 and 9.

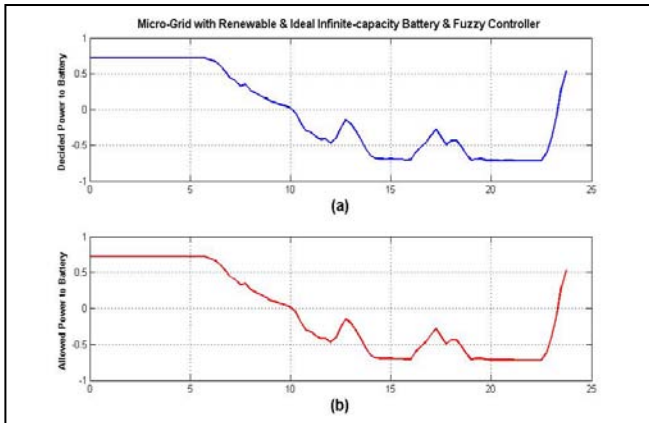


Figure 8 Output of the Fuzzy Controller, i.e. measure of the amount of power given to/taken from storage unit; scenario 2; (a) Theoretically decided (b) Practically allowed

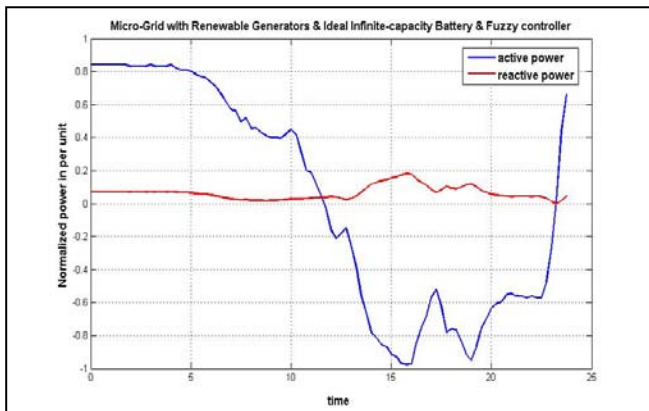


Figure 9 Power Flow of Bus 2 connected to Utility; scenario 2

Figure 8 parts a and b are matched to each other and this clearly shows that any value decided by the Fuzzy Controller for the power to be given to Battery or to be taken from it can be practical since battery unit assumed in scenario 2 is of infinite capacity. Figure 9 shows that active power is taken from the utility during first half of the day, and in the second half of day the active power is mostly being sold to the grid which can be deduced by the negative value of the blue curve in figure 9. The point is that the first part of the active power diagram is raised dramatically due to fuzzy decision making which means that the system is absorbing more active power from the grid during low-price hours and stores the power in the storage unit. Also, the second part of the active power diagram has fallen more in comparison to the same section of figure 6 which denotes on increase in the amount of power drawn from storage unit and using this power for partially charging the load and also selling the excess power to the grid

during high-price hours. This strategy results in reduction of cost function value or in other words increases the profit.

Remembering that the pricing periods are assumed to be 15 minute periods and one day is 24 hours overallly there will be 96 periods of pricing during one day period. The summation of payment/profit and the loss during each of the periods will give us the overall value of cost function for one day. The process can be extended to one week, one month, one year etc.

Output of the fuzzy inference engine which represents the power rate given to battery is shown in figure 11. Whenever the value of this variable is positive it means that power is delivered to the storage unit and if the power is drawn from the storage unit, the value will be negative.

Simulation results for scenario 3 in which ideal finite-capacity storage is added on bus 2 in Micro-Grid network are represented in figures 10 to 12.

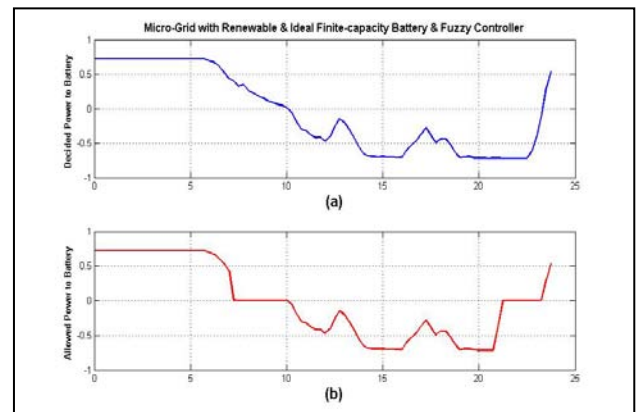


Figure 10 Output of the Fuzzy Controller; scenario 3; (a) Theoretically decided (b) Practically allowed

Figure 10 parts a and b are not matched to each other and this shows the fact that the values decided by the Fuzzy Controller for the power to be given to Battery or be taken from it might not be practical since battery unit assumed in scenario 3 is of finite capacity and the maximum and minimum limits of stored energy should be taken into account.

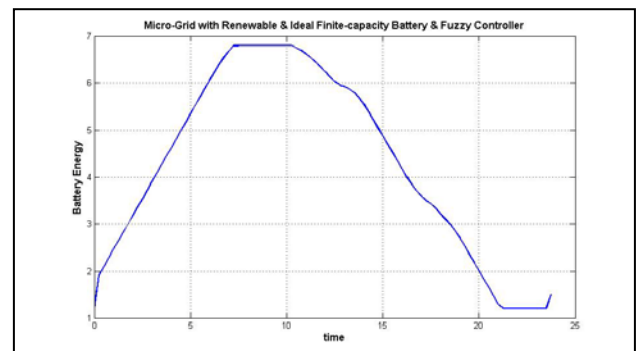


Figure 11 Measure of Energy stored in Battery; scenario 3

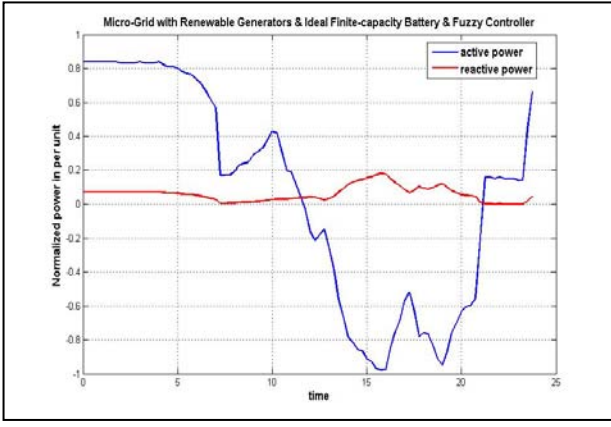


Figure 12 Power Flow of Bus 2 connected to Utility; scenario 3

The Center of Gravity, i.e. Centroid, defuzzification method is used for computing the crisp values of the output variable from the union of the Fuzzy rules. The formula used for defuzzification is shown in Eq. 2

$$y_{crisp} = \frac{\sum_{i=1}^n (\max_j (\mu_i) \times y_i)}{\sum_{i=1}^n \max_j (\mu_i)} \quad (2)$$

Where y_{crisp} stands for crisp value of output variable. i changes between 1 and n , and refers to the number of discrete point at which the calculation is being done. j changes between 1 and the number of membership functions of output variable which in this case is 5, and represents the number of membership function curve for which we are getting the membership value of i^{th} point in the universe of discourse of the output variable. Therefore, $\max_j (\mu_i)$ represents the final membership value of the i^{th} point in the universe of discourse of output, i.e. y_i . Equation 3 shows the relation between Balance, Distribution Loss and the overall Cost of Electricity.

$$Balance = Loss + Cost \quad (3)$$

In table 1, total values of distribution loss, cost, and balance on one typical day for the three scenarios mentioned in section III are summarized. It must be noted that the values in the table are unit-less, and they can be regarded as measures for payment that the end-user should make to the utility because of regular operation of Micro-Grid, or profits earned due to improved operation and control of the Micro-Grid.

Table 1. Simulation results for Loss, Cost and Balance

	Loss	Cost	Balance
Scenario 1	0.1339	1.2294	1.3632
Scenario 2	6.6039	-17.6716	-11.0677
Scenario 3	6.6039	-13.3021	-6.6982

Cost is simply the overall summation of power from/to grid multiplied by the relevant price for all 15 min periods. The overall summation of multiplication of the price and wasted power on distribution branches for all 15 min periods is defined as Loss. With no loss of generality, it is assumed that the reactive power has one tenth the value of active power.

We can see that scenario 2 will provide the consumer with the most possible profit on balance and this is because of the fact that the battery unit used in scenario 2 is assumed to be of infinite capacity. Therefore there will be chance for utmost storage of power in the battery whenever required and the battery can provide that stored power completely to the Micro-Grid for appropriate usage any time. This is not a practical case though. In scenario 3 which is the practical case compared to the second scenario, battery storage unit is assumed to be of limited capacity and therefore, maximum and minimum limits of the stored energy in the battery might prevent the control system to apply the decided action on the storage unit thoroughly. This might cause a drop in the benefits that consumer will obtain using this approach as it can be seen by comparing the values of Balance for the two scenarios 2 and 3. However, by improvements in the battery production technologies this issue can be solved to good extents.

VI. CONCLUSION

The proposed Fuzzy-Logic based control method is applied for Battery Management in Micro-Grid Systems. In the micro-grid system three buses are considered as renewable generator and storage, utility, and load (smart house). The goal was to reduce the balance which is based on distribution loss and cost. The Micro-Grid was simulated under three scenarios. Simulation results obtained for Micro-Grid under scenario 2 where the ideal infinite-capacity storage is involved with the Fuzzy controller outperform the other two scenarios. However this is not practical. In third scenario, ideal limited-capacity storage was involved and the results were satisfactory. Therefore, using fuzzy controller it is possible to reduce the cost of the Micro-Grid system, and even let the customers make profit from selling the excess power to the utility.

REFERENCES

- [1] Y. S. Manjili; A. Rajaei; B. Kelley; M. Jamshidi, "Fuzzy Control of Storage Unit for Energy Management in Micro-Grids" University of Texas at San Antonio College Of Science Conference, UTSA-COS 2011 (Best paper award winner)
- [2] C. Cho; J. Jeon; J. Kim; S. Kwon; K. Park.; S. Kim, "Active Synchronizing Control of a Microgrid" IEEE Transactions on Power Electronics, issue 99, pp., 2011
- [3] N. L. Srinivasa Rao; G. Govinda Rao; B. Ragunath, "Power Flow Studies Of The Regional Grid With Inter State Tie-Line Constraints" IEEE Conference on Power Quality, pp. 165-171, 2002.
- [4] R.D. Zimmerman; C.E. Murillo-Sánchez; R.J. Thomas, "MATPOWER's Extensible Optimal Power Flow Architecture" IEEE Power and Energy Society General Meeting, pp. 1-7, July 26-30 2009.
- [5] R.D. Zimmerman; C.E. Murillo-Sánchez; R.J. Thomas, "MATPOWER Steady-State Operations, Planning and Analysis Tools for Power Systems Research and Education" IEEE Transactions on Power Systems, vol. 26, no. 1, pp. 12-19, Feb. 2011.
- [6] S. L. Chang; L. A. Zadeh, "On Fuzzy Mapping and Control", IEEE Transactions on Systems, Man and Cybernetics, pp. 30-34, 1972.
- [7] Z. Wang; R. Yang; L. Wang, "Intelligent Multi-agent Control for Integrated Building and Micro-grid Systems" IEEE PES Innovative Smart Grid Technologies (ISGT), pp.1-7, 2011.
- [8] G.M. Gilbert; D.E. Bouchard; A.Y. Chikhani, "A Comparison Of Load Flow Analysis Using Distflow, Gauss-Seidel, And Optimal Load Flow Algorithms" IEEE Canadian Conf. on Elec. and Comp. Eng. 1998

Cognitive Radio Capacity Analysis for Smart Grid Networks

Amir Rajaei, KranthiManoj Nagothu, Brian Kelley Senior Member IEEE,
Electrical and Computer Engineering, The University of Texas at San Antonio, TX, USA

Abstract— In this paper a framework is presented based on 4G Cognitive Radio (CR) network capable of communicating with high numbers of geographically dispersed smart meters for command and control feature concurrently with private cellular network. Our approach uses pervasive smart grid systems (i.e. cloud data centers) as the central communication and optimization infrastructure supporting metropolitan area based smart meter infrastructure. In this paper, we investigate the performance of various scheduling algorithms in context with CR units to provide a satisfactory tradeoff between maximizing the system capacity, achieving fairness among cognitive users. We lay as a framework evaluation 3GPP LTE system model simulations. Our system level simulation results show that the 4G CR network model meets the smart grid protocols requirements for a multi-user CR network of Smart meters.

Keywords—4G Cognitive radio networks, cloud data center, scheduling algorithms, and smart meters

I. INTRODUCTION

The smart grid of the future is generally perceived to be an intelligent energy delivery system that supports plug-and-play integration of power, information, and security services. [1]. We consider the future smart grid as leveraging Information and Communications Technology (ICT) facilitated by the smart meter (also named as Advance Infrastructure Metering (AMI)) information networks. The smart meter enables the flow of real-time information within the power utility, between the power utility and its customers. It also provides customers and utilities the technology to optimize their energy consumption in participating in closed loop demand response; moreover, these services allow convergence of high penetrations of renewable energy components into grid and third party energy management applications for demand optimization. It is essential for AMI to be networked since it enables system wide sensing, utility and customer linkages, and future self healing capability.

Communication network infrastructures represent a very large capital expense. Much of this expenditure is due to the high prices of purchasing licensed bands either from the FCC auction process or from existing licensed band owners. We therefore analyze a novel, low cost framework based on 4G cognitive radio smart meter networks enabling command and control, demand optimization and other features. Research on CR has evolved from SDR (see [2-3]) with an objective of

efficient utilization of radio spectrum. In this paper, we analyze CR in the context of smart energy systems. Although there have been significant advances and improvements in CR hardware, algorithms, and protocols, less attention has been given to developing ubiquitous and pervasive metropolitan scale CR networks, particularly with respect to smart grid information networking[4]. A metropolitan infrastructure based CR networks is shown in Fig. 1. In this context, there are major challenges to overcome such as Secondary Users (SU) should sense the spectrum and timely model the behavior of the Primary Users (PU). The other issue is how the SUs manage the available spectrum resources and share the resources among the SUs to satisfy the smart grid protocol requirements and meeting the interference constraints suggested by the FCC Spectrum Policy Task.

In such a system, our objective for SUs (i.e. AMI) is to efficiently transmit their delay sensitive traffic over the network and meet the QoS requirements of the smart grid protocol. In this paper, we investigate different scheduling policies that maximize the downlink sum throughput in the given area and achieving fairness among the SUs. We present an opportunistic scheduling policy that exploits both maximizing the downlink sum throughput and fairness under time-varying channel conditions for multi-user CR network in a metropolitan based environment.

Several authors have defined aspects of AMI networking in smart grids. Mesh, Ethernet and cellular AMI network topology for smart grid has been proposed. In [5] the authors propose mesh networks of Zigbee based transmission architecture. Challenging issue with line of sight requirements in Zigbee is the limit of single-hop range to hundreds of feet. Inefficiencies arise when transmission distances featured by the protocols in the entire metropolitan area for AMI networking. In [6], the authors discuss communication infrastructure based on Ethernet (LAN and WAN). The approach will support automated meter readings and customer home appliance connections. However, wireline systems are not always available. Customer subscription to service must occur and wired system can be challenging to rapidly redeploy, particularly in swiftly enveloping emergencies.

The authors in [7] describe a framework for RF mesh networking interfaced with high speed WiMAX access networks. In [8], overview of architecture, hardware platform, is reported to enable CR for smart grid communications. However, to our knowledge anywhere in the literature a complete multi-user capacity analysis using CR network in

context with smart grid has been yet reported. Our work discusses the CR network infrastructure architecture from 4G perspective. We also present multi-user performance analysis of various scheduling algorithms in context with AMI units considering the delay occurred due to offloading the processes to cloud in our architecture.

The rest of the paper is organized as follows. Section II overviews the 4G CR system architecture in brief. In section III we present overall 4G CR system model detailing the sensing model and different scheduling policies and their properties. Section IV discusses the performance of the different scheduling algorithms with system level simulations and concludes this paper.

II. 4g Cognitive radio framework

A. 4G cognitive radio system architecture

We presume a LTE network as a CR LTE network (4G CR), if the LTE work is adopted the CR techniques. We consider a cloud data center infrastructure based CR network coexisting with PU network shown in Fig.1. The coverage of both the CR base station and PU network base station are similar. As depicted in the Fig. 1 at the center of the each cell, there is base-station which is shared as e Node-B for PUs and as antenna for SUs. The PU base-station only serves to PUs as it lacks the CR protocols capabilities to support SUs. However, it may consider supporting certain features in order to communicate with SUs.

A CR system does not own a license band to operate in a desired band. Hence, the spectrum access is allowed only in an opportunistic manner. The licensed user of the frequency band is always given priority access to the shared channel (time-frequency resource). Due to their priority in spectrum access, the operations of PUs are always 1st in the transmission queue so as to not be affected by unlicensed users. All the SUs have the same right to access the spectrum; SUs should compete with each other for the same unlicensed band. Thus, sophisticated spectrum sharing methods among SUs are required in this architecture. If multiple SUs network operators reside in the same unlicensed band, fair spectrum sharing among these networks is also required and different scheduling algorithms are discussed in detail in section III.

Placement of a Cognitive Radio Antenna on the BTS tower may occur in tandem with deployment of the cellular provider antenna. The CR senses the spectral environment over a wide frequency band, particularly the spectrum in the cell region. It identifies the unused bands in the spectrum. These bands could be owned by cellular companies or license television band owners, but are not limited to these bands or to licensed bands. Sensed information using the CR is relayed to cloud data center. In principle, eNode-B which terminates the air interface protocol and first point of contact for PU is located at the primary user base-station. However, in proposed architecture all the cognitive radio service, waveform service, protocols service, security service, scheduling and control services are displaced into cloud data center. The CR services identify unused frequency bands, the relevant cognitive services

residing in the cloud data center generates a clear to send (CTS) signal.

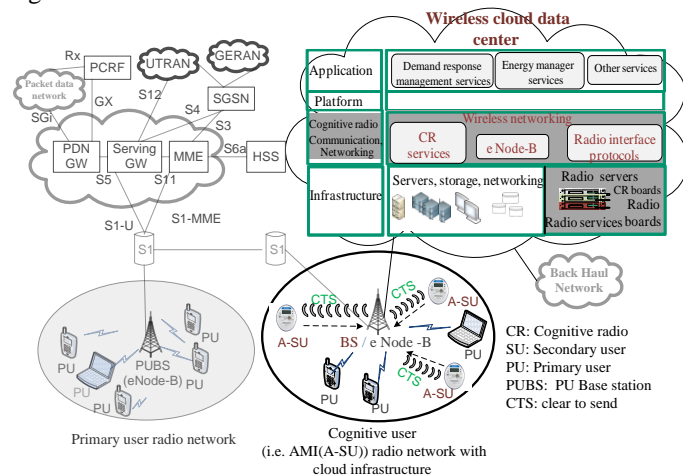


Fig. 1. 4G CR network system architecture: Scenario of multiple AMI meters serviced by cognitive radio network infrastructure enabled by cloud center coexisting with private cellular network

The CTS is sent back to the AMI meters through the feedback channel via base station. Eventually, the CR antenna relays CTS signals to every AMI in the cell region for uplink transmission.

1) *Pervasive smart grid systems*

The energy services of the future can be privately contracted services or public services. The cloud center enables convenient, on-demand network access to a shared pool of configurable, computing resources (e.g., networks, servers, storage, applications, and services) that can be rapidly provisioned and released with minimal management effort. There are different cloud computing platform classifications. Standard architectures includes Abi (or Abiquo), Nimbus Open Nebula, Azure (Microsoft), Google (App Engine), Blue (IBM) and Mosso (Rackspace). Fig.1. depicts the model for a cloud data center architecture optimized for based smart grids. Our Wireless Cloud Data (WCD) model is organized into four principle layers: application layer, platform layer, CR communication and networking layer and infrastructure layer. The first two layers are akin to existing cloud architectures. However, the lower two layers are augmented to enable the CR networking and wireless services. CR communication and networking layer provides services such as cognitive radio services, waveform services, Radio Link Control (RLC), and Medium Access Control (MAC) services. CR services, which provide spectrum management and spectrum sensing, are discussed in detail in section III. The infrastructure layer facilitates the effective integration of computing resources, storage, networks to deploy applications and operating systems. We augment our cloud infrastructure microprocessor racks with FPGA boards targeted to processing high computation rate processes typically associate with CR services, communication waveform signal processing and coding.

III. CR SYSTEM MODEL

In the paper system model 4G cellular network is considered with N_{su} secondary users sharing the spectrum simultaneously

with N_{pu} primary users. It is presumed in the context that the secondary users (i.e. AMI meters) are fixed in sense of geographical location and yields to fixed first and second statistical moments of SINR.

A. Spectrum Sensing

The spectrum sensing is one of the main layer task for CR system to obtain the spectrum usage information and the presence of PUs. Spectrum detection is based on the detection of the signal from PU through the observation of cognitive radio network.

The sensing methods can be categorized in three methods: i) Energy Detection, ii) Matched Filter, and iii) Feature Detection. The spectrum sensing method considered for this paper is Energy Detection. Since, it is particularly suitable for multiband sensing because of its low computational and implementation complexities [9-10]. We presume using OFDM modulation with M sub carriers with bandwidth W . In this paper we premised the IEEE 802.22 as it has developed air interface for opportunistic SU access to the TV spectrum in which PUs change slowly [11].

The timing model for spectrum sensing is shown in Fig. 2.a and spectrum mobility model for SUs is depicted in Fig. 2.b. The required time for channel estimation, spectrum sensing and sharing is indicated by τ . According to the [12] the given channel estimation delay is for WCDMA/HSDPA, so the scaled delay for a shorter sub-frame length in UTRAN LTE is considered for this paper. For each Resource Block (RB), there are 7 frames in time frame and 12 subcarriers and each square in Fig. 2.b is called Resource Element (RE). For example, in Fig. 2.b, RE (10, 7) means that the frequency carrier at frame 7 and subcarrier 10 is occupied by primary user 3. At each time, idle resource elements will be detected and allocated to SUs. Once a PU requests the subcarrier occupied by the active SU, SU has to leave the spectrum and try to find another idle resource element to continue transmission. In Fig. 2.a, T is time length of each frame and K is number of frames. The idle RB or hole is a band can be used by SU without interfering with PU. Supposed that received signal at SUs sampled at f_s over i th sub channel where values of discretized samples at $t = n T_s$, which T_s is $0.1\mu s$ in our framework. In discrete form, when the primary user is active, we define two hypotheses as follow:

$$\begin{cases} y_i(n) = h_i x_i(n) + u_i(n) & , \mathcal{H}_{1,i} \\ y_i(n) = u_i(n) & , \mathcal{H}_{0,i} \end{cases} \quad (1)$$

That h_i is the subchannel gain between PU transmitter and SU receiver with variance $E(|h_i|^2) = \sigma_{h,i}^2$. The signal transmitted, x_i , by PU is assumed to be independent and identically distributed (i.i.d), $\mathcal{CN}(0, \sigma_s^2)$, and u_i , the noise, is circularly symmetric complex Gaussian (CSCG) noise.

B. Energy Detection

In order to detect the RF energy in the certain subcarrier for a given PU, the CR service residing in the WCD samples on-the-air signal constructs the following test statistics as the

observed energy summation within N samples to decide on the presence of the active users in targeted subcarrier [13].

$$\mathcal{U}_i = \begin{cases} \frac{1}{N_i} \sum_{n=1}^{N_i} |h_i x_i(n) + u_i(n)|^2 & , \mathcal{H}_{1,i} \\ \frac{1}{N_i} \sum_{n=1}^{N_i} |u_i(n)|^2 & , \mathcal{H}_{0,i} \end{cases} \quad (2)$$

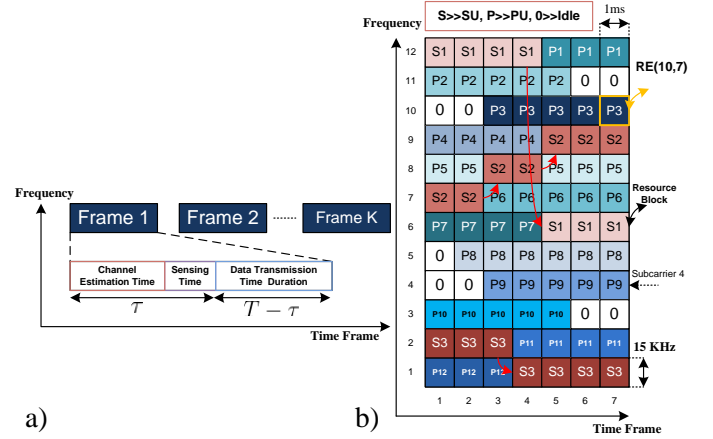


Fig. 2. a)Timing Model, b)Resource Block & Dynamic Resource Management

N_i is number of samples transmitted on duration τ_i which is equal to $N_i = \tau_i f_s$. The PDF of \mathcal{U}_i is Central Chi Square distribution with $2N_i$ degrees of freedom, $\mathcal{X}_{2N_i}^2$, for when no PU exists and on Central Chi Square distribution with $2N_i$ degrees of freedom and non-centrality parameter $2\gamma_i$, $\mathcal{X}_{2N_i}^2(2\gamma_i)$, for the state that PU exists. So:

$$\mathcal{F}_{\mathcal{U}_i}(\mathcal{U}_i) = \begin{cases} \mathcal{X}_{2N_i}^2 = \frac{1}{2^{2N_i} \Gamma(N_i)} \mathcal{U}_i^{N_i-1} e^{-\frac{\mathcal{U}_i}{2}} & , \mathcal{H}_{1,i} \\ \mathcal{X}_{2N_i}^2(2\gamma_i) = \frac{1}{2} \left(\frac{\mathcal{U}_i}{2\gamma_i} \right)^{\frac{N_i-1}{2}} e^{-\frac{2\gamma_i + \mathcal{U}_i}{2}} & , \mathcal{H}_{0,i} \end{cases} \quad (3)$$

where the signal to noise ratio (SNR) is depicted by $\gamma_i = \frac{\sigma_{x_i}^2 \sigma_{h,i}^2}{\sigma_{u_i}^2}$, $\Gamma(\cdot)$ denotes the gamma function, $I_\alpha(\cdot)$ is the first kind modified Bessel function of degree α .

Two performance parameters for spectrum sensing are probability of detection, P_d , and probability of false alarm, P_f , which is probability of when the frequency is unoccupied but we get alarm that the frequency is used. Hence, Higher P_d protects PU from interfering with SUs and smaller P_f causes better band usage efficiency. To calculate probability of detection [14]:

$$P_{d,i}(\epsilon_i, \tau_i, \gamma_i) = Pr(\mathcal{U}_i > \epsilon_i | \mathcal{H}_1) = \int_{\epsilon_i}^{\infty} p_1(x) dx \quad (4)$$

where ϵ_i is threshold and τ_i is denoted sensing time for i th subchannel.

$$P_{d,i}(\epsilon_i, \tau_i, \gamma_i) = \mathcal{Q}\left(\left(\frac{\epsilon_i}{\sigma_{u_i}^2} - \gamma_i |h_i|^2 - 1\right) \sqrt{\frac{\tau_i f_s}{2\gamma_i |h_i|^2 + 1}}\right) \quad (5)$$

Now the probability of missed detection can be defined as:

$$P_{m,i}(\epsilon_i, \tau_i, \gamma_i) = 1 - P_{d,i}(\epsilon_i, \tau_i, \gamma_i) \quad (6)$$

we have following equations for probability of false alarm,

$$P_{f,i}(\epsilon_i, \tau_i) = Pr(\mathcal{U}_i > \epsilon_i | \mathcal{H}_0) = \int_{\epsilon_i}^{\infty} p_0(x) dx \quad (7)$$

$$P_{f,i}(\epsilon_i, \tau_i) = \mathcal{Q}\left(\left(\frac{\epsilon_i}{\sigma_{u_i}^2} - 1\right)\sqrt{\tau_i f_s}\right) \quad (8)$$

Usually to evaluate the performance of energy detection, the goal is to minimize P_f for a target P_d or to maximize P_d for a target P_f . At first we assume $P_{d,i,target}$ is our target probability of detection,

$$\epsilon_i(P_{d,i,target}) = \left(\frac{\mathcal{Q}^{-1}(P_{d,i,target})}{\sqrt{\frac{\tau_i f_s}{2\gamma_i |h_i|^2}}} + \gamma_i |h_i|^2 + 1\right) \sigma_{h_i}^2 \quad (9)$$

$$P_{f,i}(\epsilon_i(P_{d,i,target}), \tau_i) = \mathcal{Q}\left(\mathcal{Q}^{-1}(P_{d,i,target}) \sqrt{2\gamma_i |h_i|^2 + 1 + \gamma_i |h_i|^2 \sqrt{\tau_i f_s}}\right) \quad (10)$$

$P_{f,i}(\epsilon(P_{d,i,target}), \tau_i)$ is the probability of false alarm regard to target $P_{d,i}$, and \mathcal{Q}^{-1} is the inverse of complementary error function. For a target $P_{f,i,target}$ we have:

$$\epsilon_i(P_{f,i,target}) = \left(\frac{\mathcal{Q}^{-1}(P_{f,i,target})}{\sqrt{\tau_i f_s}} + 1\right) \sigma_{h_i}^2 \quad (11)$$

$$P_{d,i}(\epsilon_i(P_{f,i,target}), \tau_i) = \mathcal{Q}\left(\frac{\mathcal{Q}^{-1}(P_{f,i,target}) - \gamma_i |h_i|^2 \sqrt{\tau_i f_s}}{\sqrt{2\gamma_i |h_i|^2 + 1}}\right) \quad (12)$$

$P_{d,i}(\epsilon(P_{f,i,target}), \tau_i)$ is the probability of detection when $P_{f,i}$ is targeted. As a result, in this part, probability of false alarm and detection based on $P_{d,i,target}$ and $P_{f,i,target}$, respectively, are calculated.

C. Primary User Activity Model

In this section, we present a model for primary users' activities which is directly proportional to CR network performance. In our Markov chains model, we consider two states (Busy by PU and Idle) for each subcarrier. Since each user arrival is independent, each transition follows the Poisson arrival process. Thus, the length of Busy and Idle periods are exponentially distributed. The Poisson distribution is considered in the modelling with arrival rate, α , and departure rate, β , and in simulation, the average existing users is assumed such that %80 of total spectrums are loaded by primary users in average.

$N_{tot}(nT_s) = N_{tot}(n(T_s - 1)) + \alpha(nT_s) - \beta(nT_s)$ (13) as a result, the existing users in a cell is equivalent to total existing users on previous time period added to arrival rate at current time and subtracted by current departure time as mentioned in equation (13). The transition probabilities are p^T and q^T as illustrated in Fig. 3 and the calculated steady probabilities are depicted below [15]:

$$P_{i,BUSY} = \frac{p^T}{p^T + q^T}, \quad P_{i,Idle} = \frac{q^T}{p^T + q^T}, \quad (14)$$

Eq. (14) is applied to analyze the model for identifying subcarriers states (i.e. busy or idle).

D. Optimum Sensing Time

The throughput of SU is calculated as follows [16],

$$C_i = W \log_2\left(1 + \frac{P_{i,SU} |h_{i,SU}|^2}{\mathcal{N}_0}\right) \quad (15)$$

where W is bandwidth, $P_{i,SU}$ is the power of transmitter SU and \mathcal{N}_0 is the noise power and $h_{i,SU}$ is the gain channel

between i th SU's transmitter and receiver with variance $E(|h_{i,SU}|^2) = \sigma_{h_{i,SU}}^2$.

Considering probabilities for different states gives us achievable throughput, $R_i(\tau_i)$, calculated by,

$$R_i(\tau_i) = \left(1 - \frac{\tau_i}{T}\right) (1 - P_{f,i}) P_{i,Idle} C_i \quad (16)$$

where $(1 - P_{f,i}(\epsilon_i, \tau_i)) P_{i,Idle}$ is the probability of absence of PU when we detect correctly. $(1 - \frac{\tau_i}{T})$ is the entire data transmission. Following equations can be derived,

$$\lim_{\tau_i \rightarrow 0^+} \frac{d R_i(\tau_i)}{d \tau_i} \rightarrow +\infty > 0 \quad (17)$$

$$\lim_{\tau_i \rightarrow T} \frac{d R_i(\tau_i)}{d \tau_i} < 0 \quad (18)$$

Thus, there is a τ_i between 0 and T that gives us maximum $R_i(\tau_i)$. The Fig. 4 shows the optimum sensing time based on equation (16). By Fig. 4, it can be denoted that the optimum sensing time in regard to technology limits and optimum sensing time is approximated between 3ns and 1 μ s.

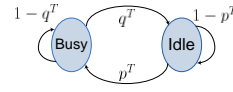


Fig. 3. Markov Chains Model

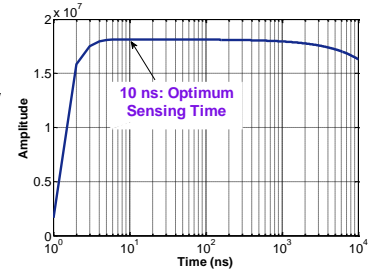


Fig. 4. Optimum Sensing Time

E. Scheduling algorithms for CR users

We consider the downlink of N_{su} secondary users are serviced by a base station within a cell. The base station allocates $RE(i,j)$ among the N_{su} SUs. At each frame multiple REs can be assigned to a single user, although each RE can be allocated to only one SU.

We assume that channel conditions vary across the subcarriers as well as secondary users. The channel conditions typically depend on the channel frequency, so they may be different for different channels. We presume typical urban area model. Moreover, scheduling of SUs also depend on the user location and the time frame. However, in our context the AMI meters are geographical stationary leading to constant SINR values.

In order to make optimal multi user scheduling decision and achieve high gain from multiplexing, the scheduler needs accurate channel quality indicator (CQI). Accuracy of CQI prediction depends on error in measuring the channel from the pilot and delays in the feeding back the information to the case-station. Feedback delay can be reduced by shrinking the size of the scheduling frame time. However, due to reduction of frame time the feedback request rate in uplink increases and eventually increasing the system overhead.

We define the peak downlink multiuser capacity for orthogonal OFDM signaling and note that it cannot exceed the Shannon capacity $\sum_{k=1}^{\min(n_T, n_R)} W_{\text{cell}} \log_2(1 + \text{SINR})$:

$$SINR = \frac{S_{Cell}}{N + I_{OtherCell}} = \frac{\frac{P_{TxCell}}{PathLoss}}{W_{Cell}G_K + \sum_{k \in Other} \frac{P_{OtherCell}}{PathLoss(k)}} \quad (19)$$

In real deployments, we can develop a modified Shannon capacity formula by replacing the cell bandwidth, W_{cell} with an effective bandwidth and βW_{eff} [17] which accounts for G-factor dependencies and protocol control, pilot, and cyclic prefix overheads. Closely related to the SINR is the G-factor, which accounts for the geometric dependencies of cell layouts and dictates the statistics of the downlink capacity. The G-factor is the average own cell power to the other cell-power plus noise ratio when considering uniform spatial distributions of transceivers within a cell.

In addition, we can define a normalized effective signal to noise ratio, SNR_{eff} , adjust SNR for both interference, G-factor statistics, and LTE implementation parameters. Defining the modified Shannon spectral efficiency for PU as

$$\beta W_{eff} \log \left(1 + \frac{\frac{S}{N+I}}{SNR_{eff}} \right) \quad (20)$$

We also define capacity of secondary user in presence of loss,

$$C = \int \sum_{SINR} (1 - \rho)(1 - \delta) \beta W_{eff} \eta \cdot \log_2 \left(1 + \frac{\frac{|h|^2 S}{N+I}}{SNR_{eff}} \right) dt \quad (21)$$

ρ is detection probability parameter and calculated by addition of false alarm detection probability (P_f) and detection probability (P_d). δ is primary user spectrum usage and we presume a average of 80% loading. β is a correction factor which nominally should be equal to one and it is discussed more detailed in. η is the spectrum sensing efficiency. The scheduler decides which SU to transmit the information at each time frames, based on the request rates the base station.

Scheduling the user with the instantaneously best link conditions is often referred as max rate scheduling. The max rate can be expressed as $k = \arg \max_i R_i$ for i th user.

Proportional fair (PF) scheduler is designed to meet the challenges of delay and fairness constraints while harnessing multi user diversity. PF scheduler tracks the average throughput, $T_k[nT_s]$, for each SU delivered in the past over sliding window of size t_c . In the time frame $[\tau]$, the base station receives rates $R_k[nT_s]$, $k=1 \dots N_{su}$ from all the active SUs and scheduler basically schedules the SU with highest PF metric value, γ that is defined as $\gamma = \frac{R_k[nT_s]}{T_k[nT_s]}$.

The average throughputs $T_k[nT_s]$ are updated using an exponentially weighted low pass-filter :

$$T_k[nT_s + 1] = \begin{cases} (1 - \frac{1}{t_c}) T_k[nT_s] + (\frac{1}{t_c}) R_k[nT_s] & k = \gamma \\ (1 - \frac{1}{t_c}) T_k[nT_s] & k \neq \gamma \end{cases} \quad (22)$$

Based on the Eq. (21) and (22) we can write as the following

$$\gamma = \frac{C = \int \sum_{SINR} (1 - \rho)(1 - \delta) \beta W_{eff} \eta \cdot \log_2 \left(1 + \frac{\frac{|h|^2 S}{N+I}}{SNR_{eff}} \right) dt}{T_k[nT_s]} \quad (23)$$

Opportunistic Scheduling (OS) is an approach to deal with both fairness among users and maximizing the capacity rate. In max rate algorithm the user with highest request rate implies giving all the system resources to particular users, yields to highly unfair scheme to all other users. However, in PF the users compete for resources not directly based on the requested rates

but based on the rates normalized by their respective average throughputs also defined as PF metric value. The downside of the PF approach is sacrificing over all throughputs. Thus OS algorithm schedules subcarriers $sc_{1,1}$ to $sc_{i,j}$ to the best secondary user based on two step criteria. First, the user who has the maximum PF metric value, γ , is selected. Second, the selected SU requested rate should be greater than the mean of all the secondary users requested rate, $\bar{R}[nT_s]$, to be scheduled as follow,

$$R[nT_s] \geq \bar{R}[nT_s] \quad (24)$$

As a result, unlike PF scheduling, the users having low throughput but high PF metric, γ , that had been chosen to access frequency will have lower priority than users with enough PF metric and higher throughput.

Algorithm: Opportunistic scheduling

- 1) for $n=1$ to N_T (simulation time)
 - 2) Update SU profile, Update γ
 - 3) Let S be the set of secondary users
 - 4) Let $RE(i,j)$ where $i=1$ to M subcarriers and $j=1$ to K be the total time frames.
 - 5) for $i=1$ to M , for $j=1$ to K
 - 6) Select the secondary user $l \in S$ with highest $\gamma(l)$
 - 7) If $R_l[nT_s] \geq \bar{R}[nT_s]$
 - 8) Update the SU profile with $S=S-\{l\}$
 - 9) Allocate $RE(i,j)$ to l th secondary user from S
 - 10) Else
 - 11) Update the SU profile with $S=S-\{l\}$
 - 12) End if, End for j, i, n
-

IV. ANALYSIS & SIMULATION RESULTS

To evaluate the performance of CR system model, system level simulations have been conducted based on 3GPP LTE system model. Table [see 15] shows the simulation parameters used for the simulations. We analyze the performance of the scheduling in terms of throughput and fairness. We first evaluate the system throughput for algorithms with varying the primary user loading within a cell. In this case, the primary user average loading is around 80% and total number of users is 500 in a cell. Over the period of time that spectrum sensing reports the number of idle resource blocks, scheduler allocates the idle REs with SUs. The Fig. 5 illustrates average capacity for three aforementioned algorithms.

Max-rate results in highest average capacity among three algorithms are followed by opportunistic and fairness algorithms. The results seem to match our expectations, since the goal of the Max-rate capacity is the user with highest request rate implies giving all the system resources to particular users. In proportional fair algorithm the users compete for resources not directly based on the requested rates but based on the rates normalized by their respective average throughputs, PF metrics. By this approach PF sacrifices the overall throughput while, achieving higher number of SUs scheduled. In OS the users having low request rate but high PF metric, γ , will have less chance to be scheduled. OS objective is to achieve higher average capacity compared to PF, while achieving decent fairness among the SUs.

Fig. 6.a and 6.b show the average number of users scheduled per one Transmission Time Interval (TTI) when 75 SUs are

active in a cell and around 20% and 30% of idle RE are available. We can see that at least 60 and 70 SUs are scheduled to idle REs by fairness algorithm. OS and max rate algorithms allocate less number of average SUs respectively.

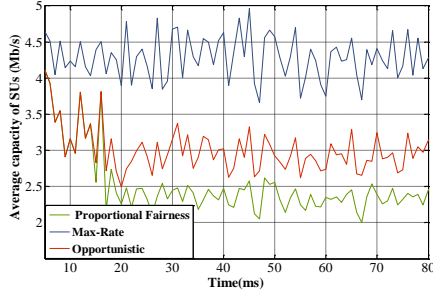


Fig. 5 Average Capacity over Time

In Fig. 7, we analyze the scheduled SUs average capacity of each algorithm in each scenario when number of active PUs varies. Based on goals of each algorithm they indicate respective positions in the results. It can be seen that the solution obtained using the proposed algorithm (OS) is quite close to the PF specifically when the active PUs are less.

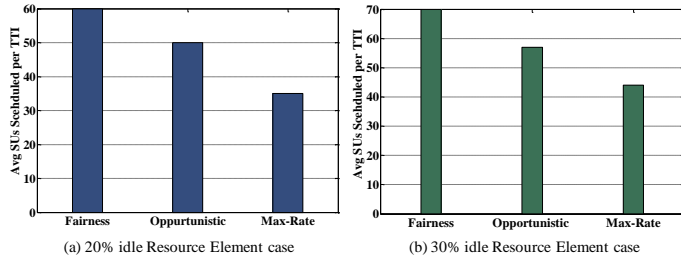


Fig. 6. Average number of users scheduled per one TTI

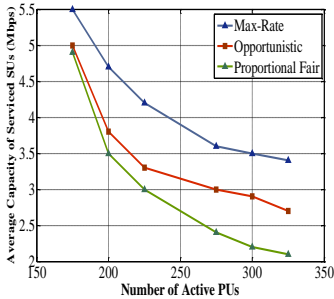


Fig. 7 Average capacity of SUs

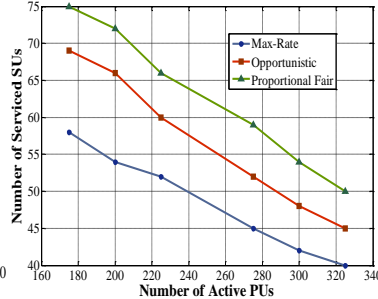


Fig. 8 Average No. of scheduled SUs

We note that the less PUs scheduled yields to high availability of idle REs. Therefore, higher number of SUs scheduled results in larger average capacity in the CR network. When the numbers of PUs are increased, the advantage of the OS algorithm over PF is more obvious (i.e. Fig.7) due to more sparse SUs. Sparse implies large variability in SUs profile (i.e. SINR, fading channel, physical location).

In Fig. 8, we analyze the average number of scheduled SUs in each scenario when number of active PUs varies. We note that the more PUs scheduled yields to less availability of idle REs and therefore less number of SU scheduled. In Fig. 7 the Max-Rate average capacity is much higher than average capacity of PF; on the contrary, Fig. 8 shows the more scheduled SUs by PF algorithm compared to Max-Rate algorithm. As a result, the OS

algorithm can balance both the performance of the cognitive radio networks in terms of achieving acceptable average capacity of secondary users and the fairness.

V. CONCLUSION

In this paper, we have analyzed the potential 4G CR network framework in context of smart grid information systems. Our system level simulation results show that the 4G CR network can achieve an average capacity of 3.5Mbps in a 3Km cell radius under the constraint of an average primary user network usage of 80%. Finally, we present that the CR capacity of a 20% usage model meets the smart grid protocols requirements for a multi-user CR network of smart meters.

REFERENCES

- [1] Smart grid Research and Development Multi- Year Program Plan (MYPP) 2010-2014.
- [2] D.D.Ariananda, M.K.Lakshmanan, H.Nikookar, "A survey on spectrum sensing techniques for cognitive radio," Cognitive Radio and Advanced Spectrum Management, 2009. CogART 2009. Second International Workshop on, pp. 74 – 79.
- [3] Brian Kelley, "Software Defined Radio for Broadband OFDM Protocols," SMC 2009, San Antonio.
- [4] Akyildiz, I. F., Lee, W.-Y., Vuran, M. C., and Mohanty, S, "Next generation dynamic spectrum access cognitive radio wireless networks: a survey," Computer Networks Journal (Elsevier), pp.2127-2159, vol. 50, May 2006.
- [5] S.-W. Luan, J.-H. Teng, S.-Y. Chan, and L.-C. Hwang, "Development of a smart power meter for AMI based on zigbee communication," in Proc. Int. Conf. Power Electron. Drive Syst., 2009, pp. 661–665.
- [6] Wenpeng Luan, Duncan Sharp and Sol Lancashire, "Smart Grid Communication Network Capacity Planning for Power Utilities," Transmission and Distribution Conference and Exposition, IEEE PES, New Orleans, USA, 2010, pp. 1–4.
- [7] B. Reid, "Oncor electric delivery smart grid initiative," in Proc. 62nd Annu. Conf. Protective Relay Engineers, 2009, pp. 8–15.
- [8] Robert C. Qiu, Zhe Chen, Nan Guo, Yu Song, Peng Zhang, Husheng Li and Lifeng Lai, "Towards A Real-time Cognitive Radio Network Testbed: Architecture, Hardware Platform, and Application to Smart Grid," Networking Technologies for Software Defined Radio (SDR) Networks, Fifth IEEE Workshop, Boston, USA, 2010, pp.1-6.
- [9] Qing Zhao; Sadler, B.M.; "A Survey of Dynamic Spectrum Access" IEEE Signal Processing Magazine, pp.79-89, vol. 24, May 2007.
- [10] Rajae, A., Saedy, M., Sahebalam, A., "Competitive spectrum sharing for cognitive radio on Scale-Free wireless networks" IEEE IWCMC, pp. 455-459, 2011.
- [11] Carlos Cordeiro, Kiran Challapali, and Dagnachew Birru, "IEEE 802.22: An Introduction to the First Wireless Standard based on Cognitive Radios" Journal of Communications, Vol. 1, No. 1, April 2006.
- [12] T.E Kolding. "Link and System performance aspects of Proportional Fair Packet Scheduling in WCDMA/HSDPA", In Proceedings of 58th IEEE Vehicular Technology Conference, Vol.3, pp. 1717-1722, October 2008.
- [13] Zhi Quan; Shuguang Cui; Sayed, A.H.; Poor, H.V.; "Optimal Multiband Joint Detection for Spectrum Sensing in Cognitive Radio Networks " IEEE Transaction on Signal Processing, pp. 1128-1140, vol. 57, November 2008.
- [14] Khalid, L.; Anpalagan, A.; "Effect of sensing errors on wideband cognitive OFDM radio networks" IEEE Biennial Symposium QBSC, pp. 273-277, 2010.
- [15] Ghosh, C.; Cordeiro, C.; Agrawal, D.P.; Rao, M.B.; "Markov chain existence and Hidden Markov models in spectrum sensing" IEEE International Conference, pp.1-6, 2009.
- [16] Zhi Quan; Shuguang Cui; Sayed, A.H.; Poor, H.V.; "Wideband Spectrum sensing in Cognitive Radio Networks " IEEE International Conference, pp. 901-906, 2008.
- [17] Preben Mogensen et.al. "LTE Capacity compared to the Shannon Bound" ,In Proceedings of 65th IEEE Vehicular Technology Conference, pp. 1234-1238, April, 2007.

**COGNITIVE RADIO NETWORKS:
SYSTEM OPTIMIZATION AND SMART GRID
APPLICATIONS**

by

AMIR RAJAEI, B.S.

THESIS

Presented to the Graduate Faculty of
The University of Texas at San Antonio
In partial Fulfillment
Of the Requirements
For the Degree of

MASTER OF SCIENCE IN ELECTRICAL ENGINEERING

THE UNIVERSITY OF TEXAS AT SAN ANTONIO
College of Engineering
Department of Electrical Engineering
July 2012

Acknowledgements

I am extremely thankful to my supervisor Dr. Mo Jamshidi for his outstanding pedagogy, valuable advice and consistent support during preparation of this research project. I hope he will be proud of me throughout future successful challenges in my career. I also express my gratitude and special thanks to my supervisor Dr. Brian Kelley for his support, patience, and encouragement throughout my graduate studies. It is not often that one finds an advisor and colleague that always finds the time for listening to the little problems and roadblocks that unavoidably crop up in the course of performing research. His technical and editorial advice was essential to the completion of this dissertation and has taught me innumerable lessons and insights on the workings of academic research in general.

July 2012

CHAPTER I. INTRODUCTION	8
CHAPTER II. COGNITIVE RADIO	12
APPLICATIONS OF COGNITIVE RADIO	12
A. <i>TV White Spaces</i>	12
B. <i>Cellular Networks</i>	13
C. <i>Military Usage</i>	13
COGNITIVE RADIO NETWORK ARCHITECTURE	13
NETWORK COMPONENTS	14
SPECTRUM MANAGEMENT FRAMEWORK.....	16
SPECTRUM SENSING	17
A. <i>Spectrum Sensing Challenges</i>	20
SPECTRUM DECISION	22
A. <i>Channel Characteristics In Cognitive Radio Networks</i>	22
B. <i>Decision Procedure</i>	23
C. <i>Spectrum Decision Challenges</i>	24
SPECTRUM SHARING.....	25
A. <i>Spectrum Sharing Challenges</i>	27
SPECTRUM MOBILITY.....	28
B. <i>Spectrum Mobility Challenges</i>	29
CHAPTER III. PROPOSED SPECTRUM DECISION AND SPECTRUM SHARING ALGORITHM... 30	
INTRODUCTION.....	30
NETWORK TOPOLOGY	31
A. <i>Random Topology</i>	32
B. <i>Scale-Free Topology</i>	32
SPECTRUM SENSING	33
A. <i>Energy Detection</i>	35
QUEUED MARKOV CHAIN MODEL FOR SPECTRUM ANALYSIS-ACCESS	38
MAX-RATE SPECTRUM SHARING	41
A. <i>Cognitive Parameters</i>	43
B. <i>Merit Function</i>	44
C. <i>Channel Indexing Function</i>	44
D. <i>Competitive Indexing Algorithm</i>	45
SHARING INCORPORATED IN MARKOV CHAIN MODEL	47
SIMULATION	48
A. <i>Simulation Results For Sensing</i>	48
B. <i>Simulation Results For Sharing</i>	50
CONCLUSION.....	53
CHAPTER IV. COGNITIVE RADIO IN SMART GRID	54
THROUGHPUT ANALYSIS ON COGNITIVE RADIO NETWORKS FOR AMI METERS IN SMART GRID.....	54
INTRODUCTION.....	54
4G COGNITIVE RADIO FRAMEWORK	56
A. <i>4G Cognitive Radio System Architecture</i>	56
B. <i>Pervasive Smart Grid Systems</i>	57
CR SYSTEM MODEL.....	58
A. <i>Primary User Activity Model</i>	59
B. <i>Optimum Sensing Time</i>	60
SCHEDULING ALGORITHMS FOR CR USERS	61
ANALYSIS & SIMULATION RESULTS	63
CONCLUSION.....	65
CHAPTER V. INTERFERENCE AWARE SCHEDULING FOR MAXIMUM CHANNEL REUSE AND MAX-CAPACITY IN SMART METER NETWORKS.....	66

CONTRIBUTIONS OF THIS THESIS ON INTERFERENCE AWARE SCHEDULING	66
SYSTEM MODEL.....	67
INTERFERENCE –AWARE SCHEDULING ALGORITHM	69
INTERFERENCE MODEL FOR SISO	72
INTERFERENCE MODEL FOR BEAMFORMING	74
SIMULATIONS AND RESULTS	74
CONCLUSION.....	78
CHAPTER VI. SMART GRID AND OPTIMIZATION	80
FUZZY CONTROL OF ELECTRICITY STORAGE UNIT FOR ENERGY MANAGEMENT OF MICRO-GRIDS	80
INTRODUCTION.....	80
SYSTEM MODEL.....	81
A. <i>Characteristics of Buses in Scenario 1</i>	83
B. <i>Characteristics of Buses in Scenario 2</i>	83
C. <i>Characteristics of Buses in Scenario 3</i>	84
PROBLEM STATEMENT	84
A. <i>Scenario 1</i>	86
B. <i>Scenario 2</i>	86
C. <i>Scenario 3</i>	86
FUZZY CONTROL APPROACH.....	87
SIMULATION RESULTS & DISCUSSIONS	89
CONCLUSION.....	96
CHAPTER VII. PARTICLE SWARM OPTIMIZATION	97
SIMULATIONS FOR PSO	99
CHAPTER VIII. CONCLUSION	104
CHAPTER IX. REFERENCES.....	107

Table of Figures

FIGURE 1 AVAILABLE CHUNKS OF SPECTRUM (WHITE SQUARES) ARE DETECTED IN FREQUENCY AND TIME AND CAN BE AGGREGATED FOR OPPORTUNISTIC USE	9
FIGURE 2 COGNITIVE OPERATIONS NEEDED FOR AN OPTIMAL DECISION.....	9
FIGURE 3 COGNITIVE RADIO NETWORK ARCHITECTURE.	14
FIGURE 4 SCALE-FREE NETWORK FORMATION WITH POWER-LAW DEGREE DISTRIBUTION	33
FIGURE 5 A)TIMING MODEL, B)RESOURCE BLOCK & DYNAMIC RESOURCE MANAGEMENT	35
FIGURE 6 WIDE SPECTRUM SENSING MODEL	38
FIGURE 7 QUEUED MARKOV CHAIN STATE MACHINE WITHOUT SHARING	39
FIGURE 8 SCALE FREE INFRASTRUCTURE AND ITS UL AND DL SPECTRUM RESOURCE MODEL	43
FIGURE 9 QUEUED MARKOV CHAIN STATE MACHINE WITH SHARING.....	48
FIGURE 10 STATE PROBABILITIES USING COMPETITIVE SHARING FOR DIFFERENT NUMBER OF USERS	49
FIGURE 11 STATE PROBABILITIES USING COMPETITIVE AND UNIFORM SHARING N=3.....	50
FIGURE 12 LOAD AND NET REQUEST IN CLUSTER A	51
FIGURE 13 LOAD WITH DIFFERENT TRAFFIC IN CLUSTER A.....	51
FIGURE 14 CAPACITY IMPROVEMENT IN CLUSTER A	52
FIGURE 15 CAPACITY IMPROVEMENT IN CLUSTER A	52
FIGURE 16 CAPACITY IMPROVEMENT FOR SCALE-FREE NETWORK	52
FIGURE 17 4G CR NETWORK SYSTEM ARCHITECTURE: SCENARIO OF MULTIPLE AMI METERS SERVICED BY COGNITIVE RADIO NETWORK INFRASTRUCTURE ENABLED BY CLOUD CENTER COEXISTING WITH PRIVATE CELLULAR NETWORK	57
FIGURE 18 MARKOV CHAINS MODEL; OPTIMUM SENSING TIME	59
FIGURE 19 AVERAGE CAPACITY OVER TIME.....	63
FIGURE 20 MAX-RATE AVERAGE CAPACITY	64
FIGURE 21 AVERAGE NO. OF SCHEDULED SUS.....	64
FIGURE 22 SISO SYSTEM MODEL DEPICTED WITH COORDINATED AND UNCOORDINATED INTERFERENCE	67
FIGURE 23 MECHANISM OF OUR REUSE MODEL.....	68
FIGURE 24 INTERFERENCE-AWARE SCHEDULER (IAS) ALGORITHM FOR PRE REUSE	69
FIGURE 25 MIMO SYSTEM MODEL WITH COORDINATED AND UNCOORDINATED INTERFERENCE	73
FIGURE 26 TOTAL CAPACITY OF A-SU IN THE CASES OF NO IAS, IAS-SISO AND IAS-BF	76
FIGURE 27 TOTAL CAPACITY OF A-SU IN THE CASES OF NO IAS, IAS-SISO AND IAS-BF	76
FIGURE 28 RELATION BETWEEN INTERFERENCE GENERATED BY REUSE AND TOTAL CAPACITY OF SCHEDULED A-SU IN THE CASES OF IAS-SISO AND IAS-BF.....	78
FIGURE 29 NUMBER OF REUSE FOR EVERY SCHEDULED A-SUS IN ONE INSTANCE.....	79
FIGURE 30 TOTAL NUMBER OF REUSES OVER ENTIRE BW IN CASES OF IAS-SISO AND IAS-BF.	79
FIGURE 31 BASIC GRID SYSTEM MODEL.....	82
FIGURE 32 THREE BUS MODEL FOR MICRO-GRID	85
FIGURE 33 FUZZY MEMBERSHIP FUNCTIONS FOR INPUT AND OUTPUT VARIABLES OF THE FUZZY CONTROLLER;	88
FIGURE 34 PROFILES OF PRICE, RENEWABLE GENERATION, AND THE LOAD	90
FIGURE 35 POWER FLOW OF BUS 1 CONNECTED TO SOLAR PANELS; SCENARIO 1.....	90
FIGURE 36 POWER FLOW OF BUS 2 CONNECTED TO UTILITY; SCENARIO 1.....	90
FIGURE 37 POWER FLOW OF BUS 3 CONNECTED TO LOAD; SCENARIO 1	91
FIGURE 38 OUTPUT OF THE FUZZY CONTROLLER, I.E. MEASURE OF THE AMOUNT OF POWER GIVEN TO/TAKEN FROM STORAGE UNIT; SCENARIO 2;	92
FIGURE 39 POWER FLOW OF BUS 2 CONNECTED TO UTILITY; SCENARIO 2.....	92
FIGURE 40 OUTPUT OF THE FUZZY CONTROLLER; SCENARIO 3;	93
FIGURE 41 MEASURE OF ENERGY STORED IN BATTERY; SCENARIO 3	94
FIGURE 42 POWER FLOW OF BUS 2 CONNECTED TO UTILITY; SCENARIO 3.....	94
FIGURE 43 MICRO GRID CONTROL BY PSO WITH LOAD, RE, AND PRICE PROFILE	99
FIGURE 44 POWER FROM BATTERY.....	99
FIGURE 45 ALL PROFILES AND BATTERY BEHAVIOR THROUGH PSO UTILIZATION	100

FIGURE 46 THE RE POWER, PRICE, AND LOAD PROFILE WHEN RE POWER IS NOT SUFFICIENT FOR GIVEN LOAD.....101

FIGURE 47 BATTERY CHARGING AND DISCHARGING STATES101

FIGURE 48 GRID POWER, PRICE, COST FUNCTION, AND POWER FROM RE102

FIGURE 49 BATTERY POWER, INPUT PROFILES AND GRID POWER103

Abstract

This thesis presents the Cognitive Radio framework for wireless networks. The proposed Cognitive Radio framework is a complete model for Cognitive Radio that describes the decision and sharing procedures in wireless networks by introducing Queued Markov Chain method.

Queued Markov Chain method is capable of considering waiting time and is very well generalized for unlimited number of secondary users. It includes the sharing aspect of Cognitive Radio.

The proposed approach in this thesis uses pervasive smart grid systems (i.e. cloud data centers) as the central communication and optimization infrastructure supporting metropolitan area based smart meter infrastructure. In this thesis, we investigate the performance of various scheduling algorithms in context with CR units to provide a satisfactory tradeoff between maximizing the system capacity, achieving fairness among cognitive users.

This thesis also addresses improvements in the multiuser capacity in unplanned networks with high levels of co-channel interference. For this, a novel opportunistic interference aware scheduling protocol ideally suited for maximum channel reuse in unplanned networks. In this thesis, we analyze the application of SISO and MIMO interference aware scheduling to maximize the capacity and number of scheduled smart meters.

Moreover, a Fuzzy Logic-based framework and Particle Swarm Optimization are proposed for control of Battery Storage Unit in Micro-Grid Systems to achieve Efficient Energy Management. Typically, a Micro-Grid system operates synchronously with the main grid and also has the ability to operate independently from the main power grid in an islanded

mode. The goal here is to control the amount of power delivered to/taken from the storage unit in order to improve a cost function, defined based on summation of payment required for purchasing power from main grid or profit obtained by selling power to the main grid and distribution power loss.

KEYWORDS

Queued Markov Chain, Cognitive Radio, Spectrum Sensing, Spectrum Decision, Spectrum Sharing, Ad Hoc, Scale-Free, Random Networks, 4G, Cloud Data Center, Scheduling Algorithms, Smart Meters, Micro-Grid Network, Power Flow Analysis, Fuzzy-Logic, Load Demand, Particle Swarm Optimization.

Chapter I. INTRODUCTION

Current wireless networks are identified by an inactive spectrum allocation policy, where governmental agencies assign wireless spectrum to licensed users on a long-term basis for large geographical regions. Recently, because of the increase in spectrum demand, this policy faces spectrum scarcity in particular spectrum bands [1].

Most of the spectrum that is interesting to operators has already been exclusively assigned. This is particularly true for spectrum below 3 GHz, which can be used for providing mobile services and indoor coverage. This means that it is difficult for new operators to get access to spectrum and for existing operators to get access to more spectrums to meet an ever increasing demand for capacity [2].

In contrast, a large portion of the assigned spectrum is used periodically, leading to underutilization of a significant amount of spectrum. Hence, dynamic spectrum access techniques were recently proposed to solve these spectrum inefficiency problems[1].

One of the ways to achieve a more efficient utilization of spectrum is Cognitive Radio (CR), which relies on the opportunistic use of frequency holes. A number of rule bodies are promoting a more liberalized use of spectrum that would also encompass a more dynamic

usage. This trend is also reflected in several standardization forums that develop methods enabling a more flexible and highly dynamic spectrum usage[2].

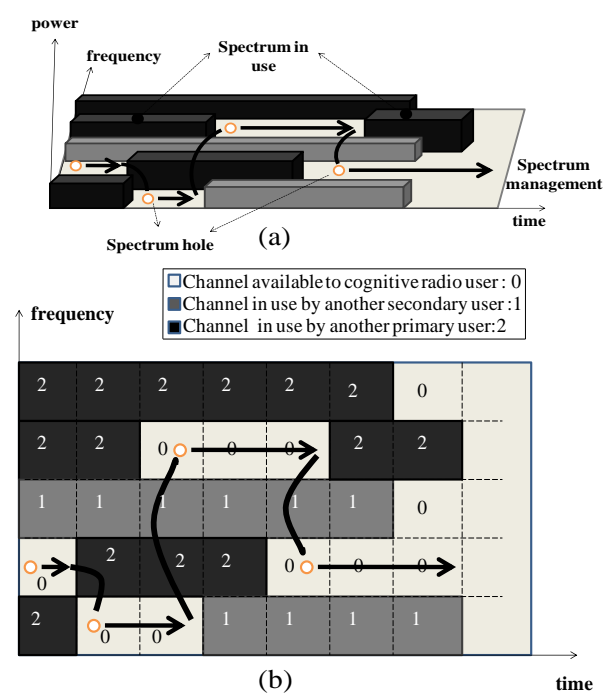


Figure 1 Available chunks of spectrum (white squares) are detected in frequency and time and can be aggregated for opportunistic use

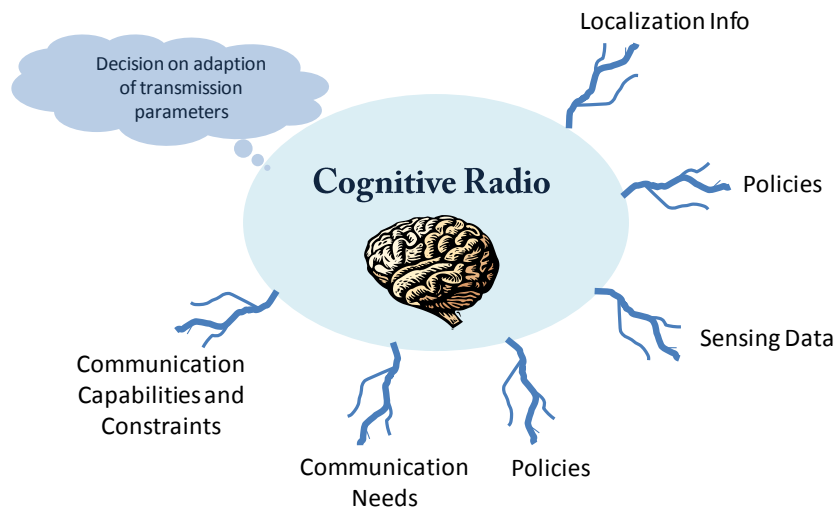


Figure 2 Cognitive operations needed for an optimal decision

This combination of a large unsatisfied demand for spectrum and the current poor spectrum utilization is unacceptable from a regulatory and political point of view. It indicates that there is a potential for offering the public better and cheaper wireless telecommunication services. Not utilized spectrum can be used by a new operator to offer services competing with existing services to enhance the competition in the market and hence reduce prices. Or it can be used by new operators to offer new types of services or by existing operators to enhance their existing services [2].

Cognitive Radio (CR) has been proposed as a way to increase the availability of spectrum resources. It is a system utilizing spectrum holes in licensed bands in an opportunistic manner. In order to implement this feature, a CR system functions along three basic steps further illustrated in Figure 1: 1 Detection of available spectrum from primary, licensed users; 2 Usage of this spectrum as secondary user; 3 Exit as quickly as possible if primary usage resumes [2].

A Cognitive Radio system is an ‘intelligent’ radio system that takes into account its knowledge about its environment and its communication needs and adapts its wireless transmissions in an optimal manner as illustrated in Figure 2[2].

The key enabling technology of dynamic spectrum access techniques is cognitive radio (CR) technology, which provides the capability to share the wireless channel with licensed users in an opportunistic manner. CR networks are envisioned to provide high bandwidth to mobile users via heterogeneous wireless architectures and dynamic spectrum access techniques. This goal can be realized only through dynamic and efficient spectrum management techniques. CR networks, however, impose unique challenges due to the high fluctuation in the available spectrum, as well as the diverse quality of service (QoS)

requirements of various applications. In order to address these challenges, each CR user in the CR network must[1]:

- Determine which portions of the spectrum are available
- Select the best available channel
- Coordinate access to this channel with other users
- Vacate the channel when a licensed user is detected [3]

These capabilities can be realized through spectrum management functions that address four main challenges: *spectrum sensing*, *spectrum decision*, *spectrum sharing*, and *spectrum mobility*. This article presents a definition, the functions, and the current research challenges of spectrum management in CR networks. [1].

Chapter II. COGNITIVE RADIO

Applications of Cognitive Radio

The development of spectrum sensing and spectrum sharing techniques enable the applications of CR in many areas. In this section, we introduce some of them.

A. TV White Spaces

The main regulatory agencies for the unlicensed use of TV white spaces are the FCC in the United States, the Office of Communications in the United Kingdom, and the Electronic Communications Committee (ECC) of the conference of European Post and Telecommunications in Europe. After many years of effort in this area, FCC released the final rules for using the TV white space in September 2010 [4], which led to the culmination of this field. Meanwhile, other agencies have been also getting progress [5]. This is based on the idea of having an accessible database (centralize-fashion) of free TV bands, otherwise called TV white space, or to sense and obtain SHs (distributed-fashion) within TV bands to utilize for SUs communication.

B. Cellular Networks

The applications of CR in cellular networks are emerging in recent years. To overcome the indoor coverage problem and adapt to traffic growth, the concept of small cells, such as femtocells, has been proposed in 3GPP LTE-Advanced (LTE-A)[6] and IEEE 802.16m [7], and companies like PicoChip driving femtocell revolution.. The femtocell unit has the function of the typical BS (eNodeB in LTE). However, the self-deployment property of the femtocells makes the centralized interference management impractical.

C. Military Usage

CR is a must-have technique for military usage. With CR, the users can recognize the enemies' communications and protect their own. Moreover, the users can search for more transmission opportunities. The US department of defense (DoD) has already established programs such as SPEAK easy radio system and next Generation (XG) to exploit the benefits of CR techniques [3].

Cognitive Radio Network Architecture

A comprehensive description of the CR network architecture is essential for the development of communication protocols that address the dynamic spectrum challenges. The CR network architecture is presented in this section.

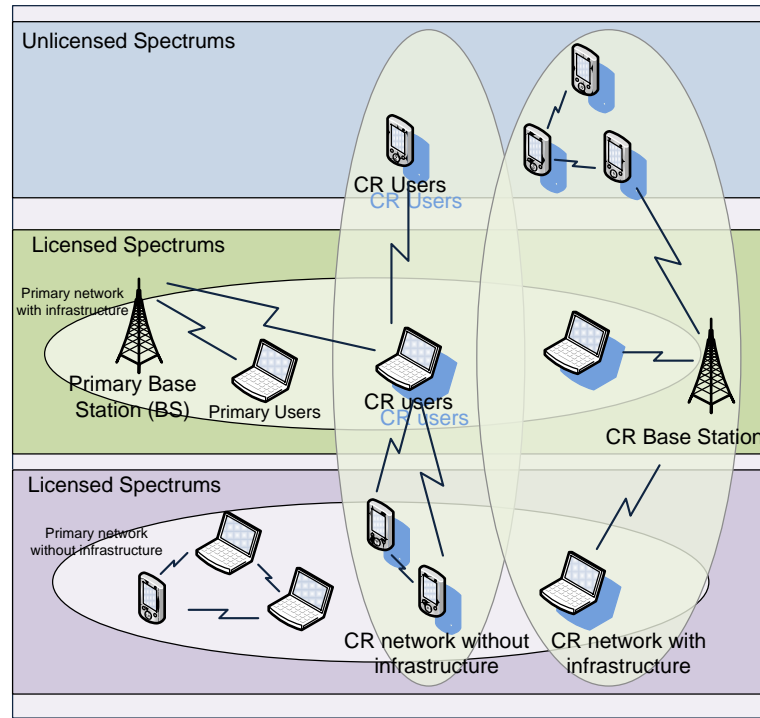


Figure 3 Cognitive radio network architecture.

Network Components

The components of the CR network architecture can be classified as shown in Fig. 3 as two groups: the *primary network* and the *CR network*. The primary network (or licensed network) is referred to as an existing network, where the *primary users* have a license to operate in a certain spectrum band. If primary networks have an infrastructure, primary user activities are controlled through *primary base stations*. Due to their priority in spectrum access, the operations of primary users should not be affected by unlicensed users. The CR network (also called the dynamic spectrum access network, secondary network, or unlicensed network) does not have a license to operate in a desired band. Hence, additional functionality is required for *CR users* to share the licensed spectrum band. CR networks also can be equipped with *CR base stations* that provide single-hop connection to CR users.

Finally, CR networks may include *spectrum brokers* that play a role in distributing the spectrum resources among different CR networks [1].

CR users are capable of accessing both the licensed portions of the spectrum used by primary users and the unlicensed portions of the spectrum through wideband access technology. Consequently, the operation types for CR networks can be classified as *licensed band operation* and *unlicensed band operation*.

- *Licensed band operation*: The licensed band is primarily used by the primary network. Hence, CR networks are focused mainly on the detection of primary users in this case. The channel capacity depends on the interference at nearby primary users. Furthermore, if primary users appear in the spectrum band occupied by CR users, CR users should vacate that spectrum band and move to available spectrum immediately [1].

- *Unlicensed band operation*: In the absence of primary users, CR users have the same right to access the spectrum. Hence, sophisticated spectrum sharing methods are required for CR users to compete for the unlicensed band [1].

As shown in Fig. 3, the CR users have the opportunity to perform three different access types:

- *CR network access*: CR users can access their own CR base station, on both licensed and unlicensed spectrum bands. Because all interactions occur inside the CR network, their spectrum sharing policy can be independent of that of the primary network.

- *CR ad hoc access*: CR users can communicate with other CR users through an ad hoc connection on both licensed and unlicensed spectrum bands.

- *Primary network access*: CR users can also access the primary base station through the licensed band. Unlike for other access types, CR users require an adaptive medium access control (MAC) protocol, which enables roaming over multiple primary networks with

different access technologies. According to the CR architecture shown in Fig. 3, various functionalities are required to support spectrum management in CR networks. An overview of the spectrum management framework and its components is provided next[1].

Spectrum Management Framework

CR networks impose unique challenges due to their coexistence with primary networks as well as diverse QoS requirements. Thus, new spectrum management functions are required for CR networks with the following critical design challenges:

- *Interference avoidance*: CR networks should avoid interference with primary networks.
- *QoS awareness*: To decide on an appropriate spectrum band, CR networks should support QoS-aware communication, considering the dynamic and heterogeneous spectrum environment.
- *Seamless communication*: CR networks should provide seamless communication regardless of the appearance of primary users. To address these challenges, we provide a directory for different functionalities required for spectrum management in CR networks.

The spectrum management process consists of four major steps:

- *Spectrum sensing*: A CR user can allocate only an unused portion of the spectrum. Therefore, a CR user should monitor the available spectrum bands, capture their information, and then detect spectrum holes.
- *Spectrum decision*: Based on the spectrum availability, CR users can allocate a channel. This allocation not only depends on spectrum availability, but is also determined based on internal (and possibly external) policies.

- *Spectrum sharing*: Because there may be multiple CR users trying to access the spectrum, CR network access should be coordinated to prevent multiple users colliding in overlapping portions of the spectrum.
- *Spectrum mobility*: CR users are regarded as visitors to the spectrum. Hence, if the specific portion of the spectrum in use is required by a primary user, the communication must be continued in another vacant portion of the spectrum. The spectrum management framework for CR network communication is illustrated in Fig.3. It is evident from the significant number of interactions that the spectrum management functions require a cross-layer design approach. In the following sections we discuss the four main spectrum management functions[1].

Spectrum Sensing

Cognitive radio (CR) can successfully deal with the growing demand and scarcity of the wireless spectrum. To increase the spectrum usage, CR technology allows unlicensed users to access licensed spectrum bands. Since licensed users have priorities to use the bands, the unlicensed users need to continuously monitor the licensed users' activities to avoid interference and collisions. How to obtain reliable results of the licensed users' activities is the main task for spectrum sensing. Based on the sensing results, the unlicensed users should adapt their transmit powers and access strategies to protect the licensed communications. The requirement naturally presents challenges to the implementation of CR.

In practice, the unlicensed users, also called secondary users (SUs), need to continuously monitor the activities of the licensed users, also called primary users (PUs), to find the spectrum holes (SHs), which is defined as the spectrum bands that can be used by the SUs

without interfering with the PUs. This procedure is called spectrum sensing [8], [9]. There are two types of SHs, namely temporal and spatial SHs [8], respectively. A temporal SH appears when there is no PU transmission during a certain time period and the SUs can use the spectrum for transmission. A spatial SH appears when the PU transmission is within an area and the SUs can use the spectrum outside that area.

This can be accomplished through a real-time wideband sensing capability to detect weak primary signals in a wide spectrum range. Generally, spectrum sensing techniques can be classified into three groups: primary transmitter detection, primary receiver detection, and interference temperature management as described in the following[1].

Transmitter detection is based on the detection of a weak signal from a primary transmitter through the local observations of CR users. Three schemes are generally used for transmitter detection: *matched filter detection*, *energy detection*, and *feature detection*[10]:

- *Matched filter detection*: When the information of the primary user signal is known to the CR user, the optimal detector in stationary Gaussian noise is the matched filter. However, the matched filter requires a priori knowledge of the characteristics of the primary user signal.
- *Energy detection*: If the receiver cannot gather sufficient information about the primary user signal, the optimal detector is an energy detector. However, the performance of the energy detector is susceptible to uncertainty in noise power. Also, energy detectors often generate false alarms triggered by unintended signals because they cannot differentiate signal types.
- *Feature detection*: In general, modulated signals are characterized by built-in periodicity or *cyclostationarity*. This feature can be detected by analyzing a spectral correlation function. The main advantage of feature detection is its robustness to uncertainty in noise power.

However, it is computationally complex and requires significantly long observation times. Due to the lack of interactions between primary users and CR users, transmitter detection techniques rely only on weak signals from the primary transmitters. Hence, transmitter detection techniques alone cannot avoid interference to primary receivers because of the lack of primary receiver information as depicted in Fig. 4a. Moreover, transmitter detection models cannot prevent the hidden terminal problem. A CR user (transmitter) can have a good line of sight to a CR receiver but may not be able to detect the primary transmitter due to shadowing. Therefore, sensing information from other users is required for more accurate primary transmitter detection — referred to as *cooperative detection*.

Cooperative detection is theoretically more accurate because the uncertainty in a single user's detection can be minimized through collaboration. Moreover, multipath fading and shadowing effects can be mitigated so that the detection probability is improved in a heavily shadowed environment. However, cooperative approaches cause adverse effects on resource constrained networks due to the overhead traffic required for cooperation[1].

There are several other spectrum sensing techniques, such as eigenvalue-based and moment-based detectors. Eigenvalue-based detector: In the multiple-antenna system, eigenvalue-based detection can be used for spectrum sensing [11],[12]. In [11], maximum-minimum eigenvalue (MME) and energy with minimum eigenvalue detectors have been proposed, which can simultaneously achieve both high probability of detection and low probability of false-alarm without requiring information of the PU transmitter signals and noise power. In most of the existing eigenvalue-based methods, the expression for the decision threshold and the probabilities of detection and false-alarm are calculated based on the asymptotical distributions of eigenvalues. To address this issue, the exact decision threshold for the probability of false-alarm for the MME detector with finite numbers of cooperative SUs and

samples has been derived in [12], which leads to our next section on cooperative spectrum sensing (CSS). Moment-based detector: When accurate noise variance and PU transmitter signal power are unknown, blind moment-based spectrum sensing algorithms can be applied[13]. Unknown parameters are first estimated by exploiting the constellation of the PU transmitter signal. When the SU does not know the PU transmitter signal constellation, a robust approach that approximates a finite quadrature amplitude modulation (QAM) constellation by a continuous uniform distribution has been developed [13].

A. Spectrum Sensing Challenges

There exist several open research challenges that must be investigated for the development of spectrum sensing techniques:

- *Interference temperature measurement*: Due to the lack of interactions between primary networks and CR networks, generally a CR user cannot be aware of the precise locations of the primary receivers. Thus, new techniques are required to measure or estimate the interference temperature at nearby primary receivers.
- *Spectrum sensing in multi-user networks*: The multi-user environment, consisting of multiple CR users and primary users, makes it more difficult to sense spectrum holes and estimate interference. Hence, spectrum sensing functions should be developed considering the multi-user environment.
- *Spectrum-efficient sensing*: Sensing cannot be performed while transmitting packets. Hence, CR users should stop transmitting while sensing, which decreases spectrum efficiency. For this reason, balancing spectrum efficiency and sensing accuracy is an important issue. Moreover, because sensing time directly affects transmission performance,

novel spectrum sensing algorithms must be developed such that the sensing time is minimized within a given sensing accuracy [1].

- *Wideband sensing:* Wideband sensing faces technique challenges and there is limited work on it. The main challenge stems from the high data rate radio-front (RF) end requirement to sense the whole band, with the additional constraint that deployed CR systems (like mobile phones) will be limited in data processing rates. To achieve reliable results, the sample rate should be above the Nyquist rate if conventional estimation methods are used, which is a challenging task. Alternatively, the RF end can use a sequence of narrowband bandpass filters to sense one narrow frequency band at a time [14]. However, a large number of RF components are needed for the whole band. For more effective SU network, a multiband sensing-time-adaptive joint detection framework has been proposed in [15], [16], which adaptively senses multiple narrowband channels jointly to maximize the achievable opportunistic throughput of the SU network while keeping the interference with the PU network bounded to a reasonably low level. Based on energy detector for narrowband sensing, the sensing time and detection thresholds for each narrowband detector are optimized jointly, which is different from the previous multiband joint detection framework in [17].

- *Synchronization:* Besides the synchronization problem for quiet sensing period, spectrum synchronization before the data transmission for non-contiguous OFDM based systems is also a challenge. To address this challenge, a scheme has been proposed in [18] to use the received training symbols to calculate a posterior probability of each subband's being active without the information of out-of-band spectrum synchronization. The proposed hard-decision-based detection (HDD) utilizes a set of adjacent subbands while the soft-decision-

based detection (SDD) uses all the subbands for detection. Both HDD and SDD schemes provide satisfactory performance while SDD performs better.

Spectrum Decision

CR networks require the capability to decide which spectrum is the best spectrum band among the available bands according to the QoS requirements of the applications. This notion is called *spectrum decision* and constitutes a rather important but as yet unexplored topic in CR networks. Spectrum decision is closely related to the channel characteristics and operations of primary users. Furthermore, spectrum decision is affected by the activities of other CR users in the network. Spectrum decision usually consists of two steps: first, each spectrum band is characterized, based on not only local observations of CR users but also statistical information of primary networks. Then, based on this characterization, the most appropriate spectrum band can be chosen. In the following we investigate the channel characteristics, decision procedures, and research challenges in CR networks [1].

A. Channel Characteristics In Cognitive Radio Networks

Because available spectrum holes show different characteristics that vary over time, each spectrum hole should be characterized considering both the time-varying radio environment and spectrum parameters, such as operating frequency and bandwidth. Hence, it is essential to define parameters that can represent a particular spectrum band as follows:

- *Interference*: From the amount of interference at the primary receiver, the permissible power of a CR user can be derived, which is used for the estimation of channel capacity.

- *Path loss*: The path loss is closely related to distance and frequency. As the operating frequency increases, the path loss increases, which results in a decrease in the transmission range. If transmission power is increased to compensate for the increased path loss, interference at other users may increase.
- *Wireless link errors*: Depending on the modulation scheme and the interference level of the spectrum band, the error rate of the channel changes.
- *Link layer delay*: To address different path loss, wireless link error, and interference, different types of link layer protocols are required at different spectrum bands. This results in different link layer delays. It is desirable to identify the spectrum bands that combine all the characterization parameters described previously for accurate spectrum decision. However, a complete analysis and modeling of spectrum in CR networks has not been developed yet [1].

B. Decision Procedure

After the available spectrum bands are characterized, the most appropriate spectrum band should be selected, considering the QoS requirements and spectrum characteristics. Accordingly, the transmission mode and bandwidth for the transmission can be reconfigured. To describe the dynamic nature of CR networks, a new metric — *primary user activity* — is proposed[19], which is defined as the probability of a primary user appearance during CR user transmission. Because there is no guarantee that a spectrum band will be available during the entire communication of a CR user, it is important to consider how often the primary user appears on the spectrum band.

However, because of the operation of primary networks, CR users cannot obtain a reliable communication channel for a long time period. Moreover, CR users may not detect any single spectrum band to meet the user's requirements. Therefore, multiple noncontiguous spectrum bands can be simultaneously used for transmission in CR networks. This method can create a signal that is not only capable of high data throughput, but is also immune to interference and primary user activity. Even if spectrum handoff occurs in one of the current spectrum bands, the rest of the spectrum bands will maintain current transmissions[1].

C. Spectrum Decision Challenges

In the development of the spectrum decision function, several challenges still remain unsolved:

- *Decision model*: Spectrum capacity estimation using signal-to-noise ratio (SNR) is not sufficient to characterize the spectrum band in CR networks. Also, applications require different QoS requirements. Thus, design of application- and spectrum-adaptive spectrum decision models is still an open issue.
- *Cooperation with reconfiguration*: CR techniques enable transmission parameters to be reconfigured for optimal operation in a certain spectrum band. For example, even if SNR is changed, bit rate and bit error rate (BER) can be maintained by exploiting adaptive modulation instead of spectrum decision. Hence, a cooperative framework with reconfiguration is required in spectrum decision.
- *Spectrum decision over heterogeneous spectrum bands*: Currently, certain spectrum bands are assigned to different purposes, whereas some bands remain unlicensed. Thus, a CR network should support spectrum decision operations on both the licensed and unlicensed bands[1].

Spectrum Sharing

The shared nature of the wireless channel requires the coordination of transmission attempts between CR users. In this respect, spectrum sharing should include much of the functionality of a MAC protocol. Moreover, the unique characteristics of CRs, such as the coexistence of CR users with licensed users and the wide range of available spectrum, incur substantially different challenges for spectrum sharing in CR networks. The existing work in spectrum sharing aims to address these challenges and can be classified by four aspects: the *architecture*, *spectrum allocation behavior*, *spectrum access technique*, and *scope*.

The first classification is based on the architecture, which can be *centralized* or *distributed*:

- *Centralized spectrum sharing*: The spectrum allocation and access procedures are controlled by a central entity. Moreover, a distributed sensing procedure can be used such that measurements of the spectrum allocation are forwarded to the central entity, and a spectrum allocation map is constructed. Furthermore, the central entity can lease spectrum to users in a limited geographical region for a specific amount of time. In addition to competition for the spectrum, competition for users can also be considered through a central spectrum policy server [20].
- *Distributed spectrum sharing*: Spectrum allocation and access are based on local (or possibly global) policies that are performed by each node distributively [21]. Distributed solutions also are used between different networks such that a base station (BS) competes with its interferer BSs according to the QoS requirements of its users to allocate a portion of the spectrum. The recent work on comparison of centralized and distributed solutions reveals

that distributed solutions generally closely follow the centralized solutions, but at the cost of message exchanges between nodes. The second classification is based on allocation behavior, where spectrum access can be *cooperative* or *noncooperative*.

- *Cooperative spectrum sharing*: Cooperative (or collaborative) solutions exploit the interference measurements of each node such that the effect of the communication of one node on other nodes is considered. A common technique used in these schemes is forming clusters to share interference information locally. This localized operation provides an effective balance between a fully centralized and a distributed scheme.

- *Non-cooperative spectrum sharing*: Only a single node is considered in non-cooperative (or non-collaborative, selfish) solutions [22]. Because interference in other CR nodes is not considered, non-cooperative solutions may result in reduced spectrum utilization. However, these solutions do not require frequent message exchanges between neighbors as in cooperative solutions. Cooperative approaches generally outperform noncooperative approaches, as well as closely approximating the global optimum. Moreover, cooperative techniques result in a certain degree of fairness, as well as improved throughput. On the other hand, the performance degradation of non-cooperative approaches are generally offset by the significantly low information exchange and hence, energy consumption. The third classification for spectrum sharing in CR networks is based on the access technology [23]:

- *Overlay spectrum sharing*: Nodes access the network using a portion of the spectrum that has not been used by licensed users. This minimizes interference to the primary network.

- *Underlay spectrum sharing*: The spread spectrum techniques are exploited such that the transmission of a CR node is regarded as noise by licensed users. Underlay techniques can utilize higher bandwidth at the cost of a slight increase in complexity. Considering this trade-off, hybrid techniques can be considered for the spectrum access technology for CR

networks. Finally, spectrum sharing techniques are generally focused on two types of solutions: spectrum sharing inside a CR network (*intranetwork spectrum sharing*) and among multiple coexisting CR networks (*internetwork spectrum sharing*), as explained in the following:

- *Intranetwork spectrum sharing*: These solutions focus on spectrum allocation between the entities of a CR network. Accordingly, the users of a CR network try to access the available spectrum without causing interference to the primary users. Intranetwork spectrum sharing poses unique challenges that have not been considered previously in wireless communication systems.
- *Internetwork spectrum sharing*: The CR architecture enables multiple systems to be deployed in overlapping locations and spectrum.

A. Spectrum Sharing Challenges

There are many open research issues for the realization of efficient and seamless open spectrum operation in CR networks, such as:

- *Common control channel*: A common control channel (CCC) facilitates many spectrum sharing functionalities. However, because a channel must be vacated when a primary user chooses a channel, implementation of a fixed CCC is infeasible. Moreover, in CR networks a channel common to all users is highly dependent on topology and varies over time[24]. Consequently, either CCC mitigation techniques must be devised or local CCCs must be exploited for clusters of nodes.
- *Dynamic radio range*: Due to the interdependency between radio range and operating frequency, the neighbors of a node may change as the operating frequency changes. So far,

there is no work addressing this important challenge in CR networks, and we advocate frequency-aware spectrum sharing techniques.

- *Spectrum unit*: Almost all spectrum decision and sharing techniques consider a channel as the basic spectrum unit. Hence, the definition of a channel as a spectrum unit is crucial in developing algorithms.
- *Location information*: An important assumption in the existing work is that secondary users know the location and transmit power of primary users so that interference calculations can be performed easily. However, such an assumption may not always be valid in CR networks.

Spectrum Mobility

The fourth step of spectrum management, as explained earlier, is *spectrum mobility* management. After a CR captures the best available spectrum, primary user activity on the selected spectrum may necessitate that the user change its operating spectrum band(s), which is referred to as spectrum mobility. Spectrum mobility gives rise to a new type of handoff in CR networks, *spectrum handoff*. Protocols for different layers of the network stack must adapt to the channel parameters of the operating frequency. Moreover, they should be transparent to spectrum handoff and the associated latency. Each time a CR user changes its frequency of operation, the network protocols may require modifications to the operation parameters. The purpose of the spectrum mobility management in CR networks is to ensure smooth and fast transition leading to minimum performance degradation during a spectrum handoff. An important requirement of mobility management protocols is information about

the duration of a spectrum handoff. This information can be provided by the sensing algorithm. After the latency information is available, the ongoing communications can be preserved with only minimum performance degradation. The intrinsic characteristics of a CR network give rise to two novel concepts: spectrum mobility and spectrum handoff. So far, there is no research effort to address the problems of spectrum handoff. Although the mobility-based handoff mechanisms that have been investigated in cellular networks may lay the groundwork in this area, there are still open research topics to be investigated[1].

A. Spectrum Mobility Challenges

The following are the open research issues for efficient spectrum mobility in CR networks:

- *Spectrum mobility in the time domain*: CR networks adapt to the wireless spectrum based on the available bands. Because these available channels change over time, enabling QoS in this environment is challenging.
- *Spectrum mobility in space*: The available bands also change as a user moves from one place to another. Hence, continuous allocation of spectrum is a major challenge [1].

Chapter III. PROPOSED SPECTRUM DECISION AND SPECTRUM SHARING ALGORITHM

Introduction

In current communication networks, the average spectrum utilization is between 15% to 85%. Cognitive Radio (CR) is a solution to increase the spectrum utilization and ultimately the network capacity leading to generating new revenue streams with higher quality of service. With increasing demand for higher capacity in wireless networks due to the rapid growth of new applications such as multimedia, the network resources such as spectrum should be used more efficiently to fulfill the need for both quantity and quality of service. This implies an optimum resource management [25],[26]. Spectrum is one of the most challenging network resources which needs to be carefully consumed. Cognitive Radio Networks (CRN) are supposed to efficiently use idle portions of the spectrum (resource grid). There are many techniques to sense the idle spectrum channels and manage them to increase the networks efficiency.

The works done in spectrum sharing has faced some challenges and can be categorized as centralized spectrum sharing vs. distributed spectrum sharing, and cooperative spectrum

sharing vs. non-cooperative spectrum sharing. Spectrum sharing can also be considered from inter or intra network perspective as either one or two operators share the resources. On the other hand, the network topology and the user distribution are determining factors that directly affect the network state of being either overloaded or underloaded. CRs can be employed in many applications. CR using dynamic spectrum access can alleviate the spectrum congestion through efficient allocation of bandwidth and flexible spectrum access. It provides additional bandwidth and versatility for rapidly growing data applications. Moreover, a CR network can also be implemented to enhance public safety and homeland security. A natural disaster or terrorist attack can destroy existing communication infrastructure, so an emergency network becomes indispensable to aid the search and rescue. CR can also improve the quality of service when frequency changes are needed due to conflict or interference, the CR frequency management software will change the operating frequency automatically even without human intervention. Additionally, the radio software can change the service bandwidth remotely to accommodate new applications. As communication networks tend to become more social-like networks, Ad hoc networks and in particular power-law distributed networks i.e. scale-free networks are proposed in this thesis to be considered for developing spectrum sharing technique then a new method for sharing the spectrum is proposed and proved to have the optimum performance in increasing the network capacity. At the end the results are presented and compared.

Network Topology

The network topology is one of the main factors in considering the traffic flow and resource management in telecommunication networks. There are different ad hoc topologies like random and scale-free discussed in network theories each presenting certain characteristics.

A. Random Topology

There are classes of networks where the nodes are attached to the network in a random way meaning that the number of connections of nodes has a normal distribution. The degree (number of links to the node) distribution of nodes in such networks is a Gaussian type distribution.

B. Scale-Free Topology

In 1999, A. L. Barabasi, and R. Albert (BA) proposed a scale-free network model based on a mechanism of growth with preferential attachment characterized with power-law distribution of the nodes degree [27]. Scale-free networks are robust to random attacks (node removal) and very well describe the nature of real world networks where there are always few nodes with much higher degree called hubs. Each new node enters the network initially with ability to have m links to existing nodes. The probability to connect to an existing node is dependent on the degree of that node meaning that the new node gets connected most probably to nodes with higher degree. The degree distribution for this model is a power-law distribution. The probability of a node to have a degree d_i is given by

$$P\{d_i\} = d_i^{-\alpha} \quad (1)$$

where $2 < \alpha < +\infty$.

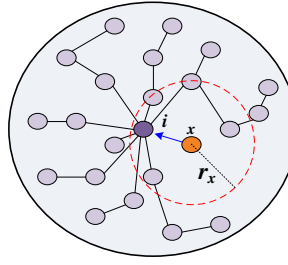


Figure 4 scale-free network formation with power-law degree distribution

The distribution tail shows the nodes with highest degree called hubs. Here we use scale-free properties to better sense network traffic and manage the resources. Since hubs have the highest degrees amongst the nodes and because of their many connections, they have big impact on overall behavior of the network [27]. Consider a cluster of having N_0 nodes and some newcomers tends to attach to this network. The newcomer starts to scan its neighborhood in a radius of r_x which is determined by minimum satisfactory bitrate. There will be some existing nodes within r_x from which only one node is selected to be connected based on scale-free algorithm and that is the node with highest degree and of course the one with the best link quality as in Figure 4.

Spectrum Sensing

The spectrum sensing is one of the main layer tasks for CR system to obtain the spectrum usage information and the presence of PUs. Spectrum detection is based on the detection of the signal from PU through the observation of cognitive radio network.

The sensing methods can be categorized in three methods: i) Energy Detection, ii) Matched Filter, and iii) Feature Detection. The spectrum sensing method considered for this thesis is

Energy Detection. Since, it is particularly suitable for multiband sensing because of its low computational and implementation complexities. We presume using OFDM modulation with M sub carriers with bandwidth W . In this thesis we premised the IEEE 802.22 as it has developed air interface for opportunistic SU access to the TV spectrum in which PUs change slowly [28].

The timing model for spectrum sensing is shown in Fig. 2.a and spectrum mobility model for SUs is depicted in Fig. 2.b. The required time for channel estimation, spectrum sensing and sharing is indicated by τ . According to the [29] the given channel estimation delay is for WCDMA/HSDPA, so the scaled delay for a shorter sub-frame length in UTRAN LTE is considered for this thesis. For each Resource Block (RB), there are 7 frames in time frame and 12 subcarriers and each square in Fig .5.b is called Resource Element (RE In Fig. 5.a. T is time length of each frame and K is number of frames. Supposed that received signal at SUs sampled at f_s over i th sub channel where values of discretized samples at $t = n T_s$, which T_s is $0.1\mu s$ in our framework. In discrete form, when the primary user is active, we define two hypotheses as follow:

$$\begin{cases} y_i(n) = h_i x_i(n) + u_i(n) & , \mathcal{H}_{1,i} \\ y_i(n) = u_i(n) & , \mathcal{H}_{0,i} \end{cases} \quad (2)$$

That h_i is the subchannel gain between PU transmitter and SU receiver with variance $E(|h_i|^2) = \sigma_{h,i}^2$. The signal transmitted, x_i , by PU is assumed to be independent and identically distributed (*i.i.d*), $\mathcal{CN}(0, \sigma_s^2)$, and u_i , the noise, is circularly symmetric complex Gaussian (CSCG) noise.

A. Energy Detection

In order to detect the RF energy in the certain subcarrier for a given PU, the CR service residing in the WCD samples on-the-air signal constructs the following test statistics as the observed energy summation within N samples to decide on the presence of the active users in targeted subcarrier [30].

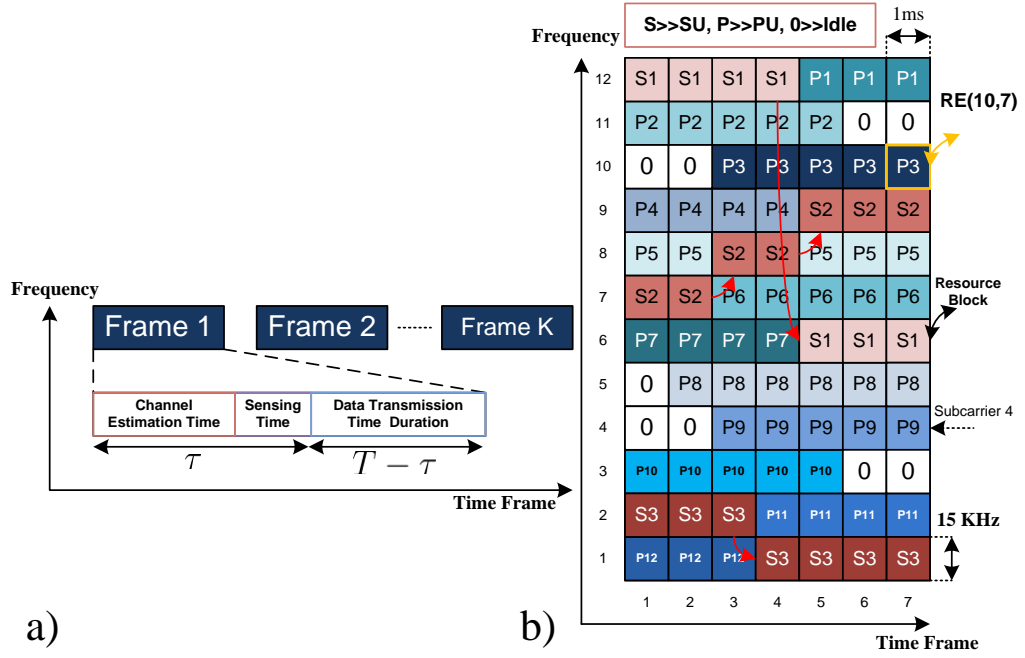


Figure 5 a)Timing Model, b)Resource Block & Dynamic Resource Management

$$\mathcal{U}_i = \begin{cases} \frac{1}{N_i} \sum_{n=1}^{N_i} |h_i x_i(n) + u_i(n)|^2, \mathcal{H}_{1,i} \\ \frac{1}{N_i} \sum_{n=1}^{N_i} |u_i(n)|^2, \mathcal{H}_{0,i} \end{cases} \quad (3)$$

N_i is number of samples transmitted on duration τ_i which is equal to $N_i = \tau_i f_s$. The PDF of \mathcal{U}_i is Central Chi Square distribution with $2N_i$ degrees of freedom, $\chi_{2N_i}^2$, for when no PU

exists and on Central Chi Square distribution with $2N_i$ degrees of freedom and non-centrality parameter $2\gamma_i, \mathcal{X}_{2N_i}^2(2\gamma_i)$, for the state that PU exists. So:

$$\mathcal{F}_{\mathcal{U}_i}(\mathcal{U}_i) = \begin{cases} \mathcal{X}_{2N_i}^2 = \frac{1}{2^{2N_i} \Gamma(N_i)} \mathcal{U}_{i,1}^{N_i-1} e^{-\frac{\mathcal{U}_{i,1}}{2}}, \mathcal{H}_{1,i} \\ \mathcal{X}_{2N_i}^2(2\gamma_i) = \frac{1}{2} \left(\frac{\mathcal{U}_{i,0}}{2\gamma_i} \right)^{\frac{N_i-1}{2}} e^{-\frac{2\gamma_i + \mathcal{U}_{i,0}}{2}} I_{N_i-1}(\sqrt{2\gamma_i \mathcal{U}_{i,0}}) \end{cases}, \mathcal{H}_{0,i} \quad (4)$$

where the signal to noise ratio (SNR) is depicted by $\gamma_i = \frac{\sigma_{x_i}^2 \sigma_{h,i}^2}{\sigma_{u_i}^2}$, $\Gamma(\cdot)$ denotes the gamma function, $I_\alpha(\cdot)$ is the first kind modified Bessel function of degree α .

Two performance parameters for spectrum sensing are probability of detection, P_d , and probability of false alarm, P_f , which is probability of when the frequency is unoccupied but we get alarm that the frequency is used. Hence, Higher P_d protects PU from interfering with SUs and smaller P_f causes better band usage efficiency. To calculate probability of detection [31]:

$$P_{d,i}(\epsilon_i, \tau_i, \gamma_i) = \Pr(\mathcal{U}_i > \epsilon_i | \mathcal{H}_1) = \int_{\epsilon_i}^{\infty} p_1(x) dx \quad (5)$$

where ϵ_i is threshold and τ_i is denoted sensing time for i th subchannel.

$$P_{d,i}(\epsilon_i, \tau_i, \gamma_i) = \mathcal{Q}\left(\left(\frac{\epsilon_i}{\sigma_{u_i}^2} - \gamma_i |h_i|^2 - 1\right) \sqrt{\frac{\tau_i f_s}{2\gamma_i |h_i|^2 + 1}}\right) \quad (6)$$

Now the probability of missed detection can be defined as:

$$P_{m,i}(\epsilon_i, \tau_i, \gamma_i) = 1 - P_{d,i}(\epsilon_i, \tau_i, \gamma_i) \quad (7)$$

We have following equations for probability of false alarm,

$$P_{f,i}(\epsilon_i, \tau_i) = \Pr(\mathcal{U}_i > \epsilon_i \mid \mathcal{H}_0) = \int_{\epsilon_i}^{\infty} p_0(x) dx \quad (8)$$

$$P_{f,i}(\epsilon_i, \tau_i) = \mathcal{Q}\left(\left(\frac{\epsilon_i}{\sigma_{u_i}^2} - 1\right)\sqrt{\tau_i f_s}\right) \quad (9)$$

Usually to evaluate the performance of energy detection, the goal is to minimize P_f for a target P_d or to maximize P_d for a target P_f . At first we assume $P_{d,i,target}$ is our target probability of detection,

$$\epsilon_i(P_{d,i,target}) = \left(\frac{\mathcal{Q}^{-1}(P_{d,i,target})}{\sqrt{\frac{\tau_i f_s}{2\gamma_i |h_i|^2}}} + \gamma_i |h_i|^2 + 1\right)\sigma_{h_i}^2 \quad (10)$$

$$P_{f,i}(\epsilon_i(P_{d,i,target}), \tau_i) = \mathcal{Q}\left(\mathcal{Q}^{-1}(P_{d,i,target})\sqrt{2\gamma_i |h_i|^2 + 1} + \gamma_i |h_i|^2 \sqrt{\tau_i f_s}\right) \quad (11)$$

$P_{f,i}(\epsilon(P_{d,i,target}), \tau_i)$ is the probability of false alarm regard to target $P_{d,i}$, and \mathcal{Q}^{-1} is the inverse of complementary error function. For a target $P_{f,i,target}$ we have:

$$\epsilon_i(P_{f,i,target}) = \left(\frac{\mathcal{Q}^{-1}(P_{f,i,target})}{\sqrt{\tau_i f_s}} + 1\right)\sigma_{h_i}^2 \quad (12)$$

$$P_{d,i}(\epsilon_i(P_{f,i,target}), \tau_i) = \mathcal{Q}\left(\frac{\mathcal{Q}^{-1}(P_{f,i,target}) - \gamma_i |h_i|^2 \sqrt{\tau_i f_s}}{\sqrt{2\gamma_i |h_i|^2 + 1}}\right) \quad (13)$$

$P_{d,i}(\epsilon(P_{f,i,target}), \tau_i)$ is the probability of detection when $P_{f,i}$ is targeted. As a result, in this part, probability of false alarm and detection based on $P_{d,i,target}$ and $P_{f,i,target}$, respectively, are calculated. The proposed wide spectrum sensing by energy detection can be shown in figure 6.

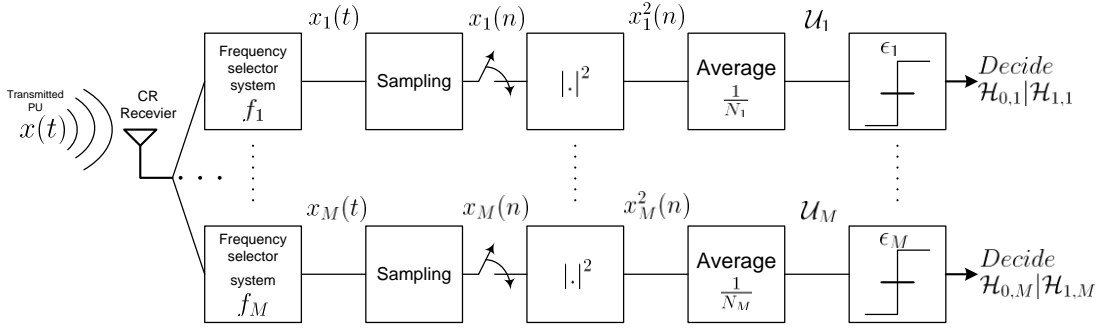


Figure 6 wide spectrum sensing model

Queued Markov Chain Model For Spectrum Analysis-Access

In this section, we consider group of secondary users that tend to access idle licensed spectrum portions in an opportunistic way. The process of sensing and decision making on the spectrum allocation is analyzed with a Markov Chain Process with a *queue state* in which, primary user has the spectrum and secondary users are waiting to access once it is released by primary user. This model is for one subcarrier and can be generalized for a resource block with multiple subcarriers.

The primary user PU is licensed to operate in the spectrum. The PU traffic is modeled as Poisson random process with arrival rate λ_p and departure rate μ_p . The secondary users are indexed by i ($i=1,2,\dots,N$) and modeled with Poisson random process as well; the arrival rate of SU is λ_i and departure rate is μ_i . All users are connected to Cognitive Radio (CR) Control Unit (CU) that controls CR network. To avoid interference with Primary Users (PU), once the PU starts using the subchannel, CU forces the Secondary Users (SU) to leave and if SUs still need to access the subchannel, CU puts them in Queue State (Sq) to find another band or wait for PU to release the subchannel. Here we assume that spectrum band is not allowed to be shared with two or more users concurrently [32], [33], [34].

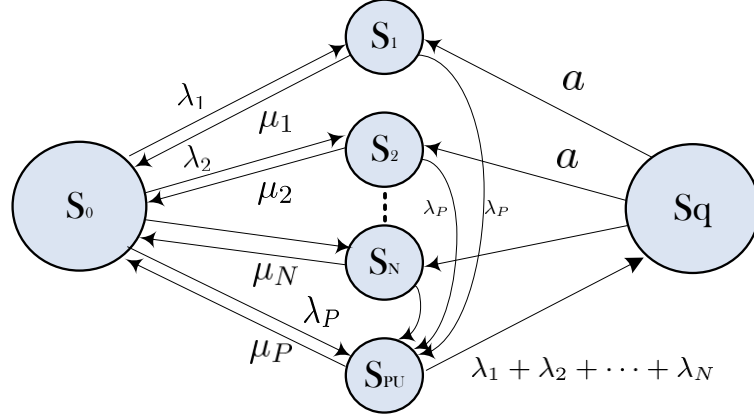


Figure 7 Queued Markov Chain State Machine without sharing

$(N+3)$ -state Markov Chain State Machine is illustrated in Figure 2, where state S_0 means that the spectrum band is idle. Without the loss of generality, the probability of transition from S_0 to S_i ($i=1,2,\dots,N$) is proportional to λ_i 's. S_0 is the state when the subchannel is idle. Inversely, the transition probability from S_i to S_0 is μ_i . If SU's are operating in subchannel, and PU shows up, SU's have to leave the subchannel. The probability of S_i to S_{PU} is proportional to arrival rate of primary user. If PU is active in the subchannel by itself i.e. S_{PU} , the transition probability from S_{PU} to S_q is proportional to summation of SU's arrival rates, $\lambda_1 + \lambda_2 + \dots + \lambda_N$, because when they request to access, due to PU's priority, they will be forced to be put in queue. In S_q state, as soon as PU leaves the subchannel, the user state changes to either of S_i whose total probabilities are proportional to departure rate of PU that are considered a_i .

The set of equations based on above Markov Chain Model is as follow:

$$\mathbf{P}\mathbf{H} = 0 \quad (14)$$

$$\Pi_0 + \Pi_1 + \Pi_2 + \dots + \Pi_N + \Pi_Q + \Pi_P = 1 \quad (15)$$

where \mathbf{H} is the matrix that characterizes the transition state of the Markov chain, and $\Pi = [\Pi_0, \Pi_1, \Pi_2, \dots, \Pi_N, \Pi_Q, \Pi_P]$ is the state probability vector for $S_0, S_1, S_2, \dots, S_N, S_q, S_{PU}$ respectively.

The \mathbf{H} matrix of our model is as follow:

$$\begin{bmatrix} \Pi_0, \Pi_1, \dots, \Pi_N, \Pi_Q, \Pi_P \end{bmatrix} \cdot \begin{bmatrix} -(\lambda_1 + \lambda_2 + \dots + \lambda_N + \lambda_p) & \lambda_1 & \dots & \lambda_N & 0 & \lambda_p \\ \mu_1 & -(\mu_1 + \lambda_p) & \dots & 0 & 0 & \lambda_p \\ \vdots & \vdots & & \vdots & \vdots & \vdots \\ \mu_N & 0 & \dots & -(\mu_N + \lambda_p) & 0 & \lambda_p \\ 0 & a_1 & \dots & a_N & -(a_1 + \dots + a_N) & 0 \\ \mu_p & 0 & \dots & 0 & \lambda_1 + \lambda_2 + \dots + \lambda_N & -(\lambda_1 + \lambda_2 + \dots + \lambda_N + \mu_p) \end{bmatrix} = \mathbf{0} \quad (16)$$

So the set of equations from (16) will be:

$$-\Pi_0(\sum_{i=1}^N \lambda_i + \lambda_p) + \sum_{i=1}^N (\Pi_i \mu_p) + \Pi_p \mu_p = 0$$

$$\Pi_0 \lambda_i - \Pi_i (\mu_i + \lambda_p) + \Pi_Q a_i = 0$$

$$-\Pi_Q \cdot (\sum_{i=1}^N a_i) + \Pi_P \cdot (\sum_{i=1}^N \lambda_i) = 0$$

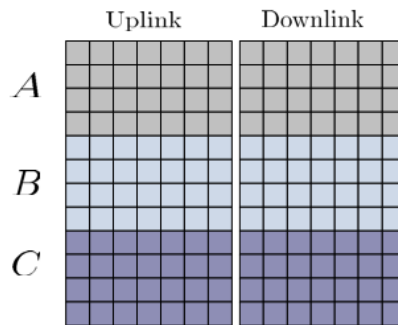
$$\lambda_p \cdot (\sum_{i=1}^N) - \Pi_P \cdot (\sum_{i=1}^N \lambda_i + \mu_p) = 0$$

With which all Π entries will be calculated with known entries of \mathbf{H} . With more complex systems, computer aided solution is required to above set of equations. This has been done for specific \mathbf{H} in simulation section.

Max-Rate Spectrum Sharing

In communication networks, there are always unused resources due to mismanagement or the traffic usage pattern. However, it is possible to share the inactive resources between different portions of the network and in some cases share them with other service providers. Therefore, implementing spectrum sharing would highly improve the spectrum utilization efficiency and reduce the request blocking rate (Grade of Service). We assume that the network topology is mainly scale free which has ad hoc properties plus that nodes are preferentially distributed mostly around hubs; different portions of the network are then categorized as clusters which have access to certain part of the resources. In this thesis we deal with a case where clusters are overloaded and needs extra resources for providing acceptable quality of service. Figure 8 shows the infrastructure of scale free inter-network interaction. Each cluster is defined with a cluster hub and a range of operation. Clusters A, B, and C each of N_A , N_B , and N_C active users are initially planned to operate in separate allocated resource blocks (AU, AD), (BU, BD), and (CU, CD), respectively as in Figure 8. Index U represents the uplink and D is for downlink communications. If a new user attaches to cluster A and all of the resources in resource block A are busy, the hub node in cluster A i.e. H_A , tries to see if there is available idle resources in neighboring clusters. The resource elements in this portion are in the form of REU and RED. For instance, $REU(i,j)$ represents the resource element for uplink at i th subcarrier and j th time slot. Now consider a new user willing to attach to cluster A by sending a request to the cluster hub, H_A . We presume at the time of request all of the resources of cluster A are occupied. The new user is not blocked at this stage like conventional communication networks. Instead, H_A starts to sense and search for potential available resources in neighboring clusters like B, and C. if the resource is available in either neighboring clusters for more than a limited period of time, it will be

granted to cluster A and finally allocated to the new user. There is a process to consider associated criteria for releasing and granting the resources from other clusters to requesting clusters. In real world applications the hubs in clusters are distinguished mainly with their degree which is the number of active links either terminated to or originated from these hub nodes. Hubs are basically supposed to have access to as many resources as the number of active links connected to them. This leads to initially interrogating the more populated clusters as opposed to handshaking with less important (lower degree) nodes. The degree of the nodes is then considered in evaluating the merit for a specific hub. The Merit function determines the merit value for each requesting node given a certain set of available resources in granting cluster. One of the main factors in merit function is that the idle resources in neighboring clusters are not idle for unlimited time. As opposed, based on the number of active users in granting clusters, there is an average number of requests coming from user side which leads to always updating a request queue. This queue will be monitored at the time of releasing the idle resource to make sure that there is no potential demand from local cluster for the idle resource.



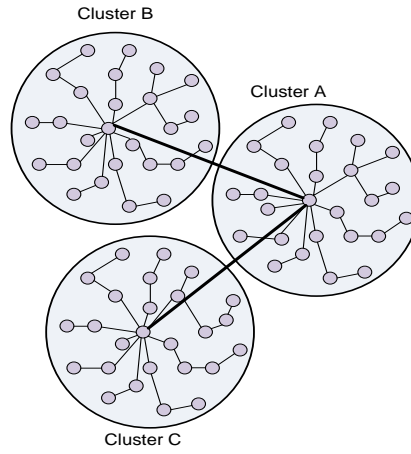


Figure 8 Scale free infrastructure and its UL and DL spectrum resource model

A. Cognitive Parameters

The hubs are presumed to be Cognitive Enabled in order to be able to sense unoccupied channels. A channel is said to be unoccupied if the instantaneous radio frequency (RF) energy (plus noise) in this channel, is less than the certain interference limit. The probability that the channel is available for a period of time is greater than a threshold p_{th} , These measures can be evaluated by the CR node through monitoring the traffic pattern. The Interference is measured using Carrier to Interference ratio ($\frac{C}{I}$) for each subcarrier. The probability of a channel to be available for a certain period of time is predicted by looking up the traffic profiles both in real time and the traffic history. Because the network has a scale-free topology, the requesting users/nodes are characterized with their degree. d_i is the degree of i th node in a cluster. The degree information of the nodes is also communicated along with the request or obtained from network statistics. Nodes with higher degree have higher priority. This information is known in the local cluster and there is no need for global information broadcast [35],[36].

Another criterion for granting the network resources to requesting users is the Customer Classification (Q_i). Each of these new users has a specific service profile with different QoS

like gold, silver and bronze. When a resource is reported to be available, it's now time to see which users of what level of quality (priority) have requested the resource. There are users with different subscription profiles which enables the decision making process directed based on the required QoS from user side. Another level of priority is also defined for emergency and security cases which dominate all incoming requests.

Signal to Noise Ratio (SNR) is important parameter that is considered for the users. Finally, the interrogated CR node from neighboring cluster reports the available channels with a set of information $(\frac{C}{I})$, p to the overloaded cluster. At the requesting cluster, d_i , Q_i are used to classify the users for granting borrowed resources.

B. Merit Function

For the reported available resources to be granted to requesting users/nodes in a fairly optimum way there needs to be a function that considers the Cognitive Parameters to calculate the merit for users/nodes.

C. Channel Indexing Function

Let R denote the set of available resources reported by the CR node. (Hub node in neighboring cluster(s)). The Channel Indexing Function (CIF) is meant for indexing the elements in R based on received Cognitive Parameters $R = \{r_1, r_2, \dots, r_L\}$ Where $r_i = \phi_i((\frac{C}{I})_i, p_i)$ for every available channel. Then CIF operates on R to generate χ

$$\Phi(R) = \chi \quad (17)$$

$\chi = \{x_1, x_2, \dots, x_L\}$ is the output of Channel Indexing Function, Φ , which consists of sorted performance indices for all available channels. U is the list of cognitive parameters collected

from requesting users/nodes from requesting clusters. $\mathbf{U} = \{u_1, u_2, \dots, u_L\}$ where $u_i = \psi_i(SNR_i, Q_i, d_i)$. Then the Merit Function is applied to calculate the merit value for requesting users.

$$\Psi(\mathbf{U}) = \mathbf{M} \quad (18)$$

where \mathbf{M} is the set of merit values for all requesting users i.e. $\mathbf{M} = \{m_1, m_2, \dots, m_L\}$. ϕ_i and ψ_i are CIF and Merit functions operating on each resource and user respectively and can be defined as:

$$\phi_i = \omega_p p_i + \omega_l \left(\frac{C}{I}\right)_i \quad (19)$$

$$\psi_i = \omega_d d_i + \omega_Q Q_i + \omega_S SNR_i \quad (20)$$

All ω parameters are set according to technical and commercial constraints. We define the SNR for target node i as the summation of uplink (UL) and downlink (DL) SNRs.

$$SNR_i = SNR_i^{UL} + SNR_i^{DL} = \frac{P_x / N_i}{r_x^2} + \frac{P_i / N_x}{r_x^2} \quad (21)$$

P_x and P_i represent the transmit power of the newcomer node x and target node i , respectively. N_x and N_i are the noise power at newcomer and target node receivers.

D. Competitive Indexing Algorithm

\mathbf{M} and χ are matched against each other to grant the best performing channel to the users/nodes with highest merit values because the users with higher value are those who require better quality of service and are in urgent need of resources to either use them or distribute them amongst their neighbors. Then the second best resource is granted to the

second user with highest merit. This process goes on until either there is no request from overloaded cluster or comes a new request from the local cluster which leads to filling up the request queue in the local cluster[37].

Cluster A sends its request to the neighboring clusters. Matrix χ is a set of performance indices for all available resources (channels) in neighboring clusters where x_i is the performance index for i th available resource element which is a function of cognitive parameters for i th subcarrier like interference and availability probability and other potential cognitive parameters that can be defined/measured as well.

Φ and Ψ are determined based on network statistics, measurements, topology and operators commercial strategies. Based on the proposed competitive algorithm for granting available resources, χ and M are sorted in descendingly and the winning channel which is the top indexed one in χ is granted to the user with highest merit value at the top of M . this process goes on until all the demands from cluster A(or all requesting clusters) are supplied. This algorithm gives optimum performance in terms of the increased capacity in the network compared to uniform allocation of resources (without indexing) in response to incoming request.

To evaluate the performance for different algorithms, We define a resource sharing performance index, $\Upsilon = M\chi^T$, which is maximized based on rearrangement inequality for proposed competitive indexing algorithm. Since χ and M are sorted, we can write:

$$x_1 \geq x_2 \geq \dots \geq x_L; m_1 \geq m_2 \geq \dots \geq m_L \quad (22)$$

Let $\sigma_k(\chi)$ and $\sigma_l(M)$ be any arbitrary permutation of χ and M . The rearrangement inequality states that for sorted matrices χ and M :

$$\sum_{i=1}^L x_i m_i \geq \sum_{i=1}^L \sigma_k(x_i) \sigma_l(m_i) \quad (23)$$

$$Y_{opt} = \sum_{i=1}^L x_i m_i \geq \sum_{i=1}^L \sigma_k(x_i) \sigma_l(m_i) = Y_{rand} \quad (24)$$

Υ_{opt} is the performance index of the proposed competitive algorithm. Υ_{opt} can be defined as different known parameters like total increased capacity if χ and M are defined appropriately.

Sharing incorporated in Markov chain model

Now, we put sharing part in our Markov Chain Model as shown in Figure 7. Because of each futures the SU's have, their chance to get spectrum from S_q is different based on our specific sharing policy shown by a_i 's. Based on different policies we considered for allocating the spectrum with SU's, the a_i 's will be different. For example, in Scale-Free Ad Hoc networks, degree is an important feature we can consider for SU that user with greater degree has more priority to get access. In our simulation, we assumed different traffic for each SU. The arrival rates is the same and departure rates are different. The first user has more priority than others in our simulation and the departure rates descending from first to last SU. So, the chance of first user is more than others, because of its less departure rate and its higher priority, and for second user is more than third user, only because of its less departure rate, and so on. As we see, if we increase the number of users, P_q (probability of being in queue) is decreasing and P_{PU} (the probability that only the primary user requested to access) decreasing. At the End, we compared the probability of SU's when number of users is 3. The only difference will be in P_1 's that in sharing method, the chance of user with priority is more (user 1) and the difference between other users is because of their different traffics.

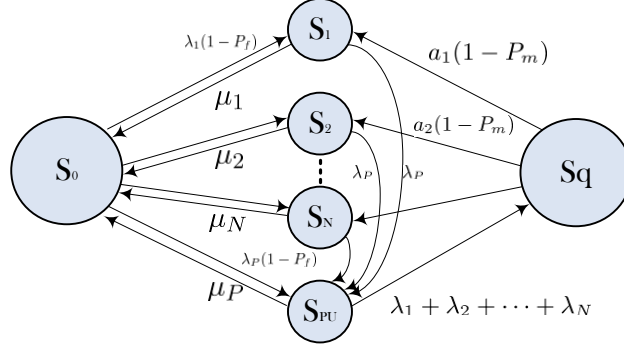


Figure 9 Queued Markov Chain State Machine with sharing

Here $P_d = 1 - P_m$.

In this model, imperfect spectrum sensing consisting of false alarm, P_f and miss-detection, P_m is also considered. If the idle channel is reported as busy, the current state does not change. So $(1 - P_f)$ is multiplied by arrival rates. In addition, when a channel is busy but reported as idle, the state S_q will not be allowed to go to S_i 's. As a result, $a_i \times (1 - P_m)$ is considered as a transition probability.

Simulation

A. Simulation Results For Sensing

SU with greater degree has more priority to get access to subchannel. In our simulation, we assumed different traffic models i.e. λ_i for each SU. We simulated a scenario with 2,3,4 and 5 secondary users and one primary user over one subchannel. $\lambda_p = 2$, $\mu_p = 4$ and $\lambda_i = 3$. The rest of parameters are assigned as in Table 1.

Table 1 Simulation traffic parameters

No.	μ_i	a_i
1	2	2
2	4	0.5
3	6	0.5
4	8	0.5
5	10	0.5

The first user is assumed to have higher degree in our scale-free model resulting in having greater parameter a_1 , which means it will have better chance than other users in the queue. The departure rates are assigned to SU's descendingly. Therefore, the probability of S_1, Π_1 will be greater than other secondary users because of its less departure rate and higher priority. also Π_2 , the probability of S_2 is more than others' since its departure rate is smaller than others' and so on. As we see in Figure 10, if we increase the number of secondary users, Π_Q (probability of S_Q) is increasing and Π_P (the probability of S_{PU}) is decreasing. At the End, we compared the probability of SU's when number of SU's is 3. The only difference between results with *uniform sharing* (all users have equal allocation chance) and *competitive sharing* (users are prioritized) will be in Π_j ($j=1,2,\dots,N$). in our simulation we assumed only first SU has higher priority in *competitive sharing*. As shown in Figure 11, Π_1 in *competitive sharing* is greater than Π_1 in *uniform sharing*.

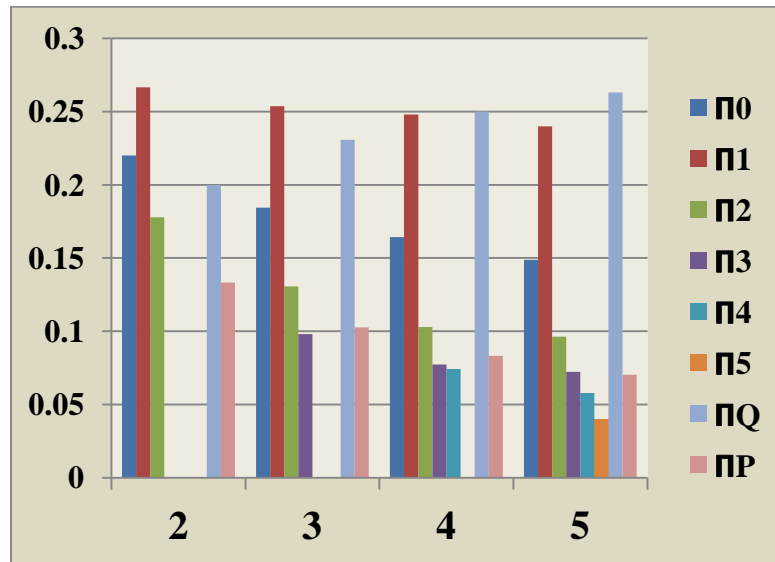


Figure 10 state probabilities using competitive sharing for different number of users

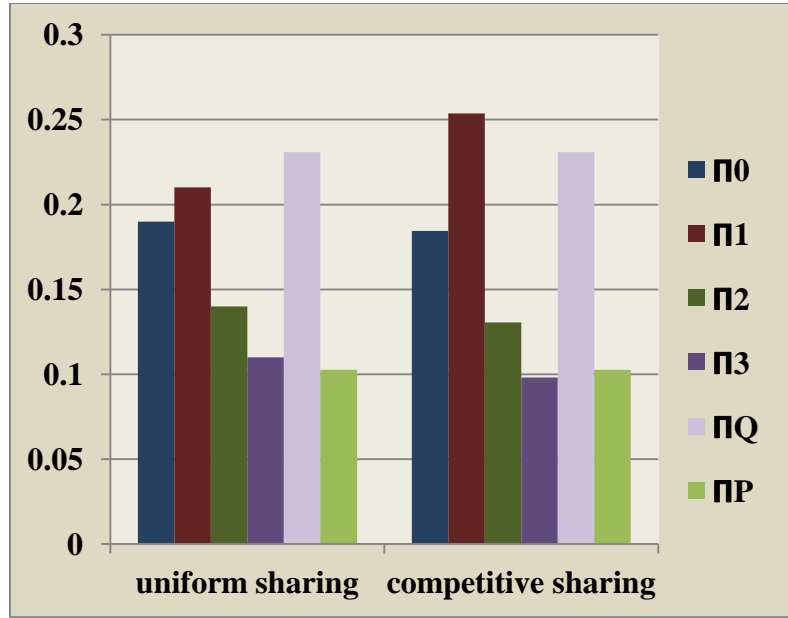


Figure 11 state probabilities using competitive and uniform sharing $N=3$

B. Simulation Results For Sharing

The network structure used in the simulation is a scale-free topology with $N=100$ nodes and three hubs each of 19, 17, and 15 links. The average degree of nodes in this network is 3.7 meaning that each user is in average connected to about 4 nodes. There are 3 clusters centered around aforementioned hubs called cluster A, B, and C respectively. Each cluster uses a typical OFDM (3GPP compliant) resource block of 12 subcarriers in 7 time slots for Uplink and another 7 time slots for Downlinks resulting total 84 resource elements. At each time instance, there are K_i incoming nodes to cluster A and K_o nodes leave this cluster drawn from Poisson distribution. Without spectrum sharing based on the distribution of the requests coming from the users side, cluster A may get overloaded. The capacity and load measures are simulated for cluster A without having the chance to borrow resources from neighboring clusters; Figure 9 demonstrates the performance of Uniform Indexing and Competitive Indexing. Our method in Spectrum Sharing outperforms the Uniform Indexing.

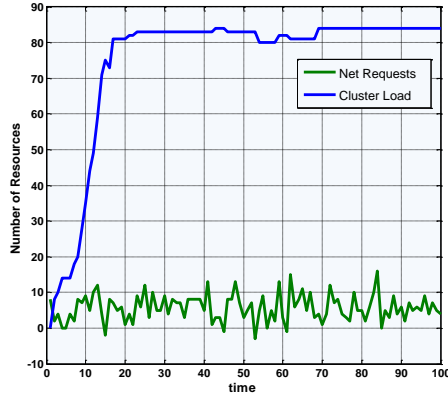


Figure 12 Load and Net Request in cluster A

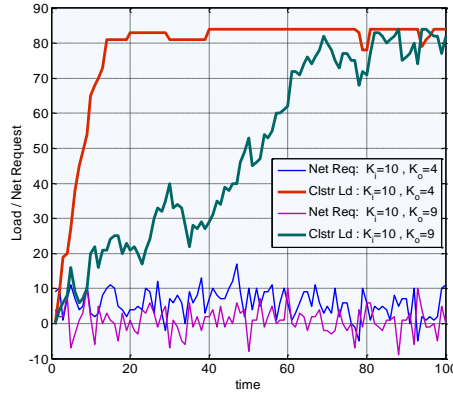


Figure 13 Load with different traffic in cluster A

As we can see in Figure 12, the network gets saturated after a certain time and all resource elements will be occupied and the capacity tends to zero. Figure 13 shows the cluster load and net request for two different incoming and outgoing traffic. To avoid user blocking, CR nodes start to search to find idle resources in neighboring clusters. If the found resources are allocated uniformly to requesting nodes, the Capacity will increase to some extent like purple line in Figure 14, but the optimum algorithm i.e. competitive indexing will outperform any *uniformly random allocation* scheme as green curve in Figure 14. Depending on the distribution of incoming request from users, the capacity increase will be different. Figure 9 shows a case where $K_i=10$ and $K_o=4$.

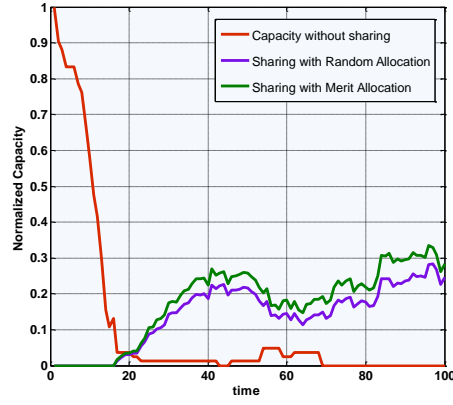


Figure 14 Capacity improvement in cluster A

Because the degree is directly proportional to the indexing performance, and in Scale-Free networks, the difference between users degree is prominent as a key factor, the outperformance of CIF compared to UI algorithm is much higher than when we apply CIF in Random Network shown in Figure 15 and Figure 16.

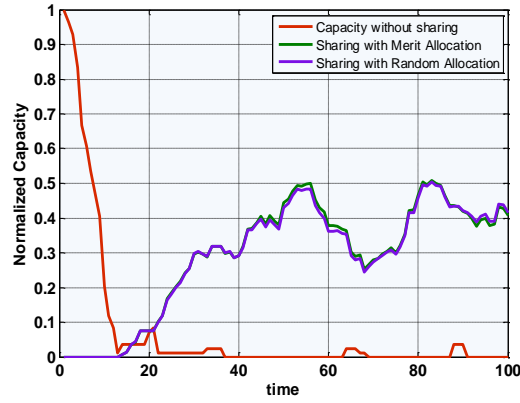


Figure 15 Capacity improvement in cluster A

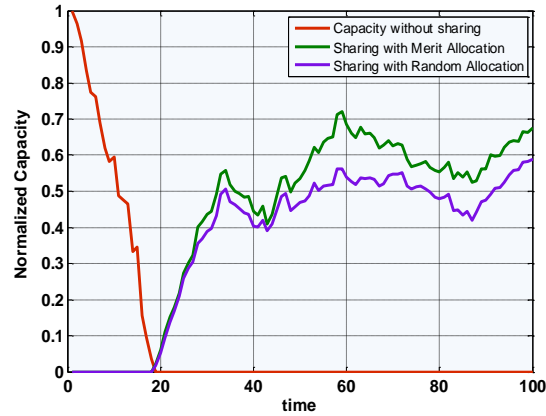


Figure 16 Capacity improvement for Scale-Free Network

Conclusion

In this thesis, we presented the Cognitive Radio framework for wireless Ad Hoc networks. The complete model describes the sensing and sharing procedures in wireless networks in general but the simulation results are for random and scale-free topologies. We introduced *Queued Markov Chain* method in spectrum sensing and *Competitive Indexing Algorithm* in spectrum sharing part. We demonstrate that our proposed *Competitive Indexing Algorithm* outperforms the *Uniform Indexing Algorithm*.

Chapter IV. COGNITIVE RADIO IN SMART GRID

Throughput Analysis on Cognitive Radio Networks for AMI Meters in Smart Grid

Introduction

We consider the future smart grid as leveraging Information and Communications Technology (ICT) facilitated by the smart meter (also named as Advance Infrastructure Metering (AMI)) information networks. The smart meter enables the flow of real-time information within the power utility, between the power utility and its customers. It is essential for AMI to be networked since it enables system wide sensing, utility and customer linkages, and future self healing capability.

Communication network infrastructures represent a very large capital expense. Research on CR has evolved from SDR (see [38],[39]) with an objective of efficient utilization of radio spectrum. In this thesis, we analyze CR in the context of smart energy systems. Although there have been significant advances and improvements in CR hardware, algorithms, and protocols, less attention has been given to developing ubiquitous and pervasive metropolitan

scale CR networks, particularly with respect to smart grid information networking [3]. A metropolitan infrastructure based CR networks is shown in Fig. 1. In this context, there are major challenges to overcome such as Secondary Users (SU) should sense the spectrum and timely model the behavior of the Primary Users (PU). The other issue is how the SUs manage the available spectrum resources and share the resources among the SUs to satisfy the smart grid protocol requirements and meeting the interference constraints suggested by the FCC Spectrum Policy Task.

In such a system, our objective for SUs (i.e. AMI) is to efficiently transmit their delay sensitive traffic over the network and meet the QoS requirements of the smart grid protocol. In this thesis, we investigate different scheduling policies that maximize the downlink sum throughput in the given area and achieving fairness among the SUs. We present an opportunistic scheduling policy that exploits both maximizing the downlink sum throughput and fairness under time-varying channel conditions for multi-user CR network in a metropolitan based environment.

Several authors have defined aspects of AMI networking in smart grids. Mesh, Ethernet and cellular AMI network topology for smart grid has been proposed. In [40] the authors propose mesh networks of Zigbee based transmission architecture. In [41], the authors discuss communication infrastructure based on Ethernet (LAN and WAN). The approach will support automated meter readings and customer home appliance connections. However, wireline systems are not always available. Customer subscription to service must occur and wired system can be challenging to rapidly redeploy, particularly in swiftly enveloping emergencies.

The authors in [42] describe a framework for RF mesh networking interfaced with high speed WiMAX access networks. In [43], overview of architecture, hardware platform, is

reported to enable CR for smart grid communications. Our work discusses the CR network infrastructure architecture from 4G perspective. We also present multi-user performance analysis of various scheduling algorithms in context with AMI units considering the delay occurred due to offloading the processes to cloud in our architecture.

4G Cognitive Radio Framework

A. 4G Cognitive Radio System Architecture

We presume a LTE network as a CR LTE network (4G CR), if the LTE work is adopted the CR techniques. We consider a cloud data center infrastructure based CR network coexisting with PU network shown in Fig.17. The coverage of both the CR base station and PU network base station are similar. As depicted in the Fig. 1 at the center of the each cell, there is base-station which is shared as e Node-B for PUs and as antenna for SUs. The PU base-station only serves to PUs as it lacks the CR protocols capabilities to support SUs. However, it may consider supporting certain features in order to communicate with SUs.

Placement of a Cognitive Radio Antenna on the BTS tower may occur in tandem with deployment of the cellular provider antenna. The CR senses the spectral environment over a wide frequency band, particularly the spectrum in the cell region. It identifies the unused bands in the spectrum. These bands could be owned by cellular companies or license television band owners, but are not limited to these bands or to licensed bands. Sensed information using the CR is relayed to cloud data center. In principle, eNode-B which terminates the air interface protocol and first point of contact for PU is located at the primary user base-station. However, in proposed architecture all the cognitive radio service, waveform service, protocols service, security service, scheduling and control services are

displaced into cloud data center. The CR services identify unused frequency bands, the relevant cognitive services residing in the cloud data center generates a clear to send (CTS) signal.

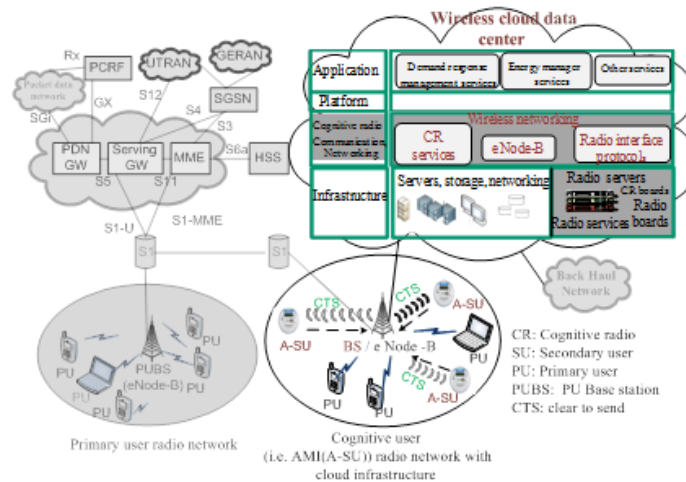


Figure 17 4G CR network system architecture: Scenario of multiple AMI meters serviced by cognitive radio network infrastructure enabled by cloud center coexisting with private cellular network

The CTS is sent back to the AMI meters through the feedback channel via base station. Eventually, the CR antenna relays CTS signals to every AMI in the cell region for uplink transmission.

B. Pervasive Smart Grid Systems

The energy services of the future can be privately contracted services or public services. The cloud center enables convenient, on-demand network access to a shared pool of configurable, computing resources (e.g., networks, servers, storage, applications, and services) that can be rapidly provisioned and released with minimal management effort. There are different cloud computing platform classifications. Standard architectures includes Abi (or Abiquo), Nimbus Open Nebula, Azure (Microsoft), Google (App Engine), Blue

(IBM) and Mosso (Rackspace). Fig.17. depicts the model for a cloud data center architecture optimized for based smart grids. Our Wireless Cloud Data (WCD) model is organized into four principle layers: application layer, platform layer, CR communication and networking layer and infrastructure layer. The first two layers are akin to existing cloud architectures. However, the lower two layers are augmented to enable the CR networking and wireless services. CR communication and networking layer provides services such as cognitive radio services, waveform services, Radio Link Control (RLC), and Medium Access Control (MAC) services. CR services, which provide spectrum management and spectrum sensing, are discussed in detail in section III. The infrastructure layer facilitates the effective integration of computing resources, storage, networks to deploy applications and operating systems. We augment our cloud infrastructure microprocessor racks with FPGA boards targeted to processing high computation rate processes typically associate with CR services, communication waveform signal processing and coding.

CR System Model

In the thesis system model 4G cellular network is considered with N_{su} secondary users sharing the spectrum simultaneously with N_{pu} primary users. It is presumed in the context that the secondary users (i.e. AMI meters) are fixed in sense of geographical location and yields to fixed first and second statistical moments of SINR.

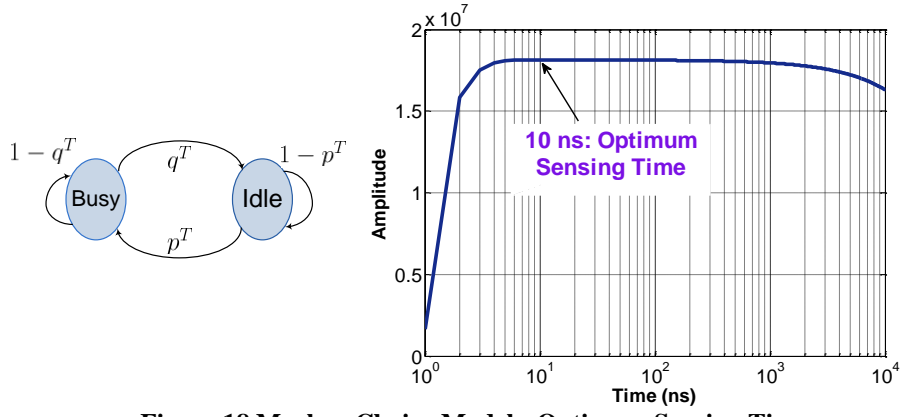


Figure 18 Markov Chains Model; Optimum Sensing Time

A. Primary User Activity Model

In this section, we present a model for primary users' activities which is directly proportional to CR network performance. In our Markov chains model, we consider two states (Busy by PU and Idle) for each subcarrier. The Poisson distribution is considered in the modeling with arrival rate, α , and departure rate, β :

$$N_{tot}(nT_s) = N_{tot}(n(T_s - 1)) + \alpha(nT_s) - \beta(nT_s) \quad (25)$$

as a result, the existing users in a cell is equivalent to total existing users on previous time period added to arrival rate at current time and subtracted by current departure time as mentioned in equation (25). The transition probabilities are p^T and q^T as illustrated in Fig. 18 and the calculated steady probabilities are depicted below [34]:

$$P_{i,BUSY} = \frac{p^T}{p^T + q^T}, P_{i,Idle} = \frac{q^T}{p^T + q^T} \quad (26)$$

Eq. (26) is applied to analyze the model for identifying subcarriers states (i.e. busy or idle).

B. Optimum Sensing Time

The throughput of SU is calculated as follows [17],

$$C_i = W \log_2 \left(1 + \frac{P_{i,SU} |h_{i,SU}|^2}{\mathcal{N}_0} \right) \quad (27)$$

where W is bandwidth, $P_{i,SU}$ is the power of transmitter SU and \mathcal{N}_0 is the noise power and $h_{i,SU}$ is the gain channel between i th SU's transmitter and receiver with variance $E(|h_{i,SU}|^2) = \sigma_{h_{i,SU}}^2$.

Considering probabilities for different states gives us achievable throughput, $R_i(\tau_i)$, calculated by,

$$R_i(\tau_i) = \left(1 - \frac{\tau_i}{T}\right) (1 - P_{f,i}) P_{i,Idle} C_i \quad (28)$$

where $(1 - P_{f,i}(\epsilon_i, \tau_i)) P_{i,Idle}$ is the probability of absence of PU when we detect correctly.

$\left(1 - \frac{\tau_i}{T}\right)$ is the entire data transmission. Following equations can be derived,

$$\lim_{\tau_i \rightarrow 0^+} \frac{d R_i(\tau_i)}{d \tau_i} \rightarrow +\infty > 0 \quad (29)$$

$$\lim_{\tau_i \rightarrow T} \frac{d R_i(\tau_i)}{d \tau_i} < 0 \quad (30)$$

Thus, there is a τ_i between 0 and T that gives us maximum $R_i(\tau_i)$. The Fig. 18 shows the optimum sensing time based on equation (28). By Fig. 18, it can be denoted that the optimum sensing time in regard to technology limits and optimum sensing time is approximated between 3ns and 1 μ s.

Scheduling algorithms for CR users

We consider the downlink of N_{su} secondary users are serviced by a base station within a cell. The base station allocates $RE(i,j)$ among the N_{su} SUs. At each frame multiple REs can be assigned to a single user, although each RE can be allocated to only one SU.

We assume that channel conditions vary across the subcarriers as well as secondary users. The channel conditions typically depend on the channel frequency, so they may be different for different channels. We presume typical urban area model. Moreover, scheduling of SUs also depend on the user location and the time frame. However, in our context the AMI meters are geographical stationary leading to constant SINR values. We also define capacity of secondary user in presence of loss,

$$C = \int \sum_{SINR} (1-\rho)(1-\delta)\beta W_{eff} \cdot \eta \cdot \log_2 \left(1 + \frac{|h|^2 S}{SNR_{eff}}\right) dt \quad (31)$$

ρ is detection probability parameter and calculated by addition of false alarm detection probability (Pf) and detection probability (Pd). δ is primary user spectrum usage and we presume a average of 80% loading. β is a correction factor which nominally should be equal to one and it is discussed more detailed in. η is the spectrum sensing efficiency. The scheduler decides which SU to transmit the information at each time frames, based on the request rates the base station.

Scheduling the user with the instantaneously best link conditions is often referred as max rate scheduling. The max rate can be expressed as $k = \arg \max_i R_i$ for i^{th} user.

Proportional fair (PF) scheduler is designed to meet the challenges of delay and fairness constraints while harnessing multi user diversity. PF scheduler tracks the average throughput, $T_k[nT_s]$, for each SU delivered in the past over sliding window of size t_c . In the time frame $[\tau]$, the base station receives rates $R_k[nT_s]$, $k=1...N_{su}$ from all the active SUs and

scheduler basically schedules the SU with highest PF metric value, γ that is defined as

$$\gamma = \frac{R_k[nT_s]}{T_k[nT_s]}.$$

The average throughputs $T_k[nT_s]$ are updated using an exponentially weighted low pass-filter :

$$T_k[nT_s + 1] = \begin{cases} (1 - \frac{1}{t_c})T_k[nT_s] + (\frac{1}{t_c})R_k[nT_s] & k = \gamma \\ (1 - \frac{1}{t_c})T_k[nT_s] & k \neq \gamma \end{cases} \quad (32)$$

Based on the Eq. (31) and (32) we can write as the following

$$\gamma = \frac{\int \sum_{SNR} (1 - \rho)(1 - \delta)\beta W_{eff} \cdot \eta \cdot \log_2(1 + \frac{|h|^2 S}{SNR_{eff}}) dt}{T_k[nT_s]} \quad (33)$$

As a result, unlike PF scheduling, the users having low throughput but high PF metric, γ , that had been chosen to access frequency will have lower priority than users with enough PF metric and higher throughput.

Algorithm: Opportunistic scheduling

- 1) for $n=1$ to N_T (simulation time)
 - 2) Update SU profile, Update γ
 - 3) Let S be the set of secondary users
 - 4) Let $RE(i,j)$ where $i=1$ to M subcarriers and $j=1$ to K be the total time frames.
 - 5) for $i=1$ to M , for $j=1$ to K
 - 6) Select the secondary user $l \in S$ with highest $\gamma(l)$
 - 7) If $R_l[nT_s] \geq \bar{R}_l[nT_s]$
 - 8) Update the SU profile with $S=S-\{l\}$
 - 9) Allocate $RE(i,j)$ to l th secondary user from S
 - 10) Else
 - 11) Update the SU profile with $S=S-\{l\}$
 - 12) End if, End for j, i, n
-

Analysis & Simulation Results

To evaluate the performance of CR system model, system level simulations have been conducted based on 3GPP LTE system model. Table (see [44]) shows the simulation parameters used for the simulations. We analyze the performance of the scheduling in terms of throughput and fairness. We first evaluate the system throughput for algorithms with varying the primary user loading within a cell. In this case, the primary user average loading is around 80% and total number of users is 500 in a cell. Over the period of time that spectrum sensing reports the number of idle resource blocks, scheduler allocates the idle REs with SUs. The Fig. 19 illustrates average capacity for three aforementioned algorithms. Max-rate results in highest average capacity among three algorithms are followed by opportunistic and fairness algorithms. In proportional fair algorithm the users compete for resources not directly based on the requested rates but based on the rates normalized by their respective average throughputs, PF metrics. In OS the users having low request rate but high PF metric, γ , will have less chance to be scheduled. OS objective is to achieve higher average capacity compared to PF, while achieving decent fairness among the SUs.

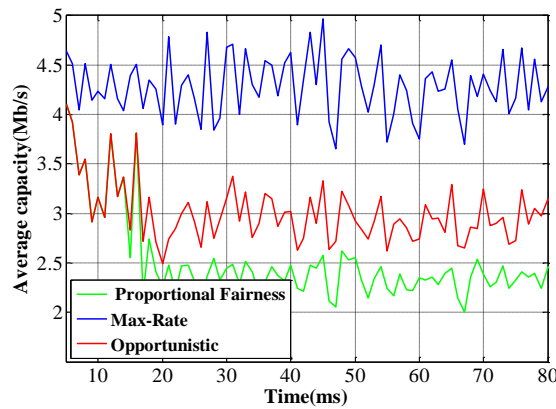


Figure 19 Average Capacity over Time

In Fig. 20, we analyze the scheduled SUs average capacity of each algorithm in each scenario when number of active PUs varies. Based on goals of each algorithm they indicate respective positions in the results. It can be seen that the solution obtained using the proposed algorithm (OS) is quite close to the PF specifically when the active PUs are less.

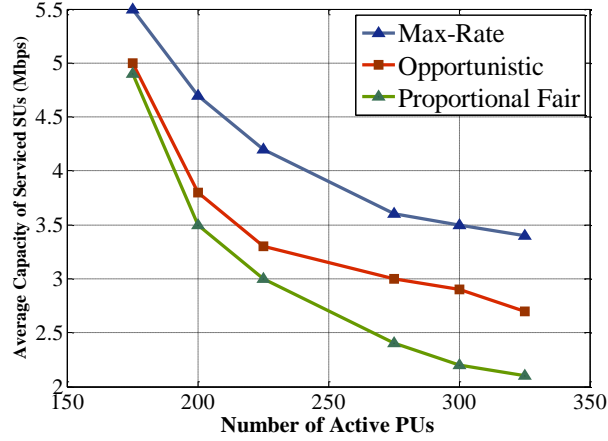


Figure 20 Max-Rate average capacity

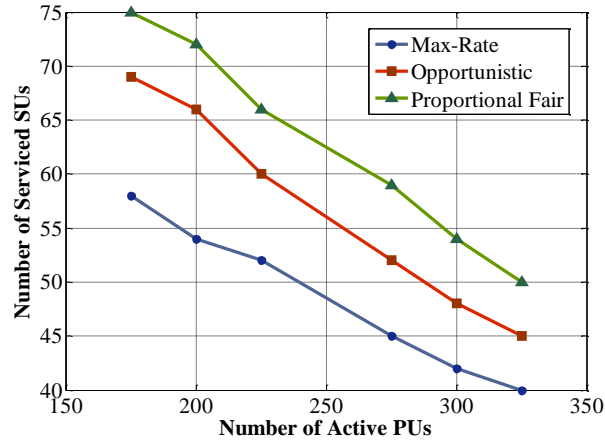


Figure 21 Average No. of scheduled SUs

We note that the less PUs scheduled yields to high availability of idle REs. Therefore, higher number of SUs scheduled results in larger average capacity in the CR network. When the numbers of PUs are increased, the advantage of the OS algorithm over PF is more obvious (i.e. Fig.20) due to more sparse SUs. Sparse implies large variability in SUs profile (i.e. SINR, fading channel, physical location).

In Fig. 21, we analyze the average number of scheduled SUs in each scenario when number of active PUs varies. We note that the more PUs scheduled yields to less availability of idle REs and therefore less number of SU scheduled.

In Fig. 21 the Max-Rate average capacity is much higher than average capacity of PF; on the contrary, Fig. 22 shows the more scheduled SUs by PF algorithm compared to Max-Rate algorithm. As a result, the OS algorithm can balance both the performance of the cognitive radio networks in terms of achieving acceptable average capacity of secondary users and the fairness.

Conclusion

In this thesis, we have analyzed the potential 4G CR network framework in context of smart grid information systems. Our system level simulation results show that the 4G CR network can achieve an average capacity of 3.5Mbps in a 3Km cell radius under the constraint of an average primary user network usage of 80%. Finally, we present that the CR capacity of a 20% usage model meets the smart grid protocols requirements for a multi-user CR network of smart meters.

Chapter V. Interference Aware Scheduling for Maximum Channel Reuse and Max-Capacity in Smart Meter Networks

Contributions of This Thesis on Interference Aware Scheduling

In this thesis, we develop a novel opportunistic interference-aware scheme based on maximum channel reuse in unplanned networks. The framework adopts the IEEE 802.22 for CR. Our model of channel reuse implies simultaneous use of intra cell physical resource elements (PRE) leading to dynamic co-channel interference on a per-PRE basis. We analyze the application of SISO and MIMO interference aware scheduling. The proposed scheduling scheme eliminates idle time-slots under the joint constraint of maximum interference and maximum capacity. We demonstrate that this approach substantially increases capacity gains for MIMO systems in multi-cell environments compared to conventional scheduling schemes discussed previously. Another distinguishing aspect of this thesis is that we analyze the smart meter network in a manner that jointly satisfies both the DOE smart grid communication protocol in terms of capacity [45] and the IEEE 802.22 protocol satisfying the FCC CR requirements.

System Model

Fig. 22 illustrates the system model under consideration in this thesis. As shown in Fig. 22, the system utilizes the CR scheme of IEEE802.22 WRAN. The TV antenna indicates service for PUs in the CR protocol. In addition, AMI is denoted as SU. The SU electronic component is alternatively named as consumer premise equipment (CPE) indicates in the CR protocol [46]. Since the 802.22 WRAN specifies a fixed point-to-multipoint wireless air interface, CR base station (BS) can manage its own cell and all associated AMIs as shown in Fig. 22. In IEEE802.22 WRAN, multiple cells are overlapped which results in uncoordinated interference from other cells as shown in Fig. 22.

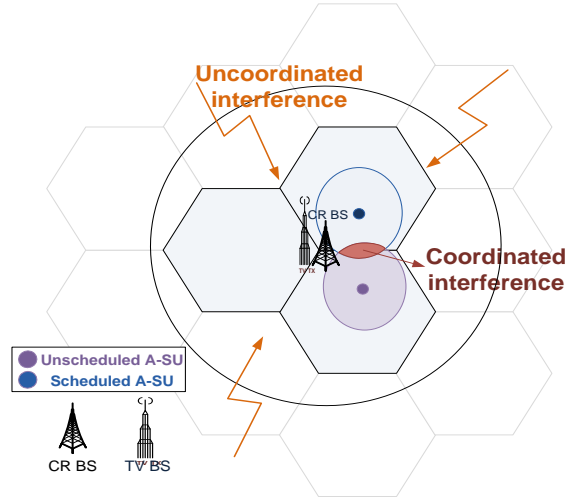


Figure 22 SISO system model depicted with coordinated and uncoordinated interference

Radio resource management in our IEEE 802.22 based CR network model involves three dimensions: frequency, time and space. Physical resource element (PRE) spans in both frequency and time dimensions. We presume a scheduler coordinating the usage of PREs in adjacent cells by opportunistically leveraging multi-user AMI frequency, time and spatial diversity. It also ensures that PRE may be simultaneously assigned to more than one A-SU

within each cell. By further assuming that orthogonally among sub-carriers can be adequately maintained, then intra-cell interference can be ignored between PU and SU. However, as previously mentioned if a PRE is simultaneously assigned to more than one A-SU meter it results in coordinated interference between A-SUs within the cell as illustrated in Fig. 22.

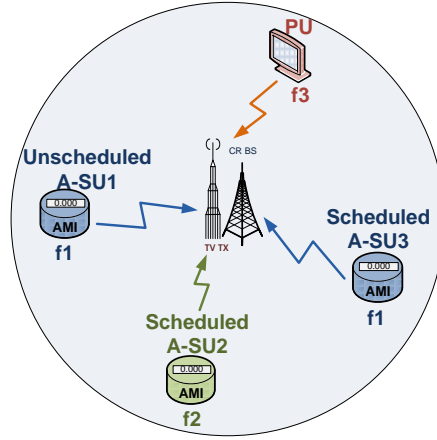


Figure 23 Mechanism of our Reuse Model

Fig. 23 shows the methodology for scheduling the PREs allocated to A-SUs. When PREs are reused, increased co-channel interference is traded off versus the allocation of additional frequency channels to unscheduled A-SUs. In Fig. 23, PU transmits over frequency f_3 ; scheduled A-SU1 transmits over frequency f_1 ; the scheduled A-SU2 transmits over frequency f_2 . We note that PU communication is disrupted if any user transmits data using frequency f_3 respectively. The system controls the interference power of the PUs to insure it remains below the maximum tolerable interference power. The diagram in Fig. 23 depicts that PUs that are unaffected. This is due to the fact that the A-SUs operate on orthogonal frequencies. However, it is possible that A-SU1 increases the co-channel interference to A-SU3 since they operate on same frequency f_1 . The main objective in this method is to determine the dynamic scheduling

of PREs that maximizes channel reuse among A-SUs and maximized multi-user capacity considering both interference and noise of existing A-SU in that particular PRE.

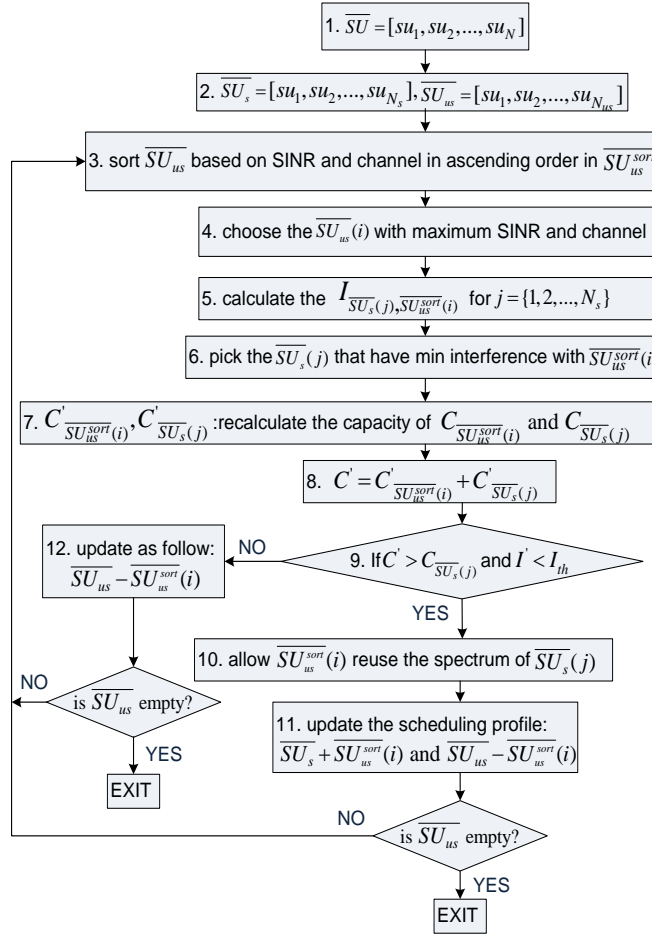


Figure 24 Interference-Aware scheduler (IAS) algorithm for PRE reuse

Interference –Aware Scheduling Algorithm

We presume the initial scheduling is performed on secondary users based on max rate algorithm (MRA) [47] . \overline{SU} is showing set of indices of all A-SUs within the cell as follow,

$$\overline{SU} = [su_1, su_2, \dots, su_N] \quad (34)$$

where N is total number of A-SUs. \overline{SU}_s is defined as the initial scheduled users through max-rate and \overline{SU}_{us} are unscheduled users. \overline{SU}_s and \overline{SU}_{us} are sub set of \overline{SU} ,

$$\overline{SU} = \overline{SU}_s \cup \overline{SU}_{us} \quad (35)$$

Furthermore, the vector of fading coefficients for the channels between the SUs and CBS is

$$\overline{H}_{SU}^{CBS}(nT) = [h_1(nT), \dots, h_N(nT)] \quad (36)$$

Fig. 3 depicts the proposed interference aware scheduling (IAS) algorithm. The scheduler selects active unscheduled users with data to send. We sort the SU_{us} by SINR and channel coefficients in ascending order represented as $\overline{SU}_{us}^{sort}$. The ascending order ensures that A-SUs with high SINR are available for exploiting interference introduced by reusing the PRE. We choose unscheduled A-SU $\overline{SU}_{us}^{sort}(i), i = \{1..N_{us}\}$ from $\overline{SU}_{us}^{sort}$ with maximum SINR and higher channel coefficients as represented in step 4 in Fig. 24. We calculate the co-channel interference between $\overline{SU}_{us}^{sort}(i)$ and $\overline{SU}_s(j), j = \{1..N_s\}$. Where N_s and N_{us} are total number of scheduled and unscheduled A-SUs respectively. Choose the $\overline{SU}_s(j)$ with minimum co-channel interference with respect to $\overline{SU}_{us}^{sort}(i)$. Co-channel interference $I' = I_{\overline{SU}_s(j), \overline{SU}_{us}^{sort}(i)}$ is evaluated in the later part of the section. In step 7, we recalculate the capacity of $\overline{SU}_s(j)$ and $\overline{SU}_{us}^{sort}$ based on updated interference I' in step 5.

If each A-SU, i , is serviced on a channel, the multiuser capacity for orthogonal OFDM signaling is given below and notes that it cannot exceed the Shannon capacity given in [47],

$$C_i = W_i \log_2 \left(1 + h_i^2(nT) \text{SINR}_i \right) \quad (37)$$

In real-world deployments, we can develop a modified Shannon capacity formula, by replacing the cell bandwidth, W_{cell} with an effective bandwidth and βW_{eff} [47] which accounts for G-factor dependencies and protocol control, pilot, and cyclic prefix overheads. Closely related to the SINR is the G-factor, which accounts for the geometric dependencies of cell layouts and dictates the statistics of the downlink capacity. The G-factor is the average own cell power to the other cell-power plus noise ratio when considering uniform spatial distributions of transceivers within a cell.

In addition, we can define a normalized effective signal to noise ratio, $SINR_{eff}$ adjust SNR for both interference, G-factor and statistics. Defining the modified Shannon spectral efficiency for PU, as we therefore define the modified A-SU capacity in

$$C_i = \beta W_{eff_i} \cdot \log_2 \left(1 + \frac{h_i^2(nT) SINR_i}{SNR_{eff}} \right) \quad (38)$$

where $SINR_i$ is the signal to interference plus noise power ratio for i^{th} A-SU. Therefore $SINR_i$ can be expresses as

$$SINR_i = \frac{P_{r_i}}{\sigma_N^2 + \sigma_I^2} \quad (39)$$

where P_{r_i} , σ_N^2 , and σ_I^2 denote the received signal power from i^{th} A-SU, the noise power, and the self-interference power at the CBS in the cell.

Using equation 5 we calculate capacity of $\overline{SU_s}(j)$ and $\overline{SU_{us}^{sort}}(i)$ as labeled as $C'_{\overline{SU_s}(j)}$ and $C'_{\overline{SU_{us}^{sort}}(i)}$.

$C'_{\overline{SU_s}(j)} < C_{\overline{SU_s}(j)}$, is due to effect of increase in interference caused due to PRE reuse. The objective of the IAS algorithm is to reuse the PRE and improve the capacity while optimally exploiting the interference variations occurred. This necessity to verify,

$$C' = C'_{\overline{SU_{us}^{sort}}(i)} + C'_{\overline{SU_s}(j)} \quad (40)$$

$$C' > C_{\overline{SU_s}(j)} \quad (41)$$

However, the other critical factor to be taken in consideration is maximum tolerable interference I_{th} . We need to check the co-channel interference $I' = I_{\overline{SU_s}(j), \overline{SU_{us}^{sort}}(i)}$ observed should be always less than I_{th} in order satisfy QoS factor and FCC requirements.

$$I' < I_{th} \quad (42)$$

In step 9, we check the conditions stated in (41) and (42). If conditions are satisfied scheduler allows $\overline{SU_{us}^{sort}}(i)$ reusing the same PREs of $\overline{SU_s}(i)$ and updates the $\overline{SU_{us}}$ and $\overline{SU_s}$ shown in step 11 and iterates the process until all $\overline{SU_{us}}$ are empty. If the conditions are not satisfies, we updated the $\overline{SU_{us}}$ as seen in step 12 and we iterates the process to step 3.

Interference Model for SISO

The OFDM transmission system with MIMO model for an A-SU as a function of sub carrier K is given by,

$$Y(k) = \mathbf{H}_{n_T \times n_R}(k) \mathbf{X}(k) + \mathbf{N}(k) + \mathbf{I}(K) \quad (43)$$

In (43), $\mathbf{Y}(k) = [Y_1[k], \dots, Y_{N_T}[k]]$ is the received signal on the k^{th} subcarrier in CR base station.

$\mathbf{H}_{n_T \times n_R}(k) = [H_1[k], \dots, H_{N_T}[k]]$ is the channel coefficients. In SISO, $n_T=1$ and $n_R=1$;

$\mathbf{X}(k) = [X_1[k], \dots, X_{N_T}[k]]$ denotes vector of transmit data at k^{th} subcarrier in CRBS from the transmitted OFDM signal in uplink model.

Our attention in this thesis is focused on smart meter equipped with multi-antenna systems. Performance can be enhanced and capacity maximized when perfect or partial channel state information (CSI) is made available at the transmitter [21]. This presumption applies well to AMI networks with fixed spatial location and wireless channels with zero Doppler. Though many MIMO approaches can be applied in multi-antenna systems, we focus on beamforming due to our focus on spatial interference.

$$\mathbf{I}_j(k) = \underbrace{\sum_{n_r} \sum_{i=1}^{N_{ns}} \mathbf{H}_{n_T \times n_R}^{i,j} x_{SU_{us}^{sot}(i)}(k)}_{\zeta_k} + \underbrace{\sum_{n_r} \sum_l \mathbf{H}_{n_T \times n_R}^{l,j} x_l(k)}_{\psi_k} \quad (44)$$

The desired the received signal at CRBS is distorted by coordinated interference aggregated in ζ_k and uncoordinated interference in ψ_k . In (44), N_{ns} is the total number of scheduled users from $\overline{SU_{us}}$ based on IAS algorithm.

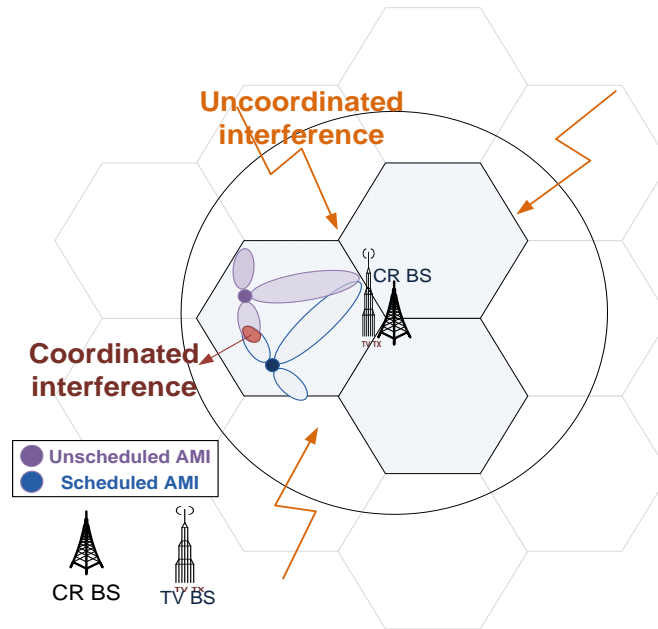


Figure 25 MIMO system model with coordinated and uncoordinated interference

Interference Model for Beamforming

The multi-antenna system offers well known motivations compared to conventional wireless communication systems. Our attention in this thesis is focused on smart meter equipped with multi-antenna systems. Performance can be enhanced and capacity maximized when perfect or partial channel state information (CSI) is made available at the transmitter [21]. This presumption applies well to AMI networks with fixed spatial location and wireless channels with zero Doppler. Though many MIMO approaches can be applied in multi-antenna systems, we focus on beamforming due to our focus on spatial interference.

Simulations and results

Numerical results exhibit the effectiveness of the proposed interference-aware scheduler for the SSIO and beamforming approach to smart meters. In this simulation, we follow the IEEE WRAN standard [46] as OFDM parameters.

Table 2 THE OFDM PARAMETERS FOR IEEE802.22 WRAN

Channel bandwidth (MHz)	6
Number (N) of subcarriers for FFT	2048
Number of data subcarriers for FFT	1440
Number of pilot subcarriers for FFT	240
Subcarrier spacing (KHz): PRE BW	3.348
Modulation	QPSK

Table 3 PARAMETERS FOR SIMULATION ANALYSIS

Cell Radius (Km)	6
Carrier frequency (MHz)	599
Cell-level user distribution	Uniform
Cell layout	Hexagonal grid, 3 sector sites
Channel Estimation	Ideal
Antenna pattern (θ_{3dB})	68
Average Primary user Loading	70%
Number of Total Users in cell	400
Number of SU in cell	100
Thermal Noise(dBm/Hz)	-174

In the simulation, we follow IEEE 802.22 for smart grid systems as given in Table 2. It is assumed to operate at 599 MHz which belongs to the VHF/UHF TV broadcast bands. In addition, the profile-A frequency selective fading channel [48] is considered for the simulation. The parameters in Table 3 also show the parameters used for simulation.

Fig. 26 exhibits total capacity of all the scheduled A-SUs in the case of conventional max-rate, IAS- SISO, IAS-BF. As shown in Fig. 26, the achieved capacity in IAS-BF and IAS-SISO in average is about five times and two times, respectively, larger than that for the case of max rate at received SINR.

As shown in figure, the capacity for the case of IAS-SISO and IAS-MIMO increases with the increase in A-SUs reusing PREs. However, capacity of the IAS-SISO and IAS-BF saturates at 15 and 70 A-SUs respectively, due to the effect of coordinated interference. Moreover, Fig. 26

shows that the average capacity for each scheduled A-SU satisfies the DOE smart grid communication protocol average capacity requirements[45].

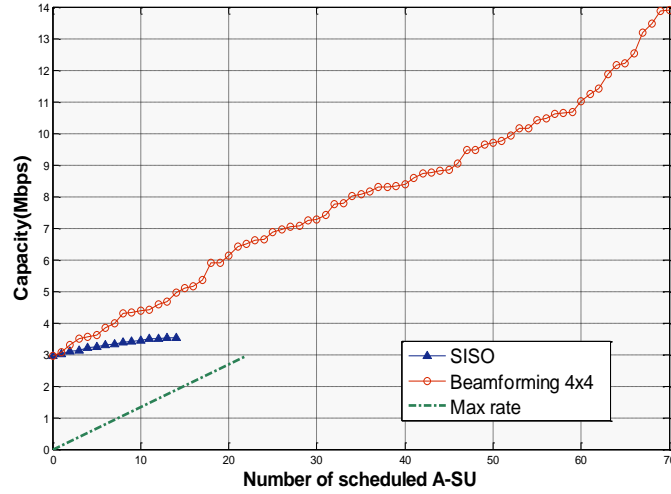


Figure 26 Total capacity of A-SU in the cases of no IAS, IAS-SISO and IAS-BF

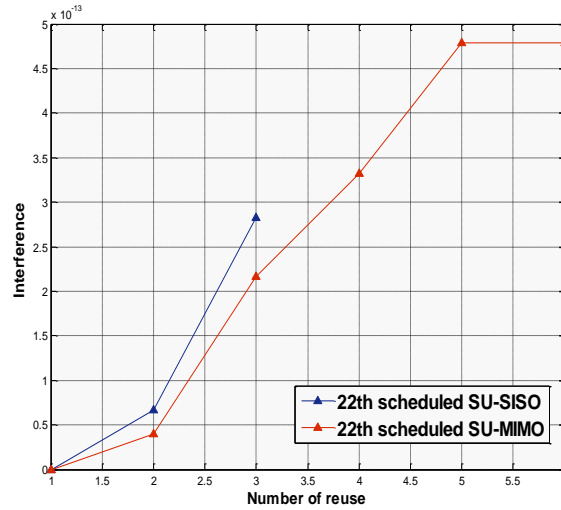


Figure 27 Total capacity of A-SU in the cases of no IAS, IAS-SISO and IAS-BF

Fig. 27 illustrates the interference and number of reuses for one of A-SUs scheduled (with index 22). As it shown in figure, after third reuse for SISO, if we add one more unscheduled A-SU with minimum interference in order to reuse the PRE, interference exceeds the threshold. This is because of high interference caused by SISO. To satisfy the condition in step 9 in Fig. 24, the

reusing is ended at 3. On the other hand, because of less interference due to side lobes in beamforming, we are able to reuse more unscheduled A-SUs till we have total interference close to I_{th} in that PRE. As a result, in Fig. 26, we have greater interference for beamforming compared to SISO, because in beamforming, the interference is closer to I_{th} than in SISO for all PREs. That is, we are taking advantage of all possible interference that can be tolerated by A-SUs.

Fig. 28 illustrates the comparison of total capacity for IAS-SISO and IAS-BF. As exhibited in Fig. 28, the proposed IAS-BF achieves greater capacity than IAS-SISO at the same interference. Moreover, capacity of the IAS-SISO and IAS-BF saturates due to the effect of coordinated interference. Although, the IAS-BF shows higher interference compared to IAS-SISO, the interference in all PREs caused by IAS-BF is still within I_{th} .

Fig. 29 illustrates the number of reuse for each scheduled A-SU. As depicted in Fig. 29a, 22 A-SUs have been scheduled by max rate algorithm. Regard to two conditions in step 9 in Fig.24, PREs of A-SU with indices 2, 6, 7, 13, 15 and 22 are reused.

Based on Fig 29, reuse of each scheduled A-SU's PREs in IAS-BF is always more than reuse in IAS-SISO. Since the interference in other A-SUs exceeds the threshold, no reuse occurred.

In Fig. 30, the total number of reuse in IAS-SISO and IAS-BF SU_s bandwidth is depicted. The figure shows that the total number in IAS-BF is always more than IAS-SISO. This is due to less interference caused by IAS-BF.

Conclusion

In this thesis we presented a novel interference aware scheduling for CR network by maximizing channel reuse in SISO and MIMO. IAS is able to utilize the opportunistic interference aware scheduling to improve the system capacity significantly. With suggested scheduling approach, we can conclude following observations. For 4Tx-4Rx Antenna IAS-BF and 1Tx- 1Rx IAS-SISO we observe an average capacity increase of 5x and 2x, respectively, larger than that for the case of max rate at received SINR. Much larger gains occur as the antenna array size increases. The comparison was done with max rate in a metropolitan area network system simulation. Our analysis has shown that the IEEE 802.22 protocol enabling FCC-CR can support future distributed smart grid communication network comprised of smart meters. Without loss of generality, our IAS also increases the number of scheduled A-SUs, which indirectly indicates the fairness among users. Developing an IAS based on fairness would be an interesting topic in future.

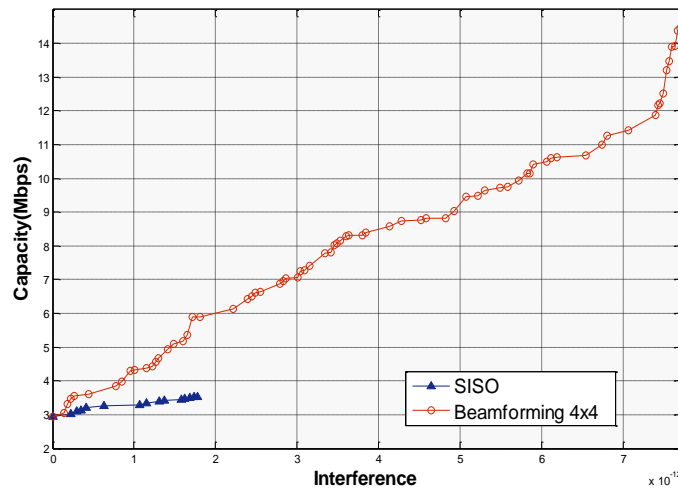


Figure 28 Relation between Interference generated by reuse and total capacity of scheduled A-SU in the cases of IAS-SISO and IAS-BF

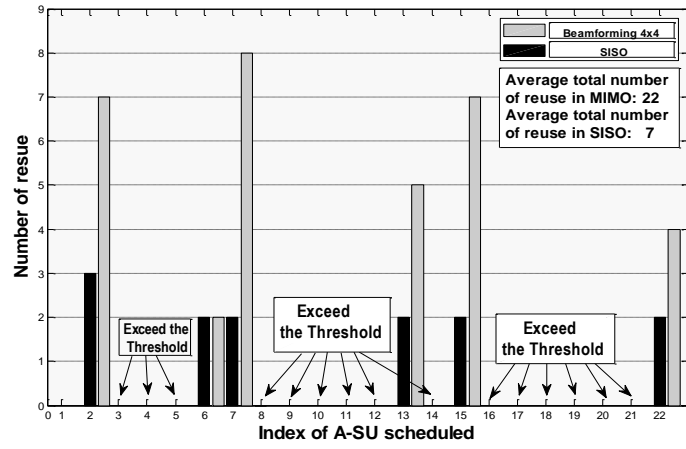


Figure 29 Number of reuse for every scheduled A-SUs in one instance.

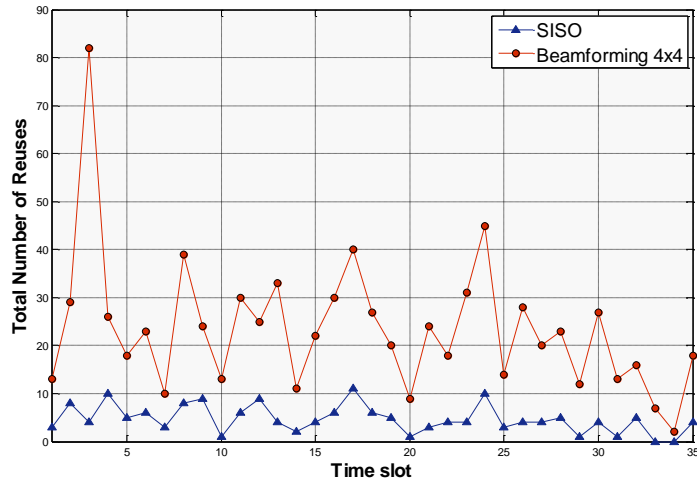


Figure 30 Total number of reuses over entire BW in cases of IAS-SISO and IAS-BF.

Chapter VI. Smart Grid and Optimization

Fuzzy Control of Electricity Storage Unit for Energy Management of Micro-Grids

Introduction

This work is partially funded by CPS Energy through Texas Sustainable Energy Research Institute at the University of Texas at San Antonio.

Micro-Grid is a small-scale grid that is designed to provide power for local communities. A Micro-Grid is an aggregation of multiple distributed generators (DGs) such as renewable energy sources, conventional generators, in association with energy storage units which work together as a power supply network in order to provide both electric power and thermal energy for small communities which may vary from one common building to a smart house or even a set of complicated loads consisting of a mixture of different structures such as buildings, factories, etc [49]. Typically, a Micro-Grid operates synchronously in parallel with the main grid. However, there are cases in which a Micro-Grid operates in islanded mode, or in a disconnected state [50]. In this article we assume that when the Micro-grid is connected to the main grid and is working

synchronously with it, the flow of electric power can be either from the main grid to the Micro-grid or vice-versa. If the flow of electric power is from the main grid towards Micro-grid it means that the Micro-grid is consuming the main grid's energy for each KiloWatt-Hour of which the consumer, here Micro-grid, must pay to the Grid. This borrowed power can be either sent to local load to be consumed or can be stored in battery for future use. But, in case the flow of power is from the Micro-Grid towards the main grid, this means that Micro-Grid is delivering power to the main grid. In other words, the excess power generated currently by the renewable electricity generators or stored previously in the batteries is being sold to the main grid, and the Micro-Grid, or in general the consumer, is making profit by selling energy to the main grid. Without loss of generality, we have assumed that the price rate for buying energy from the main grid is equal to the electricity price rate which is sold to the grid. The excess power can be sold to the grid whenever the storage unit or load don't need that power or whenever it is more beneficial to sell power to grid than to use it for supplying the load. However, in this article the main goal is to have the load completely supplied by the required power demand at all conditions. Authors have previously simulated the Micro-Grid assuming no maximum and minimum limit for the amount of energy stored in the battery unit [49]. In this article, storage unit's limits on maximum and minimum amount of stored energy are considered and the results are compared to the results of the previous work.

System Model

The model used for simulation of the Micro-grid network is a three-bus system. One of the busses in the distributed generation model is assumed to serve the renewable generators which include either solar farm, wind farm, or any other renewable generation units either in

association with battery storage unit or without storage. Another bus is assumed to be there as the grid (utility) bus which will provide the complement part of the power demanded by the local load that renewable electricity generation system cannot afford. The third bus will be the specific load to which the demanded power is to be provided. This load can be anything from a common building or a smart house, to even a group of plants and factories or a mixture of all of them. Figure 31 shows an overall Micro-Grid schematic including Renewable Electricity Generators and Storage Unit, Utility, and Local Load.

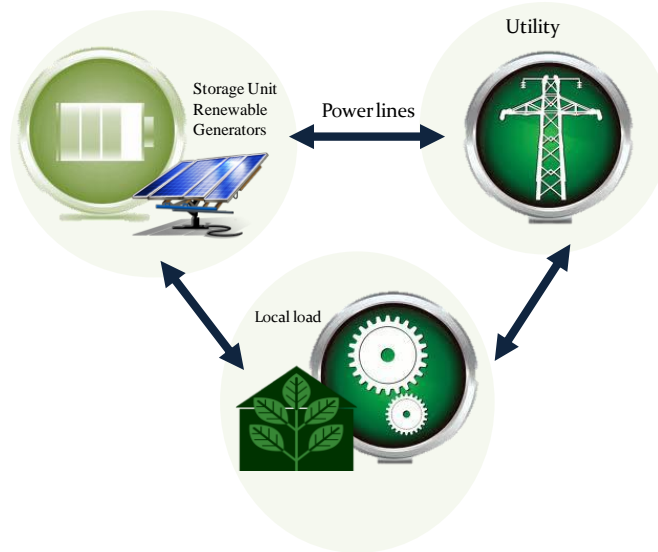


Figure 31 Basic Grid System Model

There are three scenarios defined for simulation in this article; scenario 1 deals with a Micro-Grid which includes the renewable electricity generators without any battery storage unit. Therefore there will not be any approaches required for controlling the battery storage system in this scenario. The second scenario deals with the same Micro-Grid system as mentioned in scenario one but after the battery storage unit is connected to the same bus with the renewable generators. Also, the fuzzy approach is applied in this scenario for energy management through battery unit control. The point in this scenario is that the battery storage is assumed to be an

ideal battery without any maximum or minimum limits on stored energy, i.e. infinite battery capacity. In the third scenario which is the last one, the Micro-Grid is assumed to have everything mentioned in scenario two plus the fact that maximum and minimum limits of stored energy are taken into account for storage unit and are assumed to be 85% and 15% of the nominal maximum storable energy respectively.

A. Characteristics of Buses in Scenario 1

The three buses in the model of Micro-Grid Network simulated in this article have the following characteristics in the first scenario:

Bus 1 is of type PQ and is used as the renewable electricity generation unit's bus.

Bus 2 is of type Slack (reference) and is used as the Utility (grid) bus.

Bus 3 is of type PV and is used as the Local Load bus.

B. Characteristics of Buses in Scenario 2

The characteristics of the three buses in the Micro-Grid Network model simulated in this article are as follows in the second scenario:

Bus 1 is a PQ bus and is used as the bus for renewable generation unit and infinite-capacity battery storage.

Bus 2 will be the Slack (reference) bus and is used as the Utility (grid) bus.

Bus 3 is of type PV and is used as the Local Load bus.

C. Characteristics of Buses in Scenario 3

Bus characteristics of the three buses in the Micro-Grid Network model simulated in this article are as follows in the third, i.e. last, scenario:

Bus 1 is a PQ bus and is used as the bus for renewable generation unit and finite-capacity battery storage unit.

Bus 2 will be the Slack (reference) bus and is used as the Utility (grid) bus.

Bus 3 is of type PV and is used as the Local Load bus.

This must be noted that battery units are assumed to be ideal batteries, i.e. no dynamic transient of change in the amount of stored energy in batteries are assumed, i.e. the amount of stored energy in the batteries is assumed to be changing as a pure ramp by time in both ascending and descending direction.

Problem Statement

The important point which lies behind the idea of this article is that we have assumed the real-time pricing for electricity. The update duration of pricing is assumed to be 15 minutes, which means that the price per KiloWatt-Hour of electricity consumed by the customers of the load region is updated every 15 minutes. This means that the money consumers need to pay to the utility for the same amount of energy used during different time-intervals might be different. Therefore, a function is required to be defined which takes into account the difference between amount of power given to the utility by the Micro-Grid, and the amount of power taken from the utility by the Micro-Grid. The Equation 1 represents this cost function:

$$Cost = \sum_{t=1}^T (\text{Pr}(t) \cdot (S_U(t) + S_L(t))) \quad (45)$$

where the electricity price $\text{Pr}(t)$ is determined by the CPS energy every 15 minutes for the next 15 minute period. $S_U(t)$ is the amount of power transferred to/from the Grid during each 15 minute period. If power is received from the Grid $S_U(t)$ will be positive, and if power is delivered to the grid in case of excess power generation by the renewable generation system $S_U(t)$ will appear in the equations with a negative sign. $S_L(t)$ is the amount of distribution loss which will occur on the branches we have between these three buses in the Micro-Grid system during each 15 minute period. Depending on whether the load is getting how much of its demanded power from renewable generation system and how much from the Grid, and also depending on whether the renewable generation system is producing excess power and is selling the excess power to the Grid, this power Loss will vary.

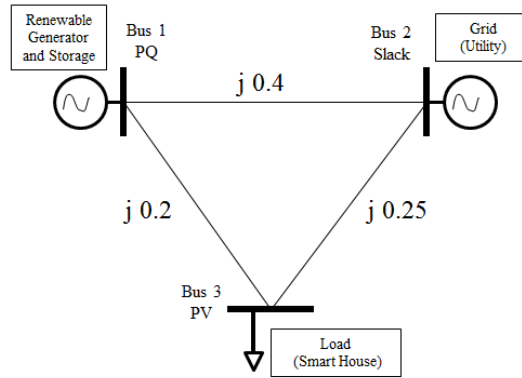


Figure 32 Three Bus Model for Micro-Grid

Figure 32 represents the three-bus model used for simulation of the Micro-Grid in different scenarios along with the branch impedances and the types of buses. Simulation is done on the

Micro-Grid system considering three scenarios. In the following the summary of these scenarios is given:

A. Scenario 1

Analysis of the Micro-Grid system profits and costs under real-time electricity pricing policy; in this scenario the simulation, analysis and study will be done on a Micro-Grid model which includes the renewable generation unit without any battery storage unit. Therefore there will not be any approaches required for controlling the battery storage system.

B. Scenario 2

Fuzzy Control of the Micro-Grid system under real-time electricity pricing policy; the cost function assumed in this scenario is the same as the cost function used in the scenario 1. The main difference here is that the storage unit exists in the network and will appear to be on the same bus with the renewable electricity generation unit. The storage unit in this scenario is assumed to be ideal with infinite capacity.

C. Scenario 3

Fuzzy Control of the Micro-Grid system under real-time electricity pricing policy; the cost function assumed in this scenario is the same as the cost function described in the two scenarios 1 and 2. In this scenario also the storage unit exists in the network on the same bus with the renewable generation unit. The critical difference between this scenario and scenario 2 is that the storage unit in this scenario is assumed to be an ideal battery with finite capacity. Therefore,

the maximum and minimum amounts of energy stored in the batteries are finite values and serve as boundaries which cannot be exceeded.

The power flow calculation and analysis in the Micro-Grid is the key to simulate the whole system. There are a number of well-known methods for calculation of power flow in the distributed generation network. There are four different types of busses considered in a distributed generation network, the characteristics of which will be calculated in power flow algorithms. These four types include PQ, PV, Slack, and isolated.

Fuzzy Control Approach

The control strategy implemented in this thesis is to use Fuzzy Logic for controlling the power flow to/from the battery storage unit in order to improve the value of the cost function introduced in section III. The three input variables to the fuzzy inference engine are Electricity Price, Renewable Generation Rate, and Load Demand. The Fuzzy inference engine serves as the controller which determines a measure of the amount of power that must be sent to/taken from the battery unit during the next time interval, i.e. 15 minute period, based on the current values of its three inputs.

The fuzzy membership functions for the three inputs price, load demand, and renewable generation rate, and also for the output variable which determines the amount of power transaction with the storage unit are shown in figure 33.

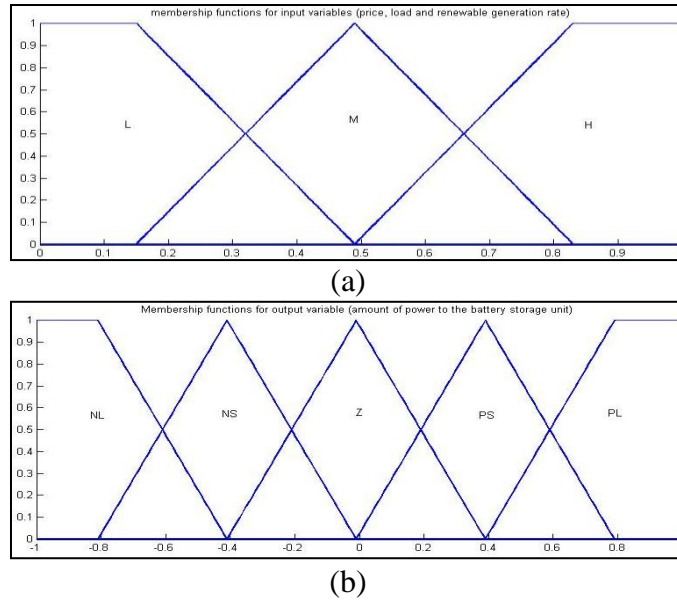


Figure 33 Fuzzy Membership functions for input and output variables of the Fuzzy Controller;
(a) inputs (b) output

The numerical values for these three input variables are normalized to the $[0 \ 1]$ interval, and then are Fuzzified using three fuzzy sets defined as Low (L), Medium (M), and High (H) as can be seen in figure 3a. The input variables after fuzzification will be fed to a fuzzy inference engine where the rule-base is applied to the input-output variables and the output will be determined by human reasoning. There is only one output variable from the fuzzy controller. This variable determines the amount of power to be stored in the battery, or to be drawn out from battery in each 15 minute interval. As represented in figure 3b, output variable fuzzy set is assumed to have five membership functions called Negative Large (NL), Negative Small (NS), Zero (Z), Positive Small (PS), and Positive Large (PL). The power drawn from the batteries can be used to complement the renewable electricity generation unit's power for providing the load's demand, can be sold to the Grid, or can be partially used for both reasons. The role of fuzzy inference engine is critically important for obtaining satisfactory results. For example two of the rules can be as follows:

IF the Price is Low, AND the Renewable Generation rate is High, AND the Load Demand is Medium, THEN the amount of Power to Battery storage system should be Positive-Large.

IF the Price is High, AND the Renewable Generation rate is Low, AND the Load Demand is Medium, THEN the amount of Power to Battery storage system should be Negative-Large.

The primary goal in these simulations is to provide the local load with all the power it demands at any circumstances. Meanwhile, this must be noted that whenever the price is high or low, the secondary goal will be to sell the most power to the main grid, and to purchase the most power possible from the main grid respectively. Under low-price electricity conditions, the action required by the rules might even require the Micro-Grid network to purchase power from grid and store it in the battery storage unit because the main point here is that the Price is low. This means by storing the energy in the batteries during low price times, the system will have enough stored energy in order to sell to the Grid during high-price periods. Even under cases of High local Load demand this will be a rational strategy. Therefore, having feasible rules predefined for the fuzzy system will help improve the cost function drastically. The proposed approach may even sometimes result in making the cost function value negative, which means that the system is making some profit instead of paying to the utility by the use of this control approach.

Simulation results & discussions

The simulation is done on the three bus system shown in figure 32. The Gauss-Seidel algorithm is implemented using Matlab for power flow calculation. Some typical data are generated for electricity price rate, time-varying Load Demand and Renewable Generation Rate. The power demand of the Load on bus 3 (Smart House) is supplied by two generators on buses 1 and 2.

Bus 1 includes solar panel and/or storage unit and bus 2 is slack which is connected to utility as shown in figure 2.

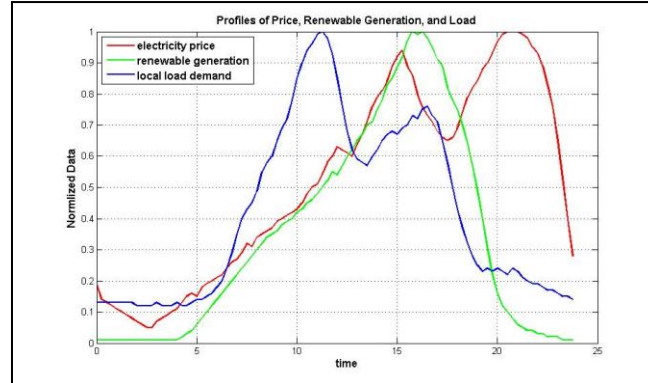


Figure 34 Profiles of Price, Renewable Generation, and the Load

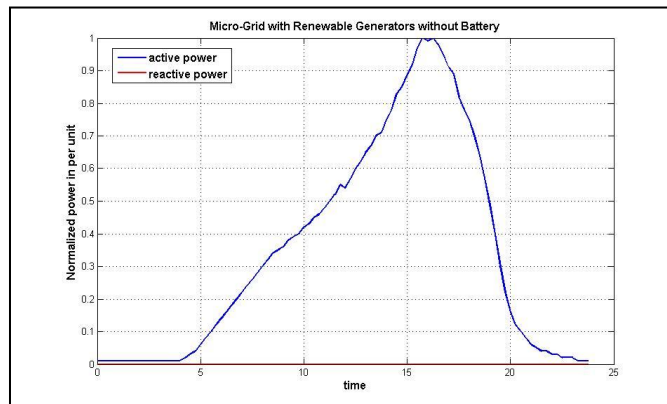


Figure 35 Power Flow of Bus 1 connected to Solar Panels; scenario 1

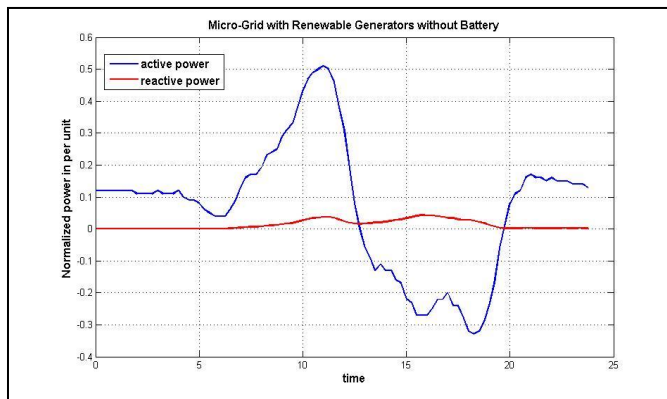


Figure 36 Power Flow of Bus 2 connected to Utility; scenario 1

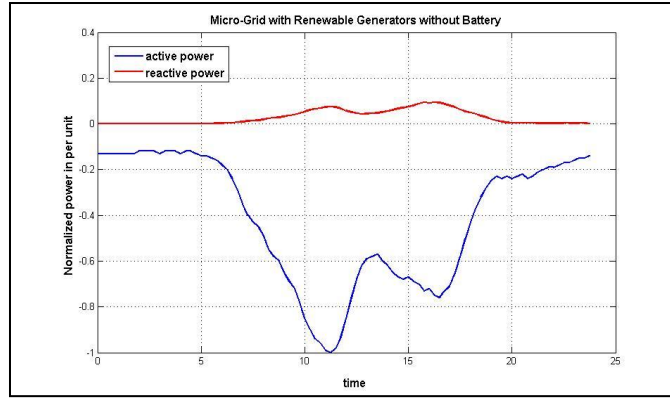


Figure 37 Power Flow of Bus 3 connected to Load; scenario 1

The numerical values of the data profile for the three input variables which are fed to the fuzzy controller are shown in figure 34 during a typical day. These variables include electricity price which is assumed to be variable as time passes, renewable electricity generation rate, and local load demand. The data is generated arbitrarily for simulation purposes only with regard to the fact that the peak electricity consumption duration of the whole region of interest for the main grid is around 8:30 pm where the electricity price gets to its maximum value. The simulation results for scenario 1 are represented in figures 35 to 37.

As it can be inferred from figure 35, the value of reactive power for bus 1 is constantly zero which corresponds to the assumption that the renewable generators do not provide reactive energy. Figure 6 shows that the active power is taken from the Utility during first half of the day time, and during most of the second half of the day the active power is being delivered to the grid. Load is evidently consuming active power regarding the blue curve represented in figure 37.

Simulation results for scenario 2 which associates ideal storage with infinite capacity to the renewable electricity generators on bus 2 are represented in figures 38 and 39.

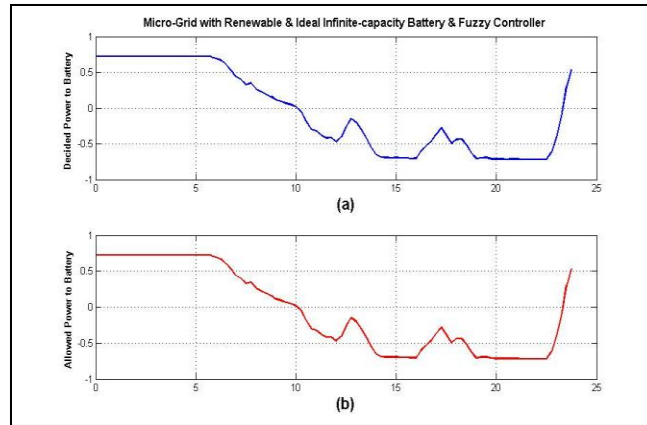


Figure 38 Output of the Fuzzy Controller, i.e. measure of the amount of power given to/taken from storage unit; scenario 2;

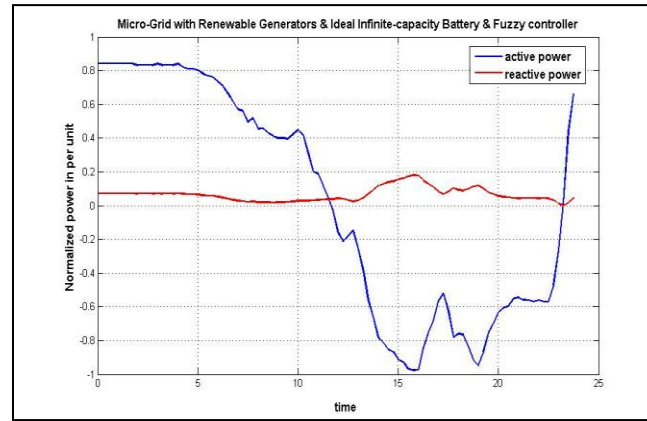


Figure 39 Power Flow of Bus 2 connected to Utility; scenario 2

Figure 38 parts a and b are matched to each other and this clearly shows that any value decided by the Fuzzy Controller for the power to be given to Battery or to be taken from it can be practical since battery unit assumed in scenario 2 is of infinite capacity. Figure 39 shows that active power is taken from the utility during first half of the day, and in the second half of day the active power is mostly being sold to the grid which can be deduced by the negative value of the blue curve in figure 39. The point is that the first part of the active power diagram is raised dramatically due to fuzzy decision making which means that the system is absorbing more active power from the grid during low-price hours and stores the power in the storage unit. Also, the second part of the active power diagram has fallen more in comparison to the same

section of figure 36 which denotes on increase in the amount of power drawn from storage unit and using this power for partially charging the load and also selling the excess power to the grid during high-price hours. This strategy results in reduction of cost function value or in other words increases the profit.

Remembering that the pricing periods are assumed to be 15 minute periods and one day is 24 hours overally there will be 96 periods of pricing during one day period. The summation of payment/profit and the loss during each of the periods will give us the overall value of cost function for one day. The process can be extended to one week, one month, one year etc.

Output of the fuzzy inference engine which represents the power rate given to battery is shown in figure 41. Whenever the value of this variable is positive it means that power is delivered to the storage unit and if the power is drawn from the storage unit, the value will be negative.

Simulation results for scenario 3 in which ideal finite-capacity storage is added on bus 2 in Micro-Grid network are represented in figures 40 to 42.

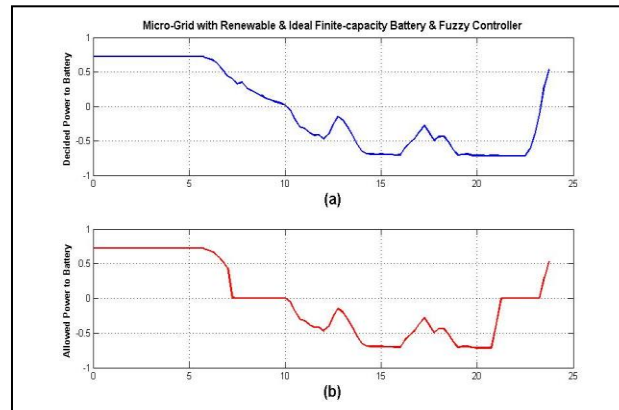


Figure 40 Output of the Fuzzy Controller; scenario 3;

Figure 40 parts a and b are not matched to each other and this shows the fact that the values decided by the Fuzzy Controller for the power to be given to Battery or be taken from it might

not be practical since battery unit assumed in scenario 3 is of finite capacity and the maximum and minimum limits of stored energy should be taken into account.

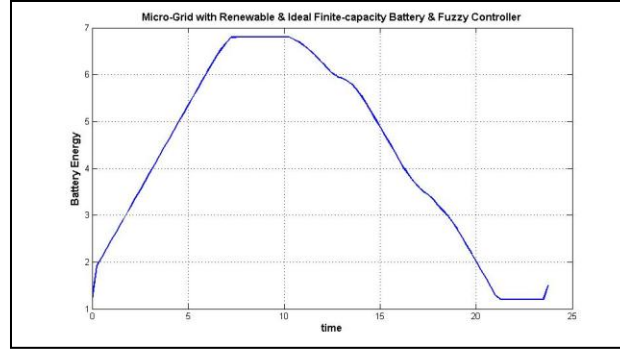


Figure 41 Measure of Energy stored in Battery; scenario 3

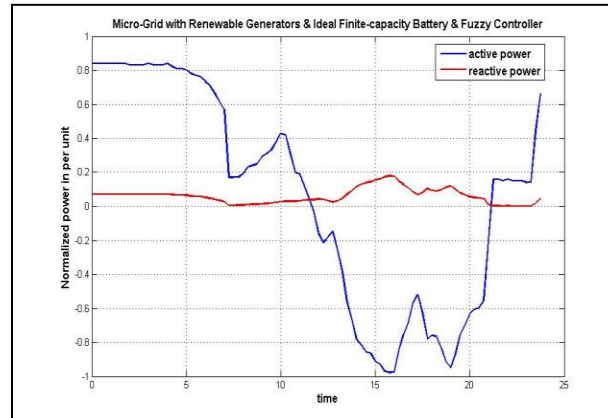


Figure 42 Power Flow of Bus 2 connected to Utility; scenario 3

The Center of Gravity, i.e. Centroid, defuzzification method is used for computing the crisp values of the output variable from the union of the Fuzzy rules. The formula used for defuzzification is shown in Eq. 46

$$y_{\text{crisp}} = \frac{\sum_{i=1}^n (\max_j(\mu_i) \times y_i)}{\sum_{i=1}^n \max_j(\mu_i)} \quad (46)$$

where y_{crisp} stands for crisp value of output variable. i changes between 1 and n , and refers to the number of discrete point at which the calculation is being done. j changes between 1 and the number of membership functions of output variable which in this case is 5, and represents the number of membership function curve for which we are getting the membership value of i^{th} point in the universe of discourse of the output variable. Therefore, $\max_j(\mu_i)$ represents the final membership value of the i^{th} point in the universe of discourse of output, i.e. y_i . Equation 47 shows the relation between Balance, Distribution Loss and the overall Cost of Electricity.

$$Balance = Loss + Cost \quad (47)$$

In table 4, total values of distribution loss, cost, and balance on one typical day for the three scenarios mentioned in section III are summarized. It must be noted that the values in the table are unit-less, and they can be regarded as measures for payment that the end-user should make to the utility because of regular operation of Micro-Grid, or profits earned due to improved operation and control of the Micro-Grid.

Table 4 Simulation results for Loss, Cost, and Balance

	Loss	Cost	Balance
Scenario 1	0.1339	1.2294	1.3632
Scenario 2	6.6039	-17.6716	-11.0677
Scenario 3	6.6039	-13.3021	-6.6982

Cost is simply the overall summation of power from/to grid multiplied by the relevant price for all 15 min periods. The overall summation of multiplication of the price and wasted power on distribution branches for all 15 min periods is defined as Loss. With no loss of generality, it is assumed that the reactive power has one tenth the value of active power.

We can see that scenario 2 will provide the consumer with the most possible profit on balance and this is because of the fact that the battery unit used in scenario 2 is assumed to be of infinite capacity. Therefore there will be chance for utmost storage of power in the battery whenever required and the battery can provide that stored power completely to the Micro-Grid for appropriate usage any time. This is not a practical case though. In scenario 3 which is the practical case compared to the second scenario, battery storage unit is assumed to be of limited capacity and therefore, maximum and minimum limits of the stored energy in the battery might prevent the control system to apply the decided action on the storage unit thoroughly. This might cause a drop in the benefits that consumer will obtain using this approach as it can be seen by comparing the values of Balance for the two scenarios 2 and 3. However, by improvements in the battery production technologies this issue can be solved to good extents.

Conclusion

The proposed Fuzzy-Logic based control method is applied for Battery Management in Micro-Grid Systems. In the micro-grid system three buses are considered as renewable generator and storage, utility, and load (smart house). The goal was to reduce the balance which is based on distribution loss and cost. The Micro-Grid was simulated under three scenarios. Simulation results obtained for Micro-Grid under scenario 2 where the ideal infinite-capacity storage is involved with the Fuzzy controller outperform the other two scenarios. However this is not practical. In third scenario, ideal limited-capacity storage was involved and the results were satisfactory. Therefore, using fuzzy controller it is possible to reduce the cost of the Micro-Grid system, and even let the customers make profit from selling the excess power to the utility.

Chapter VII. Particle Swarm Optimization

Particle swarm optimization (PSO) is inspired by social behavior of bird flocking or fish schooling, originally introduced by Eberhart and Kennedy [51] PSO is suitable for optimization problems that are relatively irregular, noisy, or dynamic Each particle updates its position based on the following factors: its best solution (Pbest), a best solution of swarm (gbest), and a best solution of its neighbors (nbest).

Pbest is the best position that each particle found by the pervious iterations. Each particle has a special Pbest. gbest is the best position that all of particles found by pervious iterations. gbest is same for all of particles. We can consider some neighbors for each particle. nbest is the best position that all of neighbors of each particle found by pervious iterations. Each particle has a special nbest.

There are several means to initialize positions of particles. One of them used in this thesis is random initialization. In random initialization, particles are placed in random positions in the space. The update equation of positions is:

$$V = c_0 X + c_1 r_1 \times (pbest - X) + c_2 r_2 \times (gbest - X) + c_3 r_3 (nbest - X) \quad (48)$$

$$X = X + V \quad (49)$$

Where c_0 , c_1 , c_2 and c_3 are constants and r_1 , r_2 and r_3 are random numbers between 0 and 1. Also, V is velocity of each particle. In this study, we consider $c_0 = 0.8$, $c_1 = 1.5$, $c_2 = 1.5$, and $c_3 = 0$ (which these amounts show the best results rather than other amounts). As mentioned before, the problem is to maximize comfort function under certain conditions. For doing this, p particles with random positions are produced. Then, their fitness (comfort function) is calculated and $pbest$ and $gbest$ are obtained.

The velocity of particles is obtained and their positions are updated. This procedure is continued iteratively until a stopping condition is satisfied. Our stopping condition is that the number of iteration reaches a maximum or the increase of the fitness (comfort function) is smaller than a given threshold (k denotes the iteration number):

$$|gbest^k - gbest^{k-1}| < \epsilon \quad (50)$$

In this study, the first one is chosen because the second one may be trapped in a local optimum.

Here, X or each particle is considered as the amount of power to be delivered or taken.

Comfort Function applied for Our Specific 3-bus Micro Grid Model:

$$comfort(p) = -e_1 \cdot (price(t))^2 \sin\left(\frac{\pi}{2}t\right) \cdot x(1, p) - price(t) \cdot (|V_{Grid}| + |Loss_{total}|). \quad (51)$$

Simulations for PSO

Figure 43 illustrates when PSO is applied for given Load, RE, and Price profile. As it shown in Figure 43, the power coming out from RE bus is completely satisfy required load and once the price in at peak and less load is needed, it consumes more power from RE to minimize cost.

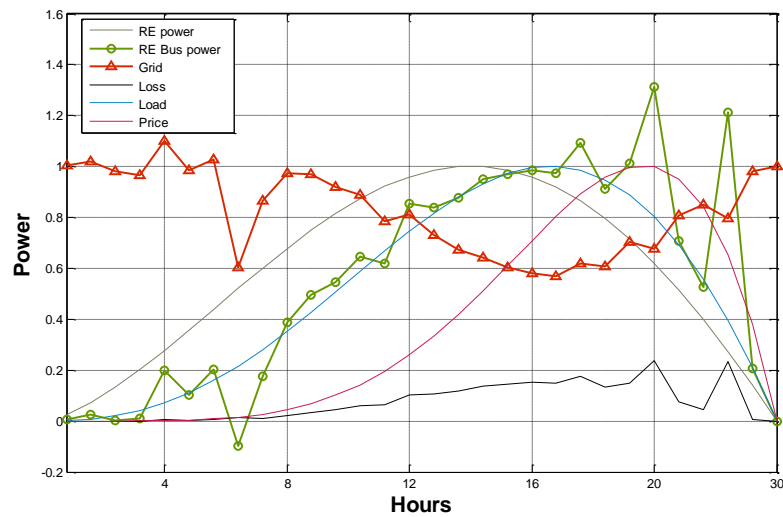


Figure 43 Micro Grid Control by PSO with Load, RE, and Price profile

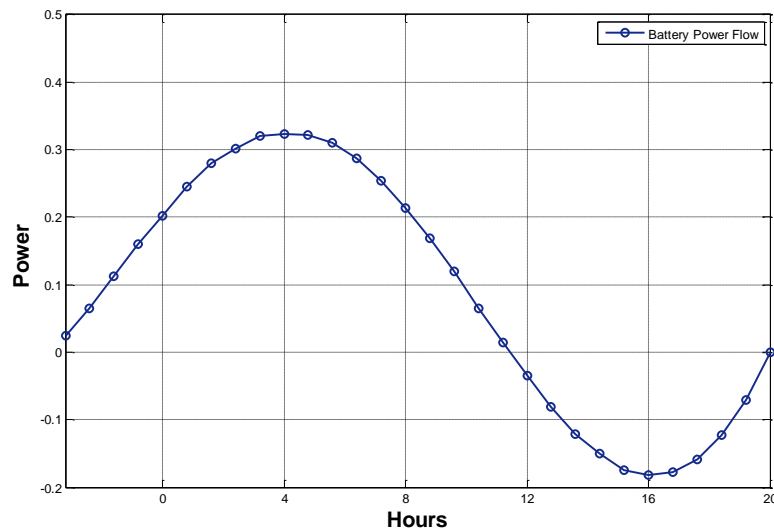


Figure 44 Power from battery

As shown in Figure 44, PSO makes battery to charge when electricity is low (0-8 hours) and discharge when price is high (8-16). Also, the stored battery in low price period is consumed for required load when price is high. This figure verifies the perfect and intelligent performance of PSO for this kind of model that every input parameter is stochastic and hard to assign fuzzy logic rules and useless to use deterministic optimization methods.

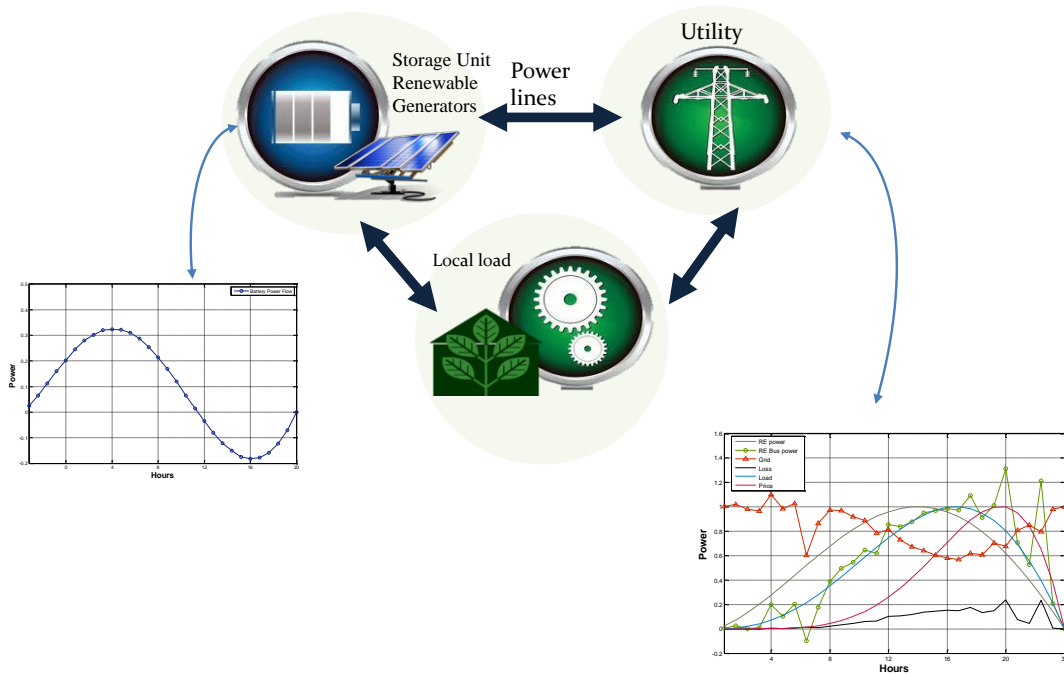


Figure 45 all profiles and battery behavior through PSO utilization

The results shown in figures (43-45) were for when the sufficient renewable energy exists. Following results will be showing for when the renewable energy is not enough.

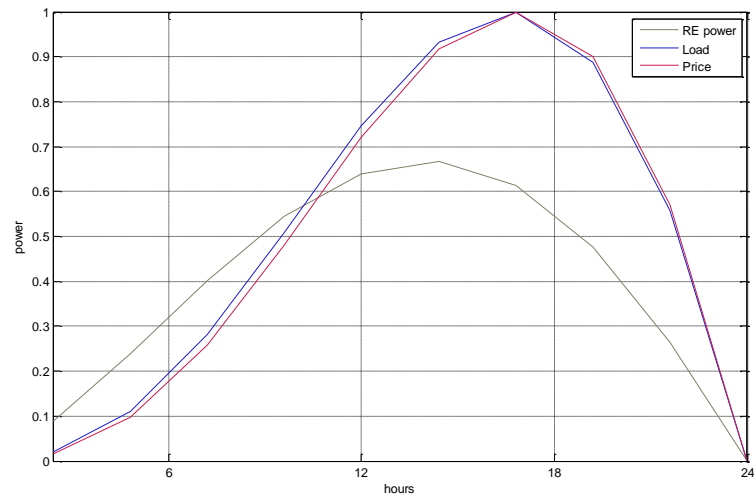


Figure 46 the RE power, price, and Load profile when RE power is not sufficient for given load

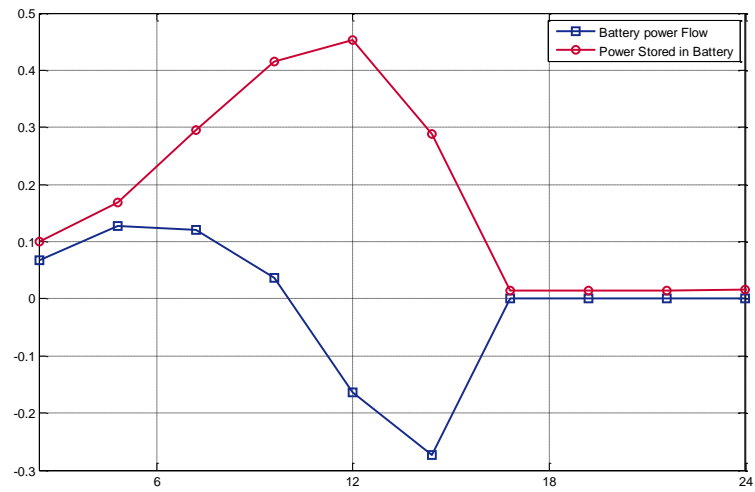


Figure 47 Battery charging and discharging states

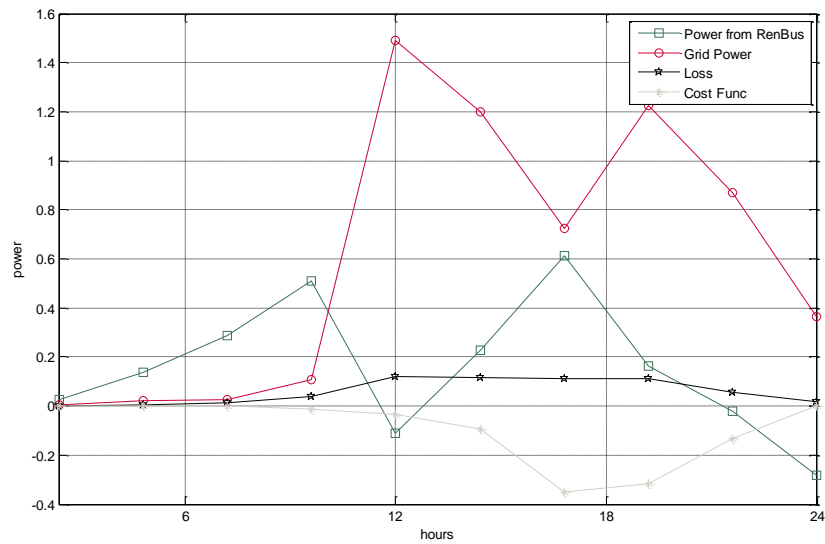


Figure 48 Grid Power, Price, Cost Function, and power from RE

As depicted in figure 46, there is no ample renewable energy for needed load. Figure 47 shows that battery stores low price power as much as possible for high price power period. As shown in 48, at hour 18, when the price has its maximum value, the battery does not let grid power to be increased and decrease the grid power as much as possible. Based upon results shown in figures 43-48, the PSO performs acceptable for Micro Grid model that has stochastic parameters.

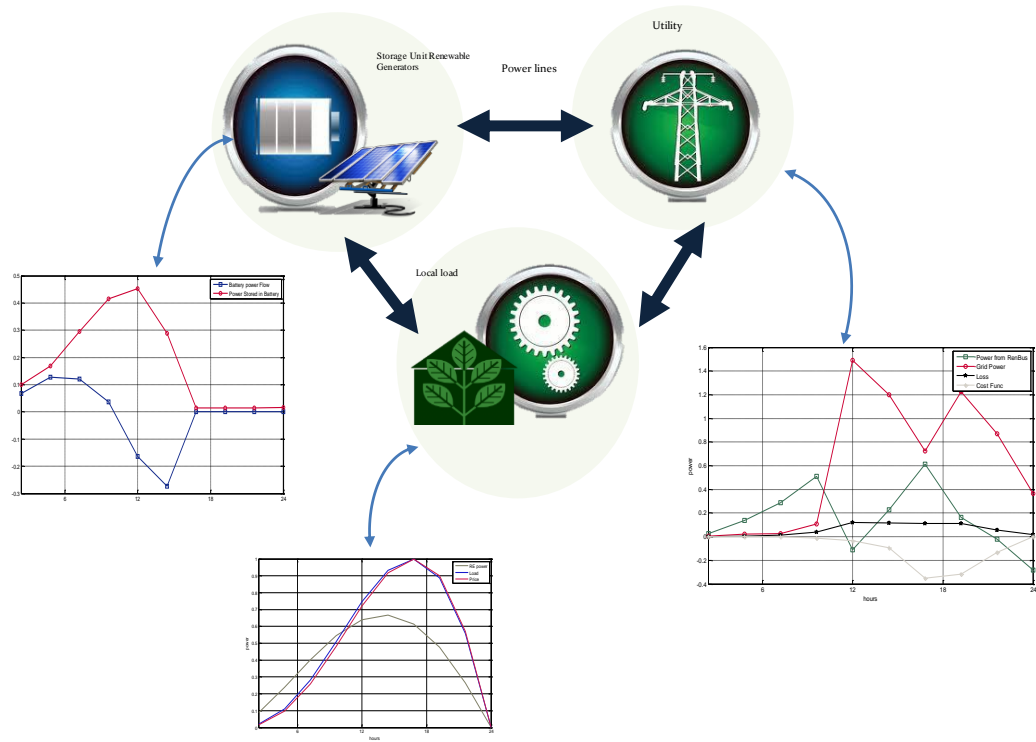


Figure 49 Battery power, input profiles and Grid Power

Chapter VIII. CONCLUSION

This thesis, presents the Cognitive Radio framework for wireless Ad Hoc networks. The proposed Cognitive Radio framework is a complete model for Cognitive Radio that describes the sensing and sharing procedures in wireless networks by introducing Queued Markov Chain method in spectrum sensing and Competitive Indexing Algorithm in spectrum sharing part.

Queued Markov Chain method is capable of considering waiting time and is very well generalized for unlimited number of secondary users. It includes the sharing aspect of Cognitive Radio. Power-law distribution of node degree in scale-free networks is important for considering the traffic distribution and resource management thus we consider the effect of the topology on sensing and sharing performances. We demonstrate that CIF outperforms Uniform Indexing (UI) algorithm in Scale-Free networks while in Random networks UI performs as well as CIF.

Also, in this thesis, a framework is presented based on 4G Cognitive Radio (CR) network capable of communicating with high numbers of geographically dispersed smart meters for command and control feature concurrently with private cellular network. Our approach uses pervasive smart grid systems (i.e. cloud data centers) as the central communication and optimization infrastructure supporting metropolitan area based smart meter infrastructure. In this thesis, we investigate the performance of various scheduling algorithms in context with CR

units to provide a satisfactory tradeoff between maximizing the system capacity, achieving fairness among cognitive users. We lay as a framework evaluation 3GPP LTE system model simulations. Our system level simulation results show that the 4G CR network model meets the smart grid protocols requirements for a multi-user CR network of Smart meters.

This thesis addresses improvements in the multiuser capacity in unplanned networks with high levels of co-channel interference. We view this as the likely system scenario for future cognitive radio (CR) networks. For this reason, this thesis presents a novel opportunistic interference aware scheduling protocol ideally suited for maximum channel reuse in unplanned networks. We present results for maximum capacity CR networks, many of which may be based upon the future IEEE 802.22 standard. In addition, we show that the IEEE 802.22 protocol enabling Federal Communication Commission (FCC)-CR can support future distributed smart grid communication network comprised of smart meters. We analyze the application of SISO and MIMO interference aware scheduling to maximize the capacity and number of scheduled smart meters. We present simulation results that show significant improvement in the total capacity and number of scheduled smart meters in comparison to traditional scheduling schemes. Finally, we show that our system meets the DOE smart grid communication protocol requirements in terms of capacity.

Moreover, a Fuzzy Logic-based framework is proposed for control of Battery Storage Unit in Micro-Grid Systems to achieve Efficient Energy Management. Typically, a Micro-Grid system operates synchronously with the main grid and also has the ability to operate independently from the main power grid in an islanded mode. Distributed renewable energy generators including solar, wind in association with batteries and main grid supply power to the consumer in the Micro-Grid network. The goal here is to control the amount of power delivered to/taken

from the storage unit in order to improve a cost function, defined based on summation of payment required for purchasing power from main grid or profit obtained by selling power to the main grid and distribution power loss, through reasonable decision making using predetermined human reasoning-based fuzzy rules. Profiles of system variables such as Consumer's Load Demand, Electricity Price Rate, and Renewable Electricity Generation Rate are assumed arbitrarily for obtaining general results. Measures of payment/profit will be extracted to compute amounts of cost and balance for the network which represents benefits of using Fuzzy logic for Storage Unit control with and without considering storage unit capacity limits. Simulation results are presented and discussed.

Chapter IX. References

- [1] Ian F. Akyildiz, Won-Yeol Lee, Mehmet C. Vuran, and Shantidev Mohanty, "A Survey on Spectrum Management in," *IEEE Communications Magazine*, April 2008.
- [2] Isabelle Tardy, Ole Grondalen, "Which Regulation for Cognitive Radio? An Operator's Perspective," *Teletronikk*, 2010.
- [3] I. F. A. e. al, "NeXt Generation/Dynamic Spectrum Access/Cognitive Radio Wireless Networks: A Survey," *Comp. Networks J*, pp. 2127-2159, 2006.
- [4] FCC, "Unlicensed Operations in the TV Broadcast Bands, Second Memorandum Opinion and Order,," 2010.
- [5] J. Wang, M. Shosh, and K. Challapali, "Emerging cognitive radio applications: a survey," *IEEE Commun. Mag*, vol. 49, p. pp. 74–81, mar 2011.
- [6] 3. S. T. 36.321, "Technical Specification Group Radio Access Network; Evolved Universal Terrestrial Radio Access; Medium Access Control," 2010.
- [7] I. S. 802.16m, "System Description Document," 2009.
- [8] J. Ma, G. Y. Li, and B. H. Juang, "Signal processing in cognitive radio," *Proc. IEEE*, p. pp. 805–823, 2010..
- [9] S. Haykin, D. J. Thomson, and J. H. Reed, "Spectrum sensing for cognitive radio," *Proc. IEEE*, p. 849–877, 2010.
- [10] D. Cabric, S. M. Mishra, and R. W. Brodersen, "Implementation Issues in Spectrum Sensing for Cognitive Radios," p. 772–76, 2004.
- [11] Y. Zeng and Y.-C. Liang, "Eigenvalue-based spectrum sensing algorithms for cognitive radio," *IEEE Trans. Commun*, p. 1784–1793, 2009.
- [12] A. Kortun, T. Ratnarajah, Sellathurai, C. M., Zhong, and C. B. Papadias, "On the performance of eigenvalue-based cooperative spectrum sensing for cognitive radio," *IEEE J. Sel. Topics Signal Process*, p. 49–55, 2011.
- [13] T. Cui, J. Tang, F. Gao, and C. Tellambura, "Moment-based parameter estimation and blind spectrum sensing for quadrature amplitude modulation," *IEEE Trans. Commun*, p. 613–623, 2011.
- [14] A. Sahai and D. Cabric, "A tutorial on spectrum sensing: Fundamental limits

- and practical challenges," *Int. Symp. on New Frontier in Dynamic Spectrum Access Networks (DySPAN)*, 2005.
- [15] P. P. Hoseini and N. C. Beaulieu, "An optimal algorithm for wideband spectrum sensing in cognitive radio systems," *Proc. IEEE Int. Conf. Commun. (ICC)*, pp. 1-6, 2010.
 - [16] P. Paysarvi-Hoseini and N. C. Beaulieu, "Optimal wideband spectrum sensing framework for cognitive radio systems," *IEEE Trans. Signal Process*, p. 1170–1182, 2011.
 - [17] Z. Quan, S. Cui, A. H. Sayed, and H. V. Poor, "Optimal multiband joint detection for spectrum sensing in cognitive radio networks," *IEEE Trans. Signal Process*, p. 1128–1140, 2009.
 - [18] D. Qu, J. Ding, T. Jiang, and X. Sun, "Detection of non-contiguous OFDM symbols for cognitive radio systems without out-of-band spectrum synchronization," *IEEE Trans. Wireless Commun*, p. 693–701, 2011.
 - [19] S. Krishnamurthy et al., "Control Channel Based MAC Layer Configuration, Routing and Situation Awareness for Cognitive Radio Networks," *Proc. IEEE MILCOM*, p. 455–60, 2005.
 - [20] O. Ileri, D. Samardzija, and N. B. Mandayam, "Demand Responsive Pricing and Competitive Spectrum Allocation via Spectrum Server," *Proc. IEEE DySPAN*, p. 194–202, 2005.
 - [21] Q. Zhao et al., "Decentralized Cognitive MAC for Opportunistic Spectrum Access in Ad Hoc Networks: A POMDP Framework," *IEEE JSAC*, pp. 589-99, 2007.
 - [22] H. Zheng and L. Cao, "Device-centric Spectrum Management," *Proc. IEEE DySPAN*, pp. 56-65, 2005.
 - [23] R. Menon, R. M. Buehrer, and J. H. Reed, "Outage Probability Based Comparison of Underlay and Overlay Spectrum Sharing Techniques," *Proc. IEEE DySPAN*, pp. 101-9, 2005.
 - [24] J. Zhao, H. Zheng, and G.-H. Yang, "Distributed Coordination in Dynamic Spectrum Allocation Networks," *Proc. IEEE DySPAN*, p. 259–68, 2005.
 - [25] Pengbo Si ; Enchang Sun ; Ruizhe Yang ; Yanhua Zhang ;, "Cooperative and distributed spectrum sharing in dynamic spectrum pooling networks," *Wireless and Optical Communications Conference (WOCC)*, pp. 1-5, 2010.
 - [26] Toroujeni, S.M.M. ; Sadough, S.M.-S. ; Ghorashi, S.A., "Time-frequency spectrum leasing for OFDM-based Dynamic Spectrum Sharing systems," *Wireless Advanced (WiAD)*, pp. 1-5, 2010.
 - [27] A.L. Barabasi, R. Albert, "Emergence of scaling in random networks," *Science*, vol. 286, pp. 509-512, 1999.
 - [28] Carlos Cordeiro, Kiran Challapali, and Dagnachew Birru, "IEEE 802.22: An Introduction to the First Wireless Standard based on Cognitive Radios," *Journal of Communications*, vol. 1, 2006.
 - [29] T. Kolding., "Link and System performance aspects of Proportional Fair Packet Scheduling in WCMS/HSDPA," *In Proceedings of 58th IEEE Vehicular*

- Technology Conference*, vol. 3, pp. 1717-1722, 2008.
- [30] Zhi Quan ; Shuguang Cui ; Sayed, A.H. ; Poor, H.V. , "Optimal Multiband Joint Detection for Spectrum Sensing in Cognitive Radio Networks," *IEEE Transaction on Signal Processing*, vol. 57, pp. 1128-1140, 2008.
 - [31] Khalid, L. ; Anpalagan, A., "Effect of sensing errors on wideband cognitive OFDM radio networks," *IEEE Biennial Symposium QBSC*, pp. 273-277, 2010.
 - [32] Ying-Chang Liang ; Yonghong Zeng ; Peh, E.C.Y. ; Anh Tuan Hoang, "Sensing-Throughput Tradeoff for Cognitive Radio Networks," *IEEE Transactions On Wireless Communications*, vol. 7, 2008.
 - [33] Yanjun Yao ; Zhiyong Feng ; Dan Miao , "Markov-based Optimal Access Probability for Dynamic Spectrum Access in Cognitive Radio Networks," *Vehicular Technology Conference (VTC 2010-Spring)*, 2010.
 - [34] Ghosh, C. ; Cordeiro, C. ; Agrawal, D.P. ; Rao, M.B. , "Markov Chain Existence and Hidden Markov Models in Spectrum Sensing," *IEEE International Conference on Pervasive Computing and Communications*, 2009.
 - [35] Akyildiz, I.F. ; Won-Yeol Lee ; Vuran, M.C. ; Mohanty, S., "A survey on spectrum management in cognitive radio networks," *Communications Magazine, IEEE*, vol. 46, pp. 40-48, 2010.
 - [36] Pengbo Si ; Hong Ji ; Yu, F.R. ; Leung, V.C.M., "Optimal Cooperative Internetwork Spectrum Sharing for Cognitive Radio Systems With Spectrum Pooling," *Vehicular Technology, IEEE Transactions on*, vol. 59, pp. 1760-1768, 2010.
 - [37] Amir Rajaei, Mahdy Saedy, Asadallah Sahebalam, "Competitive Spectrum Sharing for Cognitive Radio on Scal-Free Wireless Networks," *IEEE IWCMC Istanbul*, 2010.
 - [38] D.D.Ariananda, M.K.Lakshmanan, H.Nikookar, "A survey on spectrum sensing techniques for cognitive radio;Cognitive Radio and Advanced Spectrum Management," *Second International Workshop on*, pp. 74-79.
 - [39] B. Kelley, "Software Defined Radio for Broadband OFDM Protocols," *SMC*, 2009.
 - [40] S.-W. Luan, J.-H. Teng, S.-Y. Chan, and L.-C. Hwang, "Development of a smart power meter for AMI based on zigbee communication," *Proc. Int. Conf. Power Electron*, pp. 661-665, 2009.
 - [41] Wenpeng Luan, Duncan Sharp and Sol Lancashire, "Smart Grid Communication Network Capacity Planning for Power Utilities," *IEEE PES Transmission and Distribution Conference and Exposition*, pp. 1-4, 2010.
 - [42] B. Reid, "Oncor electric delivery smart grid initiative," in *Proc. 62nd Annu. Conf. Protective Relay Engineers*, pp. 8-15, 2009.
 - [43] Robert C. Qiu, Zhe Chen , Nan Guo , Yu Song, Peng Zhang, Husheng Li and Lifeng Lai, "Towards A Real-time Cognitive Radio Network Testbed: Architecture, Hardware Platform, and Application to Smart Grid," *Networking Technologies for Software Defined Radio (SDR) Networks, Fifth IEEE Workshop, Boston*, pp. 1-6, 2010.

- [44] Preben Mogensen et.al., "LTE Capacity compared to the Shannon Bound," *In Proceedings of 65th IEEE Vehicular Technology Conference*, pp. 1234-1238, 2007.
- [45] Department of Energy, "Communications Requirements of Smart Grid Technology", 2010.
- [46] Chawla, K., Xiaoxin Qiu, "Throughput performance of adaptive modulation in cellular systems," *IEEE , Int. Conf. Universal Personal Communications, Florence*, 1998.
- [47] "LTE Capacity Compared to the Shannon Bound," *IEEE 65th Vehicular Technology Conference, Dublin*, pp. 1234-1238, 2007.
- [48] IEEE802.22-05/0055r7, "WRAN Channel Modeling," 2005.
- [49] Y. S. Manjili; A. Rajaei; B. Kelley; M. Jamshidi, "Fuzzy Control of Storage Unit for Energy Management in Micro-Grids," *University of Texas at San Antonio College Of Science Conference, UTSA-COS*, 2011.
- [50] C. Cho; J. Jeon; J. Kim; S. Kwon; K. Park.; S. Kim, "Active Synchronizing Control of a Microgrid," *IEEE Transactions on Power Electronics*, no. 99, 2011.
- [51] J. Kennedy, R.C. Eberhart., "Particle Swarm Optimization," *In Proc .of the IEEE Int Conf. Neural Networks*, 1995.

Section 3:

Photovoltaics

Bi-Directional Multi-Mode Grid tied Converter for Solar Energy Conversion Systems¹

Elmira Mohyedinbonab, *Student Member, IEEE*, Emiliano Morales, *Member, IEEE*,
Hariharan Krishnaswami, *Member, IEEE*, Mo Jamshidi, *Fellow IEEE*.

Abstract — The rapid growing interests in renewable energy, such as solar energy, outweigh the benefit of distributed grids in current grid networks. Innovative topologies for renewable energy conversion systems that integrate with electric grids and energy storage systems are being proposed, each with limited modes of operation for the various needs in smart grid applications. In this paper, we propose a modified version of a multi-source converter, which uses a small number of elements to accomplish each task of multi-mode operation in a smart-grid. The proposed approach is verified by simulations in MATLAB. We found that by introducing an additional switch in the converter's output allows the reverse flow of current, enabling current to charge a battery from the grid while maintaining the integrity of the former modes of operation.

Index Terms—Battery Storage, Bi-directional Converters, Micro-grid, Multi-Mode Converters, Renewable Energy, Smart-grid

I. INTRODUCTION

Traditional fossil fuel power plants are built away from cities due to the air pollution they produce. Despite their steady performance, the amount of energy lost in transmission lines can be significant. This energy loss can be reduced by distributing power plants inside the city. On the other hand, with increasing the load demands, these distributed generation systems can help diminish the need for new fossil power plants. Renewable energy sources, such as solar arrays, are known for their clean source of energy, and their power plants are rapidly being built on the vicinity of cities and within the cities themselves. This paradigm shift is becoming apparent in the U.S., as renewable energy electricity generation is projected to increase from 462 billion kilowatt-hours in 2010 to 469 billion kilowatt-hours in 2015[1]. Many countries are promoting their plans to multiply their solar energy generation plants by facilitating the procurement of solar plants and offering incentives. To date, the U.S. has nine of the thirteen biggest photovoltaic solar projects in the world [2].

As renewable energies become more readily available in the residential sector, DC devices in residences can be supplied energy from the DC bus of a microgrid. There are advantages in utilizing a DC bus source as opposed to the synthesized AC source for these devices. Even though current AC/DC converters offer huge amounts of power savings thanks to the advances in power electronic conversion systems, it is still

more reliable and efficient to utilize the DC bus due to the reduced amount of components in comparison to AC-DC converters.

Solar energy is a well known and favorable type of renewable energy source, which generates DC power. However, solar, wind, and other types of renewable energies are inherently intermittent in nature, meaning they cannot supply the load demand continuously. To provide a more rigid flow of electricity, solar energy is integrated with utility grid with energy storage systems and other available renewable energy sources such as wind energy. Hybrid energy systems are capable of providing better power quality and reliability and can improve the system performance. As an example, wind and solar energy are somewhat complementary on a daily or seasonal basis [3-4]. Having an energy storage system may stabilize the energy generated from renewable sources, specifically during sporadic climate changes that can affect the output of renewable energy sources dramatically, and thus increasing the reliability of the DC bus. In this paper, we propose an amendment to an existing topology, which may serve to regulate DC voltage into an inverter or a DC bus and charge/discharge a battery storage system. The hybrid system in this paper is combination of photovoltaic, energy storage system and the utility grid. Bi-directionality of converter provides a good power exchange among sources, load and DC-voltage bus. **This concept is**

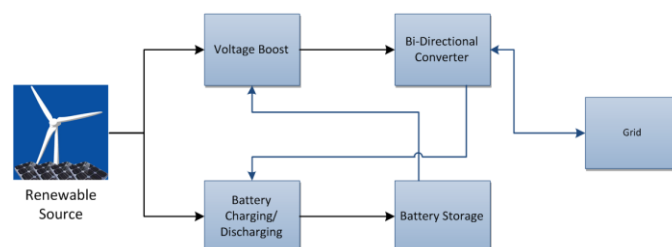


Fig. 1. The smart-grid functionality allows the battery to be charged from the grid.

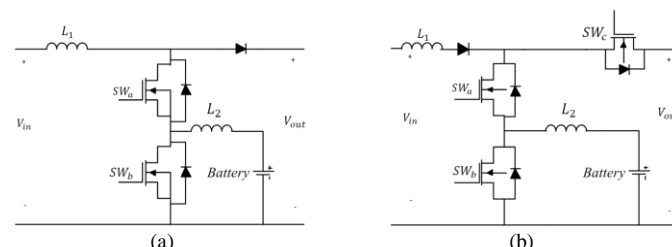


Fig. 2. (a) Original method. (b) Proposed method which places the original diode besides the L_1 inductor and places a four quadrant operating MOSFET in its place.

¹ This project was partially funded by CPS Energy through its Strategic Research Alliance with The University of Texas at San Antonio, San Antonio, TX, USA.

illustrated in Fig.1.

II. CONVENTIONAL STRUCTURE OF THE MULTI-MODE SINGLE LEG CONVERTER.

In paper [5], a novel method is proposed that utilized only two switches (single leg), one diode, and two inductors to implement different converter modes in the bi-direction operation of DC/DC converters. This was an improvement to the conventional boost and bi-directional DC/DC converters by removing a switching element from the converter, while still offering the same functionalities and modes. In [5], the battery is charged in only one mode of operation. Generated voltage can boost up/down and charge/discharge the battery at the same time a DC voltage is being supplied to the output of the circuit.

However, the methods on [5] allowed the battery to be charged from the renewable source only, and not from the grid. In this paper, the switch is re-introduced and the configuration was changed for the benefit of an additional mode. In this additional mode, the battery can be charged from the grid when the renewable source is absent or not sufficient to supply power to the battery. Despite the re-configuration of the single leg converter, the four former proposed modes of operation worked.

The placement of the switch to the proposed converter does not introduce any new switching losses during the original four modes, for the primary purpose of the switch is to act as a gate that allows current from the output into the battery, and as a diode for voltage boost operations (See fig. 2). In these four modes, the properties of the MOSFET allow the switch to behave like a diode when no pulse is felt at the gate.

The converter in [5] was limited in interactions between the renewable energy source and the battery, load, or both. By taking advantage of the bi-directionality capability of inverters, the excess grid power can be rectified by the inverter and stored in the battery. This proposed configuration allows more interaction among the renewable energy source and grid, including the battery. This useful feature is capable of storing excess power from grid and renewable energy power in the battery when the load demand drops, and may serve as smart grid function that helps regulate the utility grid.

This paper is structured as follows. In the first section, the four modes in [5] are re-tested with new configuration, and briefly describe each mode of operation. That same section will introduce and cover the new mode and derives its corresponding equations. The second section will cover the controller design and explain how to find the desired duty cycles for the MOSFET switches. In the final section, we will present our simulation results from MATLAB's Simulink followed by a conclusion, which presents the limitations of this configuration and future endeavors.

III. PROPOSED METHOD FOR THE INTERACTION BETWEEN RENEWABLE ENERGY SOURCE, BATTERY, AND GRID

The schematic for proposed configuration is shown on fig. 2. As seen on this figure, the diode is replaced with a bi-directional MOSFET and placed in series with L_1 , which will become essential to block the current from flowing into the PV source in the proposed mode of operation. The four original modes are the Main Boost Mode, the Boost-Buck Mode, the Boost-Boost Mode, the Battery Boost Mode, and the Reverse Buck Mode. In the Main Boost mode, the single leg converter increases the voltage that is supplied to the inverter. In the Boost-Buck mode, energy is stored in the battery while voltage is supplied to the inverter or DC bus simultaneously. During high load demands, the Boost-Boost mode can supply the inverter with energy from the PV source and the battery simultaneously. And during cloud cover, energy can be supplied to the inverter from the battery in Battery-Boost mode.

In cases in which grid peak shaving is desired, the battery can be charged from the grid. The grid alone can supply the current to the battery through a buck operation in the Reverse Buck Mode. Times in which is critical to charge the battery from the grid include peak shaving during inclement weather or nights, when PV source cannot provide sufficient current to charge the battery, when the load demand drops, or to store energy during times when grid energy costs are low.

A. Main Boost Mode

In this mode, SW_a and SW_b have the same duty ratio. Together, both switches form a boost converter that boosts the PV input voltage. During this mode, SW_c behaves as a diode by sending zero to its gate. The basic input to output principle of boost converters applies to this mode, where:

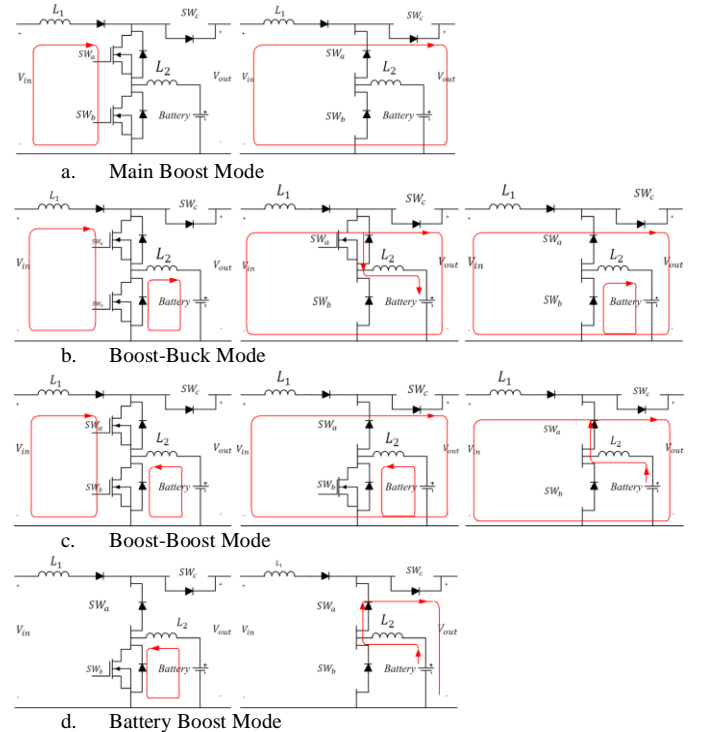


Fig. 3. The original four modes of operation still operate under the same principle as before.

$$V_{out} = \frac{V_{in}}{1-D} \quad (1)$$

In which,

$$D = \frac{T_{on}}{T_s} \quad (2)$$

B. Boost Buck Mode

For this mode, the duty ratio of SW_a is longer than SW_b . This way, the PV voltage is boosted during the time both SW_a and SW_b are “ON”. During the time SW_a remains “ON” and SW_b turns “OFF”, the PV supplies energy to the load and charges the battery. In this mode, SW_c behaves as a diode. To determine the output of the boost converter for this mode, the equations become:

$$V_{out} = \frac{V_{in}}{1-D_{boost}} \quad (3)$$

In which,

$$D_{boost} = \frac{T_{on-boost}}{T_{s-boost}} \quad (4)$$

To charge the battery, the equations become:

$$V_{batt} = D_{buck} V_{in} \quad (5)$$

Where,

$$D_{buck} = \frac{T_{on-buck}}{T_{s-boost}} \quad (6)$$

C. Boost-Boost Mode

Here, we have the opposite case from the Boost-Buck mode, in which the duty ratio of SW_b is longer than SW_a 's. This allows the battery to discharge energy to the inverter when the PV energy generation is not sufficient. During this mode, SW_c behaves as a diode. This mode boosts the input voltage while discharging the battery to supply the load. The equations for this mode are:

$$V_{out} = \frac{V_{in}}{1-D_{boost1}} \quad (7)$$

In which,

$$D_{boost1} = \frac{T_{on-boost1}}{T_s} \quad (8)$$

And

$$V_{out} = \frac{V_{batt}}{1-D_{boost2}} \quad (9)$$

In which,

$$D_{boost2} = \frac{T_{on-boost2}}{T_s} \quad (10)$$

D. Battery Boost Mode

The Battery Boost mode is useful in the case of input fault such as cloud cover, or damaged modules, etc. Since our modification to the converter, the state for SW_a is no longer

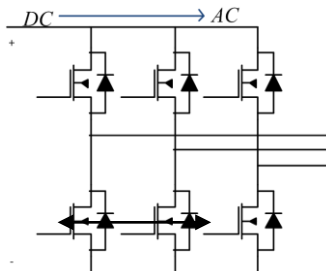


Fig. 4. A three phase full bridge inverter can act as a diode bridge rectifier in reverse when no signals are sent to the gates.

relevant while SW_c acts as a diode. In this mode, the battery supplies the inverter with energy via the mathematical equations (11) and (12).

$$V_{out} = \frac{V_{batt}}{1-D} \quad (11)$$

In which the duty ratio of SW_b is,

$$D = \frac{T_{on}}{T_s} \quad (12)$$

E. Reverse Buck Mode

The Reverse Buck Mode (RBM) benefits from the SW_c switch and makes use of the bi-directionality of the interconnected inverter. This is accomplished by either sending no pulses to the MOSFETs of the universal bridge, in essence converting the universal bridge into a full bridge rectifier (see Fig.4.), or by controlling the individual MOSFET switching cycles to achieve a desired DC voltage. Subsequently, this system converts the AC grid voltage into DC for battery charging. In this mode, we made SW_{c1} “OFF”, SW_{c2} “ON”, and SW_b “OFF”. In this way, the battery is charged from the rectified grid voltage by varying the duty of SW_a . When the SW_a is “ON”, V_{rect} is transferred to the battery and the inductor current I_{L1} increases. This is mathematically expressed as:

$$\Delta I_{L2} = \frac{V_{rect} - V_{batt}}{L_2} DT_s \quad (13)$$

Where, ΔI_{L2} is the inductor ripple current. When SW_a is “OFF”, then inductor current in L_2 decreases in the rest of the period T_s . This is expressed as

$$\Delta I_{L2} = \frac{V_{batt}}{L_2} (1-D) T_s \quad (14)$$

By equating (13) and (14), we derived the RBM input to output relation.

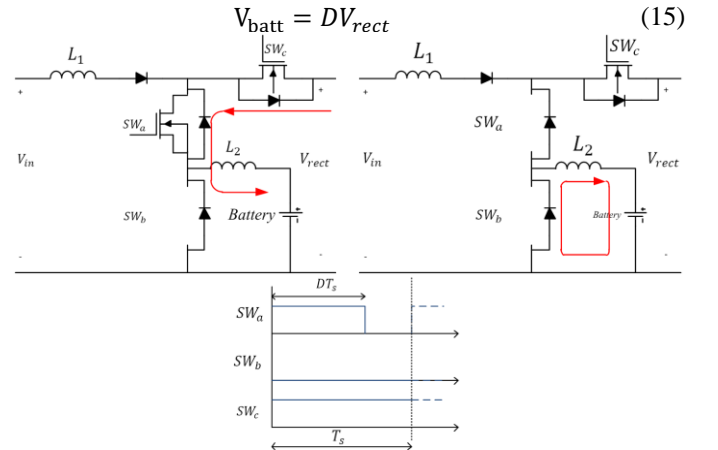


Fig. 5. Reverse Buck Mode charges the battery when SW_a is “ON” and when no renewable power source is available.

IV. CONTROL SCHEME

A control scheme was designed for proposed Reverse Buck Mode. This scheme consisted of a Lag compensator (Proportional-plus-integral controller) which increases the low-frequency loop gain, such that the output is better

regulated at DC and at frequencies below the crossover frequency. The controller transfer function is defined as:

$$G_c(s) = G_0(1 + \frac{w_L}{s})$$

where ω_L is inverted zero. PI controller integrates the error signal at low frequencies, such that the disturbance-to-output transfer function approaches zero.

We chose ω_L as one tenth the crossover frequency to avoid significant changes in the phase margin, otherwise our phase margin is corrupted and would require us to add a Lead compensator to our controller. G_0 is selected in such manner to achieve the desired crossover frequency, and has a unity loop gain at desired cross over frequency.

The Bode plot for the system is shown in fig. 6. As can be seen it has small degree phase margin which is not desired. By changing the crossover frequency, the system can achieve better stability in this mode. With this controller, the output can reach an approximately zero error in steady state and output loop disturbances are attenuated.

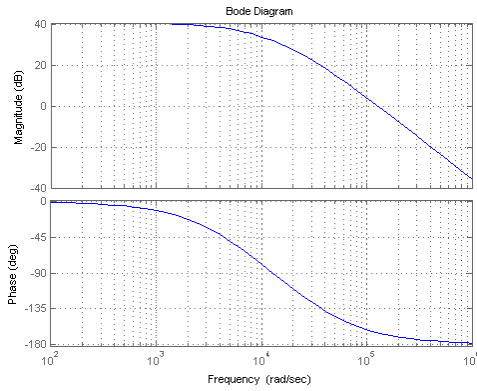


Fig. 6. converter control-to-output transfer function

As seen on fig. 7. , after setting the reference voltage on 54 volt, the steady-state error becomes zero after almost 0.14 seconds, and it reaches the desired output voltage.

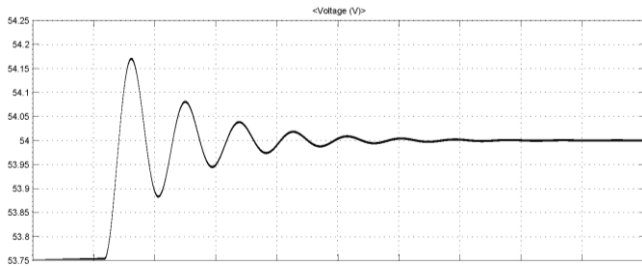


Fig. 7. output voltage transient response with PI controller

V. SIMULATION RESULTS

The three-switch multimode converter was implemented and simulated in MATLAB's Simulink. Values chosen for the different elements and modes are listed on Table I.

Table I
Simulation Parameters

Nominal Output Voltage	160V	Inductor (L1)	0.8mH
Battery Voltage	50V	Inductor (L2)	0.6mH
Initial Battery SOC%	0.5	Battery Type	NMH

The duty ratios were generated by sending control signals to a PWM generator which employed a $10\mu s$ repeating ramp waveform. Also, a similar voltage source to V_{in} was used in our model to simulate an ideal rectification from the grid. The Simulink model was run for 0.4 seconds and is depicted on fig. 8.

The battery chosen for our simulations was of a Nickel Metal Hydride with a nominal voltage of 50V. Other noteworthy parameters includes number of cells in series, and number of cells in parallel and Internal Resistance. Nonlinear model of the battery shows a good approximation of the real available NMH batteries. This battery has 42 cells in series with nominal voltage of 1.18 volt for each cell. The Maximum capacity for each cell is 7 AH. The total resistance of the battery with Internal Resistance of 0.002 Ohms for each cell is 0.0084 Ohms. Experimental validation of the model shown a maximum error of 5% (when SOC is between 10% and 100%) for charge and discharge dynamics.[Matlab help. menu].

As seen on figs 9-12, the behavior of the former four modes are not altered with the addition of SW_c and the input/output equations are not affected. fig. 9 demonstrates the Main Boost Mode, which boost the input voltage to 160V with negligible current going into the battery (ΔI_{L2}).

fig. 10 shows the Boost Buck Mode, which boosts the voltage in the beginning of the time period T_s and then charges the battery while maintaining the output voltage at its nominal value. Fig. 11 shows the Boost-Boost mode, which provides power to the grid from the grid and input sources. Fig. 12 shows the Battery Boost Mode. For this mode, the input voltage was set to zero, and the duty ratio of SW_b was regulated to provide 160V in the output. The current through inductor L_1 was effectively zero.

The Reverse Buck Mode simulation results are seen on fig. 13. The regulation of SW_a allowed the battery to be charged from the rectified grid voltage. At an initial battery state of charge (SOC) of 50%, the operating voltage of the battery was around 50V. Therefore, the battery would not charge for any duty cycle less than 0.5. This is due to duty cycle relationship of equation (15), expressed as:

$$\frac{V_{batt}}{V_{rect}} = D \approx \frac{50V}{100V}$$

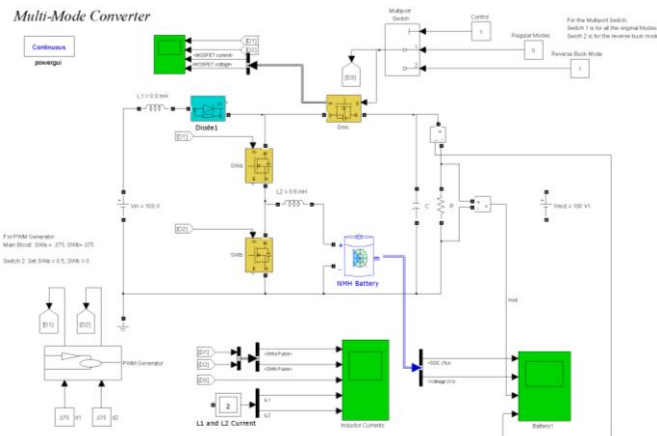


Fig. 8. Simulink model of multi-mode converter.

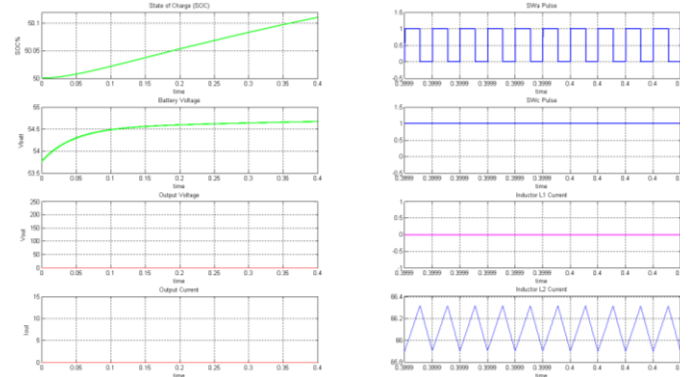
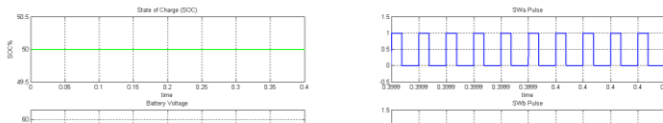


Fig. 13. Reverse Buck Mode Results.

VI. DISCUSSION

It is somewhat possible to charge the battery from two sources by modifying SW_c into a four quadrant operating



switch (that is a MOSFET configuration that allows for the positive and negative exchange of voltage and current through it). The four quadrant operating MOSFET is illustrated on fig. 14a. The four quadrant flexibility was used to preclude any current from flowing into each of the respective sources, and solely supply current to the battery. This mode is desired, since it could increase savings by storing the energy when the electric rate is low, and utilizing it when it is high in the following day(s).

In this mode, SW_a remains “ON” for the entire period while SW_{c1} is “OFF”, and SW_b becomes “ON” for $d_b T_s$ seconds. In this mode, SW_{c2} may cycle “ON” for $d_c T_s$ seconds during the remaining period $(1 - d_b) T_s$ (See Fig. 14b). Consequently, during the $d_b T_s$ the PV charges the L_1 inductor, which is the amount of energy that will be pushed into the battery when SW_b turns “OFF”. During this period of time, the grid remains disconnected from the battery. When SW_{c2} turns “ON”, the grid supplies energy to the battery for the remaining duration of time. It is during this period of time that both the PV and the grid should charge the battery.

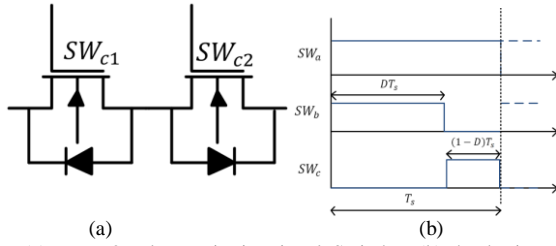


Fig.14. (a) Four Quadrant Bi-Directional Switch. (b) The basic order of switching operation to charge the battery from energy of the PV source and the rectified grid voltage simultaneously.

Formulas for two scenarios under this mode were derived. In the first scenario in which both SW_a and SW_b are “ON”, the ripple current of both inductors is calculated as follow:

$$\Delta I_{L2} = \frac{V_{bat} d_b T_s}{L_2} \quad (16)$$

And,

$$\Delta I_{L1} = \frac{V_{in} d_b T_s}{L_1} \quad (17)$$

During the time that SW_{c2} turns “ON” and SW_b is “OFF”, the ripple current of both inductors are mathematically described by:

$$\Delta I'_{L2} = \frac{V_{rect} - V_{batt}}{L_2} d_c T_s \quad (18)$$

and,

$$\Delta I'_{L1} = \frac{V_{in} - V_{rect}}{L_1} d_c T_s \quad (19)$$

However, unlike the previous method, (16) and (18) cannot be equated with (17) and (19) to find the input/output relationships. This may be due to the inequality of inductor currents (L_1 and L_2) during the short time gap which SW_b and SW_{c2} are both “OFF”. Due to this characteristic, the input/output equations cannot be derived precisely.

VII. CONCLUSIONS

This paper proposed an additional switching element to an existing method at the expense of adding a valuable capability. The goal was to add smart grid functionalities to this novel application with the introduction of minimal switching elements that ultimately reduce power electronics costs of renewable energy systems. The proposed configuration introduced more interaction between the grid and the energy storage system and while maintaining low switching losses compared to conventional boost and bi-directional DC/DC converters. While it was only possible to charge the battery from the grid with this configuration, charging the battery from both the PV source and the grid simultaneously present several challenges.

It is of active interest to introduce the ability to charge the battery from both sources simultaneously to enhance the feasibility of this topology as an economical and complete smart grid system. Topologies such as those in [6], or time shared basis flyback converters present viable approaches to this task.

VIII. REFERENCES

- [1] M. Barnes, J. Kondoh, H. Asano, J. Oyarzabal, G. Ventakaramanan, R. Lasseter, N. Hatziaargyriou, and T. Green. “Real-world microgrids - an overview,” in IEEE International Conference on System of Systems Engineering (SoSE'07), Apr. 2007, pp. 1-8.
- [2] L. Zhang, T. Wu, Y. Xing, K. Sun, and J. M. Guerrero. “Power Control of DC Microgrid Using DC Bus Signaling,” *APEC'11*, 2011, pp. 1926-1932.
- [3] Available: www.smartgridresearch.org.
- [4] Nehrir, M.H.; Wang, C.; Strunz, K.; Aki, H.; Ramakumar, R.; Bing, J.; Miao, Z.; Salameh, Z.;, “A Review of Hybrid Renewable/Alternative Energy Systems for Electric Power Generation: Configurations, Control, and Applications,” *Sustainable Energy*, IEEE Transactions on , vol.2, no.4, pp.392-403, Oct. 2011.
- [5] Taesik Park; Taehyung Kim; , “Novel multi-mode single leg converter for renewable energy conversion systems,” *Industrial Technology (ICIT), 2011 IEEE International Conference on* , vol., no., pp.198-203,14-16 March 2011
- [6] Kwang-Hwa Liu, F.C. Lee, “Topological constraints on basic PWM converters”, *PESC 1988*, pp164-172
- [7] N. Mohan, “Designing Feedback Controllers in Switch Mode DC Power Supplies,” *First Course in Power Electronics*, 2009 ed. Minneapolis, MNPERE, 2009, ch. 4, pp. (4-1)-(4-6)
- [8] R. W. Erickson and D. Maksimovic, “Controller Design,” *Fundamentals of Power Electronics*, 2nd ed. Boulder, 2001, ch. 9, pp. 331-369

Photovoltaic Microinverter using Single-stage Isolated High-frequency link Series Resonant Topology

Hariharan Krishnaswami, *Member, IEEE*,
Department of Electrical and Computer Engineering
The University of Texas at San Antonio
San Antonio, Texas, USA
E-mail: Hariharan.Krishnaswami@utsa.edu

Abstract— In this paper, PhotoVoltaic (PV) microinverter using a single-stage high-frequency ac link series resonant topology is proposed. The inverter has two active bridges, one at the front-end of PV module and the other at the output or utility side. The active bridges are interfaced through a series resonant tank and a high frequency transformer. A novel phase-shift modulation technique to regulate the current into utility is proposed. Steady-state analysis using sinusoidal approximation is presented to determine the magnitude of output current into utility. Soft-switching operation is ensured in all switches in the converter due to resonant nature of the circuit. The inverter has advantages of minimal power conversion stages, high-switching frequency operation and low switching losses and hence ideally suited for low power module integrated applications.

I. INTRODUCTION

Microinverters, also known as AC modules or Module Integrated Converters (MIC), have been shown to have high energy yield in Photovoltaic (PV) generation system due to inverters for each individual PV module [1]. The plug and play feature of MIC is especially useful for low power residential applications. Several topologies of MIC have been proposed in literature [2], [3], [4], [5] which use high-frequency link based power conversion instead of traditional dc link based systems. In [2], a MIC is proposed which uses impedance-admittance conversion theory to supply current into the utility. In [3] a push-pull based dc-ac inverter with high frequency link is proposed. It has a matrix converter with four-quadrant switches at the secondary of the transformer. A flyback-based inverter is proposed in [4] with an unique power decoupling circuit at the output of the PV module. A full-bridge based high-frequency link inverter is proposed in [5] with lowered switching frequency of the matrix converter.

The principle of power conversion in most of these topologies is through an high frequency converter followed by a matrix converter. But leakage inductance of the transformer is a non-ideality and it creates high voltages across the output side converter switches, whenever current changes direction in one switching cycle. This causes severe voltage stress on the devices and reduces reliability. Having the inductance at

the high frequency link and creating a high frequency current source which will then be rectified and fed to the utility as in [2], [6] can reduce the voltage stresses and also contribute to increased efficiency of power conversion.

In this paper a series resonant tank circuit is used at the high frequency link. The proposed converter consists of two active bridges, a high frequency transformer and a series resonant tank as shown in Fig. 1. The active bridges switch at constant switching frequency above resonant frequency. Phase-shift modulation technique between active bridges is proposed to control the current being fed to the utility as opposed to variable frequency and cycloconverter operation in [6]. The proposed principle of power conversion is similar to the dc-dc dual active bridge high power converter [7]. This principle is extended to dc-ac conversion for microinverter application with inductance replaced by a series resonant tank circuit in this paper. Four-quadrant full-bridge converter is used as the output side converter. In summary, the advantages of the proposed converter are,

- Reduced component count due to single conversion stage
- Reduced switching losses due to soft-switching operation in all the semiconductor switches
- Reduced size due to high switching frequency capability of the resonant nature of the circuit
- No adverse effect of voltage stresses on devices due to leakage inductance since it forms part of resonant circuit.

II. PROPOSED PHASE-SHIFT MODULATION

The converter shown in Fig. 1 operates above resonant frequency f_r formed by the series resonant tank inductance L and capacitance C . The output of the solar module V_{in} is connected to the active bridge through a large capacitor which filters the current ripple at twice the line frequency. The active bridge at the output-side of the converter is connected to the load or the grid through a capacitive filter for filtering the switching frequency component of the output current. The input-side active bridge is modulated using the function $m_1(t)$ in (1) and the output side active bridge is modulated using $m_2(t)$ in (2). The function $sgn(\cdot)$ is the signum function which denotes the sign of the signal. In the equations, ϕ is

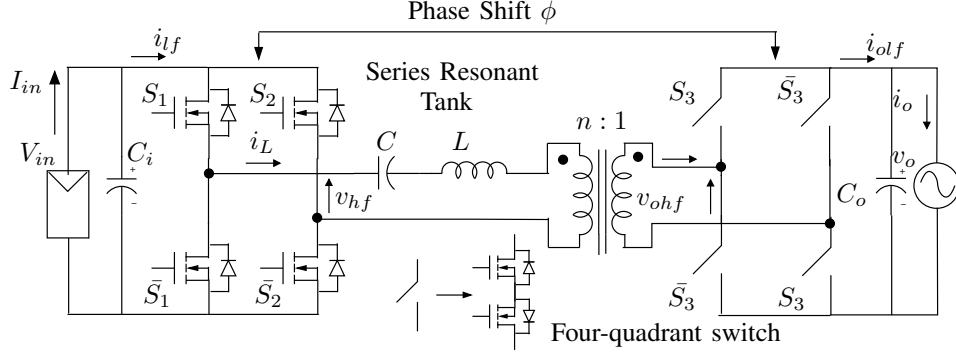


Fig. 1. Single-stage series-resonant microinverter

the phase-shift between the outputs of the active bridges v_{hf} and v_{ohf} , f_s is the switching frequency of the converter and f_o is the line frequency 60Hz . The grid voltage is defined as $v_o(t) = \hat{V}_o \sin(\omega_o t)$.

$$m_1(t) = \frac{1}{2} \left[\text{sgn}(\cos((\omega_s - \omega_o)t)) - \text{sgn}(\cos((\omega_s + \omega_o)t)) \right] \quad (1)$$

$$m_2(t) = \text{sgn}(\sin(\omega_s t - \phi)) \quad (2)$$

$$\text{where } \omega_s = 2\pi f_s; \omega_o = 2\pi f_o \quad (3)$$

The switching signals to the Mosfets in Fig. 1 can be synthesized from (1) and (2). These switching signals are shown in Fig. 2. The left and the right leg switches of the input side active bridges are phase-shifted from each other by equal angles from a fixed reference and this phase-shift angle α as shown in Fig. 2 varies linearly starting from 0 to maximum value $\frac{T_s}{2}$, then to minimum value $-\frac{T_s}{2}$ and back to zero, where $T_s = \frac{1}{f_s}$. This variation is at a low frequency equal to the line frequency f_o . In Fig. 2, this fixed reference is at $\frac{T_s}{4}$. It is known that when a low frequency voltage waveform is amplitude modulated with a high frequency square wave $m_2(t)$ as in an electronic transformer, [8], the resultant Fourier spectrum has two fundamental frequencies $f_s - f_o$ and $f_s + f_o$. Since this voltage appears across the secondary of the transformer, it is necessary to produce a voltage waveform v_{hf} across the input of the series resonant tank with two fundamental frequencies. For this reason, the modulation function $m_1(t)$ takes the form given in (1).

Due to the filtering action of the series resonant tank, it can be assumed that all higher order harmonics are negligible in magnitude. Hence, the tank current is sinusoidal with two frequencies $f_s - f_o$ and $f_s + f_o$. Control of power flow is by phase-shifting the output-side active bridge with respect to the input-side active bridge and hence termed as phase-shift modulation. The principal of power flow is similar to the power flow between two buses in power systems. This phase-shift angle ϕ is given in (2). The switching signals of the Mosfets S_1 , S_2 and S_3 are derived from the two modulation functions, as shown in Fig. 2. The switching signals can be generated

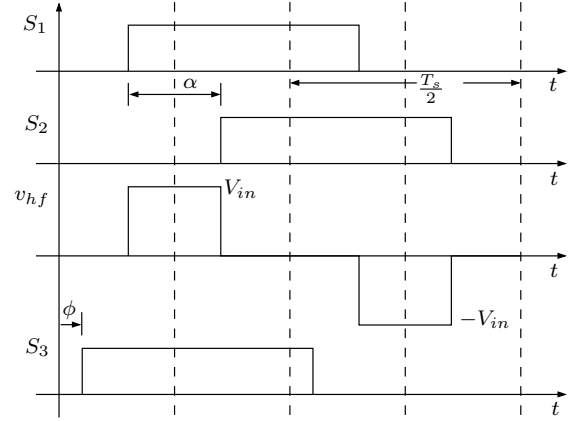


Fig. 2. Switching signals for the switches S_1 , S_2 and S_3 shown for one switching cycle

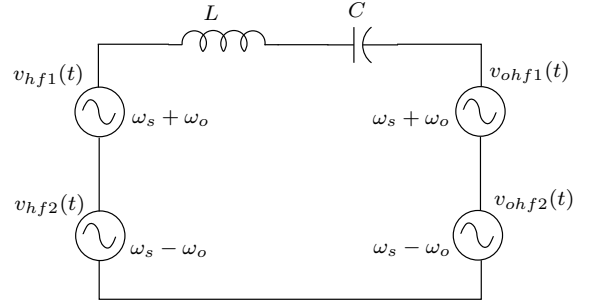


Fig. 3. Equivalent circuit for sinusoidal steady-state analysis

using a double ramp carrier wave as given in [9]. This carrier wave aids in generating positive and negative phase-shifts α .

III. STEADY-STATE ANALYSIS

Sinusoidal approximation is used in steady-state analysis since higher order harmonics are filtered by the resonant tank. Hence, only two frequencies are used in analysis, $f_s - f_o$ and $f_s + f_o$. The simplified equivalent circuit for analysis is shown in Fig. 3. The tank currents are calculated for each of the two frequencies using phasor analysis as given in (4) and (5).

TABLE I
SERIES RESONANT DC-AC CONVERTER PARAMETERS

Converter Parameter	Value
Resonant Inductor L	$10.68\mu H$
Resonant Capacitor C	$0.3\mu F$
Input voltage V_{in}	$29.1V$
Line voltage rms $V_{o(rms)}$	$120V$
Maximum power output P_{base}	$225W$
Turns ratio n	0.17
Quality factor Q	4.0

$$\hat{I}_{L1}\angle\theta_1 = \frac{\frac{2}{\pi}V_{in}\angle 0 - \frac{2}{\pi}\hat{V}_o\angle\phi}{j(\omega_s - \omega_o)L + \frac{1}{j(\omega_s - \omega_o)C}} \quad (4)$$

$$\hat{I}_{L2}\angle\theta_2 = \frac{\frac{2}{\pi}V_{in}\angle 0 - \frac{2}{\pi}\hat{V}_o\angle\phi}{j(\omega_s + \omega_o)L + \frac{1}{j(\omega_s + \omega_o)C}} \quad (5)$$

The fundamental of v_{ohf} calculated from Fourier series leads to the constants $\frac{2}{\pi}$ in the equations. The inductor current is converted to a low frequency f_o by the output side bridge through the modulation function $m_2(t)$. The average current in one switching cycle T_s can be calculated by integrating the current between the limits ϕ and $\pi + \phi$. The integration for the inductor current with frequency $\omega_s - \omega_o$ is shown in (6). Similar integration applies for the inductor current with frequency $\omega_s + \omega_o$.

$$\bar{I}_{L1} = \frac{1}{\pi} \int_{\phi}^{\pi+\phi} \hat{I}_{L1} \sin((\omega_s - \omega_o)t - \theta_1) d(\omega_s t) \quad (6)$$

The following two assumptions are used since $f_s \gg f_o$:

- The average value of the output current remains constant in one switching cycle and
- The impedance of the resonant tank remains same for variations in frequency from $f_s - f_o$ to $f_s + f_o$ and the impedance at switching frequency is used for analysis.

With the application of the above two assumptions and simplifying the equations, the resultant average output current $\bar{i}_o(t)$ is given in (7). The output current is sinusoidal with the direction of the current indicated in Fig. 1. The current is in phase with utility voltage and hence power is fed back to the utility at unity power factor. The transformer turns ratio n is included in the equation.

$$\bar{i}_o(t) = \frac{8}{\pi^2} \frac{nV_{in} \sin \phi}{Z(F - \frac{1}{F})} \sin(\omega_o t) \quad (7)$$

$$\text{where } Z = \sqrt{\frac{L}{C}}; F = \frac{\omega_s}{\omega_r}; \omega_r = 2\pi f_r = \frac{1}{\sqrt{LC}} \quad (8)$$

The analysis equations are converted to per unit representation by choosing the output power as P_{base} and the line voltage rms as V_{base} . This conversion helps in designing the system for varied power and input voltage levels. The variable d termed as voltage conversion ratio is defined in (9). Dividing (7) by the base current, the resultant normalized output current is given in (10). In Section IV, a design procedure is discussed.

$$d = \frac{V_{in}}{nV_{o(rms)}\sqrt{2}} \quad (9)$$

$$\bar{i}_{o,pu}(t) = \frac{d \sin \phi}{Q(F - \frac{1}{F})} \sin(\omega_o t) \quad (10)$$

$$\text{where } Q = \frac{Z}{\frac{8}{\pi^2} n^2 R_{base}}; R_{base} = \frac{V_{base}^2}{P_{base}} \quad (11)$$

IV. DESIGN

The design of the converter is based on the per unit equations in Section III. For the series resonant circuit, the quality factor is chosen as 4.0 or higher for validity of sinusoidal approximation. The ratio of switching frequency to resonant frequency is chosen as $F = 1.1$, to enable soft-switching operation. The voltage conversion ratio is chosen as $d = 1.0$ to enable wider range of soft-switching operation as in [7], [10]. With these chosen values, the value of phase-shift can be calculated from the required per unit current into the grid.

As an example, a 225W solar module from BP solar is chosen and the maximum power point (MPPT) mentioned in the datasheet $V_{max} = 29.1V$ and $I_{max} = 7.7A$ is used for simulation, although in real systems, MPPT can change based on sun's irradiance. MPPT can be implemented in this converter by appropriately varying the phase-shift angle ϕ . Since this converter is single-phase utility interactive, the grid voltage used in the simulation is 120V rms at a frequency of 60Hz. The switching frequency f_s is chosen as 100kHz. The converter parameters are calculated using (8) and (11). The values used in the converter simulation are summarized in Table I.

The converter can be represented using two state equations, with the inductor current and the capacitor voltage being the state variables. The input voltage V_{in} and the grid voltage $v_o(t)$ can be considered as ideal voltage sources. The state equations are given in (12-13).

$$\dot{i}_L = \frac{V_{in}}{L} m_1(t) - \frac{1}{L} v_C - \frac{n}{L} v_o(t) m_2(t) \quad (12)$$

$$\dot{v}_C = \frac{1}{C} i_L \quad (13)$$

These equations are simulated in Simulink and the ideal waveforms of the applied voltage across the tank v_{hf} , the transformer voltage v_{ohf} and the unfiltered output current i_{olf} are shown in Fig. 4 for one switching cycle T_s . In this figure, two instants are shown, which are the positive and negative peak of the grid voltage. The values used in this simulation is given in Table I.

V. SOFT-SWITCHING OPERATION

One of the advantages of operating the series resonant converter above resonant frequency is soft-switching. The

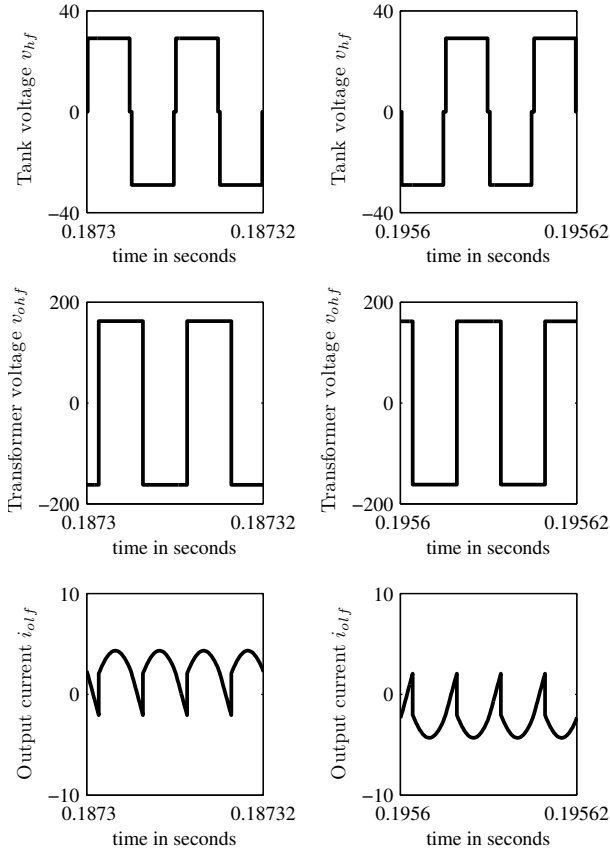


Fig. 4. Ideal waveforms of applied tank voltage v_{hf} , transformer voltage v_{ohf} and unfiltered output current i_{olf} for two switching cycles at two instants, positive and negative peak in line voltage

tank current always lags the applied tank voltage and hence Zero Voltage Switching (ZVS) in all switches in input-side converter. But, the tank voltage is not a square-wave as it has zero voltage states, as shown in Fig. 2. Hence, for low values of α , one of the legs loses ZVS operation.

Based on the current direction shown in Fig. 1, the condition for soft-switching operation in the output-side active bridge is the transformer secondary current leading the voltage across the transformer. As long as the voltage conversion ratio is unity, soft-switching operation is possible in the output-side converter also. The active bridge at the output-side uses four-quadrant switches. In order to achieve soft-switching, one of the two Mosfets in a four-quadrant switch is always kept ON based on the polarity of the line voltage. This ensures that the other switch performs ZVS, based on the condition that the transformer secondary current leads v_{ohf} . Simulation results are given in the following section to prove soft-switching operation.

VI. SIMULATION RESULTS

In this section, the simulation results from Saber[©] are presented using the converter values summarized in Table I. Simulation results of the tank current in one switching cycle along with the applied tank voltage is shown in Fig. 5 for a

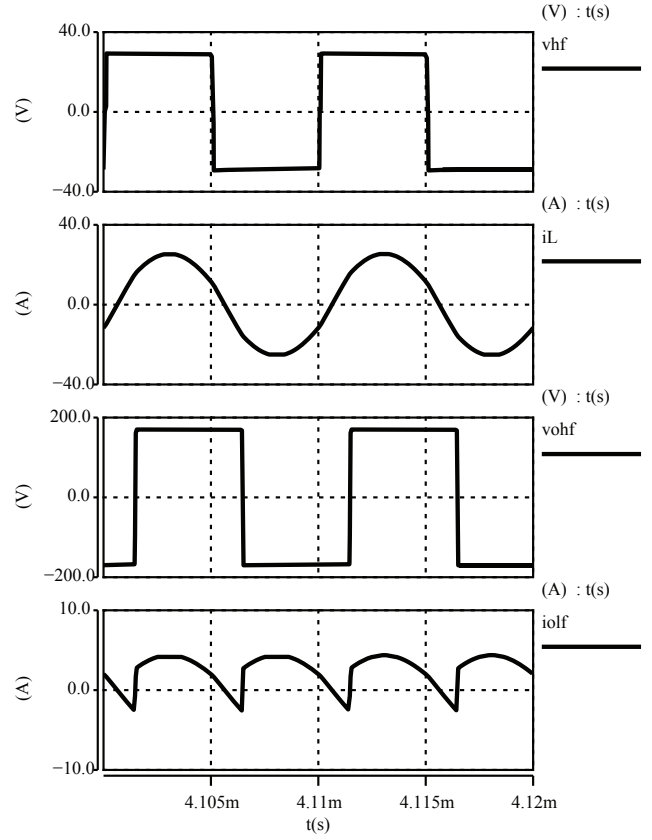


Fig. 5. Simulation results of tank current $i_L(t)$, applied tank voltage $v_{hf}(t)$, transformer voltage $v_{ohf}(t)$ and unfiltered output current $i_{olf}(t)$ shown for two switching cycles around the positive maximum of line voltage $v_o(t)$

phase-shift angle of $\alpha = 50^\circ$. The time instant during which the line voltage $v_o(t)$ is at its positive maximum is chosen for this plot. Due to the lagging nature of the current as observed from Fig. 5, soft-switching operation in the input-side bridge is ensured. The tank current leads the voltage across the transformer which ensures ZVS in output-side bridge. This is made possible by switching only one of the Mosfets in the four-quadrant switch shown in Fig. 1 according to polarity of line voltage and the other switch is ON continuously. The waveforms are repeated in Fig. 6 for the time instant at which the line voltage is at its minimum. It can be observed that soft-switching operation is ensured in this case also.

The filtered output current along with the line voltage is shown in Fig. 7. It is observed that line voltage and line current in the direction indicated in Fig. 1 are in phase and hence power is being fed to the utility. The analysis results match with the simulation results with an error of $< 5\%$ due to the sinusoidal approximation. The input current has a second harmonic component of the line frequency. The capacitor C_i at the input can be designed to filter this harmonic component. The tank current and its Fourier spectrum are shown in Fig. 8 which confirms the analysis assumption.

The converter efficiency is improved due to reduction in switching losses achieved by ZVS. Due to the use of two

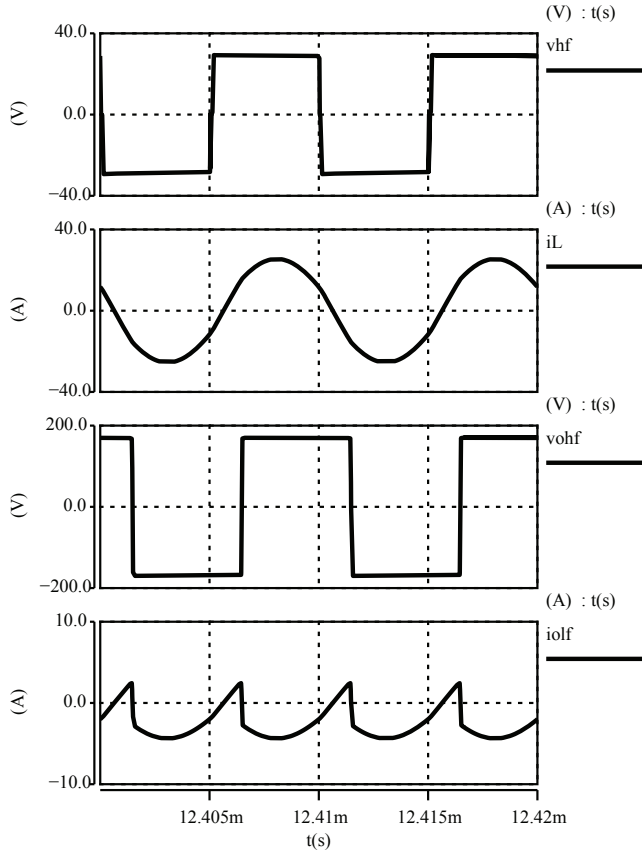


Fig. 6. Simulation results of tank current $i_L(t)$, applied tank voltage $v_{hf}(t)$, transformer voltage $v_{ohf}(t)$ and unfiltered output current $i_{olf}(t)$ shown for two switching cycles around the negative maximum of line voltage $v_o(t)$

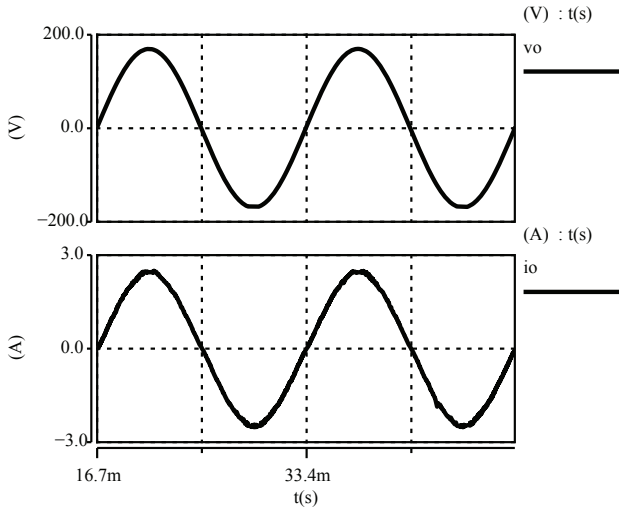


Fig. 7. Line voltage $v_o(t)$ and current $i_o(t)$ for two 60Hz cycles

semiconductor switches to realize a four-quadrant switch in the output-side converter, one of which is continuously ON based on grid voltage, the conduction losses can increase two-fold. But, since the switches are at the high voltage

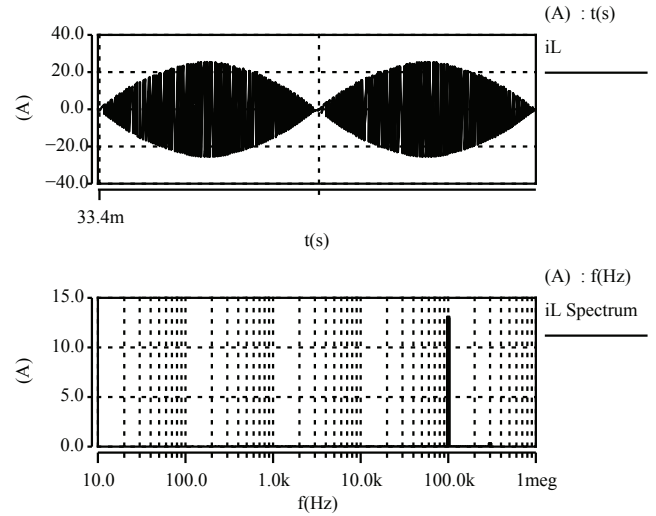


Fig. 8. Tank current $i_L(t)$ and its Fourier spectrum

side $< 200V$ and the currents are lower, it is possible to design the converter such that the effect of conduction losses on efficiency is minimal. The effect of increased cost of the converter due to addition of four-quadrant semiconductor switches in the output side converter is minimized by reduction in overall component count due to the use of single-stage power conversion as compared to the conventional two-stage dc-dc and dc-ac conversion.

VII. CONCLUSION

In this paper, a single-stage series resonant based photovoltaic microinverter is proposed. A novel phase-shift modulation technique to control the current into the grid is proposed along with steady-state analysis using sinusoidal approximation. Soft-switching operation is achieved in all the semiconductor switches. Simulation results are presented to verify the analysis. Experimental results under closed loop operation is part of further research in this project.

REFERENCES

- [1] Q. Li and P. Wolfs, "A review of the single phase photovoltaic module integrated converter topologies with three different dc link configurations," *Power Electronics, IEEE Transactions on*, vol. 23, no. 3, pp. 1320–1333, May 2008.
- [2] S. Yatsuki, K. Wada, T. Shimizu, H. Takagi, and M. Ito, "A novel ac photovoltaic module system based on the impedance-admittance conversion theory," in *Power Electronics Specialists Conference, 2001. PESC. 2001 IEEE 32nd Annual*, vol. 4, 2001, pp. 2191–2196 vol. 4.
- [3] K. de Souza, M. de Castro, and F. Antunes, "A dc/ac converter for single-phase grid-connected photovoltaic systems," in *IECON 02 [Industrial Electronics Society, IEEE 2002 28th Annual Conference of the]*, vol. 4, Nov. 2002, pp. 3268–3273 vol.4.
- [4] T. Shimizu, K. Wada, and N. Nakamura, "Flyback-type single-phase utility interactive inverter with power pulsation decoupling on the dc input for an ac photovoltaic module system," *Power Electronics, IEEE Transactions on*, vol. 21, no. 5, pp. 1264–1272, Sept. 2006.
- [5] S. Deng, H. Mao, J. Mazumdar, I. Batarseh, and K. Islam, "A new control scheme for high-frequency link inverter design," in *Applied Power Electronics Conference and Exposition, 2003. APEC '03. Eighteenth Annual IEEE*, vol. 1, Feb. 2003, pp. 512–517 vol.1.

- [6] A. Trubitsyn, B. Pierquet, A. Hayman, G. Gamache, C. Sullivan, and D. Perreault, "High-efficiency inverter for photovoltaic applications," in *Energy Conversion Congress and Exposition (ECCE), 2010 IEEE*, 2010, pp. 2803–2810.
- [7] M. H. Kheraluwala, R. W. Gascoigne, D. M. Divan, and E. D. Baumann, "Performance characterization of a high-power dual active bridge dc-to-dc converter," *IEEE Trans. Ind. Appl.*, vol. 28, no. 6, pp. 1294–1300, Nov. 1992.
- [8] M. Kang, P. Enjeti, and I. Pitel, "Analysis and design of electronic transformers for electric power distribution system," *Power Electronics, IEEE Transactions on*, vol. 14, no. 6, pp. 1133–1141, Nov 1999.
- [9] H. Krishnaswami and V. Ramanarayanan, "Control of high-frequency ac link electronic transformer," *Electric Power Applications, IEE Proceedings -*, vol. 152, no. 3, pp. 509–516, May 2005.
- [10] H. Krishnaswami and N. Mohan, "Three-port series-resonant dc-dc converter to interface renewable energy sources with bidirectional load and energy storage ports," *Power Electronics, IEEE Transactions on*, vol. 24, no. 10, pp. 2289–2297, Oct. 2009.

**VOLTAGE REGULATION AND REACTIVE POWER SUPPORT VIA
PHOTOVOLTAIC INVERTERS AS A SMART GRID
APPLICATION**

by

EMILIANO MORALES, B.A.

THESIS

Presented to the Graduate Faculty of
The University of Texas at San Antonio
In Partial Fulfillment
Of the Requirements
For the Degree of

MASTER OF SCIENCE IN ELECTRICAL ENGINEERING

THE UNIVERSITY OF TEXAS AT SAN ANTONIO
College of Engineering
Department of Electrical and Computer Engineering
December 2011

UMI Number: 1503380

All rights reserved

INFORMATION TO ALL USERS

The quality of this reproduction is dependent on the quality of the copy submitted.

In the unlikely event that the author did not send a complete manuscript and there are missing pages, these will be noted. Also, if material had to be removed, a note will indicate the deletion.



UMI 1503380

Copyright 2011 by ProQuest LLC.

All rights reserved. This edition of the work is protected against unauthorized copying under Title 17, United States Code.



ProQuest LLC.
789 East Eisenhower Parkway
P.O. Box 1346
Ann Arbor, MI 48106 - 1346

ACKNOWLEDGEMENTS

Thanks go to Dr. Hariharan Krishnaswami, and all past UTSA professors for their support and instruction. Gratitude is also extended to Mr. Richard Fryer, for shifting my research focus to the renewable energy field and placing my education first. And most importantly, thanks to all family and friends in support of my education.

Finally, a special thanks to Elmira, for her support in the multi-mode converter and for inspiring me to complete this Thesis.

December 2011

VOLTAGE REGULATION AND REACTIVE POWER SUPPORT VIA PHOTOVOLTAIC INVERTERS AS A SMART GRID APPLICATION

Emiliano Morales, M.S.
The University of Texas at San Antonio, 2011

Supervising Professor: Hariharan Krishnaswami, Ph.D.

According to the U.S. Department of Energy, there has been a rise in reactive loads in the last 20 years; reactive loads from electronic devices have risen by 40% since 1980, and are anticipated to increase by 60% by 2015. To alleviate some of the burden, the continual increase of interconnected photovoltaic (PV) inverters to grids can beneficially be employed to provide reactive power (VAR) support. Current IEEE standards preclude the active regulation of voltage by PV inverters, eliminating the possibility of providing VAR support. As these standards are anticipated to be amended, the study of VAR support by PV inverters and other renewable resources has become an active area of research.

This Thesis is supported by two years of academic and one year of graduate research. Throughout the research, it was found that a PV inveter can be broken down into two main sections, the DC side (input control) and the AC side (output control). For the output side of the inverter, reactive power control by the use of the Synchronous Reference Frame Control method will be demonstrated, a method introduced first in [18] and employed in multiple papers. This Thesis demonstrates that the control of reactive power can be achieved by this method using the Specification of Smart Inverter Interactions with Electric Grids using International Electrotechnic Commission 61850 report [19]. It was also found that this was possible under response times a little over a 60 Hz cycle.

The second part of this Thesis showcases a demonstration of a converter capable of providing multiple operation modes to the input side control of an inverter, thus eliminating the need of multiple DC-DC converters. It is demonstrated that the proposed converter configuration can provide DC boosting actions, discharging, and charging to integrated battery storage systems. The energy storage system proves to be an essential medium to absorb and inject reactive power actively. Simulation models for both aspects of PV inverters as VAR supporters were conducted using MATLAB's Simulink. Plots that demonstrate the feasibility of this approach were also provided using MATLAB.

TABLE OF CONTENTS

Acknowledgements	iv
Abstract	v
List of Tables	vii
List of Figures	viii
Chapter One: Introduction	1
1.1 PV Systems	1
1.2 PV Inverter Standards	3
1.3 Smart Grid	4
1.4 Smart Grid Functionalities	5
1.5 Literature Survey of VAR Support on Smart Grids	6
1.5.1 Integral Method	8
1.5.2 LinDistFlow Analysis	9
1.5.3 PV Inverter as UPS	10
1.5.4 Bus Linked Micro-Grid	11
1.5.5 Other Literature	11
1.6 Contributions of this Thesis	12
1.7 Organization of this Thesis	13
1.8 Conclusion	14
Chapter Two: Demonstration of Q Control	15
2.1 Modulation Techniques	16
2.1.1 Space Vector Modulation	16
2.2 Stationary Reference Frame Control	18

2.2.1 The $\alpha\beta$ Transform.....	18
2.2.2 Control of Power Flow under Stationary Reference Frame Control	19
2.3 Synchronous Reference Frame Control	20
2.3.1 The dq Transform.....	20
2.3.2 Control of Power Flow under Synchronous Reference Frame Control	21
2.4 Transfer Functions	22
Chapter Three: Simulation Results and Findings of the Q Control Model.....	23
3.1 Space Vector Modulation Setup	23
3.1 Space Vector Modulation Simulation Results	25
3.3 Synchronous Reference Frame Controller Setup.....	26
3.3.1 Controller Designs.....	26
3.3.2 Block Models.....	27
3.3.3 R-L Line Impedance Model.....	28
3.4 Synchronous Reference Frame Controller Simulation Results	29
3.4.1 Normal Energy Conservation Mode	30
3.4.2 Maximum VAR Support Mode	33
3.4.3 Fixed VAR Mode	33
3.4.4 Passive Mode	33
3.5 Other Findings	34
Chapter Four: Multi-Mode Converter for Input Side Inverter.....	37
4.1 Conventional Battery Storage Methods	37
Chapter Five: Simulation Results and Findings of the Multi-Mode Converter.....	39
5.1 Multi Mode Converter Setup	39

5.2 Multi Mode Converter Results.....	40
5.2.1 Main Boost Mode Results	41
5.2.2 Boost Buck Mode Results.....	41
5.2.3 Boost Boost Mode Results.....	43
5.2.4 Battery Boost Mode Results	45
5.2.5 Reverse Buck Mode Results	46
5.3 Other Findings	47
Conclusion	50
Bibliography	51
Vita	

LIST OF TABLES

Table 1	Major PV System Components.....	2
Table 2	Space Vector Modulation Parameters.....	24
Table 3	Synchronous Reference Frame Control Parameters	26
Table 4	Reactive Power Measurement Results.....	35
Table 5	Multi-Mode Converter Parameters	40

LIST OF FIGURES

Fig. 1	Projections for Renewables.....	1
Fig. 2	Basic Setup of a PV System.....	2
Fig. 3	Four Quadrants of Operation	6
Fig. 4	Phasor Diagrams	7
Fig. 5	Control Structure for Integral Method	8
Fig. 6	Power Regulator for Integral Method	9
Fig. 7	Diagram of Sample Radial Network.....	9
Fig. 8	Hybrid DC Micro-grid	11
Fig. 9	Breakdown of PV Inverter	12
Fig. 10	Typical Setup of a 3-Phase Inverter Without Energy Storage.....	15
Fig. 11	Space Vector Modulation	17
Fig. 12	Representation of a 3-Phase System as a Rotating Vector	18
Fig. 13	The α and β Components of Voltage and Current Vectors.....	19
Fig. 14	Stationary Reference Frame Control Structure.....	20
Fig. 15	The d and q axes in the $\alpha\beta$ Plane.....	21
Fig. 16	Synchronous Reference Frame Control Structure	22
Fig. 17	Space Vector Modulation Simulink Model Setup	24
Fig. 18	Space Vector Modulation Simulink Model	25
Fig. 19	SVM Simulink Model Results.....	26
Fig. 20	PI Controller Response Times	27
Fig. 21	Line Impedance Model	28
Fig. 22	Synchronous Rotating Reference Frame Control Simulink Model	29
Fig. 23	PV1: Normal Energy Conservation Mode Array Sample.....	30

Fig. 24	Normal Energy Conservation Mode Simulation Results.....	31
Fig. 25	PV2: Maximum VAR Support Mode Array Sample.....	32
Fig. 26	Maximum VAR Support Mode Simulation Results.....	32
Fig. 27	PV3: Fixed VAR Mode Array Sample	32
Fig. 28	Fixed VAR Mode Simulation Results	33
Fig. 29	Passive Mode Simulation Results.....	34
Fig. 30	Phase Shift Simulation Results	36
Fig. 31	Conventional Methods to Implement Energy Storage Systems	37
Fig. 32	Novel Method to Implement Energy Storage Systems.....	38
Fig. 33	Multi-Mode Converter	38
Fig. 34	Simulink Model of Multi-Mode Converter.....	39
Fig. 35	Main Boost Mode Power Flow	41
Fig. 36	Main Boost Mode Results.....	42
Fig. 37	Boost Buck Mode Power Flow	42
Fig. 38	Boost Buck Mode Results.....	43
Fig. 39	Boost Boost Mode Power Flow	43
Fig. 40	Boost Boost Mode Results.....	44
Fig. 41	Battery Boost Mode Power Flow.....	45
Fig. 42	Battery Boost Mode Results	45
Fig. 43	Reverse Buck Mode Power Flow	46
Fig. 44	Reverse Buck Mode Results	47
Fig. 45	Four Quadrant Bi-Directional Switch.....	48

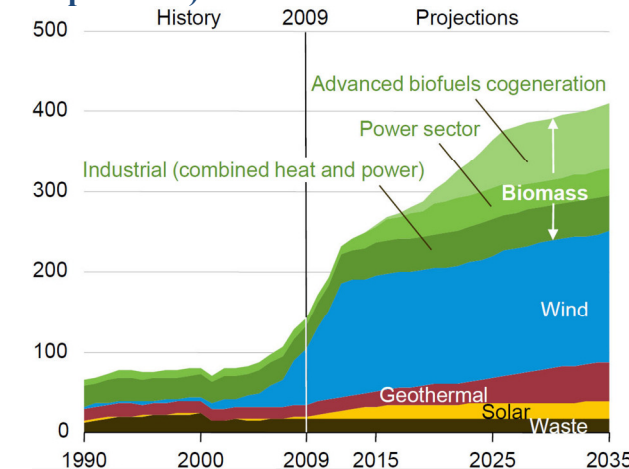
CHAPTER ONE: INTRODUCTION

This chapter provides the underlying framework and basis for this Thesis. It sets the tone by briefly introducing solar power projections, their basic setup, and the role of the inverter under current codes and standards. This chapter also contains a broad definition of smart grids, the functionalities possible under photovoltaic (PV) inverters, and followed by a summary on current literature. Finally, this chapter provides a summary on the contributions of this Thesis, followed by an outline of the organization of this document and a conclusion.

1.1 PV Systems

There are many factors to consider that are causing the ongoing increase in renewable energy penetration, such as solar, to electric grids. Major factors include rising oil and electricity costs, oil independence, and financial factors such as Federal and State incentives, utility rebates, renewable energy credits (RECs), and the continual drop in panel and system costs. As the overall consumption of energy continues to increase, coal plants continue to be the largest source of energy generation. Coal plant's total contribution is projected to fall from 45% to 43% in 2035 due to the increase in renewable energy contributions, according to projections statistics

Renewable Electricity Generation (Billion kW per Year)



Primary Energy Use (Quadrillion Btu)

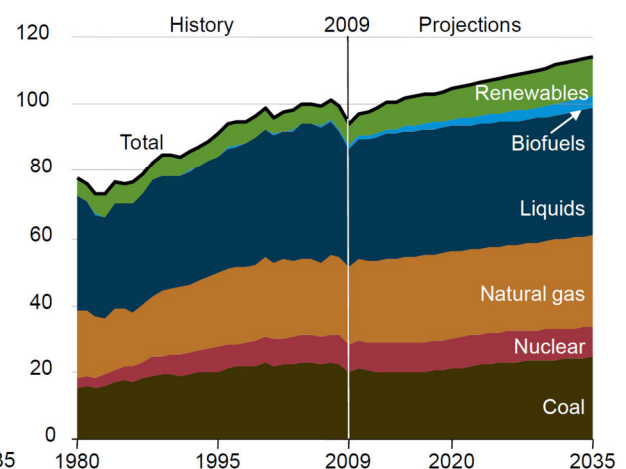


Fig. 1 Projections for renewables. Source.

*Courtesy: [1]

presented by the 2011 energy outlook report by U.S. Energy Information Administration [1]. Therefore, addressing integration issues that may arise as the penetration of Photovoltaic (PV) systems gradually increase are of paramount importance.

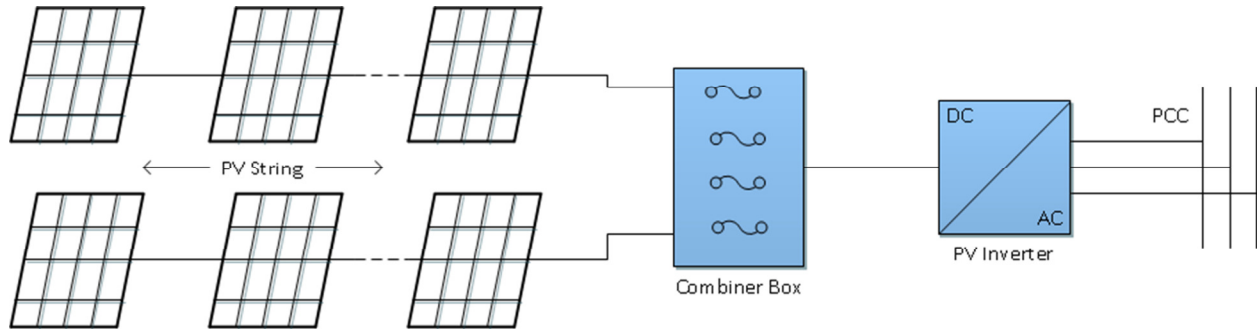


Fig. 2 Basic setup of a PV system consists of panel strings, balance of systems (BOS), and DC to AC inverters.

The basic setup of a PV system begins with PV panels, which use light from the sun to produce energy, a process known as the photoelectric effect. Panels are connected in series (strings) and parallel to form arrays that can generate DC power from a few kilo-Watts to Mega-Watt scale farms. Arrays are, in turn, connected to a DC/AC converter, most commonly referred to as an inverter. The job of the inverter goes beyond converting direct current to alternating current, but is also responsible for operating the panels at the max power point and providing voltage and frequency ride-through for abnormal transients. The inverter is then connected to the point of common coupling (PCC) via a transformer, etc. Table 1 summarizes the major components and the common types of solar panels, racking methods, BOS, and interconnection methods.

Table 1 Major PV System Components.

Major PV System Components			
Solar Panels	Racking	Balance of Systems (BOS)	Point of Common Coupling (PCC)
Polycrystalline	Roof Mounted	Disconnect Switches	Grid tied
Monocrystalline	Ground Mounted	Wires	Behind or in Front of Meter
Thin film	1 or 2 Axis Sun Tracking	Combiner Box	Islanded
Concentrated PV (CPV)		Racking	

1.2 PV Inverter Standards

The role of the inverter, and emphasis of this Thesis, is delineated by codes and standards which are constantly being amended, namely:

- UL 1741: Inverters, Converters, Controllers, and Interconnection System Equipment for Use With Distributed Energy Resources
- IEEE 519: Recommended Practices and Requirements for Harmonic Control in Electrical Power Systems
- IEEE 929: Recommended Practice for Utility Interface of Photovoltaic Systems
- IEEE 1262: Recommended Practice for Qualification of Photovoltaic Modules
- IEEE 1374: Guide for Terrestrial Photovoltaic Power System Safety
- IEEE 1547: Standard for Interconnecting Distributed Resources with Electric Power Systems

These standards also provide definitions and testing procedures that ensure PV systems are interconnected in accordance with specifications. Stipulations relevant to the operation of PV inverters covered in these standards include the response times for abnormal voltage transients that range 50-137% of the voltage at the PCC, response times for abnormal frequencies outside the ranges of 59.3-60.5 Hertz, and the total harmonic current distortion less than 5.0% requirement. Stipulations pertaining to this document include the requirement for a power factor (PF) less than 0.85 (leading or lagging) at 10% rated capacity; otherwise, the inverter should operate close to a unity PF. It is also explicitly stated in standard IEEE 1547 that the inverter cannot actively regulate voltage, a requirement anticipated to be amended to allow the future role of inverters as integral components of the smart grid.

1.3 Smart Grid

To ensure the stability and reliability of the current and aging, electric transmission and distribution (T&D) grids, a paradigm shift to a “smart grid” is in need. While most are considering this a challenging shift, a smart grid is essential to answer the reliability concerns of rising intermittent renewable penetration to grids and the increase of plug-in hybrid electric vehicles (PHEVs) on residences. As it stands, power grids today provide protection and central control through Supervisory Control and Data Acquisition (SCADA) systems, which may be too slow and limited to deal with the eminent increases.

The challenges that arise due to the growing high penetration of solar PV systems are many. Typically, sites suitable for 100+ MW solar farms are far from transmission lines and electrical stations, which call for the need of standard communication protocols between subsystems to provide automation, reduce human intervention, and troubleshoot/diagnose/heal. Another challenge of current interest is the lack of research in the new power flow patterns introduced by solar systems. Collaborative research, such as the CPSEnergy, South west Research Institute (SWRI), and the University of Texas at San Antonio (UTSA) Blue Wing Research are being initiated to study these new patterns produced by high penetration of solar farms and their impact to existing grids. The fast ramping caused by the inherent intermittent nature of solar systems is also a challenge of high interest. Current challenges that address these issues are continually being proposed, including power electronic topologies and algorithms for storage systems.

In broad terms, a smart grid is the upgrade of current grids to be able to respond to these challenges intelligently, through the use of networks and automation.

1.4 Smart Grid Functionalities

There are many different kinds of functionalities and services that can be automated for smart grids. The list of services can be as extensive as to include forty services, however six main functionalities for smart grids have been identified by the Oak Ridge National Laboratory [5], including loss compensation, scheduling & dispatch, load following, operating reserves, energy imbalance, and voltage control. Those that can be addressed by PV inverters will be discussed below.

Scheduling and dispatch have been bundled in the same category since they can be coordinated by the individual independent system operators (ISOs). Scheduling is the planning for anticipated energy load demands. Schedules can be done in terms of days/hours/minutes, and can be performed by programming PV inverters to respond to anticipated loads by making the necessary accommodations by charging and discharging storage systems at the appropriate times. In turn, dispatch is the real time control of energy resources to meet load demands. Again, to the limitation of the energy storage system's response times, the PV inverter can provide or curtail power in real time when in need.

Load following is also a service that can be provided by PV inverters. Inverters have the power electronic capability of regulating frequency and curtailing power during rapid load drops by storing excess power into its storage device. This differs from scheduling and dispatch by not being coordinated by the ISO. This function can mitigate the effect of fast power ramping caused by intermittent distributed resources such as other wind or solar systems.

Operating reserves is the supply-side of load following; in other words, they go hand-in-hand. PV systems can be made to interface with the different types of storage systems available, such as electrochemical batteries (lithium ion, sodium sulfur (NaS), lead acid, fuel cells, nickel

cadmium, etc.), flow batteries, flywheels, compressed air systems, hydro, thermal storage etc. Each storage systems have different characteristics, and the biggest challenge continues to be their cost.

Energy imbalance is introduced to correct the unavoidable imbalance between actual and scheduled flows. The Federal Energy Regulatory Commission recommends a dead-band of $\pm 1.5\%$, which again, can be accomplished by a PV inverter interfaced with a battery storage system.

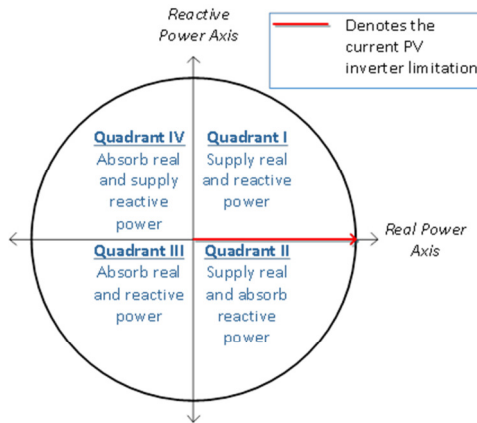


Fig. 3 Four possible quadrants of operation of PV inverters.

In basic theory, reactive power control can be achieved by regulating voltage. Dynamic control of real and reactive power, as a smart-grid functionality, is the emphasis of this Thesis. Current codes and standards prohibit the active regulation of voltage. However, a PV inverter in conjunction with a storage system can supply and absorb both real and reactive power, as depicted on

Figure 3. Reactive power control by PV inverters is an

active area of research and many methods are continually being proposed as of today. Many of the methods introduced vary in complexity, capability, and cost. One of the main contributions by this Thesis will be to model the feasibility of having PV inverters provide reactive power support.

1.5 Literature Survey of VAR Support on Smart Grids

There are many papers that present different ideas and methods to control voltage so that inverters can provide volt-ampere reactive (VAR) support. The basic principle to inject and/or

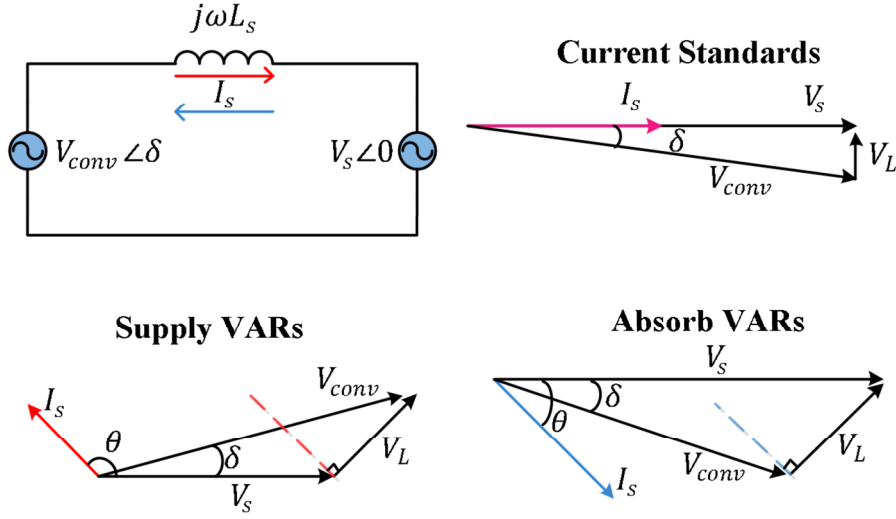


Fig. 4 Phasor diagrams of the operation modes of current inverters, inverters supplying VARs and inverters absorbing VARs.

absorb VARs by regulating voltage is by manipulating the magnitude and phase of the interconnected inverter's voltage. Explained thoroughly in [6]-[8], a common application in which an inverter is connected to the grid is presented in Figure 4. The top-right phasor diagram illustrates the operation of an inverter under unity power factor, where the converter's current is in phase with the grid voltage; when the converter voltage matches the grid voltage, the voltage across the inductor becomes zero.

As seen on the figure, in order for the inverter to supply or absorb reactive power, V_{conv} must be able to change its phase δ and magnitude. Thereby, equations for P and Q can be derived from the conventional equations in terms of V_{conv} and phase δ .

$$P = \frac{V_s^2 V_{conv}}{\omega L_s} \sin \delta \quad (1.1)$$

$$Q = \frac{V_s V_{conv} \cos \delta - V_s^2}{\omega L_s} \quad (1.2)$$

$$Q = \frac{V_s^2 - V_s V_{conv} \cos \delta}{\omega L_s} \quad (1.3)$$

Where (1.2) corresponds to the reactive power Q injected to the grid and (3) represents the reactive power absorbed. It must be noted that direct calculation of P and Q via (1.1) through (1.3) is impractical, due primarily to the fact that both equations are nonlinear and difficult to solve in real time. Therefore, methods that manipulate phase and voltage magnitudes have been explored and will be briefly described next.

1.5.1 Integral Method

This conventional method is presented in [9] and is a feedback loop based method that solves for the desired P_{ref} and Q_{ref} as illustrated in Figure 5.

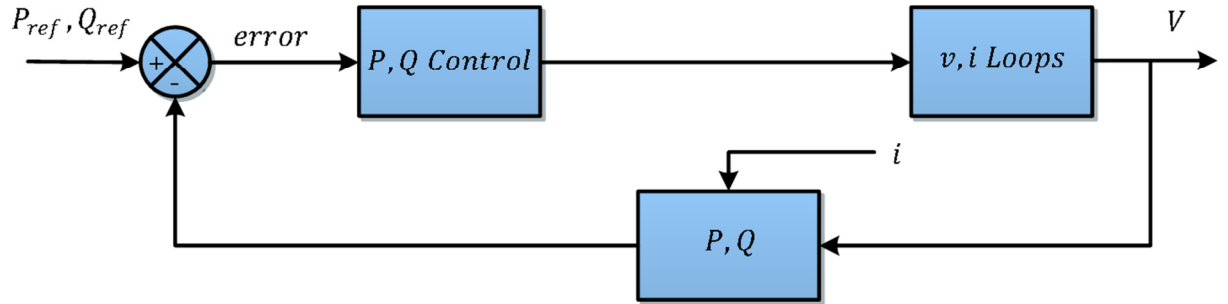


Fig. 5 Control structure for integral method.

Based on the analysis performed in [9], partial derivatives of power equations (1.1)-(1.3) show that P is sensitive to the phase δ and Q is sensitive to changes in the output converter voltage V_{conv} . This fact makes it possible to control P and Q independently. If the grid's voltage is kept as the reference for the converter phase angle, then the desired phase and voltage magnitudes can be solved by:

$$\delta_{ref} = \int [K_p(P_{ref} - P) + \omega_n] dt + \delta_0 \quad (1.4)$$

$$V_{ref} = \int K_q(Q_{ref} - Q) dt + V_0 \quad (1.5)$$

Which may be graphically represented as shown in Figure 6.

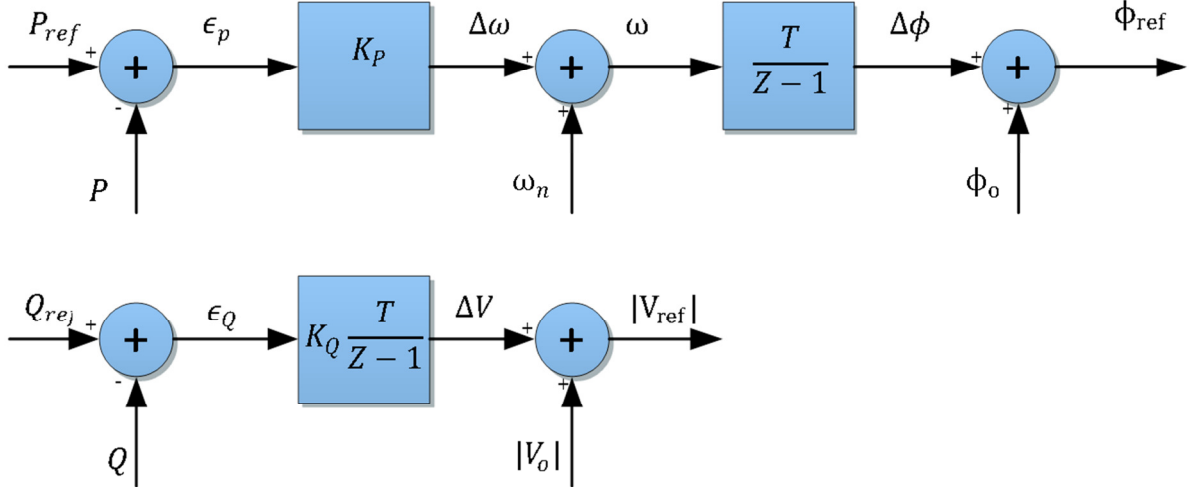


Fig. 6 Power regulator for integral method.

1.5.2 LinDistFlow Analysis

Paper [10] performs a large scale analysis of PV inverters as reactive power compensators in smart grids. To compute voltages and power flow, the authors introduce a set of equations called the LinDistFlow equations, namely:

$$P_{j+1} = P_j - p_{j+1}^{(c)} + p_{j+1}^{(g)} \quad (1.6)$$

$$Q_{j+1} = Q_j - q_{j+1}^{(c)} + q_{j+1}^{(g)} \quad (1.7)$$

Where j is the j^{th} inverter at node j , the (c) superscript denotes the power consumed, and the (g) superscript denotes the power generated at that node.

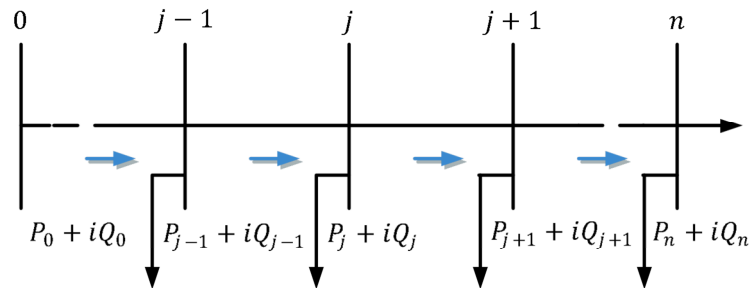


Fig. 7 Diagram of a sample radial network.

Equations (1.6)-(1.7) represent the power calculations at node $j + 1$ seen on Figure 7, where

$$P_j + iQ_j = p_j + iq_j = (p_j^{(c)} - p_j^{(g)}) + (q_j^{(c)} - q_j^{(g)}) \quad (1.8)$$

In (1.8), $q_j^{(g)}$ is the reactive power generated by the individual inverter at that node. In this analysis, reactive power was only achievable for nodes where PV inverters operated. The allowable reactive power generation on this paper was limited by:

$$|q^{(g)}| \leq \sqrt{S^2 - p^{(g)2}} \quad (1.9)$$

Equation (1.9) can be graphically represented by phasors inscribed in a circle with radius S , similar to Figure 3. The analysis was modeled with parameters typical in distribution systems where $V_0 = 7.2kV$, 250 nodes with 50% of them with PV inverters at a capacity of $2.2kVA$.

1.5.3 PV Inverters as UPS

In [11], titled “A Control Algorithm of Power Converters in Smart-Grids for Providing Uninterruptible Ancillary Services”, the authors present a method that device a control strategy to regulate both real and reactive power, providing reactive power compensation even when solar output is negligible. The PV source modeled in their simulation was mathematically represented according to the following relationship:

$$v_{pv} = V_T \log \left(\frac{I_{ph} - i_{pv} + I_0}{I_0} - r_{pv} i_{pv} \right) \quad (1.10)$$

This enabled the simulation to mimic i-v curves comparable to monocrystalline PV panels. Their control scheme included strategies that modeled MPPT, phase lock loop (PLL) functions to lock into the interconnected phase, and power flow control via the synchronous rotating frame. The synchronous rotating frame was employed in a manner such that the required current and outputs were derived from the desire P_{ref} and Q_{ref} .

1.5.4 Bus Linked Micro-Grid

One of the benefits of smart grids is its ability to improve reliability by providing power to critical loads (such as hospitals or military bases) through the innovation of micro-grids. Micro-grids can be comprised of distributed energy resources (DER) such as wind and solar. In [12], the authors propose a strategy that includes a wind turbine, a solar array, and a battery storage system in parallel to a super-capacitor in a single DC bus, and utilizes a synchronous rotating frame to regulate voltage during island modes. See Figure 8.

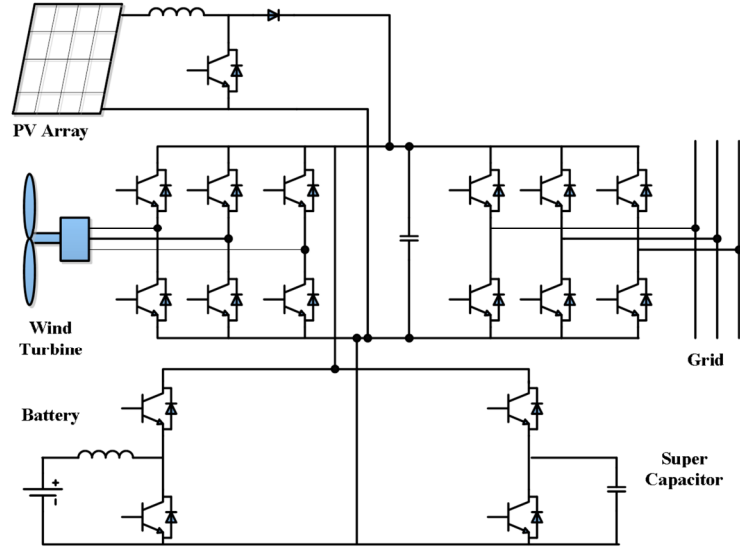


Fig. 8 Hybrid DC Micro-grid.

1.5.5 Other Literature

Methods such as [13] and [14] make use of look-up tables and direct power control (DPC) methods to actively regulate voltage. Method [14] is an enhanced modification of its predecessor, in which it proposes the use of sliding mode control schemes to generate a converter output voltage reference as an input to a space vector modulation (SVM) module. This directly addresses the issues with its former method.

Other methods, such as [15], estimate the required reactive current by making current measurements based on the inherent orthogonality of the trigonometric system.

1.6 Contributions of this Thesis

Current standards preclude the active regulation of voltage by PV inverters, compelling inverters to supply active, more commonly referred to as real, power only. As more real power is integrated to grids, a larger amount of reactive power has to be injected/absorbed by utility substations. Substations have to be able to meet the demand that is offset by the real power injected by PV systems. Measures to inject and/or absorb reactive power today include synchronous generators, which are typically localized and have a limited effect on a distribution system. Other methods include the use of capacitor banks in which reactive power is supplied by controlling switches to the capacitors. Placement of capacitor banks in these scenarios are of critical importance and in most cases, challenging to implement. Other methods include On-Load Tap Charging (OLTC) transformers and Static VAR Compensators (SVCs). However reverse power flow under high penetration of PV sources can lead to increases in voltages at the feeder end, which OLTC transformers and SVCs cannot correct. Given the eminent rise in renewable energy penetration to grids, standards are anticipated to change and allow reactive power compensation to relieve some of the burden off substations and feeders.

A PV inverter can be broken down into two major sections of control, an input and output side; see Figure 9.

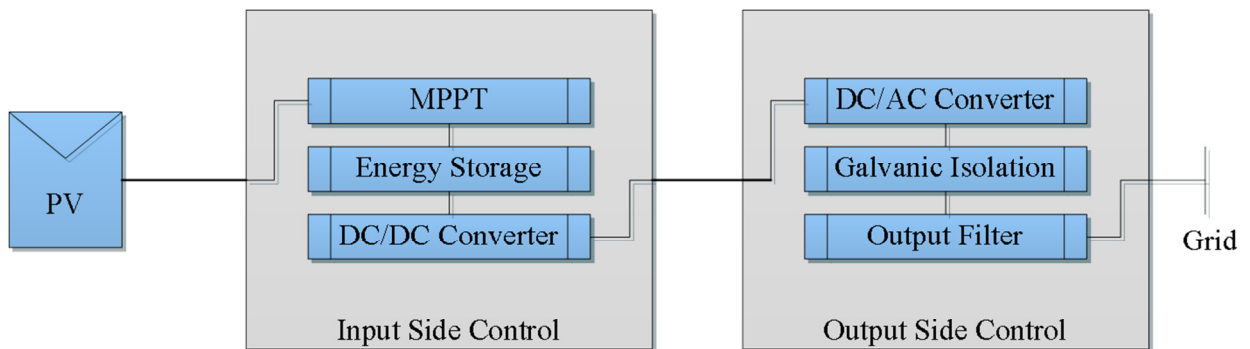


Fig. 9 Breakdown of a PV inverter.

The input side's primary tasks focus on regulating the DC voltage from the DC link (with the use of DC-DC boost converter actions) to achieve max power point tracking (MPPT). The input DC-DC boost converter action performed by the input side also serves as an isolation point between the DC link capacitor and the universal bridge DC-AC converter. As outlined in [16], the output side of a PV inverter can provide control of active power generated to the grid, control of reactive power between the inverter and the grid, control of DC-link voltage, power quality of injected power and filtering, grid synchronization, and isolation between the universal bridge converter and the grid.

The two main contributions by this Thesis are supported by 2 years of academic, and 1 year of graduate research for each of the two major sections identified in Figure 9. For the output side of the inverter, the main focus of this Thesis will be the demonstration of reactive power control by PV inverters with the use of synchronous reference frame control methods, introduced first in [18] and used in [11], [12], [16], and [17]. It will be demonstrated that control of power can be achieved using the *Specifications for Smart Inverter Interactions with Electric Grids using International Electrotechnical Commission 61850* report [19]. As an addendum to this Thesis, the second part will showcase the demonstration of a circuit capable of charging and discharging a battery storage system at the input side of Figure 9. It will be demonstrated that the input side can provide DC boosting actions, charging, and discharging capabilities using the DC bus, with minimal switching elements.

1.7 Organization of this Thesis

This document has been organized into five chapters and a conclusion. Chapter Two briefly introduces the dq -method and its role in the synchronous reference frame control strategy

to control active and reactive power injected by the inverter to the grid. Chapter Three will use the synchronous frame model and apply the specifications and guidelines found in Electric Power Research Institute's (EPRI's) report [19]. Chapter Four will demonstrate an addendum to a bi-directional multi-mode converter in the input side of the inverter that is able to provide the actions of a typical DC-DC input side converter and charge/discharge a battery in the same bus. Chapter Five will convey the simulation results of the addendum to the multi-mode converter and report findings. Finally, a recap of chapters One through Five will bridge all the gaps in the Conclusion, aiming at defending this Thesis as a holistic approach that tests the feasibility of a PV inverter that implements smart grid functionalities by regulating voltage.

1.8 Conclusion

This Chapter provided the underlying framework and basis for this Thesis. It introduced PV market trends and projections, followed by a breakdown of the basic setup of PV systems and its major components. It states the problem that is anticipated to occur if current codes and standards are not amended. This Chapter introduced the main six out of dozens of smart grid services and functionalities, and a literature survey on the different proposed methods that implement them. This Chapter included a section that explained the major contributions by this Thesis followed by a description of the organization of this document.

CHAPTER TWO: DEMONSTRATION OF P-Q CONTROL

PV arrays produce direct current (DC) power, which is injected to the input side of an inverter through a DC-DC converter. Common DC-DC converters used are Boost Converters, comprised of a switch (such as MOSFETs), inductor, and a diode, as shown on Figure 10.

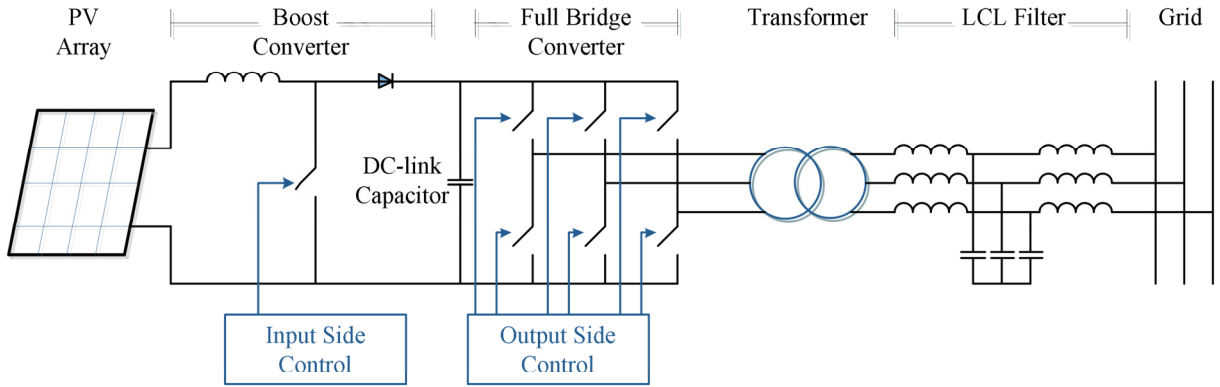


Fig. 10 Typical setup of a 3-phase PV inverter (without energy storage).

The input side control sends signals to the Boost Converter, which is in charge of boosting voltage to the Full-Bridge DC-AC Converter. This enables the Boost Converter to generate the optimal operating voltage, known as MPPT. Boost Converters are commonly employed to discharge battery systems as well. It will be demonstrated in Chapter Four and Five that a few modifications and new algorithms to the input side Boost Converter can simultaneously charge/discharge the battery in the same DC bus. DC-link capacitors are placed in between both converter stages. Capacitors are known to provide a short circuit path to AC changes in DC buses, making them a suitable choice for a filter.

Full-Bridge Converters are the most common choice of output side control, able to synthesize DC from a DC source to 3-phase alternating current (AC) voltages. The output side control sends signals to the Full Bridge Converter, which can effectively manipulate the output voltage magnitude and phase, which is the focus of this Chapter. The output is then stepped up/down by a transformer, which is then filtered before being connected to the grid.

This Chapter will begin with the research on several different kinds of modulation techniques, to achieve AC waveforms at the output of PV inverters. Two techniques that use transformations to facilitate the regulation of voltage will be presented, followed by the transfer function derivation of an inverter.

2.1 Modulation Techniques

Obsolete now, the past technique to achieve sinusoidal waveforms was through line commutation, which matched the interconnected grid waveform. Now, most inverters use pulse width modulation (PWM) to generate switching signals for the gates at the full bridge inverter. The first use of digital modulation was Sine-PWM, which its line-to-line output voltage waveform is limited by:

$$\hat{V}_{LL_{max}} = \frac{\sqrt{3}}{2} V_{in} \quad (2.1)$$

A full bridge converter can be fully exploited with the use of space vectors, which will be presented next.

2.1.1 Space Vector Modulation

Space vector modulation (SVM) is one of the most efficient techniques to perform pulse width modulation (PWM), which is 13.4% more efficient than the conventional Sine-PWM mentioned. Figure 11 demonstrates the eight vectors possible under a full bridge inverter topology. Each of the eight possible switching configurations form eight vectors, two of which are zero vectors and can be used beneficially during modulation. The eight vectors form six different sections which may be represented in phasors, where the resultant vector across any of the six sections, \vec{v}_s , is represented in (2.2).

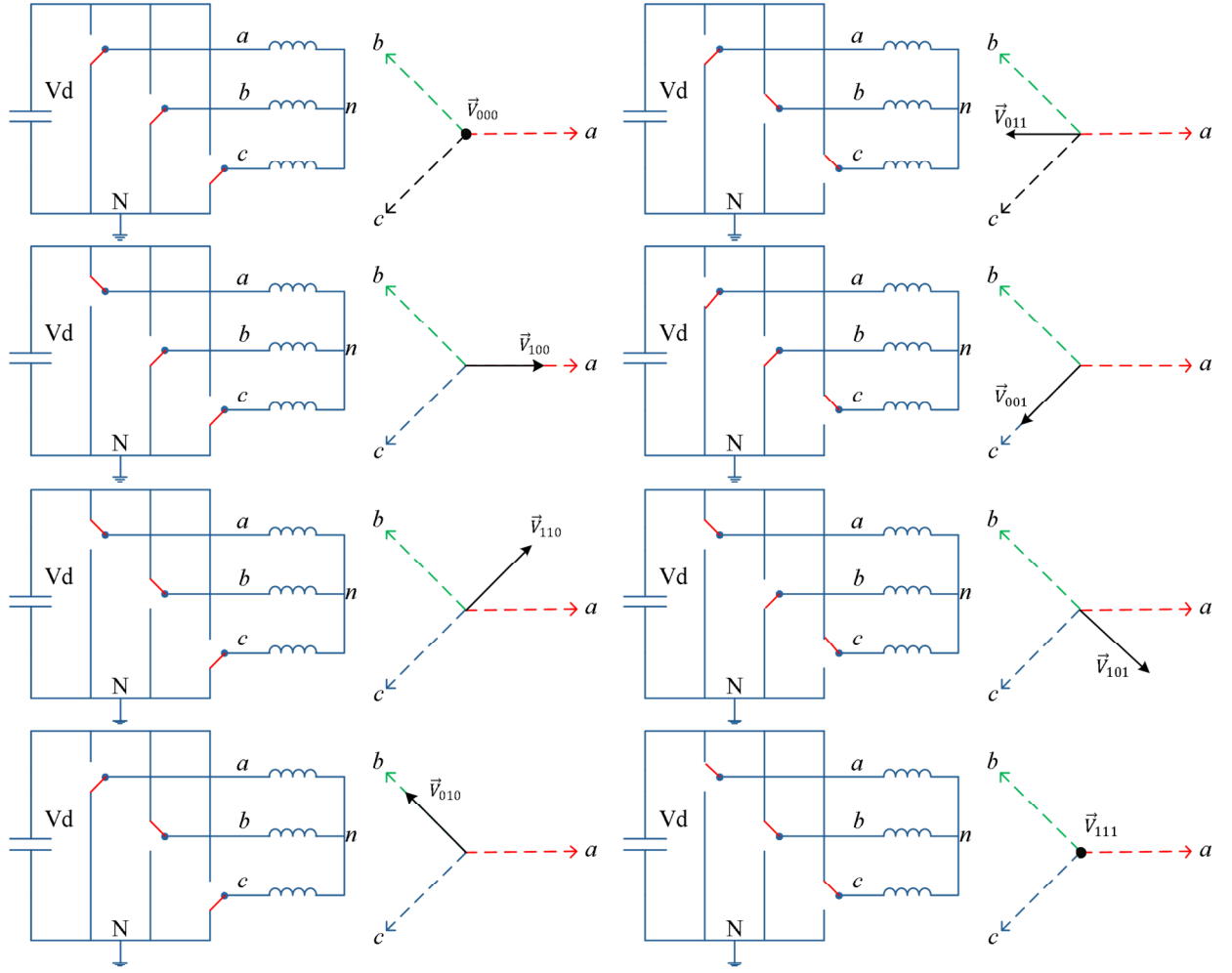


Fig. 11 Space Vector Modulation.

$$\vec{v}_s = v_a e^{j0} + v_b e^{j\frac{2\pi}{3}} + v_c e^{j\frac{4\pi}{3}} \quad (2.2)$$

By varying each of the vectors for different duty ratios in a time period T_s , the vector v_s can rotate. Representing each voltage output in terms of duty ratio $v_{an} = d_a V_d$, (2.2) may be written as:

$$v_s = V_d \left[d_a e^{j0} + d_b e^{j\frac{2\pi}{3}} + d_c e^{j\frac{4\pi}{3}} \right] \quad (2.3)$$

Therefore, in order to synthesize a vector in between \vec{V}_{100} and \vec{V}_{110} , each vector has to be varied for different time durations, such that on “average”, a vector in-between them can be achieved.

The zero vectors can be used to an advantage, since the sum of all duty ratios must equal zero in

order to synthesize any space vector \vec{v}_s . Countless methods that determine the appropriate duty ratio values have been introduced, with each choice in algorithm typically resulting in a compromise between harmonics and switching losses.

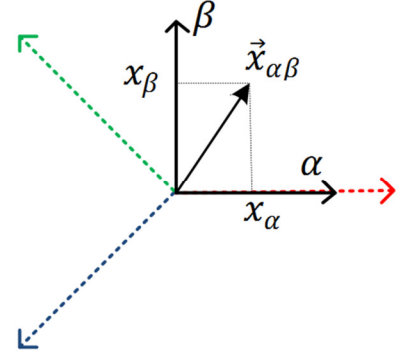


Fig. 12 Representation of 3-phase system as a rotating vector.

2.2 Stationary Reference Frame Control

2.2.1 The $\alpha\beta$ Transform

Advantages in utilizing a transformation to reduce the complexity of representing a three phase system as a whole are without question. The $\alpha\beta$ transformation can fulfill a similar advantage. It can reduce a three-phase mathematical model to 2 manageable dimensions, and permits the vectorial rotation needed for SVM. Using a synchronized vectorial rotation of ωt will lead to an analysis in DC components when the rotation effects are withdrawn.

In $\alpha\beta$ form, a three phase system X_s is represented by two rotating vectors. There are several methods to accomplish this transformation. One of the methods to accomplish this is by performing the matrix multiplication (2.4) to the magnitude of the three phases:

$$\begin{bmatrix} x_\alpha \\ x_\beta \end{bmatrix} = \sqrt{\frac{2}{3}} \begin{bmatrix} 1 & -1/2 & -1/2 \\ 0 & \sqrt{2}/3 & -\sqrt{2}/3 \end{bmatrix} \vec{x}_{abc} \quad (2.4)$$

Where the magnitude of the three phase voltages is $\vec{x}_{abc} = [x_a \ x_b \ x_c]^T$. The resulting transform can thereby represent a three-phase system into a two element vector of components x_α and x_β . Vectors x_α and x_β can then be conveniently plotted on the same axes presented on Figure11, see Figure 12. To obtain the inverse transformation, equation (2.5) is used.

$$\begin{bmatrix} x_a \\ x_b \\ x_c \end{bmatrix} = \sqrt{\frac{2}{3}} \begin{bmatrix} 1 & 0 \\ -1/2 & \sqrt{3}/2 \\ -1/2 & -\sqrt{3}/2 \end{bmatrix} \begin{bmatrix} x_\alpha \\ x_\beta \end{bmatrix} \quad (2.5)$$

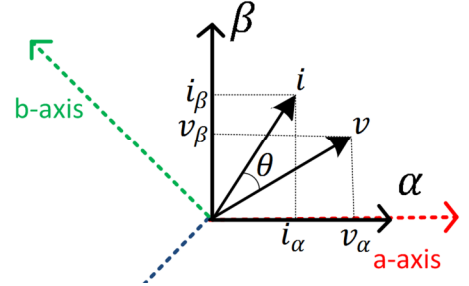


Fig. 13 The α and β components of voltage and current vectors.

2.2.2 Control of Power Flow under Stationary Reference

Frame Control

Computing the instantaneous power flow from a three-phase source by conventional methods, (2.6), can prove to be a cumbersome method to regulate active and reactive power injection.

$$P = v_a i_a + v_b i_b + v_c i_c \quad (2.6)$$

However, power can beneficially be calculated and controlled in the $\alpha\beta$ -plane, by taking advantage of the vectorial characteristics of voltage and current in the plane. It is evident to see that the current component in phase with the voltage is the real power, while the current orthogonal to voltage is the reactive component seen on Figure 13. This fact opens a new interpretation of active and reactive power in the $\alpha\beta$ -plane as (2.7) and (2.8), where θ is the angle between voltage and current.

$$P_{\alpha\beta} = \frac{3}{2} |v| |i| \cos(\theta) \quad (2.7)$$

$$Q_{\alpha\beta} = \frac{3}{2} |v| |i| \sin(\theta) \quad (2.8)$$

The active and reactive power equations (2.7) and (2.8) can also be expressed in terms of α and β vector components, by noting that (2.7) is the dot product between the current and voltage vectors while (2.8) is the cross product of the vectors shown on Figure 13. Equations (2.7) and (2.8) can be then re-written as (2.9) and (2.10) respectively.

$$P_{\alpha\beta} = \frac{3}{2} (v_\alpha i_\alpha + v_\beta i_\beta) \quad (2.9)$$

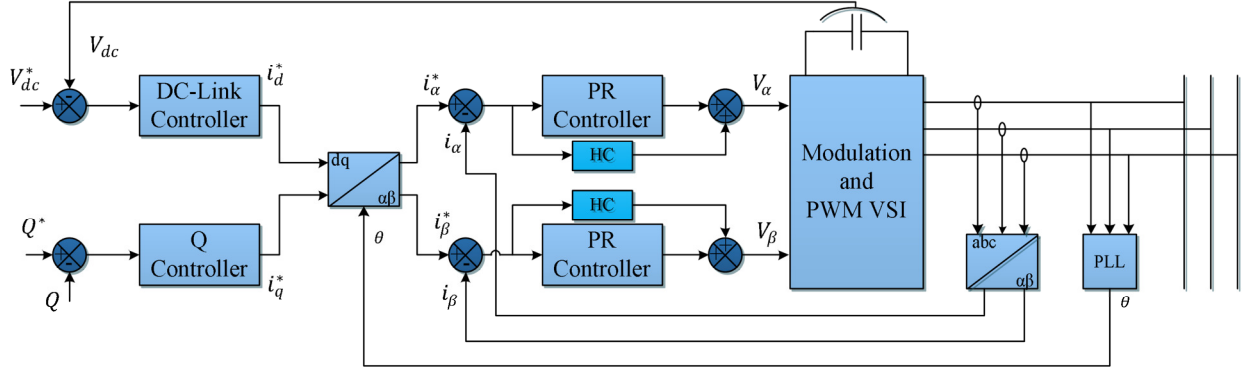


Fig. 14 *Stationary reference frame control structure.*

$$Q_{\alpha\beta} = \frac{3}{2}(v_{\alpha}i_{\beta} - v_{\beta}i_{\alpha}) \quad (2.10)$$

Where the $3/2$ constant is chosen to coincide with the classical phasor definition under the steady state conditions presented in (2.4), [18].

The $\alpha\beta$ transform opens way to structure a control loop as seen on Figure 14. Since the control variables i_{α} and i_{β} are sinusoidal in nature, the use of a proportional resonant (PR) controller is preferred. A beneficial characteristic of PR controllers is that they can achieve a high gain around resonant frequency, thus being able to eliminate the steady state error between the control signal and its reference [20].

2.3 Synchronous Reference Frame Control

2.3.1 The dq Transform

Most commonly known as dq control, the synchronous reference frame control makes use of the $\alpha\beta$ transformation and implements an additional rotating scheme that rotates at the same speed (synchronously) as the transform to perceive the resulting vector as a constant (DC value). The synchronous mapping of dq references to the $\alpha\beta$ -plane can be achieved via the Park's transformation, which is mathematically expressed in (2.11).

$$\begin{bmatrix} x_d \\ x_q \end{bmatrix} = \begin{bmatrix} \cos\theta & \sin\theta \\ -\sin\theta & \cos\theta \end{bmatrix} \begin{bmatrix} x_\alpha \\ x_\beta \end{bmatrix} \quad (2.11)$$

With Park's transformation, the former $\vec{x}_{\alpha\beta}$ is multiplied by sinusoids with an angular speed equal to $\theta = \omega t$. By matching the speed of the rotating vector with the speed of the grid, the vector $\vec{x}_{\alpha\beta}$ will appear not to be moving at all in the dq axes. Conversely, the inverse of a Park's transformation is accomplished by (2.12).

$$\begin{bmatrix} x_\alpha \\ x_\beta \end{bmatrix} = \begin{bmatrix} \cos\theta & -\sin\theta \\ \sin\theta & \cos\theta \end{bmatrix} \begin{bmatrix} x_d \\ x_q \end{bmatrix} \quad (2.12)$$

Another benefit of dq frames is the fact that they can be represented using complex phasorial representation of vectors, which is a simplified way of expressing a three phase system.

$$\vec{x}_{dq} = \vec{x}_{\alpha\beta} e^{-j\theta} \quad (2.13)$$

2.3.2 Control of Power Flow under Synchronous Reference Frame Control

To simplify the power derivations in the dq frame, the voltage vector can be made to rest on the d -axis. When the voltage vector is aligned with the d -axis, the current component in d is the real current power, while the current component orthogonal to the voltage vector is the reactive current, as seen on Figure 15. Power derivation in dq becomes simpler:

$$P = \frac{3}{2} |v| i_d \quad (2.14)$$

$$Q = \frac{3}{2} |v| i_q \quad (2.15)$$

The DC characteristics of the synchronous reference frame controllers are beneficial to PI controllers, since they can guarantee zero tracking error on constant signals [16]. The synchronous reference frame control scheme is shown on Figure 16. As seen on Figure 16, the voltage of the grid is placed as reference for the phase δ .

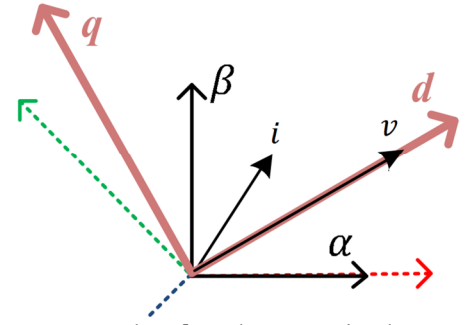


Fig. 15 The d and q axes in the $\alpha\beta$ plane.

CHAPTER THREE: SIMULATION RESULTS AND FINDINGS OF THE Q CONTROL METHOD

This chapter begins by explaining the setups for the SVM simulation model and the synchronous rotating frame model, followed by their respective results and findings.

3.1 Space Vector Modulation Setup

Space vector modulation is one of the most efficient techniques to perform PWM, which is 13.4% more efficient than conventional Sine-PWM techniques. Figure 11 demonstrated eight of the vectors possible under a full bridge topology, with each switching configurations forming the eight vectors and two resulting in zero vectors. The six non-zero vectors form six different sections. Mathematically, these vectors may be represented in phasors, where the resultant vector, \vec{v}_s can be represented as in (3.1).

$$\vec{v}_s = v_a e^{j\theta_a} + v_b e^{j\theta_b} + v_c e^{j\theta_c} \quad (3.1)$$

By varying each of the vectors for different duty ratios in a time period T_s , the rotating vector v_s , can be represented in terms of duty ratio, (3.2). As seen on Figure 11, each voltage vector varies by one bit, in which it becomes the task of a SVM PWM generator's task to solve for the duration of each bit, x , y , and z for the given time period T_s .

$$v_s \angle \theta_s = V_d [d_x e^{j\theta_x} + d_y e^{j\theta_y} + d_z e^{j\theta_z}] \quad (3.2)$$

Where θ_s is the current vector location.

Countless methods to determine the duty ratios have been proposed. With recent increasing improvements in computation power, the ability to solve for complex equations in fewer clock cycles has become an advantageous approach to solve for the duty ratios. As

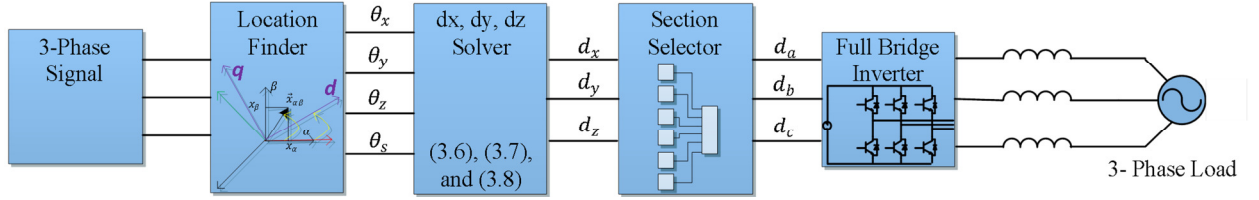


Fig. 17 Space vector modulation Simulink model setup.

conducted by this research, it is possible to solve for the duty ratios faster than the sampling frequency T_s . By noting that the $d_z e^{j\theta}$ component in (3.2) is zero, (3.2) can be broken down into its real and imaginary components, (3.3-3.4).

$$v_s \cos(\theta_s) = d_x V_d \cos(\theta_x) + d_y V_d \cos(\theta_y) \quad (3.3)$$

$$v_s \sin(\theta_s) = d_x V_d \sin(\theta_x) + d_y V_d \sin(\theta_y) \quad (3.4)$$

$$1 = d_x + d_y + d_z \quad (3.5)$$

Where (3.5) is used to solve for the third unknown, d_z . Results were as follow:

$$d_x = \frac{1}{2} \frac{v_s \cos(\theta_s) \sin(\theta_y) - v_s \cos(\theta_y) \sin(\theta_s)}{V_d \cos(\theta_x) \sin(\theta_y) - V_d \cos(\theta_y) \sin(\theta_x)} \quad (3.6)$$

$$d_y = \frac{1}{2} \frac{v_s \cos(\theta_s) \sin(\theta_x) - v_s \cos(\theta_x) \sin(\theta_s)}{V_d \cos(\theta_x) \sin(\theta_y) - V_d \cos(\theta_y) \sin(\theta_x)} \quad (3.7)$$

$$d_z = 1 + \frac{v_s \sin(\theta_s) (\cos(\theta_x) - \cos(\theta_y)) + v_s \cos(\theta_s) (\sin(\theta_x) + \sin(\theta_y))}{2V_d (\cos(\theta_y) \sin(\theta_x) - \cos(\theta_x) \sin(\theta_y))} \quad (3.8)$$

Figure 17 is a graphical representation of the setup for the model. A three phase reference signal was given to a m-file function that determines the location of the vector, outputting the current locations to another m-file. The “solver” block then transfers the results to a “section selector” block, which translates the input to duty ratios for the full bridge inverter. The model was connected to a 3-phase load with parameters shown on Table 2.

Table 2			
Vd	240 V	Sampling Frequency	100 kHz
V phase to phase	240 V	Grid Frequency	60 Hz
Inductor	1.5 mH	Phase angle of 'a'	90°

3.2 Space Vector Modulation Simulation Results

The MATLAB Simulink model is seen on Figure 18, which is based on the approach presented on Figure 17. Simulink's PowerSim blocks were used to model inductors, load, and the switches of the full bridge inverter. A ramp signal was used to generate duty cycles with a sampling frequency of 100 kHz. Figure 19 probes two locations in the model. The image to the left plots d_x , d_y , and d_z , which their sum is seen to be equal to zero. These signals were sent to a duty ratio generator, which selected the appropriate block based on the location of the rotating vector. The image to the right probes the output voltage, which verifies a line to line voltage of 240 V and a 90° phase shift. This minor demonstration shows that it is possible to manipulate the voltage magnitude and phase by the direct calculation of (3.6), (3.7), and (3.8).

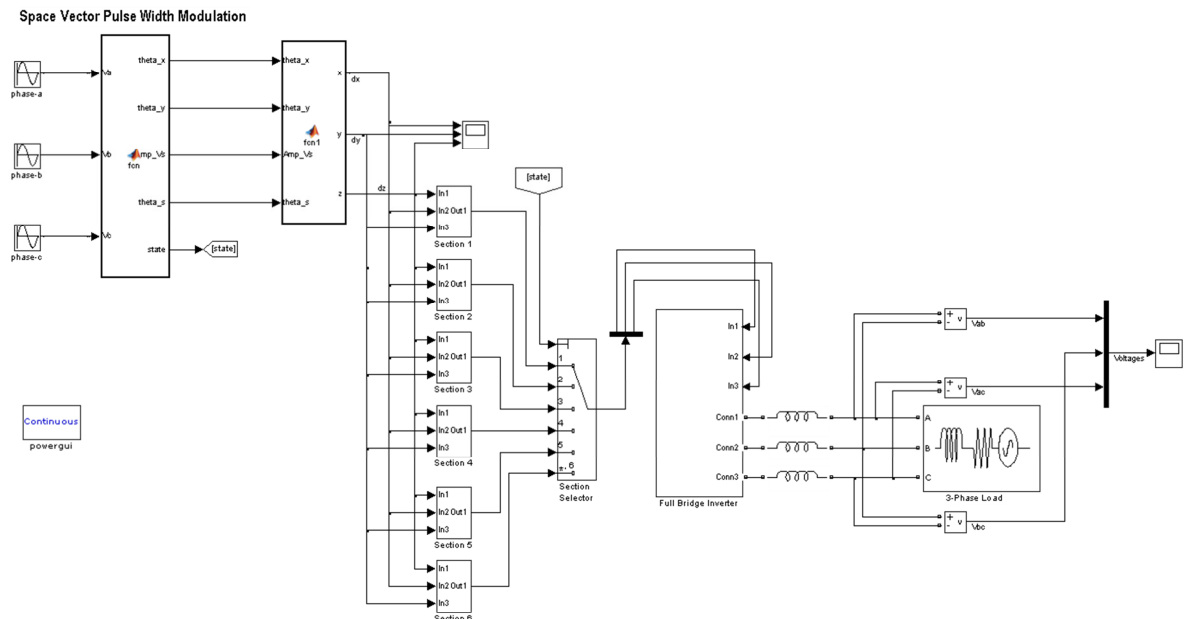


Fig. 18 Space vector modulation Simulink model.

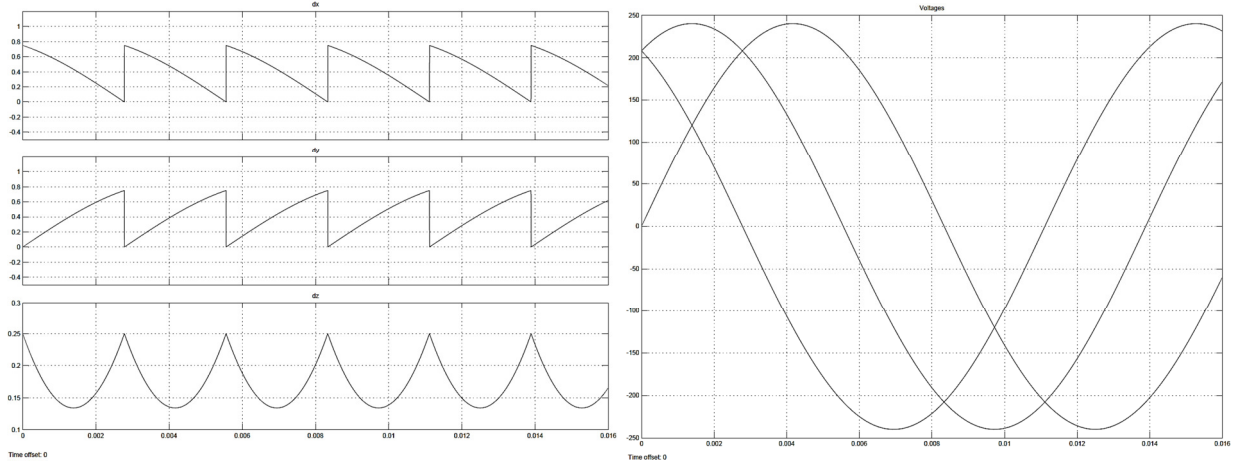


Fig. 19 SVM Simulink model results.

3.3 Synchronous Reference Frame Controller Setup

Essentially, the setup for the synchronous reference frame controller was a derivation of Figure 16 and the design was based on transfer function (2.19). This was accomplished using MATLAB's Simulink, a proven tool for modeling, simulating, and analysis of dynamic systems. Parameters for the simulation are listed on Table 3.

Table 3			
Simulation Step Size	10 μs	System Frequency	60 Hz
Simulation Error Tolerance	1 ms	Apparent Power	1.5 kVA
Simulation Run Time	1 s	Load Inductor	1.5 mH
Nominal Grid Voltage	120 V	Load Resistor	0.1 Ω

3.3.1 Controller Designs

The approach taken was designing the inner PI controllers first. This required the desired voltage vectors ingoing the inverter, e_d and e_q , to be controlled independently. Both vectors could be represented mathematically by (3.9) and (3.10).

$$e_d = L_s(x_1 - \omega i_q) + |v| \quad (3.9)$$

$$e_q = L_s(x_2 - \omega i_d) \quad (3.10)$$

Where x_1 and x_2 are the PI controller error equations represented by (3.11) and (3.12).

$$x_1 = \left(k_p + \frac{k_i}{s}\right)(i_d^* - i_d) \quad (3.11)$$

$$x_2 = \left(k_p + \frac{k_i}{s}\right)(i_q^* - i_q) \quad (3.12)$$

Where the current vector references are given by i_d^* and i_q^* . The reactive current i_q^* is supplied by the outer-loop, while real power is regulated by varying i_d^* in response to the DC-link voltage [15]. Gain values k_p and k_i for the PI controllers were chosen based on desired response times, and according to linearization of the plant model and the PID-tuner provided by the PI controller Simulink block. As shown on Figure 20, an adequate response time of 0.00259 seconds was selected, which was fast enough to clear one clock cycle by roughly $\sim 15\%$ the time.

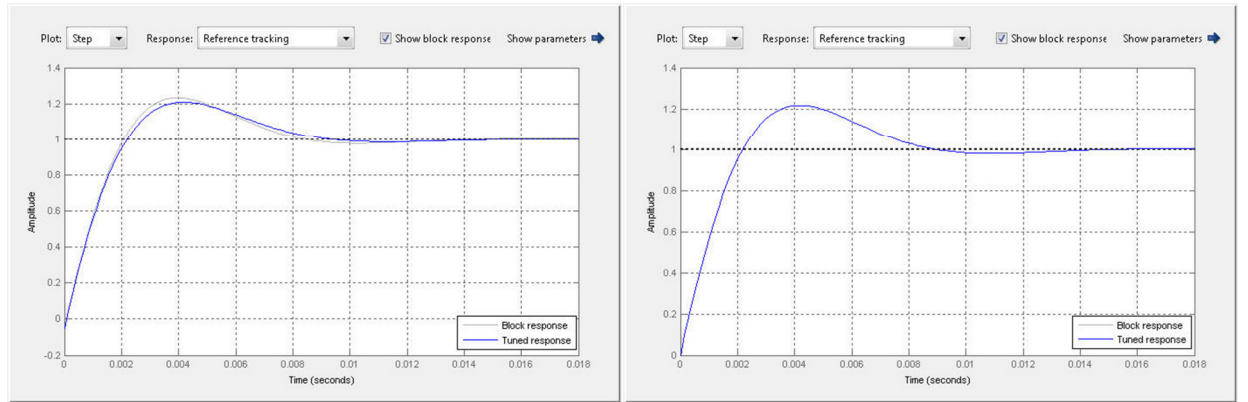


Fig. 20 PI controller response times. i_q -PI Controller (Right), i_d -PI Controller (Left).

For the purpose of the analysis, the voltage at the DC-link capacitor was assumed to be constant, eliminating the need for DC-link controller. Instead, a real power PD controller was designed to regulate the real power injection to the grid.

3.3.2 Block Models

Simulink's MATLAB Function block model was taken advantage of; to generate a block that took in as an input three sinusoidal signals, and as an output two DC values. Transforms

(2.4) and (2.11) were used to generate two 2-stage $abc \rightarrow \alpha\beta \rightarrow dq$ blocks, one for current and another for the grid voltage. The grid voltage transform block was strategically aligned along the $d - axis$ by ensuring the three grid voltage signals were synchronized directly with the transform. Conversely, to model a three phase voltage source inverter (VSI), MATLAB code for a $dq \rightarrow abc$ was generated utilizing the inverse transform relations (2.5) and (2.12).

3.3.3 R-L Line Impedance Model

To model typical line impedances, parameters from Table 3 three were used to simulate the behavior of a PV inverter connected to the grid. The model was based on the mathematical premise of the voltage across the line, given by (3.13).

$$v_{line} = L_s \left(\frac{di}{dt} \right) + i(t)R \quad (3.13)$$

Where the line current can be solved for as (3.14) and graphically depicted on Figure 21.

$$i(t) = \frac{1}{L_s} \int (v_{line} - iR) dt \quad (3.14)$$

The voltage across the line, v_{line} , was found by computing the difference between the grid voltage and the inverter's voltage, as seen on figure 21.

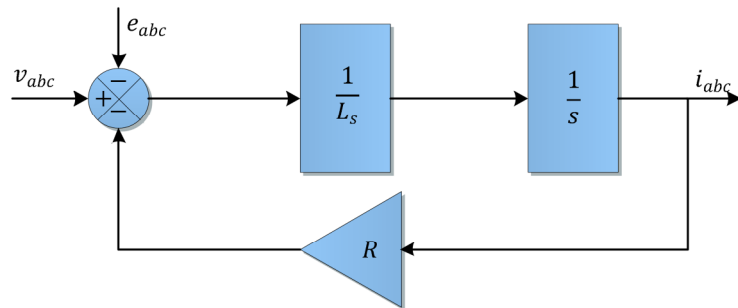


Fig. 21 Line impedance model.

3.4 Synchronous Reference Frame Controller Simulation Results

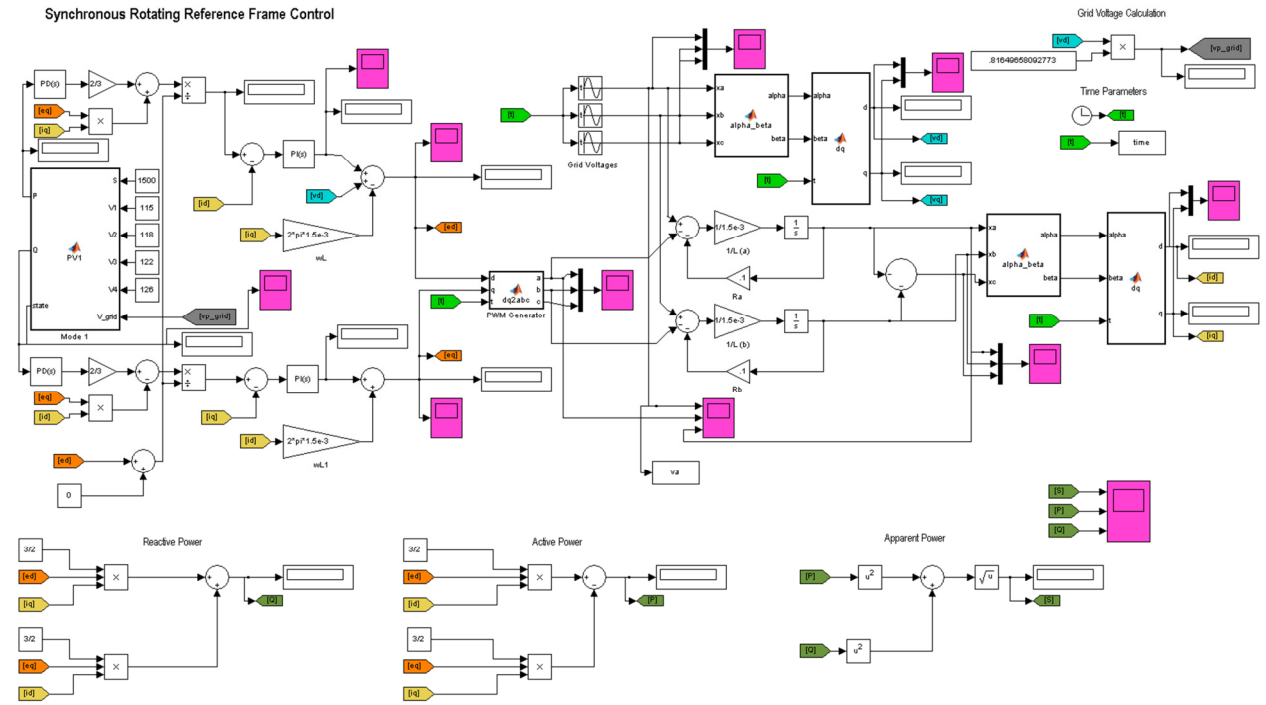


Fig. 22 *Synchronous Rotating Reference Frame Control Simulink Model*

The final Simulink model used for the demonstration and analysis of VAR control is depicted in Figure 22. The specification report for future smart inverters by the Electric Power Research Institute [19] contained suggestions for the possible future role of smart inverters. According to the U.S. Department of Energy, there has been a rise in reactive load in the last 20 years. Reactive loads from electronic devices have risen by 40% since 1980, and are anticipated to increase by 60% by 2015. Therefore, to relieve the anticipate stress, utilities will someday be able to use the reactive power support by the countless integrated smart inverters. There are several challenges that may arise if the request by the utility is not coordinated properly. For example, sending requests to many inverters of different sizes may be complex and communication traffic may cause delays which may lead to further issues. Other considerations to be taken include the precedence of user/owner control. EPRI's report [19] suggests that the

utility send a data table to inverters via an established communication protocol. The table will convey the required VAR support from all inverters capable and willing to support. Similar in procedures used by current VAR support equipment, the utility may send a Volt/VAR table to inverters which convey the information for inverters to operate. To date, EPRI has suggested four modes of operation, the Normal Energy Conservation mode, Maximum VAR Support mode, Static VAR Support mode, and the Passive mode. Simulation results and findings for each mode are presented in the following sections.

3.4.1 Normal Energy Conservation Mode

In this mode, the utility calculates the most efficient VAR levels for local inverters at specific points of power coupling (PCC), by sending an array of voltage and corresponding VAR levels, as shown on Figure 23. In the sample shown on Figure 23, the utility sends four voltage

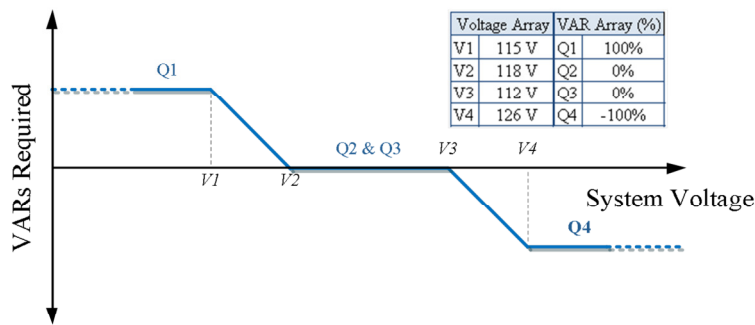


Fig. 23 PV1 - Normal Energy Conservation Mode array sample.

voltage level outside 88% to 110% off the nominal voltage [21]. Under this mode, the inverter may choose to respond to the utility's VAR demand by supplying the corresponding VAR from the table to the measured voltage at the PCC. The table shown on Figure 23 was used for the Simulink simulation model.

points of operation, all of which are within the voltage limits stipulated on the IEEE 1547 standards. The 1547 standard requires any interconnected inverter to disconnect for any grid

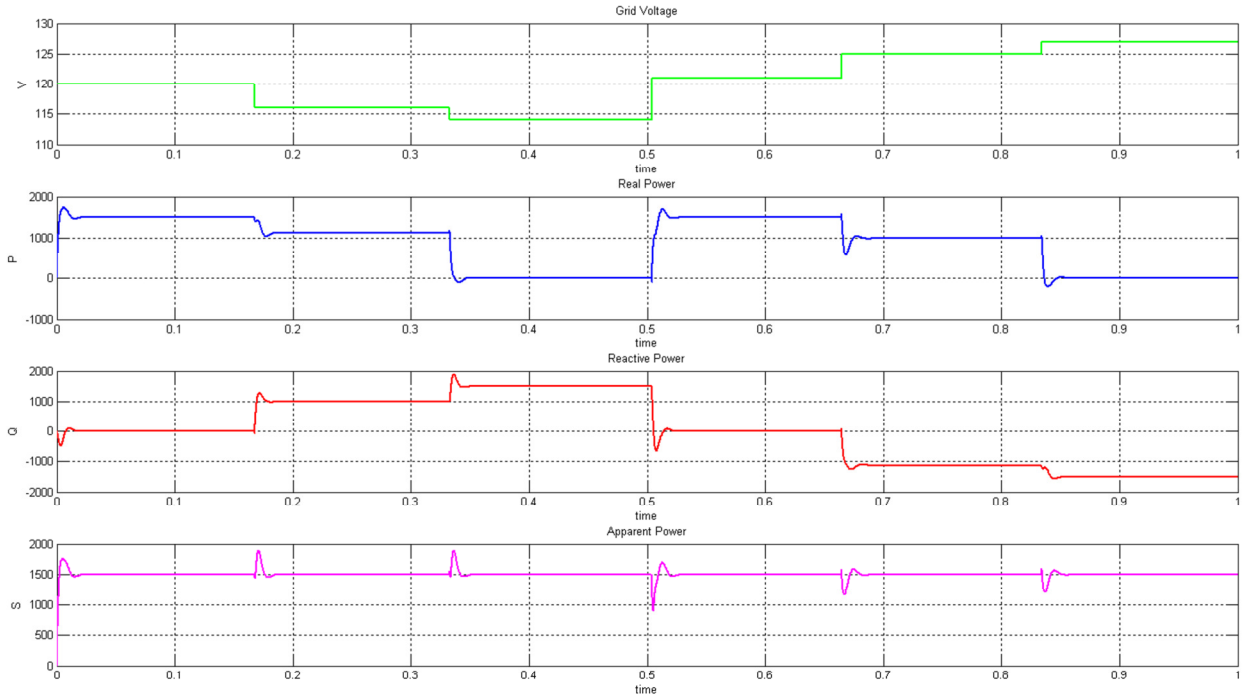


Fig. 24 *Normal Energy Conservation Mode simulation results.*

It can be demonstrated from the graphs provided by Figure 24 that the inverter can shift the PWM signals to the inverter in little over a cycle, < 0.0166 seconds. Despite a fluctuating VAR requirement modeled in Figure 24 is not likely, the response time cannot exceed less than one clock cycle due to the fact that a space vector is defined in one clock cycle.

The first grid voltage detected by the simulation was its nominal, $120V$. Thereby, only real power was supplied to the grid. In the next stage, a voltage reading of $116V$ was detected at the PCC, demanding $1000 VAR$, or 66.666% of the maximum reactive power available, while maintaining a constant apparent power throughout all the stages. In the next stage, a maximum VAR demand was sent via a $114V$ reading at the PCC, and then back to nominal operation mode in the following stage. Inductive VAR demands were tested next by changing the voltage at PCC to $125V$, demanding -75% off the maximum VARs. Finally, a full inductive stage was tested for the remainder of the simulation.

3.4.2 Maximum VAR Support Mode

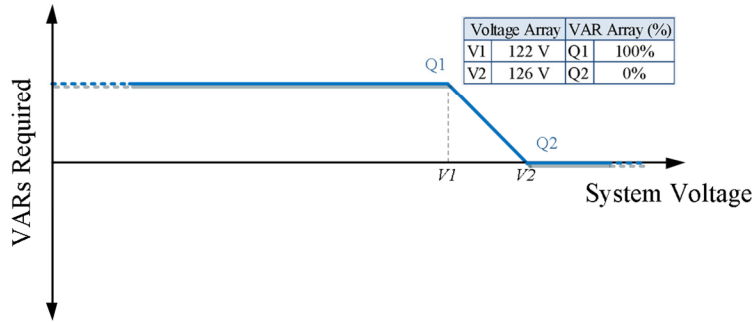


Fig. 25 PV2 – Maximum VAR Support Mode array sample.

This mode is basically the first half of the PV1 mode, in which the inverter provides 100% of capacitive (positive) VARs without exceeding V_{max} . This mode is most useful during times that the transmission line is in need

of emergency support. The function is therefore a horizontal line until it reaches Q1, where it will drop by the rules given on an interpolation of the V1 and V2 voltages. This is graphically represented in Figure 25, followed by results on Figure 26.

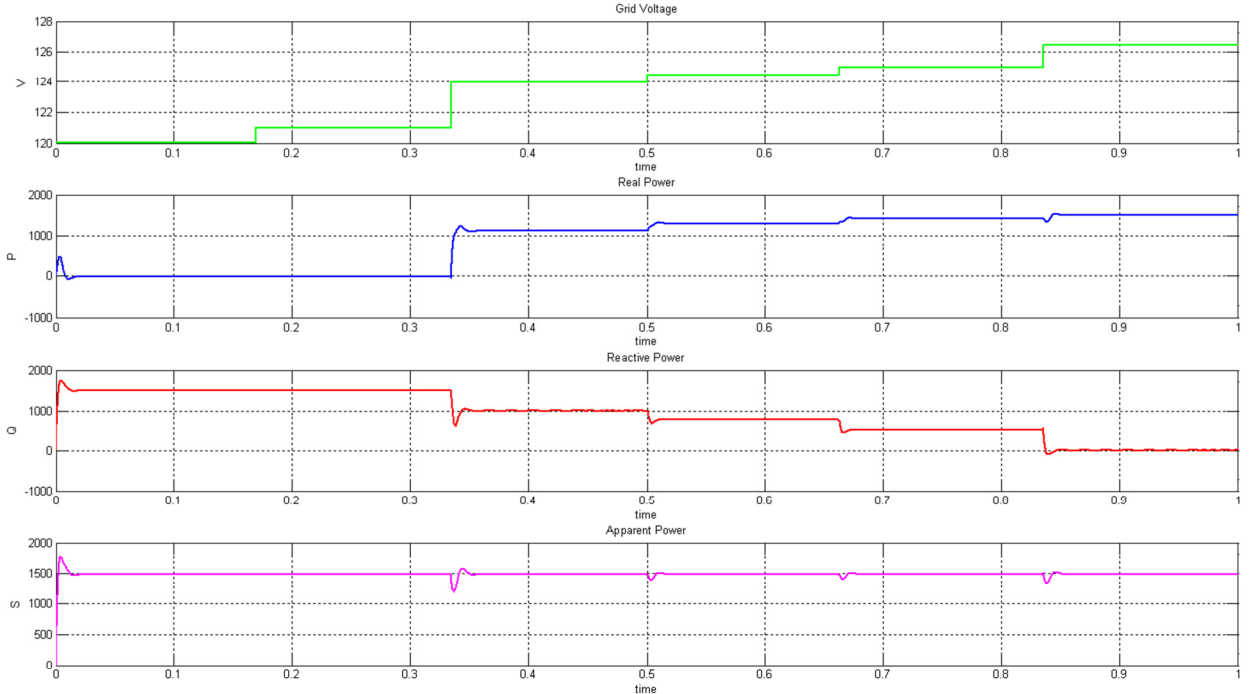


Fig. 26 Maximum VAR Support Mode simulation results.

The voltage signals felt at the PCC were 120V, 121V, 124V, 124.5V, 125V, and 126.5V.

3.4.3 Fixed VAR Mode

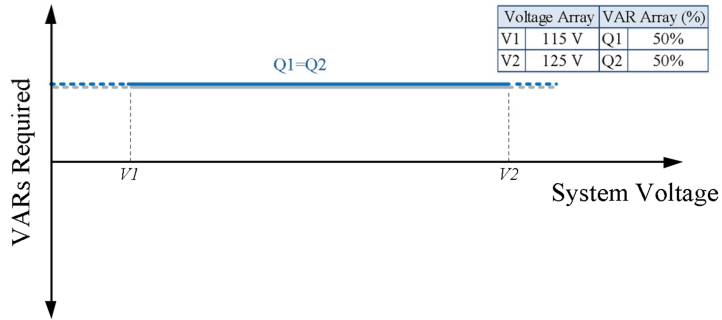


Fig. 27 PV3 – Fixed VAR Mode array sample.

a centralized, more intelligent controller will send fixed VAR requirements, managing the regulation of VARs injected to the grid.

For this mode, inverters inject a constant VAR level, regardless of voltage reading at PCC. The main objective of this mode is to free the inverter of controller requirements. This way,

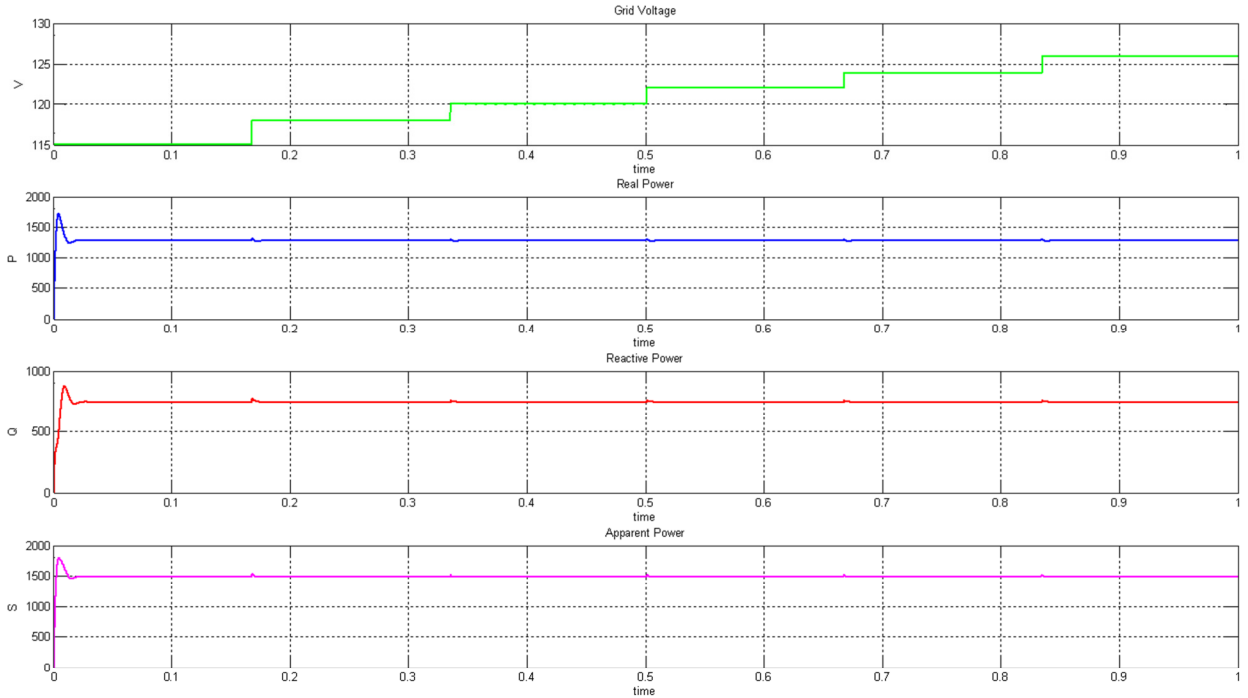


Fig. 28 Fixed VAR Mode simulation results.

3.4.4 Passive Mode

This final mode is similar to the Fixed VAR Mode, except instead of providing constant VARs, it provides constant real power. The results for this mode are shown on Figure 29.

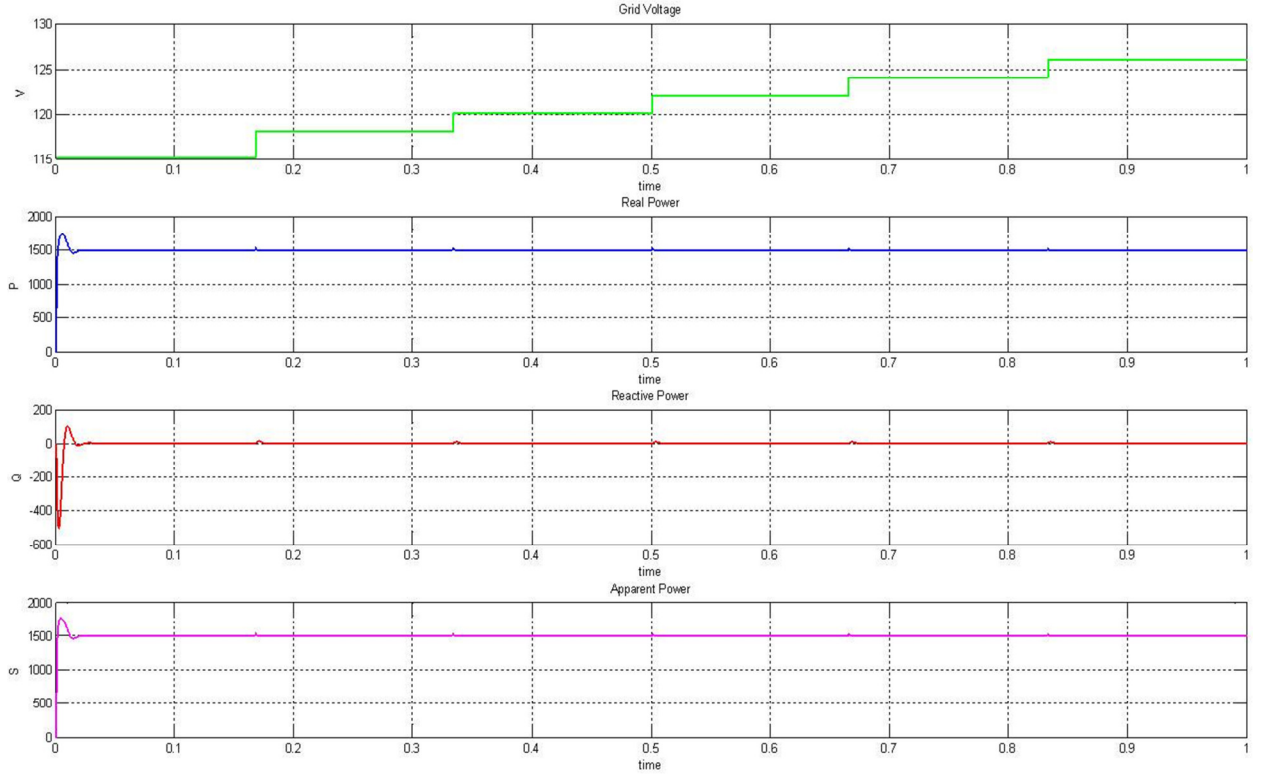


Fig. 29 *Passive Mode simulation results.*

The same voltage sequence as those of Figure 28 was sent: 115V, 118V, 120V, 122V, 124V, and 126V.

3.5 Other Findings

Due to the sudden voltage changes detected on the PCC, small perturbations that adjust to these changes can be seen on the active and reactive power graphs of Figure 28 and Figure 29. It should be noted that these perturbations are also less than a clock cycle, measuring 0.0176 seconds, for example.

The validity of the simulation model was tested via power equations (1.1), (1.2), (3.14), and (3.15) versus the method utilized in the simulation, the multiplication of dq vectors (3.17).

$$P = v_a i_a \cos(\theta) + v_b i_b \cos(\theta) + v_c i_c \cos(\theta) \quad (3.14)$$

$$Q = v_a i_a \sin(\theta) + v_b i_b \sin(\theta) + v_c i_c \sin(\theta) \quad (3.15)$$

$$S = (e_d + je_q)(i_d + ji_q) \quad (3.17)$$

Where

$$P = e_d i_d - e_q i_q \quad (3.18)$$

$$Q = e_d i_q + e_q i_d \quad (3.19)$$

Table 4				
$V_{grid} = 116V, P = 1118W, Q = 1000VAR, S = 1500VA$				
Measurement	Value	Eqn. no.	Equation	Results
θ	0.791681 rads	(1.1)	$P = \frac{v_a e_a}{X_s} \sin(\delta)$	1220.6 W
	45.36°			
δ	0.033929 rads	(1.2)	$Q = \frac{v_a e_a \cos(\delta) - v_a^2}{X_s}$	813.375 VAR
	1.944°			
$v_a(rms)$	82.024V		$S = \sqrt{(1.1)^2 + (1.2)^2}$	1466.78 VA
$e_a(rms)$	83.971V	(3.14)	$Q = v_a i_a \cos(\theta) + v_b i_b \cos(\theta) + v_c i_c \cos(\theta)$	1067.31 W
$i_a(rms)$	5.9545A	(3.15)	$P = v_a i_a \sin(\theta) + v_b i_b \sin(\theta) + v_c i_c \sin(\theta)$	1053.98 VAR
			$S = \sqrt{(3.14)^2 + (3.15)^2}$	1500.01 VA

Table 4 shows the results under PV1 Energy Conservation Mode, for a voltage at PCC of 116V. Under that situation, and using equations (3.18) and (3.19), real power required becomes 1118 Watts while the total reactive power needed becomes 1000 VAR. However, as seen by results on Table 4, using (1.1) and (1.2) to solve for active and reactive power is not as precise, due to the small shift between grid and inverter voltages, δ . The arrays stored in the simulation were accurate to the 1000th decimal, giving a change in phase of 0.0001 seconds, not enough digits to accurately derive the actual shift. Using equations (3.14) and (3.15) yielded more formidable results, due to the larger discrepancy between the voltage and current phase shift. However, the same issue arose with the 1000th decimal limitation, with a 0.0021 second phase

difference. This asserts one more advantage of using dq over conventional methods, its precision for bigger samples is remarkably accurate. Figure 30 depicts the current and voltage waveforms for this scenario.

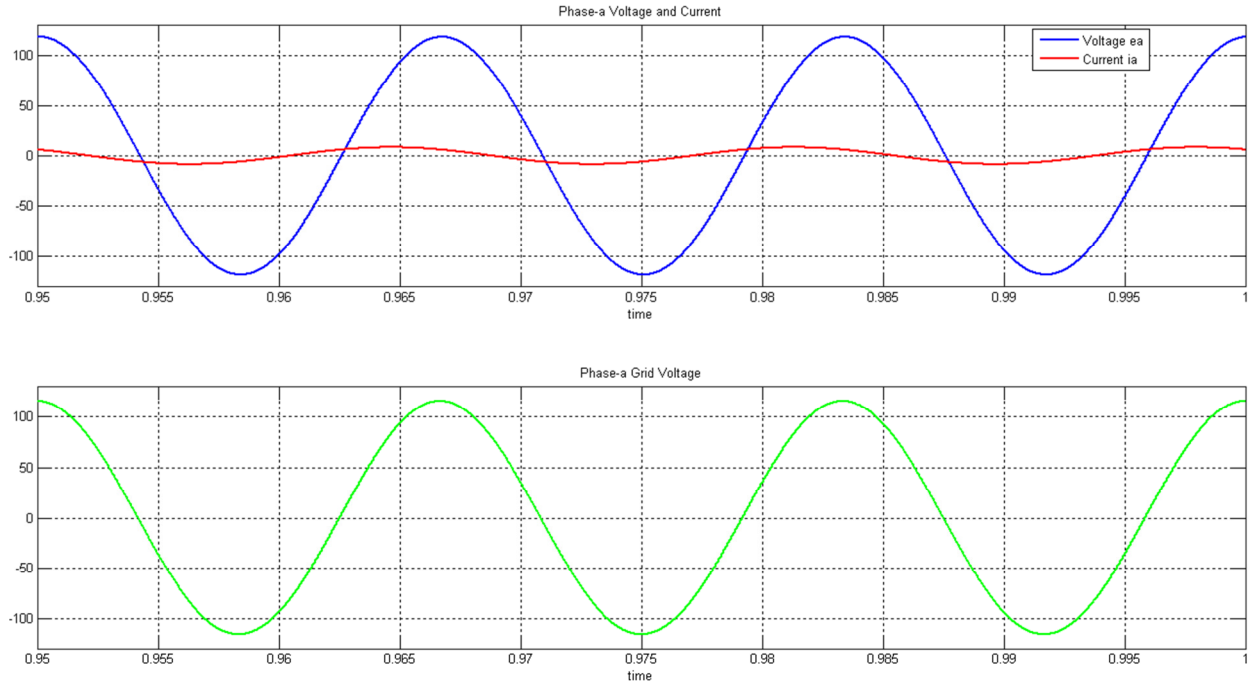


Fig. 30 *Phase shift simulation results.*

CHAPTER FOUR: MULTI-MODE CONVERTER FOR INPUT SIDE OF INVERTERS

This chapter deals with the input side controller that interfaces battery storage systems with PV arrays, as presented on Figure 9. As more and more intermittent sources are integrated into grids, the need for stability via the use of energy storage systems becomes imperative. One of the main challenges of energy storage systems is their cost, reducing the payback of PV systems. While different technologies and research on different chemical batteries are reducing the costs of storage systems, input side power electronics components can also be reduced to lower costs of storage systems. Another most important advantage of implementing energy storage systems to PV systems is the fact that it allows for the inverter to operate in all four quadrants of power flow, presented previously on Figure 3.

4.1 Conventional Battery Storage Methods

Typically, battery storage systems are integrated to PV systems as seen on Figure 31. Configurations consist of DC-DC boost converters to optimize the input for max power delivery. The boosted voltage is then supplied to inverters which are in turn connected to the grid. Both configurations offer different levels of control, with more control with increased components. The configuration on the right of Figure 31 has fewer components, but suffers from control

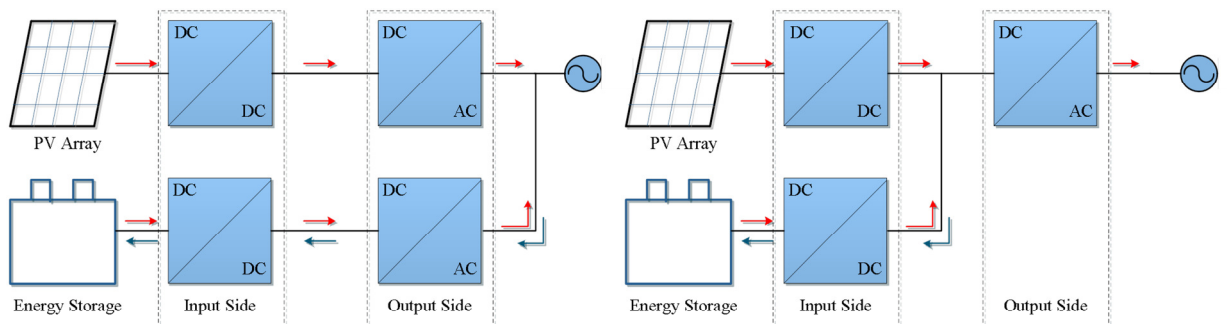


Fig. 31 Conventional methods to implement energy storage systems.

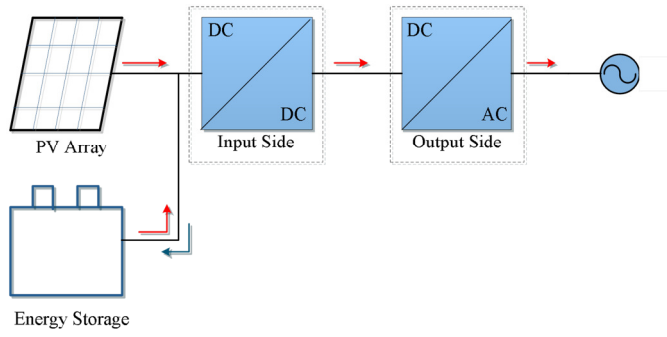


Fig. 32 Novel method to implement energy storage systems.

freedoms offered by its counterpart on the left. A novel method, introduced in [22], allows for the use of a single input side converter, which can operate in boost and buck modes to charge and discharge the battery while providing MPPT

simultaneously. This is done by utilizing two switches, one diode, and two inductors, as seen on the left circuit of Figure 33.

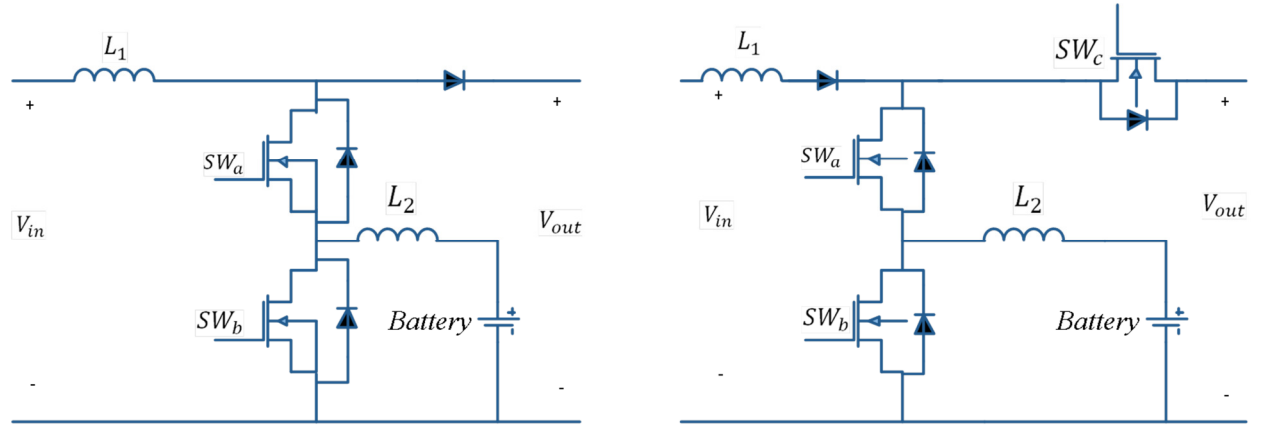


Fig. 33 Multi-Mode Converters.

However, despite its advantages, the multimode converter on [22] was limited to charging the battery from the PV system, and not from power flowing from the grid into the inverter. With the use of a bidirectional switch in place of the diode, and PWM to that switch (SW_c from Figure 33), it becomes possible to charge the battery from the grid as well. This feature allows the battery storage system to absorb real and reactive power from the grid, allowing it to operate in all four quadrants presented on Figure 3. The diode is placed next to the input bus, to prevent the flow of current into PV panels, and avoid damage to them. The new topology is able to operate in all four mode originally presented in [22], as well the additional mode aforementioned.

CHAPTER FIVE: SIMULATION RESULTS AND FINDINGS OF THE MULTI-MODE CONVERTER

5.1 Multi-Mode Converter Setup

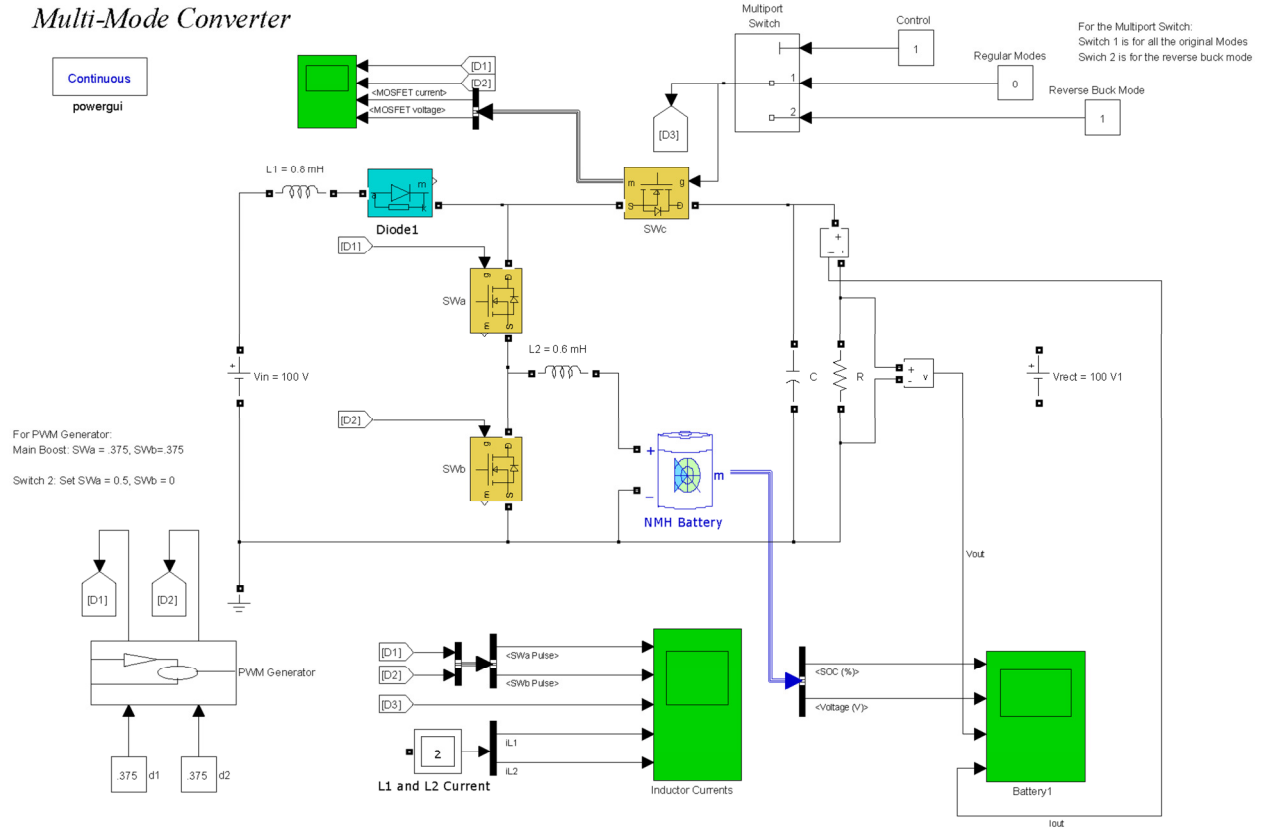


Fig. 34 Simulink model of the multi-mode converter.

The three-switch multimode converter was implemented and simulated in MATLAB's Simulink. Values chosen for the different elements and modes are listed on Table 5. The duty ratios were generated by sending control signals to a PWM generator which employed a $10\mu\text{s}$ repeating ramp waveform. A constant PV voltage source was assumed for V_{in} , and a similar voltage source was used in the model to simulate an ideal rectified voltage from the grid. The Simulink model was run for 0.4 seconds and is depicted on Figure 34.

The battery chosen for this model was of a Nickel Metal Hydride with a nominal voltage of 50V. Other parameters taken into consideration include the number of cells in series, number

of cells in parallel, and the internal resistance. The nonlinear model of the battery showed a good approximation of real available NMH batteries in the market. The battery had 42 cells in series with nominal voltage of 1.18 volt for each cell with a maximum capacity of 7 AH for each cell. The total resistance of the battery was 0.0084 Ohms, with an internal resistance of 0.002 Ohms for each cell. Experimental validation of the model showed a maximum error of 5% (when SOC is between 10% and 100%) for charge and discharge dynamics.

Table 5

Simulation Parameters

Nominal Output Voltage	160 V	Inductor (L1)	0.8mH
Battery Voltage	50 V	Inductor (L2)	0.6mH
Initial Battery SOC%	0.5	Battery Type	NMH

5.2 Multi-Mode Converter Results

As seen on the circuit to the right in Figure 33, the diode is replaced with a bi-directional MOSFET and placed in series with L_1 , which will become essential to block the current from flowing into the PV source in the additional mode of operation. The four original modes are the Main Boost Mode, the Boost-Buck Mode, the Boost-Boost Mode, the Battery Boost Mode, and the Reverse Buck Mode. In the Main Boost mode, the single leg converter increases the voltage that is supplied to the inverter. In the Boost-Buck mode, energy is stored in the battery while voltage is supplied to the inverter or DC bus simultaneously. During high load demands, the Boost-Boost mode can supply the inverter with energy from the PV source and the battery simultaneously. And during cloud cover, energy can be supplied to the inverter from the battery in Battery-Boost mode.

In cases in which grid peak shaving is desired, the battery can be charged from the grid. The grid alone can supply the current to the battery through a buck operation. This new mode

was dubbed the Reverse Buck Mode. Times in which is critical to charge the battery from the grid include peak shaving during inclement weather or nights, when PV source cannot provide sufficient current to charge the battery, when the load demand drops, or to store energy during times when grid energy costs are low.

5.2.1 Main Boost Mode Results

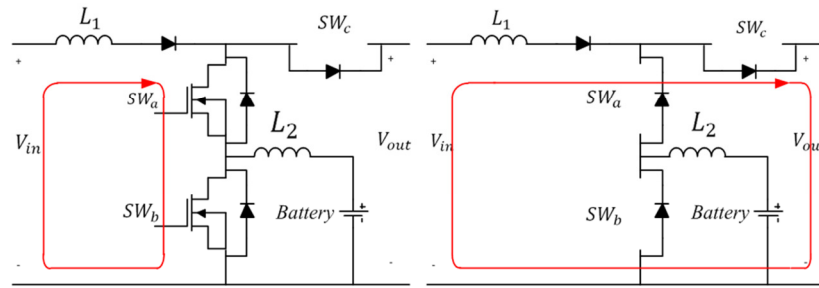


Fig. 35 Main Boost Mode power flow.

In this mode, SW_a and SW_b have the same duty ratio. Together, both switches form a boost converter that boosts the PV input voltage. During this mode, SW_c behaves as a diode by sending zero to its gate. The basic input to output principle of boost converters applies to this mode, as described in (5.1). Solving for the duty ratio, this mode yields (5.2).

$$V_{out} = \frac{V_{in}}{1-D} \quad (5.1)$$

$$D = \frac{T_{on}}{T_s} \quad (5.2)$$

The results for this mode are seen on Figure 36, where a duty ratio of 0.375 was sent to both switches, while SW_c remained off, acting as a diode.

5.2.2 Boost Buck Mode Results

For this mode, the duty ratio of SW_a is longer than SW_b . This way, the PV voltages are boosted during the time both SW_a and SW_b are “ON”. During the time SW_a remains “ON” and

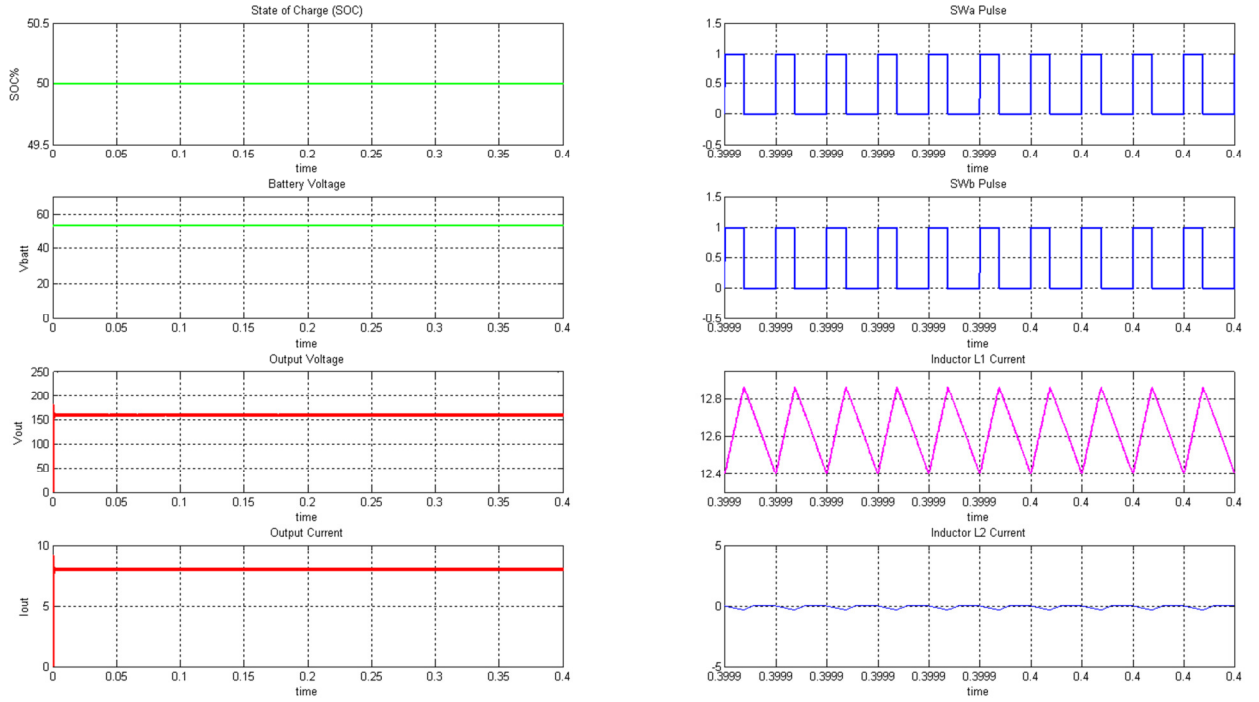


Fig. 36 Main Boost Mode results.

SW_b turns “OFF”, the PV supplies energy to the load and charges the battery. In this mode, SW_c behaves as a diode. This behavior is depicted on Figure 37. To determine the output of the converter boost operations for this mode, the output equation is (5.3), in which the duty ratio is solved as (5.4).

$$V_{out} = \frac{V_{in}}{1-D_{boost}} \quad (5.3)$$

$$D_{boost} = \frac{T_{on-boost}}{T_{s-boost}} \quad (5.4)$$

To charge the battery, the equations become (5.5), where the duty ratio is solved as (5.6).

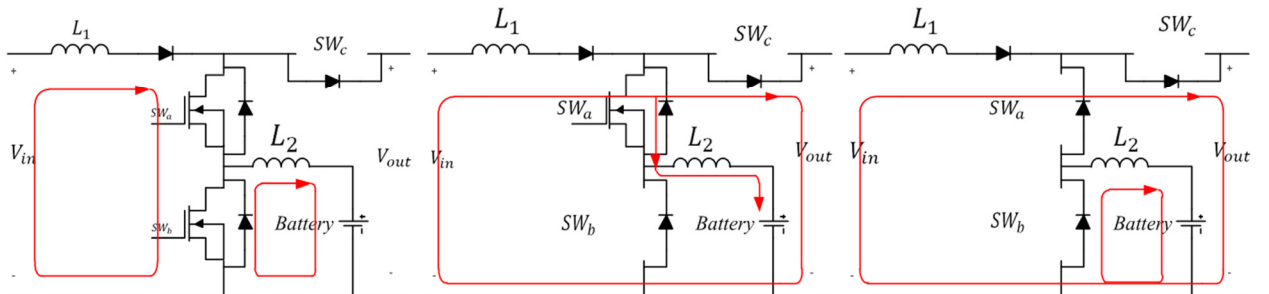


Fig. 37 Boost Buck Mode power flow.

$$V_{batt} = D_{buck} V_{in} \quad (5.5)$$

$$D_{buck} = \frac{T_{on-buck}}{T_{s-buck}} \quad (5.6)$$

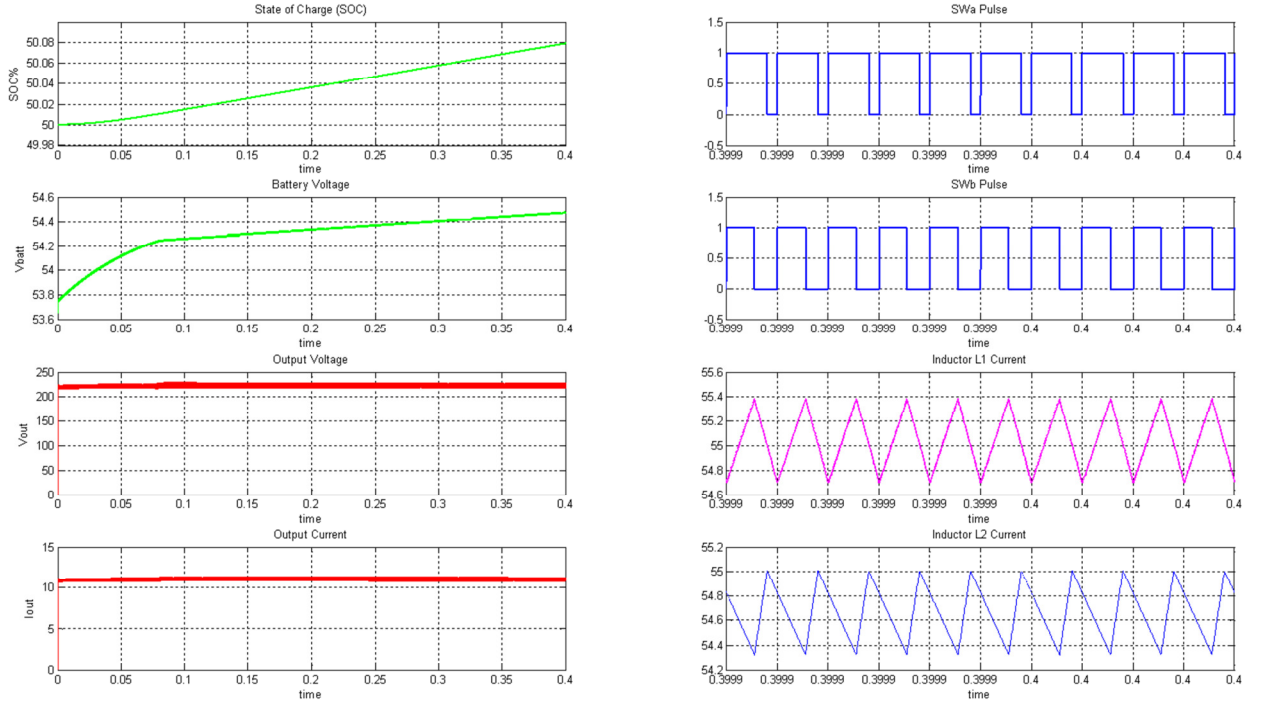


Fig. 38 Boost Buck Mode results.

5.2.3 Boost Boost Mode Results

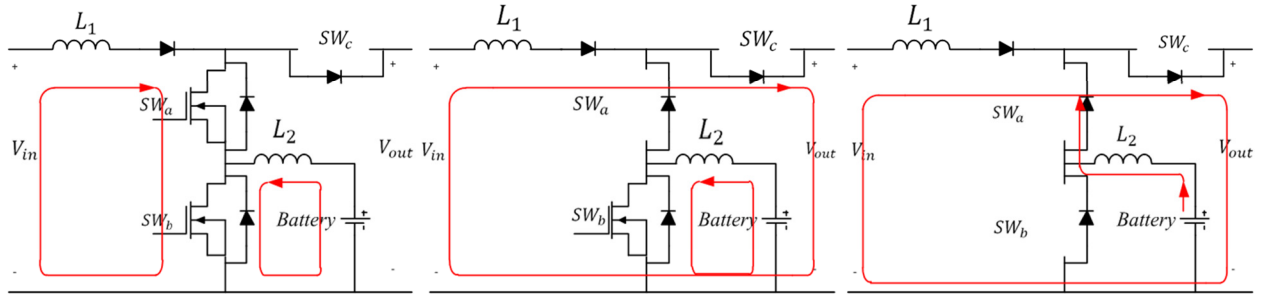


Fig. 39 Boost Boost Mode power flow.

In this mode, the opposite case from the Boost-Buck mode is the case, in which the duty ratio of SW_b is longer than SW_a 's. This allows the battery to discharge energy to the inverter when the PV energy generation is not sufficient. During this mode, SW_c behaves as a diode.

This mode boosts the input voltage while discharging the battery to supply the load. The output and duty ratio equations for this mode are (5.7) and (5.8), while the battery equations become (5.9) and (5.10). Figure 40 shows the Boost-Boost mode, which provides power to the grid from the grid and input sources.

$$V_{out} = \frac{V_{in}}{1-D_{boost1}} \quad (5.7)$$

$$D_{boost1} = \frac{T_{on-boost1}}{T_s} \quad (5.8)$$

$$V_{out} = \frac{V_{batt}}{1-D_{boost2}} \quad (5.9)$$

$$D_{boost2} = \frac{T_{on-boost2}}{T_s} \quad (5.10)$$

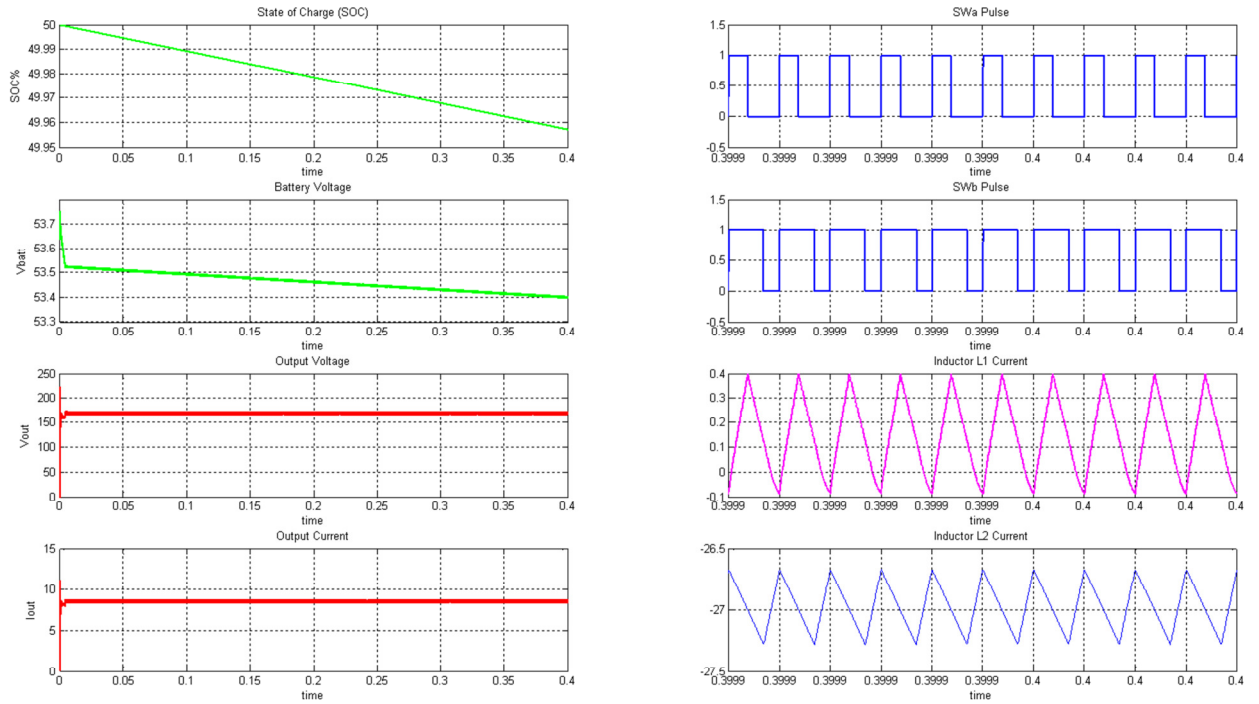


Fig. 40 Boost Boost Mode results.

5.2.4 Battery Boost Mode Results

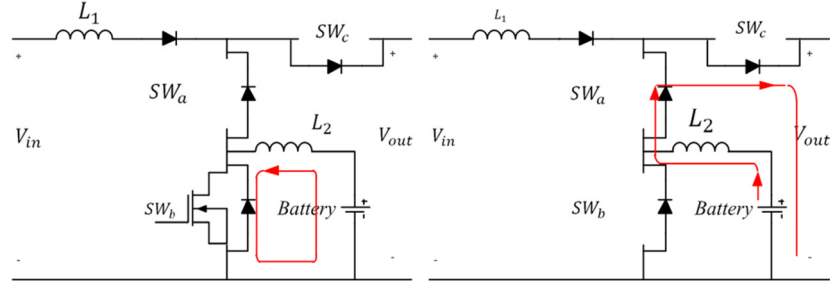


Fig. 41 Battery Boost Mode power flow.

The Battery Boost mode is useful in the case of input fault such as cloud cover, or damaged modules, etc. Since the modification to the converter, the state for SW_a is no longer relevant while SW_c acts as a diode. In this mode, the battery supplies the inverter with energy via the mathematical equations (5.11) and (5.12).

$$V_{out} = \frac{V_{batt}}{1-D} \quad (5.11)$$

$$D = \frac{T_{on}}{T_s} \quad (5.12)$$

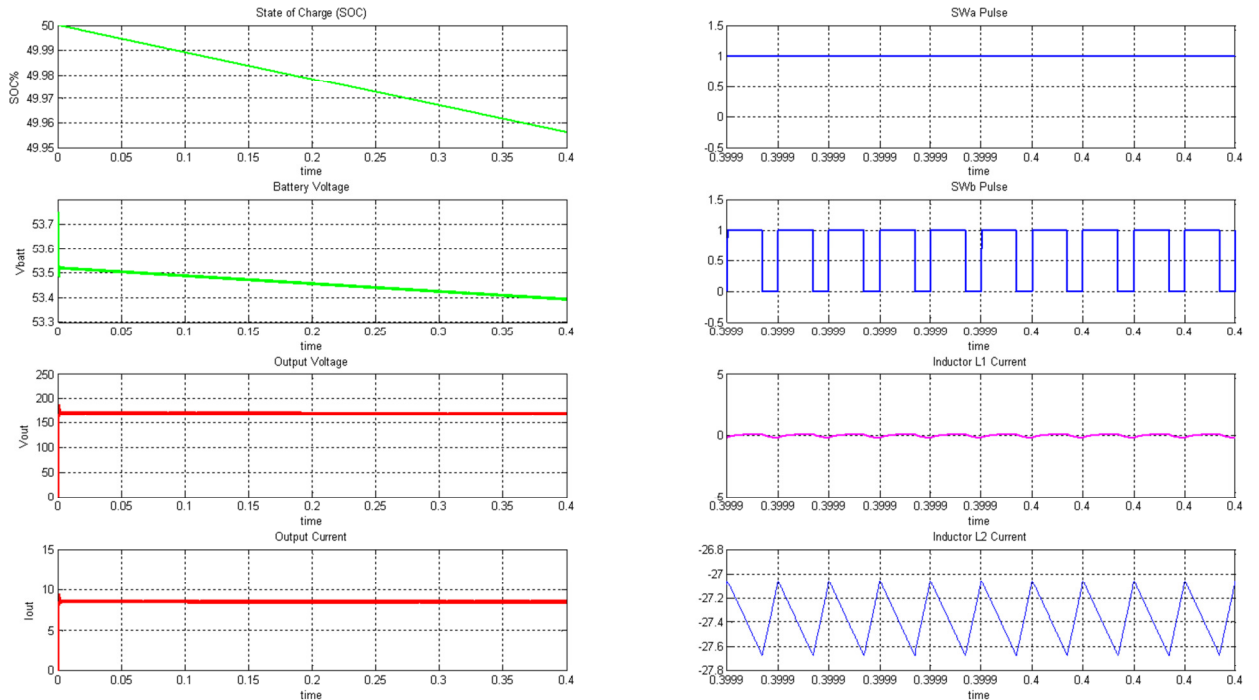


Fig. 42 Battery Boost Mode results.

5.2.5 Reverse Buck Mode Results

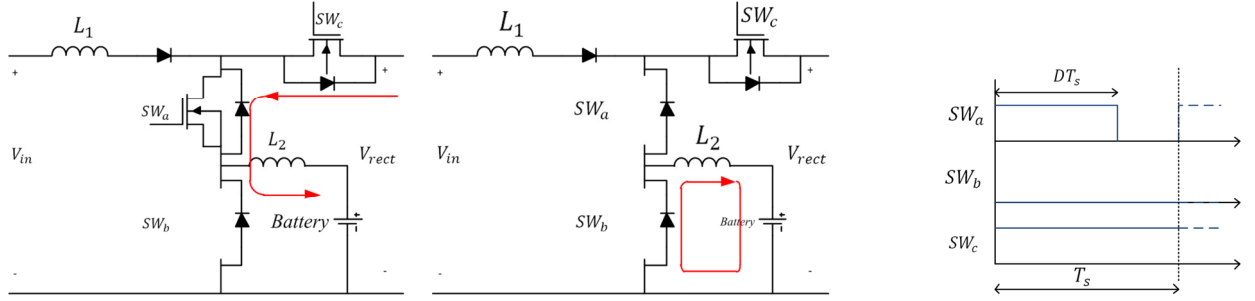


Fig. 43 Reverse Buck Mode power flow.

The Reverse Buck Mode benefits from the SW_c switch and makes use of the bi-directionality of the interconnected inverter. This is accomplished by either sending no pulses to the MOSFETs of the universal bridge, in essence converting the universal bridge into a full bridge rectifier, or by controlling the individual MOSFET switching cycles to achieve a desired DC voltage. Subsequently, this system converts the AC grid voltage into DC for battery charging. In this mode, SW_{c1} is “OFF”, SW_{c2} is “ON”, and SW_b is “OFF”. In this way, the battery is charged from the rectified grid voltage by varying the duty of SW_a . When the SW_a is “ON”, V_{rect} is transferred to the battery and the inductor current I_{L1} increases. This is mathematically expressed as (5.13).

$$\Delta I_{L2} = \frac{V_{rect} - V_{batt}}{L_2} DT_s \quad (5.13)$$

Where, ΔI_{L2} is the inductor ripple current. When SW_a is “OFF”, then inductor current in L_2 decreases in the rest of the period T_s . This is expressed as (5.14).

$$\Delta I_{L2} = \frac{V_{batt}}{L_2} (1 - D) T_s \quad (5.14)$$

By equating (5.13) and (5.14), the input to output relation is derived as (5.15).

$$V_{batt} = DV_{rect} \quad (5.15)$$

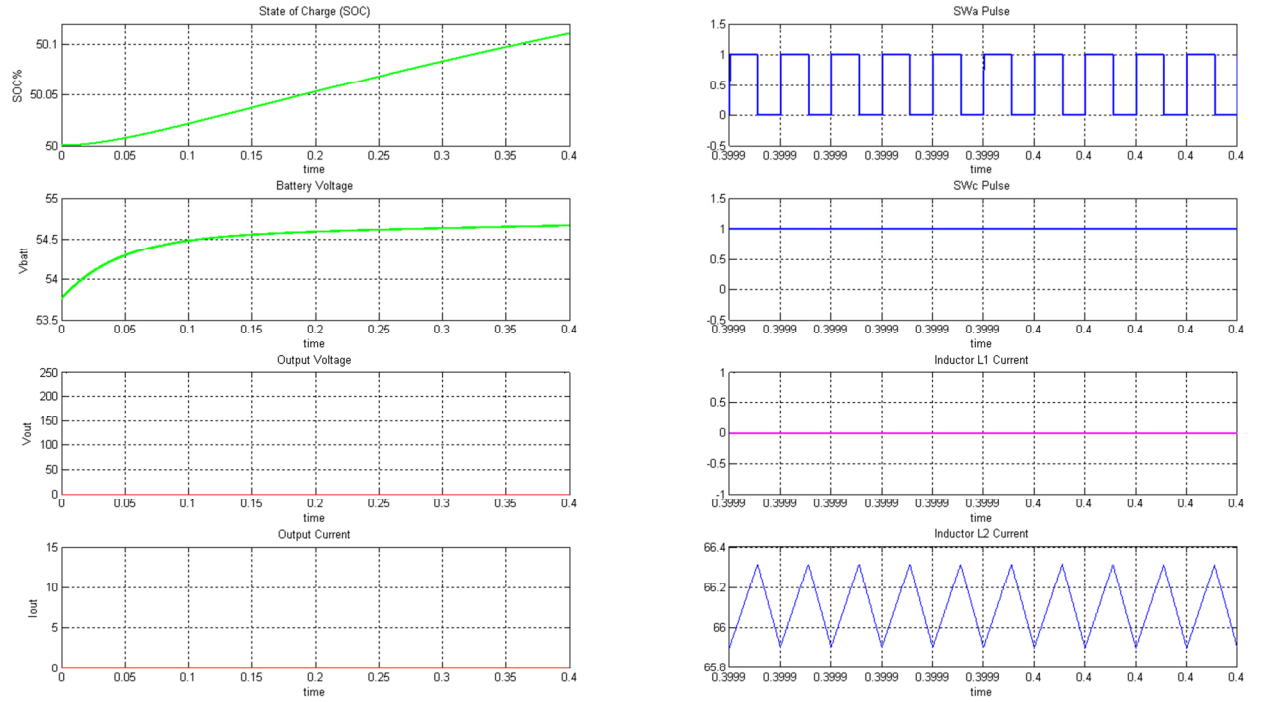


Fig. 44 Reverse Buck Mode results.

The Reverse Buck Mode simulation results are seen on Figure 44. The regulation of SW_a allowed the battery to be charged from the rectified grid voltage. At an initial battery state of charge (SOC) of 50%, the operating voltage of the battery was around 50V. Therefore, the battery would not charge for any duty cycle less than 0.5. This is due to duty cycle relationship of equation (5.15), re-expressed as (5.16).

$$\frac{V_{batt}}{V_{rect}} = D \approx \frac{50V}{100V} \quad (5.16)$$

5.3 Other Findings

The goal was to add smart grid functionalities to this novel application with the introduction of minimal switching elements that ultimately reduces power electronics costs of renewable energy systems. While it was only possible to charge the battery from the grid with

this configuration, charging the battery from both the PV source and the grid simultaneously present several challenges.

It is somewhat possible to charge the battery from two sources by modifying SW_c into a four quadrant operating switch (that is a MOSFET configuration that allows for the positive and negative exchange of voltage and current through it). The four-quadrant operating MOSFET is illustrated on Figure 45. The four-quadrant flexibility was used to preclude any current from flowing into each of the respective sources, and solely supply current to the battery. This mode is desired, for it could increase savings by storing the energy when the electric rate is low, and utilizing it when it is high in the following day(s).

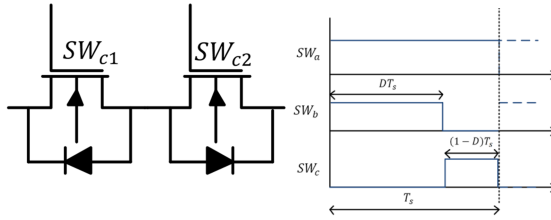


Fig.45 *Four Quadrant Bi-Directional Switch and The basic order of switching operation.*

In this mode, SW_a remains “ON” for the entire period while SW_{c1} is “OFF”, and SW_b becomes “ON” for $d_b T_s$ seconds. SW_{c2} may cycle “ON” for $d_c T_s$ seconds during the remaining period $(1 - d_b) T_s$

(See Fig. 45). Consequently, during the $d_b T_s$ the PV charges the L_1 inductor, which is the amount of energy that will be pushed into the battery when SW_b turns “OFF”. During this period of time, the grid remains disconnected from the battery. When SW_{c2} turns “ON”, the grid supplies energy to the battery for the remaining duration of time. It is during this period of time that both the PV and the grid should charge the battery. In the first scenario in which both SW_a and SW_b are “ON”, the ripple current of both inductors is calculated as (5.17) and (5.18).

$$\Delta I_{L2} = \frac{V_{bat} d_b T_s}{L_2} \quad (5.17)$$

$$\Delta I_{L1} = \frac{V_{in} d_b T_s}{L_1} \quad (5.18)$$

During the time that SW_{c2} turns “ON” and SW_b is “OFF”, the ripple current of both inductors are mathematically described by (5.19) and (5.20).

$$\Delta I'_{L2} = \frac{V_{rect} - V_{batt}}{L_2} d_c T_s \quad (5.19)$$

$$\Delta I'_{L1} = \frac{V_{in} - V_{rect}}{L_1} d_c T_s \quad (5.20)$$

However, unlike the previous method, equations (16) and (18) cannot be equated with (17) and (19) to find the input/output relationships. This is due to the inequality of inductor currents (L_1 and L_2) during the short time gap which SW_b and SW_{c2} are both “OFF”. Due to this characteristic, the input/output equations cannot be derived precisely.

CONCLUSION

Two major aspects of a PV inverter were modeled and simulated in MATLAB. Parameters were chosen consistently, to study the holistic feasibility of the dq-method, space vector modulation, and the proposed multi-mode converter. For the input side of the inverter, an existing multi-mode converter was improved by allowing additional interaction between the grid and interconnected PV systems. It was shown that the addition of an extra switch, in conjunction with a pulse width modulation scheme, were sufficient to charge an integrated battery from the grid. For the output side of the inverter, the synthesis of AC waveforms was demonstrated by using direct calculations of the SVM equations for high sampling frequencies. It was also demonstrated that the control of reactive power can be achieved using the Specifications for Smart Inverter Interactions with Electric Grids using IEC 6185 report with the synchronous reference frame, or dq, method.

BIBLIOGRAPHY

- [1] U.S. Energy Information Administration. (2011, April). Annual Energy Outlook 2011 with Projections to 2035. [On-line]. Available: www.eia.gov/forecasts/aeo/ [Oct 2011].
- [2] "IEEE Recommended Practices and Requirements for Harmonic Control in Electrical Power Systems," *IEEE Std 519-1992*, vol., no., pp.0_1, 1993
- [3] "IEEE Recommended Practice for Utility Interface of Photovoltaic (PV) Systems," *IEEE Std 929-2000*, vol., no., pp.i, 2000
- [4] Ipakchi, A.; Albuyeh, F.; , "Grid of the future," *Power and Energy Magazine, IEEE*, vol.7, no.2, pp.52-62, March-April 2009
- [5] E. Hirst and B. Kirby, "Electric-Power Ancillary Services", *ORNL/CON-426, Oak Ridge National Laboratory*, Oak Ridge, TN, January 1996.
- [6] N. Mohan, T. Underland, and W. Robbins, "Power electronics converters, applications, and design", Wiley, 3rd ed., 2003
- [7] A. Keyhani, M. N. Marwalli, and M. Dai, "Power flow control of a single distributed generation unit," in *Integration of Green and Renewable Energy in Electric Power Systems*, New Jersey: Wiley, 2010, ch. 6, pp 179-202.
- [8] N. Mohan, "First Course on Power Electronics", Minneapolis: MNPERE, 2009,
- [9] A. Keyhani, M. N. Marwalli, and M. Dai, "Power flow control of a single distributed generation unit," in *Integration of Green and Renewable Energy in Electric Power Systems*, New Jersey: Wiley, 2010, ch. 6, pp 179-202.
- [10] Turitsyn, K.; Sulc, P.; Backhaus, S.; Chertkov, M.; , "Options for Control of Reactive Power by Distributed Photovoltaic Generators," *Proceedings of the IEEE*, vol.99, no.6, pp.1063-1073, June 2011
- [11] Piegari, L.; Tricoli, P.; , "A control algorithm of power converters in smart-grids for providing uninterruptible ancillary services," *Harmonics and Quality of Power (ICHQP), 2010 14th International Conference on*, vol., no., pp.1-7, 26-29 Sept. 2010.
- [12] Bo, Dong; Li, Yongdong; Zheng, Zedong; , "Energy management of hybrid DC and AC bus linked microgrid," *Power Electronics for Distributed Generation Systems (PEDG), 2010 2nd IEEE International Symposium on*, vol., no., pp.713-716, 16-18 June 2010
- [13] T. Noguchi, H. Tomiki, S. Kondo, and I. Takahashi, "Direct power control of PWM converter without power-source voltage sensors" *IEEE Trans. Ind. Appl.*, vol. 34, no. 3, pp.473-479, May/Jun. 1998.

- [14] J. Hu; L. Shang; Y. He; Zhu, Z.Z.; , "Direct Active and Reactive Power Regulation of Grid-Connected DC/AC Converters Using Sliding Mode Control Approach," *Power Electronics, IEEE Transactions on* , vol.26, no.1, pp.210-222, Jan. 2011
- [15] J. Gong; J. Lu; D. Xie; Y. Zhang; , "A new-style dynamic var compensation control strategy," *Electric Utility Deregulation and Restructuring and Power Technologies, 2008. DRPT 2008. Third International Conference on* , vol., no., pp.1625-1630, 6-9 April 2008
- [16] Blaabjerg, F.; Teodorescu, R.; Liserre, M.; Timbus, A.V.; , "Overview of Control and Grid Synchronization for Distributed Power Generation Systems,"*Industrial Electronics, IEEE Transactions on*, vol.53, no.5, pp.1398-1409, Oct. 2006
- [17] S. Buso and P. Mattavelli. "Extension to Three Phase Inverters" in *Digital Control in Power Electronics*, USA: Morgan & Claypool Publishers, 2006, pp.81-107
- [18] Schauder, C.; Mehta, H.; , "Vector analysis and control of advanced static VAR compensators," *Generation, Transmission and Distribution, IEE Proceedings C* , vol.140, no.4, pp.299-306, Jul 1993
- [19] *Specifications for Smart Inverter Interactions with Electric Grids using International Electrotechnical Commission 61850* report
- [20] R. Teodorescu and F. Blaabjerg, "Proportional-resonant controllers. A new breed of controllers suitable for grid-connected voltage-source converters," in *Proc. OPTIM*, 2004, vol. 3, pp. 9–14
- [21] "IEEE Standard Conformance Test Procedures for Equipment Interconnecting Distributed Resources With Electric Power Systems," *IEEE Std 1547.1-2005* , vol., no., pp.0_1-54, 2005
- [22] Taesik Park; Taehyung Kim; , "Novel multi-mode single leg converter for renewable energy conversion systems," *Industrial Technology (ICIT), 2011 IEEE International Conference on* , vol., no., pp.198-203,14-16 March 2011

VITA

Emiliano Morales was born and raised in the border town of Eagle Pass, Texas. He is the first male of his extended family to graduate from a University with a Master's degree. His Bachelor degree was in Electrical Engineering and concentrated in computer engineering. His Master's research focused primarily on the renewable energy field. His future plans include becoming part of the Navy as an active duty Officer, continue his education, and traveling the world in humanitarian missions.

Section 4:

**Advance Metering
Infrastructure and
Communications**

Modified Intelligent Energy Management system in a smart house¹

Dariusz Shahgoshtasbi

Electrical Engineering Department
University of Texas at San Antonio
San Antonio, TX, USA
isjd@wacong.org

Mo Jamshidi

Electrical Engineering Department
University of Texas at San Antonio
San Antonio, TX, USA
moj@wacong.org

Abstract— Demand response has an important role in improving energy efficiency. By using it, we are able to shift electrical load from peak demand time to other periods which is usually in response to price signal. In residential level and in a dynamic pricing system which modification of energy consumption is unrecognized by a consumer, using an automated Energy Management System (EMS) should be considered. In this paper, which is the modified version of our last work, an intelligent EMS in a smart house is presented¹. It has two components, fuzzy component and intelligent lookup table. Fuzzy component is in the EMS and makes the proper output for intelligent lookup table based on its fuzzy rules and inputs. The second component which its core is an associative neural network is moved to smart appliances. So each appliance has a separate intelligent lookup table. They are able to map inputs to desired outputs. They take three types of inputs which come from fuzzy component, outside sensors and other smart appliances. So, all the appliances should send their control bits to each other. Whatever is trained in these lookup tables are different scenarios in different conditions. This system is able to find the best energy efficiency scenario in different situations.

Keywords- Energy Efficiency, Demand Response, Smart Grid, Fuzzy logic, Neural Networks.

I. INTRODUCTION

Smart Grid is a novel initiative which its aim is to deliver energy to the users and also to achieve consumption efficiency by means of bidirectional communication [2]. Combination of different hardware devices and software along with an ICT infrastructure for a bidirectional communication make the smart grid architecture. ICT has a vital rule in the smart grid architecture as it gives sustainability, creativity and intelligence to it. This electricity network is able to intelligently integrate the actions of all users which are connected to it in order to return them back to users. Users can use this information to optimize their energy consumption. Thus, one of the main objectives of smart grid is encouraging end users to participate in making decision about energy consumption in an efficient way. But in order to reach energy efficiency, such architecture is not enough. We need to add intelligence to it in different levels. In home level, the approach is to add intelligence and then encourage customers to save energy by changing their

energy consumption behavior. So, demand response can be in response to an economical signal which is mostly a pricing signal. By using demand response, we are able to shift electrical load from peak demand time to other periods which reduces the ratio of peak to average load. This can be resulted in improving efficiency, reducing costs and risk of outages. Demand response can be done on different levels like generation, transmission or end user level. A lot of works has been done on generation and transmission levels [2][3][5][6][7][8]. In the end user level, the smart grid is not only able to provide information about electricity consumption for both users and network operators, but also is able to connect renewable energy resources to the grid. In the residential or end user level demand response, challenges include real time pricing information to consumer, networking home devices, security and implementing automated Energy Management Systems (EMS) should be considered. In this paper, which is the modified version of our last work [1], an intelligent EMS system is presented. It takes inputs from the grid and by using an intelligent algorithm, tries to find effective and efficient energy consumption. It also can be matched by users' preferences and behaviors and then find optimal energy scheduling according to the dynamic notion of price. This approach is useful especially in a dynamic pricing system

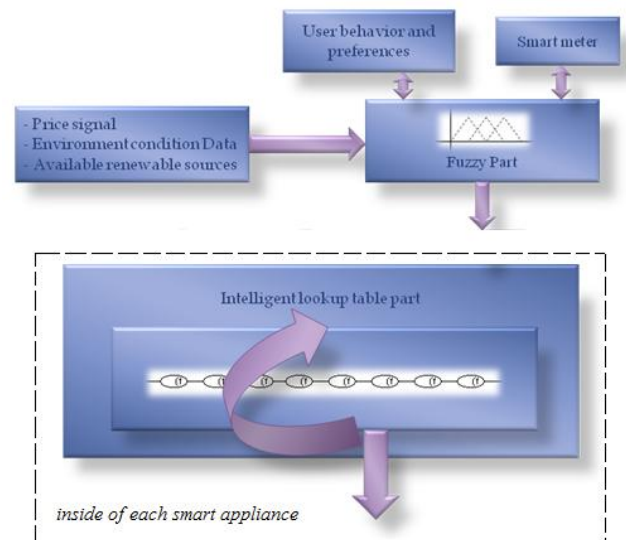


Figure 1. Modified automated EMS

¹ This work was supported, in part, by a grant from CPS Energy through Texas Sustainable Energy Research Institute and Lucher Brown Chair, the University of Texas, San Antonio, TX, USA.

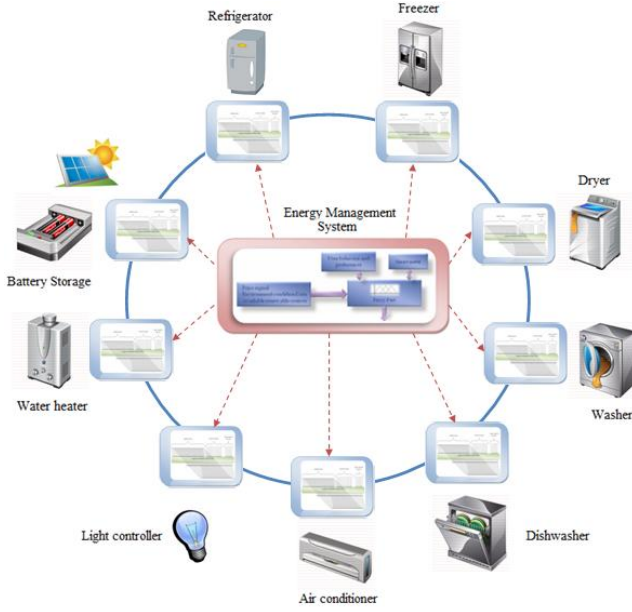


Figure 2. Smart appliances connection.

which modification of energy consumption is unrecognized by and renewable resources or can be human behavior and a consumer. The suggested system has two components as it is shown in Figure 1. The first component is a fuzzy system which its inputs can be external events like price signal, environment condition data preferences. This component which is inside the EMS has some fuzzy rules along with their membership functions which make appropriate output for the second component which is intelligent lookup table. The reason of using Fuzzy component is to get real time changeable external information and find the best system situation based on the fuzzy rules and then by using centralized defuzzification get a unique number in the output range. The second and the main component is intelligent lookup table which is moved to smart appliances. So each appliance has a separate intelligent lookup table. The reason of doing that is to have a very simple structure of neural network which will be resulted in fewer scenarios in each appliance. In this situation all of the appliances should send some control bits to each other. Therefore, they should be connected to each other as it is shown in Figure 2. The Intelligent lookup table is made by using a new topology of neural network [4]. The output part of this topology is modified. By using this modification which will be explained in section III, we are able to connect more inputs to the neural network. The first reason of using this type of neural network is that its structure is crystal type and can be easily extended for more inputs and the second reason is that it is able to act as an associative memory to map inputs to desired outputs. This paper is organized as follows. In Section II, the fuzzy component of the system is explained. In section III, the structure of the intelligent lookup table, its training and functionality are described and in section IV, the simulation of the suggested approach is shown.

II. FUZZY LOGIC COMPONENT

This component has 5 types of inputs. The first one is price signal which comes from the smart meter, the second one is battery storage situation, and the rest are environment condition

data like humidity, temperature and solar as their membership functions are depicted in Figure 3. These inputs are divided into two categories. Price signal, battery storage and solar inputs are in the first category which makes a unique and appropriate input for the intelligent lookup table. The output of this category has 7 membership functions which gives us the energy consumption situation in the grid. These 7 fuzzy sets are Neutral-, Neutral+, Normal, High-, High+, Peak- and Peak+ which are selected based on the fuzzy rules and mapping of input values to their appropriate membership functions. Finally the resulting set is defuzzified by Centriod defuzzification technique and gets a single number as (1).

$$x^* = \frac{\int \mu_i(x) x dx}{\int \mu_i(x) dx} \quad (1)$$

Where x^* is the defuzzified output, $\mu_i(x)$ is the aggregated membership function and x is the output variable. This number is rounded and its binary value goes to the intelligent lookup table. The second category of this component which contains environment condition data makes some input control signals to the second component which will be explained in the next section. The fuzzy rules and membership function values are set based on our knowledge from the grid and the environment. These values can be changed by human behavior and preferences. The behavior and preferences are logged and if there are any changes in them (like A/C setting), the system just modifies the initial membership values.

III. INTELLIGENT LOOKUP TABLE COMPONENT

A. Structure

The main part of this system has a crystal structure with cells as shown in Figure 4-a. As it can be seen, each cell is constructed of two middle neurons and four side neurons such that the two upper ones have fixed weights and the two lower ones have trainable weights. The two upper neurons and also the middle neurons have linear function and the two lower ones have a sigmoid function as (2).

$$y = \frac{1 + e^{-\lambda x}}{1 - e^{-\lambda x}} \quad (2)$$

The neurons of this layer receive their binary inputs from the previous layer. Figure 4-a can be summarized as Figure 4-b. For each cell we have:

$$f(n) = f(n-1) \times (f(input_n \times W_p) + f(\overline{input_n} \times W_q)), \quad f(0) = c \quad (3)$$

Where n is the input cell number. In Figure 4-a, if $input_n$, which is the complement of $\overline{input_n}$, gets value 1, the first and the forth neuron will fire whereas if it gets 0, the second and third neurons do so. In the training step, only active neurons are trained. The characteristic of the lower neurons is that the increasing and decreasing rate of the weight changes are not equivalent during the training step as will be explain in section III.B. In each cell, there are only two active neurons at a time and the output of that cell enters as input to the succeeding cell. If each input consists of n bits, cells would be connected as a chain up to the $(n-1)th$ input. The only remaining input is n where the output of the chained string is connected to $\frac{2^n}{2}$ of this

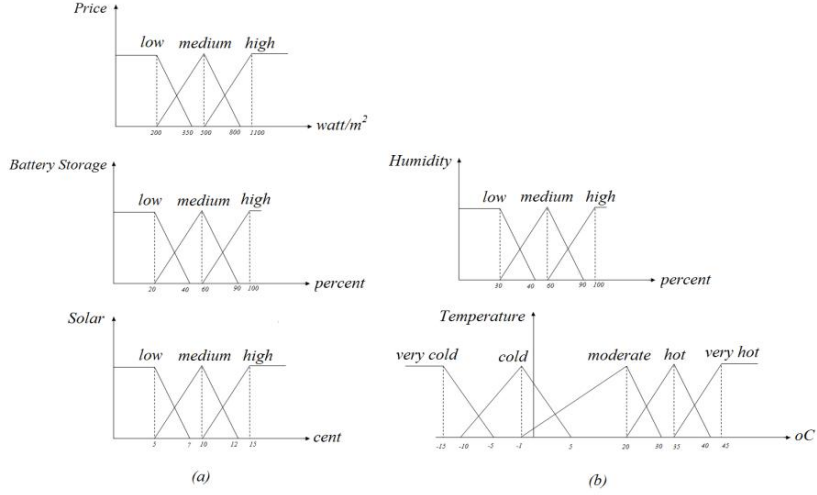


Figure 3. Fuzzy membership functions for the fuzzy component. (a): Category 1. (b): Category 2.

input cell. We call this layer the parallel layer as its cells are parallel to each other. In this layer, only one cell of input n is selected. With this selection, we reach our desired memory cell.

For networks with more than one output, $\frac{2^n}{2}$ of input cell n are added to the parallel layer for each output. These added cells are only used for adjustment of all outputs except the first one. They have no influence on the adjustment of other weights. On the other word, the weights of the network are adjusted only by the first output and the other outputs are adjusted by the weights of added input cells in the parallel layer [4]. Figure 5 shows this structure for an example network with 3 inputs and 2 outputs. The problem of using this type of network is when we have a lot of inputs, the number of cells in parallel layer increase dramatically. On the other hand, we increase the capacity of associative memory, but most of the cells in parallel layer will be never used. In order to solve the problem, instead of having $\frac{2^n}{2}$ cell in parallel layer, we consider m cells and by using a mapping table, each used output is mapped to one of these m considered cells. In order to make an intelligent lookup table by the suggested neural network, we create feedbacks from outputs of the network to its inputs as it is depicted in Figure 6. This makes a sequential system with memory. In this situation, next outputs will be made based on the present inputs and feedback outputs. As it was mentioned earlier, the system has three types of inputs; the first type comes directly from the fuzzy component and is a unique value which shows energy consumption situation in the grid. This input is connected to n first inputs of neural networks and implies the network which scenario should be started. The second type of inputs is some control bits which come either from fuzzy component or some outside sensors and the last type are feedback outputs. All of

the inputs together based on their conditions make different scenarios for the intelligent lookup table. Control bits can show for example water heater, air conditioner, refrigerator and other appliances situation in the smart house. Also they can be battery storage and solar situation which come from the fuzzy component. This intelligent lookup table should be trained based on the different inputs and control bits.

B. Learning

The algorithm of network training is a way to decode the problem to be solved [9]. The learning of this network is supervised. The single layer perceptron learning rule is used to train this network [10]:

$$W_j(t+1) = W_j(t) + \eta \times (Train_{out} - out) \times In_p \quad (4)$$

Where W is the weight, j is the input cell number, In_p is the input of that cell, out is the output of the network and $Train_{out}$ is the desired output. The important point is that using the learning rule of single layer perceptron for this multi-layer network makes learning easy. The way of using this rule is presented here. As mentioned earlier, only active neurons are trained and in each cell there is only one lower active neuron at a time. So the Eq. (4) can be rewritten as:

$$W_j(t+1) = W_j(t) + SelectNeuron \times \eta \times (Train_{out} - out) \times In_p \quad (5)$$

In each layer, the η values which have been used for the stabilization of weights are smaller when weights increase than when they decrease. This always makes weights decreasing values larger than weights increasing values. These increasing and decreasing values are reduced in subsequent layers. The reason is that in binary numbers, the bit toggle frequency is halved when we move from LSB bits toward MSB bits. Since the inputs of the suggested network are binary, considering η as mentioned, will cause the changes of weights to become slower in subsequent layers. On the other words, weights change with lower frequency for 2^n sequential

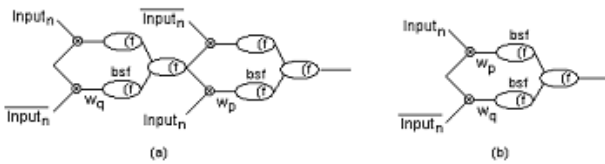


Figure 4. One cell of the network in the associative memory layer (a): Original Shape, (b): The summary of part a.

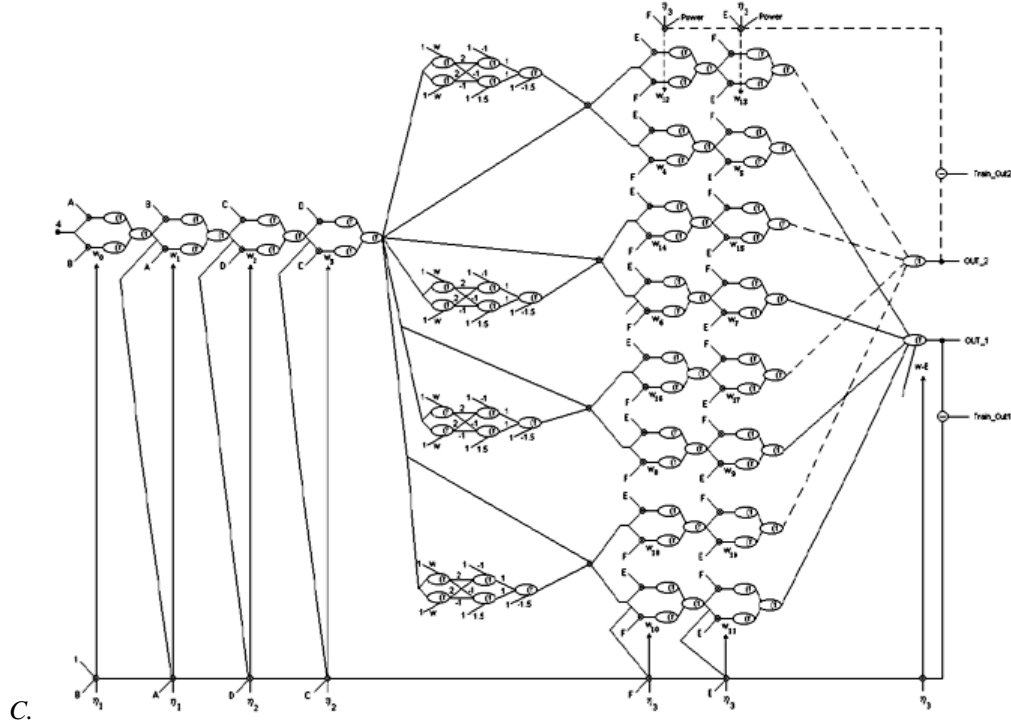


Figure 5. The structure of the associative memory layer with 3 inputs and 2 outputs. A,C,E are inputs and B,D,F are their complements.

binary inputs. Considering the first layer as MSB and moving toward parallel layer as moving to LSB, the weight toggles would be less for the neurons of input cell n which are in the last layer and frequency of changes in their inputs is more than other cells. Due to the fact that the output error creates feedbacks to all layers, the weights of all active neurons will decrease or increase if this error becomes negative or positive respectively. But since η values are not equal, their increasing and decreasing rate would be different in each layer. By this method the network can be stabilized and get adjusted to 2^n input forms which result in the convergence of weights [4]. Experiments show that in case of having more than one output, it is better to consider a coefficient *Power* to adjust the weights of all outputs except the first one to expedite the convergence of weights.

D. Functionality

This network acts as an associative memory and is able to map a set of inputs to a desired output. Whatever will be

trained in the network are different scenarios (based on different conditions) and connection between them. It can be trained in a certain time and mostly maps outputs based on the previous learning. The system will be trained when we have a new scenario or we intend to change one. This characteristic of the suggested lookup table gives the system speed and reliability which are two important items in the field of energy in a smart house. Scenarios in the mentioned intelligent lookup table are connected to each other in a way which suggest the best energy efficiency for appliances in the smart house. In fact, this system predicts outputs based on control bits and fuzzy inputs. For example, if a smart house has both battery storage and solar system and weather forecast information shows that we would have a cloudy weather in the next hours (which solar would not work), if the control bit is set and imply the battery storage needs to be charged, the system charges it in order to use its energy in the future peak hours. As it was mentioned before, each smart appliance has a separate intelligent lookup table. The first step is that all the appliances

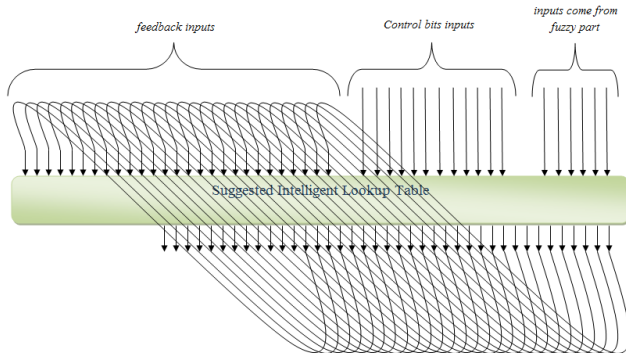


Figure 6. The intelligent lookup table structure.

Algorithm for Smart Appliances

```

1: The first highest priority node sends control bit information to the second one
2: The second one adds its control bit information to it and sends them to the third one and so on
3: The last one adds its control bit information and sends all the control bit information to the first one
4: do {
5:   fuzzy_output_change ← checkfuzzyoutput()
6: } while (fuzzy_output_change != True)
7: do {
8:   if (fuzzy_output_change == True) then
9:     findbestscenariobasedoninputs()
10:    fuzzy_output_change ← checkfuzzyoutput()
11:    a_node_control_bit_information_changes ← controlbitchanges()
12:    if (a_node_control_bit_information_changes == True) then
13:      sendcontrolbittoothers()
14: } while (True)

```

Figure 7. Algorithm for Smart Appliances.

should send their control bits to each other. We consider priority for our appliances. The priority can be in the plug which the appliances is connected to. The highest priority appliance sends its control bit information to the second one. It is clear that if the second one is turned off or is not plugged in, the third one will be considered as the second one. The second one adds its control bit information to it and sends them to the third one. This process continues to reach the last one. The last one adds its control bit information and sends all the control bit information to the first one. Therefore, all the appliances have all the control bits. After that all the intelligent lookup tables are waiting for inputs from Fuzzy component. When they

receive it, each intelligent lookup table tries to find the best scenario for its appliances based on the inputs and whatever they have been trained. This algorithm is shown in Figure 7. We just have n Scenarios which the connections between them in different situations are trained in the network.

IV. SIMULATION

For simulation of the mentioned system, we consider a smart house with water heater, air conditioner, light, solar panel, battery storage, refrigerator, freezer, dishwasher, washer and dryer. The fuzzy component of the simulation has 5 types of inputs along with membership functions as they are shown in Figure 3. In the first category, we have 15 fuzzy rules which make proper inputs for the intelligent lookup table. These fuzzy rules are shown in Figure 8. An associative memory with 38 inputs and 18 outputs is designed. Totally 4096 cells are considered for its parallel layer. The outputs of the fuzzy component enter the first six inputs of the network. We consider 12 control bits which enter the network as next inputs. These control bits are for solar, battery storage and home appliances situations. The rest inputs come from feedback

Algorithm for Energy Management System

- 1: If (cost is low) then output \leftarrow neutral_minus
- 2: If (cost is medium and battery is high and solar is high) then output \leftarrow neutral_plus
- 3: If (cost is medium and battery is high and solar is medium) then output \leftarrow neutral_plus
- 4: If (cost is medium and battery is high and solar is low) then output \leftarrow normal
- 5: If (cost is medium and battery is medium and solar is high) then output \leftarrow normal
- 6: If (cost is medium and battery is medium and solar is medium) then output \leftarrow normal
- 7: If (cost is medium and battery is medium and solar is low) then output \leftarrow high_minus
- 8: If (cost is medium and battery is low and solar is high) then output \leftarrow high_minus
- 9: If (cost is medium and battery is low and solar is medium) then output \leftarrow high_plus
- 10: If (cost is medium and battery is low and solar is low) then output \leftarrow high_plus
- 11: If (cost is high and battery is high) then output \leftarrow peak_minus
- 12: If (cost is high and battery is medium and solar is high) then output \leftarrow peak_minus
- 13: If (cost is high and battery is medium and solar is medium) then output \leftarrow peak_minus
- 14: If (cost is high and battery is medium and solar is low) then output \leftarrow peak_plus
- 15: If (cost is high and battery is low) then output \leftarrow peak_plus

Figure 8. Fuzzy rules for the intelligent Energy Management System

outputs. Seventeen different scenarios are defined and based on different conditions; proper scenarios are trained to each neural network. These scenarios are shown in Table 1. The weight changes are shown in Figure 9. As shown in this figure, the weights stabilize after 25 samples which shows that this kind of connection between neurons results in weight convergence to the desired output. The figure also shows that the weight changes in cells toward parallel layer are reduced which indicates the stabilization of the network. Figure 10 and 11 show the weight changes for two lower trainable weights in parallel layer for all of the training situations. They show that weight changes are limited and also for all of the outputs are very close to each other. For the simulation result, the mentioned house is simulated in GridLAB-D software and the results of real power with and without using the intelligent EMS during one day (24 hours) are compared. As it is shown in Figure 12, by applying the intelligent EMS in the house, the energy consumption is moved from peak hour to non-peak hour by the system.

TABLE I. SEVENTEEN DEFINED SCENARIOS FOR ENERGY EFFICIENCY IN A SMART HOUSE

No.	Scenario
1	Charge battery by grid
2	Charge battery by solar
3	Turn on water heater
4	Turn on air conditioner
5	Turn on dishwasher if programmed on
6	Turn on washer if programmed on
7	Turn on dryer if programmed on
8	Give portion of energy to dishwasher if programmed on
9	Give portion of energy to washer if programmed on
10	Give portion of energy to dryer if programmed on
11	Give portion of energy to refrigerator if needed (on)
12	Give portion of energy to freezer if needed (on)
13	Turn off dishwasher
14	Turn off washer
15	Turn off dryer
16	Get energy from battery storage
17	Turn on light controller

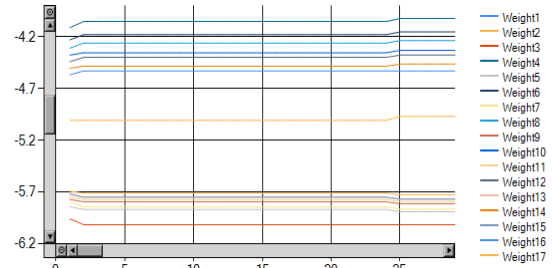


Figure 9. The value of weight changes for simulation of system with 38 inputs and 18 outputs.

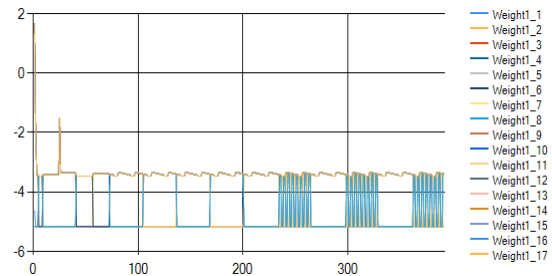


Figure 10. Weight changes for the first lower trainable weight in parallel layer for all of the training situations.

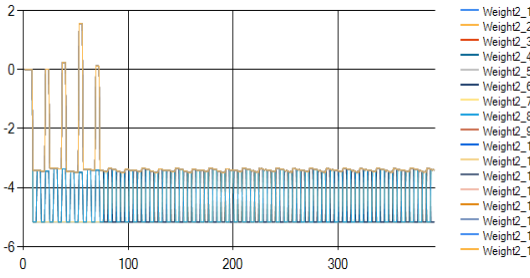


Figure 11. Weight changes for the second lower trainable weight in parallel layer for all of the training situations.

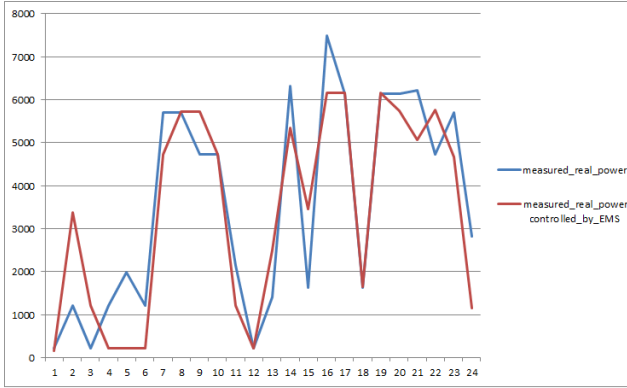


Figure 12. Comparing measured power with and without applying the intelligent EMS to the system during one day (24 hours).

V. CONCLUSIONS

The modified version of our previous work as an automated Energy management system (EMS) for residential level is presented. The suggested system has two components, fuzzy component and intelligent lookup table. The fuzzy component which is in the EMS has 15 fuzzy rules along with membership functions which makes appropriate outputs for the intelligent lookup table component. The intelligent lookup table is an associative neural network which is moved to smart appliances. Therefore, each appliance has a separate intelligent lookup table. They map inputs to desired outputs. They can be trained based on the different scenarios and connections between them. This method makes the structure of neural networks simpler which is resulted in faster convergence of weights. The intelligent lookup table has three types of inputs. The first type comes directly from the fuzzy component. The second type is control bits which come either from the fuzzy component or some outside sensors and the last type of inputs is feedbacks from its outputs. This automated energy management system is able to find the best energy efficiency scenario in different situations.

REFERENCES

- [1] D. Shahgoshtasbi, Mo Jamshidi, "Energy efficiency in a smart house with an intelligent Neuro-Fuzzy lookup table", The 6th IEEE international conference on System of Systems Engineering (SOSE 2011), Albuquerque, NM, USA, 2011.
- [2] Omid Siakani, O. Hussian, T. Dillon, A. Tabesh, "Intelligent Decision Support System for Including Consumers' Preferences in Residential Energy Consumption in Smart Grid", Second International Conference on Computational Intelligence, Modelling and Simulation, 2010.
- [3] T. R. Kuhn, "Energizing Efficiency's Potential," The Electricity Journal, vol. 19, pp. 83-87, 2006.
- [4] D. Shahgoshtasbi, "A New Topology of Neural Network for Memory Simulation", World Automation Congress, Seville, Spain, 2004.
- [5] R. Earle, E. P. Kahn, and E. Macan, "Measuring the Capacity Impacts of Demand Response," The Electricity Journal, vol. 22, pp. 47-58, 2009.
- [6] O. Sezgen, C. A. Goldman, and P. Krishnarao, "Option value of electricity demand response," Energy, vol. 32, pp. 108-119, 2007.
- [7] J. Sancho, J. Sánchez-Soriano, J. A. Chazarra, and J. Aparicio, "Design and implementation of a decision support system for competitive electricity markets," Decision Support Systems, vol. 44, pp. 765-784, 2008.
- [8] D. Coll-Mayor, M. Paget, and E. Lightner, "Future intelligent power grids: Analysis of the vision in the European Union and the United States," Energy Policy, vol. 35, pp. 2453-2465, 2007.
- [9] Cornelius T. Leondes, "Algorithms and architectures", Academic Press, 1998.
- [10] R. J. Schalkoff, "Artificial Neural Network", McGraw-Hill, International, 1997.

Energy efficiency in a smart house with an intelligent Neuro-Fuzzy lookup table¹

Dariush Shahgoshtasbi

Electrical Engineering Department
University of Texas at San Antonio
San Antonio, TX, USA
isjd@wacong.org

Mo Jamshidi

Electrical Engineering Department
University of Texas at San Antonio
San Antonio, TX, USA
moj@wacong.org

Abstract - Demand response has an important role in improving energy efficiency. By using it, we can shift electrical load from peak demand time to other periods which is usually in response to price signal. In residential level and in a dynamic pricing system which modification of energy consumption is unrecognized by a consumer, using an automated Energy Management System (EMS) should be considered. In this paper, a new intelligent EMS in a smart house is presented¹. It has two parts, fuzzy part and intelligent lookup table. Fuzzy part based on its fuzzy rules and inputs makes the proper output for intelligent lookup table. The second part which its core is an associative neural network is able to map inputs to desired outputs. It takes two types of inputs which come from fuzzy part and outside sensors. Whatever is trained in this lookup table are different scenarios in different conditions. This system is able to find the best energy efficiency scenario in different situations.

Keywords: Energy Efficiency, Demand Response, Smart Grid, Fuzzy logic, Neural Networks.

1 Introduction

Smart Grid is a novel initiative which its aim is to deliver energy to the users and also to achieve consumption efficiency by means of bidirectional communication [1]. Combination of different hardware devices and software along with an ICT infrastructure for a bidirectional communication make the smart grid architecture. ICT has a vital rule in the smart grid architecture as it gives sustainability, creativity and intelligence to it. This electricity network is able to intelligently integrate the actions of all users which are connected to it in order to return them back to users. Users can use this information to optimize their energy consumption. Thus, one of the main objectives of smart grid is encouraging end users to participate in making decision about energy consumption in an efficient way. But in order to reach energy efficiency, such architecture is not enough. We need to add intelligence to it in different levels. In home level, the approach is to add

intelligence and then encourage customers to save energy by changing their energy consumption behavior. So, demand response can be in response to an economical signal which is mostly a pricing signal. By using demand response, we are able to shift electrical load from peak demand time to other periods which reduces the ratio of peak to average load. This can be resulted in improving efficiency, reducing costs and risk of outages. Demand response can be done on different levels like generation, transmission or end user level. A lot of works has been done on generation and transmission levels [1][2][4][5][6][7]. In the end user level, the smart grid is not only able to provide information about electricity consumption for both users and network operators, but also is able to connect renewable energy resources to the grid. In the residential or end user level demand response, challenges include real time pricing information to consumer, networking home devices, security and implementing automated Energy Management Systems (EMS) should be considered. In this paper, a new intelligent EMS system is presented. It takes inputs from the grid and by using an intelligent algorithm, tries to find effective and efficient energy consumption. It also can be matched by users' preferences and behaviors and then find optimal energy scheduling according to the dynamic notion of price. This approach is useful especially in a dynamic pricing system which modification of energy consumption is unrecognized by a consumer. The suggested system has two parts as it is shown in Figure 1.

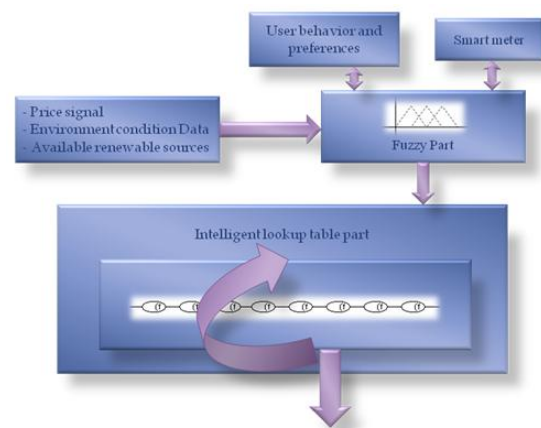


Figure 1. The suggested automated EMS

¹ This work was supported, in part, by a grant from CPS Energy through Texas Sustainable Energy Research Institute, the University of Texas, San Antonio, TX, USA

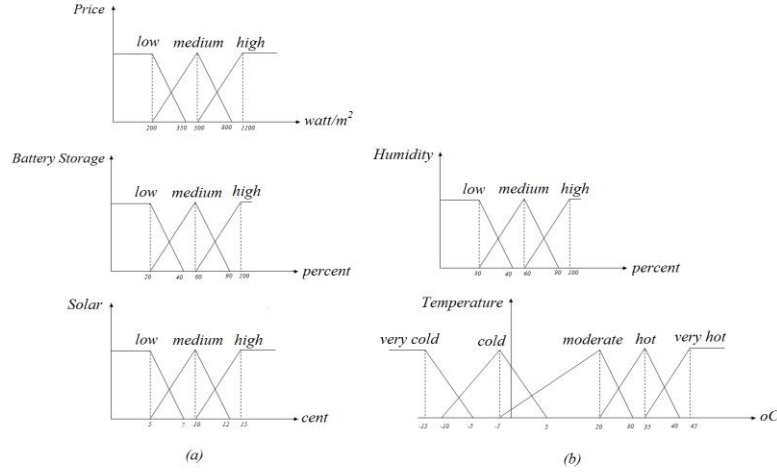


Figure 2. Fuzzy membership functions for the fuzzy part. (a): Category 1. (b): Category 2

The first part is a fuzzy system which its inputs can be external events like price signal, environment condition data and renewable resources or can be human behavior and preferences. This part has some fuzzy rules along with their membership functions which makes appropriate output for the second part which is an intelligent lookup table. The reason of using Fuzzy part is to get real time changeable external information and find the best system situation based on the fuzzy rules and then by using centralized defuzzification get a unique number in the output range. The second and the main part is an intelligent lookup table which is made by using a new topology of neural network [3]. The first reason of using this type of neural network is that its structure is crystal type and can be easily extended for more inputs and the second reason is that it is able to act as an associative memory to map inputs to desired outputs. This paper is organized as follows. In Section 2, the fuzzy part of the system is explained. In section 3, the structure of the intelligent lookup table, its training and functionality are described and in section 4, the simulation of the suggested approach is shown.

2 Fuzzy logic part

This part has 5 types of inputs. The first one is price signal which comes from the smart meter, the second one is battery storage situation, and the rest are environment condition data like humidity, temperature and solar as their membership functions are depicted in Figure 2. These inputs are divided into two categories. Price signal, battery storage and solar inputs are in the first category which makes a unique and appropriate input for the intelligent lookup table. The output of this category has 7 membership functions which gives us the energy consumption situation in the grid. These 7 fuzzy sets are Neutral-, Neutral+, Normal, High-, High+, Peak- and

Peak+ which are selected based on the fuzzy rules and mapping of input values to their appropriate membership functions. Finally the resulting set is defuzzified by Centriod defuzzification technique and gets a single number as (1).

$$x^* = \frac{\int \mu_i(x) x dx}{\int \mu_i(x) dx} \quad (1)$$

Where x^* is the defuzzified output, $\mu_i(x)$ is the aggregated membership function and x is the output variable. This number is rounded and its binary value goes to the intelligent lookup table. The second category of this part which contains environment condition data makes some input control signals to the second part which will be explained in the next section. The fuzzy rules and membership function values are set based on our knowledge from the grid and the environment. These values can be changed by human behavior and preferences. The behavior and preferences are logged and if there are any changes in them (like A/C setting), the system just modifies the initial membership values.

3 Intelligent lookup table part

3.1 Structure

The main part of this system has a crystal structure with cells as shown in Figure 3-a. As it can be seen, each cell is constructed of two middle neurons and four side neurons such that the two upper ones have fixed weights and the two lower ones have trainable weights. The two upper neurons and also the middle neurons have linear function and the two lower ones have a sigmoid function as (2).

$$y = \frac{1 + e^{-\lambda x}}{1 - e^{-\lambda x}} \quad (2)$$

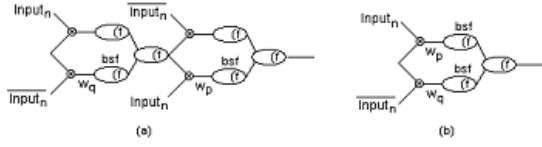


Figure 3. One cell of the network in the associative memory layer (a): Original Shape , (b): The summary of part a

The neurons of this layer receive their binary inputs from the previous layer. Figure 3-a can be summarized as Figure 3-b. For each cell we have:

$$f(n) = f(n-1) \times (f(input_n \times W_p) + f(\overline{input_n} \times W_q)), f(0) = c \quad (3)$$

Where n is the input cell number. In Figure 3-a, if $input_n$, which is the complement of $\overline{input_n}$, gets value 1, the first and the forth neuron will fire whereas if it gets 0, the second and third neurons do so. In the training step, only active neurons are trained. The characteristic of the lower neurons is that the increasing and decreasing rate of the weight changes are not equivalent during the training step as will be explain in section 3.2. In each cell, there are only two active neurons at a time and the output of that cell enters as input to the succeeding cell. If each input consists of n bits, cells would be connected as a chain up to the $(n-1)th$ input. The only remaining input is n where the output of the chained string is connected to $\frac{2n}{2}$ of this input cell. We call this layer the parallel layer as its cells are parallel to each other. In this layer, only one cell of input n is selected. With this selection, we reach our desired memory cell. For networks with more than one

output, $\frac{2n}{2}$ of input cell n are added to the parallel layer for each output. These added cells are only used for adjustment of all outputs except the first one. They have no influence on the adjustment of other weights. On the other word, the weights of the network are adjusted only by the first output and the other outputs are adjusted by the weights of added input cells in the parallel layer [3]. Figure 4 shows this structure for an example network with 3 inputs and 2 outputs. In order to make an intelligent lookup table by the suggested neural network, we create feedbacks from outputs of the network to its inputs as it is depicted in Figure 5. This makes a sequential system with memory. In this situation, next outputs will be made based on the present inputs and feedback outputs. As it was mentioned earlier, the system has two types of inputs; the first type comes directly from the fuzzy part and is a unique value which shows energy consumption situation in the grid. This input is connected to n first inputs of neural networks and implies the network which scenario should be started. The second type of inputs is some control bits which come either from fuzzy part or some outside sensors. These inputs are wired-or with feedback outputs and make different scenarios based on their conditions. These control bits can show for example water heater, air conditioner, refrigerator and other appliances situation in the smart house. Also they can be battery storage and solar situation which come from the fuzzy part. This intelligent lookup table should be trained based on the different inputs and control bits.

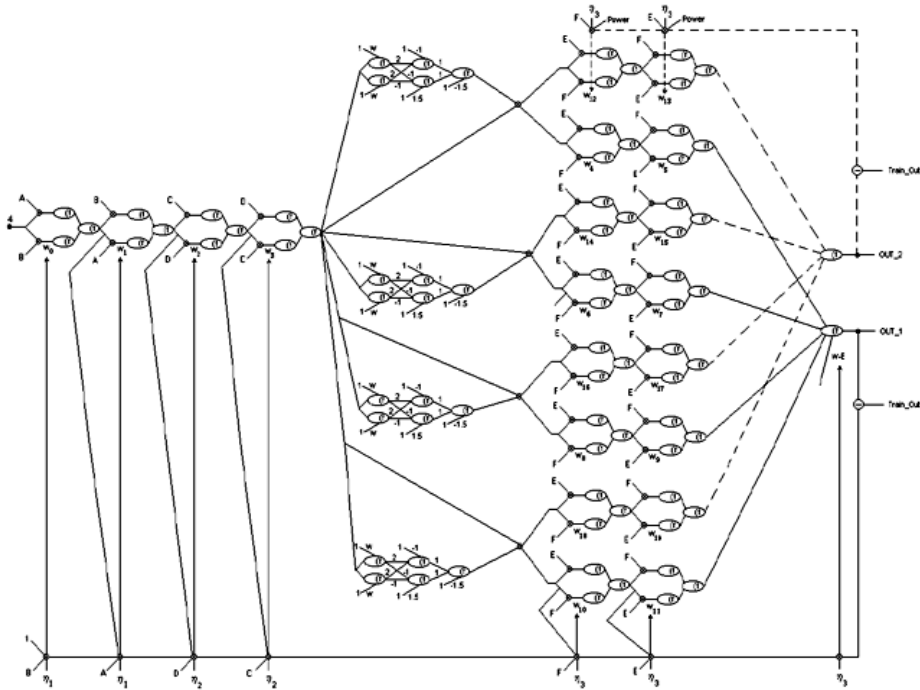


Figure 4. The structure of the associative memory layer with 3 inputs and 2 outputs. A,C,E are inputs and B,D,F are their complements.

3.2 Learning

The algorithm of network training is a way to decode the problem to be solved [8]. The learning of this network is supervised. The single layer perceptron learning rule is used to train this network [9]:

$$W_j(t+1) = W_j(t) + \eta \times (Train_{out} - out) \times In_p \quad (4)$$

Where j is the input cell number, In_p is the input of that cell, out is the output of the network and $Train_{out}$ is the desired output. The important point is that using the learning rule of single layer perceptron for this multi-layer network makes learning easy. The way of using this rule is presented here. As mentioned earlier, only active neurons are trained and in each cell there is only one lower active neuron at a time. So the Eq. (4) can be rewritten as:

$$W_j(t+1) = W_j(t) + SelectNeuron \times \eta \times (Train_{out} - out) \times In_p \quad (5)$$

In each layer, the η values which have been used for the stabilization of weights are smaller when weights increase than when they decrease. This always makes weights decreasing values larger than weights increasing values. These increasing and decreasing values are reduced in subsequent layers. The reason is that in binary numbers, the bit toggle frequency is halved when we move from LSB bits toward MSB bits. Since the inputs of the suggested network are binary, considering η as mentioned, will cause the changes of weights to become slower in subsequent layers. On the other words, weights change with lower frequency for 2^n sequential binary inputs. Considering the first layer as MSB and moving toward parallel layer as moving to LSB, the weight toggles would be less for the neurons of input cell n which are in the last layer and frequency of changes in their inputs is more than other cells. Due to the fact that the output error creates feedbacks to all layers, the weights of all active neurons will decrease or increase if this error becomes negative or positive respectively. But

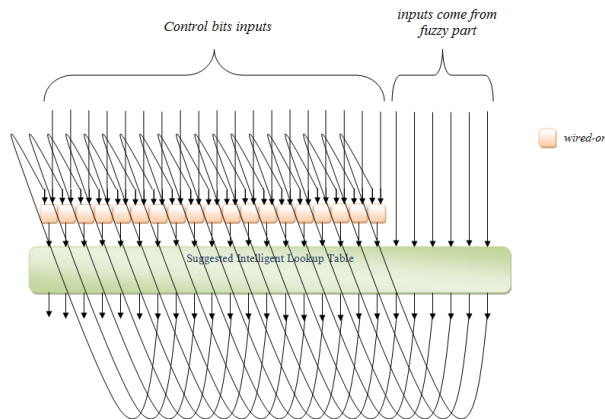


Figure 5. The intelligent lookup table structure

since η values are not equal, their increasing and decreasing rate would be different in each layer. By this method the network can be stabilized and get adjusted to 2^n input forms which result in the convergence of weights [3]. Experiments show that in case of having more than one output, it is better to consider a coefficient *Power* to adjust the weights of all outputs except the first one to expedite the convergence of weights.

3.3 Functionality

This network acts as an associative memory and is able to map a set of inputs to a desired output. Whatever will be trained in the network are different scenarios (based on different conditions) and connection between them. It can be trained in a certain time and mostly maps outputs based on the previous learning. The system will be trained when we have a new scenario or we intend to change one. This characteristic of the suggested lookup table gives the system speed and reliability which are two important items in the field of energy in a smart house. Scenarios in the mentioned intelligent lookup table are connected to each other in a way which suggest the best energy efficiency for appliances in the smart house. In fact, this system predicts outputs based on control bits and fuzzy inputs. For example, if a smart house has both battery storage and solar system and weather forecast information shows that we would have a cloudy weather in the next hours (which solar would not work), if the control bit is set and imply the battery storage needs to be charged, the system charges it in order to use its energy in

Table 1: Seventeen defined scenarios for energy efficiency in a smart house

No.	Scenario
1	Charge battery by grid
2	Charge battery by solar
3	Turn on water heater
4	Turn on air conditioner
5	Turn on dishwasher if programmed on
6	Turn on washer if programmed on
7	Turn on dryer if programmed on
8	Give portion of energy to dishwasher if programmed on
9	Give portion of energy to washer if programmed on
10	Give portion of energy to dryer if programmed on
11	Give portion of energy to refrigerator if needed (on)
12	Give portion of energy to freezer if needed (on)
13	Turn off dishwasher
14	Turn off washer
15	Turn off dryer
16	Get energy from battery storage
17	Turn on light controller

the future peak hours. We just have n Scenarios which the connections between them in different situations are trained in the network.

4 Simulation

For simulation of the mentioned system, we consider a smart house with water heater, air conditioner, light, solar panel, battery storage, refrigerator, freezer, dishwasher, washer and dryer. The fuzzy part of the simulation has 5 types of inputs along with membership functions as they are shown in Figure 2. In the first category, we have 15 fuzzy rules which make proper inputs for the intelligent lookup table. The outputs of the fuzzy part enter an associative memory with 18 inputs and 18 outputs. The outputs of the fuzzy part enter the first six inputs of the network and the rest inputs come from feedback outputs. Also we consider 10 control bits which are wired-or with feedback outputs. These control bits are for solar, battery storage and home appliances situations. Seventeen different scenarios are defined and based on different conditions are trained to the neural network. These scenarios are shown in Table 1. The changes of weights for 40 samples are shown in Figure 6. As shown in this figure, the weights stabilize after 30 samples which shows that this kind of connection between neurons results in weight convergence to the desired output. The figure also shows that the weight changes in cells toward parallel layer are reduced which indicates the stabilization of the network.

5 Conclusions

An automated Energy management system (EMS) for residential level is presented. The suggested system has two parts, fuzzy part and intelligent lookup table. The fuzzy part has 15 fuzzy rules along with membership

functions which makes appropriate outputs for the intelligent lookup table part. The intelligent lookup table is an associative neural network which maps inputs to desired outputs. It can be trained based on the different scenarios and connections between them. It has two types of inputs. The first type comes directly from the fuzzy part. The second type is feedbacks from its outputs which are wired-or with some control bits which come either from the fuzzy part or some outside sensors. This automated energy management system is able to find the best energy efficiency scenario in different situations.

References

- [1] Omid Siakani, Omar Hussian, Tharam Dillon, Azadeh Tabesh, "Intelligent Decision Support System for Including Consumers' Preferences in Residential Energy Consumption in Smart Grid", Second International Conference on Computational Intelligence, Modelling and Simulation, 2010.
- [2] T. R. Kuhn, "Energizing Efficiency's Potential," *The Electricity Journal*, vol. 19, pp. 83-87, 2006.
- [3] D. Shahgoshtasbi, "A New Topology of Neural Network for Memory Simulation", *World Automation Congress*, 2004.
- [4] R. Earle, E. P. Kahn, and E. Macan, "Measuring the Capacity Impacts of Demand Response," *The Electricity Journal*, vol. 22, pp. 47-58, 2009.
- [5] O. Sezgen, C. A. Goldman, and P. Krishnarao, "Option value of electricity demand response," *Energy*, vol. 32, pp. 108-119, 2007.
- [6] J. Sancho, J. Sánchez-Soriano, J. A. Chazarra, and J. Aparicio, "Design and implementation of a decision support system for competitive electricity markets," *Decision Support Systems*, vol. 44, pp. 765-784, 2008.
- [7] D. Coll-Mayor, M. Paget, and E. Lightner, "Future intelligent power grids: Analysis of the vision in the European Union and the United States," *Energy Policy*, vol. 35, pp. 2453-2465, 2007.
- [8] Cornelius T. Leondes, "Algorithms and architectures", *Academic Press*, 1998.
- [9] R. J. Schalkoff, "Artificial Neural Network", *McGraw-Hill, International*, 1997.

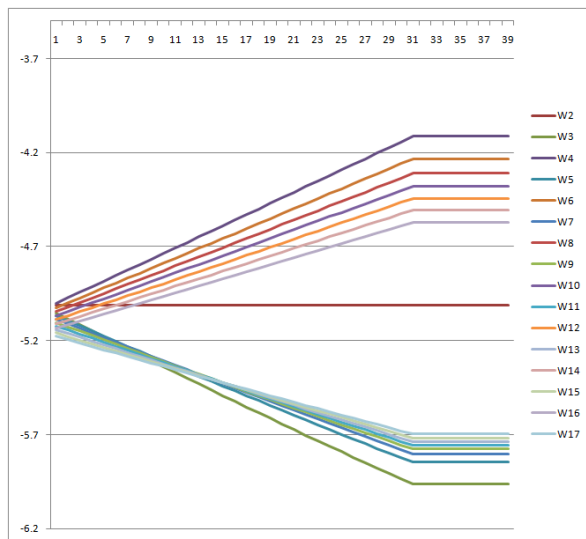


Figure 6. The value changes of weights for simulation of system with 18 inputs and 18 outputs

Fail-Safe Decentralized Architectures for Advanced Metering Infrastructure

Sai Krishna Narra and Ram Krishnan

Dept. of Electrical and Computer Engineering

University of Texas at San Antonio

Email: hrl334@my.utsa.edu and Ram.Krishnan@utsa.edu

Abstract—Advanced Metering Infrastructure (AMI) is a key component of smart grid. Current AMI solutions employ a mesh network of routers, collectors and potentially hundreds of thousands of smart meters. Typically, a command center (head end) manages this whole infrastructure. This type of security solution suffers from a single point of failure, since in most current deployments, a single instance of the command center manages the whole network. Specifically compromise of the command center (or any of its instances) implies compromise of the whole network—allowing one to arbitrarily control all the smart meters. In this paper, we propose a decentralized architecture with multiple head ends each of which is responsible for different domain of meters with some *overlap* of management amongst various head ends. The benefit of this architecture is that if there is a compromise of one head end only a subset of meters will be affected and the rest of the system can continue to operate normally. We also discuss various classes of such architectures with varying security properties and analyze them in detail.

Index Terms—Decentralized Architecture, Security Analysis, Key management.

I. INTRODUCTION

AMI (Advanced Metering Infrastructure) offers useful features like remote control of meters and two-way communication. AMI is majorly influenced by the use of smart meters which record the consumption of energy more frequently than the traditional meters and transmit that information to a central controlling center. Remote management of the smart meters in AMI is made possible by routers and collectors that facilitate hop by hop data transfer. Furthermore, the smart meter themselves act as mesh network. This is illustrated in figure 1.

A major issue in current deployments is that there is typically one logical command center that manages the whole network of meters, collectors and routers. This suffers from the problem of single point of failure. That, compromise of the command center compromises the whole network. In this paper, we develop a framework of decentralized architectures for the AMI with multiple command centers with different, yet overlapping, management responsibilities, so that if one is compromised, it minimizes the number of meters that would be affected. We specify a formal graph based model that can be used for analyzing the extent of damage in case of compromise of a node in the AMI network. We identify three classes of decentralized architectures with different cryptographic key sharing patterns. We analyze and compare the robustness of

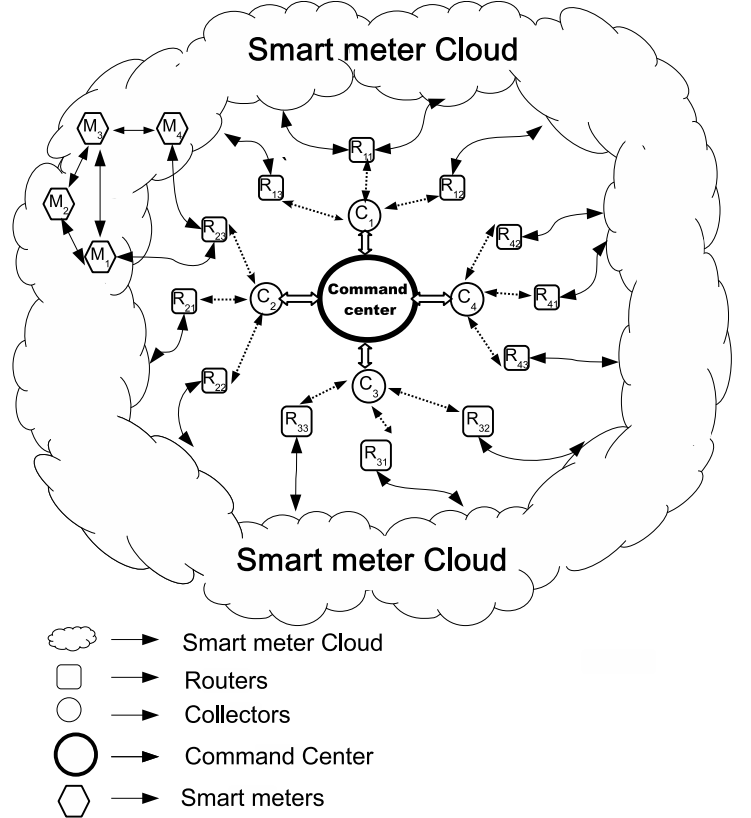


Fig. 1. High level architecture of an AMI: The meters are connected in a mesh network. Meters M_1 and M_4 transmit data directly to the router R_{23} . Other meters may transfer data to routers using multiple hops. Collectors aggregate data from routers and perform encoding/decoding and pre-processing before transmitting them to the Command Center.

these classes with respect to security in case of different kinds of compromise.

II. DECENTRALIZED AMI MODEL

In a decentralized AMI network, there are multiple head ends that manage various smart meters. For the purposes of this paper, we assume that each smart meter owns a unique key, K_U , that is shared with one or more head ends. Similarly, each head end owns a network key, K_N , that is shared with the meters that it would manage. With the knowledge of these keys, the meters and the head ends can achieve mutual authentication and confidentiality and integrity of data

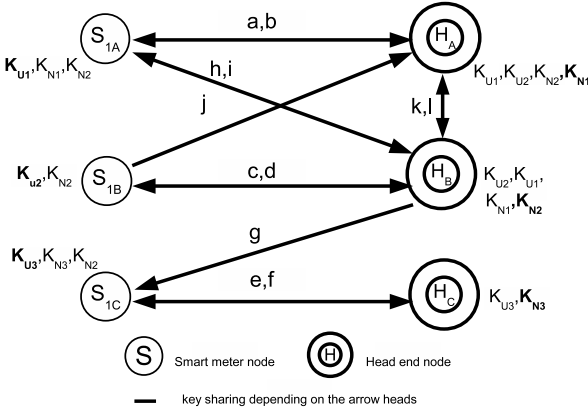


Fig. 2. Example Figure: A_1 can be a single node or a domain comprising of multiple Smart meter nodes. Then each node in a domain will have its own K_U, K_{N1}, K_{N2}

exchanged between them. (See [1] for example.)

A. Components of the Model

In this section, we develop a graph based model for decentralized AMI and formally define various requirements of this model. Later, we analyze specific classes of this model.

Definition 1 (Decentralized AMI system (dAMI-system))

A Decentralized AMI system (dAMI-system) is a directed graph $G(V, E)$ where V is a set of vertices in the graph and E is the set of edges that connect different vertices in V .

Definition 2 (Node) A node in a dAMI-system is represents a unique end point entity.

There are two different types of nodes present in the dAMI-system: Type-S and Type-H. Type-S nodes represent smart meters and are denoted using single circles in figures and Type-H nodes represent head ends and are denoted using double circles.

Note that we are only interested in modeling the smart meters and the head ends for security analysis. Specifically, devices like routers and collectors (see figure 1) are solely part of the communication infrastructure of the AMI and are not directly relevant to our study in this paper. We assume the existence of such a communication infrastructure that facilitates data transfer from one node to another in our model.

Definition 3 (Edge) An edge represents sharing of key(s) from the source node to the destination node. Nodes are only allowed to share the key(s) that it owns.

An edge represents key sharing in a Decentralized AMI system. Every Type-S node owns its unique key K_U . Similarly, every Type-H node owns its network key K_N . Figure 2 illustrates an example dAMI-system with 3 Type-S nodes and

3 Types-H nodes. This is a dAMI-system $G(V, E)$ where:

$$V = \{S_{1A}, S_{1B}, S_{1C}, H_A, H_B, H_C\}$$

$$E = \{(S_{1A}, H_A), (H_A, S_{1A}), (S_{1B}, H_B), (H_B, S_{1B}), (S_{1C}, H_C), (H_C, S_{1C}), (S_{1C}, H_B), (H_B, S_{1C}), (S_{1A}, H_B), (H_B, S_{1A}), (S_{1B}, H_A), (H_A, H_B), (H_B, H_A)\}$$

As seen, each node in the graph has knowledge of a number of keys in addition to the key it owns. A key owned by a node is indicated in bold font. The key configuration at various nodes is a result of key sharing facilitated by the edges. In the figure, for clarity, if two nodes mutually share their keys then they are represented by a single bidirectional edge. Recall that edges only represent key sharing and do not speak to the communication infrastructure.

Consider the node S_{1A} in the figure. K_{U1} is S_{1A} 's original key (bold font). K_{N1} and K_{N2} are the original keys of H_A and H_B respectively. Since there is an incoming edge into S_{1A} from both H_A and H_B , their original keys K_{N1} and K_{N2} are available at S_{1A} . Similarly, consider the node H_B . K_{N2} is the key owned by H_B . Due to the incoming edges from S_{1A} and S_{1B} , it obtains K_{U1} and K_{U2} . Further, due to an incoming edge from H_A , it also obtains K_{N1} .

Next, we introduce the concept of a domain that allows us to assign ownership of a set of smart meters to a specific head end.

Definition 4 (DOMAIN) The domain of a H-Type node is a collection of Type-S nodes with which an edge exists.

There are two types of domains: *primary* and *secondary*. A Type-S node's primary Type-H node is that node with which there is a bidirectional edge. That is, the Type-S node mutually shares keys with that Type-H node. A Type-S node's secondary Type-H node is that node with there need not be a bidirectional node. In figure 2, the primary domain of S_{1C} is H_C and its secondary domain is H_B . The naming convention allows one to identify the primary and secondary domains of a Type-S node. (The letter subscript in the Type-S node identifies the primary domain.) Note that a bidirectional edge is not prohibited between a Type-S node and its secondary domain head end. For example, S_{1A} mutually shares keys with its secondary domain H_B . In general, the secondary domain Type-H nodes act as a backup head end for any given smart meter. Partial sharing with the backup head end allows for the dAMI-system to have reduced risk while ensuring partial operation in case of compromise of the primary head end.

B. Required Properties of the dAMI-system

We define 3 core rules that are required all dAMI-systems.

- 1) In a dAMI-system, every edge that connects a Type-S node with its primary domain Type-H node should be bidirectional.
- 2) A dAMI-system should contain both types of nodes.
- 3) Each S-Type node should share an edge with at least two H-Type nodes.
- 4) Edges are not allowed between two S-Type nodes.

Note that these rules are consistent with many of the current industry solutions for AMI.

TABLE I
SECURITY STATUS OF VARIOUS CLASSES UNDER DIFFERENT COMPROMISE SCENARIOS

Compromise type	Affected edge(s)	Status of CIAu on affected edges		
		CLASS-A	CLASS- B	CLASS- C
Compromise of Type-S node key	The one connecting that Type-S node with its primary Type-H node	Only Integrity of messages is protected. CAu is lost since K_U is lost.	Only Integrity of messages is protected. CAu is lost since K_U is lost.	Only Integrity of messages is protected. CAu is lost since K_U is lost.
	The one connecting that Type-S node with its secondary Type-H node	Only Integrity of messages is protected. CAu is lost since K_U is lost.	CIAu is lost because only K_U is shared and not K_N .	Only Integrity of messages is protected. CAu is lost since K_U is lost.
Compromise of Type-S node (all keys stored at that node compromised)	The one connecting that Type-S node with its primary Type-H node	CIAu is lost because both K_U and secondary Type-H nodes K_N is lost.	CIAu is lost because both K_U and secondary Type-H nodes K_N is lost.	CIAu is lost because both K_U and secondary Type-H nodes K_N is lost.
	The one connecting the compromised Type-S node with its secondary Type-H node	CIAu is lost because both K_U and secondary Type-H nodes K_N is lost.	CIAu is lost because both K_U is lost.	CIAu is lost because both K_U and primary Type-H nodes K_N is lost.
	Those edges that connect other Type-S nodes in the same domain as the compromised node with the primary Type-H node	C- is preserved and Type-H node can authenticate S-type nodes.	C- is preserved and Type-H node can authenticate S-type nodes.	C- is preserved and Type-H node can authenticate S-type nodes.
	Those edges that connect other Type-S nodes in the same domain as the compromised node with the secondary Type-H node of the compromised node.	C- is preserved and Type-H node can authenticate S-type nodes.	C- is preserved and Type-H node can authenticate S-type nodes.	C- is preserved and Type-H node can authenticate S-type nodes.
	Those edges that connect other Type-S nodes in the same domain as the compromised node with secondary Type-H nodes that are not the same as that of the compromised node.	CIAu is achieved	C- is preserved and Type-H node can authenticate S-type nodes	CI- is preserved and Type-H node can authenticate S-type nodes.
Compromise of a Type-H node's key	Those edges between the compromised Type-H node and Type-S nodes for which the compromised node is the primary.	C- is preserved and Type-H node can authenticate S-type nodes.	C- is preserved and Type-H node can authenticate Type-S nodes.	C- is preserved and Type-H node can authenticate Type-S nodes .
	Those edges between the compromised Type-H node and Type-S nodes for which the compromised node is the secondary.	C- is preserved and Type-H node can authenticate S-type nodes.	C- is preserved and Type-H node can authenticate S-type nodes .	CI- is preserved and Type-H node can authenticate S-type nodes.
	Those edges that connect Type-S nodes for which the compromised node is primary with their respective secondary Type-H nodes.	CIAu is preserved	C- is preserved and Type-H node can authenticate Type-S nodes.	C- is preserved and Type-H node can authenticate Type-S nodes.
Compromise of a Type-H node (all keys stored at that node compromised.)	Those edges that connect the compromised Type-H node with Type-S nodes in the same domain.	CIAu is lost since both K_U and K_N are compromised	CIAu is lost since both K_U and K_N are compromised.	CIAu is lost since both K_U and K_N are compromised.
	Those edges that connect the compromised Type-H node with Type-S nodes for which the compromised node acts as secondary.	CIAu is lost since both K_U and K_N are compromised.	CIAu is lost since K_U is compromised and K_N is absent.	CIAu is lost since both K_U of secondary and K_N of primary Type-H node of the secondary Type-S domain are compromised.
	Those edges that connect the Type-S nodes for which the compromised node is primary with their respective secondary Type-H nodes.	Integrity is preserved because K_N is not compromised.	CIAu is lost since both K_U and K_N are compromised.	CIAu is lost since both K_U and K_N are compromised.
	Those edges that connect the Type-S nodes for which the compromised node is secondary with their respective primary Type-H nodes.	Integrity is preserved because K_N is not compromised.	Integrity is preserved because K_N is not compromised.	CIAu is lost since both K_U and K_N are compromised.

C. Reachability in dAMI-system

We use the term *reachability* to specify whether an edge between two nodes in the dAMI-system facilitates authentication, confidentiality and/or integrity.

Definition 5 (C-Reachability/Confidentiality Reachability:)

A node X is C-Reachable from a node Y if data can be confidentially exchanged between nodes X and Y.

Given a graph $G(V,E)$, confidentiality of data exchanged between an S-Type node P and an H-Type node Q is achieved if an edge (P,Q) exists in E. This is because such an edge would imply that P's unique key is shared with Q. For example, in figure 2, the edge from S_{1A} to H_A indicates that K_{U1} is shared between those nodes. This allows for confidential exchange of data between them.

Definition 6 (I-Reachability/Integrity Reachability:)

A node X is I-Reachable from a node Y if integrity of data exchanged between X and Y can be achieved.

Given a graph $G(V,E)$, integrity of data exchanged between an S-Type node P and an H-Type node Q is achieved if an edge (Q,P) exists in E. This is because such an edge would imply that Q's network key is shared with P. For example, in figure 2, the edge from H_A to S_{1A} indicates that K_{N1} is shared between those nodes. This means that integrity of data exchanged between them can be achieved.

Definition 7 (Au-Reachability/Authentication Reachability:)

A node X is Au-Reachable from a node Y if messages from Y can be authenticated by X.

Given a graph $G(V,E)$, authentication of messages between an S-Type node and an H-type node is achieved if edges (P,Q) and (Q,P) exists in E. That is, if any two nodes have C and I-Reachability, then they also have Au-Reachability. This is because authentication of messages from a node P to Q (where P and Q are of different types) is achieved based on the unique key of the S-Type node *and* the network key of the H-Type node. For example, in figure 2, the bidirectional edge between S_{1A} and H_A indicate that the two nodes can mutually authenticate each other's messages.

III. CLASSES OF DAMI-SYSTEM

In this section, we discuss 3 different classes of dAMI-systems. These classes specify rules in addition to the core rules defined in section II-B. For each class, a number of dAMI-systems may be developed based on these rules. We analyze the security properties of each class of systems in situations of compromise.

A. Class-A dAMI-Systems

Class-A systems are developed based on the following rules:

- 1) Only bidirectional edges are allowed.
- 2) Edges between H-Type nodes are not allowed.

B. Class-B dAMI-Systems

Class-B systems are developed based on the following rules:

- 1) Between Type-S nodes and their secondary Type-H nodes, only unidirectional edges originating from the Type-S nodes are allowed.
- 2) Edges between H-Type nodes are not allowed.

C. Class-C dAMI-Systems

- 1) Only unidirectional edges are allowed.
- 2) For every edge that connects a Type-S node with its secondary Type-H node, another edge should originate from the Type-S node's primary Type-H node and end at that secondary Type-H node.

IV. COMPARISON TABLE

Table I presents our final analysis of how class A, B and C systems compare under different compromise scenarios. In column 1, we consider two high-level compromise scenarios: 1. compromise at the smart meter level and 2. compromise at the head end level. In each of these two levels, a single key in that node may be compromised or the whole node may be compromised (leading to compromise of all the keys stored in that node). In column 2, we identify the edges that are affected by the specific compromise scenario in column 1. In column 3, we specify how CIAu-Reachability on the edges identified in column 2 is affected for class A, B and C systems.

V. CONTRIBUTIONS OF THIS PAPER

- We have specified a formal graph based model for designing decentralized architectures for Advanced Metering Infrastructure.
- We have specified properties of 3 different classes of systems and shown that systems in the same class have the same set of security properties. This is a highly useful analysis for a security architect designing a decentralized AMI system as the classes provide various key sharing choices.

REFERENCES

- [1] S. Fuloria, R. Anderson, F. Alvarez, and K. McGrath. Key management for substations: Symmetric keys, public keys or no keys? In *Power Systems Conference and Exposition (PSCE), 2011 IEEE/PES*, pages 1–6, march 2011.

Smart Grid AMI Communication Networks and Capacity Analysis Using 4G Cognitive Radio

Kranthi Manoj Member IEEE, Amir Rajaei Member IEEE, Brian Kelley Senior Member IEEE,
Mo Jamshidi Fellow IEEE

Abstract— We present a framework and analysis of a smart meter network that communicates over a 4G cognitive radio (CR) channel. We view our Advanced Metering Infrastructure (AMI) network as ideally suited for a next generation of metropolitan area smart grid systems. We define capacity analysis models of multi-user AMI meter communication in the context of smart grid networks. Our proposed 4G CR network framework is capable of communicating with high numbers of geographically dispersed smart meters for command and control feature over the unused wholes within licensed 4G cellular network bands and TV white spaces. We introduce the foundations of a new AMI meter system model that utilizes cloud data centers as the central communication and optimization infrastructure supporting metropolitan area based smart meter networks. The performance of various scheduling algorithms for AMI is presented in the context of the CR channel. Tradeoffs between maximizing the system capacity and achieving fairness among cognitive AMI users and system level capacity results for our AMI network are presented. Detailed simulations involving the CR transmission of secondary user packets in the holes of a typical 4G Cellular network indicate that our system can obtain an average capacity that meets the smart grid communication protocol requirements.

Index Terms—4g Cognitive radio networks, cloud data center, scheduling algorithms, and smart meters.

Manuscript received October, 1, 2011.

KranthiManoj Nagothu, Amir Rajee, Brian Kelley and Mo Jamshidi is with the University of Texas at San Antonio, San Antonio, TX 78249 USA; e-mail: kranthimanoj@ gmail.com, amirajae@ gmail.com, Brian.Kelley@utsa.edu, moj@ wacong.org).

This material is based upon work was supported, in part, by the Texas Sustainable Energy Conservation office (SECO) and the U.S. Department of Energy (DOE) under Grant RFA No. RE-AG1-2010 and has been supported, in part, by a grant from CPS Energy, San Antonio, TX through Texas Sustainable Energy Research Institute, University of Texas, San Antonio.

I. INTRODUCTION

The smart grid of the future is generally perceived to be an intelligent energy delivery system that supports plug-and-play integration of power, information, and security services. The services should be supportive of high penetrations of renewable energy sources. It also acts as platform for consumer and utility engagement in load management, closed loop demand response, conversion of carbon generating power to low carbon emitting sources, and economic security [1].

We anticipate that the future smart grid will leverage Information and Communications Technology (ICT) facilitated by sophisticated smart meter information networks. The smart meter (often referred to as an Advanced Metering Infrastructure (AMI)), enables the flow of real-time information to the power utility servers and between the power utility and its customers. It also provides customers and utilities with the technology to optimize their energy consumption via closed loop demand response services. Additional battery management services are necessary to integrate high penetrations of renewable energy components in the grid, to support third party energy management applications and enable dynamic optimization of distributed power sources [2-4].

While it is essential that smart meter be networked, communication network infrastructures represent a very large capital expense. Much of this expenditure is due to the high prices of purchasing licensed wireless bands either from the Federal Communications Commission (FCC) auction process or from existing licensed band owners. According to the FCC, temporal and geographical variations in the utilization of the assigned spectrum range from 15% to 85% [5]. To address this issue in the context of spectrum availability, Cognitive Radio (CR) is considered by the FCC as one of leading approaches to improve the utilization and efficiency of spectrum [6]. We, therefore analyze a new low cost wireless system based on a 4G cognitive radio AMI networks. In our context, we refer to 3GPP-LTE protocol parameters as 4G. The smart grid AMI network we describe is metropolitan in scale and principally independent of existing cellular infrastructure.

A. Related work on AMI Networks

Several authors have defined aspects of AMI networking in smart grids. Mesh, Ethernet and cellular AMI network topology for smart grid has been proposed in [7-8]. In these

works, the authors propose mesh networks of Zigbee based transmission architecture. Challenging issues remain due to line of sight requirements in Zigbee that limit the single-hop range to hundreds of feet [9]. The model details in deployment of new mesh networks necessarily imply high levels of inter-network coordination. Inefficiencies arise when transmission distances featured by the protocols in the entire metropolitan area for AMI networking. Improved alternatives include IEEE 802.11 (a, b, g, n) protocols configured as AMI mesh networks. Such networks, however, support transmission distances range from 50-200 meters, which is problematic for robust metropolitan area coverage.

In [10], the authors discuss smart grid communication infrastructure based on Ethernet (LAN and WAN). The approach will support automated meter readings and customer home appliance connections. It can also support distribution automation and substation automation. We view such systems as completely complementary to our approach and a way of introducing service diversity. However, wireline-ethernet systems are not always available. Customer subscription to service must occur and wired system can be challenging to rapidly redeploy, particularly in swiftly enveloping emergencies.

The authors in [11] describe a framework for RF mesh networking interfaced with high speed WiMAX access networks. In [11], the AMI smart meter is capable of two-way communications over a 900 MHz wireless mesh network back to a collection point at the substation/switchyard. A private high speed access network will be then utilized to connect the substation-switchyard to the corporate network. This access network typically can be fiber or an existing cellular network (i.e. WiMAX). Since smart grid is considered as critical infrastructure, resiliency and persistency in the aftermath of a major disruption is of the utmost importance. To minimize economic disturbances, it should also persist. It should also survive in instances of service provider exiting of markets or in instance where customer cannot afford paid services.

The authors in [12] discussed the use of OFDM based communication system over low voltage power lines in the CENELEC bands. Recently, the FCC has finalized the rules to make the unused spectrum in the TV bands available for unlicensed broadband wireless devices [17]. Research on CR has evolved from SDR (see [18-24]) with an objective of efficient utilization of radio spectrum. In [13] authors discuss deployment of smart utility networks in TV white spaces. In [14-16], overview of architecture, hardware platform, and key algorithms are reported to enable CR for smart grid communications.

There exists very few results on large scale deployment of CR networks and principally in context with smart grid AMI networking and to our knowledge nowhere in the literature a complete multi-user capacity analysis using CR network in context with smart grid has been not reported. In this paper, we discuss framework and infrastructure for smart grid AMI networks enabled by 4G cognitive radio. Principle features (i.e. sensing, scheduling) of 4G CR metropolitan based environment specifically from stationery AMI perspective are developed. We also present multi-user performance analysis over 4G CR channels for smart grid AMI networks.

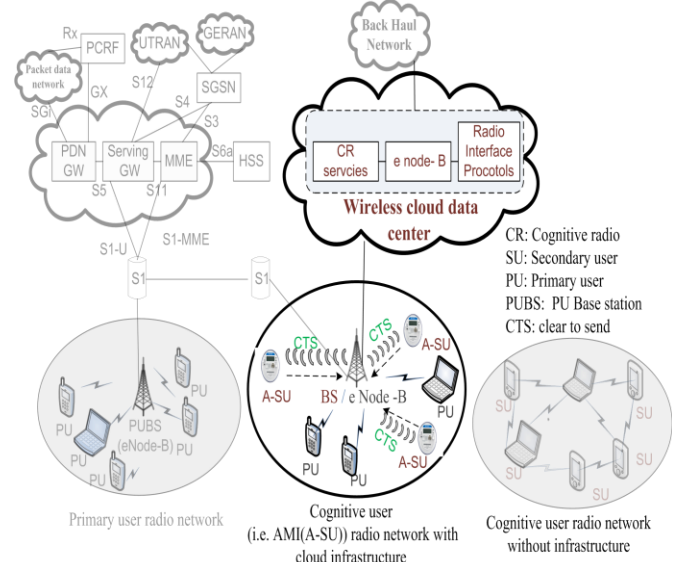


Fig. 1. System Architecture – Scenario of multiple AMI smart meters serviced by cognitive radio network infrastructure enabled by cloud center coexisting with private cellular network

II. Smart Grid Cognitive Radio in 4G Framework

A. CR Infrastructure for Smart Grid AMI networking

We begin with a discussion on the infrastructure of a CR networks optimized for smart grid AMI networking. Without a loss of generality, we adopt 3GPP LTE network parameter assumptions and in our simulations for the 4G CR AMI network. As a major point of departure from expensive cellular networks, we consider a low cost cloud data center infrastructure based CR network coexisting with private cellular network, shown in Fig. 1 and as presented in [25].

The coverage area of the cell of both the CR base station and private cellular networks (PCN) base station are similar. In our model, each cell of PCN is split into three sectors. For simplicity, we assume that the frequency band is divided equally for three sectors to avoid inter cell interference. As depicted in the Fig.1. at the center of the each cell, there is base-station which is shared as eNode-B for PU and as antenna for A-SUs.

PU end- end network architecture of LTE and various components of the network are shown in Fig.1. Primary user base-station is a component which has access to the license bands as it belongs to private cellular network. The primary user base-station only serve to PUs as it lacks the CR protocols capabilities to support A-SUs. However, it may consider supporting certain features in order for the primary network access users communicating with CR users [26].

We illustrate our smart grid AMI networks for metropolitan area based CR infrastructure as shown in Fig. 1. In principle, eNode-B which terminates the air interface protocol and first point of contact for PU is located at the primary user base-station. However, in proposed architecture all the cognitive radio service, waveform service, protocols service, security service, scheduling and control services are displaced in to cloud data center. This implies our cloud data center acts as

virtual base station to CR users. We employ cognitive radio as an integrated component of the smart grid AMI networks.

In cognitive radio systems, the absence of an owned license band to operate in a desired band dictates opportunistic spectrum access protocols. The licensed user of the frequency band is always given priority access to the shared channel (time-frequency resource). Due to their priority in spectrum access, the operations of primary users (PU) are always 1st in the transmission queue so as to not be affected by unlicensed users [27]. All the stationary A-SUs have the same right to access the spectrum. A-SUs should compete with each other for the same unlicensed band. Thus, sophisticated spectrum sharing methods among A-SUs are required in this architecture. If multiple A-SUs network operators reside in the same unlicensed band, fair spectrum sharing among these networks is also required and different scheduling algorithms are discussed in detail in section III.

Placement of a Cognitive Radio Antenna on the BTS tower may occur in tandem with deployment of the cellular provider antenna. The CR antenna senses the spectral environment over a wide frequency band, particularly the spectrum in the cell region. It identifies the unused bands in the spectrum. Sensed formation is relayed to cloud data center. The cloud data center then unrolls in order: the cognitive radio service, waveform service, protocols service, security service and other control services. The cloud data center generates a clear to send (CTS) signal. The CTS is sent back to the A-SU through the feedback channel via base station. Eventually, the CR antenna relays CTS signals to every A-SU in the cell region for uplink transmission. Detailed description about control procedures and data flow through the protocol stack is discussed in detail [25].

1) CR and Smart Grid Convergence on Cloud Data Centers

Cloud computing improves the availability of computing resources for wide varieties of software services. In our scenario of CR services residing on the cloud services, elasticity plays vital role due to high variations in the rate of users change accessing services. Cloud system services can reside far from physical locations of users.

The adoption of a cloud center enables convenient, on-demand network access to a shared pool of configurable, computing resources (e.g., networks, servers, storage, applications, and services) that can be rapidly provisioned and released with minimal management effort [28].

There are different cloud computing platform classifications. Standard architectures includes Abi (or Abiquo), Nimbus Open Nebula, Azure (Microsoft), Google (App Engine), Blue (IBM) and Mosso (Rackspace) (see [30]). Fig. 2. depicts the model for a cloud data center architecture optimized for smart grids. The layered design of wireless cloud data center (WCD) architecture is formulated on the bases from currently existing cloud architecture but extrapolated with a new additional layer of CR communication and networking as a service. Our WCD model is organized into four principle layers: application layer, platform layer, CR communication and networking layer and Infrastructure layer.

The first two layers are akin to existing cloud architectures. However, the lower two layers are augmented to enable the CR networking services. By this feature CR network service providers (CRNSP) will have the ability to leverage cloud and

provide various services. CRNSP can allocate on demand services arbitrarily at any period time with minimum latency by dynamically upgrading the connectivity between the sites and utilizing vast cloud resources (i.e. CPU, high bandwidth). For instance, we presume there is enough channel capacity for secondary users to access the spectrum. The A-SUs requests for live streaming of high definition video, CRNSPs can leverage the large abundance of resources and services provided in this layer to adapt to the scenario and provide quality services to users. It also provides a common management framework by operating the services across the distributed resources rather than operating at separate facilities with fixed resource allocation. Among the services provided are cognitive radio services, waveform services, radio link control (RLC), and medium access control (MAC) services.

The infrastructure layer facilitates the effective integration of computing resources, storage, networks to deploy applications and operating systems. We augment our cloud infrastructure microprocessor racks with FPGA boards targeted to processing high computation rate processes typically associate with CR services, communication waveform signal processing and coding. All the CR services are processed using SDR residing in the WCD. SDR enables an ability to adapt to future updated algorithms (i.e. sensing, management) via software (not hardware) upgrades in WCD featuring a novel, integrated cloud data center framework supporting CR communications and networking.

III. AMI DATA COMMUNICATION IN 4G CR CHANNELS

To leverage CR channels for AMI data communications, there are major challenges to overcome such as A-SU should sense the spectrum and estimate the time access model and behavior of the primary users (PU). Moreover, the A-SU needs to follow the interference constraints suggested by the FCC Spectrum Policy Task. Specifically, the total interference power received at each PU should not exceed a preselected interference temperature limit (ITL). In such a system, we develop a multi band energy detection sensing approach to provide more spectrum access opportunities to A-SU without interfering with PU operations. Also, the optimum sensing time is calculated to maximize the capacity in each frame time. However, the optimum time is re determined based on the practical limitations occurred during sensing.

In the sections that follow, the 4G CR network system model is considered with N_{su} secondary users sharing the spectrum simultaneously with N_{pu} primary users. It is presumed in the context that the secondary users (i.e. AMI meters) are fixed in sense of geographical location and yields to fixed first and second statistical moments of signal to interference plus noise ratio (SINR).

A. Our Model for Detecting Holes in the 4G Cellular Spectrum

The spectrum sensing is one of the main service tasks for CR layer system to obtain the spectrum usage information and to sense the presence of PUs. Spectrum detection is based on the signal classification of the PU via the observation of cognitive radio network.

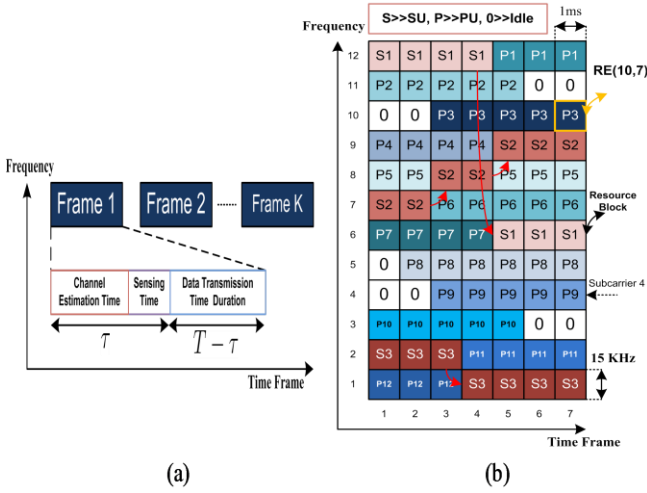


Fig. 3. (a). Timing Model. (b). Resource Block & Dynamic Resource Management

Cooperative and non-cooperative detection are common methods that are usually used in spectrum sensing. Cooperative detection by combining the observations of several cognitive radio users can be used to improve the performance of spectrum sensing. Cooperative detection can be implemented in a distributed or centralized manner. One of the goals is to use Cognitive Radio Network (CRN) efficiently; since, cooperative detection increases overhead in CRN, chose non-cooperative detection. Moreover, we try to benefit low cost and low power devices in our model which are not usually appropriate for cooperative networks. Also, unlike our goal seeking the way to maximize throughput, the cooperative method needs to multiplex the data and cooperation information that makes degradation of throughput.

The sensing methods can be categorized in three main methods: i) Energy Detection, ii) Matched Filter, and iii) Feature Detection.

Energy detection detects the spectrum by measuring the energy of the received signal in a certain frequency band. It is that is most common detection method for spectrum sensing in cognitive radio networks. Simple implementation and low computational complexities, being optimum for unknown primary users are some advantages of using energy detection.

A matched filter maximizes the output signal to noise ratio but its disadvantage is that it requires an accurate prior knowledge of every user that is not usually possible.

In feature detection, a specific feature of the user signal such as pilot, segment sync, field sync, or cyclostationarity is received. Although many of the signals used in wireless communication and radar systems possess this property, because of its high computational complexity and long observation time, it is not suitable for our model [31-33].

Hence, the method we considered for Spectrum Sensing is Energy Detection since Energy Detection is especially suitable for multiband sensing because of its low computational and implementation complexities. Our assumptions are using OFDM modulation with M subcarriers and bandwidth W. The IEEE 802.22 is considered since it has developed air interface for opportunistic secondary access to the TV spectrum in which Primary Users (PU) change slowly [34].

The timing model for spectrum sensing is shown in Fig. 3(a) and spectrum mobility model for A-SUs is depicted in Fig. 3(b). The required time for channel estimation, spectrum sensing and sharing is indicated by τ . According to the [12] the channel estimation delay is determined for WCDMA/HSDPA, so the scaled delay for a shorter sub-frame length in UTRAN LTE is considered for this paper. For each Resource Block (RB), there are 7 frames in time frame and 12 subcarriers and each square in Fig. 3(b) is called Resource Element (RE). For example, in Fig. 3(b), RE (10, 7) means that the frequency carrier at frame 7 and subcarrier 10 is occupied by primary user 3. At each time frame, idle resource elements will be detected and allocated to A-SUs. Once a PU requests the subcarrier occupied by the active A-SU, A-SU has to leave the spectrum and try to find another idle resource element to continue transmission. In Fig. 3(a), T is time length of each frame and K is number of frames. The idle RB or hole is a band can be used by A-SU without interfering with PU. Supposed that received signal at CR receivers sampled at f_s over i th sub channel where values of discretized samples at $t = n T_s$, which T_s is $0.1\mu s$ in our framework. In discrete form, when the primary user is active, we define two hypotheses as follow:

$$y_i(n) = \begin{cases} h_i x_i(n) + u_i(n), & \mathcal{H}_{1,i} \\ u_i(n) & \mathcal{H}_{0,i} \end{cases} \quad (1)$$

The parameter h_i is the subcarrier flat fading gain between PU transmitter and CR receiver with variance $E(|h_i|^2) = \sigma_{h,i}^2$. The signal transmitted, x_i , by PU is assumed to be independent and identically distributed (i.i.d), $\mathcal{CN}(0, \sigma_s^2)$, and u_i , the noise, is circularly symmetric complex Gaussian (CSCG) noise[35-36].

B. Statistical Models for Primary User Detection

In order to detect the RF energy in the certain subcarrier for a given primary user, the CR receiver samples on-the-air signal constructs the following test statistics as the observed energy summation within N samples to decide on the presence of the active users in targeted subcarrier [37].

$$\mathcal{U}_i = \begin{cases} \frac{1}{N_i} \sum_{n=1}^{N_i} |h_i x_i(n) + u_i(n)|^2, & \mathcal{H}_{1,i} \\ \frac{1}{N_i} \sum_{n=1}^{N_i} |u_i(n)|^2 & \mathcal{H}_{0,i} \end{cases} \quad (2)$$

N_i is number of samples transmitted on duration τ_i which is equal to $N_i = \tau_i f_s$. The PDF of \mathcal{U}_i is central Chi Square distribution with $2N_i$ degrees of freedom, $\chi_{2N_i}^2$, for when no PU exists and on central Chi square distribution with $2N_i$ degrees of freedom and non-centrality parameter $2\gamma_i$, $\chi_{2N_i}^2(2\gamma_i)$, for the state that PU exists. So:

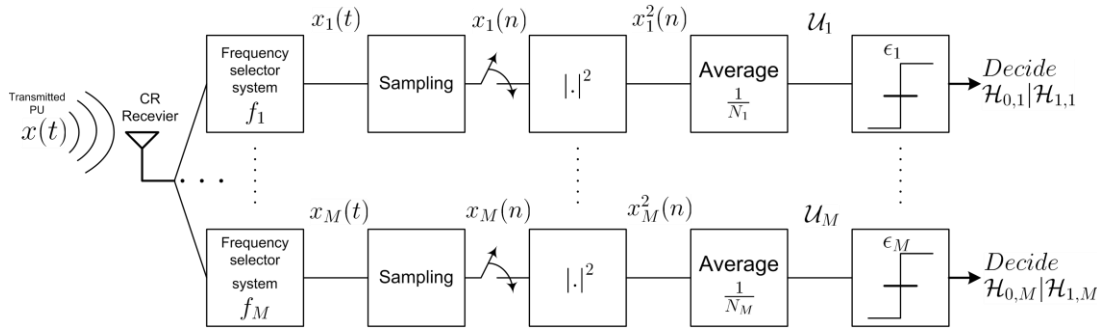


Fig. 4. Schematic for Multiple Band Sensing.

$$\mathcal{F}_{\mathcal{U}_i}(\mathcal{U}_i) = \begin{cases} \mathcal{X}_{2N_i}^2 = \frac{1}{2^{2N_i} \Gamma(N_i)} \mathcal{U}_{i,1}^{N_i-1} e^{-\frac{\mathcal{U}_{i,1}}{2}}, & \mathcal{H}_{1,i} \\ \mathcal{X}_{2N_i}^2(2\gamma_i) = \frac{1}{2} \left(\frac{\mathcal{U}_{i,0}}{2\gamma_i} \right)^{\frac{N_i-1}{2}} e^{-\frac{2\gamma_i + \mathcal{U}_{i,0}}{2}} \\ I_{N_i-1}(\sqrt{2\gamma_i \mathcal{U}_{i,0}}), & \mathcal{H}_{0,i} \end{cases} \quad (3)$$

where the signal to noise ratio (SNR) is depicted by $\gamma_i = \frac{\sigma_{x_i}^2 \sigma_{h_i}^2}{\sigma_{u_i}^2}$, $\Gamma(\cdot)$ denotes the gamma function, $I_\alpha(\cdot)$ is the first kind modified Bessel function of degree α . Two performance parameters for spectrum sensing are probability of detection, P_d , and probability of false alarm, P_f , which is probability of when the frequency is unoccupied but we get alarm that the frequency is used. Hence, Higher P_d protects PU from interfering with SUs and smaller P_f causes better band usage efficiency. To calculate probability of detection [38-39]:

$$P_{d,i}(\epsilon_i, \tau_i, \gamma_i) = Pr(\mathcal{U}_i > \epsilon_i | \mathcal{H}_1) = \int_{\epsilon_i}^{\infty} p_1(x) dx \quad (4)$$

where ϵ_i is threshold and τ_i is denoted sensing time for i th subcarrier. Using Central Limit Theorem for large N_i , under hypotheses \mathcal{H}_1 and $x_i(n)$ and $u_i(n)$ are complex valued \mathcal{U}_i is

$$\begin{aligned} \sigma_{\mathcal{U}_{i,1}}^2 &= E[|\mathcal{U}_i - \mu_{\mathcal{U}_{i,1}}|^2] \\ &= E\left[\left(\frac{1}{N_i} \sum_{n=1}^{N_i} |x_i(n) + u_i(n)|^2 - (\sigma_{x_i}^2 + \sigma_{u_i}^2)\right)^2\right] \\ &= \frac{1}{N_i} E\left[|x_i(n)|^2 + |u_i(n)|^2 + x_i(n)u_i^*(n) + x_i^*(n)u_i(n) - \sigma_{x_i}^2 - \sigma_{u_i}^2\right]^2 \end{aligned} \quad (5)$$

If $x_i(n)$ and $u_i(n)$ are real valued, \mathcal{U}_i under hypothesis \mathcal{H}_1 is:

$$\begin{aligned} \sigma_{\mathcal{U}_{i,1}}^2 &= E[|\mathcal{U}_i - \mu_{\mathcal{U}_{i,1}}|^2] \\ &= E\left[\left(\frac{1}{N_i} \sum_{n=1}^{N_i} |x_i(n) + u_i(n)|^2 - (\sigma_{x_i}^2 + \sigma_{u_i}^2)\right)^2\right] \\ &= \frac{1}{N_i} E\left[|x_i(n)|^2 + |u_i(n)|^2 + 2x_i(n)u_i(n) - \sigma_{x_i}^2 - \sigma_{u_i}^2\right]^2 \end{aligned} \quad (6)$$

That for large N_i , we have $\mu_{\mathcal{U}_i} = (\gamma_i + 1)\sigma_{u_i}^2$ and $\sigma_{\mathcal{U}_i}^2 = \frac{1}{N_i} E[|x_i(n)|^4 + |u_i(n)|^4 - (\sigma_{x_i}^2 - \sigma_{u_i}^2)^2]$.

So with assumption that the signal is PSK complex valued and using the fact that $x_i(n)$ and $u_i(n)$ are independent with zero mean and $x_i(n)$ is circularly symmetric, it can be represented by $x_i(n) = x_{i,real}(n) + j x_{i,imag}(n)$ with $E[x_{i,real}(n)] = E[x_{i,imag}(n)] = \frac{\sigma_{x_i}^2}{2}$; as a result, $E[x_i(n)^2] = 0$ and in the same way, $E[u_i(n)^2] = 0$. Therefore $\sigma_{\mathcal{U}_{i,1}} = \frac{1}{N_i}(2\lambda + 1)\sigma_{u_i}^4$ and P_d will be [40-41]:

$$P_{d,i}(\epsilon_i, \tau_i, \gamma_i) = Q\left(\left(\frac{\epsilon_i}{\sigma_{u_i}^2} - \gamma_i |h_i|^2 - 1\right) \sqrt{\frac{\tau_i f_s}{2\gamma_i |h_i|^2 + 1}}\right) \quad (7)$$

where Q is complementary error function as follow:

$$Q(x) = \frac{1}{\sqrt{2\pi}} \int_x^{\infty} \exp\left(-\frac{u^2}{2}\right) du \quad (8)$$

Now the probability of missed detection can be defined as:

$$P_{m,i}(\epsilon_i, \tau_i, \gamma_i) = 1 - P_{d,i}(\epsilon_i, \tau_i, \gamma_i) \quad (9)$$

At the same way we have following equations for probability of false alarm,

$$P_{f,i}(\epsilon_i, \tau_i) = Pr(\mathcal{U}_i > \epsilon_i | \mathcal{H}_0) = \int_{\epsilon_i}^{\infty} p_0(x) dx \quad (10)$$

$$P_{f,i}(\epsilon_i, \tau_i) = \mathcal{Q}\left(\left(\frac{\epsilon_i}{\sigma_{u_i}^2} - 1\right)\sqrt{\tau_i f_s}\right) \quad (11)$$

Usually to evaluate the performance of energy detection, the goal is to minimize P_f for a target P_d or to maximize P_d for a target P_f . At first we assume $P_{d,i,target}$ is our target probability of detection and later we obtain threshold as a function of P_d , then substitute $\epsilon_i(P_d)$ by ϵ_i in (11),

$$\epsilon_i(P_{d,i,target}) = \left(\frac{\mathcal{Q}^{-1}(P_{d,i,target})}{\sqrt{\frac{\tau_i f_s}{2\gamma_i |h_i|^2}}} + \gamma_i |h_i|^2 + 1\right)\sigma_{h_i}^2 \quad (12)$$

$$P_{f,i}(\epsilon_i(P_{d,i,target}), \tau_i) = \mathcal{Q}(\mathcal{Q}^{-1}(P_{d,i,target}) \sqrt{2\gamma_i |h_i|^2 + 1 + \gamma_i |h_i|^2} \sqrt{\tau_i f_s}) \quad (13)$$

$P_{f,i}(\epsilon_i(P_{d,i,target}), \tau_i)$ is the probability of false alarm regard to target $P_{d,i}$, and \mathcal{Q}^{-1} is the inverse of complementary error function. For a target $P_{f,i,target}$ we have:

$$\epsilon_i(P_{f,i,target}) = \left(\frac{\mathcal{Q}^{-1}(P_{f,i,target})}{\sqrt{\tau_i f_s}} + 1\right)\sigma_{h_i}^2 \quad (14)$$

$$P_{d,i}(\epsilon_i(P_{f,i,target}), \tau_i) = \mathcal{Q}\left(\frac{\mathcal{Q}^{-1}(P_{f,i,target}) - \gamma_i |h_i|^2 \sqrt{\tau_i f_s}}{\sqrt{2\gamma_i |h_i|^2 + 1}}\right) \quad (15)$$

$P_{d,i}(\epsilon_i(P_{f,i,target}), \tau_i)$ is the probability of detection when $P_{f,i}$ is targeted. As a result, in this part, probability of false alarm and detection based on $P_{d,i,target}$ and $P_{f,i,target}$, respectively, are calculated.

C. Model for Multiple Band Sensing

We present the model developed for wideband sensing as illustrated in Fig. 4. At the first step, the primary user signal is received by CR receiver at each subcarrier [42]. Next state is sampling and after sampling, the test statistics of the energy detection are obtained as the observed energy summation. At the end, in regard to each threshold, the CR decides whether the band is busy or idle. It is assumed that $\tau = [\tau_1, \tau_2, \dots, \tau_M]^T$ and $\gamma = [\gamma_1, \gamma_2, \dots, \gamma_M]^T$ as sensing time duration and the SNR for M subcarriers. Moreover the probability of false alarm and detection for all M subcarriers can be considered as $\mathbf{P}_f = [P_{f,1}, P_{f,2}, \dots, P_{f,M}]$ and $\mathbf{P}_d = [P_{d,1}, P_{d,2}, \dots, P_{d,M}]$. In the model, CR receiver can search in all frequencies and detect idle frequencies. Then, CR sends its results to scheduler and let it allocate the idle spectrums based on different policies which are set to achieve the goals like maximum total throughput and fairness allocation[43].

D. Primary User Activity Model

In this section, we present a model for primary users' activities which is directly proportional to CR network performance. In the Markov chains model, it is considered that two states (Busy by PU and Idle) are for each subcarrier. Since each user arrival is independent, each transition follows the

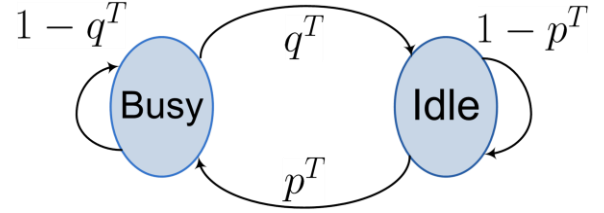


Fig. 5. Markov Chains Model.

Poisson arrival process. Thus, the length of Busy and Idle periods are exponentially distributed (or the time that user shall be served). The Poisson distribution is considered in the modelling with arrival rate, α , and departure rate, β , and in simulation, the average existing users is assumed such that 80% of total spectrums are loaded by primary users in average.

$$N_{tot}(nT_s) = N_{tot}(n(T_s - 1)) + \alpha(nT_s) - \beta(nT_s) \quad (16)$$

As a result, the existing users in a cell is equivalent to total existing users on previous time period added to arrival rate at current time and subtracted by current departure time as mentioned in equation (26). The transition probabilities are p^T and q^T as illustrated in Fig. 5. Hence, the probability transition matrix, P , in this case is given by:

$$\mathbf{P} = \begin{bmatrix} p_{b,b} & p_{b,i} \\ p_{i,b} & p_{i,i} \end{bmatrix}_{2 \times 2} = \begin{bmatrix} 1 - q^T & q^T \\ p^T & 1 - p^T \end{bmatrix}_{2 \times 2} \quad (17)$$

which results in transition rate matrix Q as:

$$\mathbf{Q} = \begin{bmatrix} -q^T & q^T \\ p^T & -p^T \end{bmatrix}_{2 \times 2} \quad (18)$$

$$\Pi \mathbf{Q} = 0 \quad (19)$$

$$\Pi = [P_{i,Busy}, P_{i,Idle}] \quad (20)$$

The calculated steady probabilities are depicted below:

$$P_{i,BUSY} = \frac{p^T}{p^T + q^T}, P_{i,Idle} = \frac{q^T}{p^T + q^T} \quad (21)$$

Eq. (21) is applied to analyse the model for identifying subcarriers states (i.e. busy or idle) [44-46].

E. Optimum Sensing time for A-SU in 4G CR network

The throughput of A-SU is calculated as follow while it can access subcarrier when PU is not using that spectrum,

$$C_i = W \log_2\left(1 + \frac{P_{i,SU} |h_{i,SU}|^2}{\mathcal{N}_0}\right) \quad (22)$$

where W is bandwidth, $P_{i,SU}$ is the power of transmitter CR and \mathcal{N}_0 is the noise power and $h_{i,SU}$ is the gain channel between i th CR transmitter and receiver with variance $E(|h_{i,SU}|^2) = \sigma_{h_{i,SU}}^2$.

Considering probabilities for different states gives us achievable throughput, $R_i(\tau_i)$, calculated [46],

$$R_i(\tau_i) = (1 - \frac{\tau_i}{T})(1 - P_{f,i}) P_{i,Idle} C_i \quad (23)$$

where $(1 - P_{f,i}(\epsilon_i, \tau_i)) P_{i,Idle}$ is the probability of absence of PU when we detect correctly. $(1 - \frac{\tau_i}{T})$ is the entire data transmission time [47].

From derivation of (23) we have:

$$\begin{aligned} \frac{d R_i(\tau_i, \epsilon_i)}{d \tau_i} = & \\ \frac{-1}{T}(1 - P_{f,i}) P_{i,Idle} C_i + (1 - \frac{\tau_i}{T}) \frac{\gamma_i |h_i|^2 \sqrt{f_s}}{2\sqrt{2\pi\tau_i}} \cdot & \\ \exp(Q^{-1}(P_{d,i, target})) \sqrt{2\gamma_i |h_i|^2 + 1 + \gamma_i |h_i|^2 \sqrt{\tau_i f_s}} & \end{aligned} \quad (24)$$

that the following equations can be derived,

$$\lim_{\tau_i \rightarrow 0^+} \frac{d R_i(\tau_i)}{d \tau_i} \rightarrow +\infty > 0 \quad (25)$$

$$\lim_{\tau_i \rightarrow T} \frac{d R_i(\tau_i)}{d \tau_i} < 0 \quad (26)$$

Thus, there is a τ_i between 0 and T that gives us maximum $R_i(\tau_i)$. Fig. 6 Shows the optimum sensing time based on equation (23). By Fig. 6, it can be denoted that the optimum sensing time in regard to technology limits and figure 4 might be between 3ns and 1μs.

F. Scheduling Approaches for AMI meters in Smart Grids

In 4G CR based AMI networks, managing the available spectrum resources and share the resources among the A-SUs requires sophisticated sharing methods for AMI meters to participating in future services (i.e. control of smart appliances, real time pricing adaptation, renewable energy management, and closed loop demand response) of smart grid.

We consider the downlinks of N_{su} A-SUs are serviced by a CR scheduling services located in cloud data centre (i.e. virtual base station) within a cell. The cloud data center allocates resource element RE (i,j) among the N_{su} A-SUs. At each frame multiple REs can be assigned to a single A-SU, although each RE can be allocated to only one A-SU. We assume that channel conditions vary across the subcarriers as well as A-SU. The channel conditions typically depend on the channel frequency, so they may be different for different channels. We presume typical urban area model. In addition, scheduling of SUs also depend on the user location and the time frame. However, in our context the AMI meters are geographical stationary leading to constant SINR values.

If each A-SU is serviced on a channel, the downlink multiuser capacity for orthogonal OFDM signaling is given below and note that it cannot exceed the Shannon capacity

$$C = \sum_{k=1}^{\min(n_T, n_R)} W_{cell} \log_2(1 + SINR):$$

$$SINR = \frac{S_{Cell}}{N + I_{OtherCell}} = \frac{\frac{P_{TxCell}}{PathLoss}}{W_{Cell}G_K + \sum_{k \in Other} \frac{P_{OtherCell}}{PathLoss(k)}} \quad (27)$$

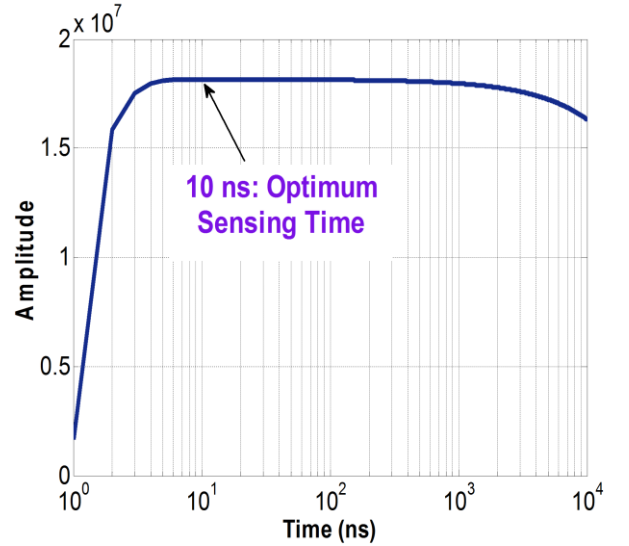


Fig. 6 Optimum Sensing Time.

In real-world deployments, we can develop a modified Shannon capacity formula, C_{MOD} , by replacing the cell bandwidth, W_{cell} with an effective bandwidth and βW_{eff} [48] which accounts for G-factor dependencies and protocol control, pilot, and cyclic prefix overheads. Closely related to the SINR is the G-factor, which accounts for the geometric dependencies of cell layouts and dictates the statistics of the downlink capacity. The G-factor is the average own cell power to the other cell-power plus noise ratio when considering uniform spatial distributions of transceivers within a cell.

In addition, we can define a normalized effective signal to noise ratio, SNR_{eff} , adjust SNR for both interference, G-factor statistics, and LTE implementation parameters. Defining the modified Shannon spectral efficiency for PU as

$$C_{MOD} = \beta W_{eff} \log \left(1 + \frac{S/(N+I)}{SNR_{eff}} \right) \quad (28)$$

We therefore define the A-SU capacity in presence of loss,

$$C = \int \sum_{SINR} (1 - \rho)(1 - \delta) \beta W_{eff} \eta \cdot \log_2 \left(1 + \frac{|h|^2 S}{SNR_{eff}} \right) dt \quad (29)$$

Where ρ is detection probability parameter and calculated by addition of false alarm detection probability (P_f) and detection probability (P_d). The parameter, δ , is primary user spectrum usage and we presume a average of 80% loading. β is a correction factor which nominally should be equal to one. η is the spectrum sensing efficiency. The scheduler decides which A-SU to transmit the information at each time frames, based on the request rates the base station.

The objective of max rate scheduling algorithm is to maximize the data rate through the system. Scheduling the user with the instantaneously best link conditions is often referred as max rate scheduling. The max rate can be expressed as $k = \arg \max_i R_i$ for i th user. The drawback of the max rate algorithm is that it is likely that a few users that are close to the base station (and have excellent channel conditions) will be allocated all the resources.

Proportional fair (PF) scheduler is designed to meet the challenges of delay and fairness constraints while harnessing multi user diversity. PF scheduler tracks the average

throughput, $T_k[nT_s]$, for each A-SU delivered in the past over sliding window of size t_c . In the time frame $[\tau]$, the base station receives rates $R_k[nT_s]$, $k=1\dots N_{su}$ from all the active A-SUs and scheduler basically schedules the A-SU with highest PF metric value, γ that is defined as $\gamma = \frac{R_k[nT_s]}{T_k[nT_s]}$.

The average throughputs $T_k[nT_s]$ are updated using an exponentially weighted low pass-filter [49]:

$$T_k[nT_s + 1] = \begin{cases} (1 - \frac{1}{t_c} T_k[nT_s] + (\frac{1}{t_c}) T_k[nT_s] & k = \gamma \\ (1 - \frac{1}{t_c} T_k[nT_s] & k \neq \gamma \end{cases} \quad (30)$$

Based on the Eq. (21) and (22) we can write as the following

$$\gamma = \frac{C = \int \sum_{SINR} (1-\rho)(1-\delta) \beta \cdot W_{eff} \cdot \eta \cdot \log_2(1 + \frac{|h|^2 S}{SINR_{eff}}) dt}{T_k[nT_s]} \quad (31)$$

Opportunistic Scheduling (OS) is an approach to deal with both fairness among users and maximizing the capacity rate. In max rate algorithm the user with highest request rate implies giving all the system resources to particular users, yields to highly unfair scheme to all other users. However, in PF the users compete for resources not directly based on the requested rates but based on the rates normalized by their respective average throughputs also defined as PF metric value. The downside of the PF approach is sacrificing over all throughputs. Thus OS algorithm schedules subcarriers $sc_{i,1}$ to $sc_{i,j}$ to the best secondary user based on two step criteria. First, the user who has the maximum PF metric value, γ , is selected. Second, the selected A-SU requested rate should be greater than the mean of all the secondary users requested rate, $\bar{R}[nT_s]$, to be scheduled as follow,

$$R[nT_s] \geq \bar{R}[nT_s] \quad (32)$$

As a result, unlike PF scheduling, the users having low throughput but high PF metric, γ , that have been chosen to access resource elements will have lower priority than users with enough PF metric and higher throughput.

Algorithm: Opportunistic scheduling

```

1) for  $n=1$  to  $N_T$  (simulation time)
2) Update A-SU profile, Update  $\gamma$ 
3) Let  $S$  be the set of secondary users
4) Let  $RE(i,j)$  where  $i=1$  to  $M$  subcarriers and  $j=1$  to  $K$  be the total time frames.
5) for  $i=1$  to  $M$ , for  $j=1$  to  $K$ 
6) Select the secondary user  $l \in S$  with highest  $\gamma(l)$ 
7) If  $R_l[nT_s] \geq \bar{R}_l[nT_s]$ 
8) Update the A-SU profile with  $S=S-\{l\}$ 
9) Allocate  $RE(i,j)$  to  $l$ th secondary user from  $S$ 
10) Else
11) Update the A-SU profile with  $S=S-\{l\}$ 
12) End if, End for  $j, i, n$ 

```

G. Inter-cell Interference coordination for Edge AMI meters

The performance of wireless cellular system is significantly limited by Inter-cell Interference (ICI). The principal reason

for ICI is spatial reuse (i.e., the reuse of resource elements such as timeslots or frequency bands) in a geographical distance, where the signal strength is reduced due to path loss, shadowing, and so on. In our 4G CR network, each A-SU suffers from ICI due to frequency reuse in other cells adopted by the primary user network frequency reuse patterns, which lead to poor resource utilization and less spectral efficient. In this paper we presume a frequency reuse of 2 is considered for PU network. Researchers proposed network-level approaches such as cooperative scheduling, multicell power control and distributed antennas as means of reducing the interference and improve spectral efficiency.

Ericson in [50-51] developed an uplink inter-cell interference co-ordination/avoidance scheme for frequency reuse. In this scheme cell users are divided in to two different groups; cell center users and edge cell users. Only a part of the frequency is used for cell-edge users with full power and should be orthogonal between neighbor cells to mitigate most of the interference. Cell-center users use the whole spectrum with restricted power to transmit/receive, and hence there will not too much ICI even the same frequency is used. In the case of CR users, as we borrow the unused resource blocks and specifically, the total interference power received at each PU should not exceed a preselected interference temperature limit (ITL) stated by FCC. There is not much flexibility to allocate RBs separately for cell edge users and cell center users.

This challenge necessitates proposing a coordinated multi-point uplink transmission scheme to improve cell-edge performance in terms of average throughput. Fig. 7. shows example scenario of A-SU present in the overlapping area of both cells representing a cell edge user. Fig. 7. depicts cell edge A-SU receives the received SINR from left BS is 10dB and no idle hole for uplink transmission. Fig. 7. also shows that left cell has high level of PU usage of RB. Cell edge A-SU receives the received SINR from right BS is 16dB and has idle hole for uplink transmission, so it performs uplink transmission with right cell BS due to unused RB availability. For the case2, Fig. 8. Shows if PUs moves from the range of the left BS to right BS and now edge A-SU receives the received SINR from left BS is 10dB and has idle hole for uplink transmission. Cell edge A-SU also receives the received SINR from right BS is 16dB and has idle hole for uplink transmission, it performs uplink transmission with both BS using coordinated multi-point uplink transmission scheme as shown in Fig .8.

To evaluate the zero delay expected transmission time for A-SU based on the allocated resource elements is defined as t_{req} for the remaining data size d_i . Let R_i denote the transmission rate of A-SU_{*i*} with m_i sub carriers allocated for transmission with bandwidth BW. According to Shannon theorem, the zero delay expected transmission time is given by

$$t_{req} = \frac{dt}{S_{ci} \cdot BW \cdot \log_2(1 + SINR_{dB})} \quad (33)$$

The zero delay expected transmission time for cell edge A-SU in case 2 as follows:

$$t_{req} = \frac{dt}{S_{ci} \cdot BW \cdot \log_2(1 + SINR_{dB})} + \frac{dt}{S'_{ci} \cdot BW \cdot \log_2(1 + SINR'_{dB})} \quad (34)$$

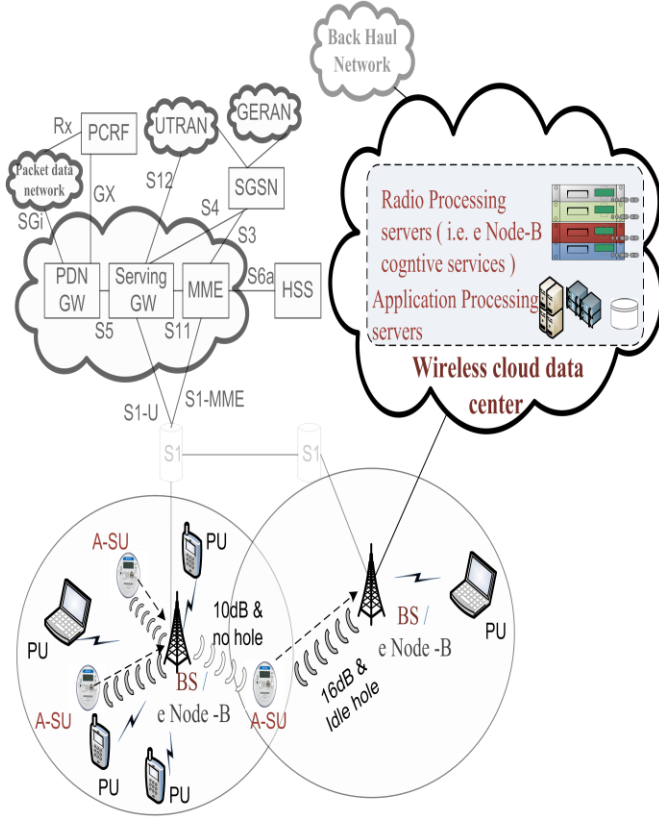


Fig. 7 Case 1 scenario: A-SU present in the overlapping cell area: High level of PU usage in the left cell and low level of P U usage in the right cell.

Where S_{ci} is the number of allocated resource element and $SINR_{dB}$ from the left cell BS, where as S_{ci}' is the number of allocated resource elements and $SINR'_{dB}$ from the right cell BS. The prime objective of the coordinated multi-point approach is to improve the cell edge user average data rates. This approach has been applied to different scheduling schemes (i.e. max rate, proportional fairness and opportunistic) using system-level simulations with hexagonal cells and analyzed in section IV.

IV. SIMULATION RESULTS & DISCUSSIONS

The environmental parameters used in simulations are shown in Table. 1. Two different sets of experiment are simulated. In the first experiment, different scheduling approaches have been analyzed in terms of throughput and fairness of A-SU. Also, the impact of active PUs to the number of A-SU that shall be served in each scheduling algorithm has been evaluated. In the second part, we analyze how coordinated multi-point approach acts on various scheduling algorithms to improve the average throughput of cell-edge users.

We adopt the 3GPP-LTE specifications (see [52]) 3-sectorial antenna (120 degree) because each site consists of three cells. Assuming 2-Dim uniform user spatial cell distribution, the obtained Probability Density Function (PDF) and Cumulative Density Function (CDF) are shown in Fig. 9. and Fig. 10. It is assumed that all users have equal session times.

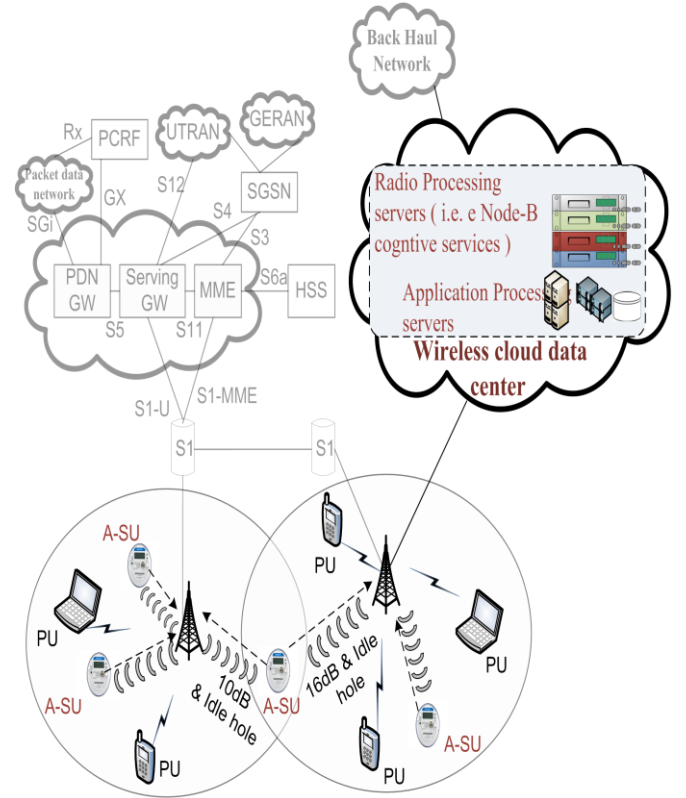


Fig. 8 Case 2 scenario: Example of edge cell user utilizing both base stations for uplink transmission using coordinated multi-point network.

A. Analysis of End to End Latency

The expected delay transmission time for A-SU is modeled as shown in Fig. 11. We presume the time to offload the processes such as CR and RAN services to the cloud data center including the fiber transmission time and wireless channel delay. The A-SU connection establishment time, $\tau_{SU} = \tau_{PU}^d + \tau_{CRA}^d + \tau_{ROF}^d + \tau_{CRS}^d + \tau_{ROF}^d + \tau_{CRBS}^d + \tau_{CSU}^d + \tau_{SU}^d$ (43) where τ_{pu}^d is time delay between PU and BS, τ_{CRA}^d is required sensing time, τ_{rof}^d is time delay caused by fiber transmission between BS and cloud data center and vice-versa, τ_{CRS}^d is time delay for cloud data center to process CR and other services, τ_{CRBS}^d is time delay between BS and A-SU device, τ_{CSU}^d is time delay for A-SU device to process the request, and τ_{SU}^d is time delay between A-SU device and base station or destination.

Latency Calculation Example

The cell radius (d) is 3 km in urban macro cell, and the speed of light (c) is 3×10^8 m/s. Therefore, the time of arrival (ToA) at the cell edge is $d/c = 10 \mu s$. In urban macro cell, the delay spread is $0.65 \mu s$ in Table 3.1 (pp. 28) of [52]. Let's assume that the delay for the strong peak of the received signal at the cell edge exhibits a uniform distribution with the minimum delay (a) of the ToA ($10 \mu s$) and the standard deviation of the delay spread ($0.65 \mu s$). In the uniform distribution, mean = $(a + b)/2$ and variance = $(b-a)^2/12$. Since $a = 10 \mu s$ and $(b-a)^2/12 = 0.65^2 (\mu s)$, $b = 12.2517 \mu s$ and mean = $11.1258 \mu s$. Therefore, we can assume that the maximum delay is $12.2517 \mu s$ in the macro cell.

$$\tau_{PU}^d = \tau_{CRBS}^d = \tau_{SU}^d = 12.2517 \mu sec \quad (44)$$

The τ_{CRA}^d and τ_{CRA}^d are very minimum; therefore delay caused by them is negligible. τ_{rof}^d is the propagation delay incurred for the signal to propagate through the medium. For a distance of about 10km the round trip delay is app. to 100 μ s. Finally, the τ_{CRS}^d the time delay for cloud data center to process CR and other services is based on the hardware specifications of provided the cloud infrastructure. A preliminary benchmark analysis for various Intel processors using VTune performance analyzer has been performed. We can tolerate the delay up to 200 μ s and to satisfy the latency requirements our system model needs minimum hardware specifications of 3.66 GHz processor and 12M cache and other network level requirements. Overall τ_{SU} delay is marginally reasonable to perform cognitive functionality on to the cloud. It can be realized due to the significant adoption of an on-demand network access to a shared pool of configurable, computing resources that can be rapidly provisioned and released by cloud data center.

B. Scheduling Performance of AMI Packets on CR Networks

To evaluate the performance of transmitting AMI packets on a CR system model, system level simulations have been conducted based on 3GPP LTE physical layer parameter assumptions. We first evaluate the system throughput for algorithms with varying the primary user loading within a cell. In this case, the primary user average loading is around 80% and total number of users is 500 in a cell. Over the period of time that spectrum sensing reports the number of idle resource elements, scheduler allocates the idle REs with A-SUs. The Fig. 12 illustrates average capacity for three aforementioned algorithms.

Max-rate scheduling algorithm results in highest average capacity among three algorithms, followed by opportunistic and fairness algorithms. The results seem to match our expectations, since the goal of the max-rate capacity is the user with highest request rate implies giving all the system resources to particular users. In proportional fair algorithm the users compete for resources not directly based on the requested rates but based on the rates normalized by their respective average throughputs, PF metrics. By this approach PF sacrifices the overall throughput while, achieving higher number of A-SUs scheduled. In OS the users having low request rate but high PF metric, γ , will have less chance to be scheduled. OS objective is to achieve higher average capacity compared to PF, while achieving decent fairness among the A-SUs.

Fig. 13.a and 13.b show the average number of users scheduled per one Transmission Time Interval (TTI) when 75 A-SUs are active in a cell and around 20% and 30% of idle RE are available. We can see that at least 60 and 70 A-SUs are scheduled to idle REs by fairness algorithm. OS and max rate algorithms allocate less number of average SUs respectively.

In Fig. 14, we analyze the scheduled A-SUs average capacity for each scheduling algorithm when number of active PUs varies. Based on goals of each algorithm they indicate respective positions in the results. It can be seen that the solution obtained using the proposed algorithm (OS) is quite close to the PF specifically when the active PUs are less.

We note that in scenario where less PU are scheduled, it yields to high availability of idle REs. Therefore, higher

number of A-SUs scheduled results in larger average capacity in the CR network. When the numbers of PUs are increased, the advantage of the OS algorithm over PF is more obvious (i.e. Fig.14) due to more sparse A-SUs. Sparse implies large variability in A-SUs profile (i.e. SINR, fading channel, physical location).

In Fig. 15, we analyze the average number of scheduled SUs in each scenario when number of active PUs varies. We note that the more PUs scheduled yields to less availability of idle REs and therefore less number of A-SU scheduled. In Fig. 14 the Max-Rate average capacity is much higher than average

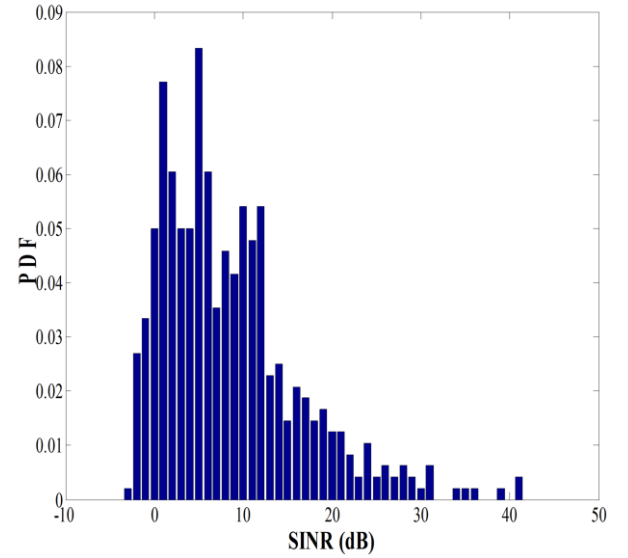


Fig. 9. PDF of SINR of all the users (i.e. PU and A-SU) within a cell.

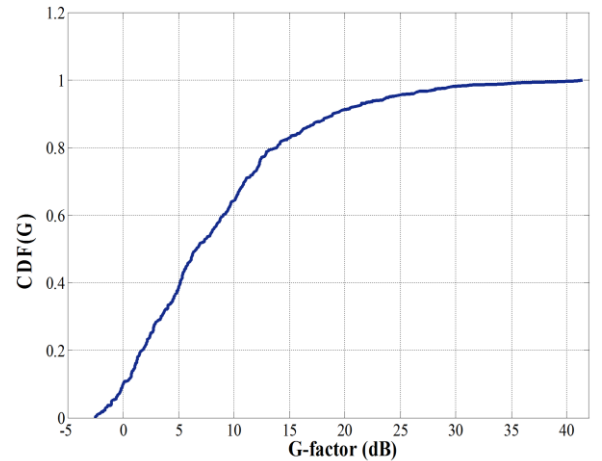


Fig. 10. G-factor CDFs for the cell.

capacity of PF; on the contrary, Fig. 15 shows the more scheduled A-SUs by PF algorithm compared to Max-Rate algorithm. As a result, the OS algorithm can balance both the performance of the cognitive radio networks in terms of achieving acceptable average capacity of A-SUs and the fairness.

C. Coordinated Multi-point Performance of AMI Edge Users

In the second experiment, we evaluate the number of cell edge A-SUs scheduled by the scheduling schemes enabled by

coordinated multi-point approach. Fig. 16(a). shows the distribution of active A-SUs in the cell. For simplicity we show the results only in the three cells. Fig. 16(b). shows the scheduling of A-SUs by the max rate algorithm. Max rate algorithm schedules the A-SU with the instantaneously best link conditions. Since the radio conditions for the different radio links within a cell typically vary independently, at each point in time there is almost some radio links whose channel quality is near its peak. Max rate schedules the A-SUs with best radio links and correspondingly high rates are achieved. This translates in to high system capacity. However, typically cell edge users have low probability to be scheduled due to low SINR which leads to low system capacity. Fig. 16(b). shows that low probability distribution of cell edge A-SU scheduled by max rate algorithm.

Fig. 16(c). shows the scheduling of A-SUs by the max rate algorithm enabled by the coordinated multi-point approach. It can be seen that the solution obtained using the proposed coordinated multi-point enables the higher probability distribution of cell edge A-SU scheduled by max rate algorithm. Fig. 17. illustrates the average capacity performance for three aforementioned scheduling algorithms using coordinated multi-point scheme.

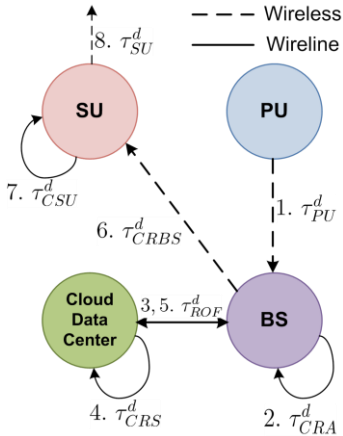


Fig. 11. End-to-End delay model.

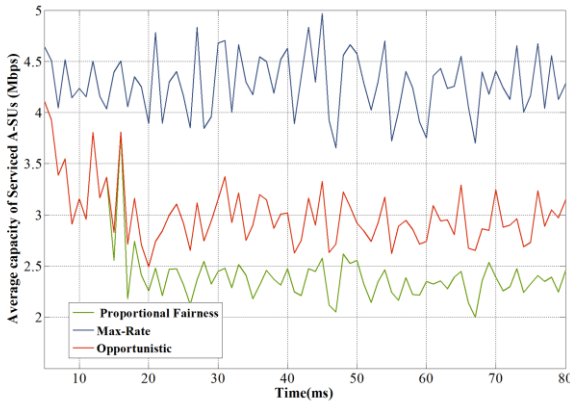
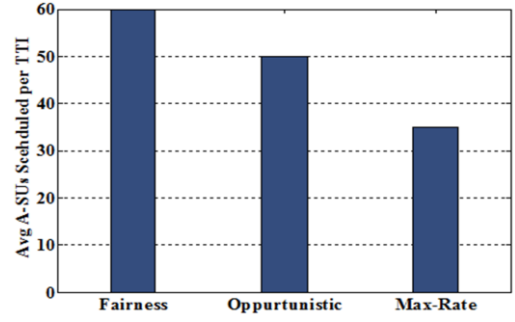
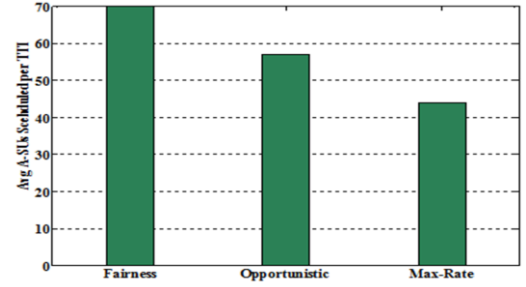


Fig. 12. Average capacity of scheduled A-SUs using different scheduling algorithms



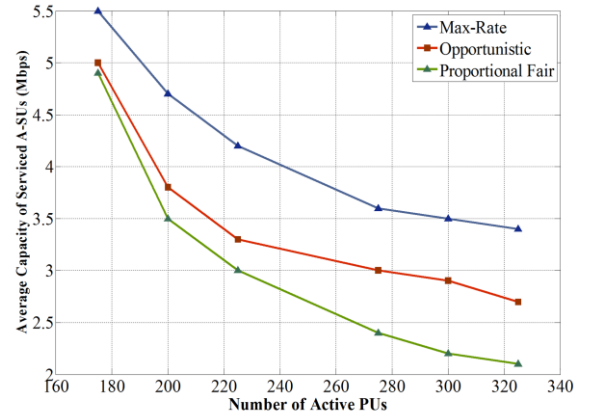
(a) 20% idle Resource Element case



(b) 30% idle Resource Element case

13. Average number of users scheduled per one TTI

Fig. 14.



Average capacity of serviced A-SUs.

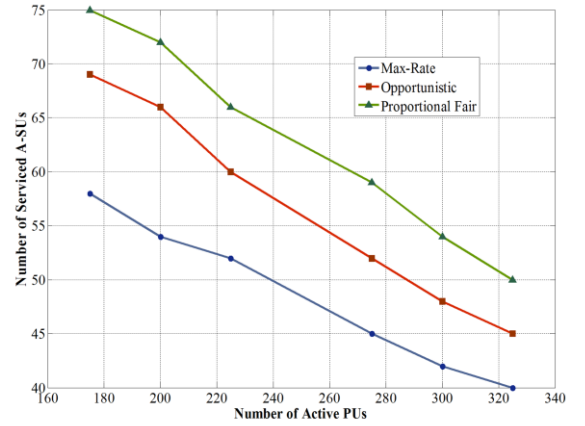


Fig. 15. Average number of serviced A-SUs

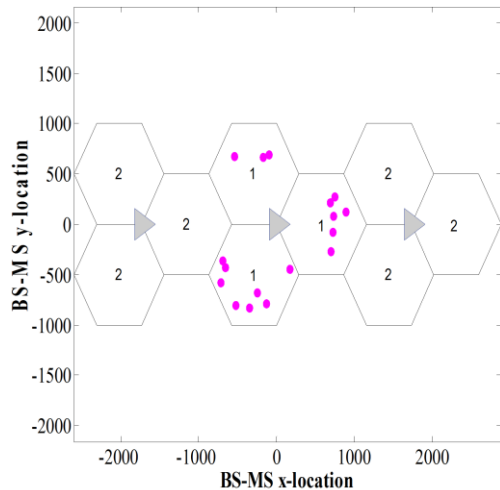
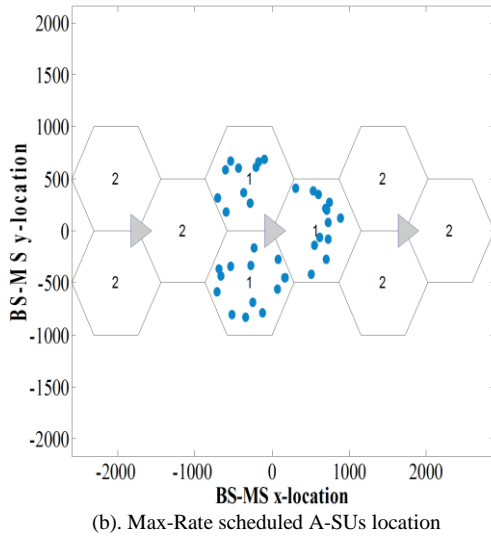
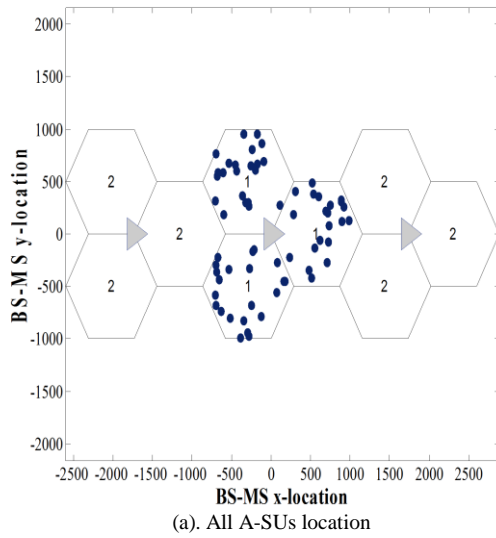


Fig. 16. A-SU Location Distribution

V. CONCLUSION

We have developed 4G CR framework model supporting AMI network in smart grids. Thus, the CR systems can be used to transmit AMI packets in the holes of a modern 4G LTE network with good performance for smart grid data communication. This paper also illustrates the use of cloud data center architectures to enable advance CR networking concepts. The integration of CR services in the cloud data center establishes software upgradability, high performance and low cost convergence architecture. We also proposed an opportunistic scheduling algorithm with multi coordinated network approach to avoid ICI and to improve the cell edge users over all throughputs without sacrificing the fairness metric of the users. Our system level simulation results show that the 4G CR network can achieve an average capacity of 3.5Mbps in a 3Km cell radius under the constraint of an average primary user network usage of 80%. We also present that the CR capacity of a 20% usage model meets the smart grid protocols requirements for a multi-user CR network of smart meters.

REFERENCES

- [1] Smart Grid Research & Development Multi-Year Program Plan (MYPP) 2010-2014.
- [2] Cameron Potter, Allison Archambault, Kenneth Westrick, "Building a Smarter Smart Grid Through Better Renewable Energy Information," IEEE Power Systems Conference and Exposition, 2009, IEEE PSCE, pp. 1-5, 2009.
- [3] Richard DeBlasio, "Standards for the Smart Grid," IEEE Energy 2030 Conference, Nov. 2008, pp1-7.
- [4] S. Massoud Amin and Bruce F. Wollenberg, "Toward a Smart Grid," IEEE Power and Energy Magazine, September, 2005, pp. 35-41.
- [5] FCC, ET Docket No 03-222 Notice of proposed rule making and order, December 2003.
- [6] Won-Yeol Lee and Ian F. Akyildiz, "Optimal Spectrum Sensing Framework for Cognitive Radio Networks" IEEE Transaction on Wireless Communications, pp. 3845-3857, vol. 7, No. 10, October 2008.
- [7] Shang-Wen Luan, Jen-Hao Teng, Shun-Yu Chan and Lain-Chyr Hwang, "Development of a Smart Power Meter for AMI Based on ZigBee Communication," in Proc. International Conference on Power Electronics and Drive Systems, Taiwan, 2009, pp. 661-665.
- [8] Coalton Bennett and Darren Highfill, "Networking AMI Smart Meters," in Proc IEEE Energy 2030 Conference, Atlanta, USA, 2008, pp.1-8.
- [9] Drew Gislason, Zigbee Wireless Networking. Elsevier Science.2008.
- [10] Wenpeng Luan, Duncan Sharp and Sol Lancashire, "Smart Grid Communication Network Capacity Planning for Power Utilities," Transmission and Distribution Conference and Exposition, IEEE PES, New Orleans, USA, 2010, pp. 1-4.
- [11] Byron Reid, "Oncor Electric Delivery Smart Grid Initiative," Protective Relay Engineers, 62nd Annual Conference, Austin, USA, 2009, pp. 8-15.
- [12] Srinivasa Prasanna, G.N. Lakshmi, et al., "Data communication over the smart grid", IEEE ISPLC 2009, pp. 273-279.
- [13] Chin-Sean, S., H. Harada, et al., "Smart utility networks in tv white space." Communications Magazine, IEEE 49(7): 132-139, July, 2011.
- [14] Robert C. Qiu, Zhe Chen, Nan Guo, Yu Song, Peng Zhang, Husheng Li and Lifeng Lai, "Towards A Real-time Cognitive Radio Network Testbed: Architecture, Hardware Platform, and Application to Smart Grid," Networking Technologies for Software Defined Radio (SDR) Networks, Fifth IEEE Workshop, Boston, USA, 2010, pp.1-6.
- [15] A. Ghassemi, S. Bavarian, and L. Lampe, "Cognitive Radio for Smart Grid Communications", IEEE SmartGridComm 2010, pp. 297-302.
- [16] Fatemeh, O.; Chandra, R.; Gunter, C.A, "Low cost and secure smart meter communications using the TV white spaces", ISRCS symposium 2010, pp. 37-42.
- [17] FCC, ET Docket No 04-186 Unlicensed Operation in the TV Broadcast Bands, September, 2010.

- [18] Jon M. Peha, "Sharing Spectrum Through Spectrum Policy Reform and Cognitive Radio," *Proceedings of the IEEE*, Vol 97, No. 4, 2009, pp. 708-719.
- [19] Chittabrata Ghosh and Dharma P. Agrawal, "Channel Assignment with Route Discovery (CARD) Using Cognitive Radio in Multi-channel Multi-radio Wireless Mesh Networks", 2006 IEEE Conference on Software Defined Radio.
- [20] Brian Kelley, "Software Defined Radio for Broadband OFDM Protocols," SMC 2009, San Antonio.
- [21] Brian Kelley, Software Defined Radio for Advanced Gigabit Cellular Systems, to appear in *DSP Handbook & Wireless, Networking, Radar, Sensor Array Processing, and Nonlinear Signal Processing*, Chapter 22, 2009.
- [22] Weifang Wang, "Spectrum Sensing for Cognitive Radio," Third International Symposium on Intelligent Information Technology Application Workshops, IEEE computer society, 2009, pp. 410-412.
- [23] D.D.Ariananda, M.K.Lakshmanan, H.Nikookar, "A survey on spectrum sensing techniques for cognitive radio," *Cognitive Radio and Advanced Spectrum Management*, 2009. CogART 2009. Second International Workshop on, pp. 74 – 79.
- [24] Akyildiz, I. F., Lee, W.-Y., Vuran, M. C., and Mohanty, S, "Next generation dynamic spectrum access cognitive radio wireless networks: a survey," *Computer Networks Journal (Elsevier)*, 2006.
- [25] Kranthimanoj Nagothu, Brain Kelley, Mo Jamshidi and Amir Raajee, "Persistent Net-AMI for Microgrid Infrastructure Using Cognitive Radio on Cloud Data Centers", accepted in *IEEE system Journal*, special edition Integration of Intermittent Renewable Energy Resources into Power grid, April 2012.
- [26] Minh-Viet, N. and L. Hwang Soo. "Effective Scheduling in Infrastructure-Based Cognitive Radio Networks." *Mobile Computing, IEEE Transactions on* vol. 10 No.6, pp. 853-867, 2011.
- [27] Qing Zhao ; Sadler, B.M. ;, "A Survey of Dynamic Spectrum Access," *IEEE Sig. Proc. Mag.*, vol 24, no.3, pp.79-89, 2007.
- [28] Shuai Zhang, Shufen Zhang, Xuebin Chen and Xiuzhen Huo," Cloud Computing Research and Development Trend", *Future Networks, ICFN '10*, Sanya, Hainan, 2010, pp. 93-97.
- [29] Bhaskar Prasad Rimal, Eumi Choi and Ian Lamb, "A Taxnomy and Survey of Cloud Computing Systems," in *Proc. Fifth International Joint Conference on INC, IMS and IDC*, 2009, pp. 44-51.
- [30] Junjie Peng, Xuejun Zhang Zhou Lei, Bofeng Zhang, Wu Zhang and Qing Li," Comparison of Several Cloud Computing Platforms," *Information Science and Engineering (ISISE)*, Dec, 2009, pp. 23-27.
- [31] Qing Zhao ; Sadler, B.M. ;, "A Survey of Dynamic Spectrum Access" *IEEE Signal Processing Magazine*, pp.79-89, vol. 24, May 2007.
- [32] Zhang Jingping," Theoretical Analysis of Combination and Detection for Short-Term Cooperative Sensing in Cognitive Radio Systems" 2nd International Conference on Education Technology and Computer (ICETC), vol. 2, pp. 381 -384, June 2010.
- [33] Akyildiz, I.F. ; Won-Yeol Lee ; Vuran, M.C. ; Mohanty, S. ; "A survey on spectrum management in cognitive radio networks" *IEEE Communications Magazine*, pp. 40-48, April 2008.
- [34] Carlos Cordeiro, Kiran Challapali, and Dagnachew Birru," IEEE 802.22: An Introduction to the First Wireless Standard based on Cognitive Radios" *Journal of Communications*, Vol. 1, No. 1, April 2006.
- [35] Digham, F. F. ; Alouini, M.-S. ; Simon, M. K. ; "On the Energy Detection of Unknown Signals Over Fading Channels" *IEEE Transactions on Communications*, vol. 55, pp. 21-24, Jan 2007.
- [36] Digham, F.F. ; Alouini, M.-S. ; Simon, M.K. ; "On the energy detection of unknown signals over fading channels" *ICC '03. IEEE International Conference on Communications*, vol. 5, pp. 3575-3579, May 2003.
- [37] Zhi Quan ; Shuguang Cui ; Sayed, A.H. ; Poor, H.V. ; "Optimal Multiband Joint Detection for Spectrum Sensing in Cognitive Radio Networks " *IEEE Transaction on Signal Processing*, pp. 1128-1140, vol. 57, November 2008.
- [38] Feng, T. ; Wang, G. ; Culver, S. ; Gidlund, M. ; "Collaborative Spectrum Sensing in Cognitive Radio System - Performance Analysis of Weighted Gain Combining" *Communication Networks and Services Research Conference (CNSR)*, pp. 1-6, May 2011.
- [39] Zhi Quan, Shuguang Cui, and Ali H. Sayed," Optimal Linear Cooperation for Spectrum Sensing in Cognitive Radio Networks" *IEEE Journal Of Selected Topics In Signal Processing*, Vol. 2, No. 1, February 2008.
- [40] Zhaoxia Song ; Zheng Zhou ; Xuan Sun ; Zhichao Qin ; "Cooperative Spectrum Sensing for Multiband under Noise Uncertainty in Cognitive Radio Networks" *IEEE International Conference ICC*, pp. 1-5, 2010.
- [41] Jiang Zhu ; Benxiong Huang ; Furong Wang ; Bo Zhang ; Wei Wu ; "AEF Analysis of Central Limit Theory Approximation in Spectrum Sensing" *WiCom '09. 5th International Conference on Wireless Communications, Networking and Mobile Computing*, pp. 1-4, 2009.
- [42] Khalid, L. ; Anpalagan, A. ; "Effect of sensing errors on wideband cognitive OFDM radio networks" *IEEE Biennial Symposium QBSC*, pp. 273-277, 2010.
- [43] Zhi Quan ; Shuguang Cui ; Sayed, A.H. ; Poor, H.V. ; "Wideband Spectrum sensing in Cognitive Radio Networks " *IEEE International Conference*, pp. 901-906, 2008.
- [44] Ghosh, C. ; Cordeiro, C. ; Agrawal, D.P. ; Rao, M.B. ; "Markov chain existence and Hidden Markov models in spectrum sensing" *IEEE International Conference*, pp.1-6, 2009.
- [45] Siddhartha Chib; Edward Greenberg; "Understanding the Metropolis-Hastings Algorithm" *The American Statistician*, Vol. 49, No. 4. (Nov., 1995), pp. 327-335.
- [46] Xiao Yu Wang, Alexander Wong, and Pin-Han Ho "Spectrum Sensing in Cognitive Radio Using a Markov-Chain Monte-Carlo Scheme" *IEEE Communications Letters*, Vol. 14, No. 9, September 2010.
- [47] Ying-Chang Liang, Yonghong Zeng, Edward C.Y. Peh, and Anh Tuan Hoang,"Sensing-Throughput Tradeoff for Cognitive Radio Networks" *IEEE TRANSACTIONS ON WIRELESS COMMUNICATIONS*, VOL. 7, NO. 4, APRIL 2008
- [48] Preben Mogensen, et al, "LTE Capacity compared to the Shannon Bound," *IEEE 65th Vehicular Technology Conference*, 2007. VTC2007-Spring, April 2007.
- [49] Davis Tse and Pramod Viswanth, "Fundamentals of Wireless Communications", Cambridge university press, 2005.
- [50] R1-050764,"Inter-cell Interference Handling for EUTRA", Ericsson, August 28-September 2,2005
- [51] R1-061374,"Downlink inter-cell interference coordination avoidance-evaluation of frequency reuse", Ericsson, May, 2006.
- [52] Lathaharan Somasegaran, "Channel Estimation and Prediction in UMTS LTE," Master Thesis (Aalborg University), 2007.

APPENDIX

Table Parameters	Value
Cell-level user distribution	Uniform
Power delay profile	3gppTU
G-factor	Ref [48]
Inter-Site DistanceCell	1732 Meters
Cell Layout	Hexagonal Grid, 3 sector sites
Network Scheduling	Frequency Domain
	Packet Scheduler
LTE-OFDM	MIMO: 1Tx, 2Rx
Deployment Spectral Efficiency	1.5bits/sec/Hz [48]
Bandwidth	20MHz
RB Bandwidth	180kHz
3dB Beam-width (θ_{3dB})	70
Maximum Attenuation (A_m)	20dB
Cognitive Radio Secondary Usage	10%
Cognitive Radio Primary Load	80%
Modulation/code rate settings	Qpsk/ 0.2-0.8
	16QAM/ 0.5-0.9
	64QAM/ 0.5-0.9
Channel Estimation	Ideal
Carrier frequency	2GHz

Table 1: Network Capacity Parameters for Cognitive Radio AMI Network

Persistent Net-AMI for Microgrid Infrastructure Using Cognitive Radio on Cloud Data Centers

Kranthimanoj Nagothu, *Student Member, IEEE*, Brian Kelley, *Senior Member, IEEE*, Mo Jamshidi, *Fellow, IEEE*, and Amir Rajaei, *Student Member, IEEE*

Abstract—We address the potential for a truly universal set of integrated wireless communication services, energy management, and control services for a next-generation of National Institute of Standards and Technology microgrid standards. Our approach uses cloud computing data center as the central communication and optimization infrastructure supporting a cognitive radio network of AMI meters which we label netbook advance metering infrastructure (Net-AMI). The Net-AMI is a novel low cost infrastructure of AMI meters that operate akin to netbooks with wireless transceiver that access to cloud data center energy services, cognitive radio services, and wireless communication services. Access occurs via cognitive radios channels. We claim that this solution solves the important problem in smart grid systems of how to develop an extensible, persistent, smart grid information network with a lifespan equivalent to that of most power systems (20–30 years). By persistence, we imply always operable, entirely software upgradeable, and independent of cellular networks. Our system is extensible and can easily handle thousands of variations in power systems, communication protocols, control, and energy optimization protocols. We formulate necessary link analysis and optimum scheduling of downlink and uplink Net-AMI packets in a multiuser cognitive radio environment.

Index Terms—Cloud data center, cognitive radio, netbook advance metering infrastructure (Net-AMI), smart grid, wireless.

I. INTRODUCTION

THE SMART grid of the future is generally anticipated to consist of an intelligent energy delivery system that supports plug-and-play integration of power, information, and security services. The future smart grid should possess a wide range of attributes that enable it to cope with information delivery, power flow distribution, intermittent energy sources, transmission line failures, energy storage systems, command and control of national infrastructure to achieve peak efficiency. In addition, as critical infrastructure it supports commerce and service needs. Resiliency and persistency in the aftermath of a major disruption is of the utmost im-

portance to minimize economic disturbances. Future services will involve autonomous control of smart appliances, real time pricing adaptation, shifting grid-tied power usage to non-peak periods, renewable energy management, and closed loop demand response [2], [3]. The services should be supportive of high penetrations of renewable energy components. It also acts as platform for consumer engagement in load management, national energy independence, and economic security [1]. In many such scenarios services, the advanced metering infrastructure (AMI) system is a central access point for communication of information flows in the smart grid and micro-grid distribution system networks.

We describe a new flexible Net-AMI infrastructure that supports the distributed smart grid. The Net-AMI network in the smart grid realm can be connoted as the firmware analogous to the PC-Netbooks [4], but integrated to the realm Net-AMI infrastructure. In addition, in our model of the processing, public and private energy services reside in customer accessible cloud data center containing remote servers. The cloud offers other services such as demodulation of home area network protocols (IEEE 802.15.4–Zigbee, Bluetooth, and Proprietary RF). Moreover, it also hosts energy manager applications with all the optimization algorithms residing in the cloud. It also provides microgrid energy optimization and other control services.

Net-AMI meters behave akin to a message relay and storage with a modicum of processing capabilities and communication and wireless interfaces. Rather than full fledged intelligent control processing devices, the Net-AMI is optimized for carrying out control tasks, accessing power system information in buildings and home area networks, and relaying (and receiving) data whose fundamental processing occurs in cloud data centers.

We define an ideal Net-AMI meter network attributes as: 1) low cost infrastructure (due to cell tower reuse and low frequency band costs) that is simultaneously rapidly deployable and can communicate wirelessly to a metropolitan wide network; 2) supports a universal set of protocols, standards, including most wireless and proprietary standards; 3) an ability to extensively adapt to future protocols via software (not hardware) upgrades; and 4) persistent power information flows of building usage and control, especially during power line disruption (e.g., convert to microgrid control due to hurricanes, lighting, transmission line failures). It should also persist if a service provider exits the market, a customer lacks paid

Manuscript received August 5, 2010; revised January 17, 2011; accepted May 25, 2011. This work was supported in part by the Texas Sustainable Energy Conservation Office and the U.S. Department of Energy under Grant RFA RE-AG1-2010, and by the Lutch Brown Chair Endowment at the University of Texas System, San Antonio.

The authors are with the University of Texas, San Antonio, TX 78249 USA (e-mail: kranthimanoj@gmail.com; brian.kelley@utsa.edu; moj@wacong.org; amirajaei@gmail.com).

Color versions of one or more of the figures in this paper are available online at <http://ieeexplore.ieee.org>.

Digital Object Identifier 10.1109/JSYST.2011.2162794

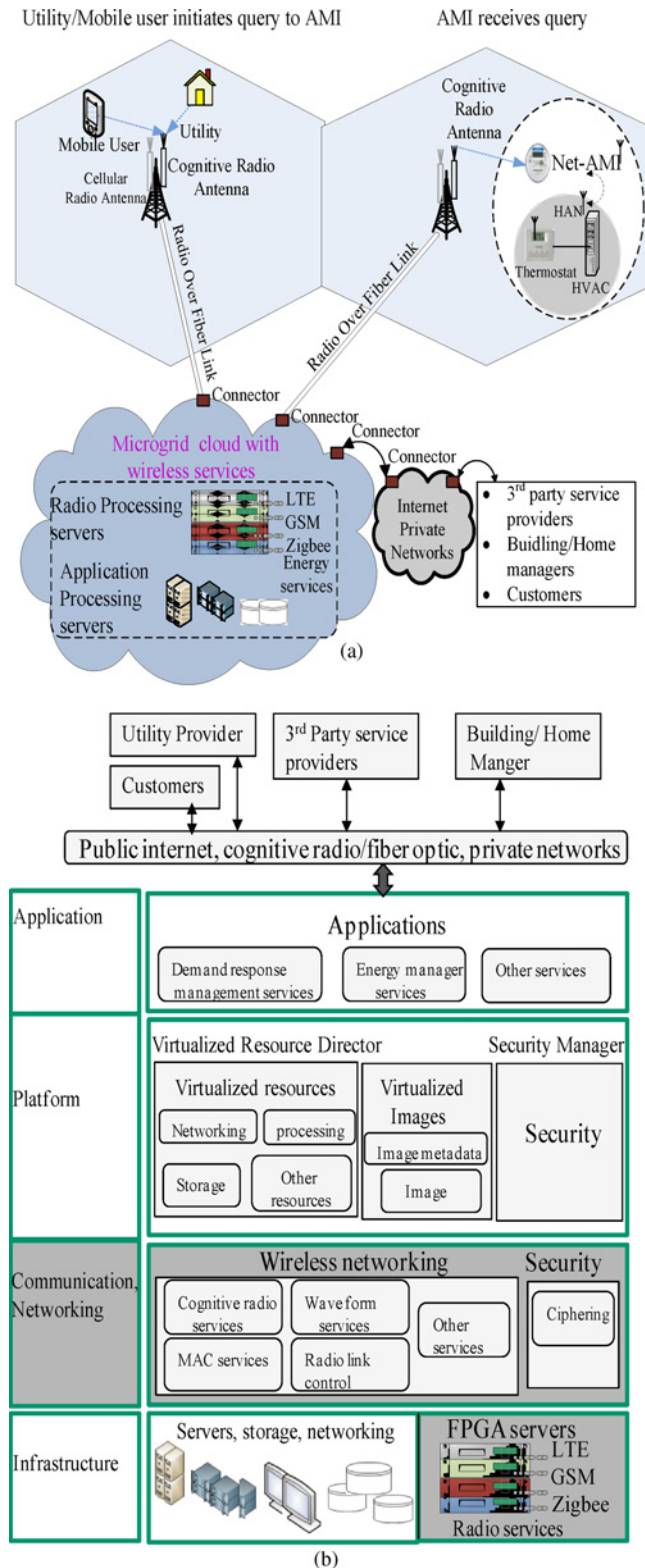


Fig. 1. (a) System architecture-wireless cloud data center facilitating cognitive radio transmission between net-AMI and mobile user/utility. (b) Model representing microgrid cloud.

services, or new proprietary protocols emerge relative to the AMI meter. A conventional approach to AMI networking involves connectivity to an Ethernet network. However, not every home or building supports Ethernet.

In this paper, we propose a persistent, low cost infrastructure enabling a distributed metropolitan area network of wireless

Net-AMI meters supportive of attributes 1–4. The network of Net-AMI meters is capable of cellular-like communications and control interactions with utility providers, mobile customers and autonomous energy management systems. Low-cost and low latency infrastructure results from leveraging the modern cellular networks base transceiver station (BTS) tower footprint to support metropolitan area Net-AMI meter coverage areas as shown in Fig. 1(a). Low cost also results from integrating existing cellular BTS towers with new Net-AMI antennas supportive of wireless metropolitan area Net-AMI networking. We employ cognitive radio as an integrated component of the smart grid [10]. We place new cognitive radio antennas on existing cellular antenna towers to leverage their infrastructure and tower height to achieve vast geographical coverage. We proffer that wireless communication enables dynamic connectivity. In addition, remote software upgrades allow modifications of existing networks components and Net-AMI meters in a flexible, amorphous manner.

A. Previous Work

Several authors have defined aspects of our proposed integrated Net-AMI network. Mesh, Ethernet and cellular AMI network topology for smart grid has been proposed in [5] and [6]. The authors proposed mesh networks of Zigbee based transmission architecture. Challenging issue with line of sight requirements in Zigbee is the limit of single-hop range to hundreds of feet [7]. The model details in deployment of new mesh networks necessarily imply high levels of inter-network coordination. Inefficiencies arise when transmission distances featured by the protocols in the entire metropolitan area for AMI networking. Improved alternatives include IEEE 802.11 (a, b, g, n) protocols configured as AMI mesh networks. Such networks, however, support transmission distances range from 50 to 200 m, which is problematic for robust metropolitan area coverage.

In [8], the authors discussed communication infrastructure based on Ethernet (LAN and WAN). The approach will support automated meter readings and customer home appliance connections. It can also support distribution automation and substation automation. We view such systems as completely complementary to our approach and a way of introducing service diversity. However, wireline systems are not always available. Customer subscription to service must occur and wired system can be challenging to rapidly redeploy, particularly in swiftly enveloping emergencies.

The authors in [9] described a framework for RF mesh networking interfaced with high speed WiMAX access networks. An issue here is how the AMI interfaces to future proprietary protocols unknown to the AMI at design time. Ideally, AMI upgrades should be done without hardware modification but via software upgrades. In [9], the AMI smart meters is capable of two-way communications over a 900 MHz wireless mesh network back to a collection point at the substation/switchyard. A private high speed access network will be then utilized to connect the substation-switchyard to the corporate network. This access network typically can be fiber or an existing cellular network (i.e., WiMAX).

The rest of this paper is organized as follows. Section II discusses core concepts such as cloud data center model, cognitive radio model, radio over fiber involved in developing Net-AMI networking infrastructure system in brief. Section III describes the overview of cognitive radio Net-AMI network system model. This section also details procedure of AMI information flow through communication protocol. Moreover, a hybrid RF-Optical communication analytical model is developed. Section IV details about study results on the overall system model and concludes this paper.

II. CORE CONCEPT IDEAS KEY TO PERSISTENT NET-AMI NETWORKING

A. Cloud Data Center System Model

The energy services of the future can be privately contracted services or public services. The centralized energy services manager resides on a cloud computing data center. The cloud center enables convenient, on-demand network access to a shared pool of configurable, computing resources (e.g., networks, servers, storage, applications, and services) that can be rapidly provisioned and released with minimal management effort [11], [12]. Cloud computing improves the availability of computing resources for wide varieties of software services. For instance, it can provide self-help services without the need for any manual interactions with service providers [13]. In our scenario of wireless cloud services, elasticity plays vital role due to high variations in the rate of users change accessing services. Cloud system services can reside far from physical locations of users.

There are different cloud computing platform classifications. Standard architectures include Abi (or Abiquo), Nimbus Open Nebula, Azure (Microsoft), Google (App Engine), Blue (IBM), and Mosso (Rackspace) (see [14]). Fig. 1(b) depicts the model for a cloud data center architecture optimized for microgrid based smart grids. Microgrids can act as an island with a set of loads, energy storage, and dynamic adjustable capability which can be detached from grid-tied power. The layered design of microgrid architecture is formulated on the bases from currently existing cloud architecture but extrapolated with a new additional layer of communication and networking as a service. Our microgrid cloud is layered into four layers.

1) *Application Layer*: This layer facilitates consumers to utilize the providers' application running on the cloud infrastructure. Applications may vary from energy services, optimization services to music and video services. Application layer is interfaced by the utility providers, customers, third party energy services providers via cognitive radio, internet or private networks. Consider an example, where a utility updates the AMI meter at any location with real-time pricing ability using an API on the cloud. The building energy manager (i.e., energy management service provider for end user) calls a different API on the cloud to access the real time pricing to evaluate and consider necessary changes to make a beneficiary decision. Eventually, the energy manager will send a control signal to net-AMI meter to allocate power flows among intermittent renewable sources, grid-tied sources, and loads to maintain equilibrium via demand response management

applications. When load demand is high and plant facilities need additional power capacity, the energy manager sends API requests to all the customers registered in demand response service to shutter devices or reduce serviceable loads (i.e., HVAC, lighting) according to a preplanned load prioritization scheme. These application services can be accessed by various partners with particular access control rights leading to a secure system. The attribute of accessing API's permits interoperability and extensibility around the cloud services supporting microgrids [15].

2) *Platform Layer*: The platform layer applications can be created using tools, software's provided by the cloud. Moreover, the layer attributes include a virtualization resource director (VRD) and security manager. The VRD allows users to create virtual machines and configure them with a specific operating system, resource allocation (i.e., CPU, memory) and software. However, the VRD has the ability to control and limit resources (i.e., CPU or memory) utilized by the users [16], [17]. This layer also supports the creation of images and image metadata.

The platform layer also dictates how security policies are created, managed and enforced in the cloud. It provides authentication, identity management mechanism to authenticate users and services based on credentials and characteristics. Trust management and policy integration enables multiple service providers to coexist and collaborate. It ensures that these features are handled securely and security breaches are effectively monitored during the interoperation process. Access controls, privacy and data management issues to be dealt with cloud. As some of the business enterprises are not comfortable storing their customer's data and applications on systems that reside outside of their on-premise datacenters. However there are large communities of researchers developing enhancements to existing solutions as well as creating mature newer solutions to above stated security related paradigms [18]–[21]. We contend that cloud computing benefits are fully realized as its adoption accelerates.

3) *Communication and Networking Layer*: This layer consists of services specifically designed to deliver networking services. By this feature AMI network service providers (ANSP) will have the ability to leverage cloud and provide various services. ANSP can allocate on demand services arbitrarily at any period time with minimum latency by dynamically upgrading the connectivity between the sites and utilizing vast cloud resources (i.e., CPU, high bandwidth). For instance, when there are large requests for a live streaming of high definition video. The ANSPs can leverage the services provided in this layer to adapt to the scenario and provide quality services to users. It also provides a common management framework by operating the services across the distributed resources rather than operating at separate facilities with fixed resource allocation. Among the services provided are cognitive radio services, waveform services, radio link control (RLC), and medium access control (MAC) services. Cognitive radio services, which provide spectrum management and spectrum sensing, are discussed further in Section III.

Waveform services represent error correction, modulation and demodulation for various protocols [i.e., long term evo-

lution (LTE), GSM]. The RLC services transport traffic between user devices and enodeB. The MAC services provide scheduling, reliability with advance transmission schemes and other services. Moreover, RLC provides ciphering (e.g., 128 bit AES) to the data. It ensures confidentiality and integrity of the signaling data. Finally, cloud communication and networking solution will lead to compelling next generation cloud communication networking services.

4) *Infrastructure Layer*: The infrastructure layer facilitates the effective integration of computing resources, storage, networks to deploy applications and operating systems. We augment our cloud infrastructure microprocessor racks with FPGA boards targeted to processing high computation rate processes typically associate with communication waveform signal processing and coding.

B. Data Center Based Microgrids and Smartgrids

Microgrids are envisaged as crucial infrastructure with a need for high levels of resiliency. Smart grid data in the cloud is obtained from various sources such as home area networks (HAN), AMI meters, transmission lines, distribution lines and vast arrays of sensor networks. Data obtained from these sources directly alter time-varying consumption and generation. Our model uses a robust, scalable data centric system that provides a (key, value). Data is stored in the form of key-value pairs [22]. The key can be the ID number of net-AMI meter or the time stamp. The value is the data associated with the key. Both the storage and retrieval is performed using keys. Flexibility is the key attribute for data centric system, which enables distributed data management and leads to horizontally scalable system. To enable redundancy, we can configure the number of replicas of any critical data with networked cloud centers. Moreover, as we rely on cloud centers to deliver critical services, system outage probabilities must be minimized. During network outages or environmental disturbances, the outage event service applications will shift the distribution equilibrium of the power system network via high speed control links to on distributed cloud resources.

In our model, we also achieve resiliency by integrating robust *cellular-like* services which are independent of cellular infrastructure and operated by utility-based network service providers. Cloud computing centers are designed to be scalable and to process large varieties of software applications. Finally, though the total power required by cloud computing systems is not insignificant, many approaches to minimizing power involving adaptive prediction algorithms to achieve optimal task allocation, minimum resource utilization, and optimum energy dissipation workloads have been proposed in [23] and [24].

C. Core Cognitive Radios Model

Cognitive radio networks (CRN) for advanced Net-AMI infrastructure enable persistent operation independent of spectral band license ownership arrangements. Persistence results from opportunistic barrowing of unused spectrum. Traditional CRN include three primary components: spectrum sensing, spectrum management (decision), and spectrum sharing. In cognitive radio systems, the licensed user of the frequency

band is always given priority access to the shared channel (time-frequency resource). Due to their priority in spectrum access, the operations of primary users (PU) are always first in the transmission queue so as to not be affected by unlicensed users [25], [26]. In our model of persistent Net-AMI wireless networking, the CRN is not required to have a license to operate in the desired spectrum. As a result, additional functionality is needed for CRN users to share the licensed spectrum band. We use a logical feedback channel model from a cognitive radio service running on a cloud data center. This is relayed to a cognitive radio antenna. In this way the Net-AMI schedules uplink transmission after the cognitive radio antenna transmits a downlink clear to send (CTS) signal. This is discussed further in Section III. In this event, the Net-AMI transmits an uplink signal over the allocated CRN band (e.g., television band, cellular band, unlicensed band). We presume procedures similar to [10].

D. Relaying RF Signals over Fiber Optics Cables

A major principal we follow revolves around relaying duplex information between the Net-AMI and cognitive radio antenna and the cloud data center in support of the Net-AMI system. This is shown in Fig. 1. In this context, we incorporate the transport of cognitive radio antennas signals, as relayed analog signals at RF, to the cloud data center at RF via fiber optic techniques. Such low loss, GHz broadband fiber optic technology has been demonstrated by researchers in [27]–[31] for use in micro cellular systems and is applied here. The technique is known as radio over fiber (ROF).

Traditionally a single radio over fiber can carry information in one direction only (simplex) and we usually require two fibers for bidirectional (duplex) communication. However, advanced wavelength division multiplexing (WDM) makes it possible to use the same fiber for duplex communication using different wavelengths [32]. WDM can be used to combine several wavelengths together. It can send them through a fiber optic network, greatly increasing the use of the available fiber bandwidth and maximizing total data throughput and wireless bandwidth.

Data centers are capable of handling enormous varieties of services, protocols, wireless standards, and new applications. The migration of the bulk hardware and software computation away from the Net-AMI and cognitive radio antenna to the flexible cloud data center enables virtually limitless extensibility of the Net-AMI network services. The benefit of this is that the cloud data center can process the universal set of wireless services, including wireless and Net-AMI meter services, allowing a virtually unlimited extensibility to the Net-AMI services and infrastructure.

III. COGNITIVE RADIO NET-AMI NETWORK SYSTEMS

We now describe the procedure for communicating data from the mobile user to an in-building network controllable by the Net-AMI as shown in Fig. 1(a). This infrastructure enables true metropolitan areas wireless via Net-AMI meter networking. In this scenario the Net-AMI meter is not formally registered with any wireless service provider. We

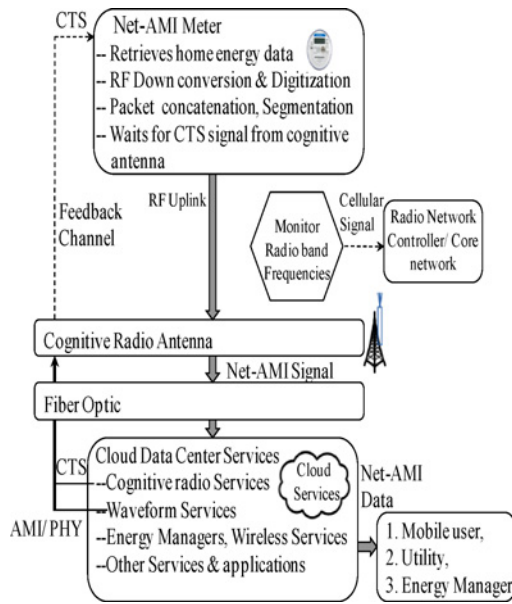


Fig. 2. Cognitive radio uplink via clear to send (CTS) presuming no cellular service.

note that the procedure enables the adoption of a new style of universal interface methodology and bounds allowing wireless connectivity among the Net-AMI meter, mobile, and the utility. Cognitive radio enables wireless connectivity between mobile user and Net-AMI. Placement of a cognitive radio antenna (CRA) on the BTS tower may occur in tandem with deployment of the cellular provider antenna. Antenna placement can also occur on utility based tower sites. By deploying CRA on existing towers, we reduce the infrastructure cost. The CRA also maintains significant antenna height, thereby reducing the path loss. Furthermore, placement of CRA on high towers sites maximize cognitive radio sensing for spectrum management services. We define sensing as the combination of signal detection and modulation classification.

The cognitive radio (CR) senses the spectral environment over a wide frequency band, particularly the spectrum in the cell region. It identifies the unused bands in the spectrum. These bands could be owned by cellular companies or license television band owners, but are not limited to these bands or to licensed bands. Sensed information using the CR is relayed over the fiber to cloud data center. The data center then unrolls in order: the cognitive radio service, waveform service, protocols service, security service, microgrid information packet and air-interface service, and the microgrid energy optimization or control services. The cloud center generates a response signal which is communicated over ROF to Net-AMI through CRA. Based on the incoming query, the Net-AMI performs several actions (i.e., collecting data from HAN) and an uplink transmission back to cloud center via ROF through CRA. The cloud center processes and analyzes Net-AMI data to generate a control signal to Net-AMI for using in building device control.

Fig. 2 depicts the flow of connection for the cognitive radio downlink presuming there is no subscription to high QoS energy management services running over cellular. In this sce-

nario, the cognitive radio identifies unused frequency bands, identifies the relevant cognitive services residing in the cloud data center, and generates a CTS signal. The CTS is sent back to the CRA through the feedback channel via radio over fiber links. Eventually, the CRA relays CTS signals to every Net-AMI meter in the cell region of CRA for uplink transmission.

A CTS signal accommodates both acknowledgment packets to send data from the Net-AMI meter and frequency band to transmit the signal and various other packets for over the air transmission (see Section IV). The Net-AMI responds to the CTS signal by sending the HAN data to CRA over the particular frequency band dedicated at this particular instant. The CRA receives the signal and forwards it via radio over fiber link to cloud data center. The cloud data center performs RF down conversion, A/D conversion and enables a plethora of Net-AMI communication standards, including proprietary utility standards.

Typically, the Net-AMI might need to interact with standards driven protocols such as GSM, LTE, HSPA, or WiFi rather than the Net-AMI meter's native communication protocol. Serendipitously, the cloud easily enables global aggregation of different protocols; it is capable of identifying the suitable protocols and supporting software definable radio wireless services. It then applies Net-AMI meter protocol services.

The rationale of this convergence of processing in the cloud is the ability for flexible, on-demand processing enabled by cloud computing. Migration of protocols and software allows for concurrent support of legacy standards and future standards defined after the Net-AMI *firmware* systems are designed. Let us consider a scenario where a Net-AMI meter's native local services are incapable of supporting a new protocol standard due to incompatibilities with HAN network and other hardware issues. In this instance, the software is virtually performed Net-AMI but physically mapped to the cloud. The Net-AMI meter relays the information to the cloud, which processes the protocol compliant responses and communicates the formatted information packets back to the Net-AMI. Such a software defined approach requires no hardware upgrades to the net-AMI, reduces system cost reduction, and improves flexibility in the system compared with existing systems.

A. Cognitive Radio Model

The prior discussion is premised on high speed communication links with broad geographic coverage. We now describe a new low cost model amalgamating cognitive radio and displacement, allowing the uplink receiver and downlink transmission at the base station to be invariant to the wireless communication protocol. In scenarios, where it is time critical due to emergency situations, we presume Net-AMI user is registered with wireless service provider in pay as you go form as shown in Fig. 1(a). The service provider handles all the principal components like demodulation and other issues in radio network controller similar to cloud center. Though smart grid is considered as critical infrastructure, build-out of an entirely new communication infrastructure would be highly expensive and not an ideal solution.

We emphasize reusing portions of existing wireless infrastructure (i.e., cell-tower) rather than solely relying on existing wireless carriers. Use of cognitive radio services and ROF concepts enables to form a persistent and resilient system as our model or using wireless carrier networks. This former does not preclude incorporating existing wireless-carrier services, but is low cost due to reuse of existing cell towers for antenna mounting (either wireless carrier towers or power utility towers), easy adaptation to future protocols through software upgrades, and no monthly recurring costs for customers using cognitive radio channels. The new components are principally software; the cost of the cloud data center is similar to the existing data center costs, with the exception of the FPGA Radio Servers.

The cloud data center offers cognitive radio applications as a spectrum management and spectrum sensing services. In regards to sensing spectrum, we propose three principal methods: matched filter detection, energy detection and feature detection [33]–[36]. In matched filter detection services, the secondary Net-AMI users must have *a priori* knowledge of primary user's signal statistics. These methods require less detection time, but generate optimal results only when detecting stationary signals in the presence of Gaussian noise [34].

Alternatively, energy detection senses the spectrum by measuring the energy of the received signal in a certain time-frequency band. Energy detection has very low computational complexities and can be implemented in the frequency domain by averaging FFT frequency bins; moreover, if the primary user's signal statistics are not known, energy detection can still be applied. However, it performs poorly in a low SNR environment and cannot distinguish signal, noise, and interference.

A third principal method is feature detection. The core idea involved in feature detection is to correlate with reoccurring parameters of the signal. For instance, many signals in wireless communication have a specific feature such as pilot, synchronization channels or cyclostationary properties that we detect and classify. Feature detection can differentiate the noise energy from the modulated signal energy and works well at low SNR. However, it requires longer and more complex processing. It also needs the prior knowledge of the PU or secondary user (SU) information statistics. The longer computation time can be reduced through the use of cooperative detection [34]. By collecting the observations from multiple cognitive radio users, we reduce detection sensitivity and detection time requirement at the expense of increased overhead and control for the cognitive radio network.

The model for spectrum sharing illustrated Fig. 3 (see [37], [38]). Fig. 3(a) illustrates the time frequency increment power, and Fig. 3(b) the (0, 1, 2) mapping of time-frequency increments to scheduled user classes.

The 0-holes can be accessed by cognitive radio users. Once accessed, such time-frequency increments are labeled as 1-holes. Other SUs are prevented from using 1-holes if it is determined by the cloud data center CR scheduler that the secondary user interference reduces the system capacity. At all times, licensed band users have highest priority. The useable CR capacity depends on the licensed user network statistics.

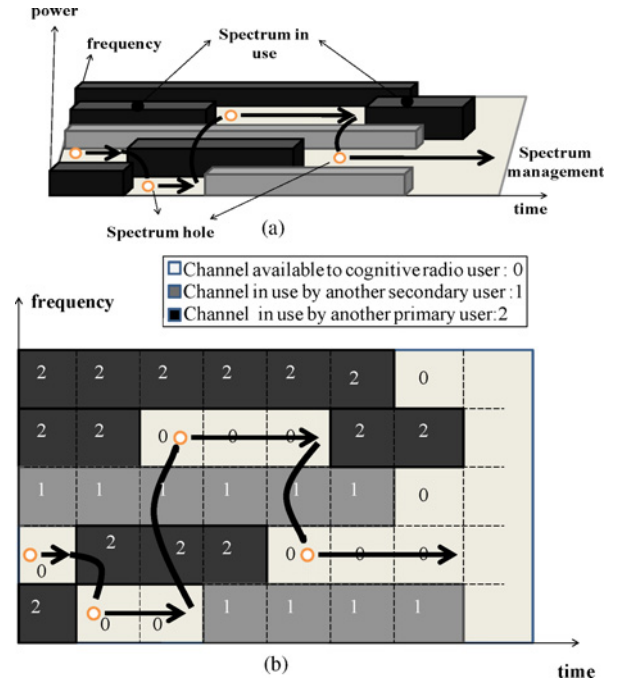


Fig. 3. (a) Spectrum sensing of time-frequency channel availability. (b) Interference avoidance based spectrum management. Primary users are detected via energy detection. Secondary users are detected via energy detection and frame type signal correlation.

To decrease system overhead, the interference temperature (IT) model [34], [35] can be used. This concept, which mitigates multiple access interference, was introduced by the FCC in order to facility the sharing of spectrum bands by SUs. In [34] and [35], improvements in the PU's QoS results by restricting the SUs transmit power so as to make the interference at PU's receiver below the given IT threshold [36], [39]. However, here we pursue a constant transmit power method and instead rely on adaptive modulation and control [40]. We make use of the method involved in the IT model. We apply the following thresholds based upon the signal-to-interference-plus-noise (SINR). Outage probability is inversely proportional to the PU's QoS. During the coherence time of the channel, the IT threshold is transmitted to SUs so as to determine the PU's channel information statistics. The cloud data center cognitive services periodically broadcast a pilot signal that includes the information about its transmit power and the maximal IT threshold, I_m .

From this, each SU can obtain the values of L_i and I_m . The parameter, L_i , defines the shadowing and distance-related average channel gain between the i th secondary user, SU_i , and base station (BTS). Then the practical maximal transmit power of the SU_i (P_i^M) is constrained by both the PU's SINR outage probability and its own maximal transmit power, P_i^{Max} . In order to protect PU's QoS, we choose the maximum cognitive radio transmit power, P_i^M , restriction of the i th Net-AMI transmit power suggested in [36], which is

$$P_i^M = \min \left\{ \frac{I_m}{L_i}, P_i^{\text{Max}} \right\}. \quad (1)$$

The term P_i^{Max} is the maximum PU power. The term $\frac{I_m}{L_i}$ is the maximum interference I_m by the primary user due to the

SU co-channel interference. The SUs compete to access the shared cognitive radio channel based on their average transmit rate, we apply the practical method max throughput algorithm with proportional fair (PMTA-PF, see [36]). This makes our cognitive radio cell spectrum sharing procedure “proportional fair” with the following scheduling rule metric:

$$i^* = \max_i \left(\frac{R_i^M}{T_i} \right) = \max_i \left(\frac{\log_2 \left(1 + \frac{(P_i^M/L_i) \|h_i\|^2}{n_i + I_p} \right)}{T_i} \right). \quad (2)$$

If the i th SU has interference plus noise which is $n_i + I_p$. The optimum scheduling strategy is to schedule user i^* if their channel has the maximum rate indicated in (2) during the time period at time t , $T_i(t)$. In order to achieve fairness among SUs, the SU who has larger transmit rate and larger average throughput will not be selected, due to its larger average throughput. The parameter, i^* , is the scheduling rule, R_i^M is the maximal transmit rate of SU_i , L_i represents the distance-dependent channel loss (>1) and shadowing effect from SU_i to cognitive radio base station, $h_i \sim CN(0, 1)$ models the normalized Rayleigh fading. I_p and n_i are the background interference plus the interference caused by SUs and i th users background noise power, respectively. In [36], the method shows an average throughput bps/Hz is not saturated until number of secondary users is less than 120 in each cell and range of throughput bits/s/Hz is about 19 kb/s to 23 kb/s.

B. System Infrastructure an Net-AMI Meter Data Flow Illustration Through the Protocol Stack

The Net-AMI meter is the major component for communication of information flows in the smart grid distribution system networks. The Net-AMI meter needs to relay time of use metering, power information, HAN information for outage management, demand response, network optimization, distribution of renewable sources and controlling home or building appliances. As we discussed in Section III, the Net-AMI meter may not be capable of processing HAN protocols due to protocol incompatibilities issues and limited processing capabilities. The Net-AMI meter’s principal architectural function is the fast communication of data to and from the cloud center. In this section, we describe how the Net-AMI meter combines all the data from various sources and hands off data to a cellular protocol [e.g., typically GSM, 3 GPP high speed packet access (HSPA), 3 GPP LTE] for over the air communication. Eventually, data is received by the cloud system for processing. In order to process the data in the cloud in a systematic way, the Net-AMI meter appends a packet header to data to enable protocol identification and message handling.

In Fig. 4(a), we illustrate an example of the mobile device initiating a control operation of in-building power system (i.e., HAN network) using the Net-AMI as relay portal. In our discussion the cognitive spectrum management (cognitive radio services) residing in cloud center, identifies the unused bands and sends a CTS signal including the query by the user to the Net-AMI meter indicating band availability. The Net-AMI responds to query (i.e., in this case it is remote

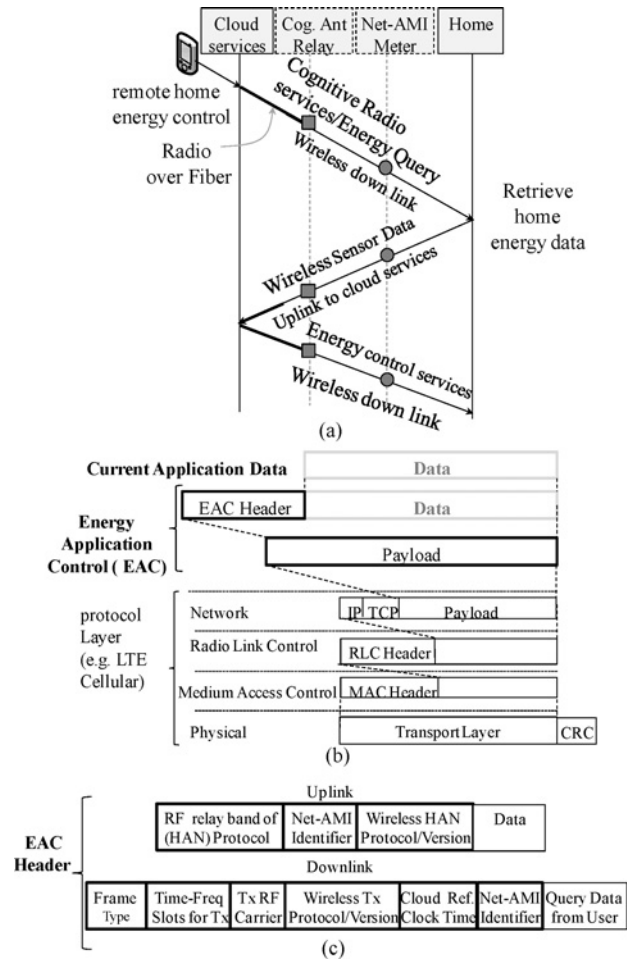


Fig. 4. Session control procedures with data flow. (a) Session control procedures. (b) Illustration of data flow through cellular protocol stack. (c) EAC uplink control frame and EAC downlink control frame (indicating CTS/query).

home energy control) and retrieves home energy data from HAN network. The Net-AMI acts a relay portal device and performs uplink transmission to the cloud center. The cloud center performs a plethora of services such as waveform processing service, protocols service and energy manager and optimization algorithms. The energy control services are displaced back to Net-AMI via ROF through CRA for in-building control operation. The Net-AMI meter performs concatenation of energy application control (EAC) header for uplink transmission as shown in Fig. 4(c). The EAC header details the type of the HAN protocol (i.e., Zigbee, Zwave, Proprietary, and WiFi), the version of protocol, and the Net-AMI identifier used for source and destination identification.

The Net-AMI meter waits for the CTS signal from CRA for uplink transmission. The CTS signal broadcasts specific information to Net-AMI meter, as shown in Fig. 4(c). The EAC header in downlink details first field as frame type. The Cloud sends CTS, query or both. This field identifies as binary 0 (CTS), query (1), and both (0, 1). The next field provides scheduling of time and frequency slots for data transfer with less interference of signals at CRA. If the Net-AMI is unable to perform transmission within a CTS time-out period, the system delays transmission until next CTS control signal. A

field indicating the type of cellular protocol (i.e., LTE, GSM, and CDMA) is included in the RF carrier frequency signal to support uplink transmission. The cloud reference time is used to account for time out scenarios based on received time slots. Finally, a Net-AMI identifier is needed for destination and source routing. Based on all these inputs, the Net-AMI meter bandpass modulates the signal to a specific RF carrier frequency and performs uplink transmission.

In Fig. 4(b), without loss of generality, we illustrate data flow through a cellular protocol stack with respect to the 3GPP-LTE protocol. The Net-AMI meter concatenates an EAC header to the data packet in the EAC layer. It inserts as information packets in the cellular protocol frame (LTE in this example). The uplink and downlink transmission of the LTE protocol are below the EAC layer. Thus, LTE applies packet retransmission to the occasional uncorrectable packet errors due to fading and pathloss. This is accomplished through a highly sophisticated two-layered retransmission scheme: a fast hybrid-ARQ protocol with low overhead feedback and support for soft combining with incremental redundancy. This is complemented with a highly reliable selective-repeat ARQ protocol in the MAC layer [41], [42]. A fixed bit 24 bit cyclic redundancy check (CRC) is performed on every block coming from above layers in physical layer. The calculation performed using CRC is appended to every transport block in order to check coherence of received signal. This process ensures data integrity and allows cellular protocols to handle the issues without our intervention. Since we included the CRC in the application layer, retransmission of packets is done in network layer.

C. Procedures for Cloud Control Services

The cloud center is the global aggregator of services and protocols, from cognitive radio services to wave form services to energy management, to microgrid control, and many other services. The cloud data center is imbued with both baseband processor servers and general processor servers. Base band processors resemble to conventional radio network controller of the cellular service providers. Demodulation, encryption, error detection are specifically processed in baseband servers and other application oriented processes are dedicated to general purpose servers.

The structural components of the downlink cognitive radio services are spectrum management and process the cognitive radio signals from the CRA to generate a CTS signal with EAC header for downlink transmission as shown in Fig. 4(c). Moreover, cloud service supports waveform services. Processes like signal processing, error correction, baseband conversion, and other modulation techniques are designated to radio processing servers. Furthermore, radio processing servers are loaded with protocol oriented applications (i.e., Zigbee, propriety RF, Wi-Fi, and Bluetooth) to process the requested services. It also provides energy home management services. These services request the necessary data from waveform services in order to monitor and analyze energy consumption, if this service has been registered or requested by the user. Similarly, if the user has renewable sources he can register with energy optimization services for optimal renewable source management. Cloud

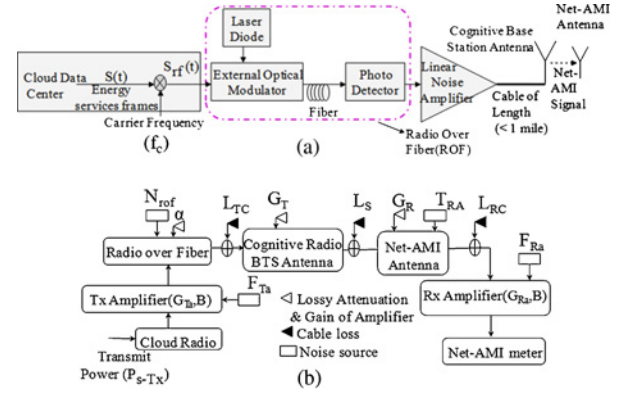


Fig. 5. Downlink models. (a) Structural cloud downlink configuration to Net-AMI. (b) Noise model of cloud source to net-AMI receiver link with losses, gains, signal components, and noise sources.

data center enables users to install any third party applications for additional services. This empowers the whole system to be flexible and extensible.

D. Hybrid Wireless (RF)-Fiber Optic Communication Model

We now analyze the communication link consisting of ROF, wireless signaling, and noise at the transmitter side and receiver side. We present an example Net-AMI network based ROF architecture using on external modulation for illustration in Fig. 5(a). For downlink transmission from Cloud data centers to Net-AMI meters the energy services signal, $s(t)$ at power P_{S-TX} is modulated to an RF band which, in turn, is converted to an RF optical light source using an external optical modulator. This signal is carried over the downlink optical fiber where the optical signal is converted back to electrical signal using a photo detector. The Net-AMI signal is relayed to a Net-AMI meter. For uplink transmission from Net-AMI meter to cloud center, the Net-AMI signal received at the cognitive radio is converted into an optical signal by modulating a light source. It is then relayed at RF over the optical fiber relay to the cloud data center. A photo detector demodulates the optical signal to obtain electrical signal which is again demodulated using RF band to process the Net-AMI signal at the cloud data center.

The, end-to-end noise, N_{RX} , contains both radio over fiber noise, and N_{ref} . Due to transmission of fiber optic data to the cognitive radio base station antenna and downlink operates from the base station transmitter to the wireless Net-AMI meter. N_{rof} noise is influenced by the linear amplifier after the lossy cable connecting the radio fiber optics and the base station linear amplifier after RF up-converter. The complete noise model of Cloud Source to Net-AMI receiver link with losses, gains, signal components, and noise sources is illustrated in Fig. 5(b).

The optical carrier's wavelength is usually selected to coincide with either the 1.3 μm window, which corresponds to minimum dispersion for standard single-mode fiber. Alternatively, an approximately 1.55 μm window obtains minimum attenuation and is compatible with the best-performing type of optical amplifier. Considering a single mode fiber and radio over the fiber noise, N_{rof} is added at the optical receiver where

the signal $s(t)$ is weak (due to the fiber and conversion losses). Considering only the dominant noise processes, the radio over fiber link noise power is sum of short noise, thermal noise and relative intensity noise (RIN) powers [43], [44].

We now analyze uplink and downlink configurations. We can improve all the following analysis by adding additional Net-AMI receive antennas, MIMO space time codes, or increasing bandwidth.

1) *Downlink: Cloud to ROF to Net-AMI Meter*: Following the approach in [45] note that we account for the noise components at the transmitter as well as the noise at the receiver, where P_{s-Tx} is the signal optical transmit power in Watts, E_b is the energy per bit in Joules, N_o is the noise power spectral density in

$\frac{watts}{Hz N_{rof}} = \langle i_{sh}^2 \rangle + \langle i_{RIN}^2 \rangle + \langle i_{th}^2 \rangle$ is the radio over fiber noise in Watts [43], [44], k is the Boltzmann's constant $= 1.38 \times 10^{-23}$ J/K, f_s is digital sampling rate, $B = 5$ MHz is the one-sided bandwidth and $B = f_s/2$. Without loss of generality, we assume an ambient temperature of $T_0^o = 290$ K, $\langle i_{sh}^2 \rangle = 2 \times R \times q \times P_s \times B$ is the shot noise variance arises from static nature of photo detection (R is the responsivity, q is the charge of the electron, P_s is the signal optical power), $\langle i_{RIN}^2 \rangle = P_{RIN} \times I_D^2 \times B$ (P_{RIN} is the RIN parameter, I_D is the average dark current of photodiode), $\langle i_{th}^2 \rangle = \frac{4 \times k \times T_0^o \times B}{R_L}$ is the mean square thermal noise (R_L is the load resistance), c is the speed of light, f_c is the carrier frequency G_{Ta} , G_{Ra} , G_T , G_R are the gain of transmit amplifier, receive amplifier, the transmit antenna, and receive antenna, respectively, F_{Ta} , F_{Ra} is the noise figure of the transmit amplifier and the receive amplifier, respectively. The receiver antenna noise is T_{RA}^o . L_s , L_{TC} , L_{RC} are the path loss, the transmit cable loss, and the receive cable loss. $L_{RoF}(dB) = -\alpha L$ (α : fiber attenuation coefficient 0.8 dB/km) is the attenuation in fiber as a function of length. As light travels along the fiber, its power decreases exponentially with distance.

We presume a wireless path loss (divergent from ideal path loss) defined as

$$L_s = 35.4 + 15.59 \text{ LOG}_e(d) \quad (3)$$

R_b is the digital bit rate and $\left(\frac{E_b}{N_o}\right)_{Rx}$ is the digital SNR at the receiver. Then, the total noise at the receiver, N_{Rx} , is

$$N_{Rx} = \frac{G_T G_R}{L_s} N_{Tx_{RoF}} + N_{Rx_{ant}} + (L_{RC} F_{Ra} - 1) \kappa G_{Ra} T_0^o B \quad (4)$$

$$N_{Tx_{RoF}} = \frac{N_{rof} G_{Ta} + (F_{Ta} - 1) k T_0^o B G_{Ta}}{L_{TC}} + \frac{(L_{TC} - 1) \kappa T_0^o B}{L_{TC}} \quad (5)$$

From (4) we see that the ROF noise, N_{rof} , manifests itself as a transmitter noise which is attenuated due to path loss. For $N_{rof} = 1e - 12$ Watts. Our simulations indicated that it is typically several orders of magnitude less than the receiver noise for reasonable assumptions of noise figures, amplifier gains, and cable losses [see Fig. 6(a)] and can be neglected. The receiver noise, noise power spectral density, receiver power, and receiver digital SNR can be derived in (6)–(10) as

$$N_{Rx} \approx N_{Rx_{ant}} + (L_{RC} F_{Ra} - 1) \kappa G_{Ra} T_0^o B \quad (6)$$

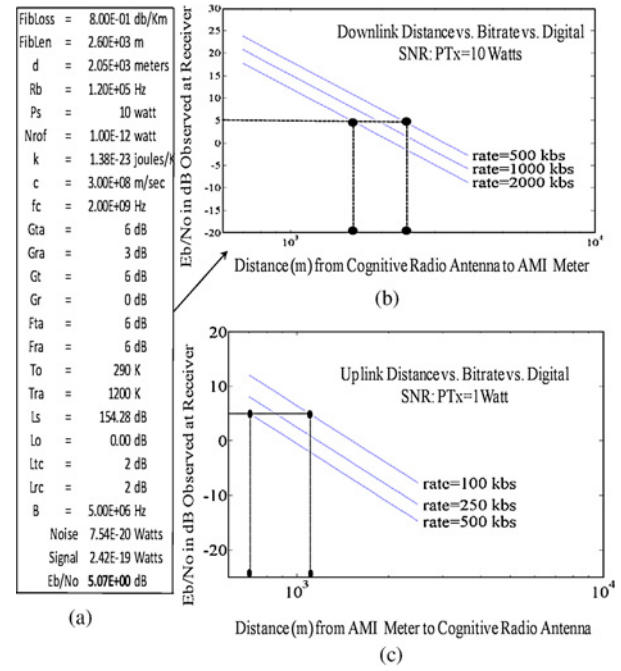


Fig. 6. Data rate versus digital SNR (E_b/N_o) computed from link analysis of combined ROF and wireless net-AMI to cognitive radio antenna. (a) Link parameters. (b) Downlink at 5 MHz, 10 Watts. (c) Uplink at 5 MHz, 1 Watt

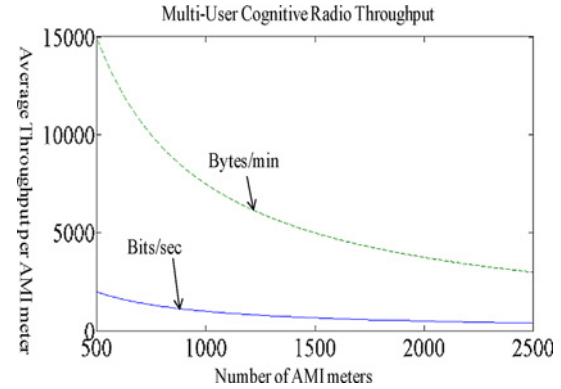


Fig. 7. Average deployment throughput as a function of the number of AMI meters in a site 3 hexagonal configuration based upon Table I.

$$N_o \triangleq \frac{N_{Rx}}{B} = \kappa G_{Ra} T_{Rx_{ant}}^o + (L_{RC} F_{Ra} - 1) \kappa G_{Ra} T_0^o \quad (7)$$

$$P_{Rx} = P_{s-Tx} \frac{G_T G_R G_{Ta} G_{Ra}}{L_s L_{TC} L_{RC} L_{RoF}} \quad (8)$$

$$\left(\frac{E_b}{N_o}\right)_{Rx} = \frac{P_{Rx}/R_b}{N_o} = \left(\frac{P_{s-Tx} G_T G_R G_{Ta} G_{Ra}}{R_b L_s L_{TC} L_{RC} L_{RoF} N_o}\right) \quad (9)$$

2) *Uplink: Net-AMI Meter to ROF to Cloud*: Let us define the uplink as the Net-AMI meter to the cognitive radio cellular antenna to Radio over fiber to the cloud data center. Noise components are principally associated with the receiver. In this instance, ROF noise occurs at the receiver. Similar to the downlink we find that

$$N_{Rx} = \kappa G_{Ra} T_{Rx_{ant}}^o B + (L_{RC} F_{Ra} - 1) \kappa G_{Ra} T_0^o B + N_{rof} \quad (10)$$

$$N_o \triangleq \frac{N_{Rx}}{B} = \kappa G_{Ra} T_{Rx_ant}^o + (L_{RC} F_{Ra} - 1) \kappa G_{Ra} T_0^o + \frac{N_{rof}}{B} \quad (11)$$

$$P_{Rx} = P_{s-Tx} \frac{G_T G_R G_{Ra}}{L_s L_{RC}} \quad (12)$$

$$\left(\frac{E_b}{N_o} \right)_{Rx} = \frac{P_{Rx}/R_b}{N_o} = \left(\frac{P_{s-Tx} G_T G_R G_{Ra}}{R_b L_s L_{RC} L_{ROF}} \right) \frac{1}{N_o}. \quad (13)$$

IV. SIMULATION RESULTS

For the downlink system, we estimate an Net-AMI meter shared channel data rate at 4.5 dB SNR, 5 MHz bandwidth, at $R_b = 2$ Mb, a 10 Watt transmitter, the CR antenna 1.7 km from the Net-AMI, and at 5 MHz bandwidth. This estimate can be improved using transmit or receive diversity and MIMO. In Fig. 5(b) we find that for constant transmit power, we can adapt the data rate to account for distance variations of the cognitive radio antenna site to the Net-AMI meter. We presume constant transmit power with adaptive modulation and coding to mitigate interference (not adaptive power control). Using (1), (9), and (13), we plot $\left(\frac{E_b}{N_o} \right)$ of the RF downlink versus bit rate and distance in Fig. 6(b). As an example, we note that when we presume a much lower uplink transmit power of 1 Watt for Net-AMI to cognitive radio antenna site (at the BTS cell tower). In this instance a 0.8 km distance supports $R_b = 240$ kb/s data rates to the cognitive radio tower. The simulation results shown in Fig. 6(c) indicated that the use of a low power 1 Watt transmitter can still result in high data rates of 250 kb/s out to 1.1 km. These methods are useful for noise limited scenarios and for system insight. From them, we now derive the optimum schedule for the uplink and downlink in an interference limited Net-AMI network based upon a cellular array configuration via [36]

$$i_{DL}^* = \max_i \left(\frac{R_i^M}{T_i(t)} \right) = \max_i \left(\frac{\log_2 \left(1 + \frac{\left(P_i^M \frac{G_T G_R G_{Ra}}{L_s L_{RC} L_{ROF}} \right) \|h_i\|^2}{BN_{oi} + I_p} \right)}{T_i(t)} \right) \quad (14)$$

$$i_{UL}^* = \max_i \left(\frac{R_i^M}{T_i(t)} \right) = \max_i \left(\frac{\log_2 \left(1 + \frac{\left(P_i^M \frac{G_T G_R G_{Ra}}{L_s L_{RC} L_{ROF}} \right) \|h_i\|^2}{BN_{oi} + I_p} \right)}{T_i(t)} \right). \quad (15)$$

The use of 2×2 MIMO Alamouti space time codes is suggested to improve the reliability of the link in fading. The throughput can also be improved by increasing the bandwidth or transmit powers. The use of 5 MHz channels is compatible with television and cellular bands.

The simulation results above evaluate individual communication links, but do not consider the dynamic aspects of the AMI communication network, its multi-user network capacity, or QoS. To address this, we now introduce a separate analysis for multi-user, cognitive radio capacity. For this, we define

TABLE I
NETWORK CAPACITY PARAMETERS FOR COGNITIVE
RADIO AMI NETWORK

Table Parameters	Value
G-factor	Reference [48]
Inter-site distance	1732 m
Layout	Hexagonal grid
Network scheduling	Frequency domain Packet scheduler
LTE-OFDM	MIMO: 1Tx, 2Rx
Deployment spectral efficiency	1.5 bits/s/Hz [48]
Bandwidth	20 MHz
Cognitive radio secondary usage	10%
Cognitive radio primary load	80%
Density of AMI meters	L/mile ²
Cell site area	$2.6 \times 1732 \text{ m}^2$
Avg. AMI CR spectral efficiency	0.05 bits/s/Hz

the peak downlink multiuser capacity for orthogonal OFDM signaling and note that it cannot exceed the Shannon capacity

$$\sum_{k=1}^{\min(n_T, n_R)} W_{\text{cell}} \log_2(1 + \text{SINR}) \quad (16)$$

$$\text{SINR} = \frac{S_{\text{Cell}}}{N + I_{\text{OtherCell}}} = \frac{P_{\text{TxCell}}}{W_{\text{cell}} G \kappa T_{\text{Comp}} + \sum_{k \in \text{Other}} \frac{P_{\text{OtherCell}}}{\text{PathLoss}(K)}} \quad (17)$$

In real deployments, we can develop a modified Shannon capacity formula by replacing the cell bandwidth, W_{cell} , with an effective bandwidth and ηW_{eff} [48] which accounts for G-factor dependencies and protocol control, pilot, and cyclic prefix overheads. Closely related to the SINR is the G-factor, which accounts for the geometric dependencies of cell layouts and dictates the statistics of the downlink capacity.

The G-factor is the average own cell power to the other cell-power plus noise ratio when considering uniform spatial distributions of transceivers within a cell.

In addition, we can define normalization an effective signal-to-noise ratio, SNR_{eff} , adjust SINR for both interference, G-factor statistics, and LTE implementation parameters. Defining the modified Shannon spectral efficiency [48] as

$$\text{SE}(G) \frac{\text{bits}}{\text{sec}} = \eta W_{\text{eff}} \log_2 \left(1 + \frac{\text{SNR}(G)}{\text{SNR}_{\text{eff}}(G)} \right). \quad (18)$$

The cell spectral efficiency can be defined as

$$\text{Cell}_{\text{SE}} = \int_{-\infty}^{\infty} \text{SE}(G) P(G) dG. \quad (19)$$

The G-factor distributions (see [48], Fig. 1) presume macro cell hexagonal layouts. Based upon these assumptions, a frequency domain packet scheduler (FDPS, see [50]) generates roughly 1.5 bits/s/Hz of deployed capacity, as shown in Table I. By using this as our cell spectral efficiency and presuming a cell loading of 80% we can support a peak to average response necessary for high QoS [49]. In our low cost model, if we allow cognitive radio channel secondary users to consume up to 10% of the capacity on average without interfering with PU-QoS, we arrive at the following results. At a macro cell deployment (see [48], [49]) using FDPS, a 1Tx-2Rx

transceiver, an AMI meter density of L AMIs per square mile, an omni directional site with hexagonal grid layout (case 3 with inter site distance of 1732 m), the 10% secondary user cognitive radio spectral efficiency per L-AMI meters in $\frac{\text{bit/s/Hz}}{\text{L-AMImeter}}$ can be approximated as

$$C_{\text{AMI}} \approx \frac{1 \text{ mile}^2}{\text{LAMI m}} \times \frac{(1609 \text{ m})^2 / \text{mile}^2}{2.6 \times (1732 \text{ m})^2} \times 10\% \times (1.5 \text{ bits/s/Hz})$$

$$= 0.05 \frac{\text{bit/s/Hz}}{\text{L-AMImeter}}. \quad (20)$$

This supports streaming of a typical TCP/IP packet of 1500 bytes every 30 s to $L = 2500$ smart meters in a shared 20 MHz cognitive radio (secondary-user) wireless channel. The network parameter assumptions are indicated in Table I.

V. CONCLUSION

We developed the key equations and models supporting persistence in Net-AMI networks. We illustrated the method of analysis for cognitive radios, which can secure time-frequency bands for wireless communication of key power service applications in a manner which is invariant to cellular or other network infrastructures. Thus, the all Net-AMI meters, whether or not high QoS services are enabled, formally register with the utility service provider and allow a basic primitive set of utility power services. The cloud data center uploads the Net-AMI network infrastructure with legacy system protocols, proprietary protocols, and future systems protocols, thereby ensuring extensible services over long time horizons. Data rates, ranges, and capacity of the cognitive radio for relatively low 1 W uplink and 10 Watt downlink configurations reveal highly reliable data rate configurations from 1–3 km, with a possibility of trading off additional range versus data rate.

ACKNOWLEDGMENT

The authors would like to thank the support of the Department of Electrical and Computer Engineering, and their colleagues, especially Dr. H. Krishnaswami, T. Shaneyfelt, J. Prevost, and the anonymous reviewers for their comments, which helped to improve this paper.

REFERENCES

- [1] *Smart Grid Research and Development Multi-Year Program Plan (MYPP) 2010–2014*.
- [2] C. Potter, A. Archambault, and K. Westrick, "Building a smarter smart grid through better renewable energy information," in *Proc. IEEE PSCE*, Mar. 2009, pp. 1–5.
- [3] R. DeBlasio, "Standards for the smart grid," in *Proc. IEEE Energy 2030 Conf.*, Nov. 2008, pp. 1–7.
- [4] S. M. Amin and B. F. Wollenberg, "Toward a smart grid," *IEEE Power Energy Mag.*, vol. 3, no. 5, pp. 35–41, Sep.–Oct. 2005.
- [5] S.-W. Luan, J.-H. Teng, S.-Y. Chan, and L.-C. Hwang, "Development of a smart power meter for AMI based on zigbee communication," in *Proc. Int. Conf. Power Electron. Drive Syst.*, 2009, pp. 661–665.
- [6] C. Bennett and D. Highfill, "Networking AMI smart meters," in *Proc. IEEE Energy 2030 Conf.*, Nov. 2008, pp. 1–8.
- [7] D. Gislason, *Zigbee Wireless Networking*. Amsterdam, The Netherlands: Elsevier Science, 2008.
- [8] W. Luan, D. Sharp, and S. Lancashire, "Smart grid communication network capacity planning for power utilities," in *Proc. Transmission Distribution Conf. Expos.*, 2010, pp. 1–4.
- [9] B. Reid, "Oncor electric delivery smart grid initiative," in *Proc. 62nd Annu. Conf. Protective Relay Engineers*, 2009, pp. 8–15.
- [10] R. C. Qiu, Z. Chen, N. Guo, Y. Song, P. Zhang, H. Li, and L. Lai, "Toward a real-time cognitive radio network testbed: Architecture, hardware platform, and application to smart grid," in *Proc. 5th IEEE Workshop Netw. Technologies Softw. Defined Radio Netw.*, Jun. 2010, pp. 1–6.
- [11] S. Zhang, S. Zhang, X. Chen, and X. Huo, "Cloud computing research and development trend," in *Proc. Future Netw. ICFN*, 2010, pp. 93–97.
- [12] M. Naghshineh, R. Ratnaparkhi, D. Dillenberger, J. R. Doran, C. Dorai, L. Anderson, G. Pacifici, J. L. Snowdon, A. Azagury, M. VanderWiele, and Y. Wolfsthal, "IBM Research Division cloud computing initiative," *IBM J. Res. Dev.*, vol. 53, no. 4, pp. 1–10, Jul. 2009.
- [13] B. P. Rimal, E. Choi, and I. Lamb, "A taxonomy and survey of cloud computing systems," in *Proc. 5th Int. Joint Conf. INC IMS IDC*, 2009, pp. 44–51.
- [14] J. Peng, X. Zhang, Z. Lei, B. Zhang, W. Zhang, and Q. Li, "Comparison of several cloud computing platforms," in *Proc. ISISE*, Dec. 2009, pp. 23–27.
- [15] Z. Wei, S. Qin, D. Jia, and Y. Yang, "Research and design of cloud architecture for smart home," in *Proc. ICSESS*, Jul. 2010, pp. 87–92.
- [16] J. Bi, Z. Zhu, R. Tian, and Q. Wang, "Dynamic provisioning modeling for virtualized multi-tier applications in cloud data center," in *Proc. 3rd IEEE Int. Conf. Cloud Comput.*, Jul. 2010, pp. 370–377.
- [17] A. Di Costanzo, M. D. De Assuncao, and R. Buyya, "Harnessing cloud technologies for a virtualized distributed computing infrastructure," *IEEE Internet Comput. J.*, vol. 13, no. 5, pp. 24–33, Sep.–Oct. 2009.
- [18] C. Wang, Q. Wang, K. Ren, and W. Lou, "Ensuring data storage security in cloud computing," in *Proc. IWQoS*, Jul. 2009, pp. 1–9.
- [19] Q. Liu, C. Weng, M. Li, and Y. Luo, "An In-VM measuring framework for increasing virtual machine security in clouds," *IEEE Security Privacy J.*, vol. 8, no. 6, pp. 56–62, Nov.–Dec. 2010.
- [20] E. Bertino, F. Paci, and R. Ferrini, "Privacy-preserving digital identity management for cloud computing," *IEEE Comput. Soc. Data Eng. Bull.*, vol. 32, pp. 1–4, Mar. 2009.
- [21] Y. Zhang and J. Joshi, "Access control and trust management for emerging multidomain environments," in *Annals of Emerging Research in Information Assurance, Security and Privacy Services*, S. Upadhyaya and R. O. Rao, Eds. Bradford, U.K.: Emerald Group Publishing, 2009, pp. 421–452.
- [22] G. DeCandia, "Dynamo: Amazon highly available key-value store," in *Proc. 21st ACM Symp. Operating Syst. Principles*, Oct. 2007, pp. 205–220.
- [23] K. Nagothu, B. Kelley, J. Prevost, and M. Jamshidi, "On prediction to dynamically assign heterogeneous microprocessors to the minimum joint power state to achieve ultralow power cloud computing," in *Proc. Asilomar Conf. Signals Syst. Comput.*, Nov. 2010, pp. 1269–1273.
- [24] K. Nagothu, B. Kelley, J. Prevost, and M. Jamshidi, "Low energy cloud computing using adaptive load prediction algorithms," in *Proc. World Autom. Congr.*, 2010, pp. 1–7.
- [25] I. F. Akyildiz, W.-Y. Lee, M. C. Vuran, and S. Mohanty, "A survey on spectrum management in cognitive radio networks," *IEEE Commun. Mag.*, vol. 46, no. 4, pp. 40–48, Apr. 2008.
- [26] Q. Zhao and B. M. Sadler, "A survey of dynamic spectrum access," *IEEE Sig. Process. Mag.*, vol. 24, no. 3, pp. 79–89, May 2007.
- [27] E. I. Ackerman and C. H. Cox, "RF fiber-optic link performance," *IEEE Microw. Mag.*, vol. 2, no. 4, pp. 50–58, Dec. 2001.
- [28] H. Al-Rawashdy, *Radio Over Fiber Technology for Next Generation*. Norwood, MA: Arctech House, 2002, ch. 1.
- [29] H. B. Kim, "Radio over fiber based network architecture," Ph.D. dissertation, Dept. Electr. Comput. Eng., Tech. Univ. Berlin Sekr FT5 Einsteinufer, Berlin, Germany, 2005.
- [30] Y. Ebine, "Development of fiber-radio systems for cellular mobile communications," in *Proc. Int. Microw. Photonics MWP*, vol. 1. 1999, pp. 249–252.
- [31] H. B. Kim, M. Emmelmann, B. Rathke, and A. Wolisz, "A radio over fiber network architecture for road vehicle communication systems," in *Proc. IEEE Vehicular Technol. Conf.*, vol. 5. Jun. 2005, pp. 2920–2924.
- [32] T. Kuri, H. Toda, J. J. V. Olmos, and K. Kitayama, "Reconfigurable dense wavelength-division-multiplexing millimeter-waveband radio-over-fiber," *J. Lightw. Technol.*, vol. 28, no. 16, pp. 2247–2257, 2010.
- [33] W. Wang, "Spectrum sensing for cognitive radio," in *Proc. 3rd Int. Symp. Intell. Inform. Technol. Applicat. Workshops*, 2009, pp. 410–412.
- [34] D. D. Ariananda, M. K. Lakshmanan, and H. Nikookar, "A survey on spectrum sensing techniques for cognitive radio," in *Proc. 2nd Int. Workshop Cognitive Radio Adv. Spectrum Manage. (CogART)*, 2009, pp. 74–79.

- [35] D. Cabric, S. M. Mishra, and R. W. Brodersen, "Implementation issues in spectrum sensing for cognitive radios," in *Proc. 38th Asilomar Conf. Signals Syst. Comput.*, vol. 1, Nov. 2004, pp. 772–776.
- [36] J. Zhang, Z. Zhang, H. Luo, A. Huang, and R. Yin, "Uplink scheduling for cognitive radio cellular network with primary user's QoS protection," in *Proc. WCNC*, 2010, pp. 1–5.
- [37] J. M. Peha, "Sharing spectrum through spectrum policy reform and cognitive radio," *Proc. IEEE*, vol. 97, no. 4, pp. 708–719, Apr. 2009.
- [38] E. G. Larsson and M. Skoglund, "Cognitive radio in a frequency planned environment: Some basic limits," *IEEE Trans. Wirel. Commun.*, vol. 7, no. 12, pp. 4800–4806, Dec. 2008.
- [39] I. Sooyeol, H. Jeon, and H. Lee, "Autonomous distributed power control for cognitive radio networks," in *Proc. IEEE 68th VTC*, Sep. 2008, pp. 1–5.
- [40] K. C. Beh, A. Doufexi, and S. Armour, "Performance evaluation of hybrid ARQ schemes of 3GPP LTE OFDMA systems," in *Proc. 18th Annu. IEEE Int. Symp. Personal Indoor Mobile Radio Commun.*, Sep. 2007, pp. 1–5.
- [41] D. Astély, E. Dahlman, A. Furuskär, Y. Jading, M. Lindström, and S. Parkvall, "LTE: The evolution of mobile broadband," *IEEE Commun. Mag.*, vol. 47, no. 4, pp. 44–51, Apr. 2009.
- [42] A. Larmo, M. Lindström, M. Meyer, G. Pelletier, and J. Torsner, "The LTE link-layer design," *IEEE Commun. Mag.*, vol. 47, no. 4, pp. 52–59, Apr. 2009.
- [43] G. Keiser, *Optical Fiber Communications*. New York: McGraw-Hill, 2000, chs. 3–6.
- [44] R. Hui and M. O. Sullivan, *Fiber Optic Measurements Techniques*. Amsterdam, The Netherlands: Elsevier/Academic Press, 2009, ch. 5.
- [45] B. Sklar, *Digital Communications: Fundamentals and Applications*, 2nd ed. Englewood Cliffs, NJ: Prentice-Hall, 2009.
- [46] R. Mardeni and T. S. Priya, "Optimized COST-231 Hata models for WiMAX path loss prediction in suburban and open urban environments," *Mod. Appl. Sci.*, vol. 4, no. 9, pp. 75–89, 2010.
- [47] B. Kelley, "Software defined radio for advanced gigabit cellular systems, to appear in DSP handbook and wireless," in *Proc. Networking Radar Sensor Array Process. Nonlinear Signal*, 2009, ch. 22.
- [48] P. E. Mogensen, W. Na, I. Z. Kovács, F. Frederiksen, A. Pokhariyal, K. I. Pedersen, T. E. Kolding, K. Hugl, and M. Kuusela, "LTE capacity compared to the Shannon bound," in *Proc. IEEE 65th Vehicular Technol. Conf.*, Apr. 2007, pp. 1234–1238.
- [49] A. B. Syed, "Dimensioning of LTE network description of models and tool, coverage and capacity estimation of 3GPP long term evolution radio interface," M.S. thesis, Dept. Elect. Eng., Helsinki Univ. Technol., Helsinki, Finland.
- [50] P. Mogensen, W. Na, I. Z. Kovacs, F. Frederiksen, A. Pokhariyal, K. I. Pedersen, K. Hugl, and M. Kuusela, "LTE capacity compared to the Shannon bound," in *Proc. IEEE 65th VTC*, Apr. 2007, pp. 1234–1238.



Kranthimanoj Nagothu (S'07) received the B.S.E.E. degree from Anna University, Chennai, India, in 2006, and the M.S.E.E. degree from the University of Texas, San Antonio, in 2009. Currently, he is pursuing the Ph.D. degree in electrical engineering with the University of Texas, San Antonio.

He is with the Autonomous Control Engineering Center and the Wireless Advanced Next-Generation Laboratory as a Graduate Research Assistant. His current research interests include communications and networking for smart grid systems, software

define radio, 4G cellular, sensor networks, low power cloud systems, system of systems and underwater robotics swarms.

Mr. Nagothu received several awards including the Best Paper Award for the ESB Student Conference 2007 at the University of Texas, San Antonio, and is a member of Eta Kappa Nu. He has been actively participating in organizing international conferences.



Brian Kelley (S'91–M'93–SM'06) received the B.S.E.E. degree from the College of Electrical Engineering, Cornell University, Ithaca, NY, and the M.S.E.E. and Ph.D.E.E. degrees from the Department of Electrical and Computer Engineering, Georgia Institute of Technology, Atlanta, where he was an Office of Naval Research Fellow and a Georgia Tech Presidential Fellow.

He is currently with the Department of Electrical and Computer Engineering, University of Texas, San Antonio. After research and development efforts

with Motorola, Austin, TX, and Freescale, Austin, he joined the faculty of the University of Texas, San Antonio, as an Assistant Professor in communications. With the University of Texas, San Antonio, he has taught numerous graduate courses in communications. He has numerous publications and is a holder of ten U.S. patents. His current research interests include software defined radio, power system communications, 4G cellular, communications, and sensor networks.

Dr. Kelley is the Chair of the San Antonio IEEE Communication and Signal Processing Chapter, and was an Associate Editor of *Computers and Electrical Engineering*, Elsevier in 2008. He is a member of Tau Beta Pi and Eta Kappa Nu.



Mo Jamshidi (S'66–M'71–SM'74–F'89) received the B.S. degree from Oregon State University, Newport, in June 1967, and the M.S. and Ph.D. degrees in electrical engineering from the University of Illinois at Urbana-Champaign, Urbana, in June 1969 and February 1971, respectively. He holds three Honorary Doctorate degrees from Odla Yourdu University, Baku, Azerbaijan, in 1999, the University of Waterloo, Waterloo, ON, Canada, and the Technical University of Crete, Crete, Greece, in 2004.

Currently, he is the Lutch Brown Endowed Chaired Professor with the University of Texas System, San Antonio. He also has been the Founding Director of the Center for Autonomous Control Engineering (ACE), University of New Mexico (UNM), Albuquerque, and moved the center to the University of Texas, San Antonio, in early 2006. He has been the Director of the International Consortium on System of Systems Engineering since 2006. He is currently organizing the U.S. System of Systems Engineering Network consisting of many academic institutions and industries in the U.S. He is also Regents Professor Emeritus of ACE with UNM. In 1999, he was a NATO Distinguished Professor of intelligent systems and control in Portugal. He has been an advisor, an IPA, or a special government employee with NASA (10 years), U.S. AFRL (9 years), and DOE (9 years) since 1984. He has over 625 technical publications, including 63 books (11 textbooks) and edited volumes. Six of his books have been translated into at least one foreign language.

Dr. Jamshidi is the Founding Editor, Co-Founding Editor or Editor-in-Chief of five journals. He is the Editor-in-Chief of the new IEEE SYSTEMS JOURNAL (inaugurated in 2007) and the Founding Editor-in-Chief of the IEEE CONTROL SYSTEMS MAGAZINE. He is a recipient of the IEEE Centennial Medal and the IEEE CSS Distinguished Member Award. He received the IEEE SMC Societies Norbert Weiner Research Achievement Award in 2005 and the IEEE SMC Distinguished Contribution Award in 2006. In 2006, he was awarded a Distinguished Alumni in Engineering at Oregon State University, Corvallis. In 2009, he was a Distinguished Fellow of the U.K. Royal Academy of Engineering, Cardiff University, Cardiff, U.K., and from 2009 to 2012 he is an Honorary Professor of Deakin University, Australia. In October 2009, he served as an Advisor to the European Commission on System of Systems Engineering. Since 2010, he has been serving on the Review Board of the U.S.–Vietnam Education Foundation of the U.S. National Research Council. From 2009 to 2010, he was a U.K. Royal Academy of Engineering Fellow with Cardiff University. In April 2010, his research paper on robotic swarms was chosen as the Best Paper at the IEEE Systems Conference, San Diego, CA, and in September 2010 his research papers on swarm robotics and UAV control systems received the First and Second Best Paper Awards at the WAC Meeting, Kobe, Japan. He is a member of the International Council on Systems Engineering. He is a fellow of ASME, AAAS, NYAS, TWAS (Developing Nations Science Academy), and an associate fellow of AIAA.



Amir Rajaei (S'11) received the B.S.E.E. degree from the Iran University of Science and Technology, Tehran, Iran, in 2010. He is currently pursuing the M.S.E.E. degree with the University of Texas, San Antonio.

His current research interests include spectrum sensing and management in cognitive radio (ad hoc and cellular networks), communications and optimization for smart grids, and he has worked on localization in speech processing.

Throughput Analysis for AMI Meters in Smart Grid on Cognitive Radio Networks

Amir Rajae¹, KranthiManoj Nagothu², Brian Kelley³, Mo Jamshidi⁴
amirajae@gmail.com¹, kranthimanoj@gmail.com², brian.kelley@utsa.edu³, moj@wacong.org⁴
Electrical and Computer Engineering, the University of Texas at San Antonio, TX, USA

Abstract— In this paper a framework is presented based on 4G Cognitive Radio (CR) network capable of communicating with high numbers of geographically dispersed smart meters for command and control feature concurrently with private cellular network. Our approach uses pervasive smart grid systems (i.e. cloud data centers) as the central communication and optimization infrastructure supporting metropolitan area based smart meter infrastructure. In this paper, we investigate the performance of various scheduling algorithms in context with CR units to provide a satisfactory tradeoff between maximizing the system capacity, achieving fairness among cognitive users. We lay as a framework evaluation 3GPP LTE system model simulations. Our system level simulation results show that the 4G CR network model meets the smart grid protocols requirements for a multi-user CR network of Smart meters.

Keywords— 4G Cognitive radio networks, cloud data center, scheduling algorithms, and smart meters

I. INTRODUCTION

The smart grid of the future is generally perceived to be an intelligent energy delivery system that supports plug-and-play integration of power, information, and security services. [1]. We consider the future smart grid as leveraging Information and Communications Technology (ICT) facilitated by the smart meter (also named as Advance Infrastructure Metering (AMI)) information networks. The smart meter enables the flow of real-time information within the power utility, between the power utility and its customers. It also provides customers and utilities the technology to optimize their energy consumption in participating in closed loop demand response; moreover, these services allow convergence of high penetrations of renewable energy components into grid and third party energy management applications for demand optimization. It is essential for AMI to be networked since it enables system wide sensing, utility and customer linkages, and future self healing capability.

Communication network infrastructures represent a very large capital expense. Much of this expenditure is due to the high prices of purchasing licensed bands either from the FCC auction process or from existing licensed band owners. We therefore analyze a novel, low cost framework based on 4G cognitive radio smart meter networks enabling command and control, demand optimization and other features. Research on CR has evolved from SDR (see [2-3]) with an objective of efficient utilization of radio spectrum. In this paper, we analyze

CR in the context of smart energy systems. Although there have been significant advances and improvements in CR hardware, algorithms, and protocols, less attention has been given to developing ubiquitous and pervasive metropolitan scale CR networks, particularly with respect to smart grid information networking[4]. A metropolitan infrastructure based CR networks is shown in Fig. 1. In this context, there are major challenges to overcome such as Secondary Users (SU) should sense the spectrum and timely model the behavior of the Primary Users (PU). The other issue is how the SUs manage the available spectrum resources and share the resources among the SUs to satisfy the smart grid protocol requirements and meeting the interference constraints suggested by the FCC Spectrum Policy Task.

In such a system, our objective for SUs (i.e. AMI) is to efficiently transmit their delay sensitive traffic over the network and meet the QoS requirements of the smart grid protocol. In this paper, we investigate different scheduling policies that maximize the downlink sum throughput in the given area and achieving fairness among the SUs. We present an opportunistic scheduling policy that exploits both maximizing the downlink sum throughput and fairness under time-varying channel conditions for multi-user CR network in a metropolitan based environment.

Several authors have defined aspects of AMI networking in smart grids. Mesh, Ethernet and cellular AMI network topology for smart grid has been proposed. In [5] the authors propose mesh networks of Zigbee based transmission architecture. Challenging issue with line of sight requirements in Zigbee is the limit of single-hop range to hundreds of feet. Inefficiencies arise when transmission distances featured by the protocols in the entire metropolitan area for AMI networking. In [6], the authors discuss communication infrastructure based on Ethernet (LAN and WAN). The approach will support automated meter readings and customer home appliance connections. However, wireline systems are not always available. Customer subscription to service must occur and wired system can be challenging to rapidly redeploy, particularly in swiftly enveloping emergencies.

The authors in [7] describe a framework for RF mesh networking interfaced with high speed WiMAX access networks. In [8], overview of architecture, hardware platform, is reported to enable CR for smart grid communications. However, to our knowledge anywhere in the literature a complete multi-user capacity analysis using CR network in context with smart grid has been yet reported. Our work discusses the CR network infrastructure architecture from 4G

perspective. We also present multi-user performance analysis of various scheduling algorithms in context with AMI units considering the delay occurred due to offloading the processes to cloud in our architecture.

The rest of the paper is organized as follows. Section II overviews the 4G CR system architecture in brief. In section III we present overall 4G CR system model detailing the sensing model and different scheduling policies and their properties. Section IV discusses the performance of the different scheduling algorithms with system level simulations and concludes this paper.

II. 4g Cognitive radio framework

A. 4G cognitive radio system architecture

We presume a LTE network as a CR LTE network (4G CR), if the LTE work is adopted the CR techniques. We consider a cloud data center infrastructure based CR network coexisting with PU network shown in Fig.1. The coverage of both the CR base station and PU network base station are similar. As depicted in the Fig. 1 at the center of the each cell, there is base-station which is shared as e Node-B for PUs and as antenna for SUs. The PU base-station only serves to PUs as it lacks the CR protocols capabilities to support SUs. However, it may consider supporting certain features in order to communicate with SUs.

A CR system does not own a license band to operate in a desired band. Hence, the spectrum access is allowed only in an opportunistic manner. The licensed user of the frequency band is always given priority access to the shared channel (time-frequency resource). Due to their priority in spectrum access, the operations of PUs are always 1st in the transmission queue so as to not be affected by unlicensed users. All the SUs have the same right to access the spectrum; SUs should compete with each other for the same unlicensed band. Thus, sophisticated spectrum sharing methods among SUs are required in this architecture. If multiple SUs network operators reside in the same unlicensed band, fair spectrum sharing among these networks is also required and different scheduling algorithms are discussed in detail in section III.

Placement of a Cognitive Radio Antenna on the BTS tower may occur in tandem with deployment of the cellular provider antenna. The CR senses the spectral environment over a wide frequency band, particularly the spectrum in the cell region. It identifies the unused bands in the spectrum. These bands could be owned by cellular companies or license television band owners, but are not limited to these bands or to licensed bands. Sensed information using the CR is relayed to cloud data center. In principle, eNode-B which terminates the air interface protocol and first point of contact for PU is located at the primary user base-station. However, in proposed architecture all the cognitive radio service, waveform service, protocols service, security service, scheduling and control services are displaced into cloud data center. The CR services identify unused frequency bands, the relevant cognitive services residing in the cloud data center generates a clear to send (CTS) signal.

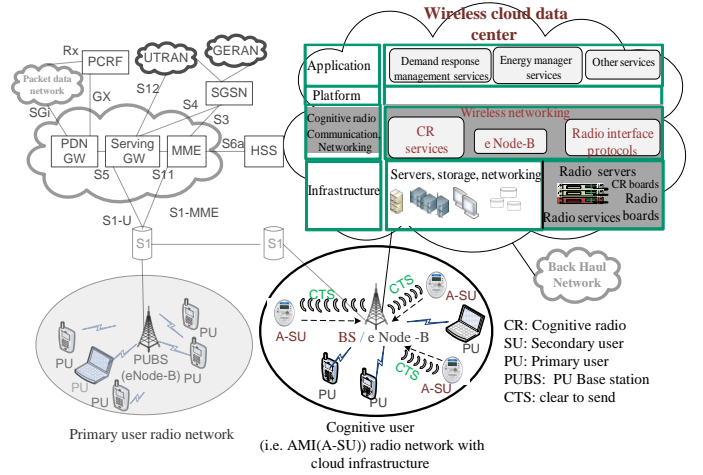


Fig. 1. 4G CR network system architecture: Scenario of multiple AMI meters serviced by cognitive radio network infrastructure enabled by cloud center coexisting with private cellular network

The CTS is sent back to the AMI meters through the feedback channel via base station. Eventually, the CR antenna relays CTS signals to every AMI in the cell region for uplink transmission.

1) Pervasive smart grid systems

The energy services of the future can be privately contracted services or public services. The cloud center enables convenient, on-demand network access to a shared pool of configurable, computing resources (e.g., networks, servers, storage, applications, and services) that can be rapidly provisioned and released with minimal management effort. There are different cloud computing platform classifications. Standard architectures includes Abi (or Abiquo), Nimbus Open Nebula, Azure (Microsoft), Google (App Engine), Blue (IBM) and Mosso (Rackspace). Fig.1. depicts the model for a cloud data center architecture optimized for based smart grids. Our Wireless Cloud Data (WCD) model is organized into four principle layers: application layer, platform layer, CR communication and networking layer and infrastructure layer. The first two layers are akin to existing cloud architectures. However, the lower two layers are augmented to enable the CR networking and wireless services. CR communication and networking layer provides services such as cognitive radio services, waveform services, Radio Link Control (RLC), and Medium Access Control (MAC) services. CR services, which provide spectrum management and spectrum sensing, are discussed in detail in section III. The infrastructure layer facilitates the effective integration of computing resources, storage, networks to deploy applications and operating systems. We augment our cloud infrastructure microprocessor racks with FPGA boards targeted to processing high computation rate processes typically associate with CR services, communication waveform signal processing and coding.

III. CR SYSTEM MODEL

In the paper system model 4G cellular network is considered with N_{su} secondary users sharing the spectrum simultaneously with N_{pu} primary users. It is presumed in the context that the secondary users (i.e. AMI meters) are fixed in sense of

geographical location and yields to fixed first and second statistical moments of SINR.

A. Spectrum Sensing

The spectrum sensing is one of the main layer task for CR system to obtain the spectrum usage information and the presence of PUs. Spectrum detection is based on the detection of the signal from PU through the observation of cognitive radio network.

The sensing methods can be categorized in three methods: i) Energy Detection, ii) Matched Filter, and iii) Feature Detection. The spectrum sensing method considered for this paper is Energy Detection. Since, it is particularly suitable for multiband sensing because of its low computational and implementation complexities [9-10]. We presume using OFDM modulation with M sub carriers with bandwidth W . In this paper we premised the IEEE 802.22 as it has developed air interface for opportunistic SU access to the TV spectrum in which PUs change slowly [11].

The timing model for spectrum sensing is shown in Fig. 2.a and spectrum mobility model for SUs is depicted in Fig. 2.b. The required time for channel estimation, spectrum sensing and sharing is indicated by τ . According to the [12] the given channel estimation delay is for WCDMA/HSDPA, so the scaled delay for a shorter sub-frame length in UTRAN LTE is considered for this paper. For each Resource Block (RB), there are 7 frames in time frame and 12 subcarriers and each square in Fig. 2.b is called Resource Element (RE). For example, in Fig. 2.b, RE (10, 7) means that the frequency carrier at frame 7 and subcarrier 10 is occupied by primary user 3. At each time, idle resource elements will be detected and allocated to SUs. Once a PU requests the subcarrier occupied by the active SU, SU has to leave the spectrum and try to find another idle resource element to continue transmission. In Fig. 2.a, T is time length of each frame and K is number of frames. The idle RB or hole is a band can be used by SU without interfering with PU. Supposed that received signal at SUs sampled at f_s over i th sub channel where values of discretized samples at $t = n T_s$, which T_s is $0.1\mu s$ in our framework. In discrete form, when the primary user is active, we define two hypotheses as follow:

$$\begin{cases} y_i(n) = h_i x_i(n) + u_i(n) & , \mathcal{H}_{1,i} \\ y_i(n) = u_i(n) & , \mathcal{H}_{0,i} \end{cases} \quad (1)$$

That h_i is the subchannel gain between PU transmitter and SU receiver with variance $E(|h_i|^2) = \sigma_{h,i}^2$. The signal transmitted, x_i , by PU is assumed to be independent and identically distributed (i.i.d), $\mathcal{CN}(0, \sigma_s^2)$, and u_i , the noise, is circularly symmetric complex Gaussian (CSCG) noise.

B. Energy Detection

In order to detect the RF energy in the certain subcarrier for a given PU, the CR service residing in the WCD samples on-the-air signal constructs the following test statistics as the observed energy summation within N samples to decide on the presence of the active users in targeted subcarrier [13].

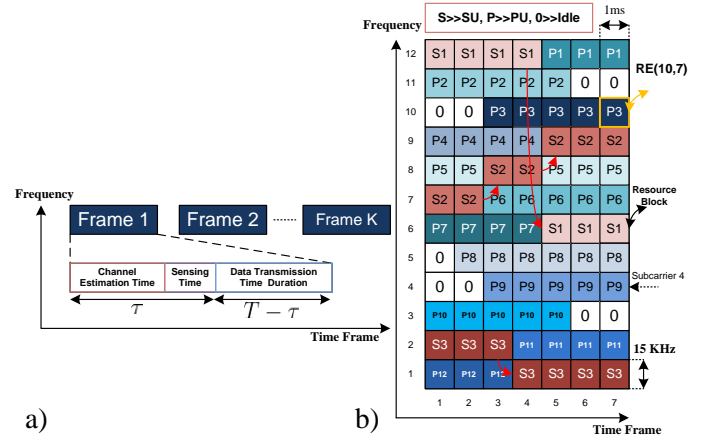


Fig. 2. a)Timing Model, b)Resource Block & Dynamic Resource Management

$$\mathcal{U}_i = \begin{cases} \frac{1}{N_i} \sum_{n=1}^{N_i} |h_i x_i(n) + u_i(n)|^2 & , \mathcal{H}_{1,i} \\ \frac{1}{N_i} \sum_{n=1}^{N_i} |u_i(n)|^2 & , \mathcal{H}_{0,i} \end{cases} \quad (2)$$

N_i is number of samples transmitted on duration τ_i which is equal to $N_i = \tau_i f_s$. The PDF of \mathcal{U}_i is Central Chi Square distribution with $2N_i$ degrees of freedom, $\mathcal{X}_{2N_i}^2$, for when no PU exists and on Central Chi Square distribution with $2N_i$ degrees of freedom and non-centrality parameter $2\gamma_i$, $\mathcal{X}_{2N_i}^2(2\gamma_i)$, for the state that PU exists. So:

$$\mathcal{F}_{\mathcal{U}_i}(\mathcal{U}_i) = \begin{cases} \mathcal{X}_{2N_i}^2 = \frac{1}{2^{N_i} \Gamma(N_i)} \mathcal{U}_i^{N_i-1} e^{-\frac{\mathcal{U}_i}{2}} & , \mathcal{H}_{1,i} \\ \mathcal{X}_{2N_i}^2(2\gamma_i) = \frac{1}{2} \left(\frac{\mathcal{U}_i}{2\gamma_i} \right)^{\frac{N_i-1}{2}} e^{-\frac{2\gamma_i + \mathcal{U}_i}{2}} & , \mathcal{H}_{0,i} \end{cases} \quad (3)$$

where the signal to noise ratio (SNR) is depicted by $\gamma_i = \frac{\sigma_{x_i}^2 \sigma_{h,i}^2}{\sigma_{u_i}^2}$, $\Gamma(\cdot)$ denotes the gamma function, $I_\alpha(\cdot)$ is the first kind modified Bessel function of degree α .

Two performance parameters for spectrum sensing are probability of detection, P_d , and probability of false alarm, P_f , which is probability of when the frequency is unoccupied but we get alarm that the frequency is used. Hence, Higher P_d protects PU from interfering with SUs and smaller P_f causes better band usage efficiency. To calculate probability of detection [14]:

$$P_{d,i}(\epsilon_i, \tau_i, \gamma_i) = Pr(\mathcal{U}_i > \epsilon_i | \mathcal{H}_1) = \int_{\epsilon_i}^{\infty} p_1(x) dx \quad (4)$$

where ϵ_i is threshold and τ_i is denoted sensing time for i th subchannel.

$$P_{d,i}(\epsilon_i, \tau_i, \gamma_i) = \mathcal{Q}\left(\left(\frac{\epsilon_i}{\sigma_{u_i}^2} - \gamma_i |h_i|^2 - 1\right) \sqrt{\frac{\tau_i f_s}{2\gamma_i |h_i|^2 + 1}}\right) \quad (5)$$

Now the probability of missed detection can be defined as:

$$P_{m,i}(\epsilon_i, \tau_i, \gamma_i) = 1 - P_{d,i}(\epsilon_i, \tau_i, \gamma_i) \quad (6)$$

we have following equations for probability of false alarm,

$$P_{f,i}(\epsilon_i, \tau_i) = Pr(\mathcal{U}_i > \epsilon_i | \mathcal{H}_0) = \int_{\epsilon_i}^{\infty} p_0(x) dx \quad (7)$$

$$P_{f,i}(\epsilon_i, \tau_i) = \mathcal{Q}\left(\left(\frac{\epsilon_i}{\sigma_{u_i}^2} - 1\right) \sqrt{\tau_i f_s}\right) \quad (8)$$

Usually to evaluate the performance of energy detection, the goal is to minimize P_f for a target P_d or to maximize P_d for a target P_f . At first we assume $P_{d,i,target}$ is our target probability of detection ,

$$\epsilon_i(P_{d,i,target}) = \left(\frac{\mathcal{Q}^{-1}(P_{d,i,target})}{\sqrt{\frac{\tau_i f_s}{2\gamma_i |h_i|^2}}} + \gamma_i |h_i|^2 + 1 \right) \sigma_{h_i}^2 \quad (9)$$

$$P_{f,i}(\epsilon_i(P_{d,i,target}), \tau_i) = \mathcal{Q}\left(\frac{\mathcal{Q}^{-1}(P_{d,i,target})}{\sqrt{\frac{\tau_i f_s}{2\gamma_i |h_i|^2}}} + \gamma_i |h_i|^2 + 1\right) \quad (10)$$

$P_{f,i}(\epsilon(P_{d,i,target}), \tau_i)$ is the probability of false alarm regard to target $P_{d,i}$, and \mathcal{Q}^{-1} is the inverse of complementary error function. For a target $P_{f,i,target}$ we have:

$$\epsilon_i(P_{f,i,target}) = \left(\frac{\mathcal{Q}^{-1}(P_{f,i,target})}{\sqrt{\tau_i f_s}} + 1 \right) \sigma_{h_i}^2 \quad (11)$$

$$P_{d,i}(\epsilon_i(P_{f,i,target}), \tau_i) = \mathcal{Q}\left(\frac{\mathcal{Q}^{-1}(P_{f,i,target}) - \gamma_i |h_i|^2 \sqrt{\tau_i f_s}}{\sqrt{2\gamma_i |h_i|^2 + 1}}\right) \quad (12)$$

$P_{d,i}(\epsilon(P_{f,i,target}), \tau_i)$ is the probability of detection when $P_{f,i}$ is targeted. As a result, in this part, probability of false alarm and detection based on $P_{d,i,target}$ and $P_{f,i,target}$, respectively, are calculated.

C. Primary User Activity Model

In this section, we present a model for primary users' activities which is directly proportional to CR network performance. In our Markov chains model, we consider two states (Busy by PU and Idle) for each subcarrier. Since each user arrival is independent, each transition follows the Poisson arrival process. Thus, the length of Busy and Idle periods are exponentially distributed. The Poisson distribution is considered in the modelling with arrival rate, α , and departure rate, β , and in simulation, the average existing users is assumed such that %80 of total spectrums are loaded by primary users in average.

$N_{tot}(nT_s) = N_{tot}(n(T_s - 1)) + \alpha(nT_s) - \beta(nT_s)$ (13)
as a result, the existing users in a cell is equivalent to total existing users on previous time period added to arrival rate at current time and subtracted by current departure time as mentioned in equation (13). The transition probabilities are p^T and q^T as illustrated in Fig. 3 and the calculated steady probabilities are depicted below [15]:

$$P_{i,BUSY} = \frac{p^T}{p^T + q^T}, \quad P_{i,Idle} = \frac{q^T}{p^T + q^T}, \quad (14)$$

Eq. (14) is applied to analyze the model for identifying subcarriers states (i.e. busy or idle).

D. Optimum Sensing Time

The throughput of SU is calculated as follows [16],

$$C_i = W \log_2 \left(1 + \frac{P_{i,SU} |h_{i,SU}|^2}{N_0} \right) \quad (15)$$

where W is bandwidth, $P_{i,SU}$ is the power of transmitter SU and N_0 is the noise power and $h_{i,SU}$ is the gain channel between i th SU's transmitter and receiver with variance $E(|h_{i,SU}|^2) = \sigma_{h_{i,SU}}^2$.

Considering probabilities for different states gives us achievable throughput, $R_i(\tau_i)$, calculated by,

$$R_i(\tau_i) = \left(1 - \frac{\tau_i}{T} \right) (1 - P_{f,i}) P_{i,Idle} C_i \quad (16)$$

where $(1 - P_{f,i}(\epsilon_i, \tau_i)) P_{i,Idle}$ is the probability of absence of PU when we detect correctly. $(1 - \frac{\tau_i}{T})$ is the entire data transmission. Following equations can be derived,

$$\lim_{\tau_i \rightarrow 0^+} \frac{d R_i(\tau_i)}{d \tau_i} \rightarrow +\infty > 0 \quad (17)$$

$$\lim_{\tau_i \rightarrow T} \frac{d R_i(\tau_i)}{d \tau_i} < 0 \quad (18)$$

Thus, there is a τ_i between 0 and T that gives us maximum $R_i(\tau_i)$. The Fig. 4 shows the optimum sensing time based on equation (16). By Fig. 4, it can be denoted that the optimum sensing time in regard to technology limits and optimum sensing time is approximated between 3ns and 1μs.

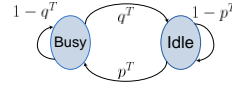


Fig. 3. Markov Chains Model

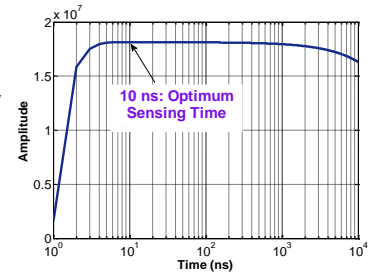


Fig. 4. Optimum Sensing Time

E. Scheduling algorithms for CR users

We consider the downlink of N_{su} secondary users are serviced by a base station within a cell. The base station allocates $RE(i,j)$ among the N_{su} SUs. At each frame multiple REs can be assigned to a single user, although each RE can be allocated to only one SU.

We assume that channel conditions vary across the subcarriers as well as secondary users. The channel conditions typically depend on the channel frequency, so they may be different for different channels. We presume typical urban area model. Moreover, scheduling of SUs also depend on the user location and the time frame. However, in our context the AMI meters are geographical stationary leading to constant SINR values.

In order to make optimal multi user scheduling decision and achieve high gain from multiplexing, the scheduler needs accurate channel quality indicator (CQI). Accuracy of CQI prediction depends on error in measuring the channel from the pilot and delays in the feeding back the information to the case-station. Feedback delay can be reduced by shrinking the size of the scheduling frame time. However, due to reduction of frame time the feedback request rate in uplink increases and eventually increasing the system overhead.

We define the peak downlink multiuser capacity for orthogonal OFDM signaling and note that it cannot exceed the Shannon capacity $\sum_{k=1}^{\min(n_T, n_R)} W_{cell} \log_2(1 + \text{SINR})$:

$$\text{SINR} = \frac{S_{Cell}}{N + I_{OtherCell}} = \frac{\frac{P_{TxCell}}{\text{PathLoss}}}{W_{Cell} G_K + \sum_{k \in \text{Other}} \frac{P_{OtherCell}}{\text{PathLoss}(k)}} \quad (19)$$

In real deployments, we can develop a modified Shannon capacity formula by replacing the cell bandwidth, W_{cell} with an effective bandwidth and βW_{eff} [17] which accounts for G-factor dependencies and protocol control, pilot, and cyclic prefix overheads. Closely related to the SINR is the G-factor, which accounts for the geometric dependencies of cell layouts and dictates the statistics of the downlink capacity. The G-factor is the average own cell power to the other cell-power plus noise ratio when considering uniform spatial distributions of transceivers within a cell.

In addition, we can define a normalized effective signal to noise ratio, SNR_{eff} , adjust SNR for both interference, G-factor statistics, and LTE implementation parameters. Defining the modified Shannon spectral efficiency for PU as

$$\beta W_{eff} \log \left(1 + \frac{S}{SNR_{eff}} \right) \quad (20)$$

We also define capacity of secondary user in presence of loss,

$$C = \int \sum_{SINR} (1-\rho)(1-\delta) \beta W_{eff} \eta \cdot \log_2 \left(1 + \frac{|h|^2 S}{SNR_{eff}} \right) dt \quad (21)$$

ρ is detection probability parameter and calculated by addition of false alarm detection probability (P_f) and detection probability (P_d). δ is primary user spectrum usage and we presume a average of 80% loading. β is a correction factor which nominally should be equal to one and it is discussed more detailed in. η is the spectrum sensing efficiency. The scheduler decides which SU to transmit the information at each time frames, based on the request rates the base station.

Scheduling the user with the instantaneously best link conditions is often referred as max rate scheduling. The max rate can be expressed as $k = \arg \max_i R_i$ for i th user.

Proportional fair (PF) scheduler is designed to meet the challenges of delay and fairness constraints while harnessing multi user diversity. PF scheduler tracks the average throughput, $T_k[nT_s]$, for each SU delivered in the past over sliding window of size t_c . In the time frame $[\tau]$, the base station receives rates $R_k[nT_s]$, $k=1 \dots N_{su}$ from all the active SUs and scheduler basically schedules the SU with highest PF metric value, γ that is defined as $\gamma = \frac{R_k[nT_s]}{T_k[nT_s]}$.

The average throughputs $T_k[nT_s]$ are updated using an exponentially weighted low pass-filter :

$$T_k[nT_s + 1] = \begin{cases} (1 - \frac{1}{t_c}) T_k[nT_s] + (\frac{1}{t_c}) R_k[nT_s] & k = \gamma \\ (1 - \frac{1}{t_c}) T_k[nT_s] & k \neq \gamma \end{cases} \quad (22)$$

Based on the Eq. (21) and (22) we can write as the following

$$\gamma = \frac{C = \int \sum_{SINR} (1-\rho)(1-\delta) \beta W_{eff} \eta \cdot \log_2 \left(1 + \frac{|h|^2 S}{SNR_{eff}} \right) dt}{T_k[nT_s]} \quad (23)$$

Opportunistic Scheduling (OS) is an approach to deal with both fairness among users and maximizing the capacity rate. In max rate algorithm the user with highest request rate implies giving all the system resources to particular users, yields to highly unfair scheme to all other users. However, in PF the users compete for resources not directly based on the requested rates but based on the rates normalized by their respective average throughputs also defined as PF metric value. The downside of the PF approach is sacrificing over all throughputs. Thus OS

algorithm schedules subcarriers $sc_{i,1}$ to $sc_{i,j}$ to the best secondary user based on two step criteria. First, the user who has the maximum PF metric value, γ , is selected. Second, the selected SU requested rate should be greater than the mean of all the secondary users requested rate, $\bar{R}[nT_s]$, to be scheduled as follow,

$$R[nT_s] \geq \bar{R}[nT_s] \quad (24)$$

As a result, unlike PF scheduling, the users having low throughput but high PF metric, γ , that had been chosen to access frequency will have lower priority than users with enough PF metric and higher throughput.

Algorithm: Opportunistic scheduling

- 1) for $n=1$ to N_T (simulation time)
 - 2) Update SU profile, Update γ
 - 3) Let S be the set of secondary users
 - 4) Let $RE(i,j)$ where $i=1$ to M subcarriers and $j=1$ to K be the total time frames.
 - 5) for $i=1$ to M , for $j=1$ to K
 - 6) Select the secondary user $l \in S$ with highest $\gamma(l)$
 - 7) If $R_l[nT_s] \geq \bar{R}_l[nT_s]$
 - 8) Update the SU profile with $S=S-\{l\}$
 - 9) Allocate $RE(i,j)$ to l th secondary user from S
 - 10) Else
 - 11) Update the SU profile with $S=S-\{l\}$
 - 12) End if, End for j, i, n
-

IV. ANALYSIS & SIMULATION RESULTS

To evaluate the performance of CR system model, system level simulations have been conducted based on 3GPP LTE system model. Table [see 15] shows the simulation parameters used for the simulations. We analyze the performance of the scheduling in terms of throughput and fairness. We first evaluate the system throughput for algorithms with varying the primary user loading within a cell. In this case, the primary user average loading is around 80% and total number of users is 500 in a cell. Over the period of time that spectrum sensing reports the number of idle resource blocks, scheduler allocates the idle REs with SUs. The Fig. 5 illustrates average capacity for three aforementioned algorithms.

Max-rate results in highest average capacity among three algorithms are followed by opportunistic and fairness algorithms. The results seem to match our expectations, since the goal of the Max-rate capacity is the user with highest request rate implies giving all the system resources to particular users. In proportional fair algorithm the users compete for resources not directly based on the requested rates but based on the rates normalized by their respective average throughputs, PF metrics. By this approach PF sacrifices the overall throughput while, achieving higher number of SUs scheduled. In OS the users having low request rate but high PF metric, γ , will have less chance to be scheduled. OS objective is to achieve higher average capacity compared to PF, while achieving decent fairness among the SUs.

Fig. 6.a and 6.b show the average number of users scheduled per one Transmission Time Interval (TTI) when 75 SUs are active in a cell and around 20% and 30% of idle RE are available. We can see that at least 60 and 70 SUs are scheduled

to idle REs by fairness algorithm. OS and max rate algorithms allocate less number of average SUs respectively.

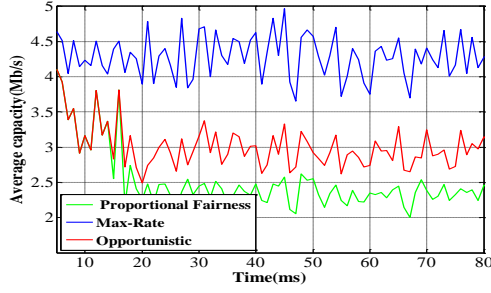


Fig. 5 Average Capacity over Time

In Fig. 7, we analyze the scheduled SUs average capacity of each algorithm in each scenario when number of active PUs varies. Based on goals of each algorithm they indicate respective positions in the results. It can be seen that the solution obtained using the proposed algorithm (OS) is quite close to the PF specifically when the active PUs are less.

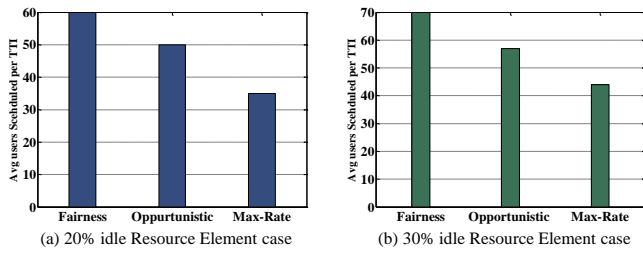


Fig. 6. Average number of users scheduled per one TTI

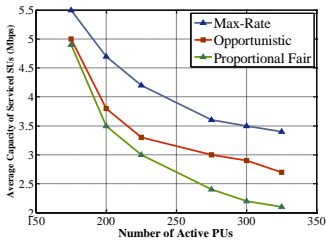


Fig. 7 Max-Rate average capacity

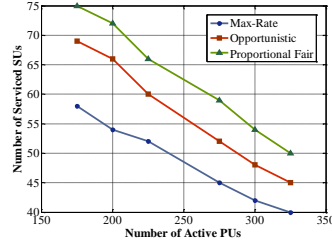


Fig. 8 Average No. of scheduled SUs

We note that the less PUs scheduled yields to high availability of idle REs. Therefore, higher number of SUs scheduled results in larger average capacity in the CR network. When the numbers of PUs are increased, the advantage of the OS algorithm over PF is more obvious (i.e. Fig.7) due to more sparse SUs. Sparse implies large variability in SINR profile (i.e. SINR, fading channel, physical location).

In Fig. 8, we analyze the average number of scheduled SUs in each scenario when number of active PUs varies. We note that the more PUs scheduled yields to less availability of idle REs and therefore less number of SU scheduled.

In Fig. 7 the Max-Rate average capacity is much higher than average capacity of PF; on the contrary, Fig. 8 shows the more scheduled SUs by PF algorithm compared to Max-Rate algorithm. As a result, the OS algorithm can balance both the performance of the cognitive radio networks in terms of

achieving acceptable average capacity of secondary users and the fairness.

V. CONCLUSION

In this paper, we have analyzed the potential 4G CR network framework in context of smart grid information systems. Our system level simulation results show that the 4G CR network can achieve an average capacity of 3.5Mbps in a 3Km cell radius under the constraint of an average primary user network usage of 80%. Finally, we present that the CR capacity of a 20% usage model meets the smart grid protocols requirements for a multi-user CR network of smart meters.

REFERENCES

- [1] Smart grid Research and Development Multi- Year Program Plan (MYPP) 2010-2014.
- [2] D.D.Ariananda, M.K.Lakshmanan, H.Nikookar, "A survey on spectrum sensing techniques for cognitive radio," Cognitive Radio and Advanced Spectrum Management, 2009. CogART 2009. Second International Workshop on, pp. 74 – 79.
- [3] Brian Kelley, "Software Defined Radio for Broadband OFDM Protocols," SMC 2009, San Antonio.
- [4] Akyildiz, I. F., Lee, W.-Y., Vuran, M. C., and Mohanty, S., "Next generation dynamic spectrum access cognitive radio wireless networks: a survey," Computer Networks Journal (Elsevier), pp.2127-2159, vol. 50, May 2006.
- [5] S.-W. Luan, J.-H. Teng, S.-Y. Chan, and L.-C. Hwang, "Development of a smart power meter for AMI based on zigbee communication," in Proc. Int. Conf. Power Electron. Drive Syst., 2009, pp. 661–665.
- [6] Wenpeng Luan, Duncan Sharp and Sol Lancashire, "Smart Grid Communication Network Capacity Planning for Power Utilities," Transmission and Distribution Conference and Exposition, IEEE PES, New Orleans, USA, 2010, pp. 1-4.
- [7] B. Reid, "Oncor electric delivery smart grid initiative," in Proc. 62nd Annu. Conf. Protective Relay Engineers, 2009, pp. 8–15.
- [8] Robert C. Qiu, Zhe Chen, Nan Guo, Yu Song, Peng Zhang, Husheng Li and Lifeng Lai, "Towards A Real-time Cognitive Radio Network Testbed: Architecture, Hardware Platform, and Application to Smart Grid," Networking Technologies for Software Defined Radio (SDR) Networks, Fifth IEEE Workshop, Boston, USA, 2010, pp.1-6.
- [9] Qing Zhao; Sadler, B.M.; "A Survey of Dynamic Spectrum Access" IEEE Signal Processing Magazine, pp.79-89, vol. 24, May 2007.
- [10] Rajace, A., Saedy, M., Sahebalam, A., "Competitive spectrum sharing for cognitive radio on Scale-Free wireless networks" IEEE IWCMC, pp. 455-459, 2011.
- [11] Carlos Cordeiro, Kiran Challapali, and Dagnachew Birru, "IEEE 802.22: An Introduction to the First Wireless Standard based on Cognitive Radios" Journal of Communications, Vol. 1, No. 1, April 2006.
- [12] T.E Kolding. "Link and System performance aspects of Proportional Fair Packet Scheduling in WCDMA/HSDPA", In Proceedings of 58th IEEE Vehicular Technology Conference, Vol.3, pp. 1717-1722, October 2008.
- [13] Zhi Quan; Shuguang Cui; Sayed, A.H.; Poor, H.V.; "Optimal Multiband Joint Detection for Spectrum Sensing in Cognitive Radio Networks" IEEE Transaction on Signal Processing, pp. 1128-1140, vol. 57, November 2008.
- [14] Khalid, L.; Anpalagan, A.; "Effect of sensing errors on wideband cognitive OFDM radio networks" IEEE Biennial Symposium QBSC, pp. 273-277, 2010.
- [15] Ghosh, C.; Cordeiro, C.; Agrawal, D.P.; Rao, M.B.; "Markov chain existence and Hidden Markov models in spectrum sensing" IEEE International Conference, pp.1-6, 2009.
- [16] Zhi Quan; Shuguang Cui; Sayed, A.H.; Poor, H.V.; "Wideband Spectrum sensing in Cognitive Radio Networks" IEEE International Conference, pp. 901-906, 2008.
- [17] Preben Mogensen et.al. "LTE Capacity compared to the Shannon Bound", In Proceedings of 65th IEEE Vehicular Technology Conference, pp. 1234-1238, April, 2007.

On the Foundations of Ultra-Low Power Scale Free Sensor Networks For Cluster to Cluster Communications

Mahdy Saedy¹, *Member, IEEE*, Brian Kelley², *Senior Member, IEEE*

Electrical and Computer Engineering Dept.
University of Texas at San Antonio
San Antonio, USA

1. Mahdy.Saedy@utsa.edu , gmail.com}, 2. Brian.Kelley@utsa.edu

Abstract— this paper introduces a new foundation for ultra-cooperative communications based on very low SNR channels between mobile sensor nodes grouped in spatially distributed clusters. In this new framework, we define a cluster entity as a sensor network of wireless nodes with, but not limited to, scale-free topology. We define physical wireless scale-free model for the clusters that extends the abstract scale-free model developed by Barabasi-Albert for network graphs to the wireless channel. Our air interface model is based on OFDM with Rayleigh flat fading channels and AWGN. For intra-cluster communications, we have developed the new concept of consensus in a wireless network framework to improve the performance. This new approach is ideal for distributed long-range low power sensor networks with ultra-low power signals well below the noise floor. For a cluster size of 100 nodes, we achieve BER of 10^{-5} at an SNR of -25 dB in Rayleigh fading. This method enables reliability in both fading channels for intra-cluster communications and can support ultra-long range or ultra-low power communications links. We establish the fundamental principles involving the relationship between cluster sizes, and communication performance and illustrate 7X gains in range performance using HATA path loss models.

I. INTRODUCTION

Wireless sensors are widely used in industrial facilities, structural health monitoring, and remote environments requiring pervasive closed loop sensor control of electro-mechanical systems. As future applications demand more transmit range and higher data rates, sensor networks are increasingly limited by battery capacity limits. Our sensor model framework considers a large network of sensors nodes powered by a small sustainable source, such as milliwatt and nanowatt photo-voltaic. The power amplifier and signal processing applications are two major energy-consuming aspects in wireless sensor nodes. In traditional low power sensor networks, the limited power nodes support short range communications. A key aspect of the approach is the capability to jointly enable either long-range or low-power sensor

communications via our ultra-cooperative transmission model. A second distinguishing feature of our network is the use of sensor network formation using low-power 4G OFDM protocols. However, low power 4G wireless may appear to be contradictory, it is well known in microprocessor systems that power drain calculations are defined from average power consumption computed over the duty cycle of sleep mode to wake-mode transmission of the microelectronics (sensors). Moreover, OFDM systems well-publicized peak-to-average transmit power issues have controllable solutions [21]. Unlike the traditional methods of [22], our sensor network framework can embrace a large number of nodes, considerable 100MHz bandwidths, and high data rate applications at low power. Simultaneously, low cost, integrated microelectronics and solar power supplies are increasingly available as off-the-shelf components. These technology trends in sensor devices allow for large-scale sensor network deployments (e.g. wall-paper sensors).

Though there is no formal 4G standard at the present time, it is generally accepted that IMT-Advanced derived from 100 MHz LTE-Advanced will be the dominant technology. We specifically indicate the following key points of departure for traditional wireless sensor networks: (1) the concept of ultra-scale cooperation, (2) the use of multi-carrier OFDM with Rayleigh flat fading channels (3) a sensor networks where the fundamental entity of communication is a cluster of nodes rather than an individual sensor node. Within this new context, we introduce a novel method of information transfer between or within clusters of nodes based upon consensus theory [1], which we discuss in Section III. In doing so, we propose the wireless domain extension to the network science of [1]. Our new wireless models therefore evolve from graph theories and findings on social networks behavior models. We consider our clusters of sensors nodes to represent a complex network.

Complex networks pervade in all disciplines of science and humanities. The typical examples of complex networks include electrical power networks, metabolic networks, and

social networks in the World-Wide Web [8]. In particular, we invoke a scale-free network model for connected graphs [9]. In 1999, A. L. Barabasi, and R. Albert (BA) first proposed an abstract scale-free network model based on a mechanism of growth with preferential attachment characterized by a power-law distribution of the node degree (i.e. connections). A motivation for this topology is based upon the robustness against random link failure (node removal) [9]. To reiterate, we consider this paper to be major extension of the field of network science and graph theory to the realm of wireless sensor network communications.

The physical model of sensor network communications we invoke relies upon a topological interaction of sensor nodes within an entity defined by us as a cluster (see Section II.B.1). Our wireless links are modeled as Rayleigh flat faded with AWGN [2]. By applying graph theories like Graph Laplacians and spectral properties of Laplacian Matrices of a graph [1][4], we introduce new dissemination properties for sensor networks. An important property we invoke is that derives from a class of propagation known as Gossip [12]. The theory of propagation we invoke, known as consensus theory, is a class of Gossip propagations theory. In a network of dynamics, consensus means to reach an agreement regarding a certain quantity of interest that depends on the state of all agents. A consensus algorithm (or protocol) is an interaction rule that specifies the information exchange between an agent and all of its neighbors on the network. The consensus concept has been studied previously in field of cooperative control systems [1]. *We illustrate the protocols for message communication for scale free clusters networks via consensus theory.* Figure 1 illustrates our pervasive sensor network model with scale free link topology.

In this paper, we solve the emergent problem of optimally utilizing coordinated sensors in such a way as to match the desired transmission range, battery lifetime, and data rates to sensor transmission power limits. Our new protocols introduced in both [15] and [1], enable moderate data rate links capable of operation in low signal to noise (SNR) environments. In section 2, we introduce the sensor network topology. Section 3 advances the concept of consensus in a cluster of sensor nodes. In section 4, the cooperative relaying model for communications is developed and a three-cluster system is developed. We also formulate new models of resource allocation. In section 5 we present simulation results for a complete model of three-cluster sensor system.

II. NETWORK FORMATION AND TOPOLOGY

In order to formulate the network behavior and the connectivity of nodes in clusters we use the graph theory and the findings in network topology studies [8]. Consider a network of N —coupled, wireless sensor nodes with topology $G = (V, E)$. In our context, $V = \{v_1, v_2, \dots, v_N\}$ denotes the

network vertices and E is the edge set of V in which each sensor node, v_i , communicates with its neighbors. $N_i = \{v_j \in V : \{i, j\} \in E\}$ represents the neighbor set of v_i in V . We assume sensor nodes communicate primarily within their own immediate neighborhood. For an undirected graph, the degree or cardinality is simply defined as $d_i = |N_i|$.

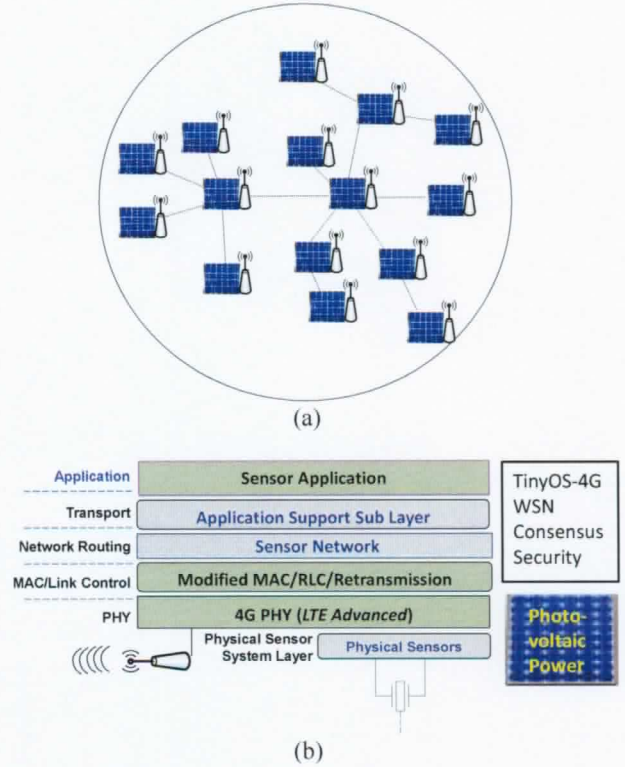


Figure 1 (a) wireless sensor network: sensors attached to photo voltaic panels (b) wireless sensor node protocol stack and system architecture.

A. Prior Scale-Free Network Model of Barabasi-Albert

Scale-free networks are based on a model of link connectivity where the “rich get richer.” This rule can be perceived as a form of preferential wireless link attachment. We note that this feature is analogous to social network behavior. This network is built on a connected primary graph of m_0 nodes. Each new node is added to the network with m edges ($m < m_0 = 3$) [2]. For the new node v_j , the probability of connection to existing node v_i is given below where a is the attraction factor and d_i is the degree of node v_i . In our wireless context, the *preferential attachment probability* is defined as:

$$\Pi_{v_j \rightarrow v_i} = \frac{(a + d_i)}{\sum_{v_k \in N_i} (a + d_k)} \quad (1)$$

Equation (1) defines the probability that new node v_j , connects to an existing node v_i . In (1), $-m < a < \infty$. The degree

Mahdy Saedy is with the University of Texas at San Antonio, San Antonio, TX 78249 USA (Phone; 512-814-7414; e-mail: Mahdy.Saedy@gmail.com). Brian Kelley is with the University of Texas at San Antonio, San Antonio, TX 78249 USA (210-706-0854; fax: 210-458-7191; e-mail: Brian.Kelley@utsa.edu.).

This work was supported, in part, by the Texas Sustainable Energy Conservation office (SECO) and the U.S. Department of Energy (DOE) under Grant RFA No. RE-AG1-2010 at the University of Texas System at San Antonio Campus, San Antonio, TX, USA.)

distribution for this model is a power-law distribution. Figure 2 illustrates the degree distribution of a scale-free wireless sensor network. When the probability that a node has a degree d_i is described by a power law degree distribution, the resulting network topology is scale free [2][5][13]. From (1) nodes are more likely to be connected or attached to other nodes with higher degree (i.e. higher number of links). Therefore,

$$p(d_i) = d_i^{-\gamma(a,m)} \quad (2)$$

In Equation (2), γ is the *distribution exponent* and $2 < \gamma < \infty$.

From empirical analysis, we find the selection of $\gamma = 3 + \frac{a}{m}$ leads to optimum results.

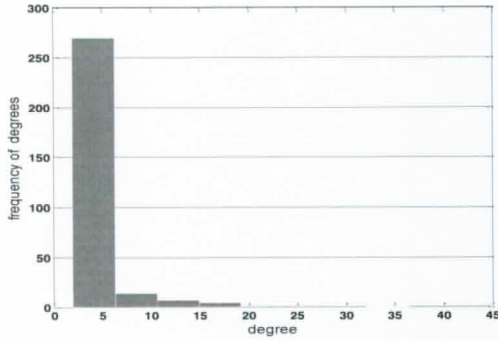


Figure 2. Degree distribution for a scale-free cluster of size $N=300$

B. Definition of Cluster in Wireless Domain

In this section, we propose an extension of the abstract model of Barabasi-Albert (BA) to the wireless channel. This framework establishes a relationship between the abstract network theory of the BA model and the real spatial distributions associated with physical sensor node locations. The traditional BA model does not consider spatial distribution [2]. In Equation (3), we introduce the use of a joint random variable that relates the power law distribution of the node degree to the 2-Dim spatial distribution of node location.

$$\begin{bmatrix} x_i \\ y_i \end{bmatrix} = \begin{bmatrix} \frac{\sum_{v_j \in N_i} d_j x_j}{\sum_{v_j \in N_i} d_j}, \frac{\sum_{v_j \in N_i} d_j y_j}{\sum_{v_j \in N_i} d_j} \end{bmatrix}^T \quad (3)$$

A hypothetical example of the resulting spatial distribution is illustrated this in Figure 3. The location (x_i, y_i) is the location of node i . The degree of node i , d_i , is bounded between lower and upper cut-offs d_{\min} and d_{\max} . If we define $d_{\min} \triangleq m$ and d_{\max} is the highest degree in the network. The probability of the highest degree node having a degree greater than d_{\max} is:

$$1 - F_K(d_{\max}) = \Pr\{k \geq d_{\max}\} = \int_{d_{\max}}^{+\infty} p_K(k) dk = \frac{1}{N} \quad (4)$$

When $p(d) = d^{-\gamma}$, this yields:

$$d_{\max} = mN^{\frac{1}{\gamma-1}} \quad (5)$$

1) Definition of a Wireless Cluster

The commoditization of sensors has prompted us to base communication on clusters of nodes rather than individual nodes. To avoid ambiguity is the association of nodes with clusters, we select a connection criterion for node j to connect to node i based upon the capacity of link $e_{ij} = \{i, j\}$:

$$C_{ij} = W_{ij} \log_2 \left(1 + \frac{P_i |h_{ij}|^2 r_{ij}^{-\alpha} g}{N_0 + I_i} \right) \geq R_{th} \quad (6)$$

Table 1 summarizes the wireless sensor network parameters.

TABLE I
WIRELESS SYSTEM PARAMETERS

Symbol	Description
C_{ij}	Wireless link capacity between node i and node j .
R_{th}	Bit rate threshold for link establishment.
W_{ij}	Wireless channel bandwidth of link $e_{ij} \in E$.
P_i	Transmit power of node i .
h_{ij}	fading channel coefficient between nodes i and j with zero-mean complex Gaussian random distribution : $h_{ij} \sim CN(0, \sigma^2)$. $ h_{ij} $ has Rayleigh distribution
r_{ij}	Distance between node i and node j
g	path loss constant ^a .
α	Path loss exponential: $2 \leq \alpha \leq 4$
N_0	noise power

^a path loss constant depends on the pat loss model adopted for the system.

The parameter R_{th} is the minimum required bit rate. In Equation (6), the connected nodes yield an edge set with a graph described by $G=(V,E)$ where the edge set, E , is $E = \{(v_i, v_j) \in V, C_{ij} \geq R_{th}\}$. The set E defines the topology that we label a *cluster*.

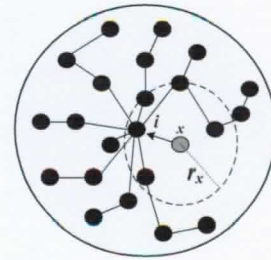


Figure 3 Network formation into a cluster with scale-free topology. The new node v enters the cluster and starts to scan the neighborhood within r_x range. According to Preferential Attachment, it picks up to m nodes which have highest number of links within r_x .

In order to quantify the connectivity of a set of nodes in a cluster we define a new matrix of coefficient values called the capacity adjacency matrix. The matrix entries, a_{ij} are defined in the following way:

$$A = \begin{cases} a_{ij} = \frac{C_{ij}}{W_{ij}} & , \text{ for } \frac{C_{ij}}{W_{ij}} \geq \frac{R_{th}}{W_{ij}} = \frac{1}{2} \\ 0 & , \text{ otherwise} \end{cases} \quad (7)$$

Without a loss of generality, we choose the threshold ratio $(R_{th}/W_{ij}) \triangleq 0.5$ as a minimum non-zero coefficient for the matrix. The matrix A , defined as the *Cluster Capacity Adjacency Matrix (CCAM)*, defines the wireless link capacity between nodes. We use the concept of consensus based upon the wireless adjacency matrix to radically increase diversity gain as a function of the number of nodes.

III. COMMUNICATION VIA INTRA-CLUSTER CONSENSUS

In cooperative networks, the group consensus is a way to improve the overall behavior of cooperating nodes. In wireless sensor networks, the consensus is used to increase the reliability of intra-cluster communications. Conversely, in a cluster with sensor agents, consensus means to reach an agreement regarding a certain quantity of interest that depends on the state of all agents. This state or *state vector* could be any characteristic assigned to a node like frequency, phase, and velocity. In general, a complex vector of information obtained from environment is the state vector of the node. A consensus algorithm is an interaction rule that specifies the information exchange. As in Figure 4, concurrent information flows to each node acting as agent and all of its neighbors in cluster. An updating of the agent's state vector occurs at each iteration. If the vector, $\bar{x}_i(t)$, is assigned to node i at time t , then the matrix of all vectors at time t in the cluster is

$\mathbf{X}(t) = [\bar{x}_1(t), \bar{x}_2(t), \dots, \bar{x}_N(t)]^T$. In this paper we label one-dimensional vectors $\bar{x}_i(t)$ and matrices $\mathbf{X}(t)$. The continuous-time dynamical protocol for updating vectors is then written as:

$$\frac{dx_i(t)}{dt} = \sum_{v_j \in N_i} (x_i(t) - x_j(t)) \quad (8)$$

Equivalently, a matrix representation of (8) can be written as:

$$\dot{\mathbf{X}}(t) = -\mathbf{L}\mathbf{X}(t) \quad (9)$$

The matrix \mathbf{L} is generally referred to as the graph *Laplacian Matrix* of the network [1][8]. For a cluster with communication delay and wireless channel, the channel coefficient is h_{ij} as defined in Table 1. The link delay, τ_{ij} , is associated with the edge link, e_{ij} . From (9), we arrive at:

$$\frac{dx_i(t)}{dt} = \sum_{v_j \in N_i} (x_i(t - \tau_{ij}) - h_{ij}x_j(t - \tau_{ij}) + n_i(t)) \quad (10)$$

For simplicity, we approximate the time-delay in all links as $\tau \approx \mu_\tau = E\{\tau_{ij}\}$. Defining τ as the synchronous update interval,

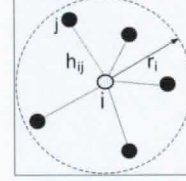


Figure 4. a wireless sensor neighborhood with single antenna 4G compliant sensor nodes. The wireless link is established based on passing a capacity threshold R_{th} and falling within the range r_i of sensor node.

and considering λ_N , the largest eigenvalue of \mathbf{L} , the maximum tolerated delay time for stability of dynamical system, τ_{max} , in Equation (9) is [1][5]:

$$\tau < \tau_{max} = \frac{\pi}{2\lambda_N} \quad (11)$$

In the wireless domain, Equation (11) determines the bound for total update time. If the system updates take place at $t = nT_u$

then $\mathbf{X}(n) = [x_1(n), x_2(n), \dots, x_N(n)]^T$. We now describe the consensus by letting $\Omega: \mathbb{R}^N \rightarrow \mathbb{R}$ be a multi-input single-output operation that generates the decision (observation) value: $y(n) = \Omega(\mathbf{X}(n))$. We say that all the nodes of the cluster-graph have reached consensus with respect to $\mathbf{X}(n)$ in finite time, if and only if the vectors of all pairs of nodes meet the following criteria— $\lim_{k \rightarrow \infty} \|x_i(n) - x_j(n)\| = 0$. The operation $\|\cdot\|$ is 2-norm of a vector. From (9), the stable equilibrium will be $x_{ss} = \Omega(\mathbf{X}(0))$ [1]. If the network is a connected graph, the eigenvalues are $\lambda_1 \leq \lambda_2 \leq \dots \leq \lambda_N = 2d_{max}$ [9]. It is known that the speed of convergence increases as λ_2 increases. The parameter λ_2 is called algebraic connectivity. Recalling that the neighborhood of v_i is N_i , the state vector equation of node v_i at iteration $(n+1)$ can be written as [1][9]:

$$x_i(n+1) = \frac{1}{d_i+1} \left(x_i(n) + \sum_{v_j \in N_i} (a_{ij}x_j(n) + n_i(n)) \right) \quad (12)$$

In matrix form, this can be rewritten as:

$$\mathbf{X}(n+1) = (\mathbf{I}_N + \mathbf{D}_G)^{-1} (\mathbf{I}_N + \mathbf{A}) \mathbf{X}(n) \quad (13)$$

Defining \mathbf{D}_G as the diagonal matrix of node degree values, we can decompose \mathbf{L} into two matrices, \mathbf{D}_G and (adjacency) \mathbf{A} ,

such that $\mathbf{L} = \mathbf{D}_G - \mathbf{A}$. Defining $\mathbf{P} = (\mathbf{I}_N + \mathbf{D}_G)^{-1}(\mathbf{I}_N + \mathbf{A})$, the discrete time update protocol will be:

$$\mathbf{X}(n+1) = \mathbf{P}\mathbf{X}(n) \quad (14)$$

$$\mathbf{X}(n) = \mathbf{P}^n \mathbf{X}(0) \quad (15)$$

Noting that Ψ belongs to a set of convergent update protocols as shown in (12), the dynamical protocol can be written as:

$$\mathbf{X}(n+1) = \Psi(\mathbf{X}(n), \mathbf{X}(0), \mathbf{P}) \quad (16)$$

It is important to indicate that the disagreement between node i and node j at each iteration n , is define as the absolute difference between the state vector of nodes i and j , $\|x_i(n) - x_j(n)\|$. This difference is measured over the set of neighbors, N_i . Thus,

$$\Delta_i(x_i(n)) = \sum_{v_j \in N_i} \|x_i(n) - x_j(n)\| \quad (17)$$

The overall disagreement in the sensor network is the summation of all local nodal disagreements,

$$\Delta(n) = \sum_i \Delta_i(x_i(n)) = \sum_i \sum_{v_j \in N_i} \|x_i(n) - x_j(n)\| \quad (18)$$

Equation (18) represents the overall disagreement between all nodes and is a measure of how convergent the consensus protocol (Ψ) is. The parameter, $\Delta(n)$, is denoted as a super martingale process [7]. It converges to zero since $\lim_{n \rightarrow \infty} E\{\Delta\} = 0$ and $\lim_{n \rightarrow \infty} \Pr(x_i(n) \rightarrow x_{ss}) = 1, \forall i$. This implies that x_{ss} is the steady state (vector) value of the sensor nodes. So all nodes in the cluster reach consensus and the disagreement tends to zero as $n \rightarrow \infty$ [7][9]. The imbalance is shown in Figure 10. Figure 11 shows how vectors of all nodes asymptotically converge to x_{ss} .

A. Convergence Rate of a Wireless Cluster

All nodes in the cluster start from the initial state value and the updated protocol drives the nodes to reach a consensus. The time to reach consensus is defined as number of iterations where the absolute difference between any arbitrary pair of nodes is less than a certain small value, ϵ , where $0 < \epsilon < 1$. The consensus time is dependent on the topology, initial state of nodes and the residual tolerable difference, ϵ , [11][12]. Therefore,

$$T_c = \sup_{x_i(0) \neq x_{ss}} \inf \left\{ k : \Pr \left(\left\| \frac{x_i(n) - x_{ss}}{x(0) - x_{ss}} \right\| \geq \epsilon \right) \leq \epsilon \right\} \quad (19)$$

Using the Markov's inequality, we can show that

$$\frac{0.5 \text{Log}(\epsilon^{-1})}{\text{Log}(\lambda_2(\mathbf{P}))^{-1}} \leq T_c \leq \frac{3 \text{Log}(\epsilon^{-1})}{\text{Log}(\lambda_2(\mathbf{P}))^{-1}} \quad (20)$$

Figure 11 illustrates the convergence for a cluster of 25 nodes. Figure 12 shows a loose dependence of convergence time and cluster size for a scale-free topology. Figure 12 shows the convergence performance of both random and scale-free topologies.

IV. PROBLEM SETUP AND SYSTEM MODEL

In section III we introduced the intra-cluster cooperative scheme. In this section, we will consider the clusters as macro entities and introduce the concept of the inter-cluster cooperation protocol.

A. Basic information relaying using Log-Likelihood Ratio

The use of relays in cooperative communications has been well investigated [16]. In [15], the authors have introduced a new method in which the relay node calculates the well-known Log-Likelihood Ratios (LLRs) for the code bits transmitted by the source node and transmits quantized versions of these LLRs to the destination node. The destination combines the LLR values received from the source-destination link and the quantized LLRs from the source-relay link to improve bit estimates. In fact, a major element of the reliability gain derives from increased spatial diversity of nodes.

B. Cluster Relaying Using Log-Likelihood Ratio

In this section we use the method discussed in [15]. However, S,R and D are clusters of nodes instead of individual nodes. There can be multiple relays between S and D. In fact, the relay cluster uses received symbols from a source cluster to calculate the LLR values. Information transfer between S and D occurs in 6 steps:

- (1) the Source seeding,
- (2) S-R transmission,
- (3) R convergence,
- (4) R-D transmission,
- (5) D convergence, and
- (6) D detection.

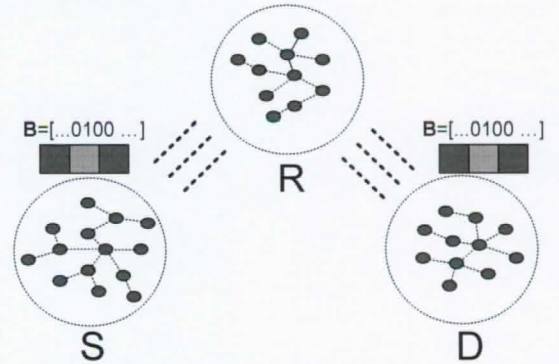


Figure 5. The basic relay model with one relay, source and destination nodes. Similarly, the basic cluster-to-cluster relay model contains one relay cluster based on the relay model in [15]

For any number of relays, the above sequence of transmission, convergence and detection is repeated. For this reason, we

focus principally on steps 1 through 4. The three-cluster system in Figure 5 is representative of our new communication scheme. After the convergence stage in the relay (R) cluster, we use the consensus state vector in the relay cluster to seed the destination (D) cluster for the next hop. We choose to define cluster transmission in a 3-phase framework.

1) *Phase 1: source seeding*

Phase 1 involves initialization step for the source cluster state. Information is disseminated via a convergence protocol defined in section III. We seed the nodes in S with information symbols in different ways:

- a. all nodes at once
- b. few nodes
- c. cluster head

Here we use approach (a) to seed the source cluster S.

2) *Phase 2 involves long-range transmission between clusters. Phase 2: inter-cluster transmission (SR Transmission)*

We choose orthogonal frequency division multiplexing (OFDM) as our physical layer model. Let time slot $T_o = T_{\text{symb}} + T_{\text{CP}}$ be the transmit time allocated to nodes in S and each node in S uses a different subcarrier. We can define a frame structure and resource allocation as shown in Fig. 5 and 6. For our protocol, we first perform packetization and modulation. Without a loss of generality, we choose QPSK modulations. The simulation result for the three-cluster system consisting is shown in Figure 13. Let V be a length N_v vector of modulated data symbols, each of which is b -bits (e.g. for QPSK, $b = 2$). The symbol vector to be transmitted will be:

$$\bar{X}^S = [x^S(0), x^S(1), \dots, x^S(N_v - 1)]^T \quad (21)$$

During each period, T_o , all nodes in S transmit the data vector symbol $\bar{X}^S = [x^S(0), x^S(1), \dots, x^S(N_v - 1)]^T$ every $T_o = (T_{\text{symb}} + T_{\text{CP}})$ seconds. Note that $n=0, 1, 2, \dots, (N_v - 1)$ and $x_i^S(k, n) = x^S(n)$ is node i symbol at time n in k th subcarrier. (k, n) is based on 3GPP resource grid standard[19],[20]. The symbol sequence to be transmitted from node i in S using subcarrier k will be:

$$X_i^S = [x_i^S(k, 0), x_i^S(k, 1), \dots, x_i^S(k, N_v - 1)]^T \quad (22)$$

$i = 1, 2, \dots, N_S$. N_S is the number of nodes in S and N_{FFT} is the number of available subcarriers. One implementation of time-frequency matrix (scheduling matrix) for symbols will be:

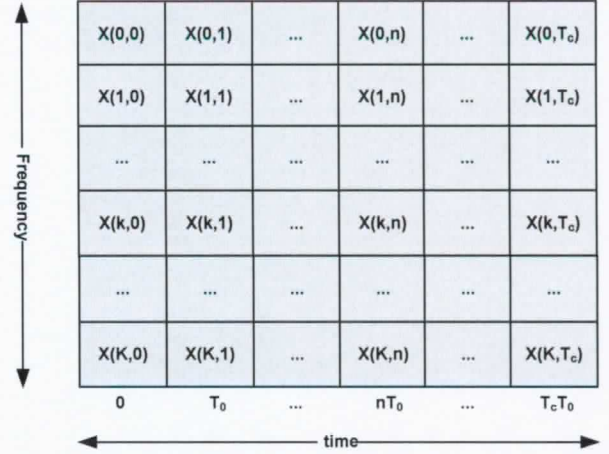


Figure 6. Time-frequency plane. The 100 MHz 4G frequency band supports $K=6665$ frequency subcarriers. For T_o , the system clock rate, the convergence time, is $T_{\text{converge}} = T_c T_o$.

$$X^S = \begin{pmatrix} x_1^S(0, 0) & \dots & x_1^S(0, N_v - 1) \\ \vdots & \ddots & \vdots \\ x_{N_S}^S(N_S - 1, 0) & \dots & x_{N_S}^S(N_S - 1, N_v - 1) \end{pmatrix} \quad (23)$$

We can use efficient permutation operators to manage the resources in (23). Of course $N_S \leq N_{\text{fft}}$ is the required number of available subcarriers. In cases where $N_S > N_{\text{fft}}$, data block \bar{X}^S needs to be scheduled with regards to N_v , N_S and N_{fft} . The resources can be reused, but interference will generally become the limiting factor in capacity. This is overcome in section 5. Each node in R receives signal from all nodes in S in different subcarriers. For example, if node j in R receives the n th data symbol from node i in S using k th subcarrier over the channel with coefficient $h_{ij}^{SR}(n, k)$ (presuming block fading that is constant over T_o), then:

$$x_j^R(k, n) = h_{ij}^{SR}(k, n) x_i^S(k, n) + n_j^R(k, n) \quad (24)$$

Define N_R as the number of nodes in R. The indexed nodes have parameters $j = 1, 2, \dots, N_R$. Then, at the end of T_o , each node j in R will have a vector of all received symbols from nodes in S:

$$X_j^R(n) = [x_j^R(0, n), x_j^R(1, n), \dots, x_j^R(N_S - 1, n)]^T \quad (25)$$

At the end of T_o , each node in R computes its LLR pair, $\begin{bmatrix} L_0 \\ L_1 \end{bmatrix}$, based on received symbols from nodes in S in each subcarrier k :

$$L_{0,j}(k, n) = \frac{2q \operatorname{Re}\{x_j^R(k, n)\}}{\sigma_j^2(k, n)} \quad (26)$$

$$L_{1,j}(k,n) = \frac{2q \operatorname{Im}\{x_j^R(k,n)\}}{\sigma_j^2(k,n)} \quad (27)$$

The noise power at node j , $\sigma_j^2(k,n)$, is the receiver noise power at node j . The superposition of all (QPSK) LLR values summed over all subcarriers will be:

$$L_{0,j}(n) = \sum_{k=1}^{N_s} L_{0,j}(k,n) \quad (28)$$

$$L_{1,j}(n) = \sum_{k=1}^{N_s} L_{1,j}(k,n) \quad (29)$$

Phase 2 will be completed by initializing nodes in R with LLR values computed in (28) and (29).

3) Phase 3: intra-cluster communications and convergence using LLRs

In phase 3 the destination cluster detects the data sent from the source cluster. Also, in Phase 3, we define T_0 as the time given to nodes in R to exchange their LLRs. This information exchange carried out through consensus protocol compensates for the poor reception in some nodes and improves the overall performance since all nodes reach a *consensus* on what LLR value to use for detection. Although each node m in node j neighborhood from R uses a different subcarrier namely p , all neighbors of node j communicate their LLRs in T_0 .

$$L_{0,j}(n+1) = \frac{1}{d_i + 1} \left(a_{ji} L_{0,j}(n) + \sum_{v_m \in N_j} (a_{mj} L_{0,m}(n)) \right) \quad (30)$$

$$L_{1,j}(n+1) = \frac{1}{d_i + 1} \left(a_{ji} L_{1,j}(n) + \sum_{v_m \in N_j} (a_{mj} L_{1,m}(n)) \right) \quad (31)$$

Then we see that:

$$\mathbf{L}_b(n+1) = \mathbf{P} \mathbf{L}_b(n) \quad (32)$$

The bit-vector is $b = 0, 1, \dots, \log_2^M - 1$. After T_c iterations, all nodes in R are ready to pass on their LLR values to destination cluster exactly in the same way as in phase 2 for SR transmission. Nodes in destination cluster will use their LLR values to detect the information since each node in cluster D will then have:

$$L_{0,m}(n) = \sum_{k=1}^{N_R} L_{0,m}(k,n) \quad (33)$$

$$L_{1,m}(n) = \sum_{k=1}^{N_R} L_{1,m}(k,n) \quad (34)$$

This way the information is transferred from source cluster to destination cluster through relay cluster.

V. INTERFERENCE MITIGATION AND RESOURCE MANAGEMENT IN WSNs

We desire to define a property here that allows for unbounded growth in the number of sensor nodes. For this, we now derive a procedure for spatial expansion of the network that avoids interference-limited scenarios. Our model for resource allocation follows the 3GPP LTE-Advanced standard [19]. Every 20 MHz sub-channel provides 1200 sub-carriers and the system resource grid scales up to 5 sub-channels.

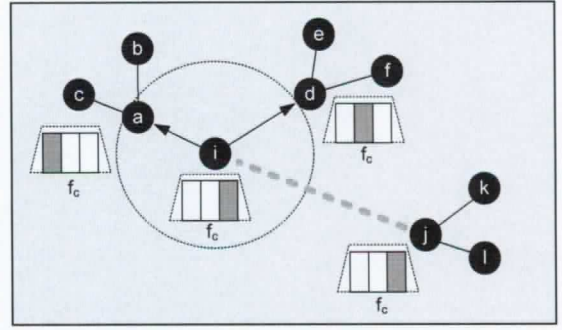


Figure 7. Interference model and coordination between neighbors. All nodes in the serving area of cluster that use the same sub-carrier portion of a sub-channel and the same carrier frequency for upconversion introduce the interference.

Figure 7 illustrates the case where node i is within connection range to nodes a and d . For node i to be able to connect to node a it uses its own *node ID* to initially map it to sub-carrier portion in corresponding sub-channel 1,2,...,5. The interference comes from any node j that uses the same carrier frequency and the same sub-carrier portion. Let N_i be the number of interfering nodes. Then the total interference received at node i is:

$$I_i = \sum_{j=1}^{N_i} P_T r_{ij}^{-\alpha} \quad (35)$$

In (35), r_{ij} represents the distance between nodes i and j .

A. Noise-limited Interference Model vs. Interference-Limited in Wireless Sensor Network

In this section, we want to introduce a method with which nodes coordinate amongst themselves to mitigate the interference and push it down to noise level in the cluster. In this scenario, the spatial expansion of cluster and attachment of new nodes to the network will not increase the total interference in the cluster and our model can support the indefinite number of nodes by relaxing the interference from network size. The link capacity between any pair of nodes (i,j) is based on (6) Where N_0 is the noise power at node i receiver and I_i is the total interference at node i . P_T is the

transmit power of all nodes since we set constant transmit power. For a *noise-limited* scenario, we intend to push and maintain the interference level down to noise level where $I_i \approx N_0$ and noise is the dominant source of distortion. This ensures that the highest interference level introduced to node i is about the same level as noise power. With this assumption (i.e. $I_i \approx N_0$), we solve the problem backwards and from equation (12) we see that:

$$I_i = \sum_{j=1}^{N_i} P_T r_{ij}^{-\alpha} \square P_T r_{eq,i}^{-\alpha} \approx N_0 \quad (36)$$

Then the *noise-limited equivalent interference distance* from node i is as follows:

$$r_{eq,i} = \left(\sum_{j=1}^{N_i} r_{ij}^{-\alpha} \right)^{-\frac{1}{\alpha}} \quad (37)$$

We point out that nodes at a distance greater than $r_{eq,i}$, have average interference power introduced by node i . The interference will be bounded by the noise power level at node i 's receive antenna. In fact, $r_{eq,i}$ indicates the threshold for node i at which the system noise and interference are approximately equivalent. In other words, for any node with the same transmit power, P_T , the expected value of $r_{eq,i}$ is:

$$E\{r_{eq,i}\} = \bar{r}_{eq} = \int \left(\sum_{j=1}^{N_i} z_{ij}^{-\alpha} \right)^{-\frac{1}{\alpha}} p_{z_{ij}}(z_{ij}) dz_{ij} \quad (38)$$

The parameter $z_{ij} = |z_i - z_j| = \sqrt{(x_i - x_j)^2 + (y_i - y_j)^2}$ and variables $z_i = x_i + jy_i$ and $z_j = x_j + jy_j$ are 2-dimensional random variables representing the location of nodes and $p_{z_{ij}}(z_{ij}) = p_z(z)$ is the PDF of z . Then we can rewrite (38) as:

$$E\{r_{eq,i}\} = \bar{r}_{eq} = \int \left(\sum_{j=1}^{N_i} z_{ij}^{-\alpha} \right)^{-\frac{1}{\alpha}} p_z(z) dz \quad (39)$$

$$\bar{r}_{eq} = \left(\frac{N_0}{P_T} \right)^{-\frac{1}{\alpha}} \quad (40)$$

The parameter \bar{r}_{eq} is the average inter-nodal distance that guarantees noise-level interference between any pair of nodes and is called *equivalent average resource reuse distance*. Figure 8. Illustrates the protocol for inserting new nodes and selecting the safe resource elements to avoid harsh interference.

$$r_{ave} = \frac{\sqrt{A}}{\sqrt{N_i}} \quad (41)$$

Then the actual equivalent average resource reuse distance is:

$$r_{eq,actual} = N_i^{-\frac{1}{\alpha}} r_{ave} \quad (42)$$

The realistic low bound for \bar{r}_{eq} and actual values for r_{ave} and $r_{eq,actual}$ are given in Table 2.

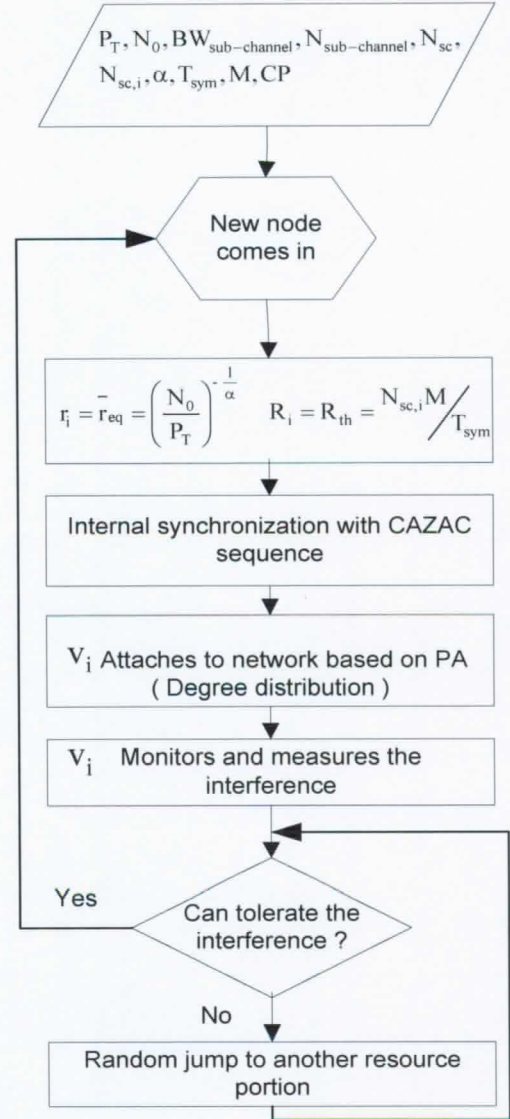


Figure 8. protocol for insertion of new nodes and camping on least interfered portion of resource block i.e. set of sub-carriers.

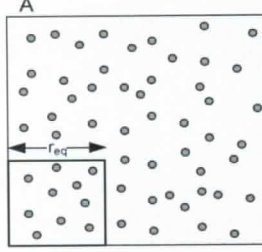


Figure 9. reuse distance that guarantees the noise-limited communications across the cluster.

VI. SIMULATION RESULTS OF CLUSTERS

We used Table 2 to perform our simulation. The simulation results show a significant performance of our proposed method. The diversity gained from the number of nodes i.e. cluster size clearly improves the performance. This simulation is for a scenario where QPSK is used as modulation scheme and Intra-cluster SNR is 20 dB higher than that of inter-cluster. The symbol rate for cluster-to-cluster communications is calculates as:

$$R_{\text{sym}} = \frac{\text{number of QPSK symbols}}{\text{TS2}}$$

$$R_b = \log_2^M \times R_{\text{sym}} = 2 \times \frac{1}{7.143 \times 10^{-5}} = 28 \text{ Kbps}$$

For higher data rate we can choose higher order modulations. For 64-QAM, $R_b = 6 \times R_{\text{sym}} = 84 \text{ kbps}$ as based upon Table 2. In Figure 13, we see an $N=50$ cluster can communicate with a BER of 10^{-4} in Rayleigh Fading. For this we assume an OFDM sampling rate of 15.36 MHz and a sub-carrier spacing of 15 KHz. Table 3 supports an $N=50$ cluster with each transmit node support 10 QPSK channels for a cluster data rate for 280 Kbps. we present a link budget for an example of our $N=50$ wireless sensor cluster transmitting 35 miles at 1 mW transmission power in Rayleigh Fading. The Rx SNR is presumed 3 dB higher than the Rx E_b/N_0 since the ratio of bandwidth to data rate is 3 dB. Using $(E_b/N_0)_{\text{Rx}} = P_T G_R G_T / (R_b \kappa T L_s)$ where $L_s = 136 \text{ dB}$ is the estimated ideal path loss, R_b is the desired bit rate, κ is the Boltzmann constant, and T is the ambient noise temperature in Kelvin. Utilizing Figure 13, for a transmit power, P_T , of 1 mW, we illustrate via link budget analysis for a cluster bit rate of $R_b = 0.28 \text{ Mbps}$ generates a digital margin of 0.7dB dB. For comparison, under ideal path loss our conventional 1Tx-1Rx sensor supports a data range of 293 meters with the same transceiver noise figure. Thus, for long range, the wireless sensor cluster improves the range by a factor of 6.8 to 2000 meters for a Hata Path loss model at 900MHz and a cluster of size $N=50$. Thus, the wireless sensor cluster improves the range by a factor of 6.8 to 2000 meters for a Hata Path loss model at 900MHz and a cluster of size $N=50$. Similarly, for an ultra-low power wireless sensor, a 1 Nano-Watt transmitter can be extended from a range of 9.5 meters to 60.5 meters for $N=50$.

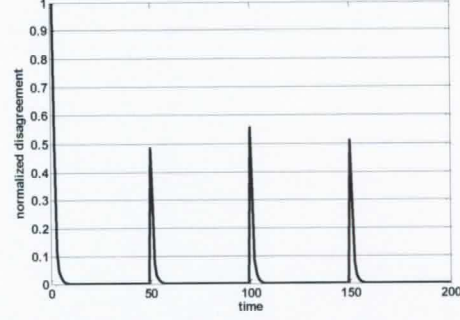


Figure 10. imbalance in the network and cooperative recovery. In the case of node malfunctioning or link failure in any part of the network, the cooperative algorithm gets the system back to consensus state. In this example we perturbed the highest degree node with 100% and 50% of the consensus value (steady state value).

TABLE II
EXAMPLE NETWORK OF 4G WSN

Parameter	Value	Description
Input parameters		
A	1120×1120 m ²	Sensor farm area
N	5000	Number of sensors
α	3.4	Path loss exponent: $2 \leq \alpha \leq 4$
$\tau_{ij} = \tau$	1 μs	Channel time delay
P_T	0.1 mW	Sensor transmit power
N_0	$1 \times 10^{-7} \text{ W}$	Noise power
$BW_{\text{sub-channel}}$	100 MHz	System bandwidth in 2.3GHz-2.5GHz range
$N_{\text{sub-channel}}$	5	Number of sub-channels
N_{sc}	1200	Sub-carriers per sub-channel
$N_{\text{sc},i}$	4	Sub-carriers per sensor node based on the application
Δf	Sub-carrier spacing	15 KHz
M	6	Modulation order 64-QAM
R_i	Bit rate of node i	$\frac{M \times N_{\text{sc},i}}{T_{\text{sym}}}$
CP	4.69 μsec	Can extend to 16.67 μsec
T_{sym}	71.4 μsec	Symbol duration = $\frac{1}{\Delta f + \text{CP}}$
Output parameters and performance		
r_{eq}	1330.7 m	Reuse distance
Average interference	$2.38 \times 10^{-15} \text{ W}$	Realistic lower bound of interference
Average bitrate	336 Kbps	
r_{ave}	354.17 m	actual inter-nodal distance
$r_{\text{eq,actual}}$	180 m	Actual reuse distance

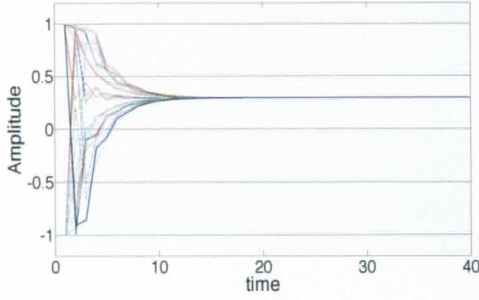


Figure 11. an example of convergence for one-dimensional node vector x in a cluster of 25 nodes vs. number of iterations.

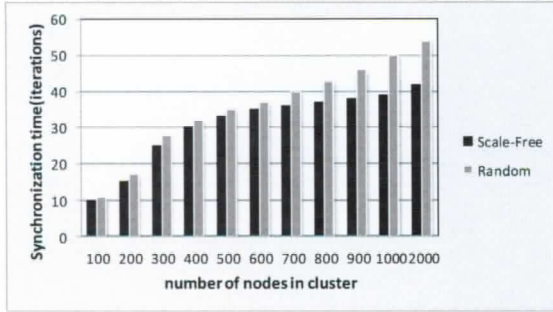


Figure 12. the convergence time of a wireless scale-free cluster for different cluster sizes. For small clusters the convergence time grows exponentially while as the cluster size scales up, the convergence time saturates for larger number of nodes. Convergence performance of scale-free topology vs. random topology can also be seen here.

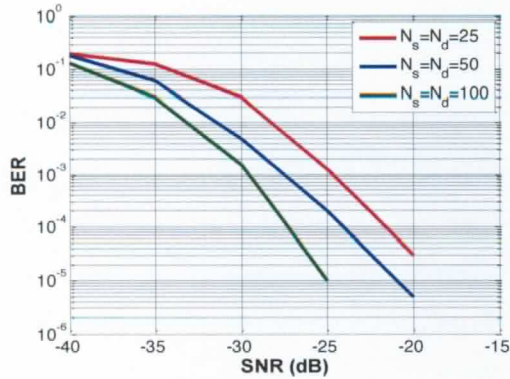


Figure 13. Performance of a three-cluster system in Rayleigh fading for different cluster sizes.

TABLE III
SENSOR CLUSTER NETWORK IMPROVEMENT

Parameter	Ultra Low Power (1 Nano-Watt Tx)		Ultra Long Range (1 milli-Watt Tx)	
	Conventional SISO Node-to-Node	50 Node Cluster Cluster-to-Cluster	Conventional SISO Node-to-Node	50 Node Cluster Cluster-to-Cluster
Ant. Height Ht	6 m	6 m	10 m	10 m
Ant. Height Hr	6 m	6 m	10 m	10 m
Tx power: Pt	-90.00 dBw	-90.00 dBw	-30.00 dBw	-30.00 dBw
Ant. Gain Tx: Gt	1.00 dB	1.00 dB	1.00 dB	1.00 dB
Ant. Gain Rx: Gr	1.00 dB	1.00 dB	1.00 dB	1.00 dB
Distance: d	9.5 meters	60.5 meters	293.0 meters	2000.0 meters
Carrier freq.: f_c	9.00E+08 Hz	9.00E+08 Hz	1.50E+09 Hz	1.50E+09 Hz
Ant. Temp Ta	1400.00 deg	1400.00 deg	1400.00 deg	1400.00 deg
Required: Eb/No	4.00 dB	-28.00 dB	4.00 dB	-28.00 dB
Therm. noise: kTo	-197.14 dBw/Hz	-197.14 dBw/Hz	-197.14 dBw/Hz	-197.14 dBw/Hz
Noise Figure: F	3.00 dB	3.00 dB	3.00 dB	3.00 dB
Bit rate: R	2.50E+05 bits/sec	2.50E+05 bits/sec	2.50E+05 bits/sec	2.50E+05 bits/sec
Hata Path Loss	49.6 dB	81.6 dB	109.6 dB	141.6 dB
Actual Rx Power	-137.6 dBw	-169.6 dBw	-137.6 dBw	-169.6 dBw
Rx Eb/No	5.5 dB	-26.5 dB	5.5 dB	-26.5 dB
Min Demod. Rx	-138.3 dBw	-170.3 dBw	-138.3 dBw	-170.3 dBw
Margin	0.7 dB	0.7 dB	0.7 dB	0.7 dB

VII. CONCLUSION

In this paper, we have developed a framework for communications between clusters of nodes (sensors) over low SNR, Rayleigh fading channels. For the first time, our method used the concept of consensus to improve the overall performance of the whole cluster in a cooperative fashion. The diversity gained from the number of nodes enables reliable communications. The simulation shows that this diversity gives more reliability as the cluster size increases. We believe that the performance can be further improved by using error correction codes and as far as the data rate, higher order modulations can provide higher bit rates for the system.

ACKNOWLEDGMENT

We greatly acknowledge the support of CPS Energy, the Texas Sustainable Energy Research Institute (TSERI), and SECO-DOE under grant No. RFA RE-AG1-2010, CS1094 and CS1038. We also acknowledge the support of our colleagues in ECE within the College of Engineering at the University of Texas at San Antonio.

REFERENCES

- [1] R. Olfati-Saber, J. Alex Fax, and Richard M. Murray, "Consensus and Cooperation in Networked Multi-Agent Systems", Proceedings of the IEEE Vol., No. 1, January 2007
- [2] A.L. Barabasi, R. Albert, "Emergence of scaling in random networks", Science, Vol. 286, pp. 509-512, 1999.
- [3] G. Grimmett and D. Stirzaker, "probability and Random Processes" Oxford University Press, 3rd edition 2001
- [4] R. O. Saber and R. M. Murray, "Consensus protocols for networks of dynamic agents", in Proc. 2003 Am. Control Conf., 2003, pp. 951-956. Consensus in Scale-free Networks
- [5] Xin Biao Lu, Jin Qing Fang, "Consensus in Scale-free Networks", IEEE Conference, 2006
- [6] R. Olfati-Saber, Richard M. Murray, "Consensus Problems in Networks of Agents With Switching Topology and Time-Delays", IEEE transactions on automatic control, vol. 49, no. 9, september 2004
- [7] J. Yu, L. Wang, "Group Consensus of Multi-agent Systems with Undirected Communication Graphs", Proceedings of the 7th Asian Control Conference, Hong Kong, China, August 27-29, 2009
- [8] A. Barrat, M. Barthélemy, and A. Vespignani, "Dynamical Processes on Complex Network", New York, Cambridge University Press, 2008

- [9] H. Wang, Y. Guo, Consensus "On Scale-free Network", American Control Conference Westin Seattle Hotel, Seattle, Washington, USA June 11-13, 2008
- [10] F. Tan, D. Liu, and X. Guan, "Consensus Value of Multi-agent Networked Systems with Time-delay", IEEE Conference, 2009
- [11] D. Ustebay, B. Oreshkin, and M. Coates, "Rates of Convergence for Greedy Gossip with Eavesdropping", Forty-Sixth Annual Allerton Conference Allerton House, UIUC, Illinois, USA September 23-26, 2008
- [12] S. Boyd, A. Ghosh, "Randomized Gossip Algorithms", IEEE transactions on information theory, vol. 52, no. 6, June 2006
- [13] P. L. Krapivsky, S. Redner, "Finiteness and fluctuations in growing networks", J. Phys. A, Vol. 35, pp. 9517-9534, 2002.
- [14] J. A. Fax and R. M. Murray, "Information flow and cooperative control of vehicle formations", IEEE Trans. Autom. Control, vol. 49, no. 9, pp. 1465-1476, Sep. 2004.
- [15] S. Schwandt, G. Matz, "A Practical Forwarding Scheme for Wireless Relay Channels Based on the Quantization of Log-Likelihood Ratios"
- [16] M. Saedy, B. Kelley, "Consensus-Based Cognitive Radio Assisted Cooperative Communications", ACM Int. Conf. 2011. USA.
- [17] Mahdy Saedy and Brian Kelley, "Consensus-Based Cooperative Communications for Clustered Mobile Wireless Sensor-Actuator Networks", International Journal of Mobile Network Design and Innovation. 2011.
- [18] Mahdy Saedy and Brian Kelley, "Distributed Distributed Cooperative Synchronization for Large-Scale 4G Wireless Sensor Networks Using CAZAC Sequences", pages 56-71, DOI: 10.4018/jitn.2012010104, International Journal of Mobile Network Design and Innovation. 2012.
- [19] Third Generation Partnership Project, www.3gpp.org, 3GPP TS 36.211.
- [20] Amitava Ghosh, Rapeepat Ratasuk, Brian Classon, Vijay Nangia, Robert Love, Dale Schwent, David Wilson, "Uplink Control Channel Design for 3GPP LTE", 18th Annual IEEE International Symposium on Personal, Indoor and Mobile Radio Communications, September 2007.



Mahdy Saedy (Student member of IEEE), Ph.D. Candidate, received his B.Sc. in Electrical Engineering from Ferdowsi University of Mashhad, Iran in 1999. He attended IUST (Iran University of Science and Technology) in Tehran, Iran to

complete his M.Sc. in Electrical Engineering and Communications and graduated in 2002. During his Masters' he worked as GSM Engineer for two years. He then joined MicroModje Industries Company, which was active in telecom projects as Wireless Communications Technical Manager. With his experience in telecom, he joined Ericsson Company as Technical Solution Manager mainly for 2G and 3G projects. In 2009, he attended The University of Texas at San Antonio for Ph.D. degree and has been active in research since then. His focus is 4G/LTE, Cooperative and Cognitive Communications, Security and Complex Networks. He is the board member of IEEE Communication Society/Signal processing -Central Texas Section, Austin Chapter. He was the winner of Who's Who Award among American Universities and Colleges in 2010.



Brian Kelley (Senior Member of IEEE) is an Assistant Professor with the University of Texas at San Antonio's (UTSA's) Department of Electrical and Computer Engineering (ECE). Dr. Kelley received his BSEE

from Cornell University's College of Electrical Engineering in Ithaca NY. He received his MSEE and PhDEE from Georgia Tech's ECE Department where he was an Office of Naval Research Fellow and a Georgia Tech Presidential Fellow. After R&D efforts with Motorola and Freescale, Dr. Kelley joined the faculty of the University of Texas at San Antonio as an Assistant Professor in Communications. At UT-San Antonio, he has taught numerous graduate courses in communications. Dr. Kelley's current research interests include Software Define Radio, smart grid information systems, 4G Cellular Communications, and sensor networks. He is a Senior Member of the IEEE, Chair of the San Antonio IEEE Communication and Signal Processing Chapter, and Associate Editor of Computers & Electrical Engineering, Elsevier, 2008, Associate Editor of the IEEE Systems Journal, and a member of the Texas Sustainable Energy Research Institute (TSERI). He has numerous publications, is a holder of 10 US patents and is a member of Tau Beta Pi and Eta Kappa Nu.



One UTSA Circle - San Antonio, TX 78249 - 210-458-7970